Abstract

Measuring the Geometry and Topology of Non-Hermitian Systems

Chitres Guria

2026

In this thesis, we study qualitatively new non-Hermitian phenomena that occur when the parameters of coupled harmonic oscillators are tuned (like mass, spring constant, and damping), while monitoring their motion. We consider both forms of tuning: static and real time. These phenomena are demonstrated experimentally using the membrane-in-the-middle (MIM) optomechanical system.

We first describe how tuning the parameters statically along a closed loop results in braiding of the system's eigenvalues, and the manner in which they braid determined by how the loop encircles the system's double degeneracies. We find that for a system of $N > 2$ coupled harmonic oscillators, the topology of the degeneracies and the braids have a distinct increase in complexity, compared to the widely studied $N = 2$ case. In particular for $N > 2$, the degeneracies are knotted, and the braids are non-Abelian. We demonstrate these features experimentally for an $N = 3$ system.

We then study the interplay of Berry phase with non-Hermiticity. For non-degenerate non-Hermitian systems, it is predicted that the Berry phase is a complex number, whose imaginary part represents a "geometric" loss/gain unique to non-Hermitian systems. We demonstrate these features experimentally in the real time evolution of a lossy two-mode system. Furthermore, we show that the interplay of the system's intrinsic loss and the geometric gain allows us to demonstrate a novel form of amplification.

Finally, for degenerate non-Hermitian systems, the Berry phase is predicted to be a real discrete-valued topological property of the control loop. The distinctive nature of this Berry phase is shown to be solely due to the non-trivial topology of the degeneracies. The adiabatic evolution that gives rise to this Berry phase is also responsible for generating novel dynamical phases. We experimentally demonstrate these predictions by tuning and monitoring a lossy doubly-degenerate system in real time. Complementary to the previous case, the novel dynamical phase, combined with the degenerate system's loss, allows us to demonstrate yet another novel form of amplification.

Measuring the Geometry and Topology of Non-Hermitian Systems

A Dissertation
Presented to the Faculty of the Graduate School
of
Yale University
in Candidacy for the Degree of
Doctor of Philosophy

by
Chitres Guria

Dissertation Director: Jack G. E. Harris

May 2026

Contents

List of Figures . . . vi
List of Tables . . . xi
Acknowledgments . . . xv

1 Introduction 1
1.1 Context of Non-Hermitian physics . . . 2
1.1.1 Brief historical account . . . 2
1.1.2 Parallel development of $\mathcal{PT}$-symmetric physics . . . 3
1.1.3 Current state-of-the-field . . . 4
1.2 Motivation . . . 4
1.3 Thesis outline . . . 6

2 Theoretical background 9
2.1 Topological structure of non-Hermitian eigenvalue spectrum . . . 10
2.1.1 Control loops and spectral flow . . . 10
2.1.2 Illustrating N-mode spectral flow . . . 14
2.1.3 Further remarks . . . 20
2.2 Non-Hermitian geometric phase . . . 28
2.2.1 Control loops and geometric phases . . . 28
2.2.2 Adiabatic theorem . . . 29
2.2.3 Illustrating the non-degenerate non-Hermitian geometric phase . . . 35
2.2.4 Illustrating the degenerate non-Hermitian geometric phase . . . 45
2.3 Cavity Optomechanical platform for Non-Hermitian physics . . . 62
2.3.1 Single mode optomechanics . . . 62
2.3.2 Two-mode optomechanics . . . 67
2.3.3 Three-mode optomechanics . . . 73

3 Knotted non-Hermitian degeneracies and non-commuting braids 78
3.1 Experimental apparatus, control and readout . . . 80
3.1.1 Experimental setup . . . 80

3.1.2 Control parameters . . . 80
3.1.3 Measurement of eigenspectra . . . 82
3.2 Locating EP degeneracies . . . 83
3.2.1 Locating the EP_3 degeneracy . . . 83
3.2.2 Locating the EP_2 degeneracies . . . 89
3.2.3 Tracing the knotted EP_2 degeneracies . . . 92
3.3 Eigenvalue braids . . . 97
3.3.1 Characterizing the braid group B_3 . . . 97

4 A new membrane-in-the-middle platform 105
4.1 MIM design and construction . . . 106
4.1.1 Design considerations . . . 106
4.1.2 A new room-temperature MIM system . . . 110
4.2 Fabry-Perot cavity . . . 114
4.2.1 Design and construction . . . 114
4.2.2 Mode-matching and optical alignment . . . 116
4.2.3 Bare cavity characterization . . . 119
4.3 Membrane . . . 127
4.3.1 Membrane characterization . . . 128
4.4 Membrane in the middle of a Fabry-Perot cavity . . . 134
4.4.1 Integrating the membrane with the Fabry-Perot cavity . . . 134
4.4.2 MIM characterization: Part I . . . 138
4.4.3 MIM characterization: Part II . . . 142
4.5 Benchmarking a tunable non-Hermitian system . . . 150
4.5.1 Characterizing Floquet-coupled membrane modes: Part I . . . 150
4.5.2 Characterizing Floquet-coupled membrane modes: Part II . . . 154
4.5.3 Introducing the blue-detuned control tone . . . 157
4.5.4 Evaluating system stability near an EP_2 . . . 161
4.6 System control and stabilization . . . 163
4.6.1 Optical and electrical setups . . . 163
4.6.2 Feedback and stabilization . . . 169
4.6.3 Evaluating system stability via its parameters . . . 172

5 Complex geometric phase of non-Hermitian systems 177
5.1 Measuring ϕ_B . . . 178
5.2 Geometric character of ϕ_B . . . 185
5.2.1 Part I: Varying the manner of control path traversal . . . 185
5.2.2 Part II: Varying the shape of the control path . . . 187
5.2.3 Part III: Multiple repetitions of a control path . . . 192
5.3 Imaginary geometric phase for open control paths . . . 195

5.4 Further insights into non-Hermitian adiabatic evolution . . . 197

6 A geometric amplifier 199
6.1 Defining SSGG . . . 200
6.2 Identifying control loops that produce SSGG . . . 203
6.2.1 SSGG with "simple" control loops . . . 204
6.2.2 SSGG with "non-simple" control loops . . . 215
6.3 Measuring SSGG . . . 217
6.3.1 Control loop family I . . . 217
6.3.2 Control loop family II . . . 220
6.4 Further remarks on SSGG . . . 224
6.4.1 Comparison to a parametric amplifier . . . 224
6.4.2 Additional analysis and views of SSGG data . . . 224
6.4.3 Driving a mechanical oscillator into nonlinearity using SSGG . . . 228

7 Topological and discrete geometric phase of non-Hermitian degeneracies 232
7.1 Measuring $\phi_{B,\mathbf{deg}}$ . . . 233
7.1.1 Locating $\boldsymbol{EP_2}$ degeneracy . . . 233
7.1.2 Constructing $\boldsymbol{\mathcal{C}_{\mathbf{deg}}}$ . . . 236
7.1.3 Measurement of real time dynamics in $\boldsymbol{\mathcal{EP}_2}$ . . . 238
7.1.4 Measuring $\phi_{\mathbf{deg}}$ and isolating $\phi_{B,\mathbf{deg}}$ . . . 247
7.2 Topological and geometric character of $\phi_{B,\mathbf{deg}}$ . . . 251
7.2.1 Part I: Homotopically distinct $\boldsymbol{\mathcal{C}_{\mathbf{deg}}}$ . . . 251
7.2.2 Part II: Varying the shape of $\boldsymbol{\mathcal{C}_{\mathbf{deg}}}$ . . . 254
7.2.3 Part III: Varying the manner of $\boldsymbol{\mathcal{C}_{\mathbf{deg}}}$ traversal . . . 268
7.3 Robustness of dynamics in $\boldsymbol{\mathcal{EP}_2}$ . . . 272
7.3.1 Robustness of $\phi_{B,\mathbf{deg}}$ measurements . . . 272
7.3.2 Stepping off $\boldsymbol{\mathcal{EP}_2}$ . . . 274
7.4 A novel $\sqrt{\boldsymbol{T}}$-dynamical phase and a $\sqrt{\boldsymbol{T}}$-amplifier . . . 283
7.4.1 The $\sqrt{\boldsymbol{T}}$-dynamical phase . . . 283
7.4.2 Defining SS$\sqrt{\boldsymbol{T}}$G . . . 287
7.4.3 Tuning up a $\sqrt{\boldsymbol{T}}$-amplifier . . . 291
7.4.4 Measuring SS$\sqrt{\boldsymbol{T}}$G . . . 293

8 Conclusion and outlook 296
8.1 Possible future directions . . . 297

Appendix 305

A Methods for Chapter 2 306

A.1 Numerical simulations of N-mode spectral flow . . . 306
A.2 Relation to studies of non-Hermitian band structure . . . 310
A.3 Further remarks on non-Hermitian geometric phase . . . 311
A.4 Mapping the control loops in $\mathcal{EP}_2$ to $\mathbb{R}\mathbf{P}^3$ . . . 320

B Methods for Chapter 3 **324**
B.1 Extracting the spectrum from mechanical susceptibility . . . 324
B.2 Projections of the hypersurface $\mathcal{S}$ . . . 328
B.3 Description of 2D control spaces used in the case study . . . 330
B.4 Rastering the hypersurface $\mathcal{S}$ . . . 331
B.5 Data analysis I: 2D sheets . . . 332
B.6 Data analysis II: eigenvalue braids . . . 335
B.7 Data fitting and theoretical calculations . . . 337
B.8 System parameters . . . 340

C Methods for Chapter 4 **343**
C.1 Mode-matching routine . . . 343
C.2 Membrane modes . . . 345
C.3 Non-tunability of (2,5) and (3,5) membrane modes . . . 349
C.4 Fits to optomechanical model . . . 351
C.5 Instrument calibrations . . . 355

D Methods for Chapter 5 **359**
D.1 Protocol for measuring $\boldsymbol{\beta}(T)$ . . . 359
D.2 Extracting state vector from ringdown measurements . . . 364
D.3 Measuring the propagator matrix $U(T)$ . . . 368
D.4 Estimating the asymptote of $\boldsymbol{\beta}(T)$ . . . 370
D.5 System parameters . . . 374

E Methods for Chapter 5 **376**
E.1 Additional views of SSGG data . . . 376

F Methods for Chapter 7 **385**
F.1 Initial state preparation . . . 385
F.2 On Jordan and Schur decompositions . . . 399
F.3 Data acquisition, processing and fitting . . . 408
F.4 Estimating the asymptote of $\boldsymbol{\beta}_{\mathrm{deg}}(T)$ . . . 418
F.5 Additional views of SS$\sqrt{T}$G data . . . 420
F.6 System parameters . . . 422

Bibliography **424**

List of Figures

2.1 Spectral flow: $\boldsymbol{N = 2}$ . . . 15
2.2 Degenerate subspace: $\boldsymbol{N = 3}$ . . . 17
2.3 Spectral flow: $\boldsymbol{N = 3}$ - part I . . . 18
2.4 Spectral flow: $\boldsymbol{N = 3}$ - part II . . . 19
2.5 Spectral flow: $\boldsymbol{N = 3}$ - part III . . . 26
2.6 Control loops and real time evolution of state vector . . . 38
2.7 Control loops in $\boldsymbol{\mathcal{EP}_2}$ . . . 54
2.8 Real time evolution in $\boldsymbol{\mathcal{EP}_2}$ . . . 58
2.9 Optomechanical control via DBA . . . 65
2.10 Floquet coupling schematic . . . 70

3.1 Experimental setup, control and readout . . . 81
3.2 Preliminary search for $\boldsymbol{EP_3}$ . . . 84
3.3 Locating $\boldsymbol{EP_3}$ - part I . . . 86
3.4 Locating $\boldsymbol{EP_3}$ - part II . . . 87
3.5 Locating $\boldsymbol{EP_3}$ - part III . . . 88
3.6 The locations of the sixty-one 2D sheets within the hypersurface $\boldsymbol{\mathcal{S}}$ . . . 90
3.7 Locating $\boldsymbol{EP_2}$ points on the hypersurface $\boldsymbol{\mathcal{S}}$ . . . 91
3.8 The measured knot of $\boldsymbol{EP_2}$ via four different indicators - part I . . . 94
3.9 The measured knot of $\boldsymbol{EP_2}$ via four different indicators - part II . . . 95
3.10 The measured knot of $\boldsymbol{EP_2}$ via four different indicators - part III . . . 96
3.11 Measurements of eigenvalue braids - part I . . . 98
3.12 Measurements of eigenvalue braids - part II . . . 99
3.13 Measurements of eigenvalue braids - part III . . . 100
3.14 Equivalent eigenvalue braids from "different" loops . . . 101
3.15 Different braids by encircling the "same" $\boldsymbol{EP_2}$ points . . . 103
3.16 Measuring the basepoint dependence of homotopy equivalence . . . 104

4.1 Mechanical design of the room-temperature MIM system . . . 111
4.2 Vacuum chamber . . . 113

4.3 Cavity design . . . 115
4.4 Mode-matching . . . 117
4.5 Bare cavity characterization - part I . . . 121
4.6 Bare cavity characterization - part II . . . 125
4.7 The membrane, its mounting and its modes . . . 128
4.8 Characterization of membrane modes . . . 130
4.9 Characterizing the degeneracy breaking of doublets . . . 133
4.10 MIM cavity design and membrane alignment . . . 135
4.11 Spectroscopy of MIM cavity . . . 139
4.12 Alternate views and analysis of MIM cavity spectroscopy . . . 141
4.13 DBA characterization . . . 143
4.14 Photothermal effect characterization . . . 147
4.15 Spectroscopy of Floquet-coupled (3,3) and (5,2) modes . . . 151
4.16 Spectroscopy of Floquet-coupled (3,3) and (5,3) modes . . . 152
4.17 Static eigenvalue braiding of Floquet-coupled (3,3) and (5,2) modes . . . 155
4.18 Real time dynamics of Floquet-coupled (3,3) and (5,2) modes . . . 156
4.19 Characterizing the blue-detuned control tone . . . 158
4.20 Spectroscopy near $\boldsymbol{EP_2}$ over time . . . 162
4.21 Optical and electrical setup I . . . 164
4.22 Optical and electrical setup II . . . 168
4.23 System and control parameters over time - part I . . . 174
4.24 System and control parameters over time - part II . . . 175
4.25 System and control parameters over time - part III . . . 176

5.1 Preparation of the initial state vector $\vec{\boldsymbol{c}}^{(a)}(\boldsymbol{0})$, and its evolution to $\vec{\boldsymbol{c}}^{(a)}(\boldsymbol{T})$ along a control loop . . . 179
5.2 Preparation of the initial state vector $\vec{\boldsymbol{c}}^{(b)}(\boldsymbol{0})$, and its evolution to $\vec{\boldsymbol{c}}^{(b)}(\boldsymbol{T})$ along a control loop . . . 180
5.3 Measurement of the propagator matrix $\boldsymbol{U}(\boldsymbol{T})$ . . . 181
5.4 Measurement of $\boldsymbol{\beta}(\boldsymbol{T})$ . . . 183
5.5 Geometric character of $\boldsymbol{\phi_B}$ - part I . . . 186
5.6 Geometric character of $\boldsymbol{\phi_B}$ - part IIA . . . 188
5.7 Geometric character of $\boldsymbol{\phi_B}$ - part IIB . . . 189
5.8 Geometric character of $\boldsymbol{\phi_B}$ - part IIC . . . 191
5.9 Geometric character of $\boldsymbol{\phi_B}$ - part III . . . 194
5.10 Imaginary geometric phase for open control paths . . . 196
5.11 Measurement and numerical simulation of $\boldsymbol{\beta_{ij}}(\boldsymbol{T})$ . . . 198

6.1 Conditions for achieving SSGG . . . 202
6.2 Range of "simple" control loops that result in SSGG - part I . . . 206
6.3 Range of "simple" control loops that result in SSGG - part II . . . 208

6.4 Range of "simple" control loops that result in SSGG - part III 210
6.5 Range of "simple" control loops that result in SSGG - part IV 212
6.6 Union of all "simple" control loop ranges that result in SSGG 214
6.7 Range of a class of "non-simple" control loops that result in SSGG . . . 216
6.8 Verifying conditions for achieving SSGG: for Control loop family I 218
6.9 SSGG for Control loop family I 219
6.10 Verifying conditions for achieving SSGG: for Control loop family II 222
6.11 SSGG for Control loop family II 223
6.12 Geometric phase of Control loops that produce SSGG - family I 225
6.13 Geometric phase of Control loops that produce SSGG - family II 226
6.14 Driving the system into non-linear regime using SSGG - part I 229
6.15 Driving the system into non-linear regime using SSGG - part II 230

7.1 Locating $\boldsymbol{EP_2}$ degeneracy via spectroscopy 234
7.2 Control loops in $\boldsymbol{\mathcal{EP}_2}$ 237
7.3 Protocol for real time dynamics measurements in $\boldsymbol{\mathcal{EP}_2}$ 239
7.4 Preparing and measuring the initial state vector $\vec{\boldsymbol{x}}(\boldsymbol{0})$, and its evolution to $\vec{\boldsymbol{x}}(\boldsymbol{T})$ along a control loop in $\boldsymbol{\mathcal{EP}_2}$: state vector component I 241
7.5 Preparing and measuring the initial state vector $\vec{\boldsymbol{x}}(\boldsymbol{0})$, and its evolution to $\vec{\boldsymbol{x}}(\boldsymbol{T})$ along a control loop in $\boldsymbol{\mathcal{EP}_2}$: state vector component II 242
7.6 Spectroscopy at $\boldsymbol{EP_2}$ 244
7.7 Measurement of real time dynamics in $\boldsymbol{\mathcal{EP}_2}$ - part I 246
7.8 Measurement of real time dynamics in $\boldsymbol{\mathcal{EP}_2}$ - part II 248
7.9 Topological character of $\phi_{B,\mathbf{deg}}$ - part IA 252
7.10 Topological character of $\phi_{B,\mathbf{deg}}$ - part IB 253
7.11 Topological character of $\phi_{B,\mathbf{deg}}$ - part IIA(i) 255
7.12 Topological character of $\phi_{B,\mathbf{deg}}$ - part IIA(ii) 256
7.13 Spectroscopically locating $\boldsymbol{EP_2}$ with a variety of $\angle\boldsymbol{R}$ 259
7.14 Topological character of $\phi_{B,\mathbf{deg}}$ - part IIB(i) 262
7.15 Topological character of $\phi_{B,\mathbf{deg}}$ - part IIB(ii) 263
7.16 Spectroscopically locating $\boldsymbol{EP_2}$ with arbitrary $\boldsymbol{R}$ 266
7.17 Topological character of $\phi_{B,\mathbf{deg}}$ - part IIC(i) 267
7.18 Topological character of $\phi_{B,\mathbf{deg}}$ - part IIC(ii) 267
7.19 Geometric character of $\phi_{B,\mathbf{deg}}$ 269
7.20 $\sqrt{\boldsymbol{T}}$ dynamical phase for distinct traversals of a $\boldsymbol{\mathcal{C}_{\mathbf{deg}}}$ 270
7.21 $\phi_{B,\mathbf{deg}}$ measured repeatably for over 40 hours 273
7.22 Stepping off $\boldsymbol{EP_2}$ 275
7.23 Measuring of real time dynamics off $\boldsymbol{\mathcal{EP}_2}$ - part I 278
7.24 Measuring of real time dynamics off $\boldsymbol{\mathcal{EP}_2}$ - part II 279
7.25 Analysis of real time dynamics off $\boldsymbol{\mathcal{EP}_2}$ 282

7.26 Conditions for achieving SS$\sqrt{\boldsymbol{T}}$G . . . 290
7.27 Setup for demonstrating SS$\sqrt{\boldsymbol{T}}$G . . . 292
7.28 Measuring SS$\sqrt{\boldsymbol{T}}$G . . . 294

8.1 A possible route to measure metric tensor for the non-Hermitian case . . 300
8.2 A possible route to measure eigenvectors . . . 301

A.1 Representing $\mathbb{R}\mathbf{P}^{\mathbf{2}}$ and $\mathbb{R}\mathbf{P}^{\mathbf{3}}$ . . . 321

B.1 Sheets that constitute the case study of 2D control spaces . . . 331
B.2 Assembling the control loops for Fig. 3.11 . . . 336
B.3 Characterizing the optomechanical coupling via DBA measurements . . . 341

C.1 Membrane modes - set I . . . 346
C.2 Membrane modes - set II . . . 347
C.3 Membrane modes - set III . . . 348
C.4 Non-tunability of (2,5) and (3,5) modes . . . 350
C.5 Fit to optomechanical model corresponding to Fig. 4.15 . . . 352
C.6 Fit to optomechanical model corresponding to Fig. 4.16 . . . 353
C.7 Fit to optomechanical model corresponding to Fig. 4.19 . . . 354
C.8 VOA calibration . . . 356
C.9 Control AOM calibration . . . 357

D.1 Complex-averaging for state vectors $\vec{\boldsymbol{c}}^{(a)}(\mathbf{0})$ and $\vec{\boldsymbol{c}}^{(a)}(\boldsymbol{T})$ . . . 362
D.2 Complex-averaging for state vectors $\vec{\boldsymbol{c}}^{(b)}(\mathbf{0})$ and $\vec{\boldsymbol{c}}^{(b)}(\boldsymbol{T})$ . . . 363
D.3 Examples of asymptote analysis of $\mathbf{Re}(\boldsymbol{\alpha}(\boldsymbol{T}))$ and $\boldsymbol{\beta}(\boldsymbol{T})$ . . . 371
D.4 Summary of all $\boldsymbol{\phi_B}$ measurements . . . 372

E.1 Preparation of the initial state vector $\vec{\boldsymbol{c}}^{(a)}(\mathbf{0})$, and its evolution to $\vec{\boldsymbol{c}}^{(a)}(\boldsymbol{T})$ along control loops that produce SSGG - family I, part I . . . 377
E.2 Evolution to state vector $\vec{\boldsymbol{c}}^{(a)}(\boldsymbol{T})$ along control loops that produce SSGG - family I, part II . . . 378
E.3 Evolution to state vector $\vec{\boldsymbol{c}}^{(a)}(\boldsymbol{T})$ along control loops that produce SSGG - family I, part III . . . 379
E.4 Evolution to state vector $\vec{\boldsymbol{c}}^{(a)}(\boldsymbol{T})$ along control loops that produce SSGG - family I, part IV . . . 380
E.5 Preparation of the initial state vector $\vec{\boldsymbol{c}}^{(a)}(\mathbf{0})$, and its evolution to $\vec{\boldsymbol{c}}^{(a)}(\boldsymbol{T})$ along control loops that produce SSGG - family II, part I . . . 381
E.6 Evolution to state vector $\vec{\boldsymbol{c}}^{(a)}(\boldsymbol{T})$ along control loops that produce SSGG - family II, part II . . . 382
E.7 Evolution to state vector $\vec{\boldsymbol{c}}^{(a)}(\boldsymbol{T})$ along control loops that produce SSGG - family II, part III . . . 383

E.8 Evolution to state vector $\vec{\boldsymbol{c}}^{(a)}(\boldsymbol{T})$ along control loops that produce SSGG - family II, part IV 384

F.1 Evaluating initial state preparation protocols - part I 388
F.2 Evaluating initial state preparation protocols - part II 390
F.3 Experimental verification of initial state preparation protocol II - part I . 395
F.4 Experimental verification of initial state preparation protocol II - part II . 396
F.5 Experimental verification of initial state preparation protocol II - part III . 397
F.6 Experimental verification of initial state preparation protocol II - part IV . 399
F.7 Complex averaging for the initial state vector $\vec{\boldsymbol{x}}(\boldsymbol{0})$, and its evolution to $\vec{\boldsymbol{x}}(\boldsymbol{T})$ along a control loop in $\boldsymbol{\mathcal{EP}_2}$: state vector component I 409
F.8 Complex averaging for the initial state vector $\vec{\boldsymbol{x}}(\boldsymbol{0})$, and its evolution to $\vec{\boldsymbol{x}}(\boldsymbol{T})$ along a control loop in $\boldsymbol{\mathcal{EP}_2}$: state vector component II 410
F.9 Complex averaging for spectroscopy at $\boldsymbol{EP_2}$ 411
F.10 Ringdown spectroscopy of $\boldsymbol{R_{\text{eff}}}$ 417
F.11 Tracking the phase of motion undergoing SS$\sqrt{\boldsymbol{T}}$G 421

List of Tables

2.1 Various spaces of a general complex traceless $\mathbf{2} \times \mathbf{2}$ matrix 24

3.1 Locating $\boldsymbol{EP_3}$ via minima of $\boldsymbol{d}$ measured in 2D sheets 85

4.1 Comparing simulated MIM systems with the previous generation 109
4.2 Summary of $\boldsymbol{\kappa}$ measurements 122
4.3 Fit parameters of DBA characterization 145
4.4 Fixed parameters of DBA characterization 145
4.5 Summary of spectroscopy measurements in Sec. 4.5 160
4.6 System and control parameters measured over $\sim$1 month 173

7.1 Spectroscopic properties of the first $\boldsymbol{EP_2}$ candidate 245
7.2 Coordinates of $\boldsymbol{EP_2}$ candidates accessed in Sec. 7.2.2.1 257
7.3 Spectroscopic properties of $\boldsymbol{EP_2}$ candidates accessed in Sec. 7.2.2.1 . . . 258
7.4 Coordinates of $\boldsymbol{EP_2}$ candidates accessed in Sec. 7.2.2.2 260
7.5 Spectroscopic properties of $\boldsymbol{EP_2}$ candidates accessed in Sec. 7.2.2.2 . . . 261
7.6 Coordinates of $\boldsymbol{EP_2}$ candidates accessed in Sec. 7.2.2.3 264
7.7 Spectroscopic properties of $\boldsymbol{EP_2}$ candidates accessed in Sec. 7.2.2.3 . . . 265

B.1 System parameters 342

C.1 DBA characterization of (2,5) and (3,5) modes 351

D.1 System parameters 375

F.1 System parameters 423

Acknowledgments

This is perhaps the most important section of my thesis. The work described in this thesis would not have been possible without the contributions of many people, and I would like to acknowledge them here. From the outset, it is impossible to acknowledge every single person's contribution, but I will try!

The person who is the most instrumental to this endeavor is Jack G. E. Harris, my thesis advisor. It all began with you telling me "Here are four independent ways we measured the motional sideband asymmetry of a mechanical mode ... ..."[1]. I was hooked instantly, as this was kind of rigor I had imagined, then. Through all these years, I have learned many valuable lessons from you, both physics and otherwise. At the end of it, I have come a full circle in appreciating your qualities as a physicist, but have realized something even more important - your qualities as a human being. I thank you for everything you have provided me, and for being an inspiration.

The next person who is as instrumental is Yogesh S.S. Patil. There could be moments in life when you hit a jackpot, and it was mine when I joined forces with you. Over all these years, you have a been a mentor, a friend, and another figure of inspiration. Sensei! thank you for all you have done for me, and for the Jack Harris Lab.

Talking about hitting jackpots, I hit it again when I got the chance to work with Judith Höller. To quantify someone's contribution is not straightforward, but here is an attempt: Your degenerate space Berry phase paper (your Ph.D. thesis) is the most (the second most) cited document in my thesis - thirty-nine (thirty-eight) times, and miles

[1]It was May 2018, and I was yet to embark on this journey with you.

ahead of anything else. I can only wish to continue collaborating with you, for as long as I do physics, and honestly, it does not matter what physics we do!

The majority of the work in this thesis was done with Justin R. Lane. Together, we built the new MIM system from scratch, and made it all happen! You imbued me with a disciplined and a methodical approach to our work - like a zen. In parallel, you also introduced me the other world of microwaves, qubits and their friends. I thank you for all the guidance and wisdom you provided, on all occasions.

To be working on the MIM experiment, at its birthplace is something special. I would like thank the past and the present Jack Harris lab members for their contributions and support throughout: Benjamin M. Zwickl, William E. Shanks, Jeff D. Thompson, Jack C. Sankey, Andrew M. Jayich, Nathan Flowers-Jacobs, Mitchell J. (Woody) Underwood, David R. Mason, Anya D. Kashkanova, Alexey Shkarin, Charles D. Brown, Luyao Jiang, Nenad Kralj, Sean Frazier, Parker A. Henry, Yiqi Wang, Jiaxin (Lucy) Yu, Yiming Zhang, Mehmet Tuna Uysal, Giovanna Truong, Juan Recaoro, Jinuk Kim, Ingrid Slattery, Akshai J. Pillai, Tongjun Liu, and Toni D. Montalvo, Theophilus Human, Lijie Yin, Anna-Lydia Vieli, Yilin Li, Igor Brandão Cavalcanti Moreira, Yinchen Hao, Gaurav Nirala, Yijun Zhang, Erin McGee.

I would like to thank our collaborators: Prof. Nicholas Read, Prof. Ramy El-Ganainy, Prof. Sahin K. Ozdemir, Prof. Qi Zhong, Prof. Kater Murch, Prof. Hugo Ribeiro, and Vishnuteja R. Chavva, and my committee members: Prof. Nicholas Read, Prof. Peter T. Rakich, Prof. Konrad W. Lehnert and Prof. Kater Murch. Over these years, I have had many insightful discussions with Prof. Charles D. Brown, Prof. John D. Teufel, Prof. Uroš Delić, Prof. Aashish Clerk, Prof. Florian Marquardt, Prof. Jakob Reichel, Prof. Mark I. Dykman, Prof. John P. Davis, Prof. Konrad W. Lehnert, Prof. Kater Murch, Prof. David C. Moore, Prof. Li Ge, Prof. David DeMille, Cedric C. Wilson, Shankar Ganesh, Thomas W. Penny, Aaron Markowitz, Varun Jorapur, Ako Jamil, Gabriel T. Assumpcao, Qian Wang, Jiaxiang Wang, Benjamin Seigel, Zhen Han, Yu-Han Tseng, Kavya Sahay, Andrew Neely, and for that I express my sincere gratitude. I would also like to thank the Yale physics department, especially: Sidney B. Cahn, Daphne O. Klemme, Francisco Lopez, Stacey Watts, and Rona Ramos, the Yale machine shop and its members: Vincent

Bernardo, Craig Miller and David Johnson, for the continued support. The work described here would be impossible without the funding agencies via: AFOSR FA9550-21-1-0202 (MURI), AFOSR FA9550-15-1-0270, as well as the Vannevar Bush Faculty Fellowship N00014-20-1-2628.

Before starting this journey, I was a very fortunate undergrad with several research opportunities. For that I express my gratitude to my undergrad advisor Prof. Saikat Ghosh, as well as the Sandoghdar division in Max Planck Institute for the Science of Light, Erlangen and its members: Prof. Vahid Sandoghdar, Prof. Stephan Götzinger, Prof. Daqing Wang, Hrishikesh Kelkar, André Pscherer, Jan Renger, and Tobias Utikal.

Outside of the lab, I would like to thank the New Haven Ultimate (frisbee) group, the New Haven Bicycling Club (NHBC) and the Yale Cycling Team for keeping me sane, rejuvenating me to go back to the lab, and trying once more. Thanks also to the people at Good Nature market for keeping open and feeding me at unreasonable hours.

Finally, it is your turn now: Mum, Dad and Pengfei. The three of you have seen it all, the good but also the difficult. You have been perennially supportive, extremely patient and equal parts tolerant. I cannot thank you enough. However, if this goes through, the three of you will have a second Ph.D. - this is as much yours as it is mine.

For Dada

Chapter 1

Introduction

A linear dynamical system of coupled harmonic oscillators is one the most ubiquitous concepts in physical sciences. It provides a robust mathematical description for a wide range of phenomena - from simple oscillating pendulum to gravitational waves, vibrations of a musical instrument to vibrations of atoms in a typical solid and so on.

Formally, a linear dynamical system is governed by

$$\boxed{\frac{d\boldsymbol{x}}{dt} = -iH\boldsymbol{x}} \tag{1.1}$$

where $\boldsymbol{x}$ is an N-dimensional vector specifying the state of the system and H is an $N \times N$ matrix that specifies the time evolution of the system, and N is taken to be finite.

Eq. (1.1) is a famous equation. It is so famous, that it does not have a name! In fact, it has many names and incarnations. It is Hamilton's equation for N masses coupled to each other by springs [1], Maxwell's laws for N modes of the electromagnetic field [2], Schrödinger equation for an isolated (closed) quantum system with N levels [3], or Lindblad equation for an open quantum system whose density matrix has N components [4]. It is also seen in a range of fields such as control theory [5], predator-prey dynamics [6], stock markets [7] and finances [8].

The ubiquity of Eq. (1.1) is complemented by the simplicity of its solution. If H is a

constant, the solutions can be written via its eigensystem. The eigensystem consists of a multiset[1] $\boldsymbol{\lambda}$, the N eigenvalues of H (they are the roots of the characteristic polynomial of H [9]), and a set $\mathbf{u}$ of N eigenvectors or generalized eigenvectors of H. When H is time varying, exact or approximate solutions can be constructed out of $\boldsymbol{\lambda}$ and $\mathbf{u}$, giving rise to important concepts such as the adiabatic theorem [10, 11], Berry phase [12, 13] and the Landau-Zener-Stückelberg-Majorana dynamics [14–18].

However, it is the form of H that determines broad qualitative and quantitative features $\boldsymbol{\lambda}$ and $\boldsymbol{x}$ via $\mathbf{v}$. It is commonplace to study Eq. (1.1) when H is a Hermitian matrix, i.e., $H^\dagger = H$ where $(^\dagger)$ denotes conjugate transpose. For example: Quantum mechanics of a closed N level system. In such a case, the system undergoes a unitary evolution and as such it is lossless (or gainless), its N eigenvalues are all purely real, and its N eigenvectors form an orthonormal basis, which spans the Hilbert space containing $\boldsymbol{x}$ [3].

1.1 Context of Non-Hermitian physics

The physical systems we encounter in our daily life are generically subject to loss or gain and can be non-reciprocal. For example: a system of N coupled and damped classical harmonic oscillators. For such open systems, their H can be any arbitrary complex matrix with complex eigenvalues, non-orthogonal eigenvectors (or generalized eigenvectors), and the system evolves non-unitarily, i.e., the system's state can grow or decay in amplitude. Such open systems are generally studied under the domain of non-Hermitian physics.

1.1.1 Brief historical account

In its early days (before 1980), non-Hermitian physics was considered as a simple perturbative extension of its Hermitian counterpart, and useful approximations for open quantum systems were derived [19, 20]. However, in the intervening years, non-Hermitian phenomena were found to be dramatically distinct and with no analogues in Hermitian systems. These early observations include the possibility of complex degeneracies in the eigenvalue

[1] A multiset, also known as a bag, is a set of elements where repetition is allowed.

spectrum, termed as "exceptional points (EP)" where H is no longer diagonalizable[1]. In the neighborhood of an EP, the eigenspectrum has a branch-point behavior as a function of the system's parameters and as such, encircling an EP permutes the eigensystem [21–26].

In addition, the real time dynamical behavior of non-Hermitian systems was found to be in stark contrast to their Hermitian counterparts. For example, the usual adiabatic theorem was no longer applicable to non-Hermitian systems, and the non-Hermitian adiabatic theorem was formulated [11, 27]. The possibility of encircling EP degeneracies in real time was predicted to inherit some of the topological character of the static system [23, 25], with additional features such as non-reciprocity in its dependence on the initial conditions of the system, the sense in which the EP is encircled, and the duration of encircling [28–30]. It is important to note that encircling EP degeneracies in real time, by default falls outside the purview of the non-Hermitian adiabatic theorem, and rather relies on a newer notion of quasi-adiabaticity [30]. These quasi-adiabatic and semi-topological features were observed for the first time in 2016, by two breakthrough experiments detailed in Refs. [31, 32], respectively.

1.1.2 Parallel development of $\mathcal{PT}$-symmetric physics

In 1998, $\mathcal{PT}$-symmetric quantum mechanics [33] was put forward as an alternative to the conventional one wherein the requirement of a Hermitian H is relaxed, and instead an H that is symmetric under inversion of space (parity, $\mathcal{P}$) and time ($\mathcal{T}$) is required. Formally, H and the $\mathcal{PT}$ operator commute, i.e., $[\mathcal{PT}, H] = 0$. As a result, a $\mathcal{PT}$-symmetric system can be governed by a non-Hermitian H with real eigenvalues and unitary evolution. Fast forward to 2007-2010, and the field saw a breakthrough. It was the realization that $\mathcal{PT}$-symmetric quantum mechanics can be mapped onto classical wave propagation in optical systems. As an equally important consequence of this mapping, work in the optical domain expanded upon $\mathcal{PT}$-symmetric physics by systematically breaking the $\mathcal{PT}$ symmetry as a function of system's parameters [34–37], and the points in parameter space where this transition occurs are precisely EP degeneracies. This breakthrough can

[1]The term exceptional points (EP) was coined originally by T. Kato in 1960s, in the first edition of Ref. [21].

be considered as the inflection point for $\mathcal{PT}$-symmetric physics and to a certain extent, for the field of non-Hermitian physics.

1.1.3 Current state-of-the-field

In the years following the above breakthroughs, a huge body of work has proliferated in complementary directions [38]:

(a) Understanding uniquely non-Hermitian phenomena, such as the appearance of topology in the system's eigenvalue spectrum [39–45]; the often counterintuitive interplay of loss and gain [46–52]; and adapting Hermitian condensed matter models to the non-Hermitian domain [53, 54], for e.g. the bulk-boundary correspondence and the non-Hermitian skin-effect [55–60].

(b) Building novel useful devices and developing novel and robust control and sensing capabilities using uniquely non-Hermitian effects [32, 51, 52, 61–69].

In addition, the above activities encompass a wide variety of physical settings: cold atoms [70, 71], optics [51, 52], microwaves [72, 73], electronics [64, 74], acoustics [75], optomechanics [32, 61], and qubits [76, 77].

1.2 Motivation

The author's contribution to the work described in this thesis began in November, 2019. By then, the membrane-in-the-middle (MIM) optomechanical platform [78–81] was an established front runner in the field of non-Hermitian physics, and had produced some of the above mentioned breakthroughs [32, 61]. The motivation behind the work described in this thesis is three-fold.

(i) Despite a large number of results in the field of non-Hermitian physics, some basic aspects lacked a clear and complete understanding. One of them is the relation between a system's parameters and its eigenvalue spectrum, a phenomenon known as spectral flow. Results on this front had been restricted to systems with $N = 2$ modes [32, 61, 76] which cannot generalize to arbitrary N. There were a few results

on higher N focused on systems either with special symmetries, or tuning them in an incomplete parameter space, or a combination of both [82–86].

(ii) Another area that remained less clear was the manifestation of Geometric phase in the real time dynamics of non-Hermitian system, and as such, they are expected to be qualitatively distinct from their Hermitian counterparts [87–89]. Adiabatic evolution is a cornerstone of Hermitian dynamics, and a paradigmatic setting in which Geometric phases [12] are studied. The large body of work mentioned above had explored quasi-adiabatic evolution, and geometric phases was beyond its domain. Strict non-Hermitian adiabatic evolution and the non-Hermitian adiabatic theorem [11, 27] were yet to be demonstrated.

(iii) A further impetus to this work was to explore purely topological real time evolution that is generated by the underlying topology of non-Hermitian system. Briefly, the static spectrum of the non-Hermitian systems have topological structures such as braids, knots, links, balls, and so on. Can these structures be put to use for real time evolution? An important insight is that such topological operations may be robust against fluctuations, which in turn has had a profound impact on many Hermitian physical settings [90]. Subsequently, theoretical work in Refs. [88, 89] indeed predicted such a case for degenerate non-Hermitian systems.

In the picture of a system of coupled harmonic oscillators, the above ideas represent complementary aspects of studying Eq. (1.1), and sets stage for the rest of this thesis. In particular, sometimes we will be interested in fully parameterizing the matrix H, i.e., all of its elements, and studying the real time evolution it generates, while on other occasions we will be interested only in the eigenspectrum of H, i.e., parameterized by the coefficients of the characteristic polynomial of H.

The goal of this thesis is to experimentally study each of the three ideas mentioned above. We will utilize the MIM platform to study a system of $N = 2$ or 3 coupled Harmonic oscillators whose parameters can be tuned statically or in real time, and measure the system's motion. Below we detail the specific contents of this thesis.

1.3 Thesis outline

The contents of this thesis are organized as follows:

Chapter 2

This chapter provides the theoretical description of the uniquely non-Hermitian effects that we wish to study, and also models the optomechanical system that is deployed for experimentally investigating these effects. The chapter is divided into three parts.

Part I

This part (Sec. 2.1) describes spectral flow in a system of N coupled oscillators. The discussion is based on our previously published work in Refs.[43, 91]. Additional technical details for this part are in Appendices A.1 and A.2.

Part II

This part (Sec. 2.2) describes the non-Hermitian adiabatic theorem and the corresponding geometric phase when a non-Hermitian system is adiabatically evolved. Specifically, we describe two cases: **(i)** when the system is non-degenerate throughout the evolution, and **(ii)** when the system is degenerate throughout the evolution. Parts of this discussion are based on a manuscript that has been submitted for publication [92], while others are adapted from Refs.[88, 89]. Additional technical details for this part are in Appendices A.3 and A.4.

Part III

The final part of this chapter (Sec. 2.3) details the optomechanical model that governs the MIM platform.

Chapter 3

This chapter provides an experimental demonstration of spectral flow of an $N = 3$ coupled oscillator system based on a pre-existing MIM platform [93, 94], and is adapted

from our work in Ref. [43]. This demonstration is then utilized to clarify several surprising past results regarding eigenvalue permutation when viewed from a various perspectives, and is adapted from our work in Ref. [91]. Additional technical details for this chapter are in Appendix B.

Chapter 4

This chapter details the construction and operation of a new MIM platform that is tailored for studying non-Hermitian physics of a few coupled oscillator systems whose parameters can be tuned, both statically and in real time. Additional technical details for this chapter are in Appendix C.

Chapter 5

This chapter provides an experimental demonstration of the complex geometric phase of a non-degenerate $N = 2$ mode non-Hermitian system that is tuned adiabatically, and is based on the new MIM platform described in Chapter 4. Parts of this chapter are adapted from Ref. [92]. Additional technical details for this chapter are in Appendix D.

Chapter 6

In this chapter, we employ the geometric gain obtained from the complex geometric phase of non-Hermitian systems to illustrate a counterintuitive result: A collection of lossy oscillators under "slow" modulation can produce gain via the geometric gain, and thereby a novel form of amplification. We refer to this mechanism as "steady state geometric gain" (SSGG). This chapter provides a platform-agnostic definition of SSGG, illustrates its broad accessibility via numerical simulations and an experimental demonstration using the new MIM platform. Parts of this chapter are adapted from Ref. [92]. Additional technical details for this chapter are in Appendix E.

Chapter 7

This chapter provides an experimental demonstration of the topological and discrete geometric phase of non-Hermitian degeneracies. Specifically, we consider an $N = 2$

mode non-Hermitian system adiabatically tuned in its degenerate subspace, using the new MIM platform. We also demonstrate a novel $\sqrt{T}$-dynamical phase, that is expected for such evolution, and is subsequently employed to demonstrate yet another novel form of amplification: "steady state $\sqrt{T}$ gain" (SS$\sqrt{T}$G). Similar to SSGG, SS$\sqrt{T}$G illustrates that a system of coupled lossy and degenerate elements subject to "slow" modulation can produce useful gain. Additional technical details for this chapter are in Appendix F.

Chapter 8

This chapter concludes this thesis, and provides a list of directions that one could explore in future, with our new MIM platform.

Chapter 2

Theoretical background

In this chapter, we provide the theoretical background for the work reported in this thesis. The chapter is divided into three parts. The first part (Sec. 2.1) illustrates how topology arises in the spectrum of a system of coupled harmonic oscillators, specifically, the phenomenon known as spectral flow. In the second part (Sec. 2.2), we discuss geometric phases in the most general setting, and elucidate their uniquely non-Hermitian features. The last part (Sec. 2.3) describes the optomechanical platform. By harnessing the optomechanical interactions between laser light circulating inside a high-finesse optical cavity and a thin millimeter-sized Silicon-Nitride membrane, we model an arbitrarily tunable non-Hermitian system.

2.1 Topological structure of non-Hermitian eigenvalue spectrum

We motivated in Chapter 1 the idea that the eigenvalue spectrum of a linear system of N coupled harmonic oscillators quite generically has a topological structure. In particular, upon tuning the parameters of the coupled oscillator system, its degeneracies form a knotted structure while the non-degenerate eigenvalue spectrum traces out a braid. In this section, we elaborate on these generic features for an arbitrary N-mode non-Hermitian system (Sec. 2.1.1) and illustrate them with examples (Sec. 2.1.2). These discussions closely follow [43, 91], and for a more mathematically steeped discussion, the reader is referred to [95] (its chapter 2 and references therein). In the final Sec. 2.1.3 as well as in Secs. A.1 and A.2, we provide some context and additional details that may further clarify our description and its relation to other work in this field.

2.1.1 Control loops and spectral flow

The eigenvalue spectrum of a generic N-mode non-Hermitian system can be regarded as an unordered set of N points in the complex plane. They are the N complex eigenvalues $\boldsymbol{\lambda} = \{\lambda_1, \lambda_2, ..., \lambda_N\}$ of H. H is the $N \times N$ matrix that governs the time evolution of the system, referred to as the dynamical matrix or the "Hamiltonian". The task of finding $\boldsymbol{\lambda}$ is straightforward: they are simply the roots of the characteristic polynomial p_N of H. $p_N = \lambda^N - \gamma_1\lambda^{N-1} + \gamma_2\lambda^{N-1} + ... + (-1)^N\gamma_N$ is completely specified by its N complex coefficients $\Gamma \equiv (\gamma_1, \gamma_2, ..., \gamma_N)$, which is an ordered set and these coefficients have polynomial expressions in terms of the elements of H. For example: $\gamma_1 = \mathrm{Tr}(H)$, $\gamma_N = \mathrm{Det}(H)$. Equivalently, $p_n(\lambda)$ can be factored out as $\prod_{i=1}^{N}(\lambda - \lambda_i)$ in which the roots λ_i maybe repeated and the coefficients Γ are polynomials in λ_i, such as $\gamma_1 = \sum_{i=1}^{N}\lambda_i$, $\gamma_2 = \sum_{i,j:i<j}\lambda_i\lambda_j$, ..., $\gamma_N = \prod_{i=1}^{N}\lambda_i$.

We now identify a few key ideas. We will sketch them out loosely below, and their formal description is detailed immediately after.

The first idea is that the coefficients of p_N i.e., Γ, smoothly and completely param-

eterize the eigenvalue spectrum $\boldsymbol{\lambda}$ [21, 26, 96]. To be specific, smoothly varying the elements of Γ causes the eigenvalues to vary smoothly. This naturally leads to regarding these coefficients as defining a space: the control space $\mathcal{L}_N$, and each coefficient as a control knob that tunes $\boldsymbol{\lambda}$.

The second idea is to realize that root finding amounts to a bijective mapping between the ordered set of N complex numbers Γ and the unordered set of N complex numbers $\boldsymbol{\lambda}$. Such a mapping has an uncertainty as seen in the following example: suppose we vary the elements of Γ along a smooth closed path. We are guaranteed the same (unordered) set of $\boldsymbol{\lambda}$ at the start and the end of this path, by construction. However, in the absence of any other information, we do not know how the individual elements of $\boldsymbol{\lambda}$ are mapped - and to be concrete, they could have been transported in any manner: trivially[1] or non-trivially[2]. Such mapping, when viewed topologically are distinct, and is what we will describe below as 'spectral flow'. We now formalize these ideas below.

2.1.1.1 Describing the control space $\mathcal{L}_N$

The starting point of this discussion is that we have a control space $\mathcal{L}_N$, given by the coefficients Γ of p_N and the corresponding N eigenvalues $\boldsymbol{\lambda}$. They are related as: **(a)** $\boldsymbol{\lambda}$ are the roots of p_N, and **(b)** Γ are polynomials in $\boldsymbol{\lambda}$. We are interested in how $\boldsymbol{\lambda}$ change with Γ, and not their absolute value. Thus, without loss of generality, $\boldsymbol{\lambda}$ can be defined up to a complex offset as it merely shifts all of its elements by an equal amount on the complex plane. In particular, we take H to be traceless such that $\gamma_1 = \mathrm{Tr}(H) = \sum_{i=1}^{N} \lambda_i = 0$ (we provide further justification in Sec. 2.1.3.1). This leaves us with $N-1$ complex parameters $(\gamma_2, \gamma_3, ..., \gamma_N)$ that define the control space $\mathcal{L}_N$, which is simply $\mathbb{C}^{N-1}$ i.e., $\mathcal{L}_N \cong \mathbb{C}^{N-1} \cong \mathbb{R}^{2N-2}$, where we use $\cong$ to denote topological isomorphism, i.e, homeomorphism [97] of respective spaces throughout this thesis. We note that $\mathcal{L}_N$ is a topologically trivial space.

[1] An example would be when $\boldsymbol{\lambda}$ is constant throughout the mapping.

[2] An example would be the first two elements of $\boldsymbol{\lambda}$ swapped their positions during the mapping, i.e., $\overline{\boldsymbol{\lambda}} = (\lambda_1, \lambda_2, ..., \lambda_N)$ got smoothly mapped to $(\lambda_2, \lambda_1, ..., \lambda_N)$. Here we used $\overline{\boldsymbol{\lambda}}$ to denote ordered $\boldsymbol{\lambda}$, with the ordering done using some sane algorithm.

2.1.1.2 Partitioning $\mathcal{L}_N$ into non-degenerate ($\mathcal{G}_N$) and degenerate ($\mathcal{V}_N$) subspaces

$\mathcal{L}_N$ can be partitioned into two distinct subspaces:

- $\boldsymbol{\mathcal{G}_N}$

  This is the space of points in $\mathcal{L}_N$ for which the corresponding $\boldsymbol{\lambda}$ are non-degenerate.

- $\boldsymbol{\mathcal{V}_N}$

  This is the space of points in $\mathcal{L}_N$ for which the corresponding $\boldsymbol{\lambda}$ are degenerate. Equivalently, $\mathcal{V}_N$ consists of the points for which the discriminant D of p_N vanishes. Degeneracy is a complex constraint given by $\lambda_i = \lambda_{j\neq i}$ and $\{i, j\} \in \{1, 2, 3, ..., N\}$ i.e., there exist at least two degenerate eigenvalues. This renders $\mathcal{V}_N$ with one (two) complex (real) dimensions lesser than $\mathcal{L}_N$. This fact is generally stated as: "*For non-Hermitian matrices,..., degeneracies are of (real) codimension two, that is points in a two-parameter space and curves in a three-parameter space*"[25]. However, we emphasize that $\mathcal{V}_N$ contains degeneracies of all orders as they satisfy $D = 0$. Said in another way, an N-mode non-Hermitian system will have degeneracies of order two up to N.

While $\mathcal{L}_N$ is topologically trivial, that need not be the case for $\mathcal{G}_N$ and $\mathcal{V}_N$. To further describe these subspaces, we vary parameters in $\mathcal{G}_N$ along smooth closed curves[1] ($\mathcal{C}$: a control loop) with a fixed starting point (which by construction is also the ending point). Traversing a control loop $\mathcal{C}$ smoothly transports $\boldsymbol{\lambda}$ back to itself [21, 26, 96] and such an evolution of N distinct points in the complex plane is called a braid of N strands [43, 91, 95, 98, 99]. For the rest of this discussion, all $\mathcal{C}$s lie exclusively in $\mathcal{G}_N$. As for $\mathcal{V}_N$, one can think of it as a hole in $\mathcal{L}_N$ of (real) codimension two, which can be encircled by control loops in $\mathcal{G}_N$ in various ways. In Sec. 2.1.3.3, we provide further clarification on encircling $\mathcal{V}_N$.

2.1.1.3 Equivalence classes of eigenvalue braids and control loops

Now consider two distinct control loops $\mathcal{C}_1$ and $\mathcal{C}_2$ that share a common starting (and ending) point. We refer to such control loops as based control loops and focus only on

[1] Curves by definition are one dimensional objects.

such loops - unless mentioned otherwise. $\mathcal{C}_1$ and $\mathcal{C}_2$ result in distinct eigenvalue braids. If one of the eigenvalue braids can be continuously deformed into the other, while keeping its end points (also referred to as basepoints) fixed and its strands non-intersecting throughout the deformation, then the two braids are topologically equivalent. Formally, such braids are isotopic, and belong to an isotopy equivalence class b.

Now let us focus on the control loops that produce isotopically equivalent eigenvalue braids. Such loops can be continuously deformed into each other within $\mathcal{G}_N$. Subsequently, the based control loops that give rise to isotopically equivalent braids are topologically equivalent, and belong to an equivalence class: the homotopy equivalence class of based control loop ℓ. See Refs. [100, 101] for an intuitive description of homotopy and isotopy.

To summarize, there is a one-to-one correspondence between the topology of control loops and the topology of the resulting eigenvalue braids. Loosely speaking, topologically equivalent control loops result in topologically equivalent eigenvalue braids and formally, the correspondence is between the homotopy classes of based loops and the isotopy equivalence classes of braids [43, 91, 95, 98, 99].

2.1.1.4 Definition of spectral flow

We define spectral flow produced by a control loop $\mathcal{C}$ to be the isotopy equivalence class b of the corresponding braid of eigenvalues.

2.1.1.5 The Braid group and the fundamental group of control loops

We now observe that braids with a common base point can be concatenated (or composed) with each other to produce another such braid. With concatenation as the operation, the braid isotopy equivalence classes b form the braid group of N strands: B_N, also known as the Artin braid group [102]. Similarly, concatenating two based control loops would produce another based control loop, and the homotopy classes of control loops ℓ form the fundamental group π_1 of the subspace $\mathcal{G}_N$ with concatenation as the group operation. Loosely speaking, the fundamental group provides a catalog of all topologically distinct control loops. From the previous discussion, $\pi_1(\mathcal{G}_N) \simeq B_N$ where $\simeq$ is used to

denote group isomorphism [103] throughout this thesis.

2.1.1.6 A "picture" of $\mathcal{L}_N$, $\mathcal{G}_N$ and $\mathcal{V}_N$

For $N > 2$, B_N is a non-Abelian group, which renders $\pi_1(\mathcal{G}_N)$ non-Abelian. More specifically, based control loops that belong to distinct homotopy classes do not commute i.e., the order in which we concatenate two based control loops matters. Recall that $\mathcal{L}_N$ has a trivial topology, whereas $\mathcal{G}_N$ consists of loops whose order of concatenation matter, thus making it topologically non-trivial. This naturally leads to the question below:

Q: *Where did this non-trivial topology come from?*

A: The non-trivial topology can be solely attributed to the non-trivial geometry of the degenerate subspace $\mathcal{V}_N$, which carves out a hole of (real) codimension two in $\mathcal{L}_N$, and the control loops in $\mathcal{G}_N$ can wind around this hole in various homotopically inequivalent ways. The spectral flow of the corresponding eigenvalue braid is determined by how the control loop encircles $\mathcal{V}_N$.

We note that in comparison, the widely studied $N = 2$ case is topologically "simpler" as B_2 is an Abelian group, $\mathcal{L}_2$ is the complex plane and $\mathcal{V}_2$ is a 0-dimensional space i.e., just a point. It will be explicitly shown in Sec. 2.1.2, that the based control loops in $\mathcal{G}_2$ commute, can be simply labeled by an integer and composing them simply amounts to adding these integers modulo 2. This increase in the complexity of the topology as N increases past 2 is the crux of this discussion[1] and the work described in Chapter 3. Some concrete examples are worked out below.

2.1.2 Illustrating N-mode spectral flow

In this section, we work out the spectral flow for various N, describe their control spaces $\mathcal{L}_N$, degenerate $\mathcal{V}_N$ and non-degenerate $\mathcal{G}_N$ subspaces, and the corresponding eigenvalue braids.

[1] To be specific, the complexity we are referring is that for $N > 2$, the loops cannot be labeled by an integer.

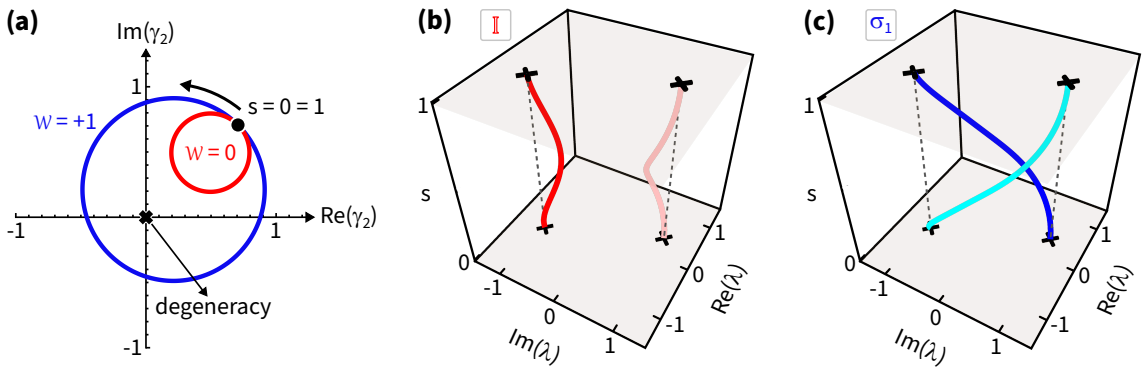

Figure 2.1: Spectral flow: $N = 2$. (a) The control space $\mathcal{L}_2$ is the complex plane, spanned by a complex parameter γ_2. The degenerate subspace $\mathcal{V}_2$ is the origin of the complex plane $\{0\}$, indicated by a black cross. Two control loops in $\mathcal{G}_2$, each parametrized by $0 \leq s \leq 1$ are shown. Red curve: a loop that does not enclose the origin (winding number $\mathcal{W} = 0$), blue curve: a loop that encloses the origin in counter-clockwise sense ($\mathcal{W} = 1$), black disk: common base point that corresponds to $s = 0 = 1$, black arrow: sense in which the control loops are traversed. **(b)** Eigenvalue braid calculated for the red loop in (a). The braid strands map trivially back to themselves: $\mathbb{I}$. **(c)** Eigenvalue braid calculated for the blue loop in (a). The braid strands swap: σ_1. In both (b,c), s indexes the corresponding control loop's coordinate, the black crosses show $\boldsymbol{\lambda}$ at the basepoint and the dashed lines are guides to the eye. Details of the corresponding numerical simulation are given in Sec. A.1.

$N = 2$

For $N = 2$, the parameter space: $\mathcal{L}_2 \cong \mathbb{C}$, i.e., the complex plane (Sec. 2.1.1.1). To identify the degenerate subspace, we recall that it is where the discriminant D of the characteristic polynomial p_2 vanishes. Applying the traceless H constraint: $\gamma_1 = \mathrm{Tr}(H) = \lambda_1 + \lambda_2 = 0$ we are left with $p_2(\lambda) = \lambda^2 + \gamma_2$ and $D = -4\gamma_2$. We note that γ_2 is the (complex) coordinate in $\mathbb{C} \cong \mathbb{R}^2$ and $\gamma_2 = 0$ is the only solution for $D = 0$. Thus $\mathcal{V}_2 \cong \{0\}$, the origin of the complex plane. Subsequently, $\mathcal{G}_2 \cong \mathbb{C} \setminus \{0\}$, the complex plane without the origin. The fundamental group of $\mathcal{G}_2$: $\pi_1(\mathcal{G}_2) \simeq B_2$, the braid group of two strands. B_2 is isomorphic to $\mathbb{Z}$: the group of integers under addition. This is reflected in the fact that control loops $\mathcal{C}$ in $\mathcal{G}_2$ are classified by their winding around the origin with a winding number $\mathcal{W}$. Concatenating such control loops provides a new control loop whose winding number is simply the sum of the winding numbers of the individual control loops used in concatenation. Finally, B_2 is characterized by an identity element $\mathbb{I}$ and a generator σ_1, where $\sigma_i(\sigma_i^{-1})$ indicates that strand i has crossed over (under) strand $i + 1$, the strands are counted from the left (in the view used for the figures below), and operations are written symbolically from right to left as the braid is read from bottom to top [104]. The winding number of the control loops that result in

the corresponding braids are $\mathcal{W} = 0$ for $\mathbb{I}$ and $\mathcal{W} = +1$(-1) for $\sigma_1(\sigma_1^{-1})$. These results are illustrated in Fig. 2.1 via simple numerical simulations with further details in Sec. A.1.

$N = 3$

For $N = 3$, the parameter space: $\mathcal{L}_3 \cong \mathbb{C}^2$. Repeating the procedure from the previous case, we have $\gamma_1 = 0$, $p_3(\lambda) = \lambda^3 + \gamma_2\lambda + \gamma_3$ and $D = -4{\gamma_2}^3 - 27{\gamma_3}^2$. Here, $\{\gamma_2, \gamma_3\}$ are the (complex) coordinates in $\mathbb{C}^2 \cong \mathbb{R}^4$. To isolate the solutions for $D = 0$, we represent $\{\gamma_2, \gamma_3\}$ in their polar form i.e.,$\gamma_2 = re^{i\theta}$ and $\gamma_3 = \rho e^{i\phi}$. For the ease of illustration, we constrain them to lie on a 3-sphere centered at the origin with a radius R i.e., $|\gamma_2|^2 + |\gamma_3|^2 = R^2$. This constraint will be relaxed later in this section. The corresponding solutions to $D = 0$ are given by $\{re^{i(2\alpha-\pi/3)}, \rho e^{3i\alpha}\}$ where $0 \leq \alpha \leq 2\pi$, $4r^3 = 27\rho^2$ and $r^2 + \rho^2 = R^2$ with $r > 0, \rho > 0$. We elaborate on these solutions and describe the structure of $\mathcal{V}_3$ below:

- The trivial solution $r = 0 = \rho$, the origin of $\mathcal{L}_3$ corresponds to a triple degeneracy i.e.,$\lambda_1 = \lambda_2 = \lambda_3 = 0$, where we applied the traceless H condition.
- For non-zero r and ρ, the solution to $D = 0$ is a trefoil knot ($\mathcal{K}$) on a 3-sphere of radius R and corresponds to double degeneracies. We note that $\mathcal{K}$ is a one-dimensional object - a curve. The specific values of r and ρ are constrained by $4r^3 = 27\rho^2$ and the choice of R. More specifically, $r = r_0$ is the positive real root of Eq. (2.1) and $\rho_0 = \sqrt{\frac{4}{27}r_0^3}$.
$$\frac{4}{27}r_0^3 + r_0^2 - R^2 = 0 \tag{2.1}$$
Different values of R provide the second dimension to the space of double degeneracies.
- For a particular scaling of γ_2 and γ_3 as given by: $\gamma_2 \to a^2\gamma_2 \neq 0$ and $\gamma_3 \to a^3\gamma_3 \neq 0$ with a being any complex number and $|a| > 0$, $D \to a^6 D$. Thus the solution to $D = 0$ remains a trefoil knot ($\mathcal{K}$) but lies on a different 3-sphere, i.e.,has a different radius given by $R' = |a|^4 r_0^2 + |a|^6\rho_0^2$, where r_0, ρ_0 are determined above.

With these features, $\mathcal{V}_3$ consists of a triply degenerate point at the origin $\{0\}$ and all double degeneracies that are the cone of the trefoil knot $\mathcal{K}$ i.e., $\mathcal{K} \times \mathbb{R}_{>0}$. These degeneracies altogether form a two-dimensional subspace as expected. They are illustrated

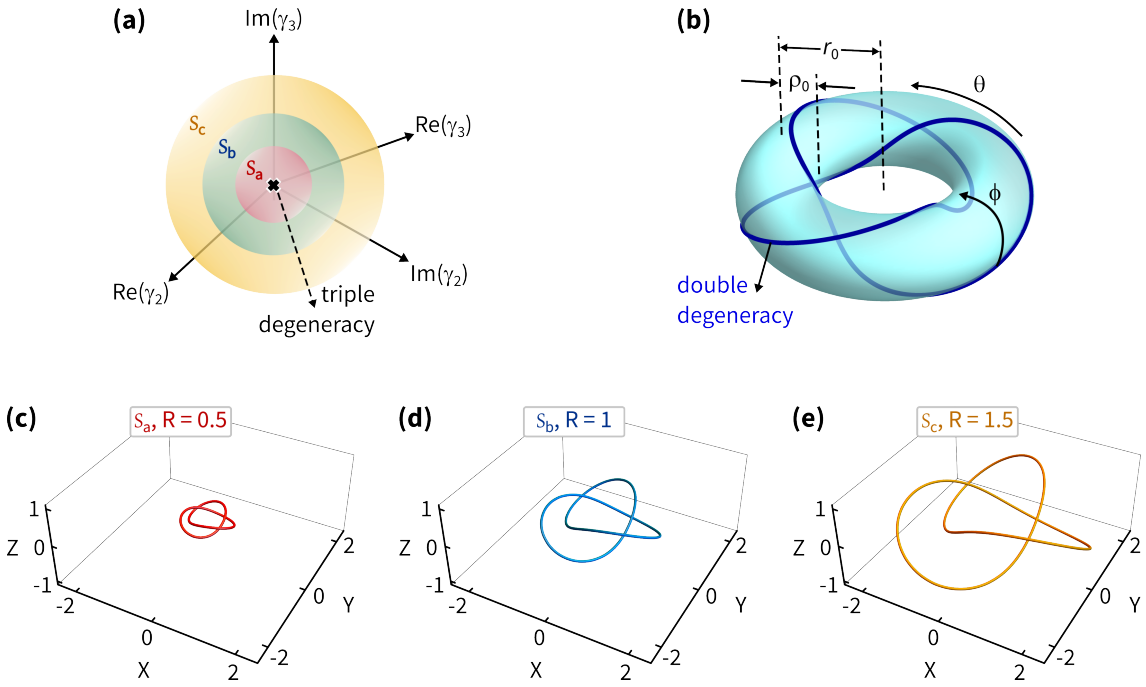

Figure 2.2: Degenerate subspace: $N = 3$. **(a)** A cartoon schematic of $\mathcal{L}_3$, spanned by complex parameters γ_2, γ_3. The triple degeneracy is the origin of $\mathcal{L}_3$, indicated by a black cross, which is enclosed by 3-spheres: $\mathcal{S}_\mathrm{a}$ (red, radius $R = 0.5$), $\mathcal{S}_\mathrm{b}$ (blue, $R = 1$) and $\mathcal{S}_\mathrm{c}$ (yellow, $R = 1.5$). **(b)** The unit 3-sphere $\mathcal{S}_\mathrm{b}$ and the corresponding degeneracies, which are all two-fold. They are represented in Hopf coordinates [105], following Ref. [106]. where $\mathcal{S}_\mathrm{b}$ is represented as torus (light blue) with toroidal radius r_0 (between the center of the torus and the center of the tube), toroidal angle θ, poloidal (tube) radius ρ_0 and poloidal angle ϕ. For this case, $r_0 = 0.937$ and $\rho_0 = 0.349$. The double degeneracies (dark blue curve) form a trefoil knot $\mathcal{K}$. **(c-e)** Double degeneracies corresponding to 3-spheres $\mathcal{S}_\mathrm{a}$, $\mathcal{S}_\mathrm{b}$ and $\mathcal{S}_\mathrm{c}$, respectively, represented in standard stereographic projection [107]. The coordinates X, Y and Z are defined in Sec. A.1. The double degeneracies altogether form a cone of $\mathcal{K}$, that converges to the triple degeneracy at the origin.

in Fig. 2.2.

The control space: $\mathcal{G}_3 \cong \mathbb{C}^2 \setminus (\mathcal{K} \times \mathbb{R}_{\geq 0})$. Identifying $\mathbb{C}^2$ with $\mathbb{R}^4$ and subsequently $\mathbb{R}^4 \cong \mathcal{S}_3 \times \mathbb{R}_{\geq 0}$ [108, 109] where $\mathcal{S}_3$ is the unit 3-sphere, we have $\mathcal{G}_3 \cong \mathcal{S}_3 \setminus \mathcal{K}$. Since $\pi_1(\mathcal{G}_3) \simeq B_3$, we have $\pi_1(\mathcal{S}_3 \setminus \mathcal{K}) \simeq B_3$. Finally, B_3 is characterized by an identity element $\mathbb{I}$ and two generators σ_1, σ_2. The control loops are identified by how they wrap around the trefoil knot, and the corresponding braids are expressed by their braid-word [110]. This highlights the fact that the control loops cannot be characterized by a number like in the $N = 2$ case, and their identification requires systematic analysis that keeps track of how braid strands cross over or under each other[1]. However, the simple case of identity braid corresponds to control loops that do not wrap around the trefoil knot. We

[1]Formally, via the Reidemeister moves [111, 112].

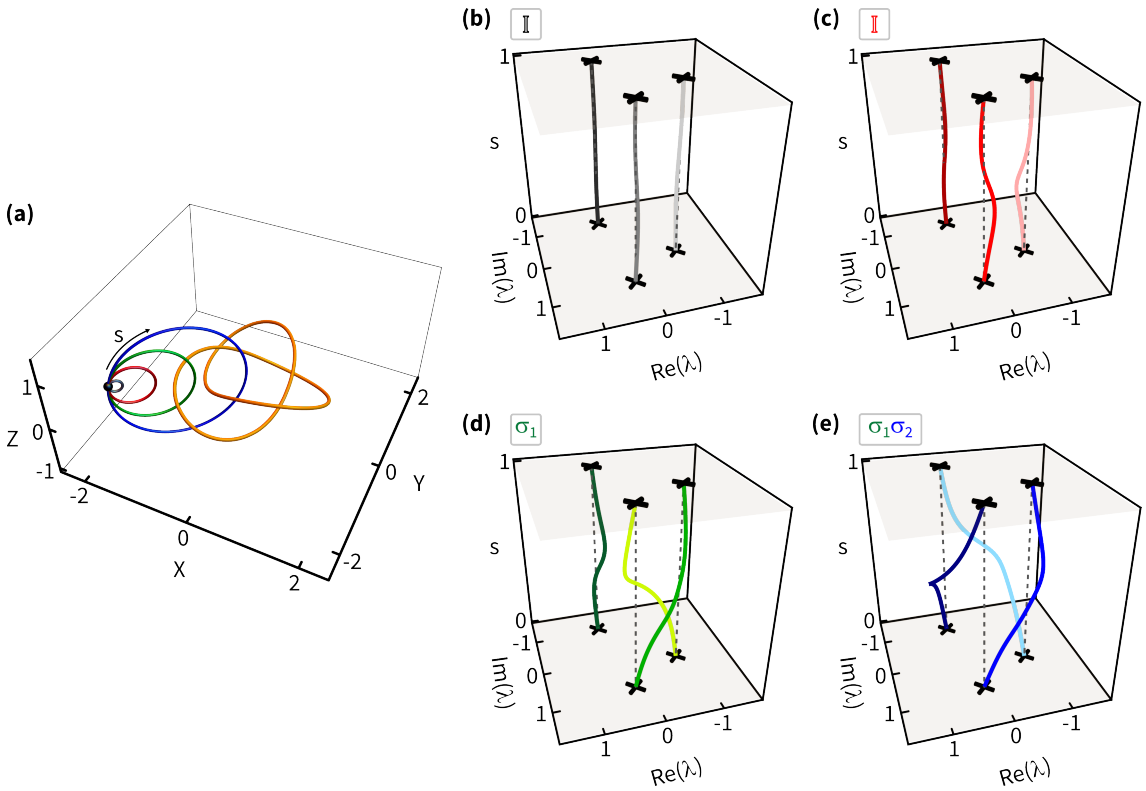

Figure 2.3: Spectral flow: $N = 3$ - part I. (a) Stereographic projection of a unit 3-sphere enclosing the origin in $\mathcal{L}_3$, with the trefoil knot of double degeneracies (orange curve) and four control loops (black, red, green, blue curves). The control loops are parameterized by $0 \leq s \leq 1$, share a common basepoint (black sphere) and their sense of traversal is indicated (black arrow). **(b-e)** Eigenvalue braids calculated for the black, red, green and blue loops in (a), respectively. They trace out the identity braid in (b,c), σ_1 in (d) and $\sigma_1\sigma_2$ in (e). In (b-e), s indexes the corresponding control loop's coordinate, the black crosses show $\boldsymbol{\lambda}$ at the basepoint and the dashed lines are guides to the eye. The coordinates X, Y and Z, and the details of the corresponding numerical simulation are given in Sec. A.1.

also note that control loops corresponding to σ_1 and σ_2, respectively, do not commute, highlighting the non-Abelian nature of B_3. We numerically simulate these results and illustrate them in Figs. 2.3 and 2.4. These simulations closely follow those in Refs. [43, 91] and further details are provided in Sec. A.1.

To conclude this discussion, we remark on our choice of the 3-surface that encloses the origin of $\mathcal{L}_3$ (which corresponds to the triple degeneracy). The choice of a 3-sphere centered at the origin simplifies the analysis presented here, and does not alter the conclusions. However, for completeness, we note the intersection of any arbitrary 3-surface $\mathcal{S}_{\text{arb}}$ with the doubly-degenerate subspace would result in a trefoil knot ($\mathcal{K}$) if $\mathcal{S}_{\text{arb}}$ satisfies the following conditions [43, 95]:

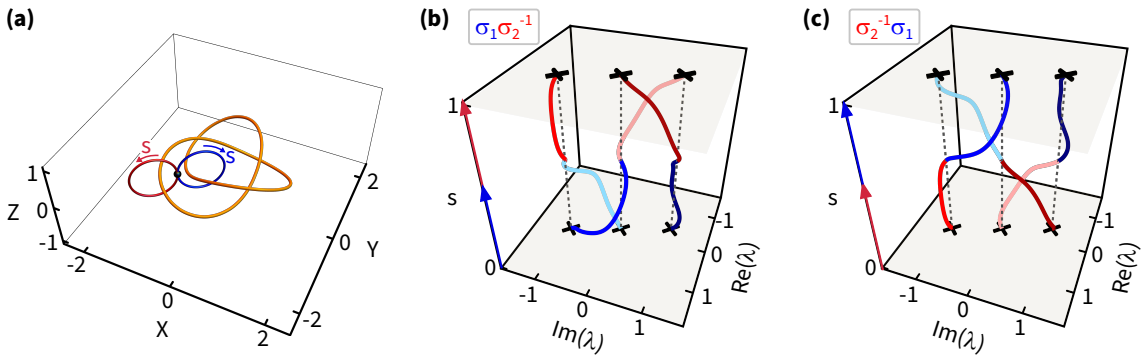

Figure 2.4: Spectral flow: $N = 3$ - part II. (a) Stereographic projection of a unit 3-sphere enclosing the origin in $\mathcal{L}_3$, with the trefoil knot of double degeneracies (orange curve) and two non-commuting control loops (blue and red curves). The control loops are parameterized by $0 \leq s \leq 1$, share a common basepoint (black sphere) and their sense of traversal is indicated (red and blue arrows, respectively). **(b)** Eigenvalue braid $\sigma_1\sigma_2^{-1}$ calculated when first performing the blue control loop ($0 \leq s < 0.5$) followed by the red control loop ($0.5 \leq s \leq 1$) in (a). **(c)** Eigenvalue braid $\sigma_2^{-1}\sigma_1$ calculated when first performing the red control loop ($0 \leq s < 0.5$) followed by the blue control loop ($0.5 \leq s \leq 1$) in (a). In (b-c), s indexes the corresponding control loop's coordinate, the black crosses show $\boldsymbol{\lambda}$ at the basepoint and the dashed lines are guides to the eye. The two braids can be seen to be topologically inequivalent thereby highlighting the non-commuting nature of the two control loops. The coordinates X, Y and Z, and the details of the corresponding numerical simulation are given in Sec. A.1.

1. It has the topology of a 3-sphere $\mathcal{S}_3$.

2. It surrounds the origin without passing through it or intersecting itself.

3. It is everywhere transverse [113] to the local action of an infinitesimal scaling (say, by $a \to 1 + \epsilon$, ϵ being small). Intuitively, rescaling the 3-surface should not "run parallel", anywhere on the 3-surface. Any two such 3-surfaces are isotopy equivalent (through a rescaling that depends on the position on the 3-surface).

However, if a 3-surface does not satisfy the above conditions, then its intersection with the doubly-degenerate subspace may produce structures in addition to $\mathcal{K}$, in the form of isolated points, closed loops or more $\mathcal{K}$s. We emphasize that none of these structures have any additional topological features other than what is described above. However, for simplicity of interpreting and understanding these results, especially those from experiments (as in Chapter 3), a 3-surface that follows the above conditions is desirable.

$N \geq 4$

For $N = 4$, the parameter space: $\mathcal{L}_4 \cong \mathbb{C}^3$. Repeating the procedure as before, we have $\gamma_1 = 0$, $p_4(\lambda) = \lambda^3 + \gamma_2\lambda^2 + \gamma_3\lambda + \gamma_4$ and D is given by Eq. (2.2).

$$D = 16\gamma_2^4\gamma_4 - 4\gamma_2^3\gamma_3^2 - 128\gamma_2^2\gamma_4^2 + 144\gamma_2\gamma_3^2\gamma_4 - 27\gamma_3^4 + 256\gamma_4^3 \tag{2.2}$$

Note that $\{\gamma_2, \gamma_3, \gamma_4\}$ are the (complex) coordinates in $\mathbb{C}^3 \cong \mathbb{R}^6$. Making any further progress similar to the $N = 2$ and 3 case is an unwieldy task due to the non-trivial dimensionality of the control space, the respective degenerate and non-degenerate subspaces. While, some general results follow from our discussion in Sec. 2.1.1: $\pi_1(\mathcal{G}_N) \simeq B_N$, and $\pi_1(\mathcal{S}^N \setminus \mathcal{V}_N) \simeq B_N$, where $\mathcal{S}^N$: N-sphere, explicitly deciphering the structure of $\mathcal{V}_N$ for $N > 3$, is beyond the scope of this thesis.

2.1.3 Further remarks

This section is devoted to provide additional details that may improve the clarity of our description above. We also provide some context and relate our description to other work in this field.

2.1.3.1 Tracelessness of H

In the above description we used the fact that H can be taken to be traceless. We note that this simplifies the analysis, and does not alter the generality of the results. We justify this assumption below.

To focus this discussion, we will work with an arbitrary N-mode system and consider a control loop parameterized by $0 \leq s \leq 1$, for which H(s) is not assumed to be traceless and to be specific, $\mathrm{Tr}(H(\mathrm{s}))$ may vary with s. The N eigenvalues of H ($\boldsymbol{\lambda}$), viewed as a function of s, will trace out a braid of N strands [43, 91, 95, 98, 99]. For each value of s along the braid, $\mathrm{Tr}(H(s))$ sets the average of $\boldsymbol{\lambda}$. Intuitively, if we remove the trace of H for each value of s, i.e., replace $H(s)$ with $H(s) - \mathbb{I}\ \mathrm{Tr}(H(s)/N$ where $\mathbb{I}$ is the identity matrix, this amounts to translating $\boldsymbol{\lambda}$ as a whole, in the complex plane. Despite the fact that this translation may be different for each value of s, since it is applied to $\boldsymbol{\lambda}$

as a whole, the topological character of the braid remains unchanged.

Formally, this follows from the result [114] that shifting the center of the eigenvalue braid by an amount that varies with s gives a family of homeomorphisms that define an ambient isotopy (the ambient space i.e., where the braids live: $\mathbb{C} \times \mathbb{I}$, where $\mathbb{I}$ is the unit interval). Such an operation leaves the braid's isotopy equivalence class unchanged.

2.1.3.2 Generic nature of eigenvalue degeneracies

As described above, the degenerate subspace corresponds to $D = 0$ i.e., at least two of the eigenvalues are degenerate. In this section, we list some of the generic characteristics of these degeneracies.

1. For any N-mode system, the most generic type of degeneracies of order $m \leq N$ render H to contain a Jordan block of dimension m, via similarity transformation (i.e.,change of basis) [88, 115]. These degeneracies are commonly known as exceptional points of order m or EP_m, even though they are not isolated points for $N > 2$. In particular, degeneracies of order m form a (real) codimension $2(m-1)$ subspace, and double degeneracies, i.e., $m = 2$ correspond to the lowest (real) codimension of two [25].

2. Degeneracies corresponding to EP are defective i.e., H is not fully diagonalizable and its right eigenvectors coalesce (as do its left eigenvectors). Consequently, right (left) eigenvectors by themselves are unable to span the columns (rows) of H. However, this situation is remedied by using generalized right eigenvectors, which has been dubbed as "revealing the missing dimensions at EP"[116].

3. At an EP, the eigenvector degeneracy can be generically encoded by requiring a quantity $E = \mathrm{Det}(S)^{-2}$ to vanish [43]. Here S is an $N \times N$ matrix whose elements are given by $s_{ij} = T_{ij}(T^{-1})_{ij}$, where T diagonalizes H, i.e., $\mathrm{Diag}(H) = T^{-1}HT$ and the columns (rows) of $T(T^{-1})$ are the right (left) eigenvectors of H.

This can be seen as follows: At an EP right (left) eigenvectors are unable to span the columns (rows) of H. Consequently, at least two[1] projections of a generic vector onto both the left and right eigenvectors would diverge. This implies that at

[1]As the lowest order EP are order two.

least two columns of S diverge, hence $\mathrm{Det}(S)$ diverges and $E = \mathrm{Det}(S)^{-2}$ vanishes. We list some notable properties of E below:

- As defined above, E has an undesirable property of depending explicitly on the choice of basis, i.e., the basis in which we express the right and left eigenvectors.
- E does not depend on the arbitrary nonzero scaling of the eigenvectors because of the multiplication of matrix elements of T with those of T^{-1} in the definition of S.
- Taking the square of $\mathrm{Det}(S)$ ensures that E does not depend upon the ordering of the eigenvectors, and is single-valued. The definition of E in terms of the reciprocal of $\mathrm{Det}(S)$ is just a convention chosen so that it vanishes at an EP, similar to D.

We will now explicitly work out an example following [43] that shows $E \to 0$ generically as we approach an EP_2, and that its phase winds by 2π when such a point is encircled. Without loss of generality, we focus this discussion on a 2×2 traceless H as close to an EP_2 only the two-dimensional subspace spanned by the two coalescing eigenvectors is relevant. The general form of T that evolves smoothly away from an EP_2 is given by Eq. (2.3) (see also Eq. (9) of Ref. [88]).

$$T \sim V \begin{bmatrix} 1 & 1 \\ -\sqrt{z} & \sqrt{z} \end{bmatrix} \tag{2.3}$$

where $z = \mathrm{Det}(H)$, $|z| \to 0$ and $z = 0$ at a second-order EP (an EP_2). The first column of V i.e.,$(V_{11}, V_{21})^{\mathrm{T}}$ defines the unique (right) eigenvector at $z = 0$. All that can be said, in general, about the z-independent basis transformation matrix V is that $\mathrm{Det}(V) \neq 0$, which follows from $\mathrm{Det}(T) \neq 0$ when $z \neq 0$. After some algebra, we obtain:

$$S \sim \frac{1}{2} \begin{bmatrix} 1 + \frac{V_{11}V_{21}}{\sqrt{z}\mathrm{Det}(V)} & 1 - \frac{V_{11}V_{21}}{\sqrt{z}\mathrm{Det}(V)} \\ 1 - \frac{V_{11}V_{21}}{\sqrt{z}\mathrm{Det}(V)} & 1 + \frac{V_{11}V_{21}}{\sqrt{z}\mathrm{Det}(V)} \end{bmatrix} \tag{2.4}$$

with $|z| \to 0$. Subsequently, $E \sim z\left(\mathrm{Det}(V)/V_{11}V_{21}\right)^2$. This shows that as long as V_{11} and V_{21} are non-zero, $E \to 0$ as $|z| \to 0$ and its phase winds by 2π when $z = 0$

is encircled. To complete this example, we note that V_{11} and V_{21} are generically non-zero. In comparison, for V_{11} or V_{21} to vanish would require fine-tuning all the matrix elements of the traceless H (i.e., six real parameters), while we require only two linearly independent real control parameters to access a second-order degeneracy: $z = 0$ and the space around it.

4. To conclude this discussion, we note that there may exist degeneracies that are not EP. In particular, some degeneracies may not be defective i.e., only eigenvalues $\boldsymbol{\lambda}$ and not the eigenvectors coalesce. However, we emphasize that such "non-defective" or Hermitian degeneracies (also known as "Diabolical points" (DP) [117]) are not generic when H can be any complex matrix. We illustrate this claim by listing all possible degeneracies for a general complex 2×2 matrix, H.

However, before delving into this discussion, we clarify that up until now, we were solely concerned about the spectrum of H i.e., $\boldsymbol{\lambda}$ which are parameterized by the coefficients of the characteristic polynomial (p_N). For this particular discussion, we are interested in fully parameterizing H i.e., all of its elements. We recall that $\boldsymbol{\lambda}$ are the roots of p_N of H and the coefficients of p_N are invariant under similarity transformations of H. This result has a wide range of consequences, of which we focus on the following aspect: A family of H that are related by similarity transformations result in the same $\boldsymbol{\lambda}$, and this family of H also forms an equivalence class. We now turn to discuss the relevant spaces of a general complex 2×2 matrix, H.

As before, without loss of generality we consider a traceless H, and its most general 2×2 incarnation is given by Eq. (2.5).

$$H = (\mathbf{B}_{\mathrm{Re}} + i\mathbf{B}_{\mathrm{Im}}).\vec{\sigma} \tag{2.5}$$

where H is represented as a pair of vectors $\mathbf{B}_{\mathrm{Re,Im}}$, each in $\mathbb{R}^3$ and $\vec{\sigma}$ is the Pauli vector [118]. The full control space of H spans $\mathbb{R}^6$ and some of its notable subspaces are listed in Table 2.1, below.

As illustrated in Table 2.1, EPs are simply more numerous than DPs and thus, are more likely to be encountered upon arbitrary tuning of H. In fact, EPs are more

Matrix space	Geometry	Dimensions	Condition
All H	$\mathbb{R}^6$	6	All $\mathbf{B}_{\mathrm{Re,Im}}$
Hermitians	$\mathbb{R}^3$	3	$\mathbf{B}_{\mathrm{Im}} = 0$
$\mathcal{DP}$	$\mathbb{R}^0$	0	$\mathbf{B}_{\mathrm{Re}} = 0 = \mathbf{B}_{\mathrm{Im}}$
$\mathcal{EP}$	$\mathbb{R}\mathrm{P}^3 \times \mathbb{R}$	4	$\mathbf{B}_{\mathrm{Re}} \cdot \mathbf{B}_{\mathrm{Im}} = 0, \lvert\mathbf{B}_{\mathrm{Re}}\rvert = \lvert\mathbf{B}_{\mathrm{Im}}\rvert$
$\mathcal{PT}$ symmetric	$\mathbb{R}\mathrm{P}^3 \times \mathbb{R}^2$	5	$\mathbf{B}_{\mathrm{Re}} \cdot \mathbf{B}_{\mathrm{Im}} = 0$

Note: **(i)** H is taken to be traceless, **(ii)** For this exercise, we count the real dimensions.

Table 2.1: Various spaces of a general complex traceless 2×2 matrix. $\mathcal{DP}$: the space of all matrices that correspond to "diabolical point" (DP) degeneracies; $\mathcal{EP}$: the space of all matrices that correspond to "exceptional point" (EP) degeneracies; $\mathbb{R}\mathrm{P}^3$: real-projective space, topologically equivalent to a 3-ball with antipodal surface points identified; $\mathcal{PT}$: the space of all matrices that are $\mathcal{PT}$ symmetric i.e., they commute with the $\mathcal{PT}$ operator [119, 120].

numerous than all Hermitian H, which may further highlight their ubiquity. We also note that *all* 2×2 traceless Hs that correspond to EP are similar to a 2×2 Jordan block, and the degenerate eigenvalue is 0. A similar analysis for $N \times N$ matrices with $N > 2$ reveal the ubiquity of EPs over DPs, and they are explicitly worked out in Ref. [115]. Finally, to include tracefull matrices, one simply includes two more real parameters that correspond to a complex-valued trace.

2.1.3.3 Clarifying encircling of degeneracies

In the preceding sections we discussed that (eigenvalue) degeneracies form a (real) codimension two subspace and encircling them with control loops results in eigenvalue braids. In this section, we explicitly clarify the order of degenerate subspaces which can be encircled with control loops.

For smooth closed curves encircling an object is a mathematically valid operation iff the object is of (real) codimension two. By comparison, EP_2 (degeneracies of order 2) are of (real) codimension two, and so can be encircled with a control loop. In contrast, $EP_{m>2}$ have (real) codimension greater than two, and hence cannot be encircled with a control loop. With this information, we refurnish a conclusion from Sec. 2.1.1: Topologically (in)equivalent control loops result in topologically (in)equivalent eigenvalue

braids and topological (in)equivalence is determined by how control loops encircle the EP_2 subspace.

Despite the above reasoning, work on non-Hermitian systems have instances of encircling $EP_{m>2}$ [83–86, 121–126]. While our previous reasoning concludes that such encircling is not meaningful, we attribute these results to the fact that analyzing the behavior of an N-mode system in a restricted control space, that does not span the entire space of eigenvalues may have apparent surprises. As such, it can result in situations where $EP_{m>2}$ "appear" as a (real) codimension two object in the restricted control space.

2.1.3.4 Consequences of accessing a restricted control space: Part I

The dimensionality of the control space grows linearly in the number of modes considered. Thus, despite their straightforward mathematical description (as in Sec. 2.1.1), the high dimensionality makes visualization of relevant subspaces hard. Furthermore, it may not be practical for experiments to have linearly independent control knobs that span the entire control space i.e., $(2N-2)$ (real) control parameters for N modes. Thus, several works on such systems have proceeded by considering a low-dimensional "slice" in the full control space [83–86, 121–131]. Such a "slice" is typically 2D. However, such a simplification may not always capture the key topological features of the full space and consequently may produce surprising results. One such behavior is already mentioned in the previous section, where the use of a restricted control space caused $EP_{m>2}$ to appear as (real) codimension two objects. In this section, we elaborate on the idea of using 2D control slices ($\mathcal{B}$: spanned by (real) parameters $\mathbf{b} = (b_1, b_2)$) in the full control space ($\mathcal{L}_N$) and study the topological structure in the evolution of eigenvalues ($\boldsymbol{\lambda}$) when the system's parameters $\mathbf{b}$ are varied along a control loop.

For $N = 2$, $\mathcal{L}_2$ is the complex plane, and a generic $\mathcal{B}$ will contain a single point where $\boldsymbol{\lambda}$ is degenerate, an EP_2. Control loops in $\mathcal{B} \setminus EP_2$ with odd winding number around the EP_2 result in a permutation of $\boldsymbol{\lambda}$. However for $N > 2$, a generic $\mathcal{B}$ will contain isolated EP_2 that correspond to degeneracies between various mode pairs [21, 26, 115]. In such systems, the relationship between a control loop, the EP_2, and the resulting permutation of $\boldsymbol{\lambda}$ is less intuitive than for $N = 2$. In particular, there is no simple

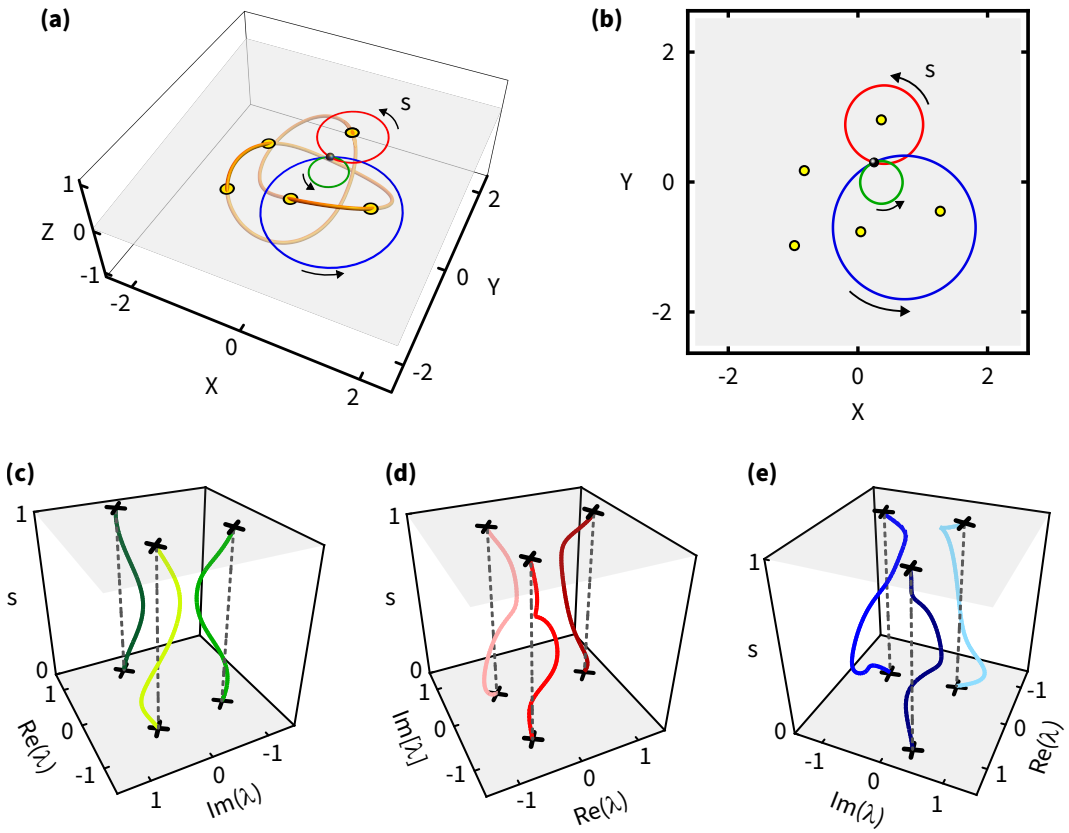

Figure 2.5: Spectral flow: $N = 3$ - part III. (a) Stereographic projection of a unit 3-sphere enclosing the origin in $\mathcal{L}_3$, with the trefoil knot $\mathcal{K}$ of double degeneracies (orange curve) The gray plane shows an example of a 2D control slice ($\mathcal{B}$). The yellow discs are the five intersections of $\mathcal{B}$ with $\mathcal{K}$. The red, green, and blue control loops all lie in $\mathcal{B}$, are parameterized by $0 \leq s \leq 1$ and have a common basepoint (black sphere). **(b)** The control slice $\mathcal{B}$, showing the five EP_2 it contains (yellow circles) and the three control loops. **(c-e)** Eigenvalue braids calculated for each of the control loops. s indexes the corresponding control loop's coordinate, the black crosses show $\boldsymbol{\lambda}$ at the basepoint and the dashed lines are guides to the eye. The coordinates X, Y and Z, and the details of the corresponding numerical simulation are given in Sec. A.1. This figure is adapted from Ref. [91].

correspondence between a loop's topology (formally, its homotopy class in $\overline{\mathcal{B}} \equiv \mathcal{B} \backslash EP_2$) and the resulting permutation of $\boldsymbol{\lambda}$. For example: loops that are homotopy equivalent in $\overline{\mathcal{B}}$ all give the same permutation, but homotopy inequivalent loops do not necessarily give distinct permutations.

As shown in Ref. [131], the permutation associated with a given loop can be calculated by introducing branch cuts (BCs) into $\mathcal{B}$ for $\boldsymbol{\lambda}$, and tracking the manner in which the loop crosses these BCs [121, 131]. This approach has the advantage of being straightforward to visualize, as it only involves quantities that are defined in the 2D space $\mathcal{B}$. It is also relevant to the many experimental systems that offer just two control parameters.

However, relying on the BCs can obscure the topological relationship between control loops and EP_2s.

We illustrate these features by numerically simulating a system of $N = 3$ modes. As described in Sec. 2.1.2, the EP_2 form a trefoil knot $\mathcal{K}$ and is illustrated in Fig. 2.5(a) as the orange curve. Also shown in Fig. 2.5(a) is an example of a 2D control slice $\mathcal{B}$ (gray plane). This particular choice of $\mathcal{B}$ intersects $\mathcal{K}$ at five distinct locations: one of them is tangential (topmost), which is obtained via fine-tuning. The remaining four are generic transverse intersections [113]. Fig. 2.5(b) depicts $\mathcal{B}$ and the five EP_2s within it. We then consider three based control loops in $\mathcal{B}$. Viewed in $\mathcal{B}$ (as in Fig. 2.5(b)), they enclose zero, one, and two EP_2s, and so are not homotopic in $\overline{\mathcal{B}}$. However, it is straightforward to see from Fig. 2.5(a) that they are homotopic in the full control space. As a result, these control loops all result in the same eigenvalue braid. In fact, each of these loops is contractible, and so results in the identity braid (and hence the identity permutation). This agrees with the explicit calculation of $\boldsymbol{\lambda}$ around each control loop, shown in Fig. 2.5(c). These simulations are wholly adapted from [91] and further details are provided in Sec. A.1. In Chapter 3, we provide further illustrations of such cases by experimentally investigating an $N = 3$ mode system.

2.2 Non-Hermitian geometric phase

In Chapter 1, we motivated that the geometric phase or the Berry phase is expected to differ qualitatively between Hermitian and non-Hermitian systems. In this section, we discuss geometric phase and elaborate on its uniquely non-Hermitian features. We begin with a brief review of geometric phase in Sec. 2.2.1. We then state the adiabatic theorem applicable to Hermitian and non-Hermitian systems, in Sec. 2.2.2, and detail their respective geometric phases. We subsequently illustrate the non-degenerate (Sec. 2.2.3) and the degenerate (Sec. 2.2.4) non-Hermitian geometric phase, with concrete examples of the $N = 2$ mode system. In Secs. A.3 and A.4, we provide supplementary discussions and provide context to other work in the field.

2.2.1 Control loops and geometric phases

In Sec. 2.1, we described how tuning a system's parameters would tune its eigenvalues along a braid. We continue with the same theme, but instead focus on the system's state (or state vector) now. In particular, we focus on the following strategy:

1. The system is prepared in some initial state.

2. The system's parameters are varied smoothly around a closed path (a control loop, $\mathcal{C}$) in the space of these parameters, such that the system is strictly non-degenerate throughout.

3. At the end of this variation, the system's state has changed by an overall phase factor, $e^{-i\phi}$.

Under these conditions, ϕ includes a contribution ϕ_B, known as the geometric or Berry phase [13], which is **(i)** determined solely by the shape of $\mathcal{C}$, **(ii)** independent of the duration of the traversal around $\mathcal{C}$, and **(iii)** independent of the manner in which $\mathcal{C}$ is traversed. This robust relationship – between the shape of a loop and the effect of transporting a system around it – arises in many physical settings [132, 133], and has a historically rich conception [134–136].

There are several ways in which the above conditions can be met and consequently,

the geometric phase ϕ_B maybe isolated. These include protocols that follow the adiabatic theorems for Hermitian [10] and non-Hermitian [11, 88] systems, respectively, wherein a crucial idea is to initialize the Hermitian (non-Hermitian) system in any (least-dissipative) eigenvector and then vary the system's parameters "slowly" in real time [12] (formalized in Sec. 2.2.2). Such adiabatic processes result in parallel transport of the system's state vector, by construction. The resulting 'parallelly transported' state vector encodes the holonomy of the control loop, and the geometric phase is a convenient measure of such holonomy (see Chapter 1.1 of Ref. [134]). There also exist protocols that side-step adiabaticity [137] and utilize holonomy in a more geometric sense [138–140]. In such non-adiabatic protocols, the system parameters can be varied without any speed-limits iff the control loop is reverse-engineered to prevent any diabatic transitions into other states [141, 142]. Such reverse-engineering is generically non-trivial for actual experimental systems. Finally, one may consider tuning the system's parameters statically, evaluate (or measure) the system's eigenvectors, and advisedly "stitch" them together to obtain ϕ_B [143, 144]. Loosely speaking, this protocol probes how eigenvectors "twist" and "turn", statically as a function of parameters. Going forward, we restrict our discussions exclusively to protocols that obey respective adiabatic theorems.

2.2.2 Adiabatic theorem

The adiabatic theorem is a cornerstone for linear dynamical systems described by Eq. (1.1). Analytic solutions to Eq. (1.1) are easily obtained if the elements of the system's dynamical matrix H are constant in time. On the contrary, their explicit form is difficult to write down for a general, time-dependent H. However, if the elements of H vary at a "slow" rate $\sim 1/T$, where T is the total time duration of the variation, the asymptotic behavior of the solutions become tractable again. Such "slow" variations are the domain of adiabatic theorems. In this section, we state Hermitian and non-Hermitian adiabatic theorems and discuss the outcomes of the "slow" variation of parameters, one of them being the geometric phase.

2.2.2.1 Non-degenerate Hermitian case

For Hermitian systems, for finite-dimensional systems [10] and for infinite-dimensional systems [145], if a control loop[1] tunes H "slowly" in a time duration $t = T$ while remaining strictly non-degenerate, and the initial state is an eigenvector of $H(t = 0)$, the initial state evolves so as to always be an eigenvector of $H(t)$ that is smoothly connected to the eigenvector of $H(t = 0)$, and in the limit of large-T (i.e., $T \to \infty$) it returns asymptotically to itself at the end of the loop, up to an overall adiabatic phase factor, $e^{-i\phi}$

$$\vec{c}(0) = \vec{u} \to \vec{c}(T) \sim e^{-i\phi}\ \vec{u} \tag{2.6}$$

where $\vec{c}(0)$ denotes the initial state vector at $t = 0$, $\vec{u}$ the non-degenerate eigenvector which is assumed to vary continuously with parameters, $\vec{c}(T)$ the final state at $T = T$, ϕ the adiabatic phase, and $\sim$ denotes the asymptotic behavior as $T \to \infty$. The corrections to the right-hand side of Eq. (2.6) are of order $\mathcal{O}(1/T)$ for H that are first-order differentiable in time t [10], and higher-order corrections can be shown for H that are higher-order differentiable [27]. Similarly, ϕ can be expressed as a series in orders of $1/T$

$$\phi(T) = \int_0^T \lambda(t)\, dt\ - \phi_B + \frac{q_1}{T} + \frac{q_2}{T^2} + \mathcal{O}\left(\frac{1}{T^3}\right) \tag{2.7}$$

where λ is the (real) non-degenerate eigenvalue which characterizes a phase that grows linearly in T - known as the linear dynamical phase, ϕ_D. ϕ_B is the (real) T-independent part - the geometric phase or the Berry phase. q_p are the (real) coefficients of $1/T^p$ terms, for $p \in \mathbb{N}$. As $T \to \infty$, ϕ_D and ϕ_B are the only terms that survive[2] in Eq. (2.7).

One can show that ϕ_B is given by

$$\phi_B = \oint_{\mathcal{C}} \mathbf{A} \cdot\ d\mathbf{R},\ \ \mathbf{A} = i\ \vec{u} \cdot \nabla_{\mathbf{R}} \vec{u} \tag{2.8}$$

where $\mathbf{R}$ denotes the control parameters that are varied and constitute the control loop, $\oint_{\mathcal{C}} d\mathbf{R}$ the line integral along the control loop $\mathcal{C}$, $\nabla_{\mathbf{R}}$ the gradient in $\mathbf{R}$, $(\cdot)$ an inner

[1] To be specific, we take the control loop of a fixed shape and the manner in which it is traversed.

[2] Another intuitive way to see why ϕ_B cannot be neglected is due to the fact that it appears in the argument of $e^{-i\phi} = \mathrm{Cos}(\phi) - i\mathrm{Sin}(\phi)$.

product and $\mathbf{A}$ the Berry connection, which is generically taken analogous to the vector potential in electromagnetism. Subsequently, one may apply Stokes' theorem, ϕ_B is then given by a surface integral of the Berry curvature or Berry flux: $\nabla_{\mathbf{R}} \times \mathbf{A}$, over a surface defined by $\mathcal{C}$.

2.2.2.2 Non-degenerate non-Hermitian case

Adiabatic transport for non-Hermitian systems is strikingly different from its Hermitian counterpart. For a Hermitian system, *all* non-degenerate eigenvectors can undergo adiabatic transport as in Eq. (2.6). In contrast, for non-Hermitian systems, only the eigenvector corresponding to the eigenvalue with the largest imaginary part is amenable to strict adiabatic transport similar to Eq. (2.6), iff such an eigenvector exists. Such eigenvectors, also known as the "dominant" eigenvector/mode or the "least-dissipative" eigenvector/-mode, have the largest (slowest) rate of growth (decay)[1].

During adiabatic evolution along a generic control loop, the system's state tends to transition into the least-dissipative eigenvector (conditional on its existence), despite the choice of the initial state - and to be clear, the initial state can be chosen distinct from the least-dissipative eigenvector. This can be expressed as

$$\vec{\mathrm{c}}(0) = \sum_{j=1}^{N} a_j \vec{\mathrm{u}}_j \rightarrow \vec{\mathrm{c}}(T) \sim e^{-i\phi}\ a_1 \vec{\mathrm{u}}_1 \tag{2.9}$$

where $\vec{\mathrm{u}}_j$ denotes a (right) eigenvector of the non-degenerate N-mode system, of which $\vec{\mathrm{u}}_1$ is the least-dissipative eigenvector. a_j are the complex amplitudes with $a_1 \neq 0$, and the ϕ is the complex adiabatic "phase". The corrections to the right-hand side of Eq. (2.9), specifically $a_1 \vec{\mathrm{u}}_1$, are given in orders of $1/T$ [11], and are determined by the differentiability of H, similar to the Hermitian case, above.

The adiabatic phase ϕ also generalizes from the Hermitian case and splits into linear dynamical phase (ϕ_D, linear in T), geometric phase (ϕ_B, T-independent) [87, 146] and corrections in orders of $1/T$, as in Eq. (2.7), with the following changes and features:

[1] To be specific, we are addressing right eigenvectors, and throughout this chapter the phrase 'least-dissipative eigenvector' implies least-dissipative right eigenvector.

1. The real eigenvalue becomes the complex least-dissipative eigenvalue, $\lambda \to \lambda_1$.

2. The real geometric phase becomes a generic complex number.

3. The real coefficients q_n become complex.

4. As $T \to \infty$, ϕ_D and ϕ_B are the only terms that survive.

In addition, we reiterate that the adiabatic phase ϕ is applicable only for the least-dissipative eigenvector, if such a mode exists.

As shown in Ref. [87, 146], the complex ϕ_B can be expressed as

$$\phi_B = \oint_{\mathcal{C}} \mathbf{A} \cdot d\mathbf{R}, \ \mathbf{A} = i \ \vec{\mathrm{v}} \cdot \nabla_{\mathbf{R}} \vec{\mathrm{u}} \tag{2.10}$$

which is similar to Eq. (2.8) except for the use of left ($\vec{\mathrm{v}}$) and right ($\vec{\mathrm{u}}$) eigenvectors, respectively and the Berry connection $\mathbf{A}$ is now a complex vector. Further work on $\mathbf{A}$ reveals an algebraic analogy to the Hermitian case. However, there are important distinctions as well, and we detail them in Sec. 2.2.3.

In the above case, we have implicitly assumed that there indeed exists a unique least-dissipative eigenvector throughout the adiabatic evolution, which may not be the case in general. As discussed in Sec. 2.1, control loops generically produce braids of eigenvalues which may change the identity of the least-dissipative one during the control loop. As a result, the non-Hermitian adiabatic theorem does not apply to such cases.

In this view, the non-Hermitian adiabatic theorem may appear more restrictive than its Hermitian counterpart. This has naturally led to work in this field that: **(i)** employs a weaker notion of adiabaticity - "quasi-adiabaticity" (Sec. A.3.3 - part **2**), **(ii)** tries to side-step adiabatic evolution partially, in favor of shortcuts-to-adiabaticity schemes [141, 142, 147–149] or completely, in favor of static characterization, or to a specifically limited extent **(iii)** fully embrace the non-Hermitian adiabatic theorem and restrict oneself to control loops that explicitly obey it. The work described in this thesis (Chapters 5, 6 and 7) exclusively falls in the third category.

2.2.2.3 Degenerate case

In so far, we have restricted ourselves to control loops that render the system to be strictly non-degenerate. However, the story of tuning a system's parameters and monitoring the system's state becomes richer, when we include control loops that render the system to be strictly degenerate i.e., throughout the entire loop. Important results have been obtained for Hermitian degenerate systems and more recently, non-Hermitian degenerate systems. The theoretical results and predictions for each of them are stated below.

Hermitian degenerate systems

For an N-mode Hermitian system, that is m-fold degenerate for $2 \leq m \leq N$, it was shown in Refs. [150, 151]:

1. A state initialized as any one of the eigenvectors corresponding to the degenerate subspace can be transported adiabatically, similar to the Hermitian non-degenerate case.

2. For a control loop $\mathcal{C}_{\text{deg}}$ that renders the system strictly degenerate throughout, the geometric phase factor is an $m \times m$ unitary matrix, which encodes the holonomy of $\mathcal{C}_{\text{deg}}$. This unitary matrix, also known as the Wilson loop, is given by a path-ordered integral of a Berry connection matrix, which solely depends on the geometry of the space of Hermitian degeneracies, and is a generalization of the Berry connection in the non-degenerate case. For $m = N$, the Berry connection matrix is trivial, i.e. equal to the zero matrix. For $m \neq N$, if the subsystem is non-trivially embedded[1] in the larger (N-mode) system, the gauge potential was shown to be non-trivial [150]. We note that if for $m \neq N$, the m-fold degenerate subsystem is independent from the larger N-mode system, i.e., has constant embedding, the resulting gauge potential is trivial once again.

3. A state initialized as any one of the eigenvectors corresponding to the degenerate subspace transforms via this geometric unitary matrix under adiabatic evolution.

4. For the non-trivial case of $m \neq N$, upon concatenation of $\mathcal{C}_{\text{deg}}$, the corresponding

[1] To be clear, by non-trivial embedding we mean that the embedding is not constant along the control loop.

matrices that encode their holonomy are generically non-commuting, thereby demonstrating the non-Abelian nature of the holonomy.

Non-Hermitian degenerate systems

For non-Hermitian systems, recent theoretical results [88, 89] have shown that in the space of degeneracies of $N \times N$ dynamical matrices ($H_{\rm deg}$), that are equivalent to an $m \times m$ Jordan block [152] i.e., correspond to $m^{\rm th}$ order EP: $\mathcal{EP}_m$, with $2 \leq m \leq N$, for certain classes of control loops in $\mathcal{EP}_m$ and a choice of initial state, the state returns to itself and acquires a complex phase $\phi_{\rm deg}$. Below, we state the theoretical results for two distinct cases given by: **(i)** $m = N$, and **(ii)** $m < N$.

(i) $m = N$

For $m = N$, $\phi_{\rm deg}$ can be given as a Puiseux series [153]:

$$\phi_{\rm deg}(T) = \sum_{r=0}^{N} T^{1-r/N} \int_0^1 a_r(s) ds + \mathcal{O}(T^{-1/N}) \tag{2.11}$$

where $a_r(s)$ are complex functions of $H'(s) = J_N - \mathcal{A}_J(s)/T$, with $\mathcal{A}_J$ the matrix of Berry connection, generalized from the Hermitian case. H' is the matrix that governs the real time evolution of the state vector and $0 \leq s \leq 1$. The complex dynamical phase (i.e., the T-dependent phase), includes the well-known linear in T part ($r = 0$ term) and fractional powers of T ($1 \leq r < N$ terms), which provide a "stretched exponential" adiabatic evolution. It was shown that the T-independent term ($r = N$ term):

1. Remarkably encodes the holonomy of loops in $\mathcal{EP}_N$ and hence is a geometric phase $\phi_{B,\rm deg}$.

2. However, the Berry curvature in the space of $\mathcal{EP}_N$ is identically zero.

3. Despite the zero Berry curvature, $\phi_{B,\rm deg}$ can be obtained by an analogous equation involving $\mathcal{A}_J$. It is precisely given by

$$\phi_{B,\rm deg} = \frac{1}{N} \oint_{\mathcal{C}} {\rm Tr}(\mathcal{A}_J)\, ds \tag{2.12}$$

and has a non-trivial and a purely real value given by $2\pi n/N$, where n is the winding number of the control loop $\mathcal{C}_{\rm deg}$ in $\mathcal{EP}_N$. The fundamental group of $\mathcal{EP}_N$: $\pi_1(\mathcal{EP}_N) \cong \mathbb{Z}_N$, the cyclic group of order N [88, 89], where the winding number of $\mathcal{C}_{\rm deg}$ determines its homotopy class [154]. Thus, the T-independent term is topological, and it takes discrete values.

4. Upon concatenating $\mathcal{C}_{\rm deg}$s, the resulting $\phi_{B,\rm deg}$ does not depend on the order of concatenation and thus the holonomy is Abelian.

This is in contrast to the corresponding Hermitian case where the geometric phase factor is trivially zero. One of the conditions under which these results hold is that the state being transported is the least-dissipative eigenvector of $H'(s) = J_N - \mathcal{A}_J(s)/T$ for all $s \in [0, 1]$. We detail these properties, provide some intuition, and work out a concrete example for the case of $N = 2$, in Sec. 2.2.4.

(ii) $m < N$

For $m < N$, one can again express $\phi_{\rm deg}$ as a Puiseux series, similar to Eq. (2.11), for a class of loops in $\mathcal{EP}_m$ and a choice of initial state. Subsequently the T-independent term yet again encodes the holonomy of the control loop in $\mathcal{EP}_m$ [89].

However, for this case, the corresponding Berry curvature is generically non-zero and complex-valued and the resulting $\phi_{B,\rm deg}$ is a generic complex number. Although, any further discussion on this matter is beyond the scope of this thesis, we refer the reader to Ref. [89] for a detailed study.

2.2.3 Illustrating the non-degenerate non-Hermitian geometric phase

In this section, we work out the complex geometric phase for an $N = 2$ mode non-Hermitian system for a simple class of control loops and list its salient features. We subsequently provide a geometric intuition for it, describe its numerical calculation for arbitrary control loops, show that the imaginary part of this geometric phase is well-defined for open control paths (i.e., non-loops) and give a teaser for a novel mechanism

for realizing an amplifier using the non-Hermitian geometric phase.

2.2.3.1 Geometric phase for "simple" control loops

The dynamical matrix H of a two-mode system is conveniently represented via a pair of three-vectors $\mathbf{B}_{\mathrm{Re,Im}}$ in $\mathbb{R}^3$, as in Eq. (2.5), supplemented with a complex trace $\mathcal{T}$.

$$H = (\mathbf{B}_{\mathrm{Re}} + i\mathbf{B}_{\mathrm{Im}}).\vec{\sigma} + \mathcal{T}\,\mathbb{I}/2 \tag{2.13}$$

where $\vec{\sigma}$ is the Pauli vector, and $\mathbb{I}$ is the identity matrix. A control loop $\mathcal{C}$ corresponds to $\mathbf{B}_{\mathrm{Re,Im}}$ tracing out a closed path in $\mathbb{R}^3$ as shown in Fig. 2.6(a). Subsequently, $\mathbf{B}_{\mathrm{Re,Im}}$ are set by the control parameters $\mathbf{R}$, and $\mathcal{C}$ is defined parametrically via $\mathbf{R}(s)$, where $0 \leq s \leq 1$ and $\mathbf{R}(0) = \mathbf{R}(1)$. A particular real time traversal of $\mathcal{C}$ is given by choosing the total duration of the control loop, T and a function $s(t/T)$, with $s(0) = 0$ and $s(1) = 1$.

A particularly simple class of loops consists of fixing the lengths and the relative orientation of $\mathbf{B}_{\mathrm{Re,Im}}$, and rigidly rotating them around the z-axis once as shown in Fig. 2.6(b), at a constant rate. Such "simple" control loops can be encoded as

$$H(s) = \begin{bmatrix} A & Be^{i\theta(s)} \\ Ce^{-i\theta(s)} & -A \end{bmatrix} + \frac{\mathcal{T}(s)}{2}\,\mathbb{I} \tag{2.14}$$

where A, B and C are constant complex numbers that set the lengths $\mathbf{B}_{\mathrm{Re,Im}}$ and their relative orientation. θ is a real parameter that sets the azimuthal angle of $\mathbf{B}_{\mathrm{Re,Im}}$ (in the x,y-plane). Setting $\theta(s) = 2\pi s$ and varying s from 0 to 1, affects a full rotation of $\mathbf{B}_{\mathrm{Re,Im}}$ around the z-axis, at a constant rate. For this case, $\mathbf{B}_{\mathrm{Re,Im}}$ are explicitly given by

$$\begin{aligned} [\mathbf{B}_{\mathrm{Re}}.\mathbf{x}]\,(s) &= \tfrac{\mathrm{Re}(B+C)}{2}\,\mathrm{Cos}(\theta(s)) - \tfrac{\mathrm{Im}(B-C)}{2}\,\mathrm{Sin}(\theta(s)) \\ [\mathbf{B}_{\mathrm{Re}}\cdot\mathbf{y}]\,(s) &= -\tfrac{\mathrm{Re}(B+C)}{2}\,\mathrm{Sin}(\theta(s)) - \tfrac{\mathrm{Im}(B-C)}{2}\,\mathrm{Cos}(\theta(s)) \\ [\mathbf{B}_{\mathrm{Re}}\cdot\mathbf{z}]\,(s) &= \mathrm{Re}(A) \end{aligned} \tag{2.15}$$

$$\begin{aligned}
\left[\mathbf{B}_{\mathrm{Im}} \cdot \mathbf{x}\right](s) &= \tfrac{\mathrm{Re}(B-C)}{2}\ \mathrm{Sin}(\theta(s)) - \tfrac{\mathrm{Im}(B+C)}{2}\ \mathrm{Cos}(\theta(s)) \\
\left[\mathbf{B}_{\mathrm{Im}} \cdot \mathbf{y}\right](s) &= \tfrac{\mathrm{Re}(B-C)}{2}\ \mathrm{Cos}(\theta(s)) - \tfrac{\mathrm{Im}(B+C)}{2}\ \mathrm{Sin}(\theta(s)) \\
\left[\mathbf{B}_{\mathrm{Im}} \cdot \mathbf{z}\right](s) &= \mathrm{Im}(A)
\end{aligned} \tag{2.16}$$

Finally, we allow for an arbitrary complex trace $\mathcal{T}(s)$ with $\mathcal{T}(0) = \mathcal{T}(1)$. As will be shown below, the complex geometric phase is independent of $\mathcal{T}(s)$.

The eigenvalues of H in Eq. (2.14) are

$$\lambda_{\pm}(s) = \mathcal{T}(s)/2 \pm \sqrt{A^2 + BC} \tag{2.17}$$

and the corresponding right (left) eigenvectors $\vec{\mathrm{u}}$ ($\vec{\mathrm{v}}$) are, up to an overall complex scaling factor, given by

$$\vec{\mathrm{u}}_{\pm}(s) = \begin{bmatrix} Be^{i\theta(s)} \\ \pm\lambda - A \end{bmatrix}, \vec{\mathrm{v}}_{\pm}(s) = \pm\frac{1}{2\lambda Be^{i\theta(s)}} \begin{bmatrix} \pm\lambda + A \\ Be^{i\theta(s)} \end{bmatrix} \tag{2.18}$$

where $\lambda = \sqrt{A^2 + BC}$, '+' is chosen to denote the least-dissipative eigenvector and '$-$' denotes the other mode. We note that this choice of eigenvectors satisfy the normalization condition (the dot product between two vectors is defined as $\vec{\mathrm{a}} \cdot \vec{\mathrm{b}} = \mathrm{a}_1\mathrm{b}_1 + \mathrm{a}_2\mathrm{b}_2$). For "simple" control loops, we only need to consider the Berry connection $\mathbf{A}$ along the θ direction of the parameter space, which is readily computed to be [12, 87, 146]

$$\mathbf{A}_{\pm} \cdot \boldsymbol{\theta} = i\vec{\mathrm{v}}_{\pm} \cdot \partial_{\theta}\vec{\mathrm{u}}_{\pm} = -\frac{1}{2}\left(1 \pm \frac{A}{\lambda}\right) \tag{2.19}$$

and the geometric phase for a control loop in which θ: $0 \to 2\pi$ is simply given by

$$\phi_{B,\pm} = \int_0^{2\pi} \mathbf{A}_{\pm} \cdot \boldsymbol{\theta}\ d\theta = -\pi\left(1 \pm \frac{A}{\lambda}\right) = \pm\pi\left(1 - \frac{A}{\lambda}\right) \tag{2.20}$$

where in the last equality we have used the fact that $\phi_{B,\pm}$ is defined modulo 2π.

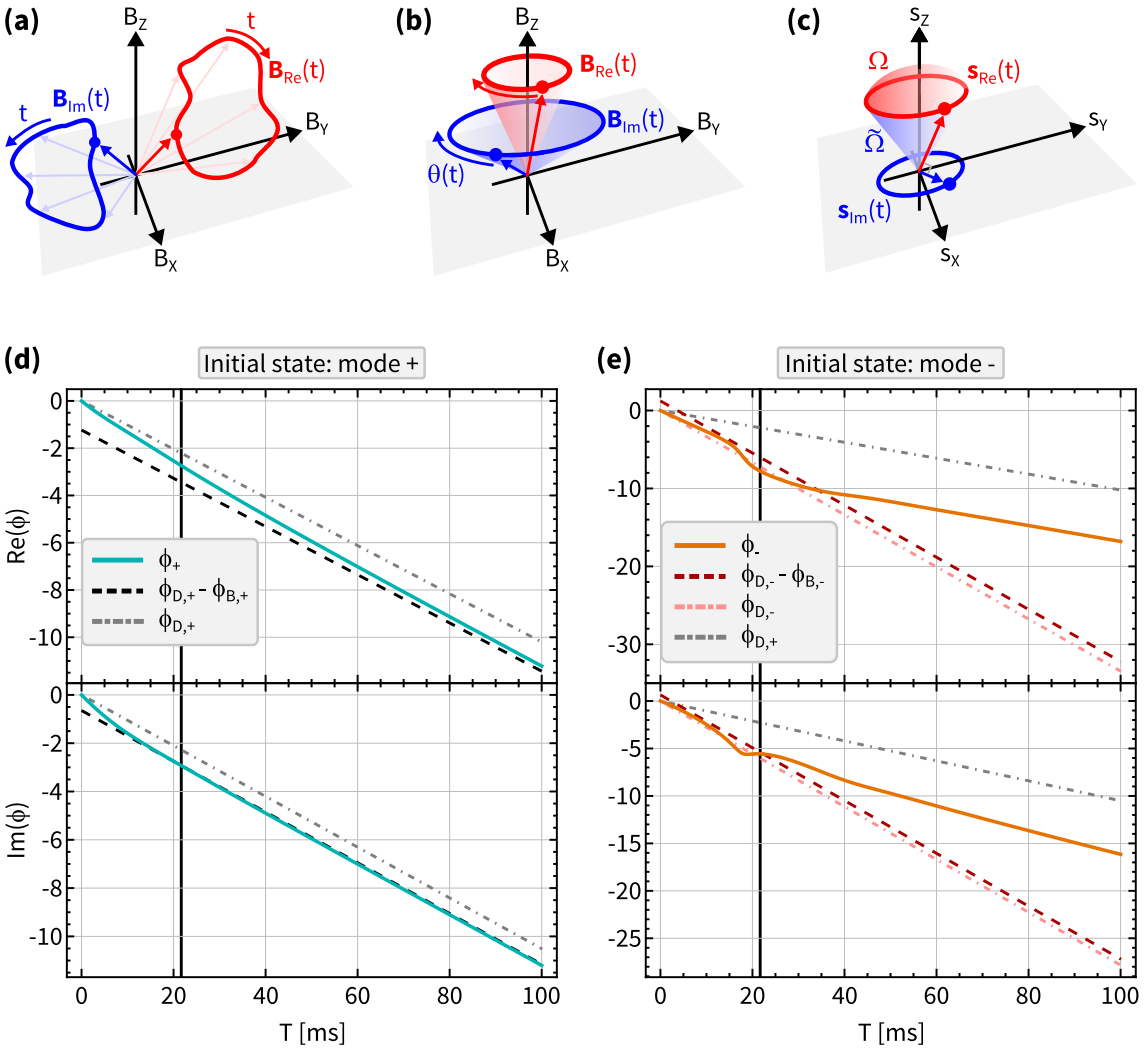

Figure 2.6: Control loops and real time evolution of state vector. **(a)** A generic control loop. Circles: the starting and the stopping point of the loop, at $t = 0, T$, respectively; curves: $\mathbf{B}_{\mathrm{Re,Im}}$; arrows are a guide to the eye. **(b)** A "simple" control loop. **(c)** "simple" control loop re-parametrized in terms of $\mathbf{s}_{\mathrm{Re,Im}}$ to obtain geometric intuition for the non-Hermitian ϕ_B (see Sec. 2.2.3.2). **(d)** Numerically simulated real time evolution of the system when initialized in the least-dissipative eigenvector $(+)$. For this case, $\mathcal{T}(s) = -2\pi(34.7 + 30.5i)$ Hz, $A = 2\pi(14.1 + 4.6i)$ Hz, $B = -2\pi(14.2 + 13.5i)$ Hz and $C = -2\pi(12.5 + 15i)$ Hz. Cyan curve: $\phi_+(T)$; dashed black curve: $\phi_{D,+} - \phi_{B,+}$; dot-dashed gray curve: $\phi_{D,+}$; black vertical line: characteristic adiabatic time scale $T_{\mathrm{ad}} = 2\pi/|\lambda_+ - \lambda_-| \sim 22$ ms. Top panel: $\mathrm{Re}(\phi_+(T))$; bottom panel: $\mathrm{Im}(\phi_+(T))$. **(e)** Same as **(d)** but the system in initialized in the other mode $(-)$. Orange curve: $\phi_+(T)$; dashed maroon curve: $\phi_{D,-} - \phi_{B,-}$; dot-dashed pink curve: $\phi_{D,-}$; dot-dashed gray curve: $\phi_{D,+}$. Top panel: $\mathrm{Re}(\phi_-(T))$; bottom panel: $\mathrm{Im}(\phi_-(T))$.

Some salient features of the geometric phase

Based on this exercise with "simple" control loops, we now list some of the salient features of the geometric phase ϕ_B.

1. Since A, λ are generically complex numbers, ϕ_B is generically complex [87, 146]. This is an important distinction between the Hermitian and the non-Hermitian case (where ϕ_B is purely real). The real part of ϕ_B affects the phase of the system's oscillations while the imaginary part affects their magnitude. ϕ_B is also seen to be independent of the trace $\mathcal{T}$ of H, similar to the Hermitian case.

Additionally, we recover the well-known result from the Hermitian case by setting $\mathbf{B}_{\mathrm{Im}} = 0$. This corresponds to A, λ being real. The resultant ϕ_B is real and is precisely the half of the solid angle subtended by the control loop at the origin of $\mathbb{R}^3$ [12].

2. In Eq. (2.20), we predict a geometric phase for both modes, $\phi_{B,+}$ for the least-dissipative eigenvector $(+)$ and $\phi_{B,-}$ for the other mode $(-)$, which are equal in magnitude but opposite in sign. However, only the least-dissipative eigenvector is amenable to adiabatic evolution [11], and as a result, adiabatic protocols allow for isolating $\phi_{B,+}$, only.

To illustrate this effect, we numerically simulate the real time evolution of the state vector when it is prepared in mode $(+)$ and $(-)$ and H is varied along "simple" loops, given by H in Eq. (2.14), with a choice of $\{\mathcal{T}(s), A, B, C\}$. We find that for large T, the state initially in mode $(+)$ acquires a phase $\phi_+(T)$ consistent with Eq. (2.7). In particular, $\phi_+(T)$ approaches $\phi_{D,+}(T) - \phi_{B,+}$, where $\phi_{D,+}(T)$ is the linear dynamical phase for mode $(+)$. This is shown in Fig. 2.6(d).

In contrast, as shown in Fig. 2.6(e), the phase acquired by the state initially in mode $(-)$, $\phi_-(T)$ does not obey Eq. (2.7). Specifically, for large T, mode $(-)$ acquires a linear dynamical phase $\sim \phi_{D,+}$, which further highlights non-Hermitian Adiabatic theorem (see Eq. (2.9)). It is indeed an interesting curiosity that for large T, $\phi_-(T)$ appears to have a $\sim$constant offset from $\phi_{D,+}$, potentially indicating something geometric (i.e., $\propto T^0$). We relegate its further investigation for a future work. See also Sec. 5.4 for additional insights.

Going forward, we will only discuss the geometric phase for the least-dissipative eigenvector, unless mentioned otherwise, and for notational simplicity we define $\phi_B \equiv \phi_{B,+}$.

3. Analogous to the Hermitian case, the non-Hermitian ϕ_B changes by a sign if the direction of traversing the control loop is reversed. Similarly, as in the Hermitian case, ϕ_B is additive upon multiple repetitions of the same control loop.

$$s \to 1 - s \implies \phi_B \to -\phi_B \tag{2.21}$$

$$s \to ns \implies \phi_B \to n\phi_B \; \forall \; n \in \mathbb{N} \tag{2.22}$$

4. While we parametrized the control loop via $\theta(s) = 2\pi s$, ϕ_B as given in Eq. (2.20) is independent of this parameterization. This highlights an important property of ϕ_B: it is independent of the manner in which we traverse the control loop.

These features of the non-Hermitian ϕ_B for the non-degenerate case are experimentally demonstrated in Chapters 5 and 6.

2.2.3.2 Geometric intuition

A large body of work on Hermitian geometric phase has provided important intuitions and visuals about how it manifests as a holonomy when vectors are parallel-transported, and its relation to geometric and topological entities such as the solid angle and the Chern number, respectively [12, 132, 138, 150, 155–157]. In this section, we provide a similar intuition for the complex geometric phase.

While "simple" loops are convenient for evaluating the geometric phase, we now consider arbitrary control paths by parameterizing them in complex spherical coordinates [158] as:

$$H = \lambda \begin{bmatrix} \mathrm{Cos}(\upsilon) & \mathrm{Sin}(\upsilon)e^{-i\Theta} \\ \mathrm{Sin}(\upsilon)e^{i\Theta} & -\mathrm{Cos}(\upsilon) \end{bmatrix} = \mathbf{B} \cdot \vec{\sigma} \tag{2.23}$$

with

$$\mathbf{B} = \lambda \begin{bmatrix} \mathrm{Sin}(\upsilon)\ \mathrm{Cos}(\Theta) \\ \mathrm{Sin}(\upsilon)\ \mathrm{Sin}(\Theta) \\ \mathrm{Cos}(\upsilon) \end{bmatrix} \tag{2.24}$$

and $\lambda, \Theta, \upsilon \in \mathbb{C}$. We have omitted the trace of H as it plays no role in the geometric phase. In these coordinates, the eigenvalues are given by $\pm\lambda$, and left ($\vec{\mathrm{u}}$) and right ($\vec{\mathrm{v}}$) eigenvectors are given by

$$\begin{aligned} \vec{\mathrm{u}}_+ &= \begin{bmatrix} \mathrm{Cos}(\upsilon/2) \\ \mathrm{Sin}(\upsilon/2)e^{i\Theta} \end{bmatrix}, \quad \vec{\mathrm{u}}_- = \begin{bmatrix} \mathrm{Sin}(\upsilon/2)e^{-i\Theta} \\ -\mathrm{Cos}(\upsilon/2) \end{bmatrix}, \\ \vec{\mathrm{v}}_+ &= \begin{bmatrix} \mathrm{Cos}(\upsilon/2) \\ \mathrm{Sin}(\upsilon/2)e^{-i\Theta} \end{bmatrix}, \quad \vec{\mathrm{v}}_- = \begin{bmatrix} \mathrm{Sin}(\upsilon/2)e^{i\Theta} \\ -\mathrm{Cos}(\upsilon/2) \end{bmatrix} \end{aligned} \tag{2.25}$$

where '$+$' is chosen to denote the least-dissipative eigenvector and '$-$' denotes the other mode. The Berry connection is readily computed to be

$$\mathbf{A}_\pm = i\vec{\mathrm{v}}_\pm \cdot \nabla \vec{\mathrm{u}}_\pm = \mp \frac{1}{2}\left(1 - \mathrm{Cos}(\upsilon)\right)\boldsymbol{\Theta} \tag{2.26}$$

We note that the Berry connection $\mathbf{A}_\pm$ is a vector in control parameter space, and ∇ is the gradient operator in this space. Thus, when considering a generic path in parameter space, we only have to consider the projection of the path to the complex Θ plane. We now consider a simplification in which we constrain Θ to be real, similar to the "simple" loops. In particular, we take $\mathrm{Re}(\Theta) = -\theta$, where θ appears in the "simple" loops (Sec. 2.2.3.1). For such simple loops, we have for the least-dissipative eigenvector

$$\begin{aligned} \phi_B &= \int_0^{2\pi} \mathbf{A}_+ \cdot \boldsymbol{\theta}\ d\theta = \pi(1 - \mathrm{Cos}(\upsilon)) \\ &= \pi(1 - \mathrm{Cos}(\upsilon_{\mathrm{Re}})\mathrm{Cosh}(\upsilon_{\mathrm{Im}}) + i\mathrm{Sin}(\upsilon_{\mathrm{Re}})\mathrm{Sinh}(\upsilon_{\mathrm{Im}}) \end{aligned} \tag{2.27}$$

where $\upsilon = \upsilon_{\mathrm{Re}} + i\upsilon_{\mathrm{Im}}$. It was noted in Ref. [87, 146] that the line integral of $\mathbf{A}_\pm$ over a control loop $\mathcal{C}$ may be converted, via Stokes' theorem, into the surface integral of a curvature over the area bounded by $\mathcal{C}$. Indeed, in complete analogy to the Hermitian Berry

curvature, this curvature may be written (in $\mathbb{C}^3$) as the field strength tensor associated with a "magnetic field"

$$\mathbf{R}_{\pm} = \mp \frac{\mathbf{B}}{2|\mathbf{B}|^3} \tag{2.28}$$

where $\mathbf{B}$ is defined in Eq. (2.24). See also Eq.45 of Ref. [158]. Therefore, the complex geometric phase can be interpreted as a flux enclosed by $\mathcal{C}$ in the presence of a monopole source of "magnetic field" that is located at $\mathbf{B} \cdot \mathbf{B} = 0$. Note that this is the location where H is degenerate.

Despite this algebraic analogy between the Hermitian and non-Hermitian case, there are also important differences. As shown before (Sec. 2.1.3.2), in the Hermitian case, the space of $\mathbf{B}$ is $\mathbb{R}^3$, with a sole degenerate point at $\mathbf{B} = 0$. However, in the non-Hermitian case, the space of $\mathbf{B}$ is $\mathbb{C}^3 \simeq \mathbb{R}^6$ and the degeneracy i.e., $\mathbf{B} \cdot \mathbf{B} = 0$, occurs in a four-dimensional subspace, making the relationship between $\mathcal{C}$ and ϕ_B challenging to visualize. Some progress can be made by decomposing

$$\frac{\mathbf{B}}{\lambda} = \mathrm{Cosh}(\upsilon_{\mathrm{Im}}) \begin{bmatrix} \mathrm{Sin}(\upsilon_{\mathrm{Re}})\ \mathrm{Cos}(\theta) \\ \mathrm{Sin}(\upsilon_{\mathrm{Re}})\ \mathrm{Sin}(\theta) \\ \mathrm{Cos}(\upsilon_{\mathrm{Re}}) \end{bmatrix} + i\mathrm{Sinh}(\upsilon_{\mathrm{Im}}) \begin{bmatrix} \mathrm{Cos}(\upsilon_{\mathrm{Re}})\ \mathrm{Cos}(\theta) \\ \mathrm{Cos}(\upsilon_{\mathrm{Re}})\ \mathrm{Sin}(\theta) \\ -\mathrm{Sin}(\upsilon_{\mathrm{Re}}) \end{bmatrix} = \mathbf{s}_{\mathrm{Re}} + i\mathbf{s}_{\mathrm{Im}} \tag{2.29}$$

where $\mathbf{s}_{\mathrm{Re,Im}}$ are vectors in $\mathbb{R}^3$. It can be readily verified that $\mathbf{s}_{\mathrm{Re}} \cdot \mathbf{s}_{\mathrm{Im}} = 0$. For "simple" loops discussed earlier (Sec. 2.2.3.1) and in the limit of $|\mathbf{B}_{\mathrm{Im}}| \ll |\mathbf{B}_{\mathrm{Re}}|$ or $\upsilon_{\mathrm{Im}} \ll 1$, which is relevant to many of the measurements shown in Chapter 5, the real part of ϕ_B simplifies to

$$\mathrm{Re}(\phi_B) = \pi(1 - \mathrm{Cos}(\upsilon_{\mathrm{Re}})) + \mathcal{O}({\upsilon_{\mathrm{Im}}}^2) \tag{2.30}$$

which is approximately equal to one-half the solid angle Ω subtended by $\mathbf{s}_{\mathrm{Re}}$, similar to the Hermitian case. For the imaginary part of ϕ_B, we note that $|\mathbf{s}_{\mathrm{Re}}| = \mathrm{Cosh}(\upsilon_{\mathrm{Im}}) = 1 + \mathcal{O}({\upsilon_{\mathrm{Im}}}^2)$ and $|\mathbf{s}_{\mathrm{Im}}| = \mathrm{Sinh}(\upsilon_{\mathrm{Im}}) = |\upsilon_{\mathrm{Im}}| + \mathcal{O}({\upsilon_{\mathrm{Im}}}^3)$ and observe that the area of the mantle of the cone swept by $\mathbf{s}_{\mathrm{Re}}$ (see Fig. 2.6(c)) is $\widetilde{\Omega} = \pi\mathrm{Sin}(\upsilon_{\mathrm{Re}}) + \mathcal{O}({\upsilon_{\mathrm{Im}}}^2)$, and we have

$$\mathrm{Im}(\phi_B) = \pi(\mathrm{Sin}(\upsilon_{\mathrm{Re}})\mathrm{Sinh}(\upsilon_{\mathrm{Im}})) = \widetilde{\Omega}|\mathbf{s}_{\mathrm{Im}}| + \mathcal{O}({\upsilon_{\mathrm{Im}}}^2) \tag{2.31}$$

In the limit of $\upsilon \in \mathbb{R}$, which corresponds to $|\mathbf{s}_{\mathrm{Im}}| = 0$, this reduces to the stan-

dard (real) Hermitian geometric phase, even for H with complex eigenvalues λ. These intuitions are illustrated in Fig. 2.6(c).

2.2.3.3 Numerical method for calculating the geometric phase

For control loops that are not "simple" (Eq. (2.14)) there is no simple expression for ϕ_B, and thus we calculate it numerically as follows. We first discretize the loop into K equal steps, each starting at $s_k = k/K$ with $k = 0, 1, 2, ..., K$. In analogy to the Hermitian case (Eq. 3.6 in Ref. [143], Eq. 4 in Ref. [144]), the non-Hermitian ϕ_B can then be expressed as

$$\phi_{B,\pm} \approx -i \operatorname{Log}\left(\prod_{k=0}^{K-1} \vec{\mathrm{v}}_{\pm}(s_{k+1}).\vec{\mathrm{u}}_{\pm}(s_k)\right) \tag{2.32}$$

Thus, we calculate the geometric phase by computing the left and right eigenvectors at each step s_k (while ensuring there is a consistent choice of gauge between all K steps) and multiplying the chain of inner products above. For closed loops, this formulation is invariant to gauge choice, as $\vec{\mathrm{u}} \to e^{i\alpha}\vec{\mathrm{u}}$ and $\vec{\mathrm{v}} \to e^{-i\alpha}\vec{\mathrm{v}}$ for all $\alpha \in \mathbb{R}$. All such calculations presented in this thesis use $K = 20{,}000$.

2.2.3.4 Gauge-invariance of the imaginary part of the Berry connection

In this section, we show that the imaginary part of the Berry connection is gauge-invariant, from which it follows that the imaginary part of the geometric phase is also gauge independent, regardless of whether or not the path is closed [159]. This discussion is similar to that of Refs. [12, 160].

To begin, consider a choice of right and left eigenvectors $\vec{\mathrm{u}}_{\pm}, \vec{\mathrm{v}}_{\pm}$ that obey the joint normalization condition:

$$\vec{\mathrm{v}}_i.\vec{\mathrm{u}}_j = \delta_{ij} \tag{2.33}$$

An arbitrary state vector $\vec{\mathrm{d}}$ may be decomposed as $\vec{\mathrm{d}} = d_+\vec{\mathrm{u}}_+ + d_-\vec{\mathrm{u}}_-$ with complex coefficients $d_{\pm} = \vec{\mathrm{v}}_{\pm} \cdot \vec{\mathrm{d}}$. In this case, a state vector $\vec{\mathrm{d}}$ that is proportional to the eigenvector $\vec{\mathrm{u}}_i$ has population $|d_i|^2$.

Now, consider a different choice of right eigenvectors $\vec{\mathrm{u}}'_{\pm} = x_{\pm}\vec{\mathrm{u}}_{\pm}$ with nonzero

complex constants $|x_\pm|$. To satisfy the normalization condition above, the corresponding left eigenvectors must be $\vec{\mathrm{v}}'_\pm = \vec{\mathrm{v}}_\pm/x_\pm$. However, upon making this choice, the population of $\vec{\mathrm{d}}$ in eigenmode $\vec{\mathrm{u}}'_i$ is

$$|d'_i|^2 = |\vec{\mathrm{v}}'_i \cdot \vec{\mathrm{d}}|^2 = \left|\frac{\vec{\mathrm{v}}_i}{x_i} \cdot \vec{\mathrm{d}}\right|^2 = |d_i|^2/|x_i|^2 \tag{2.34}$$

where the population depends explicitly on $|x_i|$. Since the population of a mode encodes an absolute physical quantity (For example: for a system of coupled harmonic oscillators, it is proportional to the energy stored in an oscillator), it must be independent of the choice of gauge, i.e.,the choice of $\vec{\mathrm{u}}_\pm, \vec{\mathrm{v}}_\pm$. This is ensured by imposing an additional normalization condition:

$$|\vec{\mathrm{u}}^*_\pm . \vec{\mathrm{u}}_\pm|^2 = 1 \tag{2.35}$$

where $(*)$ denotes complex conjugation. Thus with condition Eq. (2.35), any choice of right eigenvectors, i.e.,choice of gauge, obeys $\vec{\mathrm{u}}'_\pm = x_\pm \vec{\mathrm{u}}_\pm$ with $|x_\pm| = 1$. Put another way, to preserve the gauge independence of populations, the only allowed gauge transformations of right eigenmodes $\vec{\mathrm{u}}_\pm$ are unitary complex numbers, just as in the Hermitian case. Under such gauge transformations, the real part of the Berry connection changes but the imaginary part does not. Subsequently, the imaginary component of the geometric phase is gauge-invariant for any path, including open ones. We empirically demonstrate this facet of the complex ϕ_B in Chapter 5.

2.2.3.5 Geometric amplifier: A prelude

For a control loop with $\mathrm{Im}(\phi_B) < 0$, the geometric phase contributes gain to the normal mode, and the amplitude of its motion should actually increase if this geometric gain exceeds the dynamical loss. For example, if $\mathrm{Im}(\phi_B) < \mathrm{Im}(\phi_D) < 0$. For any control loop $\mathcal{C}$, it is impossible to meet this condition in the large-T limit, as $\mathrm{Im}(\phi_B) \propto T^0$ while $\mathrm{Im}(\phi_D) \propto T^1$ and in this limit, the gain or loss of the normal mode would be dictated solely by $\mathrm{Im}(\phi_D)$.

However, for a given T that is compatible with the notion of adiabatic theorem, we have found that it is possible to find $\mathcal{C}$, such that the geometric gain amplifies the normal

mode's motion, regardless of how large T is. We give a teaser of this new mechanism for building an amplifier, by noting that for an advisedly chosen $\mathcal{C}_{\text{amp}}$, we can have a control loop duration T^* such that

$$T^* = \frac{\text{Im}(\phi_B)}{\text{Im}(\int_0^1 \lambda_+(s)ds)} \tag{2.36}$$

where the geometric gain (i.e., $\text{Im}(\phi_B) < 0$) has canceled the dynamical loss (i.e., $\text{Im}(\int_0^1 \lambda_+(s)ds) < 0$) for a control loop duration T^*. Now in order to arbitrarily extend T^*, we recall the additive property of ϕ_B upon repetitions of $\mathcal{C}_{\text{amp}}$, formally $\mathcal{C}_{\text{amp},n}$ (Sec. 2.2.3.1) and observe that

$$T_n^* = n\left(\frac{\text{Im}(\phi_B)}{\text{Im}(\int_0^1 \lambda_+(s)ds)}\right) = nT_{n=1}^* \forall\ n \in \mathbb{N} \tag{2.37}$$

We will give the full illustration of this Geometric amplifier in Chapter 6.

2.2.4 Illustrating the degenerate non-Hermitian geometric phase

In this section, we detail the topological and discrete geometric phase $\phi_{B,\text{deg}}$ corresponding to the space of degenerate $N \times N$ dynamical matrices: $\mathcal{EP}_N$, the space of highest order EP (EP_N). Such matrices are similar to an $N \times N$ Jordan block J_N. We start by stating the theoretical results and predictions of Refs. [88, 89] and provide some intuition for $\phi_{B,\text{deg}}$ (Sec. 2.2.4.1). We then highlight its broad accessibility in tunable systems and discuss its robustness to perturbations (Sec. 2.2.4.2). We conclude this section by working out an example of a general degenerate $N = 2$ mode system, and illustrate $\phi_{B,\text{deg}}$ (Sec. 2.2.4.3).

2.2.4.1 Topological and discrete geometric phase

This section details adiabatic transport in $\mathcal{EP}_N$. We show that upon initializing the system in the least-dissipative eigenvector of $H' = J_N - \epsilon\mathcal{A}_J$: the dynamical matrix that governs evolution in $\mathcal{EP}_N$, the system returns to itself and acquires a complex phase $\phi_{\text{deg}}(T)$ given by Eq. (2.11), in the adiabatic limit ($T \to \infty$). We then discuss the T-independent part of $\phi_{\text{deg}}(T)$ and show that: **(a)** It encodes the holonomy of the control loop in $\mathcal{EP}_N$ - and thus a geometric phase $\phi_{B,\text{deg}}$, **(b)** $\phi_{B,\text{deg}}$ is real-valued and discrete,

and depends solely on the homotopy class of the loop in $\mathcal{EP}_N$, i.e., it is topological.

Traversing control loops in $\mathcal{EP}_N$

For this discussion, we smoothly parameterize $\mathcal{EP}_N$ by the control parameters of $H_{\rm deg}$: $\mathrm{R}_{\rm deg}$, which form a (complex) N^2-N+1 dimensional space. The dimensionality can be understood as follows: an arbitrary complex $N\times N$ matrix is parameterized by arbitrary N^2 complex numbers. The condition that all N complex eigenvalues equal imposes $N-1$ complex constraints, leaving an N^2-N+1 (complex) dimensional parameter space.

A control loop in $\mathcal{EP}_N$: $\mathcal{C}_{\rm deg}$ is defined parametrically by $\mathrm{R}_{\rm deg}(s)$, with $0\leq s\leq 1$ and $\mathrm{R}_{\rm deg}(0)=\mathrm{R}_{\rm deg}(1)$. The system is then evolved in real time t for total duration of T and its evolution is given by

$$i\epsilon\partial_s\vec{c}=H_{\rm deg}\vec{c} \tag{2.38}$$

as in Eq. (1.1), where $\vec{c}$ is the state vector being evolved, with $\epsilon=1/T$ and $s=t/T$. For simplicity, we take $H_{\rm deg}$ to be traceless, which reduces the (complex) dimension of $\mathcal{EP}_N$ to N^2-N. A key point is to note that $H_{\rm deg}$ is a defective $N\times N$ matrix and Eq. (2.38) can be systematically studied under a similarity transformation (change of basis) that reduces it to a single Jordan block[1]: J_N. This similarity transformation is accomplished by an $N\times N$ matrix M, whose columns are given by the unique right eigenvector and $N-1$ generalized right eigenvectors of $H_{\rm deg}$. Upon this similarity transformation, Eq. (2.38) reads as

$$i\epsilon\partial_s\vec{c}_J=H'\vec{c}_J=(J_N-\epsilon\mathcal{A}_J)\vec{c} \tag{2.39}$$

where $\vec{c}=M\vec{c}_J, M^{-1}H_{\rm deg}M=J_N$ and $\mathcal{A}_J=iM^{-1}\frac{\partial M}{\partial s}$ is the matrix of Berry connection. As $\mathcal{C}_{\rm deg}$ is a (closed) loop, we have: $M(s=0)=M(s=1)$ and $\mathcal{A}_J(s=0)=\mathcal{A}_J(s=1)$.

Identifying initial states amenable to adiabatic evolution: Part I

Our interest lies in the solutions of Eq. (2.39) in the adiabatic limit, i.e. $T\to\infty\Rightarrow\epsilon\to 0$, such that the initial state returns to itself and acquires a complex phase. In this limit, the

[1]However, see a discussion in Sec. 7.3.2 and F.2 regarding the pitfall of working with the Jordan normal form, and how Schur decomposition remedies it for general considerations of $N=2$ case.

second term ($\epsilon\mathcal{A}_J$) of H' in Eq. (2.39) can be treated as a perturbation to the first term (J_N). Now the important idea is that while both $H_{\rm deg}$ and J_N are not diagonalizable (the characteristic feature of EP degeneracies), the perturbation on J_N, i.e., $H' = J_N - \epsilon\mathcal{A}_J$ generically is. This means we can apply the non-Hermitian adiabatic theorem to the expectedly non-degenerate H'. The following discussion is a recipe to find the asymptotic form of the eigenvalues of H': $\boldsymbol{\lambda'}$, and then select the least-dissipative eigenvalue λ'_+. λ'_+ provides the adiabatic complex phase via $\phi_{\rm deg}(T) = T\int_0^1 \lambda'_+(s)ds$ for the least-dissipative eigenvector of H'. The following recipe is adapted from [88, 89].

The characteristic equation of H' can be expressed as

$$(\lambda')^N + \sum_{r=0}^{N-1} b_r(\lambda')^r = 0 \tag{2.40}$$

where b_r can expressed in terms of the elements of H'. We also note that b_r for all $r = 0, 1, ..., N-1$ are order $\mathcal{O}(\epsilon)$ as $\epsilon \to 0$. This can be seen simply by noting that the eigenvalues of J_N are identically zero, and therefore the non-zero contribution comes from $\epsilon\mathcal{A}_J$, which in leading order is $\propto \epsilon$. Explicitly, they are given by

$$b_r = \epsilon\sum_{i=0}^{r} \mathcal{A}_{J_{N-r+i,i+1}} + \mathcal{O}(\epsilon^2) \tag{2.41}$$

Now it can be shown that in the limit $\epsilon \to 0$, $b_0 = \epsilon\mathcal{A}_{J_{N,1}}$ is the only term that contributes to the solutions of λ'_μ in Eq. (2.40), at leading order in ϵ, provided $b_0/\epsilon \neq 0$ [88, 89]. Consequently, these solutions can be expressed as $\lambda'_\mu = (e^{2\pi i\mu/N})(-\epsilon\mathcal{A}_0)^{1/N}$, at leading order in ϵ, for $\mu = 0, 1, ..., N-1$. Here we replaced $\mathcal{A}_{J_{N,1}} = \mathcal{A}_0$ and chose its principle branch, $\angle\mathcal{A}_0 \in (-\pi/N, \pi/N]$. The next order correction of λ'_μ is $\propto \epsilon^{2/N}$ and is given by $-(e^{4\pi i\mu/N})b_1(-b_0)^{2/N-1}/N$. Iteratively solving for each eigenvalue, one obtains the Puiseux expansion of λ'_μ [88, 89]

$$\begin{aligned}\lambda'_\mu &= (e^{2\pi i\mu/N})\epsilon^{1/N}(-\mathcal{A}_0)^{1/N} - (e^{4\pi i\mu/N})\epsilon^{2/N}(\mathcal{A}_{J_{N-1,1}} + \mathcal{A}_{J_{N,2}})(-\mathcal{A}_0)^{2/N-1}/N + ... \\ &= \sum_{r=1}^{\infty}(e^{2\pi i\mu r/N})\epsilon^{r/N}a_r\end{aligned} \tag{2.42}$$

and coefficients $a_r \equiv a_r(s)$. a_r can be seen to be independent of μ, because if λ'_μ in Eq. (2.42) satisfies the characteristic equation (Eq. (2.40)) for a value of μ, then it does for all μ.

Identifying initial states amenable to adiabatic evolution: Part II

Having obtained λ'_μ, we wish to identify the unique least-dissipative eigenvalue λ'_+. It corresponds to choosing a particular μ such that $\mathrm{Im}(\lambda'_\mu)$ has the largest value for all $s \in [0,1]$. The existence of such unique least-dissipative eigenvector is ensured by [88, 89]:

1. $\mathcal{A}_0 \neq 0$ for all $s \in [0,1]$.

2. $\mathcal{A}_0$ does not make a full circuit around the origin as s varies from 0 to 1 via the constraint $|\angle \mathcal{A}_0| < \pi$. Such an $\mathcal{A}_0$ does not touch or cross the negative real axis. Intuitively, allowing $\mathcal{A}_0$ to make a full circuit around the origin causes λ'_μ to braid, and specifically cause a net cyclic permutation.

As a result, for all $s \in [0,1]$, $\epsilon \to 0$, and for a given choice of $\mathcal{A}_0$ that satisfies the above conditions, λ'_+ is identified for the value of μ for which $\mathrm{Im}(\lambda'_\mu)$ is the largest value. However, if $\mathcal{A}_0 = 0$, additional analysis is required which is deemed beyond the scope of this thesis, and we never consider such cases.

Calculating $\phi_{\mathbf{deg}}(T)$ and isolating $\phi_{B,\mathbf{deg}}$

Subsequently, the appropriate value of μ is chosen and the corresponding adiabatic phase is then given by

$$\phi_\mu = \frac{1}{\epsilon}\int_0^1 \lambda'_\mu ds = \sum_{r=1}^{N} (e^{2\pi i \mu r/N})\epsilon^{r/N-1}\int_0^1 a_r(s) ds \tag{2.43}$$

where $r = N$ corresponds to the $\mathcal{O}(\epsilon^0)$ term, the T-independent phase. In particular it encodes the holonomy of $\mathcal{C}_{\mathrm{deg}}$ [88, 89]. This can be seen heuristically by observing that the calculations shown here are analogous to the non-degenerate case, and its value is

given by

$$\phi_{B,\mathrm{deg}} = -\int_0^1 a_N(s)ds \tag{2.44}$$

To obtain a_N, we evaluate the trace of H' i.e. $\mathrm{Tr}(H') = \sum_{\mu=0}^{N-1} \lambda'_\mu$ via Eq. (2.42). We observe that

$$\begin{aligned}\sum_{\mu=0}^{N-1} \lambda'_\mu &= \sum_{\mu=0}^{N-1}\sum_{r=1}^{N-1}(e^{2\pi i\mu r/N})\epsilon^{r/N}a_r + \sum_{\mu=0}^{N-1} a_N + \sum_{\mu=0}^{N-1}\sum_{r=N+1}^{\infty}(e^{2\pi i\mu r/N})\epsilon^{r/N}a_r \\ &= 0 + Na_N + 0\end{aligned} \tag{2.45}$$

where we have suggestively decomposed the above into three terms. The first term is 0 as the complex coefficients a_r for $r = 1, 2, ..., N-1$ are multiplied with N unitary complex numbers $e^{2\pi i\mu r/N}$, uniformly distributed around complex origin. The same exact reasoning holds for the complex coefficients a_r for $r = N+1, N+2, ..., 2N-1, 2N+1, ...3N-1, 3N+1, ...$, and a portion of the third term is 0. Finally, we are left with complex coefficients a_r for $r = 2N, 3N, ...$ for the third term. To evaluate these terms, we utilize: $\sum_{\mu=0}^{N-1} \lambda'_\mu = \mathrm{Tr}(H') = \mathrm{Tr}(J_N - \epsilon\mathcal{A}_J) = 0 - \epsilon\mathrm{Tr}(\mathcal{A}_J)$. Consequently, $a_{2N} = a_{3N} = ... = 0$ as they correspond to the coefficients of $\epsilon^2, \epsilon^3, ...$ terms in $\sum_{\mu=0}^{N-1} \lambda'_\mu$, respectively. Thus, we have

$$a_N = \frac{1}{N}\mathrm{Tr}(\mathcal{A}_J) \tag{2.46}$$

and

$$\phi_{B,\mathrm{deg}} = -\frac{1}{N}\int_0^1 \mathrm{Tr}(\mathcal{A}_J(s))ds \bmod 2\pi \tag{2.47}$$

A special class of loops in $\mathcal{EP}_N$

An important special class of loops $\mathcal{C}_{\mathrm{deg,sp}}$ exist in $\mathcal{EP}_N$ for which $\mathcal{A}_J$ is independent of s. In such a case, the coefficients in Eq. (2.41) are constant for each value of r. As a result, if the initial state (i.e., $s = 0$) is any one of the eigenvectors of H', the state evolves as the smoothly connected eigenvector as s is varied from 0 to 1. Subsequently,

any such eigenvector is amenable to the adiabatic transport as described above. Such loops are called "straight loops", with

$$M(s) = M(0)e^{is\mathcal{A}_J} \tag{2.48}$$

where we utilized: $M^{-1}M = \mathbb{I} = MM^{-1}$, thus $[\frac{\partial M}{\partial s}, M^{-1}] = 0$ i.e., $\frac{\partial M}{\partial s}$ and M^{-1} commute, which results in $M(s) = M(0)e^{i\int_0^s \mathcal{A}_J(s')ds'}$ and Eq. (2.48) follows.

One can then immediately calculate $\phi_{B,\mathrm{deg}}$ for traversing a "straight loop" in $\mathcal{EP}_N$ as:

$$\begin{aligned} e^{i\phi_{B,\mathrm{deg}}} &= \left[e^{i\mathrm{Tr}(\mathcal{A}_J)}\right]^{-1/N} \\ &= \left[\mathrm{Det}(e^{i\mathcal{A}_J})\right]^{-1/N} \\ &= \left[\mathrm{Det}(M(1))/\mathrm{Det}(M(0))\right]^{-1/N} \\ &= \left[\mathrm{Det}(M(0))/\mathrm{Det}(M(1))\right]^{1/N} \end{aligned} \tag{2.49}$$

where the N^{th} root is defined by imposing continuity on $\mathrm{Det}(M(s))^{1/N}$, and we used Eq. (2.48), the identity $\mathrm{Det}(e^K) = e^{\mathrm{Tr}(K)}$ [161] where K is a square matrix, and that $\mathrm{Det}(M^{-1}) = 1/\mathrm{Det}(M)$.

Salient features of $\phi_{B,\mathbf{deg}}$ and $\mathcal{EP}_N$ subspace

In this section, we describe some salient features of $\phi_{B,\mathrm{deg}}$ in Eq.(2.47) and of the structure of the degenerate subspace $\mathcal{EP}_N$ of an N mode system.

1. We first comment on the form of $\phi_{B,\mathrm{deg}}$ given by Eq. (2.47). We note that $\phi_{B,\mathrm{deg}}$ is proportional to a line integral of the Berry connection, which one may recognize as encoding the holonomy of $\mathcal{C}_{\mathrm{deg}}$, similar to its non-degenerate counterpart.

However, the fact that $\phi_{B,\mathrm{deg}}$ is proportional to the line integral of the trace of the Berry connection, i.e., it takes the "entire" Berry connection matrix into account, is a crucial distinction from its non-degenerate counter part, In particular, the non-degenerate case takes specific elements of the Berry connection matrix for a given

initial state. Explicitly: **(a)** for the Hermitian non-degenerate case, $\phi_{B,i} = \int_0^1 \mathcal{A}_{ii} ds$ (Eq. (2.8)) for a state vector initialized as its i^{th} eigenvector and then transported adiabatically, and **(b)** for the non-Hermitian non-degenerate case, $\phi_{B,+} = \int_0^1 \mathcal{A}_{++} ds$ (Eq. (2.19)) for a state vector initialized as its least-dissipative eigenvector and then transported adiabatically.

2. We note that although "straight loops" exist in $\mathcal{EP}_N$, $\mathcal{A}_J$ is not constant in general. Intuitively, variations in $\mathcal{A}_J$ that contribute at $\mathcal{O}(T^0)$, appear proportional to $\int_0^1 \partial_s \text{Log}(\mathcal{A}_0) ds$. Since one of the conditions that guarantee the existence of a unique least-dissipative eigenvector throughout the evolution along $\mathcal{C}_{\text{deg}}$ is that $\mathcal{A}_0$ does not make a circuit around the origin, $\int_0^1 \partial_s \text{Log}(\mathcal{A}_0) ds = 0$. This result is calculated in Refs.[88, 89] for any N, and we show this explicitly for the $N = 2$ case in Sec. A.3.2 via Eqs. (A.16) and (A.17).

As a result Eq. (2.49) holds for a general $\mathcal{C}_{\text{deg}}$, for which a unique least-dissipative eigenvector of $H' = J_N - \epsilon \mathcal{A}_J$ exists throughout.

3. We now comment on the form of $\phi_{B,\text{deg}}$ given by Eq. (2.49). Notice that for any $\mathcal{C}_{\text{deg}}$, $\text{Det}(M(0))/\text{Det}(M(1)) = 1$. However, choosing the N^{th} root is non-trivial and specifically requires the knowledge of homotopy class of $\mathcal{C}_{\text{deg}}$ in $\mathcal{EP}_N$. This naturally requires an examination of the geometry and the topology of $\mathcal{EP}_N$ subspace. It can be shown that the fundamental group of $\mathcal{EP}_N$: $\pi_1(\mathcal{EP}_N) \cong \mathbb{Z}_N$, the cyclic group of order N [88, 89], and thereby it is the winding number ($\mathcal{W}$) of $\mathcal{C}_{\text{deg}}$ in $\mathcal{EP}_N$ that determines its homotopy class.

From this result, $\mathcal{C}_{\text{deg}}$ with $\mathcal{W} \mod N = 0$ is contractible in $\mathcal{EP}_N$, whereas $\mathcal{W} \mod N \neq 0$ corresponds to a non-contractible $\mathcal{C}_{\text{deg}}$ in $\mathcal{EP}_N$. Finally, we determine $[\text{Det}(M(0))/\text{Det}(M(1))]^{1/N} = e^{i2\pi(\mathcal{W} \mod N)/N}$, and thus using Eq. (2.49):

$$\phi_{B,\text{deg}} = 2\pi(\mathcal{W} \mod N)/N \tag{2.50}$$

which demonstrates its dependence of the homotopy class of $\mathcal{C}_{\text{deg}}$, and also that it is real and discrete.

4. Finally, we note that the Berry curvature for $\mathcal{EP}_N$ is identically zero, and follows

from the same reasoning as for its Hermitian counterpart, i.e., the embedding of the degenerate subspace in the degenerate subspace itself, does not change as function of parameters or when parameters are tuned in real time. As a result, it does not contribute to $\phi_{B,\mathrm{deg}}$, same as its Hermitian counterpart.

However as shown above, $\phi_{B,\mathrm{deg}}$ is non-trivial for the non-Hermitian case as compared to its Hermitian counterpart where it is trivially zero. This highlights an important distinction between the two cases. As such the unique topological nature of $\phi_{B,\mathrm{deg}}$ in the non-Hermitian case arises solely from the non-trivial topology of $\mathcal{EP}_N$.

2.2.4.2 Broad accessibility and robustness to perturbation

In this section, we first clarify that the topological $\phi_{B,\mathrm{deg}}$ is broadly accessible, and not just a result of fine-tuning. We then discuss its robustness to perturbations away from the $\mathcal{EP}_N$ subspace.

In Sec. 2.2.4.1, we found that $\mathcal{EP}_N$ forms a (complex) $N^2 - N + 1$ dimensional subspace in the (complex) N^2 dimensional parameter space of arbitrary complex $N \times N$ matrices. For this discussion, we recall the procedure that led to this result: *All N complex eigenvalues being equal imposes $N - 1$ complex constraints*. If we then take the following viewpoint, where we can vary up to $2(N-1)$ (real) control parameters that solely tune these constraints (and by construction, the system stays in the $\mathcal{EP}_N$ subspace, albeit respecting new constraints). Then even if these specific $2(N-1)$ (real) control parameters are noisy, we obtain the same value of $\phi_{B,\mathrm{deg}}$ for the corresponding loop in $\mathcal{EP}_N$, as long as the noise does not alter the homotopy class of the loop. This illustrates the notion of accessibility, and some form of resilience to tuning parameters that are "noisy".

This leaves us with the other class of perturbations that do cause the system to leave the $\mathcal{EP}_N$ subspace. One can show that if such perturbations are of order $\mathcal{O}(1/T)$ and traceless, $\phi_{B,\mathrm{deg}}$ remains unchanged [88, 89]. This follows simply from the fact that such a perturbation would leave $\mathrm{Tr}(\mathcal{A}_J(s))$ unchanged up to order $\mathcal{O}(1/T)$ and $\phi_{B,\mathrm{deg}} = -\frac{1}{N}\int_0^1 \mathrm{Tr}(\mathcal{A}_J(s))ds$.

2.2.4.3 Example: $N = 2$

In this section, we provide a concrete illustration of $\phi_{B,\mathrm{deg}}$, by working out an example of an $N = 2$ mode system tuned in the $\mathcal{EP}_2$ subspace. We begin by describing the topology of $\mathcal{EP}_2$ and the control loops therein. We then parameterize them, and subsequently consider adiabatic transport. The result of this adiabatic transport is discussed in several limiting and special cases.

Topology of $\mathcal{EP}_2$ subspace

To describe the topology of $\mathcal{EP}_2$, we consider H as given in Eq. (2.13). H is degenerate when $\mathbf{B}_{\mathrm{Re}} \cdot \mathbf{B}_{\mathrm{Im}} = 0$ where $(\cdot)$ denotes the inner product, and $|\mathbf{B}_{\mathrm{Re}}| = |\mathbf{B}_{\mathrm{Im}}|$. For non-zero $\mathbf{B}_{\mathrm{Re,Im}}$, these degeneracies are EP_2 and form the $\mathcal{EP}_2$ subspace. Now consider a pair of unit vectors $\mathbf{b}_{\mathrm{Re,Im}}$ such that $\mathbf{b}_{\mathrm{Re}} \cdot \mathbf{b}_{\mathrm{Im}} = 0$ and $\mathbf{B}_{\mathrm{Re,Im}} = |\mathbf{B}_{\mathrm{Re,Im}}|\, \mathbf{b}_{\mathrm{Re,Im}}$. The space of all orientations of the $\mathbf{b}_{\mathrm{Re,Im}}$ pair form the special orthogonal group in $\mathbb{R}^3$: $\mathrm{SO}(3)$ [162]. Furthermore, $\mathrm{SO}(3) \cong \mathbb{R}\mathrm{P}^3$, the real 3-dimensional projective space, which is topologically equivalent to a 3-ball with its antipodal surface points identified [88, 89, 162]. Its fundamental group, $\pi_1(\mathbb{R}\mathrm{P}^3) \cong \mathbb{Z}_2$: the group of integers under addition modulo 2, and as such it is doubly connected [154]. Therefore, we have $\mathcal{EP}_2 \cong \mathbb{R}\mathrm{P}^3 \times \mathbb{R}$, where the second factor represents $\mathrm{Log}(|\mathbf{B}_{\mathrm{Re}}|)$, which is contractible (i.e., it has trivial fundamental group: $\pi_1 = \{1\}$). As a result the fundamental group of $\mathcal{EP}_2$ subspace, $\pi_1(\mathcal{EP}_2) \cong \mathbb{Z}_2$, i.e., it is also doubly connected.

From the discussion in Sec. 2.2.4.1 and above, control loops in $\mathcal{EP}_2$ can be associated with a winding number $\mathcal{W}$. Their homotopy class is determined by $\mathcal{W} \bmod 2$, which is either 0 (i.e., contractible to a point) or 1 (not contractible). They can be visualized in two complementary ways as described below, and are illustrated in Fig. 2.7.

(a) As equal length and relatively perpendicular $\mathbf{B}_{\mathrm{Re,Im}}$ tracing out a closed curve in $\mathbb{R}^3$. From the above discussion, this amounts to the corresponding pair $\mathbf{b}_{\mathrm{Re,Im}}$ to change its orientation continuously, with the same starting and ending orientation. We refer this as a *full rotation* [163]. Since $\mathrm{SO}(3) \cong \mathbb{R}\mathrm{P}^3$, we have $\pi_1(\mathrm{SO}(3)) \cong \mathbb{Z}_2$, and thus there are two classes of such *full rotations*: **(i)** topologically trivial, and the corresponding control loop is contractible to a point with its winding number

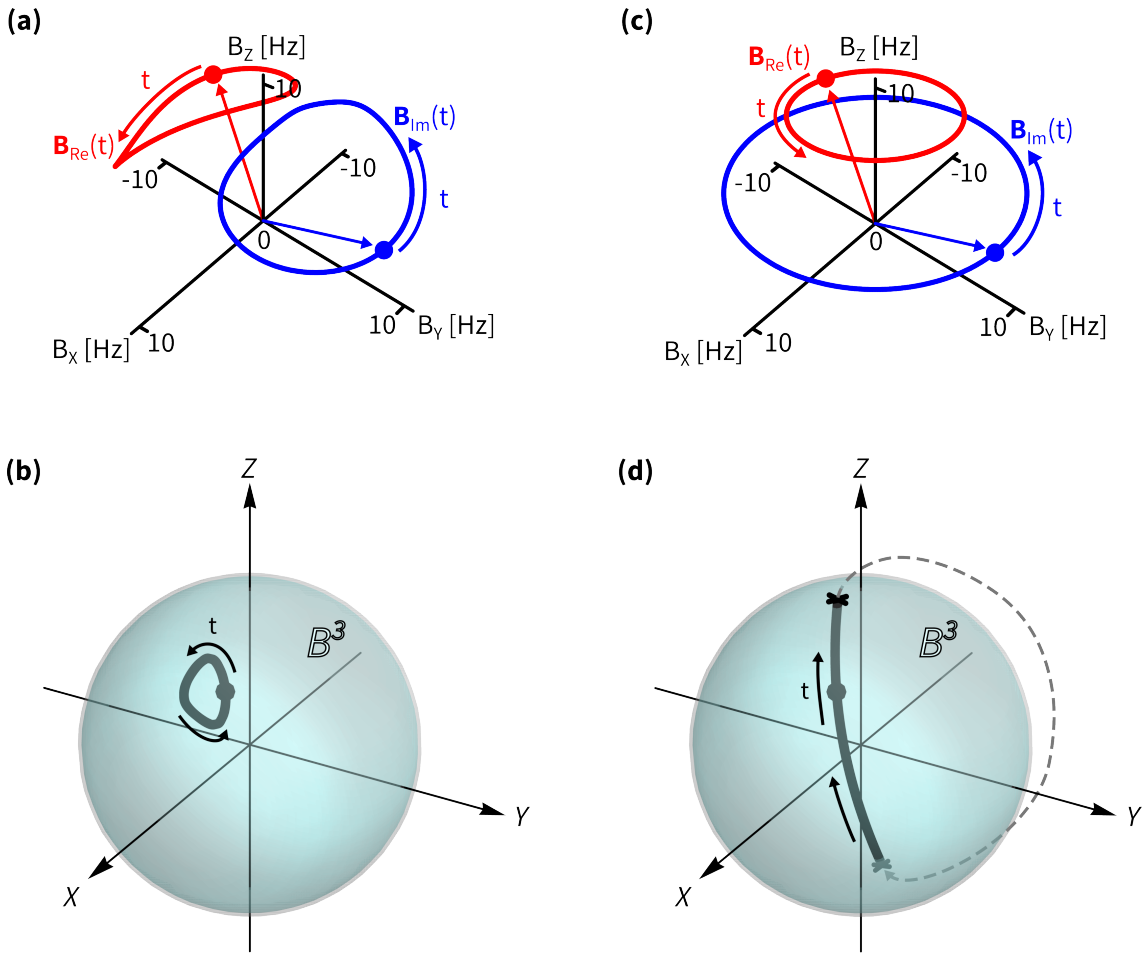

Figure 2.7: Control loops in $\mathcal{EP}_2$. **(a)** A contractible control loop in $\mathcal{EP}_2$ parameterized by H_{deg} in Eq. (2.51), shown using equal length and relatively perpendicular $\mathbf{B}_{\mathrm{Re,Im}}$ in $\mathbb{R}^3$. Circles: the starting and the stopping point of the loop, at $t = 0, T$, respectively; curves: $\mathbf{B}_{\mathrm{Re,Im}}$; arrows are a guide to the eye. For this control loop, $R(s)/2\pi = 10e^{i(0.5+0.8\,\mathrm{Sin}(\pi s)^2)}$ Hz, $p = 1, \mathcal{T}(s)/2\pi = 0$ and $\theta(s) = -2\mathrm{Sin}(\pi s + \pi/4)^2 - 0.4$. Note that for this loop, adiabatic evolution is not possible. **(b)** Same as (a) but the control loop (black curve with black disk as the starting point) is shown in $\mathbb{R}\mathrm{P}^3$ space, which in turn is represented as a 3-ball, B^3 (gray-cyan sphere, see Sec. A.4). **(c)** Same as (a) but showing a non-contractible loop. For this control loop, $R(s)/2\pi = 10e^{0.5i}$ Hz, $p = 1, \mathcal{T}(s)/2\pi = 0$ and $\theta(s) = -2\pi s - 1.4$. Note that for this loop, adiabatic evolution is possible. **(d)** Same as (c) but the control loop (black curve with black disk as the starting point) is shown in $\mathbb{R}\mathrm{P}^3$ space, represented as B^3.

$\mathcal{W} \bmod 2 = 0$, and **(ii)** topologically non-trivial, and the corresponding control loop is not contractible with $\mathcal{W} \bmod 2 = 1$.

(b) As closed paths mapped to $\mathbb{R}\mathrm{P}^3$ (see Sec. A.4).

Parameterizing the $\mathcal{EP}_2$ subspace, and the corresponding control loops

From our discussion in Sec. 2.2.4.1, $\mathcal{EP}_2$ is spanned by a $2(N^2-N+1)=6$ (real) dimensional parameter space. As a result, H in Eq. (2.14) can be re-parameterized as $H_{\rm deg}$ to span $\mathcal{EP}_2$. It is given by

$$H_{\rm deg} = \frac{\mathcal{T}}{2}\,\mathbb{I} + R\begin{bmatrix} 1 & pe^{i\theta} \\ -e^{-i\theta}/p & -1 \end{bmatrix} \tag{2.51}$$

where $R\in\mathbb{C}^{\times}$, $\mathcal{T}\in\mathbb{C}$, and both $(p,\theta)\in\mathbb{R}$. The four real parameters: $\{\mathrm{Re}(R),\mathrm{Im}(R),p,\theta\}$ completely span the space[1] of $\mathcal{EP}_2$ corresponding to the traceless part of $H_{\rm deg}$. The complex parameter $\mathcal{T}$ simply denotes the trace of $H_{\rm deg}$ and specifies its degenerate eigenvalue: $\lambda_{\rm deg}=\mathcal{T}/2$. As a result, $\{\mathrm{Re}(R),\mathrm{Im}(R),p,\theta,\mathrm{Re}(\mathcal{T}),\mathrm{Im}(\mathcal{T})\}$ are our six control knobs that completely span the $\mathcal{EP}_2$ subspace. Finally, Eqs. (2.14) and (2.51) are related by: $\{A=R, B=Rp, C=-R/p\}$ with the degeneracy condition $\sqrt{A^2+BC}=0$.

Adiabatic transport in $\mathcal{EP}_2$

As a first example, we perform a "simple" loop in $\mathcal{EP}_2$ subspace that is amenable to adiabatic transport. To accomplish that, we set $\theta(s)=(\theta_0-2n\pi s)$ defined modulo 2π with $n\in\mathbb{N}$. We vary s from 0 to 1 in duration T, while $\{R,p,\theta_0\}$ are fixed. This corresponds to rigidly rotating the fixed equal length and relatively perpendicular $\mathbf{B}_{\rm Re,Im}$ with arbitrary overall orientation, n times around the z axis at a constant rate. The trace $\mathcal{T}$ may vary. However, it will be shown below that it plays no role in the geometric phase. Following the prescription in Sec. 2.2.4.1, we have $H'(s,T)=\mathcal{T}(s)\,\mathbb{I}/2+J_2-\mathcal{A}_J(s)/T$, and explicitly

$$H'(s) = \begin{bmatrix} \mathcal{T}(s)/2 & 1 \\ 0 & \mathcal{T}(s)/2 \end{bmatrix} - \frac{\partial_s\theta}{T}\begin{bmatrix} cR & -c(1-cR) \\ -R & (1-cR) \end{bmatrix} \tag{2.52}$$

where we used $\vec{u}_1=\left(1,-e^{-i\theta(s)}/p\right)^{\rm T}$ as the unique right eigenvector of $H_{\rm deg}$ and $\vec{u}_2=\left(c,(1/R-c)e^{-i\theta(s)}/p\right)^{\rm T}/2$ as a generalized right eigenvector $H_{\rm deg}$ with $c\in\mathbb{C}$. The

[1] $\mathbb{C}^{\times}$ is the set of all nonzero complex numbers. More precisely, $R=0$ is excluded from the parameter space, as for $R=0$ the resulting $H_{\rm deg}$ is diagonal, which does not belong to $\mathcal{EP}_2$.

Berry connection matrix $\mathcal{A}_J = iM^{-1}\frac{\partial M}{\partial s}$, where the columns of M are composed of $\vec{u}_{1,2}$. Substituting $\partial_s\theta = -2n\pi$ renders $\mathcal{A}_J$ to be a constant matrix, and thus in the language of Sec. 2.2.4.1 and Ref. [88, 89], such "simple" loops correspond to "straight loops" in $\mathcal{EP}_2$. See Sec. A.3.2 for further discussion about general control loops in $\mathcal{EP}_2$ that allow adiabatic evolution.

Subsequently, the eigenvalues of H' in Eq. (2.52) are given by:

$$\lambda'_{\pm}(s) = \frac{\mathcal{T}(s)}{2} + \frac{\partial_s\theta}{2T} \pm \frac{\sqrt{\partial_s\theta(4RT + \partial_s\theta)}}{2T} \tag{2.53}$$

with the corresponding right eigenvectors

$$\vec{u}\,'_{\pm}(s) = M^{-1}(s)\begin{bmatrix} 1 + \frac{\partial_s\theta}{2RT} \pm \sqrt{\frac{\partial_s\theta}{RT}\left(1 + \frac{\partial_s\theta}{4RT}\right)} \\ -e^{i\theta(s)}/p \end{bmatrix} \tag{2.54}$$

where '$+$' is chosen to denote the least-dissipative eigenvector and '$-$' denotes the other mode. In the limit $T \to \infty$, $\lambda'_{\pm} \to \lambda_{\mathrm{deg}}$ and $\vec{u}\,'_{\pm} \to M^{-1}\vec{u}_1 = (1,0)^{\mathrm{T}}$.

Following the prescription in Refs. [88, 89] and as described in Sec. 2.2.4.1, if we prepare an initial state as the least-dissipative eigenvector of H', i.e., $\vec{u}\,'_{+}$, and vary θ adiabatically (i.e., T is large) and strictly monotonically to ensure the uniqueness of $\vec{u}\,'_{+}$, we expect the final state to be given by $\vec{c}(T) = e^{-i\phi_{\mathrm{deg}}(T)}\vec{c}(0)$, where the complex valued $\phi_{\mathrm{deg}}(T)$ is exactly given by

$$\begin{aligned}
\phi_{\mathrm{deg}}(T) &= T\int_0^1 \lambda'_{+}(s)ds \\
&= T\int_0^1 \frac{\mathcal{T}(s)}{2}ds + \int_0^1 \frac{\partial_s\theta}{2}ds + \int_0^1 \frac{\sqrt{\partial_s\theta(4RT + \partial_s\theta)}}{2}ds \qquad (2.55)\\
&= T\int_0^1 \frac{\mathcal{T}(s)}{2}ds + n\pi \bmod 2\pi + i\int_0^1 \sqrt{n\pi(2RT - n\pi)}ds \qquad (2.56)\\
&= T\int_0^1 \frac{\mathcal{T}(s)}{2}ds + (n \bmod 2)\,\pi + i\sqrt{n\pi(2RT - n\pi)} \qquad (2.57)
\end{aligned}$$

where the first term of Eqs. (2.55)-(2.57) is the linear dynamical phase $\phi_{\mathrm{LD,deg}} \propto T$. The

second term is the time-independent part $\phi_{B,\mathrm{deg}} \propto T^0$, and Eq. (2.56) follows from Eq. (2.55) straightforwardly. It is real, and is precisely determined by the homotopy class of the control loop i.e., $n \bmod 2$ in this case. More explicitly, for even (odd) n, the control loop parametrized by $\theta(s) = (\theta_0 - 2n\pi s) \bmod 2\pi$ with fixed $\{R, p\}$ is contractible (non-contractible) in the $\mathcal{EP}_2$ subspace (see also Sec. A.4). In Sec. A.3.2, we explicitly show that allowing $\{R, p\}$ to vary in the control loop will leave this result unchanged. Finally for the third term, we replaced $\theta(s) = (\theta_0 - 2n\pi s) \bmod 2\pi$ in Eq. (2.55) to obtain Eq. (2.56), and for a constant R, we have Eq. (2.57). It represents additional dynamical phases which can be expanded in fractional powers of T and $1/T$, as a Puiseux series given in Eq. (2.11), and we provide more details in Sec. A.3.1.2.

In the large T limit, i.e., $T \to \infty$, $\phi_{\mathrm{deg}}(T)$ simplifies to

$$\phi_{\mathrm{deg}}(T) - \phi_{\mathrm{LD,deg}} = n\pi \bmod 2\pi + i\sqrt{2n\pi RT} + \mathcal{O}(1/\sqrt{T}) \tag{2.58}$$

where we used $2RT \gg n\pi$. We numerically simulated an $N = 2$ mode system for a choice of fixed $\{R, p, \mathcal{T}\}$, with $\theta(s) = (0 - 2\pi ns) \bmod 2\pi$ and Fig. 2.8(a) illustrates the complex valued $\phi_{\mathrm{deg}}(T) - \phi_{\mathrm{LD,deg}}$. Specifically, it highlights that the real part of $\phi_{\mathrm{deg}}(T) - \phi_{\mathrm{LD,deg}}$ has an intercept of magnitude π and a $\sqrt{T}$ contribution. The imaginary part has a zero intercept with a "stretched exponential" gain given by $\mathrm{Im}(i\sqrt{2\pi RT})$ for large T (see also Fig. 1.2 of Ref. [89]).

Special case of positive real-valued R

As shown in Eq. (2.58), for a generic complex (but fixed) R, the asymptotic form of $\phi_{\mathrm{deg}}(T) - \phi_{\mathrm{LD,deg}}$ and consequently its real-part has a $\propto \sqrt{T}$ contribution, which diverges as $T \to \infty$. While it may not represent a fundamental impediment to isolate $\phi_{B,\mathrm{deg}}$ from $\phi_{\mathrm{deg}}(T) - \phi_{\mathrm{LD,deg}}$, the story may be simplified if one were to 'somehow' eliminate the $\sqrt{T}$-contribution. Furthermore, such a situation would be desirable for actual experiments where it is a useful strategy to nullify dynamical phases that diverge as $T \to \infty$, thereby isolating the finite geometric part more 'naturally' from the raw data. Such instances can be found in experiments with superconducting qubits [164–168] and NV centers in diamond [169, 170], in the Hermitian case. The following discussion illustrates how one

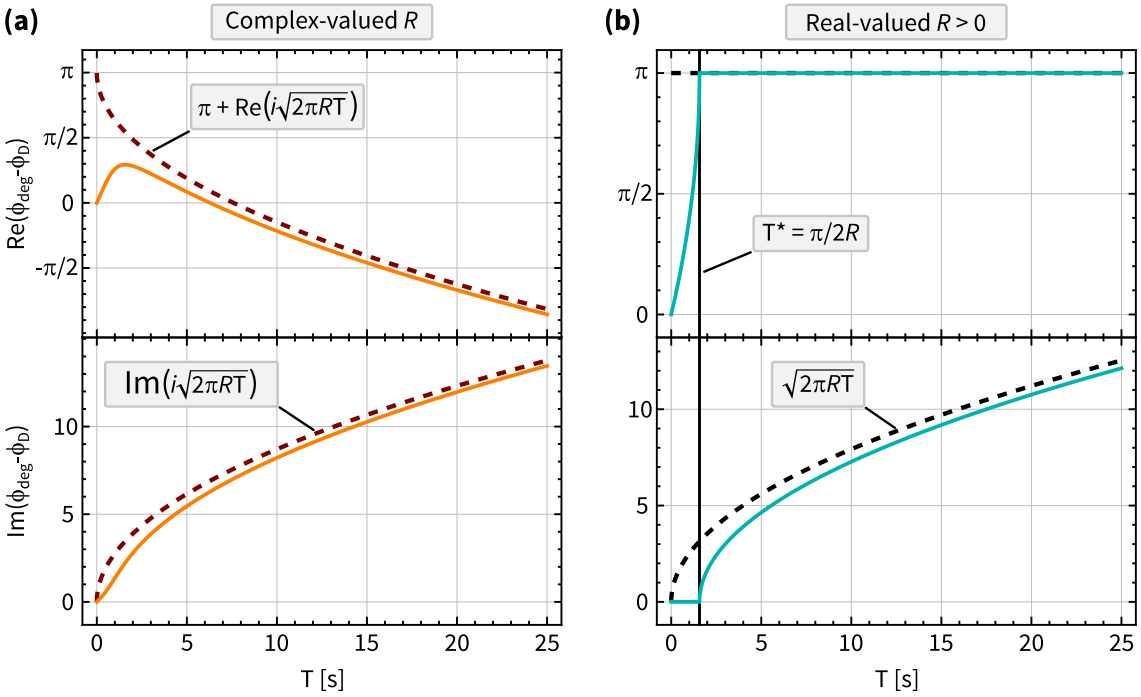

Figure 2.8: Real time evolution in $\mathcal{EP}_2$. (a) Numerically simulated real time evolution in $\mathcal{EP}_2$, for a constant complex-valued R. For this simulation, $R/2\pi = (1+i)$ Hz, $p = 17, \mathcal{T}(s)/2\pi = (1-i)$ Hz and $\theta(s) = -2\pi ns$. Orange curve: $\phi_{\rm deg}(T) - \phi_D$; dashed red curve: $\pi + \mathrm{Re}(i\sqrt{2\pi RT})$ for the top panel and $\mathrm{Im}(i\sqrt{2\pi RT})$ for the bottom panel. **(b)** Same as panel (a) but for a positive real-valued R. For this simulation, $R/2\pi = 1$ Hz, $p = 17, \mathcal{T}(s)/2\pi = (1-i)$ Hz and $\theta(s) = -2\pi ns$. Cyan curve: $\phi_{\rm deg}(T) - \phi_{\rm LD,deg}$; dashed black curve: π for the top panel and $\sqrt{2\pi RT}$ for the bottom panel; black vertical line: $T^* = n\pi/2R = \pi/2R$ for this case.

may eliminate the $\sqrt{T}$-contribution from the real part of $\phi_{\rm deg}(T) - \phi_{\rm LD,deg}$.

Case 1. Real-valued and constant $R > 0$, "simple" control loops

The simplest situation in which one can eliminate the $\sqrt{T}$-contribution is to constrain $R(s)$ to be a positive real-valued constant. In that case, Eq. (2.56) predicts an exact result: **(a)** For $T_s = n\pi/2R$, $\phi_{\rm deg}(T_s) - \phi_{\rm LD,deg} = n\pi$ and **(b)** For $T \geq T_s = n\pi/2R$, $\mathrm{Re}(\phi_{\rm deg}(T) - \phi_{\rm LD,deg}) = n\pi$. A numerical simulation corresponding to real-valued $R > 0$ is illustrated in Fig. 2.8(b).

Case 2. Real-valued and constant $R > 0$, "non-simple" control loops

"Non-simple" loops with positive real-valued constant R, are parameterized by $\theta(s) = -2n\pi k(s)$ with $n \in \mathbb{N}$ and $0 \leq s \leq 1$ with real valued $k(s) \neq s$, $k(0) = 0$, $k(1) = 1$

and $\partial_s k(s) > 0 \implies \partial_s \theta < 0$, where the last condition is strictly required to guarantee a unique least-dissipative eigenvector [88, 89] throughout the control loop. An analysis similar to case 1 (above) shows that there indeed exists: **(a)** A particular solution, i.e., for $T = T_s$, $\phi_{\rm deg}(T_s) - \phi_D = n\pi$, and **(b)** A general solution, i.e., for $T \geq T^*$, $\mathrm{Re}(\phi_{\rm deg}(T \geq T^*) - \phi_D) = n\pi$.

To obtain T_s we investigate the third term of Eq. (2.55), further. Consider the integral $\mathcal{Q} = \int_0^1 \sqrt{\partial_s k(4RT - 2n\pi\partial_s k)} ds$. Using the Cauchy-Schwarz inequality [171], we have

$$0 \leq |\mathcal{Q}| \leq \sqrt{\int_0^1 |4RT\partial_s k - 2n\pi(\partial_s k)^2|\, ds} = \sqrt{\left|4RT - 2n\pi \int_0^1 (\partial_s k)^2 ds\right|} \tag{2.59}$$

Consequently,

$$0 \leq |\mathcal{Q}| \leq \sqrt{\left|4RT - 2n\pi \left(\int_0^1 \partial_s k ds\right)^2\right|} \leq \sqrt{4RT - 2n\pi} \tag{2.60}$$

where we used the Cauchy-Schwarz inequality for the second integral, and assumed $4RT \geq 2n\pi$. For $T_s = n\pi/2R$, $|\mathcal{Q}|$ is identically zero as $\sqrt{4RT_s - 2n\pi}$ vanishes and thus we have $\phi_{\rm deg}(T_s) - \phi_D = n\pi$. Remarkably, the value of T_s here is equal to the value obtained in case 1, above.

We now search for a T^* such that $\mathrm{Re}(\phi_{\rm deg}(T \geq T^*) - \phi_D) = n\pi$. Similar to case 2 above, if we can show that $\mathrm{Im}(\mathcal{Q}) = 0$ for $T \geq T^*$, our task is complete. Observe that $\mathrm{Im}\left(\sqrt{\partial_s k(4RT - 2n\pi\partial_s k)}\right) = \sqrt{\partial_s k}\ \mathrm{Im}\left(\sqrt{(4RT - 2n\pi\partial_s k)}\right)$ as we constrained $\partial_s k > 0$. Subsequently, one can ensure $\mathrm{Im}\left(\sqrt{4RT - 2n\pi\partial_s k}\right) = 0$ for all $s \in [0, 1]$ by choosing $T^* = \frac{n\pi}{2R}(\partial_s k)_{\max}$, where $(\partial_s k)_{\max}$ denotes the largest slope of $k(s)$ for $0 \leq s \leq 1$. Distinct control loops would require distinct values of T^*, as given by the corresponding values of $(\partial_s k)_{\max}$, and our task is complete.

Case 3. Real-valued $R(s) > 0$, "simple" control loops

For "simple" control loops, i.e, $\theta(s) = -2n\pi s$ with real-valued but varying $R(s) > 0$ for $0 \leq s \leq 1$ and $R(0) = R(1)$, one recomputes $\mathcal{A}_J$, followed by H', its eigenvalues $\boldsymbol{\lambda'}$, and

thus $\phi_{\rm deg}(T)$. This exercise is carried out in Sec. A.3.2, and the resulting $\phi_{\rm deg}(T)-\phi_{\rm LD,deg}$ is adapted from Eq. (A.17) as

$$\phi_{\rm deg}(T) - \phi_{\rm LD,deg} = n\pi \mod 2\pi \\ + i\int_0^1 \sqrt{2n\pi R(s)T + (\partial_s {\rm Log}(R)/2 - in\pi)^2}ds \tag{2.61}$$

Now consider the second term of Eq. (2.61), which we denote as $i\mathcal{I}(T)$. The task at hand is to show that for $T \geq T^*$, $\mathcal{I}(T \geq T^*)$ is real-valued, and thus ${\rm Re}(\phi_{\rm deg}(T \geq T^*)-\phi_D) = n\pi \mod 2\pi$. A general solution that guarantees this is given by its integrand being real i.e., ${\rm Im}\left(\sqrt{2n\pi R(s)T + (\partial_s {\rm Log}(R)/2 - in\pi)^2}\right) = 0$ for all $s \in [0,1]$, and $T \geq T^*$. Unfortunately, this cannot be ensured due to the $in\pi$ term.

However, one can work in the large T limit such that

$${\rm Re}\left(\phi_{\rm deg}(T) - \phi_{\rm LD,deg}\right) = n\pi \mod 2\pi + \sqrt{\frac{n\pi}{8T}}\int_0^1 \frac{\partial_s {\rm Log}(R)}{\sqrt{R(s)}}ds + \mathcal{O}\left(\frac{1}{T^{3/2}}\right) \tag{2.62}$$

where we assumed $2n\pi R(s)T \gg \{(\partial_s {\rm Log}(R))^2, n^2\pi^2, n\pi\partial_s {\rm Log}(R)\}\ \forall\ s \in [0,1]$. As a result, in the limit $T \to \infty$, ${\rm Re}\left(\phi_{\rm deg}(T) - \phi_{\rm LD,deg}\right)$ in Eq. (2.62) asymptotes to $\phi_{B,\rm deg} = n\pi \mod 2\pi$. While it may resemble the non-degenerate Hermitian case (or the real part of non-degenerate non-Hermitian case), the approach to $\phi_{B,\rm deg}$ is distinct. In this case, the approach is $\mathcal{O}(1/\sqrt{T})$, whereas for the non-degenerate counterpart, it is $\mathcal{O}(1/T)$.

Case 4. Real-valued $R(s) > 0$, "non-simple" control loops

This represents a combination of cases 2 and 3, from above. As result, one can combine the corresponding analysis to produce a modified version of Eq. (2.62) given by

$${\rm Re}\left(\phi_{\rm deg}(T) - \phi_{\rm LD,deg}\right) = n\pi \mod 2\pi + \sqrt{\frac{n\pi}{8T}}\int_0^1 \sqrt{\frac{\partial_s k}{R(s)}}\partial_s {\rm Log}(R)ds + \mathcal{O}\left(\frac{1}{T^{3/2}}\right) \tag{2.63}$$

where we utilized $\theta(s) = -2n\pi k(s)$, as in case 2, and subsequently, $2n\pi R(s)T\partial_s k \gg \{(\partial_s \mathrm{Log}(R))^2, (n\pi\partial_s k)^2, n\pi\partial_s k\, \partial_s \mathrm{Log}(R)\}\ \forall\ s \in [0,1]$. As a result, in the limit $T \to \infty$, $\mathrm{Re}\left(\phi_{\mathrm{deg}}(T) - \phi_{\mathrm{LD,deg}}\right)$ in Eq. (2.63) asymptotes to $\phi_{B,\mathrm{deg}} = n\pi \mod 2\pi$, and the approach is $\mathcal{O}(1/\sqrt{T})$.

This concludes our analysis for the special case of positive real-valued R. It will be empirically demonstrated in Chapter 7 that such R are abundantly accessible, which simplifies the measurement of the topological $\phi_{B,\mathrm{deg}}$. We provide further intuition on parameterizing H_{deg} as in Eq. (2.51), and for R in Chapter 7.

2.3 Cavity Optomechanical platform for non-Hermitian physics

In this section, we describe the interactions between light that is trapped inside a high-finesse optical cavity, and a mechanically compliant object in the cavity. The light exerts radiation pressure force on the mechanics, thereby modifying the mechanics' motion, which in turn modulates the light by changing its amplitude and phase (or frequency). The remarkable ability to use radiation pressure to tune the mechanics' motion [172–176] and simultaneously detect it interferometrically [174–177], has resulted in many groundbreaking observations [178–187], and it forms the backbone of all experiments reported in this thesis.

In the following, we outline a canonical model that describes the optomechanical interaction between an optical cavity mode and a mechanical mode. We specifically highlight the optical control and measurement of the mechanical motion. We then extend this description for controlling and measuring two and three mechanical modes that are "coupled" to each other via an intermediary optical cavity mode. We subsequently connect them to a system of $N = 2$ or 3 coupled harmonic oscillators, respectively, whose parameters can be tuned over a wide range, and subsequently show that they are well poised to experimentally investigate the theoretical predictions in Secs. 2.1 and 2.2. A detailed derivation of the optomechanical model presented here can be found in Refs. [43, 61, 94, 95, 188].

2.3.1 Single mode optomechanics

A canonical cavity optomechanical system consists of two linear harmonic oscillators: an optical cavity mode and a mechanical mode coupled via radiation pressure. The classical Hamiltonian function $H_{\mathrm{full},1}$ of such a system is given by

$$H_{\mathrm{full},1} = \hbar\left(\Omega - \frac{i\kappa}{2}\right) a^* a + \hbar\left(\omega^{(0)} - \frac{i\gamma^{(0)}}{2}\right) \tilde{c}^*\tilde{c} + \hbar g_0(\tilde{c} + \tilde{c}^*)|a|^2 \tag{2.64}$$

which is composed of three terms. The first term describes the optical cavity mode with resonance frequency Ω, linewidth κ, and complex-valued amplitude a in units of the square-root of the number of photons, and * denotes complex conjugation. The second term describes the mechanical mode with bare (natural) resonance frequency $\omega^{(0)}$, bare damping rate $\gamma^{(0)}$ and complex-valued amplitude $\tilde{c}$ in units of zero-point fluctuation of mechanics (x_{ZPF}). The third term corresponds to the radiation pressure mediated interaction between the optical cavity mode and the mechanical mode. It is characterized by the coupling strength g_0, the real valued mechanical amplitude ($\tilde{c}+\tilde{c}^*$) and the optical mode's intensity ($|a|^2$). Intuitively, the coupling strength is quantified as the shift in resonance frequency of the optical cavity, $\Omega \to \Omega + g_0$ for x_{ZPF} amount of displacement of the mechanical mode. We note that while the present description is intended to be purely classical, the appearance of the reduced Plank's constant $\hbar$, zero-point fluctuation x_{ZPF} and quantification of optical field as number of photons, is only to conform with the broader literature on optomechanics.

For our experiments, the general setting involves driving the optical cavity with several laser tones, but here we begin by considering the case of just one tone. Such a drive is given by an complex amplitude a_{in}:

$$a_{\mathrm{in}} = e^{-i((\Omega+\Delta)t+\theta)}\sqrt{\frac{P}{\hbar(\Omega+\Delta)}} \tag{2.65}$$

which is parameterized by the laser tone's power P, detuning from the cavity resonance Δ and phase θ. Subsequently, the dynamics of a and $\tilde{c}$ are governed by Hamilton's equations of motion:

$$\begin{aligned}
\dot{a} &= -\left(\frac{\kappa}{2} - i\Omega + ig_0(\tilde{c}+\tilde{c}^*)\right)a + \sqrt{\kappa_{\mathrm{in}}}a_{\mathrm{in}} \\
\dot{\tilde{c}} &= -\left(i\omega^{(0)} + \frac{\gamma^{(0)}}{2}\right)\tilde{c} - ig_0|a|^2 + c_{\mathrm{in}}
\end{aligned} \tag{2.66}$$

where κ_{in} denotes the input coupling rate for driving laser tone, and c_{in} denotes additional mechanical drives, which includes the intrinsic Brownian noise force. The system we are concerned with has the following hierarchy of rates: $\kappa \gg \{g_0, \gamma^{(0)}\}$. This allows us to

linearize the optomechanical interaction by considering the optical mode $a = \bar{a} + d$ with $d \ll \bar{a}$. By adiabatically eliminating it from the equation of motion for the mechanical mode, we have:

$$\dot{\tilde{c}} = -i\left(\omega^{(0)} - \frac{i\gamma^{(0)}}{2} + \sigma\right)\tilde{c} + c_{\mathrm{in}} \tag{2.67}$$

where

$$\sigma = -i\kappa_{\mathrm{in}} g_0^2 \frac{P}{\hbar(\Omega + \Delta)} |\chi_c(\Delta)|^2 \left(\chi_c(\omega^{(0)} + \Delta) - \chi_c(\omega^{(0)} - \Delta)\right) \tag{2.68}$$

and $\chi_{\mathrm{c}}(\omega) = (\kappa/2 - i\omega)^{-1}$ is the optical cavity susceptibility. We note that in order to obtain Eqs. (2.67) and (2.68), we made the following assumptions:

(a) The mechanical mode has a high quality (Q) factor i.e. $\omega^{(0)}/\gamma^{(0)} \gg 1$, such that $\tilde{c}$ and $\tilde{c}^*$ are independent of each other.

(b) As an extension of $\kappa \gg \{g_0, \gamma^{(0)}\}$, the mechanical mode experiences almost a constant optical cavity susceptibility evaluated at its resonance frequency i.e. $\chi_{\mathrm{c}}(\omega) \to \chi_c(\omega^{(0)})$.

2.3.1.1 Optomechanical control

As seen in Eqs. (2.67) and (2.68), the optomechanical interaction tunes the mechanical resonance, both in its frequency and damping rate via the complex-valued σ, the optomechanical "self-energy" [175]. The frequency tuning is known as the "optical-spring" effect and results from the real part of σ, while the damping results from the imaginary part of σ, and together they constitute the dynamical backaction effect (DBA) [172, 173, 175].

It can be shown that the range of tunability via σ implicitly depends on the ratio $\kappa/\omega^{(0)}$ with its scale set by the optomechanical coupling strength g_0. The magnitude of this control is tuned via the laser tone's power P and its detuning from the cavity resonance Δ, respectively and they form the relevant control knobs. We illustrate and quantify this control in Fig. 2.9(a). For these simulations, we modeled the optomechanical system as the membrane-in-the-middle (MIM) platform [78, 79], in which $\sigma(P, \Delta)$ can

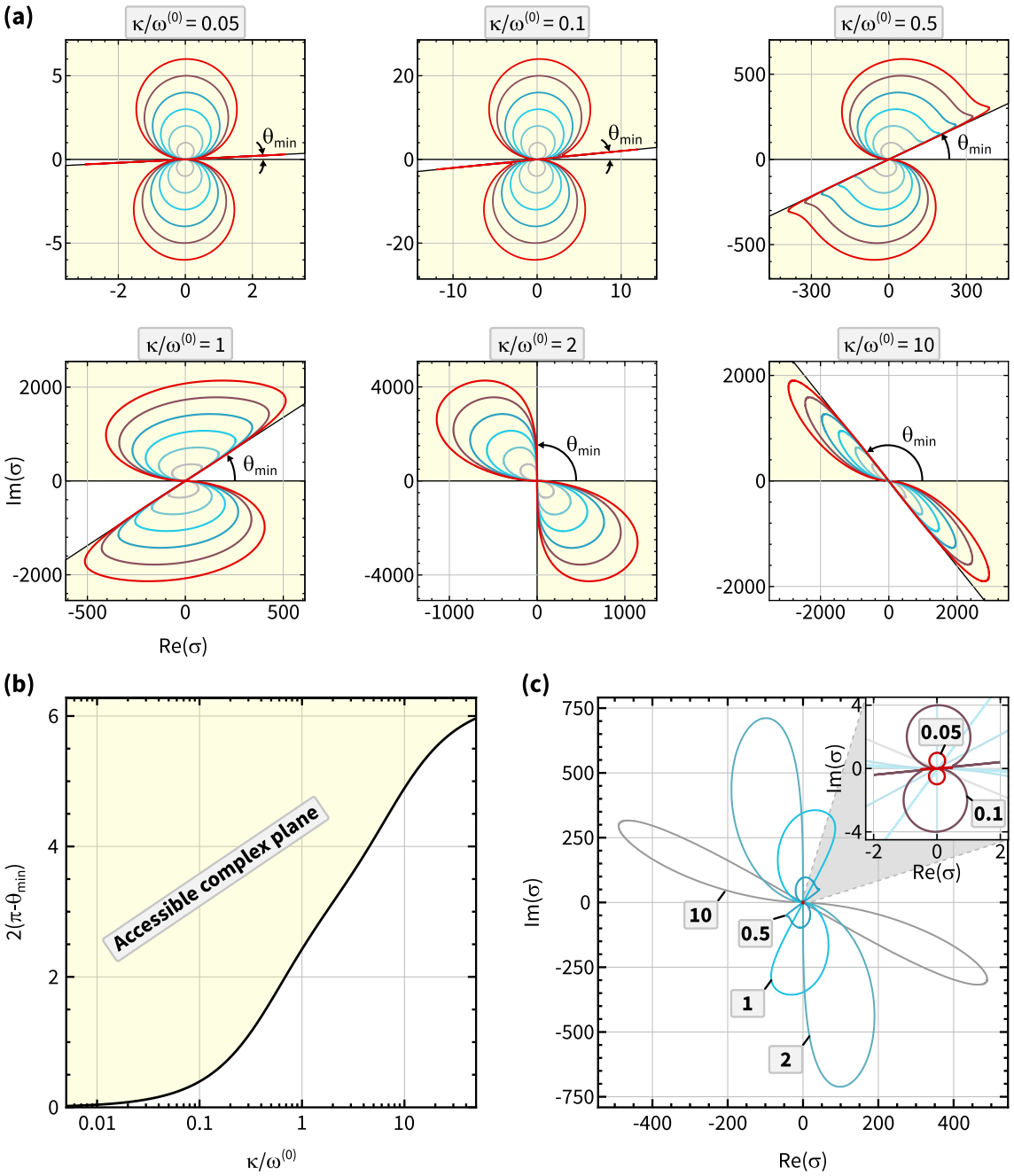

Figure 2.9: Optomechanical control via DBA. (a) Optical spring $\mathrm{Re}(\sigma)$ and optical damping $\mathrm{Im}(\sigma)$ as a function of laser tone's power P and detuning from cavity resonance Δ, for several ratios of $\kappa/\omega^{(0)}$. In each panel, σ is parametrically plotted as a function of $\Delta/\omega^{(0)} \in$ [-20,20], for $100 \leq P \leq 600$, in steps of 100. Gray to red curves indicate low to high P values. The accessible complex plane is shaded in yellow with its bounds demarcated by $\pm\theta_{\mathrm{min}}$ and the x-axis. σ is given in units of $\mathcal{J}P$. **(b)** The accessible of the complex plane of eigenvalues. It is quantified by $2(\pi - \theta_{\mathrm{min}})$ and plotted as a function of $\kappa/\omega^{(0)}$. **(c)** Trade-off between accessibility of complex plane and the size of σ, as a function of $\kappa/\omega^{(0)}$. For this plot, σ is parametrically plotted as a function of $\Delta/\omega^{(0)} \in$ [-20,20] with $P = 100$. $\kappa/\omega^{(0)}$ values for each curve are labeled.

be re-expressed from Eqs. (58,59) of Ref. [175] as

$$\mathrm{Re}(\sigma) = \frac{2\alpha|r_c|^2\mathcal{F}^2\Omega g(x_m)^2}{\pi^2 c^2 m\omega^{(0)}}\frac{w^3 P}{w^2+x^2}\left(\frac{x+1}{w^2/4+(x-1)^2}+\frac{x-1}{w^2/4+(x-1)^2}\right)$$

$$\mathrm{Im}(\sigma) = \frac{2\alpha|r_c|^2\mathcal{F}^2\Omega g(x_m)^2}{\pi^2 c^2 m\omega^{(0)}}\frac{w^4 P}{w^2+x^2}\left(\frac{1}{w^2/4+(x-1)^2}-\frac{1}{w^2/4+(x-1)^2}\right) \quad (2.69)$$

where we substituted: $x \equiv \Delta/\omega^{(0)}, w \equiv \kappa/\omega^{(0)}, \kappa_{\mathrm{in}} = \alpha/\kappa, g_0 = \frac{2|r_c|\Omega g(x_m)\kappa\mathcal{F}}{\pi c}$ with $g(x_m) = \frac{\mathrm{Sin}(2\Omega x_m/c)}{\sqrt{1-|r_c|^2\mathrm{Cos}(2\Omega x_m/c)^2}}$. $|r_c|$ and m denote the absolute reflectance and the mass of the membrane, $\mathcal{F}$ denotes the optical cavity finesse, and x_m denotes the position of the membrane inside the optical cavity.

The factors $\mathcal{J} = \frac{2\alpha|r_c|^2\mathcal{F}^2\Omega g(x_m)^2}{\pi^2 c^2 m\omega^{(0)}}$ and r specify the parameters of the MIM optomechanical system. For these simulations, σ is given in units of $\mathcal{J}P$ and w is varied via κ while holding $\omega^{(0)}$ fixed[1]. They show that for $\kappa/\omega^{(0)} \ll 1$ (known as the resolved-sideband regime) one can tune the mechanical resonance over the entire complex plane (see also [94, 189]). The range of this control is explicitly illustrated in Fig. 2.9(b). However, for small $\kappa/\omega^{(0)}$, there is a trade-off between accessibility of the complex plane and the magnitude of σ for a fixed input power. This is illustrated in Fig. 2.9(c). With these features in mind, one may design a system with appropriate $\kappa/\omega^{(0)}$ and input power handling capabilities.

2.3.1.2 Optomechanical readout

We now turn our attention to the optical mode $a = \bar{a} + d$. Its first part $\bar{a}$ represents the optical cavity's coherent response to being driven by laser tones (one tone in this case) and is given by

$$\bar{a} = -\sqrt{\kappa_{\mathrm{in}}}\chi_c(\Delta)\sqrt{\frac{P}{\hbar(\Omega+\Delta)}} \quad (2.70)$$

and the second part d encodes the optical mode's fluctuations resulting from the mechanical motion.

$$d = -ig_0\bar{a}\chi_c(\omega^{(0)})(\tilde{c}+\tilde{c}^*) \quad (2.71)$$

[1]A quick note on units: $\mathcal{J}$ has units of $(\mathrm{energy})^{-1}$, P has units of $(\mathrm{energy/time})$ and as expected σ has units of (Hz).

where we used assumption **(b)** from Sec. 2.3.1. We see that the optical mode's fluctuations are proportional to the mechanical motion, scaled by optomechanical coupling strength g_0, the amount of light circulating in the cavity $\bar{a}$, and filtered by the cavity susceptibility $\chi_c(\omega)$. This illustrates the optomechanical readout: by appropriately monitoring the amplitude/phase fluctuations of the light leaving the cavity, one has a direct record of the mechanical motion. While we are concerned with a single mechanical mode in this section, the above readout scheme can be adapted to simultaneously measure the motion of multiple mechanical modes coupled to an optical mode, by monitoring d resulting from each mechanical mode.

2.3.2 Two-mode optomechanics

In this section, we extend our model to include two mechanical modes which are non-degenerate to begin with, and are coupled to a common optical mode. The main aim here is to derive an optomechanical system that can experimentally explore the non-Hermitian geometric phase for arbitrarily tunable $N = 2$ coupled harmonic oscillators, as described in Sec. 2.2.

For such a system, the classical Hamiltonian function is given by

$$H_{\text{full},2} = \hbar\left(\Omega - \frac{i\kappa}{2}\right) a^* a + \sum_{j=1}^{2} \hbar\left(\omega_j^{(0)} - \frac{i\gamma_j^{(0)}}{2}\right) \tilde{c}_j^* \tilde{c}_j + \sum_{j=1}^{2} \hbar g_j (\tilde{c}_j + \tilde{c}_j^*)|a|^2 \quad (2.72)$$

where we simply added one more mechanical mode to Eq. (2.64), and the single-photon optomechanical coupling strengths are denoted by g_j for $j \in \{1, 2\}$. As before, the optical mode is driven by laser tones - two in this case.

$$a_{\text{in}} = e^{-i\Omega t} \sum_{m=1}^{2} \sqrt{\frac{P_m}{\hbar(\Omega + \Delta_m)}} e^{-i(\Delta_m t + \theta_m)} \quad (2.73)$$

parameterized by two powers P_m, with respective detunings from the optical cavity resonance Δ_m and respective phases θ_m for $m \in \{1, 2\}$. The dynamics of a, $\tilde{c}_j$ are given

by Hamilton's equation of motion:

$$\begin{aligned}
\dot{a} &= -\left(\frac{\kappa}{2} - i\Omega + \sum_{j=1}^{2} ig_j(\tilde{c}_j + \tilde{c}_j^*)\right) a + \sqrt{\kappa_{\rm in}} a_{\rm in} \\
\dot{\tilde{c}}_1 &= -\left(i\omega_1^{(0)} + \frac{\gamma_1^{(0)}}{2}\right) \tilde{c}_1 - ig_1|a|^2 + c_{\rm in,1} \\
\dot{\tilde{c}}_2 &= -\left(i\omega_2^{(0)} + \frac{\gamma_2^{(0)}}{2}\right) \tilde{c}_2 - ig_2|a|^2 + c_{\rm in,2}
\end{aligned} \tag{2.74}$$

Continuing with the same hierarchy of rates i.e. $\kappa \gg \{g_j, \gamma_j^{(0)}\}$, we linearize the optomechanical interaction as before with the optical mode $a = \bar{a} + d$, with $d \ll \bar{a}$ and adiabatically eliminate it from the equation of motion for the mechanical modes. Furthermore, we constrain the intracavity beat-note between the two driving laser tones to have frequency $|\Delta_{12}| = |\Delta_1 - \Delta_2| \approx |\omega_1^{(0)} - \omega_2^{(0)}|$, and make the following approximations:

(a) The mechanical modes have high Q (i.e., Q $\gg$ 1), such that $\tilde{c}_j$ is independent of $\tilde{c}_j^*$, as for the single mechanical mode case (Sec. 2.3.1).

(b) Since the mechanical modes have high Q $\gg$ 1, they are only susceptible to forces with frequency components near their resonance frequencies $\omega_j^{(0)}$, with the susceptibility bandwidth set by their damping rates $\gamma_j^{(0)}$.

(c) As a result of $\kappa \gg \{g_j, \gamma_j^{(0)}\}$, the mechanical modes experience almost a constant optical cavity susceptibility evaluated at its resonance frequency i.e. $\chi_{\rm c}(\omega) \to \chi_c(\omega_j^{(0)})$, same as the single mechanical mode case (Sec. 2.3.1).

Subsequently, the equations of motion for the mechanical modes are:

$$\dot{\vec{c}}_{\rm lab} = -iH_{\rm lab}\vec{c}_{\rm lab} \tag{2.75}$$

just as Eq. (1.1), in the lab frame, where $\vec{c}_{\rm lab} = (\tilde{c}_1, \tilde{c}_2)^{\rm T}$ with

$$H_{\rm lab} = \begin{bmatrix} \omega_1^{(0)} - \dfrac{i\gamma_1^{(0)}}{2} + \displaystyle\sum_{m=1}^{2} \sigma_{mm,1} & \sigma_{12} e^{i(\Delta_{12} t + \theta_{12})} \\ \sigma_{21} e^{-i(\Delta_{12} t + \theta_{12})} & \omega_2^{(0)} - \dfrac{i\gamma_2^{(0)}}{2} + \displaystyle\sum_{m=1}^{2} \sigma_{mm,2} \end{bmatrix} \tag{2.76}$$

where

$$\begin{aligned}
\sigma_{mm,j} &= -i\kappa_{\rm in} g_j^2 \frac{P_m}{\hbar(\Omega + \Delta_m)} |\chi_c(\Delta_m)|^2 \left(\chi_c(\omega_j^{(0)} + \Delta_m) - \chi_c(\omega_j^{(0)} - \Delta_m) \right) \\
\sigma_{12} &= -i\kappa_{\rm in} g_1 g_2 \frac{\sqrt{P_1 P_2}}{\hbar\sqrt{(\Omega + \Delta_1)(\Omega + \Delta_2)}} \chi_c(\Delta_1)^* \chi_c(\Delta_2) \left(\chi_c(\omega_1^{(0)} + \Delta_1) \right. \\
&\quad \left. - \chi_c(\omega_1^{(0)} - \Delta_2) \right) \\
\sigma_{21} &= -i\kappa_{\rm in} g_1 g_2 \frac{\sqrt{P_1 P_2}}{\hbar\sqrt{(\Omega + \Delta_1)(\Omega + \Delta_2)}} \chi_c(\Delta_2)^* \chi_c(\Delta_1) \left(\chi_c(\omega_2^{(0)} + \Delta_2) \right. \\
&\quad \left. - \chi_c(\omega_2^{(0)} - \Delta_1) \right) \\
\Delta_{12} &= \Delta_1 - \Delta_2, \ \theta_{12} = \theta_1 - \theta_2
\end{aligned} \tag{2.77}$$

Qualitatively, this arrangement allows each laser tone to vary each mechanical modes' stiffness and damping via the DBA as in the single mechanical mode case (Sec. 2.3.1.1), while the intracavity beat-note provides tunable coupling between the mechanical modes. This beat-note is similar to periodically driven Floquet systems [190], and here the analogous Floquet-drive is $1/\Delta_{12}$ periodic . Henceforth, we refer to such system as Floquet-driven systems, and the coupling it generates is referred as Floquet coupling. We illustrate this coupling in Fig. 2.10 and briefly sketch the idea below (see also [94, 95, 188]):

1. Consider the two driving laser tones to be detuned by $\Delta_1 \approx -\omega_1^{(0)}$ and $\Delta_2 \approx -\omega_2^{(0)}$, respectively, from the optical cavity resonance.

2. Each of these laser tones has sidebands resulting from the mechanical modes' motion [175]. For this present arrangement, some of the anti-stokes motional sidebands are $\sim$resonant with the optical cavity resonance, and hence get amplified via the cavity susceptibility. These sidebands overlap with each other given by our construction i.e.,

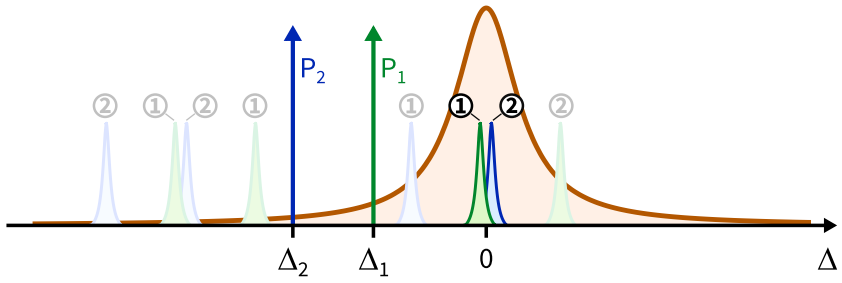

Figure 2.10: Floquet coupling schematic. Optical spectrum. Orange: cavity mode; green vertical arrow: control tone 1 with power P_1 and detuning from cavity resonance $\Delta_1 \approx -\omega_1^{(0)}$, blue vertical arrow: control tone 2 with power P_2 and detuning from cavity resonance $\Delta_2 \approx -\omega_2^{(0)}$. Motional sidebands of each tone are shown as skinny Lorentzians. Green Lorentzian: motional sideband of control tone 1 due to mechanical mode ①, $\sim$ resonant with cavity mode; blue Lorentzian: motional sideband of control tone 2 due to mechanical mode ②, $\sim$ resonant with cavity mode; faded green Lorentzian: off-resonant motional sidebands of control tone 1; faded blue Lorentzian: off-resonant motional sidebands of control tone 2. Each motional sideband is labeled with ⓘ, corresponding to the mechanical with resonance frequency $\omega_i^{(0)}$.

$$\Delta_1 - \Delta_2 \approx \omega_1^{(0)} - \omega_2^{(0)}.$$

3. Now we consider the beat-notes between a driving laser tone and a resonant anti-stokes motional sideband. In particular, consider the following two beat-note pairs: **(a)** between laser tone 1 and anti-stokes motional sideband 2 and **(b)** between laser tone 2 and anti-stokes motional sideband 1. Their intensity beat-notes and the corresponding radiation pressure forces have frequencies $(\Omega + \Delta_1) - (\Omega + \Delta_2 + \omega_2^{(0)}) \approx \omega_1^{(0)}$ and $(\Omega+\Delta_2)-(\Omega+\Delta_1+\omega_1^{(0)}) \approx \omega_2^{(0)}$, respectively. We thus see that motion of mechanical mode 1(2), creates a force nearly on resonance with mechanical mode 2(1), hence the coupling.

4. While we restricted our sketch to red-detuned laser tones, one can derive a similar story for two blue-detuned laser tones or a red-blue detuned pair of tones. For the blue-detuned tones, it is the stokes sideband that would get amplified by the optical cavity susceptibility.

We also observe that $H_{\rm lab}$ is explicitly time-dependent even if all of its parameters are held fixed, owing to the intracavity beat-note that appears in the off-diagonal, $e^{\pm\Delta_{12}t}$. The analysis is simplified if we remove this particular time dependence (but not the time dependence resulting from variations of control parameters $P_{1,2}, \Delta_{1,2}, \theta_{1,2}$). This is

accomplished by a unitary transformation $S_{\mathcal{R}}$:

$$S_{\mathcal{R}} = \begin{bmatrix} e^{i\left(-\Delta_{12}+\omega_1^{(0)}+\omega_2^{(0)}\right)t/2} & 0 \\ 0 & e^{i\left(\Delta_{12}+\omega_1^{(0)}+\omega_2^{(0)}\right)t/2} \end{bmatrix} \tag{2.78}$$

or equivalently,

$$S_{\mathcal{R}} = \begin{bmatrix} e^{i\left(\omega_1^{(0)}+\frac{\eta}{2}\right)t} & 0 \\ 0 & e^{i\left(\omega_2^{(0)}-\frac{\eta}{2}\right)t} \end{bmatrix} \tag{2.79}$$

where $\eta = \omega_2^{(0)} - \omega_1^{(0)} - \Delta_{12}$. In this frame $\mathcal{R}$, the equations of motion for the mechanical modes are given by

$$\dot{\vec{c}} = -iH\vec{c} \tag{2.80}$$

where $\vec{c} = (c_1, c_2)^{\mathrm{T}} = S_{\mathcal{R}}\vec{c}_{\mathrm{lab}}$ and $H = S_{\mathcal{R}}H_{\mathrm{lab}}S_{\mathcal{R}}^{-1} + i\dot{S}_{\mathcal{R}}S_{\mathcal{R}}^{-1}$.

Under this simplification, the time-dependence of H is solely contained in the time-dependence of its control parameters $P_{1,2}, \Delta_{1,2}, \theta_{12}$:

$$H = \begin{bmatrix} \dfrac{-\eta - i\gamma_1^{(0)}}{2} + \displaystyle\sum_{m=1}^{2}\sigma_{mm,1} & \sigma_{12}e^{i\theta_{12}} \\ \sigma_{21}e^{-i\theta_{12}} & \dfrac{\eta - i\gamma_2^{(0)}}{2} + \displaystyle\sum_{m=1}^{2}\sigma_{mm,2} \end{bmatrix} \tag{2.81}$$

and it is convenient to re-define $\Delta_{1,2}$ as $\Delta_1 = -\omega_1^{(0)} + \delta$ and $\Delta_2 = -\omega_2^{(0)} + \delta + \eta$, with $\{\delta, \eta\}$ now being the two detuning control knobs. Upon diagonalization of H, we obtain its eigenvalues $\vec{\Lambda} = (\lambda_+, \lambda_-)^{\mathrm{T}}$ in the frame $\mathcal{R}$. These are analogous to one of the 'quasi-frequencies' for Floquet-driven systems, which are defined modulo the Floquet-drive frequency, Δ_{12}. We note that they are independent of θ_{12}. While a constant θ_{12} can always be set to zero by a time-independent change of coordinates, that is not possible for a time varying θ_{12}. We also note that, in the absence of control tones (i.e. $P_1 = P_2 = 0$), the magnitude of (the real part of) the eigenvalue non-degeneracy is $|\eta|$.

In the lab frame, the mechanical motion (as inferred via d in Eq. (2.71)) will contain

components near both $\omega_1^{(0)}$ and $\omega_1^{(0)}$ [94, 188]. In this anticipation, we define:

$$\vec{\Lambda}_1 = (\Lambda_{1+}, \Lambda_{1-})^{\mathrm{T}} = \left(\omega_1^{(0)} + \frac{\eta}{2} + \lambda_+, \omega_1^{(0)} + \frac{\eta}{2} + \lambda_-\right)^{\mathrm{T}} = \omega_1^{(0)} + \frac{\eta}{2} + \vec{\Lambda}$$

$$\vec{\Lambda}_2 = (\Lambda_{2+}, \Lambda_{2-})^{\mathrm{T}} = \left(\omega_2^{(0)} - \frac{\eta}{2} + \lambda_+, \omega_2^{(0)} - \frac{\eta}{2} + \lambda_-\right)^{\mathrm{T}} = \omega_2^{(0)} - \frac{\eta}{2} + \vec{\Lambda} \tag{2.82}$$

which are useful when considering the mechanical response in the lab frame, and are two more examples of the infinite number of 'quasi-frequencies' of such Floquet-driven systems.

2.3.2.1 Experimentally realizing the non-Hermitian geometric phase for an $N = 2$ system

H in Eq. (2.81) can be easily compared to the general H for a system of $N = 2$ coupled harmonic oscillators, as defined in Eq. (2.14). Their respective elements are related by:

$$A = -\frac{\eta}{2} - i\left(\frac{\gamma_1^{(0)} - \gamma_2^{(0)}}{4}\right)\sum_{m=1}^{2}\left(\frac{\sigma_{mm,1} - \sigma_{mm,2}}{2}\right),$$

$$B = \sigma_{12},\ C = \sigma_{21},\ \theta = \theta_{12},$$

$$\mathcal{T} = -i\left(\frac{\gamma_1^{(0)} + \gamma_2^{(0)}}{2}\right)\sum_{m=1}^{2}(\sigma_{mm,1} + \sigma_{mm,2}) \tag{2.83}$$

Thus, along with the resolved-sideband condition, the above relations would allow us explore the non-Hermitian geometric phase for the $N = 2$ case, specifically as illustrated in Secs. 2.2.3 and 2.2.4. However, for completeness we note that the two laser tone scheme described above does not represent the most general parameterization of a 2×2 matrix, even if we satisfy the resolved-sideband condition. It can be shown that $\sigma_{12,21}$ appear almost symmetrically about $\chi_c(\delta)$, which effectively fixes the relative contribution of the $\sigma_{\mathrm{x,y}}$ components [191]. While a time varying θ_{12} parametrically tunes the $\sigma_{\mathrm{x,y}}$ components in real time, a four laser tone system as described in Ref. [192] provides full control over all 2×2 matrices - both statically and in real time, provided we satisfy the resolved-sideband condition.

2.3.3 Three-mode optomechanics

In this section, we extend the optomechanical Floquet-coupling for a system of three non-degenerate mechanical modes, coupled to a common optical mode. The primary goal here is to derive an optomechanical system that can experimentally explore the spectral flow for $N = 3$ coupled harmonic oscillators. This treatment is exactly the same as the two mechanical mode case (Sec. 2.3.2) and we briefly outline the procedure to obtain the relevant equations of motions for the three mechanical modes, analogous to Eqs. (2.80) and (2.81).

The starting point is yet again to define the classical Hamiltonian function

$$H_{\mathrm{full},3} = \hbar\left(\Omega - \frac{i\kappa}{2}\right) a^* a + \sum_{j=1}^{3} \hbar\left(\omega_j^{(0)} - \frac{i\gamma_j^{(0)}}{2}\right) \tilde{c}_j^* \tilde{c}_j + \sum_{j=1}^{3} \hbar g_j (\tilde{c}_j + \tilde{c}_j^*)|a|^2 \quad (2.84)$$

where a third mechanical mode was added to Eq. (2.72). We then proceed to drive the cavity with three laser tones parameterized three powers P_m, detunings from the optical cavity resonance Δ_m and respective phases θ_m for $m \in \{1, 2, 3\}$.

$$a_{\mathrm{in}} = e^{-i\Omega t} \sum_{m=1}^{3} \sqrt{\frac{P_m}{\hbar(\Omega + \Delta_m)}} e^{-i(\Delta_m t + \theta_m)} \quad (2.85)$$

We subsequently obtain the Hamilton's equation of motion for a, $\tilde{c}_j$ for $j \in \{1, 2, 3\}$, continue with the same hierarchy of rates and linearized optomechanical iteration, constrain the relative detuning between the three drive laser tones as $|\Delta_{ij\neq i}| = |\Delta_i - \Delta_j| \approx |\omega_i^{(0)} - \omega_j^{(0)}|$ for $\{i, j\} \in \{1, 2, 3\}$ to provide tunable optical-spring, optical-damping and Floquet-coupling, and apply the same approximations as in Sec. 2.3.2. As a result, the equations of motion for the mechanical modes are:

$$\dot{\vec{c}}_{\mathrm{lab}} = -iH_{\mathrm{lab}}\vec{c}_{\mathrm{lab}} \quad (2.86)$$

just as Eq. (1.1), in the lab frame where $\vec{c}_{\mathrm{lab}} = (\tilde{c}_1, \tilde{c}_2, \tilde{c}_3)^{\mathrm{T}}$ with

$$H_{\rm lab} = \begin{bmatrix} \omega_1^{(0)} - \frac{i\gamma_1^{(0)}}{2} + \sum_{m=1}^{3} \sigma_{mm,1} & \sigma_{12} e^{i(\Delta_{12}t+\theta_{12})} & \sigma_{13} e^{i(\Delta_{13}t+\theta_{13})} \\ \sigma_{21} e^{-i(\Delta_{12}t+\theta_{12})} & \omega_2^{(0)} - \frac{i\gamma_2^{(0)}}{2} + \sum_{m=1}^{3} \sigma_{mm,2} & \sigma_{23} e^{i(\Delta_{23}t+\theta_{23})} \\ \sigma_{31} e^{-i(\Delta_{13}t+\theta_{31})} & \sigma_{32} e^{-i(\Delta_{23}t+\theta_{32})} & \omega_3^{(0)} - \frac{i\gamma_3^{(0)}}{2} + \sum_{m=1}^{3} \sigma_{mm,3} \end{bmatrix} \tag{2.87}$$

where

$$\sigma_{mm,j} = -i\kappa_{\rm in} g_j^2 \frac{P_m}{\hbar(\Omega+\Delta_m)} |\chi_c(\Delta_m)|^2 \left(\chi_c(\omega_j^{(0)} + \Delta_m) - \chi_c(\omega_j^{(0)} - \Delta_m) \right)$$

$$\sigma_{mn\neq m} = -i\kappa_{\rm in} g_m g_n \frac{\sqrt{P_m P_n}}{\hbar\sqrt{(\Omega+\Delta_m)(\Omega+\Delta_n)}} \chi_c(\Delta_m)^* \chi_c(\Delta_n) \left(\chi_c(\omega_m^{(0)} + \Delta_m) - \chi_c(\omega_m^{(0)} - \Delta_n) \right)$$

$$\Delta_{mn} = \Delta_m - \Delta_n, \ \theta_{mn} = \theta_m - \theta_n \tag{2.88}$$

As before, the explicit time dependence of $H_{\rm lab}$ given by the $e^{\pm i\Delta_{mn}t}$ terms in its off-diagonal and can be removed to simplify analysis. It is accomplished by applying a unitary transformation U

$$U = \begin{bmatrix} e^{i\left(\omega_1^{(0)}+\eta\right)t - i\theta_1} & 0 & 0 \\ 0 & e^{i\omega_2^{(0)}t - i\theta_2} & 0 \\ 0 & 0 & e^{i\left(\omega_3^{(0)}+\eta\right)t - i\theta_3} \end{bmatrix} \tag{2.89}$$

where $\Delta_1 = \omega_1^{(0)} + \delta, \Delta_2 = \omega_2^{(0)} + \delta + \eta, \Delta_3 = \omega_3^{(0)} + \delta$. Under this transformation, the equations of motion for the mechanical modes are:

$$\dot{\vec{c}} = -iH\vec{c} \tag{2.90}$$

where $\vec{c} = (c_1, c_2, c_3)^{\rm T} = U\vec{c}_{\rm lab}$ and $H = UH_{\rm lab}U^{-1} + i\dot{U}U^{-1}$, which is explicitly given

by

$$H = \begin{bmatrix} -\eta - \frac{i\gamma_1^{(0)}}{2} + \sum_{m=1}^{3} \sigma_{mm,1} & \sigma_{12} & \sigma_{13} \\ \sigma_{21} & -\frac{i\gamma_2^{(0)}}{2} + \sum_{m=1}^{3} \sigma_{mm,2} & \sigma_{23} \\ \sigma_{31} & \sigma_{32} & -\eta - \frac{i\gamma_3^{(0)}}{2} + \sum_{m=1}^{3} \sigma_{mm,3} \end{bmatrix} \quad (2.91)$$

where the control knobs are now the three powers $P_{1,2,3}$ and a common detuning δ. The differential detuning η is fixed to a constant value. We justify this choice further in Sec. 2.3.3.1. For studying spectral flow, we are solely concerned with the eigenvalues of H in Eq. (2.91), which are obtained simply by diagonalizing it.

2.3.3.1 Experimentally simulating $N = 3$-mode spectral flow

In this section, we evaluate the suitability of the optomechanical system we described above to explore the $N = 3$ -mode spectral flow. The key features that would make it possible are: **(a)** the ability to tune H and bring it to an EP_3 degeneracy, **(b)** the ability to tune H in the neighborhood of the EP_3 and span the entire space of eigenvalues. This will allow us to explore the space of two-fold degeneracies, which are predicted to form a trefoil knot, and the non-Abelian braids of the non-degenerate eigenvalue spectra. We now elaborate on each of these features below.

(a) Tuning to an EP_3

H in Eq. (2.91) is a complicated function of the experimental control knobs $\{P_{1,2,3}, \delta\}$, fixed control parameter η and fixed system parameters $\{\Omega, \omega_{1,2,3}^{(0)}, \gamma_{1,2,3}^{(0)}, \kappa, \kappa_{\text{in}}, g_{1,2,3}\}$, and we did not find an analytic means for determining values of the control knobs that correspond to a three-fold degeneracy. Instead, we searched numerically over a wide range of these control knobs. This search revealed several three-fold degeneracies. The one used in the actual experimental implementation, as described in Chapter 3 was chosen for its readily accessible $\{P_{1,2,3}, \delta\}_{EP_3}$ values.

(b) Spanning the neighborhood of EP_3

In order to check whether the four experimental control knobs $\{P_{1,2,3}, \delta\}$ span the space of all eigenvalues around an EP_3 degeneracy, we use the inverse function theorem to argue about the existence of a map between these four parameters and the two complex coefficients (x, y) of the characteristic polynomial of H_0 in the vicinity of $\{P_{1,2,3}, \delta\}_{EP_3}$ (see also [89]). For simplicity, here we use H_0, the traceless version of H defined as: $H_0 = H - \mathrm{Tr}(H)\mathbb{I}/3$, where $\mathbb{I}$ is the identity matrix. In this case, $x = \mathrm{Det}(H_0) = \prod_{i=1}^{3} \lambda_{0,i}$ and $y = \mathrm{Tr}(H_0^2)/2 = \sum_{i=1}^{3} \lambda_{0,i}^2/2$, where $\{\lambda_{0,i}\}$ are the eigenvalues of H_0 for $i \in \{1, 2, 3\}$.

In particular, we consider the Jacobian J of this map, where

$$J = \begin{bmatrix} \frac{\partial \mathrm{Re}(x)}{\partial P_1} & \frac{\partial \mathrm{Re}(x)}{\partial P_2} & \frac{\partial \mathrm{Re}(x)}{\partial P_3} & \frac{\partial \mathrm{Re}(x)}{\partial \delta} \\ \frac{\partial \mathrm{Im}(x)}{\partial P_1} & \frac{\partial \mathrm{Im}(x)}{\partial P_2} & \frac{\partial \mathrm{Im}(x)}{\partial P_3} & \frac{\partial \mathrm{Im}(x)}{\partial \delta} \\ \frac{\partial \mathrm{Re}(y)}{\partial P_1} & \frac{\partial \mathrm{Re}(y)}{\partial P_2} & \frac{\partial \mathrm{Re}(y)}{\partial P_3} & \frac{\partial \mathrm{Re}(y)}{\partial \delta} \\ \frac{\partial \mathrm{Im}(y)}{\partial P_1} & \frac{\partial \mathrm{Im}(y)}{\partial P_2} & \frac{\partial \mathrm{Im}(y)}{\partial P_3} & \frac{\partial \mathrm{Im}(y)}{\partial \delta} \end{bmatrix} \tag{2.92}$$

and the derivatives are evaluated at $\{P_{1,2,3}, \delta\}_{EP_3}$. J is continuously differentiable in $\{P_{1,2,3}, \delta\}$ because (x, y) are smooth functions in the elements of H_0, which in turn are continuously differentiable in $\{P_{1,2,3}, \delta\}$, over the range of their values used in the actual experimental implementation. Therefore, if $\mathrm{Det}(J) \neq 0$, the experimental control knobs span the same space as (x, y), in the neighborhood of the EP_3. As shown in the $N = 3$ example in Sec. 2.1.2, (x, y) parametrize the entire space of eigenvalues around the EP_3 located at $x = 0 = y$. In Chapter 3, we explicitly verify $\mathrm{Det}(J) \neq 0$ for the experimental system used therein.

The connection between the experimental control parameters and the coefficients of the characteristic polynomial in the neighborhood of EP_3, can also be understood by noting that any traceless matrix in the neighborhood of an EP_3 can be brought to the canonical form via similarity transformation. The canonical form is also known as the

Arnol'd-Jordan normal form [96, 115] and is given by

$$\underline{H_0} = \begin{bmatrix} 0 & 1 & 0 \\ 0 & 0 & 1 \\ x & y & 0 \end{bmatrix} \tag{2.93}$$

where (x, y) are the same two complex coefficients of the characteristic polynomial as described previously. $\underline{H_0}$ may also be regarded as the companion matrix of the characteristic polynomial. This form highlights the fact that the non-vanishing of $\mathrm{Det}(J)$ ensures the existence of a linear relationship between the experimental control parameters and the matrix elements of H_0.

Chapter 3

Knotted non-Hermitian degeneracies and non-commuting braids

In this chapter, we provide an experimental demonstration of spectral flow for an $N = 3$-mode non-Hermitian system, in a cavity optomechanical platform. We begin with a brief description of the experimental apparatus, its control parameters that tune the dynamical matrix H of the three-mode system, and its readout (Sec. 3.1). The control parameters span the full control space $\mathcal{L}_3$, provide access to a threefold degeneracy EP_3 and all eigenspectra in its neighborhood [96]. We measure eigenspectra on a hypersurface enclosing the EP_3, and find that the twofold degeneracies EP_2 form a trefoil knot $\mathcal{K}$ (Sec. 3.2). We show that varying the control parameters in a closed loop, i.e., a control loop $\mathcal{C}$ in the non-degenerate subspace, produces an eigenvalue braid determined by how $\mathcal{C}$ encircles $\mathcal{K}$ (Sec. 3.3). These braids are shown to form the braid group B_3 and we demonstrate its non-Abelian nature. The above content is adapted from Ref. [43, 91] and also detailed in Ref. [95].

We follow up these demonstrations with an examination of eigenvalue braiding and the permutations they produce when the control loops are constrained to a 2D "slice" $\mathcal{B}$ in $\mathcal{L}_3$ (Sec. 3.3.1.1). We show that such a simplification may not capture the key topological features of the full space, and appear to produce surprising and anomalous results. We resolve these anomalies by examining them within $\mathcal{L}_3$. We also include a discussion of when the basepoint (i.e., the starting and the ending point) of control loops

is allowed to vary, and the resulting eigenvalue braids and permutations. These contents are adapted from Ref. [91]. Additional technical details for the experimental apparatus, the measurements and their analyses are given in Appendix B.

3.1 Experimental apparatus, control and readout

This section describes the experimental apparatus, its control and primary measurements that enable all subsequent experimental demonstrations of spectral flow for an $N = 3$-mode non-Hermitian system.

3.1.1 Experimental setup

The experimental setup is shown schematically in Fig. 3.1(a). It comprises a high finesse Fabry-Perot optical cavity with a silicon-nitride ($\mathrm{Si_3N_4}$) membrane placed in the middle, and is housed inside a cryostat. The experiment focuses on three vibrational "drumhead" modes of the membrane (pink box in Fig. 3.1(a)) whose dimensions are specified to be: 1 mm (length)×1 mm (width)×50 nm (thickness). The modes' bare eigenvalues (i.e., in the absence of optomechanical effects) are $\tilde{\boldsymbol{\lambda}}^{(0)} = \{\tilde{\lambda}_1^{(0)}, \tilde{\lambda}_2^{(0)}, \tilde{\lambda}_3^{(0)}\} = 2\pi\times\{352243-2.2i,\ 557217-1.9i,\ 704837-1.8i\}$ Hz, where the real (imaginary) parts give each mode's oscillation frequency (amplitude damping rate). We note that frequencies related to the mechanical modes are denoted with a tilde when given in the lab frame, and without a tilde in the frame $\mathcal{R}$ as described in Sec. 2.3.3 and below. The full set of system parameters is listed in Table B.1. A detailed description of the experimental setup can be found in Refs.[43, 93–95, 188].

3.1.2 Control parameters

The dynamical matrix H governing the system of the three mechanical modes is controlled using the dynamical back-action (DBA) effect of cavity optomechanics [172–175]. This is accomplished by driving the optical cavity using three laser tones produced from a single laser ('control' laser Fig. 3.1(a)), via an acousto-optic modulator (cAOM). The DBA from each tone induces a complex-valued shift in each mechanical mode's eigenvalue. In addition, each pair of tones gives rise to an intracavity intensity beat-note, which induces a complex-valued coupling between pairs of modes whose frequency difference is comparable to the beat-note frequency. In the resolved sideband regime ($\kappa \ll \tilde{\omega}_{1,2,3}^{(0)}$, where $\tilde{\omega}_i^{(0)} = \mathrm{Re}(\tilde{\lambda}_i^{(0)})$, these shifts and couplings can be tuned over the complex plane by

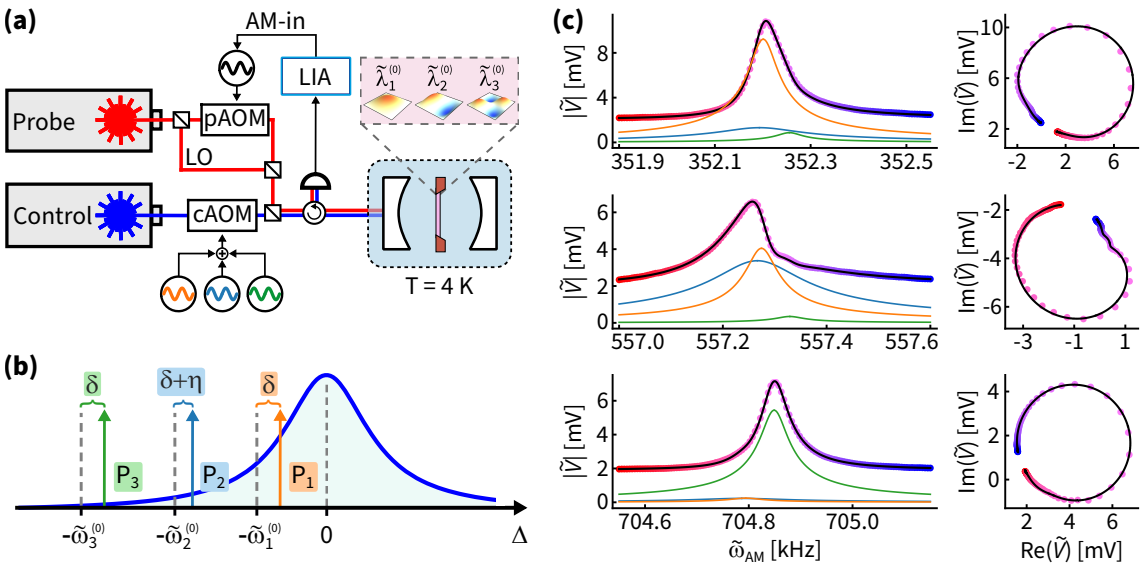

Figure 3.1: Experimental setup, control and readout. **(a)** A Si_3N_4 membrane (red) is placed in the middle of a Fabry-Perot optical cavity (white) in a cryostat (blue). Three of the membrane's modes (pink box) are tuned using three tones generated from the "control" laser via an AOM (cAOM). The membrane is driven by modulating the "probe" laser's intensity via amplitude modulating the RF drive to a second AOM (pAOM). The probe laser also provides a local oscillator (LO) which generates a signal $\tilde{V}$ that is proportional to the membrane's displacement and is monitored via a lock-in amplifier (LIA). **(b)** The detunings Δ of the three control tones with respect to the cavity resonance. Dark blue: the magnitude of the cavity's optical susceptibility. The parameter $\eta = -2\pi \times 100$ Hz is chosen to provide an optimal frame $\mathcal{R}$. **(c)** A measurement of the membrane's mechanical susceptibility for representative value of control parameters Ψ. For each frequency range, the left panel: $|\tilde{V}(\tilde{\omega}_{\mathrm{AM}})|$ and the right panel: parametric plot of $\tilde{V}$. Each data point is colored by the value of $\tilde{\omega}_{\mathrm{AM}}$. Black lines: global fit to all the data shown here. The fit returns the system's eigenvalues $\boldsymbol{\lambda}$ in the frame $\mathcal{R}$ and relative complex amplitude of each mode s_{ij}. The magnitude of each mode's contribution (as determined from the fit) is shown as the orange, green, and light blue curves in the left-hand column.

varying the tones' power P_k and detunings Δ_k relative to the optical cavity resonance with $k \in \{1, 2, 3\}$. These effects are formally discussed in Sec. 2.3. For these experiments, we vary the control tones' common detuning δ and their powers $P_{1,2,3}$. The relative detunings of the control tones are fixed via $\eta = -2\pi\times$ 100 Hz and $\tilde{\omega}^{(0)}_{1,2,3}$, and they define a frame $\mathcal{R}$ in which the three mechanical modes are almost degenerate for $P_{1,2,3} = 0$ (the real-part of the non-degeneracy in $\mathcal{R}$ is set by η). The arrangement of the laser tones in relation to the cavity resonance is shown schematically in Fig. 3.1(b). Within $\mathcal{R}$, the mechanical modes can be described by the equation of motion

$$\dot{\mathbf{x}}(t) = -iH(\Psi)\mathbf{x}(t) + \mathbf{f}(t) \tag{3.1}$$

where $\mathbf{x}(t) = (x_1(t), x_2(t), x_3(t))^{\mathrm{T}}$ and $\mathbf{f}(t) = (f_1(t), f_2(t), f_3(t))^{\mathrm{T}}$ are the modes' complex-valued amplitudes and the external forces driving, respectively. The control parameters are specified as $\Psi = \{\delta, P_1, P_2, P_3\}$. While the above equation is the generic equation of motion for any linear system, we emphasize the form of $H(\Psi)$ realized here: specifically, the parameters Ψ provide sufficient control to tune the system to an EP_3 in $\mathcal{R}$, and they completely and smoothly parametrize all of the complex eigenvalues in a neighborhood of the EP_3 point. An explicit expression for $H(\Psi)$ is given in Eq. (2.91).

3.1.3 Measurement of eigenspectra

The eigenspectrum is determined by measuring the membrane's mechanical susceptibility. This is accomplished using a separate laser ('probe' laser Fig. 3.1(a)) to exert an oscillatory force on the membrane at frequency $\tilde{\omega}_{\mathrm{AM}}$ by modulating its intensity via another acousto-optic modulator (pAOM), and to record a heterodyne signal $\tilde{V}$ proportional to the membrane's response. Fig. 3.1(c) shows a representative measurement of the membrane's susceptibility recorded for values of $\tilde{\omega}_{\mathrm{AM}}$ in a 800 Hz window centered at $\tilde{\omega}_k^0$, for $k \in \{1, 2, 3\}$. This data is fit to a sum of three complex Lorentzians with $\boldsymbol{\lambda}$ and s_{ij} for $\{i, j\} \in \{1, 2, 3\}$ as fit parameters. The real (imaginary) parts of $\boldsymbol{\lambda}$ capture the center frequency (width) of each Lorentzian, while s_{ij} encode the relative complex amplitude of mode j probed near $\tilde{\omega}_i^0$, and as shown in Sec. 2.1.3.2, it encodes the information about the eigenvectors. For the measurement in Fig. 3.1(c), $\Psi = \{2\pi\times$46 kHz, 109.4 μW, 376.8 μW, 77 μW$\}$ and the fit provided $\boldsymbol{\lambda} = 2\pi \times \{49.67-84.98i$, 57.64$-29.83i$, 112.22$-26.32i\}$ Hz in $\mathcal{R}$ and $\{s_{11}, s_{12}, s_{21}, s_{22}\} = \{0.059 + 0.46i,\ 0.22 - 0.11i,\ 1.01 - 0.52i,$ -0.057 $+ 0.50i\}$. The remaining s_{ij} are calculated via constrains $\sum_j s_{ij} = 1 = \sum_j s_{ji}$ for $i, j \in \{1, 2, 3\}$ (see Sec. B.1). In the remainder of this, $\{\boldsymbol{\lambda}, s_{ij}\}$ are determined by data and fits as described here.

3.2 Locating EP degeneracies

In this section, we describe experiments that locate the triple degeneracy (EP_3), the double degeneracies (EP_2s) on a hypersurface surrounding the EP_3 point, which are then subsequently shown to trace the knot of EP_2s.

3.2.1 Locating the EP_3 degeneracy

This section describes the protocol for experimentally identifying the EP_3. Alternative approaches to identifying EP_3s are given in Refs.[39, 82–84, 127, 131, 193–198]. In particular, Ref. [95] carries out an analysis using the mathematical construction of Hopf Invariant to quantify the *topological* proximity to an EP_3.

We identify the value of control parameters $\Psi_{EP_3} = \{\delta_{EP_3}, P_{1,EP_3}, P_{2,EP_3}, P_{3,EP_3}\}$ that corresponds to EP_3 through the quantity $d = |\lambda_1 - \lambda_2| + |\lambda_2 - \lambda_3| + |\lambda_3 - \lambda_1|$. It may be visualized as the perimeter of the triangle formed by the system's three eigenvalues $\boldsymbol{\lambda}$ in the complex plane. At Ψ_{EP_3} the three eigenvalues are equal, and so $d = 0$.

The first step was to estimate Ψ_{EP_3} via a numerical search with the system parameters obtained via single-tone DBA characterization (see Secs. B.8 and 4.4.3). The system parameters are given in Table B.1. This search revealed several EP_3s and we proceeded with the Ψ_{EP_3} given below, as it corresponded to the most readily accessible value of control parameters.

$$\Psi_{EP_3}^{(\mathrm{thy})} = \{2\pi \times 49.7 \text{ kHz}, 115\ \mu\text{W}, 387\ \mu\text{W}, 285\ \mu\text{W}\} \tag{3.2}$$

In the next step, we fixed three of the control parameters to these values, and scanned the fourth (say Ψ_i). At each value of Ψ in the one-dimensional scan, $\boldsymbol{\lambda}$ is measured and converted to $d(\Psi)$. This measurement is affectionately named: "*Whirlpool scan*" [95]. The experimental estimate $\Psi_{EP_3}^{(\mathrm{est})}$ is then updated with the value of Ψ_i that minimizes d over that scan. This process is then iterated for different choices of Ψ_i. The estimate resulting from these one-dimensional scans is given below and a set of these

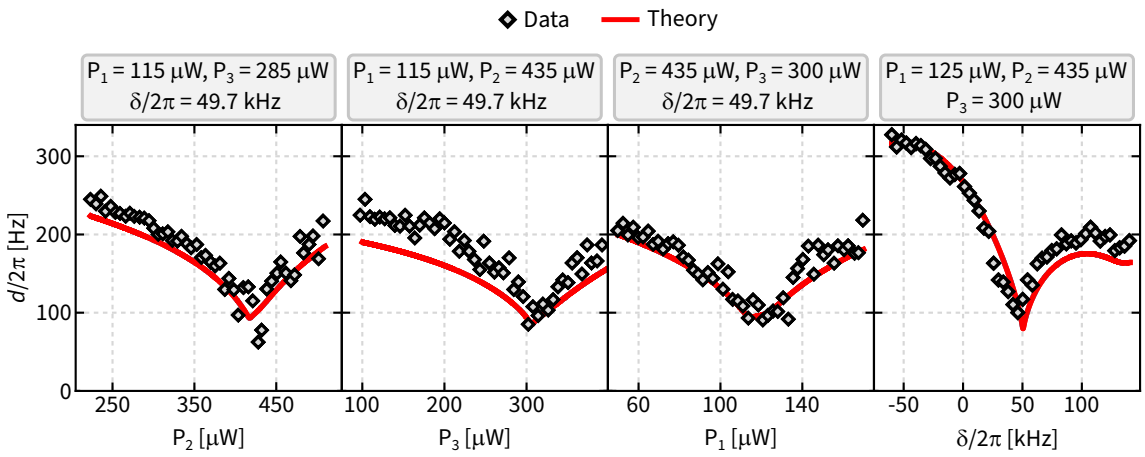

Figure 3.2: Preliminary search for EP_3. The quantity $d(\Psi)$ (which ideally vanishes at Ψ_{EP_3}), measured by scanning each of the four control parameters (one in each panel of the figure, while holding the other three fixed) through the theoretically estimated location of the EP_3 point $\Psi_{EP_3}^{(\mathrm{thy})}$. Each panel constitutes a "*Whirlpool scan*". Gray diamonds: measured $d(\Psi)$. The minima in $d(\Psi_i)$ in the i^{th}-panel provides an improved estimate for the location of the EP_3 point as $\Psi_{EP_3}^{(\mathrm{est})}$, which is subsequently used in refined scans in its neighborhood. The red curve is theoretically calculated $d(\Psi)$ from H using the best-fit optomechanical parameters obtained by fitting the knot of EP_2s (see Sec. B.7.1). The best-fit optomechanical parameters are given in Table B.1.

one-dimensional scans is illustrated in Fig. 3.2.

$$\Psi_{EP_3}^{(\mathrm{est})} = \{2\pi \times 49.7 \text{ kHz}, 125 \text{ μW}, 435 \text{ μW}, 300 \text{ μW}\} \tag{3.3}$$

To further refine the estimate of Ψ_{EP_3}, we measure $d(\Psi)$ on 2D sheets that pass through $\Psi_{EP_3}^{(\mathrm{est})}$. For each 2D sheet, two control parameters are scanned while the other two are fixed, resulting in a total of six sheets. They are shown in Figs. 3.3, 3.4 and 3.5 for data, filtered data and theory prediction, respectively. For each of these illustrations, three sheets with a common fixed value of Ψ_i are arranged in a 3D view. Near Ψ_{EP_3}, $d(\Psi)$ is expected to scale as $d \sim |\Psi - \Psi_{EP_3}|^{1/3}$ [21, 26]. However in practice, the sharp cusp in $d(\Psi_{EP_3})$ is broadened by fluctuations in Ψ and system parameters. A numerical simulation corroborating this feature can be found in Ref. [95]. Nevertheless, $d(\Psi)$ is shown to be minimized in the neighborhood of $\Psi_{EP_3}^{(\mathrm{est})}$ in the raw data. The filtered data is utilized to obtain a quantitative estimate of Ψ_{EP_3} by identifying the minima in $d(\Psi)$ in each 2D sheet (Sec. B.5.3). The result of this analysis is tabulated in Table 3.1. The mean location of these minima is taken as the experimentally identified EP_3 with the

error set by the standard deviation from the mean.

$$\Psi_{EP_3}^{(\mathrm{exp})} = \{2\pi \times 54(7)\ \mathrm{kHz},\ 128(8)\ \mu\mathrm{W},\ 428(3)\ \mu\mathrm{W},\ 304(15)\ \mu\mathrm{W}\} \tag{3.4}$$

	Parameter 1			
Sheet	$\delta/2\pi$ **(kHz)**	P_1 **(μW)**	P_2 **(μW)**	P_3 **(μW)**
Parameter 1 × δ	–	134	431	293
Parameter 1 × P_1	47.8	–	429	321
Parameter 1 × P_2	52.5	122	–	299
Parameter 1 × P_3	61.9	124	425	–
Mean	54.1	128	428	304
Std. Dev.	7.2	8	3	15

Table 3.1: Locating EP_3 via minima of d measured in 2D sheets. For each 2D sheet, two control parameters are held fixed to the expected $\Psi_{EP_3}^{(\mathrm{est})}$ (Eq. (3.3)), and the other two parameters are rastered. Measurements of $\boldsymbol{\lambda}$ provide d and their minima are identified algorithmically. The identified minima are reported for all six 2D sheets along with their mean location and its standard deviation. The mean and the standard deviation determine $\Psi_{EP_3}^{(\mathrm{exp})}$ (Eq. (3.4)).

The theory prediction of $d(\Psi)$ as calculated from H using the best-fit optomechanical parameters obtained by fitting the knot of EP_2s (see Sec. B.7.1), and these parameters given in Table B.1. It compares favorably with the measurements above, and with the calculated value of $\Psi_{EP_3}^{(\mathrm{knot})}$ given by:

$$\Psi_{EP_3}^{(\mathrm{knot})} = \{2\pi \times 60.2\ \mathrm{kHz},\ 116\ \mu\mathrm{W},\ 477\ \mu\mathrm{W},\ 329\ \mu\mathrm{W}\} \tag{3.5}$$

Having located the EP_3, we have an important question to answer:

Q: *Can we span the full control space surrounding this EP_3 and access all eigenspectra?*

A: We provide two answers to this question, below:

(i) We verify that $\mathrm{Det}(J) \neq 0$ when evaluated at EP_3, where J is the Jacobian of

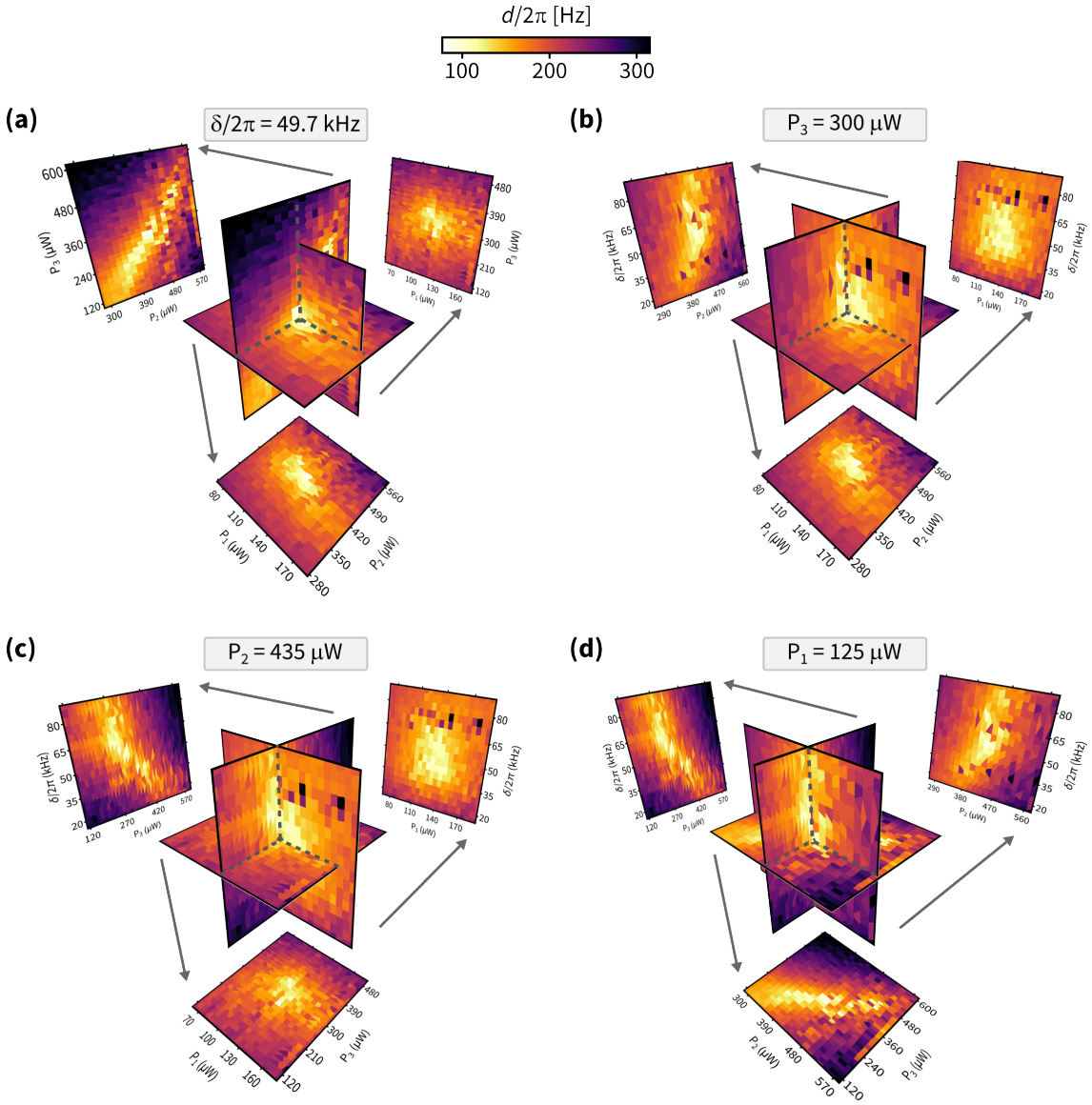

Figure 3.3: Locating EP_3 - part I. The quantity $d(\Psi)$ (which ideally vanishes at Ψ_{EP_3}), measured on six 2D sheets passing through $\Psi_{EP_3}^{(\mathrm{est})}$ the location of the EP_3 estimated from "*Whirlpool scans*" as shown in Fig. 3.2. Panels **(a-d)** show raw data for $d(\Psi)$ in a 3D view, to illustrate that it is minimized in the neighborhood of estimated location of EP_3, while one of the control parameters are held fixed estimated $\Psi_{EP_3,i} = \{\delta_{EP_3}, P_{3,EP_3}, P_{2,EP_3}, P_{1,EP_3}\}$, respectively. For each panel, we also show the full view of the corresponding 2D sheets identified by gray arrows.

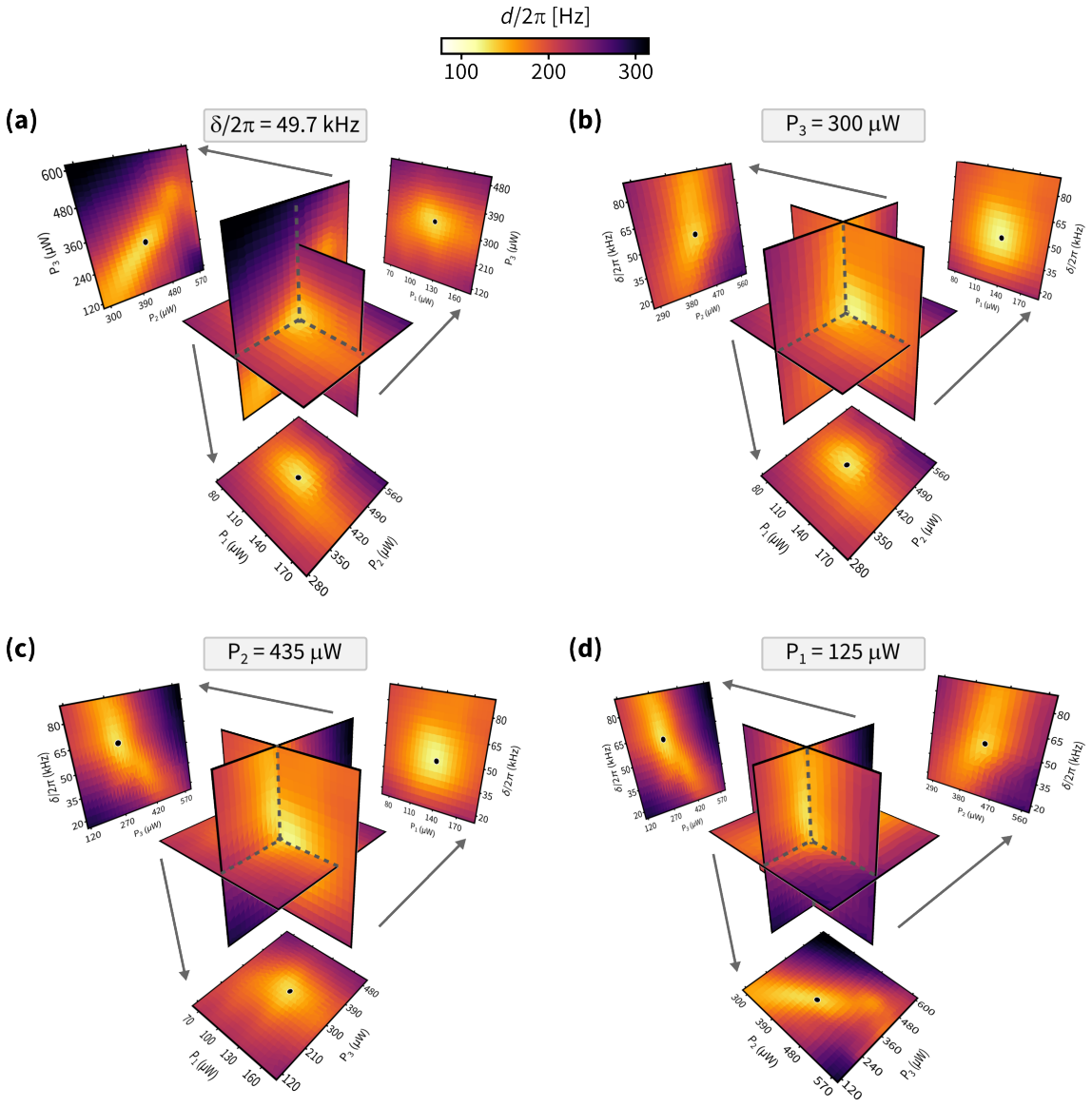

Figure 3.4: Locating EP_3 - part II. The quantity $d(\Psi)$ (which ideally vanishes at Ψ_{EP_3}), measured on six 2D sheets passing through $\Psi_{EP_3}^{(\mathrm{est})}$ the location of the EP_3 estimated from "*Whirlpool scans*" as shown in Fig. 3.2. Panels **(a-d)** show filtered data for $d(\Psi)$ in a 3D view, for a quantitative estimate the location of EP_3 by identifying the minima in $d(\Psi)$, while one of the control parameters are held fixed estimated $\Psi_{EP_3,i} = \{\delta_{EP_3}, P_{3,EP_3}, P_{2,EP_3}, P_{1,EP_3}\}$, respectively. The identified minima in $d(\Psi)$ in each 2D sheet is indicated by a black disk. For each panel, we also show the full view of the corresponding 2D sheets identified by gray arrows.

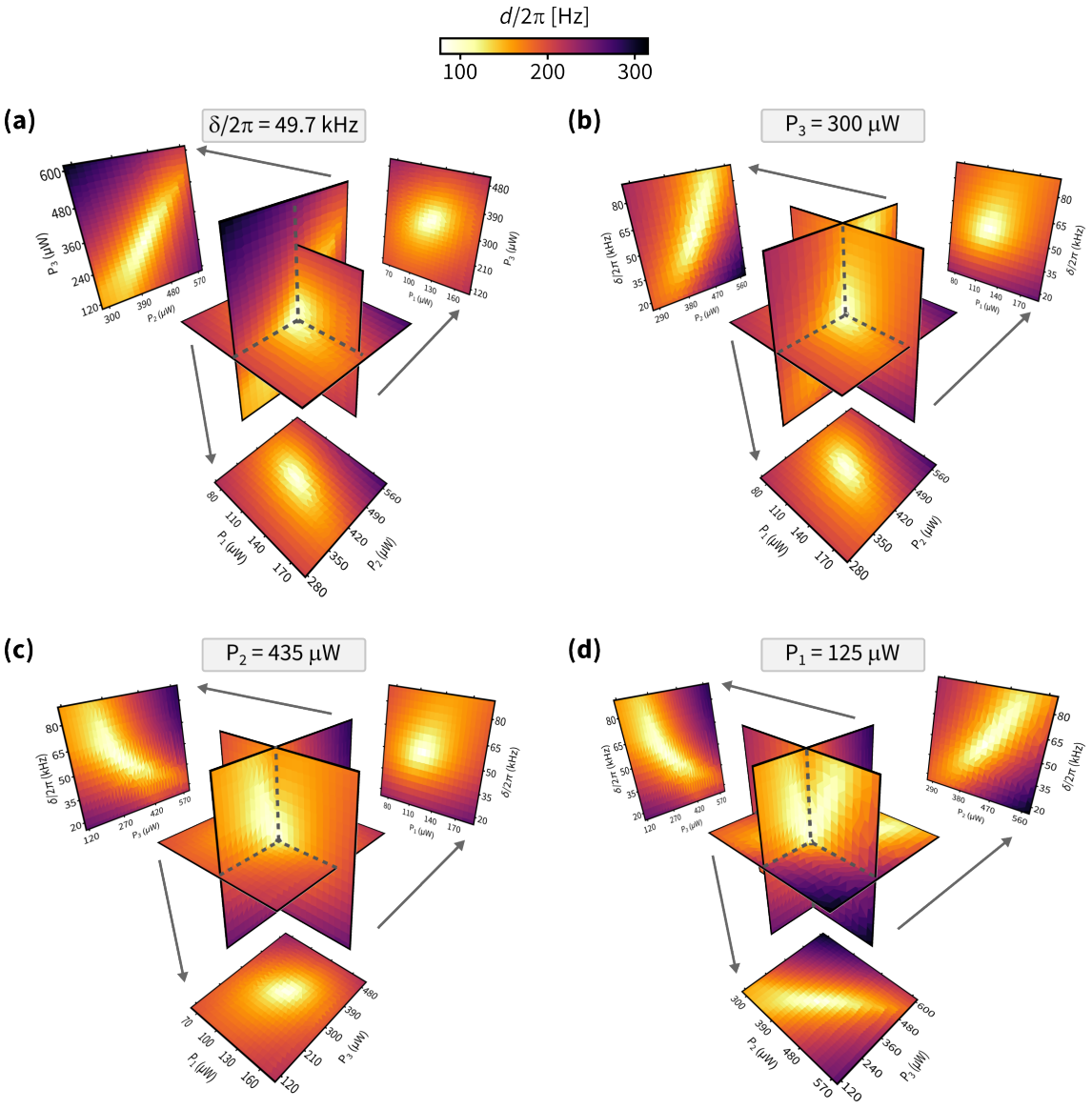

Figure 3.5: Locating EP_3 - part III. The quantity $d(\Psi)$ (which ideally vanishes at Ψ_{EP_3}), calculated for six 2D sheets passing through $\Psi_{EP_3}^{(\mathrm{est})}$ the location of the EP_3 estimated from "*Whirlpool scans*" as shown in Fig. 3.2. Panels **(a-d)** show numerical calculations for $d(\Psi)$ in a 3D view, while one of the control parameters are held fixed estimated $\Psi_{EP_3,i} = \{\delta_{EP_3}, P_{3,EP_3}, P_{2,EP_3}, P_{1,EP_3}\}$, respectively. $d(\Psi)$ is calculated from H with the best-fit optomechanical parameters obtained by fitting the knot of EP_2s (see Sec. B.7.1). The best-fit optomechanical parameters are given in Table B.1. For each panel, we also show the full view of the corresponding 2D sheets identified by gray arrows.

the map between the coefficients of the characteristic polynomial of H, and Ψ (see Sec. 2.3.3.1). Numerical calculation of $\mathrm{Det}(J)$ at EP_3 results in $\mathrm{Det}(J) \approx 10^{30}\ (2\pi\text{Hz})^9/\text{W}^3$. This value is non-zero. More precisely, it is of the order of magnitude expected from the form of J (see Eq. (2.92) and Sec. 2.3.3.1) and is roughly equal to $\left|\lambda^{(\mathrm{typ})}\right|^{10}/(\Delta P)^3(\Delta\delta)$ where $\left|\lambda^{(\mathrm{typ})}\right|/2\pi \approx 50$ Hz is the typical magnitude of the eigenvalue in the neighborhood Ψ_{EP_3}, and $\Delta P \approx 5$ μW and $\Delta\delta/2\pi \approx 10$ kHz are the typical scales of the control parameters over which $\boldsymbol{\lambda}$ vary.

(ii) We empirically demonstrate the spectral flow on a hypersurface enclosing the EP_3 point and verify its salient characteristics, i.e. that the EP_2s form a trefoil knotted structure, and control loops in the non-degenerate subspace result in non-commuting eigenvalue braids that belong to the braid group B_3. They are presented in the upcoming sections.

3.2.2 Locating the $\boldsymbol{EP_2}$ degeneracies

In this section, we describe measurements of eigenspectra on a hypersurface surrounding the EP_3 point and locate the double degeneracies, the EP_2s.

To study the spectrum on a hypersurface surrounding Ψ_{EP_3}, we measured $\boldsymbol{\lambda}$ on the boundary of a four-dimensional (4D) hyperrectangle $\mathcal{S}$ centered close to Ψ_{EP_3}. Specifically, $\mathcal{S}$ bounds the region: -10 kHz $\leq \delta/2\pi \leq$ 105.6 kHz, 22 μW $\leq P_1 \leq$ 240 μW, 289 μW $\leq P_2 \leq$ 675 μW, 78 μW $\leq P_3 \leq$ 702 μW. It consists of eight polyhedrons (referred to as "faces"), each with one element of Ψ fixed to its minimum or maximum value, while the remaining three elements of Ψ range from their minimum value to their maximum value. An animated visualization of $\mathcal{S}$ is shown in Ref. [199]. Ψ was densely rastered over sixty-one distinct two-dimensional (2D) 'sheets' within $\mathcal{S}$ and they are shown in Fig. 3.6. For each datapoint in each sheet, we measure $\boldsymbol{\lambda}$ and s_{ij} as described in Sec. 3.1.3 and construct the discriminant D and the eigenvector indicator E (see Sec. 2.1.3.2).

$$D = (\lambda_1 - \lambda_2)^2(\lambda_2 - \lambda_3)^2(\lambda_3 - \lambda_1)^2 \tag{3.6}$$

$$E = \mathrm{Det}(S)^{-2} \tag{3.7}$$

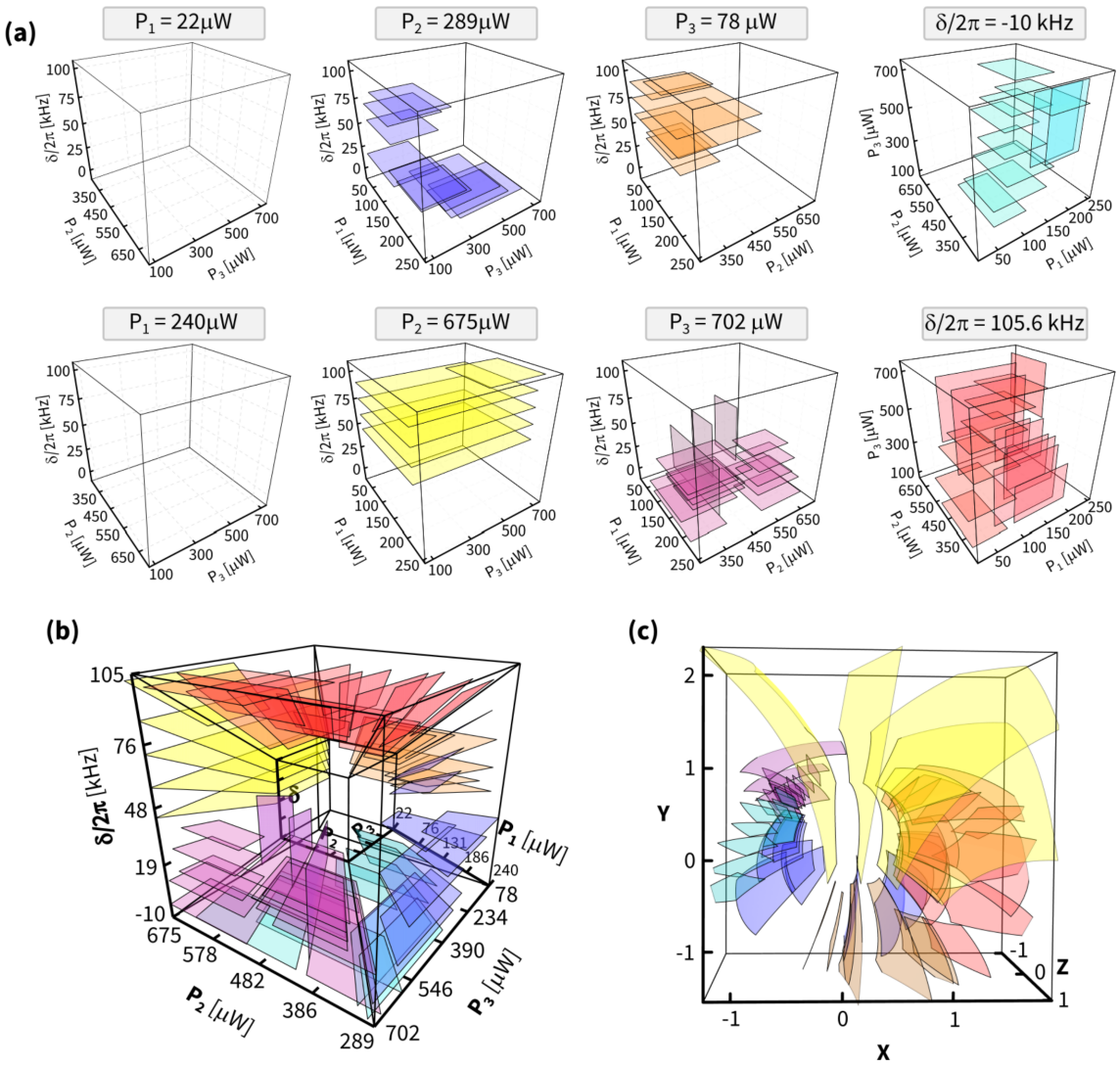

Figure 3.6: The locations of the sixty-one 2D sheets within the hypersurface $\mathcal{S}$. The sheets are color-coded by the 3D face in which they lie. **(a)** The sheets are shown within each of the eight 3D faces of $\mathcal{S}$. **(b)** The same sheets as in (a), shown using the "rectilinear stereographic" projection. The thin black lines show the boundary of each sheet. Note that in this projection, all of the sheets are contained within the plot's bounding box. **(c)** The same sheets as in (a), shown using the standard stereographic projection. The thin black lines show the boundary of each sheet. Thin gray lines show where a sheet exits the plot's bounding box.

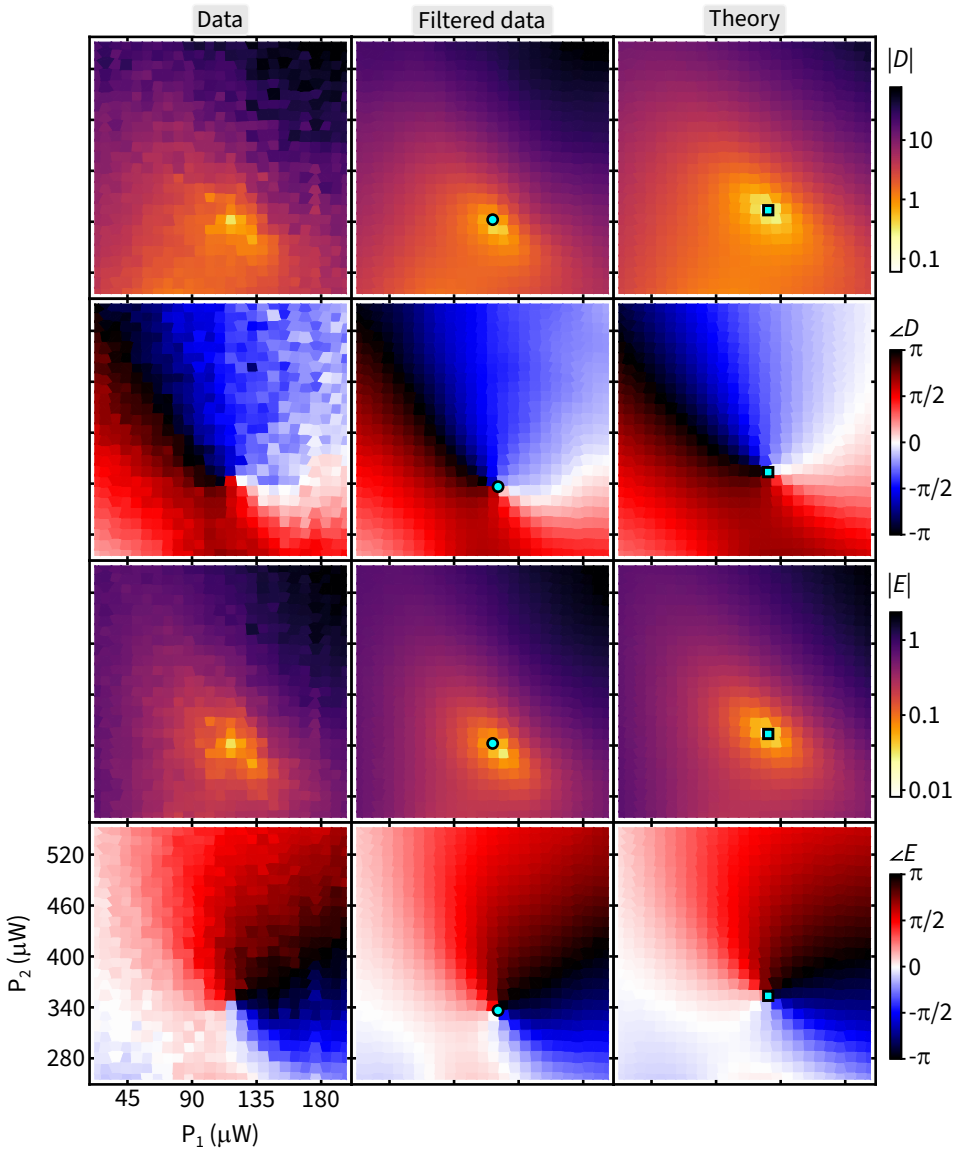

Figure 3.7: Locating EP_2 points on the hypersurface $\mathcal{S}$. The complex-valued quantities D and E measured on a typical 2D sheet in the hypersurface $\mathcal{S}$. The units of D are $10^{10} \times (2\pi \text{ Hz})^6$. For this sheet, the nominally fixed control parameters are: $P_3 = 78$ μW and $\delta/2\pi = 60$ kHz. Left column, raw data. Middle column, data after outlier rejection and smoothing. Cyan circles show algorithmically identified Ψ_{EP_2}. Right column, D and E calculated from optomechanics theory. Cyan squares, Ψ_{EP_2} determined from this calculation.

where S is the matrix formed by s_{ij}. Data from a typical sheet is shown in Fig. 3.7(first column), and data from all sixty-one data-sheets are shown in Ref. [200].

Both D and E are complex-valued, and vanish at an EP_2 point. More specifically at an EP_2 point, $|D| = |E| = 0$ and $\angle D, \angle E$ have a 2π winding. However, we emphasize that they provide complementary information: $D = 0$ reflects the eigenvalue degeneracy while $E = 0$ reflects the eigenvector degeneracy (see Sec. 2.1.3.2). Furthermore, D and E are derived from different aspects of the fits to $\tilde{V}(\tilde{\omega}_{\mathrm{AM}})$ (see Sec. 3.1.3 and B.1), and thus reflect partially independent features of the data.

We constructed appropriate algorithms to identify minima[1] in $|D|, |E|$ (Sec. B.5.3) and phase winding in $\angle D, \angle E$ (Sec. B.5.4) in our data. The values of Ψ tagged as a minima or a vortex constitute the list of measured EP_2 points: Ψ_{EP_2}s. Fig. 3.7 (second column) illustrate the identified Ψ_{EP_2} as cyan disks and agree well with the theoretical calculations (Sec. B.7.2) shown in Fig. 3.7 (third column) and the corresponding Ψ_{EP_2} from theory are shown as cyan squares.

3.2.3 Tracing the knotted EP_2 degeneracies

In this section, we illustrate the list of measured of EP_2 points that were obtained in the previous section: Sec. 3.2.2.

Figs. 3.8 shows measured Ψ_{EP_2} using the four indicators: minima in $|D|, |E|$ and phase-vortices in $\angle D, \angle E$, separately. They are depicted using two projections of the hypersurface $\mathcal{S}$. The first projection is the standard stereographic projection (top row, see also Sec. B.2.1), while the later uses a projection that is more steeped in the actual experiment and easily connected to the control parameters (bottom row), and we refer to it as "rectilinear-stereographic" projection (Sec. B.2.2). We note that both projections are isomorphic to each other and generically preserve the topology of $\mathcal{S}$ and knot equivalence classes. In both projections, the measured Ψ_{EP_2} are seen to trace out a curve that forms

[1]As in the case of locating EP_3, locating EP_2 suffers from a similar problem i.e., the sharp cusp in $|D| \sim |\Psi - \Psi_{EP_2}|^{1/2}$ and $|E| \sim |\Psi - \Psi_{EP_2}|^{1/2}$ are broadened by fluctuations in Ψ and system parameters. However, EP_2 identification is more robust than EP_3. This is because we use filtered complex valued quantities D, E for EP_2s, rather than a real valued quantity d for EP_3. Filtering is more effective in averaging the random fluctuations in measured D and E than d, arising from random fluctuations in Ψ and system parameters.

a trefoil knot $\mathcal{K}$. For ease of identification, especially when distinct portions of $\mathcal{K}$ happen to pass close to each other in a given projection, each Ψ_{EP_2} is colored according to the value of ϑ as defined below:

$$\vartheta = \mathrm{Arg}\left(\frac{2\prod_{i=1}^{3}\overline{\lambda_i}}{\sum_{i=1}^{3}\overline{\lambda_i}^2}\right) \tag{3.8}$$

where $\overline{\lambda_i} = \lambda_i - \sum_{i=1}^{3}\lambda_i/3$ for $i \in \{1,2,3\}$. ϑ runs from 0 to 2π around $\mathcal{K}$. It is simply the complex argument of the non-degenerate member of $\overline{\boldsymbol{\lambda}}$, and so is readily determined from the data. Fig. 3.9 shows all measured Ψ_{EP_2} plotted together, highlighting the good agreement between the four independent indicators. Figs. 3.8 and 3.9 also shows the theoretically predicted $\mathcal{K}$ obtained by fitting measured Ψ_{EP_2} and they match well to the measurements. Details regarding the fit to Ψ_{EP_2}s and generating the theory curves are discussed in Sec. B.7.

To further illustrate the measurements of EP_2s and simplify visualization, we algorithmically join the measured Ψ_{EP_2} that are "next to" each other (as defined below) and explicitly show the trefoil knot $\mathcal{K}$, independently from the measurements. We start by coordinatizing each Ψ_{EP_2} as Ω given by

$$\Omega_i = \{X_i, Y_i, Z_i, \mathrm{Cos}(\vartheta_i), \mathrm{Sin}(\vartheta_i)\} \tag{3.9}$$

where $\{X, Y, Z\}$ represent Ψ_{EP_2} in the standard stereographic projection. For each Ω, we find the nearest and the next nearest neighbor based on their Euclidean distance (the L^2 distance). Using this information, we sort the list of degeneracies so that the nearest neighbors are the adjacent elements of Ψ_{EP_2}. We then interpolate the sorted list with a cubic spline. This exercise is illustrated in Fig. 3.10 where Ψ_{EP_2}s obtained by each of the four indicators were independently sorted and interpolated as described above, and are shown in both projections of $\mathcal{S}$. For simplicity, going forward we will use $\mathcal{K}$ obtained from interpolating Ψ_{EP_2}s that were identified by phase-vortices in $\angle D$.

Animated illustrations of the trefoil knot $\mathcal{K}$ are shown in Ref. [201] for the "rectilinear stereographic" projection of $\mathcal{S}$ and in Ref. [202] for both projections of $\mathcal{S}$.

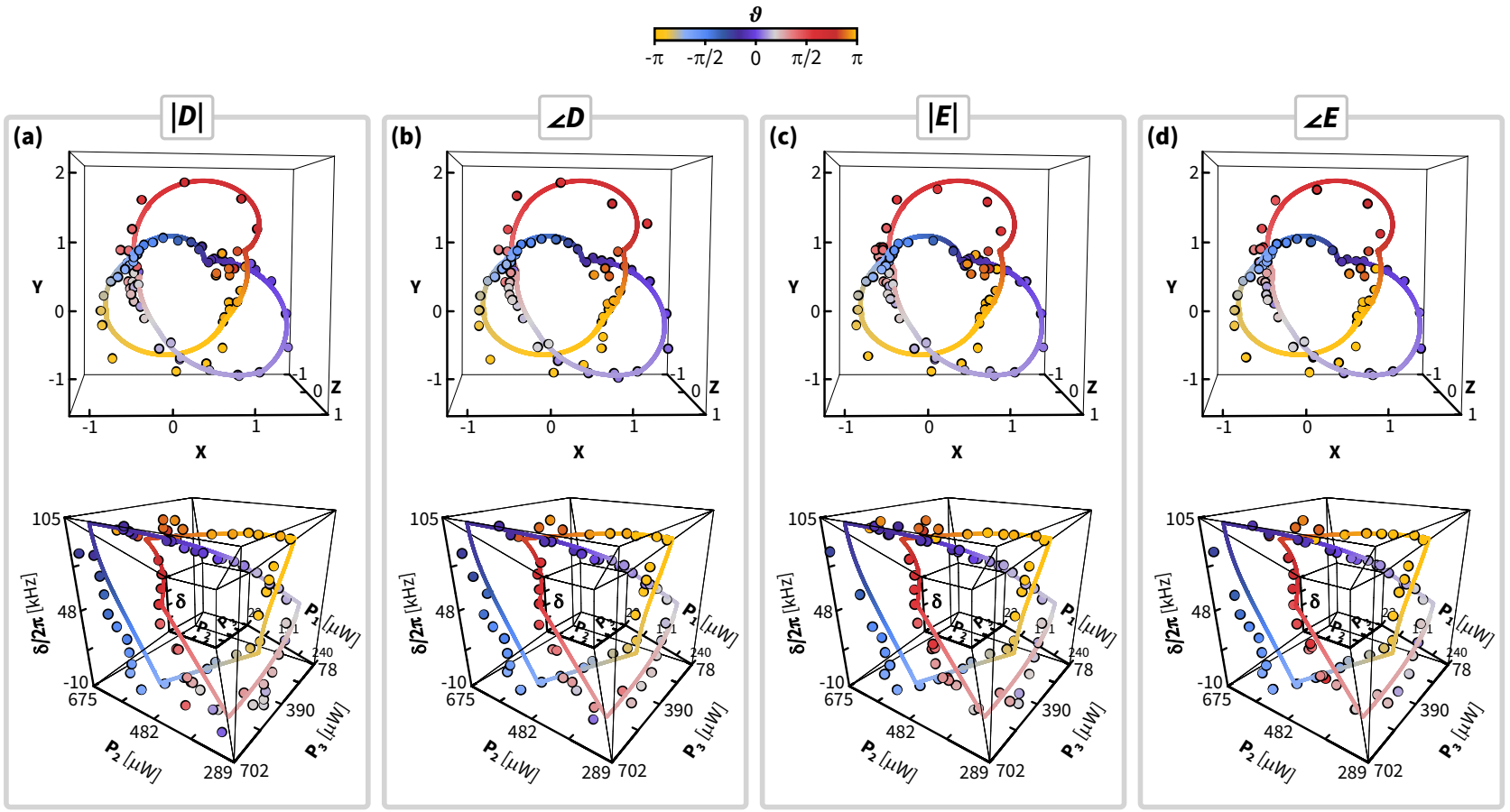

Figure 3.8: The measured knot of EP_2 via four different indicators - part I. (a) All of the EP_2 locations Ψ_{EP_2} shown in standard stereographic projection of hypersurface $\mathcal{S}$ (top panel), and "rectilinear stereographic" projection (bottom panel). Disks: measured Ψ_{EP_2} via minima identification in magnitude of D and solid curve: best fit to all the measured Ψ_{EP_2}. Both measurement and fit are colored according to the measured and the fitted value of ϑ coordinate along the trefoil knot of EP_2, respectively. **(b)** Same as (a) but measured Ψ_{EP_2} are identified via phase-vortex of D. **(c)** Same as (a) but measured Ψ_{EP_2} are identified via minima in magnitude of E. **(d)** Same as (a) but measured Ψ_{EP_2} are identified via phase-vortex of E. Measurements of Ψ_{EP_2} from all four indicators independently trace out a trefoil knot of EP_2.

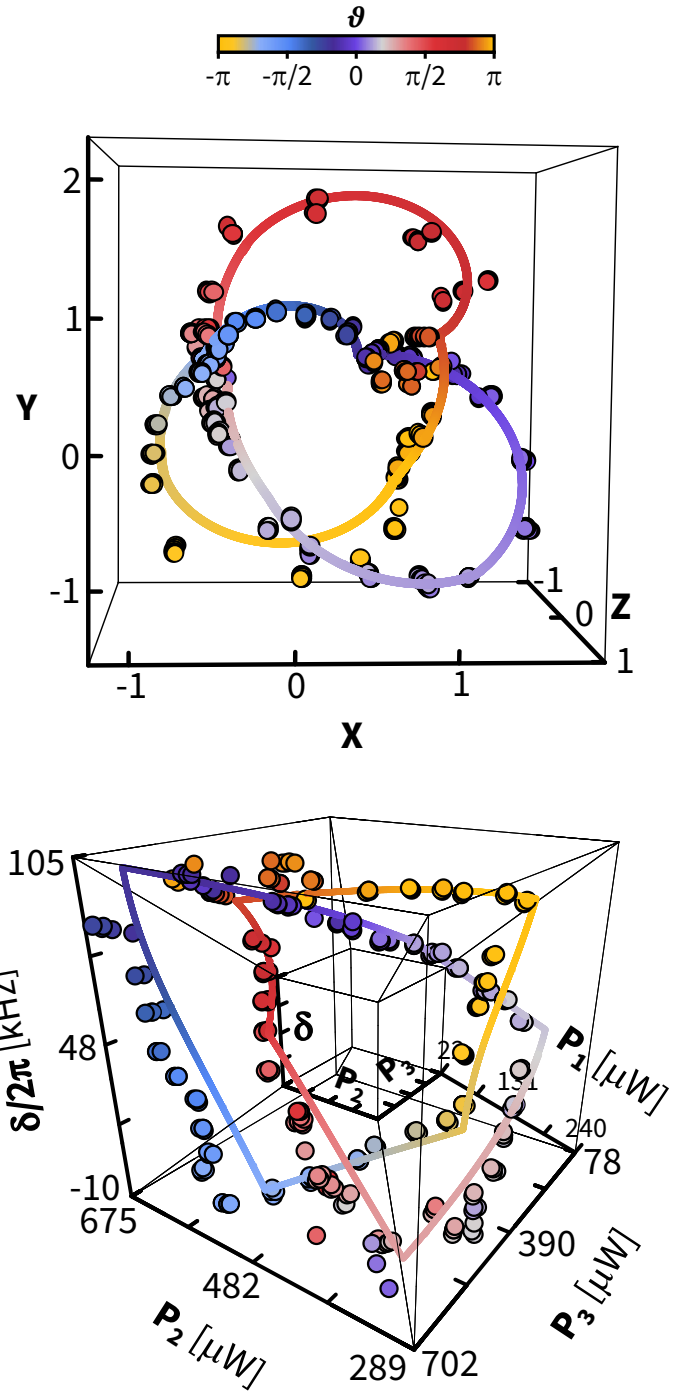

Figure 3.9: The measured knot of EP_2 via four different indicators - part II. All of the EP_2 locations Ψ_{EP_2} shown in standard stereographic projection of hypersurface $\mathcal{S}$ (top panel), and "rectilinear stereographic" projection (bottom panel). Disks: measured Ψ_{EP_2} via all four indicators i.e., minima identification in magnitude of D, E and phase-vortex identification of D, E, all placed together. Solid curve: best fit to all the measured Ψ_{EP_2}. Both measurement and fit are colored according to the measured and the fitted value of ϑ coordinate along the trefoil knot of EP_2, respectively. Measurements of Ψ_{EP_2} from all four indicators that independently trace out a trefoil knot of EP_2, are in mutual agreement.

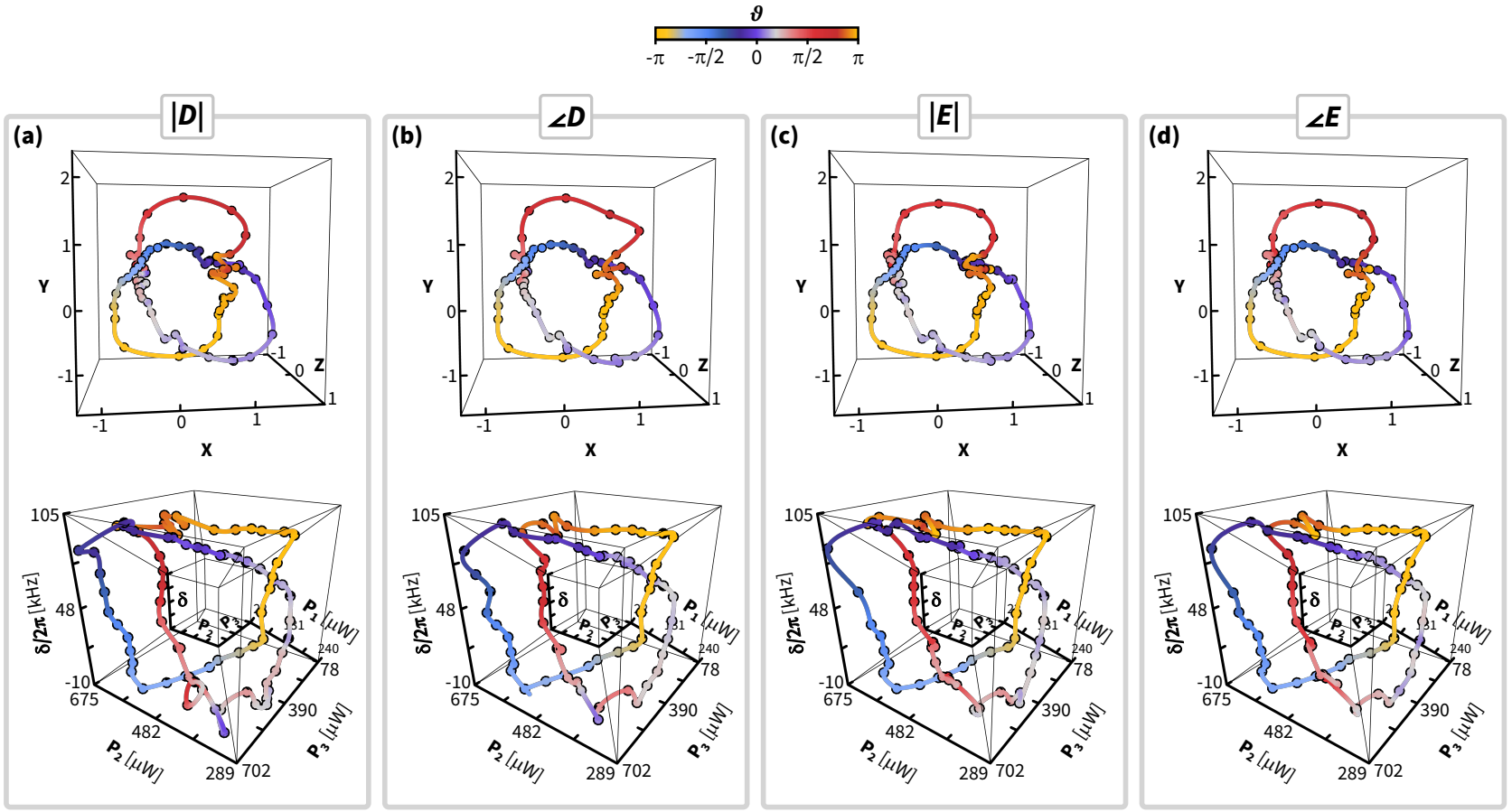

Figure 3.10: The measured knot of EP_2 via four different indicators - part III. (a) All of the EP_2 locations Ψ_{EP_2} shown in standard stereographic projection of hypersurface $\mathcal{S}$ (top panel), and "rectilinear stereographic" projection (bottom panel). Disks: measured Ψ_{EP_2} via minima identification in magnitude of D. Solid curve: cubic spline that algorithmically joins the identified Ψ_{EP_2}. Both measurement and spline are colored according to the measured value of ϑ coordinate along the trefoil knot of EP_2. **(b)** Same as (a) but measured Ψ_{EP_2} are identified via phase-vortex of D and then joined algorithmically with a cubic spline. **(c)** Same as (a) but measured Ψ_{EP_2} are identified via minima in magnitude of E and then joined algorithmically with a cubic spline. **(d)** Same as (a) but measured Ψ_{EP_2} are identified via phase-vortex of E and then joined algorithmically with a cubic spline. Measurements of Ψ_{EP_2} from all four indicators are explicitly and unambiguously shown to independently trace out a trefoil knot of EP_2.

3.3 Eigenvalue braids

Having identified the degeneracies, we now turn to the non-degenerate spectra. In this section, we describe measurements that illustrate braiding of non-degenerate $\boldsymbol{\lambda}$ when Ψ is varied around a control loop $\mathcal{C}$ in the non-degenerate subspace. The eigenvalue braids are then shown to form the braid group B_3 via its generators, several exemplary group elements and its non-Abelian character.

3.3.1 Characterizing the braid group B_3

When Ψ is varied along a control loop $\mathcal{C}$ from a given homotopy class ℓ, $\boldsymbol{\lambda}(\Psi)$ is expected to form a braid, whose equivalence class b is determined by ℓ (Sec. 2.1.1). To demonstrate this, we select pixels from the dataset described above (the sixty-one sheets) that trace out three distinct $\mathcal{C}$s with a common basepoint. In particular, each $\mathcal{C}$ belongs to a different ℓ. This is shown in Fig. 3.11(a-c). The corresponding $\boldsymbol{\lambda}(\Psi)$ for each $\mathcal{C}$ is illustrated in Fig. 3.11(d-f) and resulting eigenvalue braids form $b = \mathbb{I}, \sigma_1, \sigma_2\sigma_1$, respectively. Here, $\mathbb{I}$ is the identity and $\sigma_i(\sigma_i^{-1})$ indicates that the braid strand i has crossed over (under) the braid strand $i+1$. The braid strands are counted from left in the view used for the figures and the operations are written from right to left, as the braid word is read from bottom to top [104]. The braids σ_1 and $\sigma_2\sigma_1$ are the generators the braid group B_3 and their corresponding $\mathcal{C}$s (Fig. 3.11(b,c)) can be concatenated to produce any eigenvalue braid. The topological correspondence between the control loop's ℓ and the b it produces is a robust feature of the data and it is further illustrated in Figs.3.12-3.16, which show eigenvalues braids produced by several other control loops.

The non-Abelian character of B_3 is demonstrated in Fig. 3.13. Fig. 3.13(a) shows $\mathcal{C}$s (red, blue) that belong to different ℓ. Fig. 3.13(b) shows $\boldsymbol{\lambda}(\Psi)$ as Ψ is stepped first around the blue loop and then around the red loop, whereas Fig. 3.13(c) shows $\boldsymbol{\lambda}(\Psi)$ as Ψ is stepped first around the red loop and then around the blue loop. The former gives $b = \sigma_1^{-1}\sigma_2^{-1}$, while the latter gives $b = \sigma_2^{-1}\sigma_1^{-1}$. The inequivalence of these braids can be seen directly from the fact that they result in different permutations of $\boldsymbol{\lambda}$. This also demonstrates that encircling a degeneracy is not characterized by a number (as in the

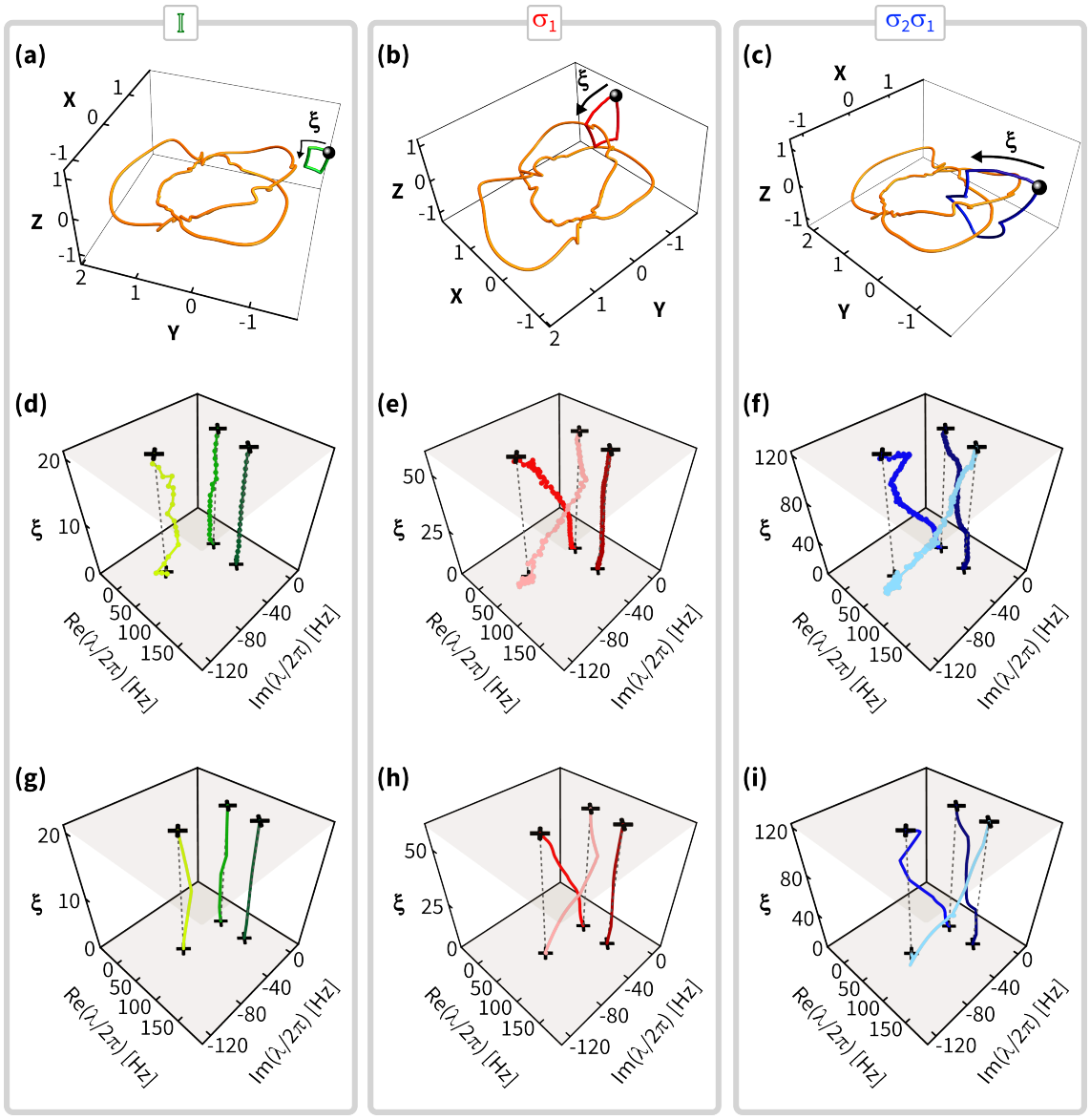

Figure 3.11: Measurements of eigenvalue braids - part I. (a-c) Three control loops (green (a), red (b), blue (c)) in $\mathcal{S}$, each from a different homotopy equivalence class and share a common basepoint (black sphere). The measured knot $\mathcal{K}$ is shown as the orange curve in the standard stereographic projection. **(d–f)** The eigenvalue spectrum $\boldsymbol{\lambda}(\Psi)$ as Ψ is varied around the corresponding loop shown in (a–c), respectively. ξ indexes the values of Ψ along each control loop. The black crosses show $\boldsymbol{\lambda}$ at the basepoint. The dashed lines are guides to the eye. The measured $\boldsymbol{\lambda}$ traces out the braids: $\mathbb{I}$ (d), σ_1 (e) and $\sigma_2\sigma_1$ (f). These braids characterize the braid group B_3, as they represent the identity element and the two generators of the group, respectively. **(g-i)** The eigenvalue spectrum as calculated using the optomechanical parameters determined from fitting the knot of EP_2s.

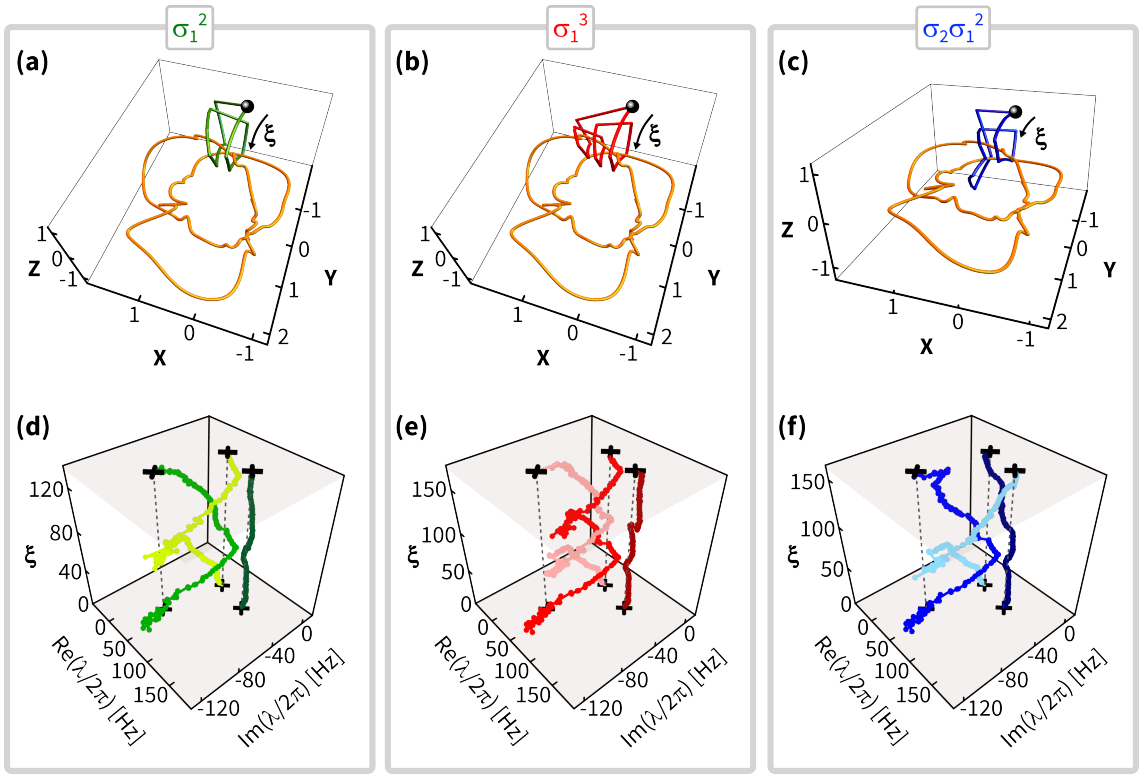

Figure 3.12: Measurements of eigenvalue braids - part II. (a-c) Three control loops (green (a), red (b), blue (c)) in $\mathcal{S}$, each from a different homotopy equivalence class, share a common basepoint (black sphere) and, are non-self intersecting. The measured knot $\mathcal{K}$ is shown as the orange curve in the standard stereographic projection. **(d–f)** The eigenvalue spectrum $\boldsymbol{\lambda}(\Psi)$ as Ψ is varied around the corresponding loop shown in (a–c), respectively. ξ indexes the values of Ψ along each control loop. The black crosses show $\boldsymbol{\lambda}$ at the basepoint. The dashed lines are guides to the eye. The measured $\boldsymbol{\lambda}$ traces out the braids: σ_1^2 (d), σ_1^3 (e) and $\sigma_2\sigma_1^2$ (f). These braids represent additional elements of the braid group B_3, obtained by concatenating control loops that produce the group generators σ_1 and σ_2.

$N = 2$ case), but by a braid equivalence class.

3.3.1.1 Consequences of accessing a restricted control space: Part II

So far, we have experimentally demonstrated various features of spectral flow in the full space of control parameters. However, we recall our discussion in Sec. 2.1.3.4 and observe that the dimensionality of the control space grows linearly in the number of modes (i.e. N) considered. Thus, despite their straightforward mathematical description (as in Sec. 2.1.1), their high dimensionality makes visualization of the relevant subspaces hard, and in many cases it may not be practical to span the full space of control parameters i.e., $2(N-1)$ (real) parameters for N modes. As a result, it may sometimes be a helpful simplification to consider a low-dimensional "slice" in the full control space. Below, we

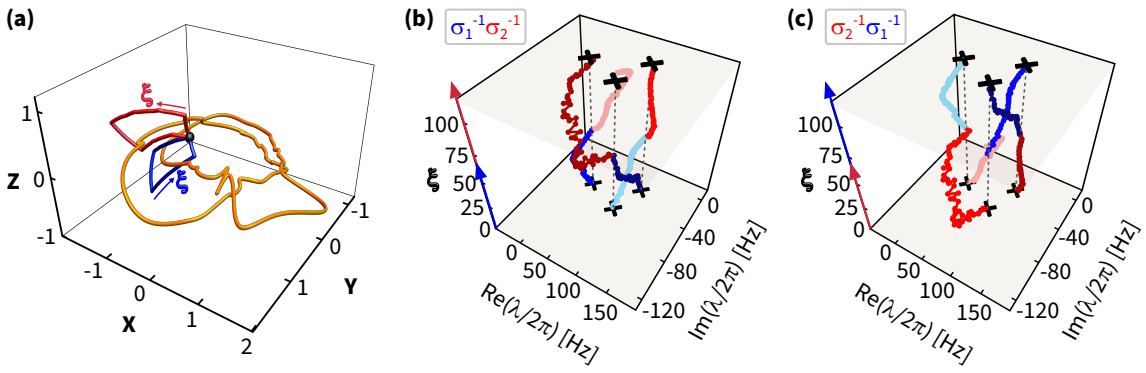

Figure 3.13: Measurements of eigenvalue braids - part III. (a) Two control loops (blue, red) that belong to different homotopy equivalence classes. They are non-intersecting, except that they have a common basepoint (black sphere). The measured knot is shown as the orange curve in the standard stereographic projection. **(b)** The spectrum $\boldsymbol{\lambda}(\Psi)$ as Ψ is varied around the control loop formed by concatenating the two loops in (a). Specifically, the blue loop is traversed first ($1 \leq \xi \leq 57$), and then the red loop ($58 \leq \xi \leq 116$). The black crosses show $\boldsymbol{\lambda}$ at the basepoint. The dashed lines are guides to the eye. **(c)** The spectrum $\boldsymbol{\lambda}(\Psi)$ as Ψ is varied first around the red loop ($1 \leq \xi \leq 59$), and then the blue loop ($60 \leq \xi \leq 116$). In both cases, the loops are traversed in the sense indicated by the arrows in (a). The braids in (b) and (c) are inequivalent, highlighting the non-Abelian nature of the braid group B_3, and the non-commutation of the two control loops in (a).

study two such cases using our data and illustrate that such a simplification does not capture the key topological features of the full space, and the results may look surprising at first. See for e.g. Fig. 2.5. Finally, we also illustrate the role of the basepoint of control loops.

Case I: Equivalent eigenvalue braids from "different" loops

To examine the effect of control loops viewed in either the full control space or in a 2D subspace, we take the region $\mathcal{B}^{(1)}$ shown in Fig. 3.14(a) as our first example of a 2D control space, and consider the two loops shown as green and blue in Fig. 3.14(a). These loops share a common basepoint, and are clearly not homotopic in $\overline{\mathcal{B}}^{(1)}$ (defined as $\mathcal{B}^{(1)}$ without the two EP_2 points). However, Figs. 3.14(b,c) show that these loops are homotopic in $\mathcal{G}_3$ (defined as full control space $\mathcal{L}_3$ minus the degeneracies $\mathcal{V}_3$, formally $\mathcal{G}_3 = \mathcal{L}_3 \setminus \mathcal{V}_3$), and that each loop is contractible to a point. Measurements of $\boldsymbol{\lambda}$ at several positions along each loop are shown in Figs. 3.14(d,e), and they demonstrate that these loops produce isotopic braids (in this case, the identity braid), as expected from Fig. 3.14(b,c). This illustrates one of the striking features similar to Fig. 2.5: the braid traced out by $\boldsymbol{\lambda}$ is determined by the loop's homotopy class in full control space, and not

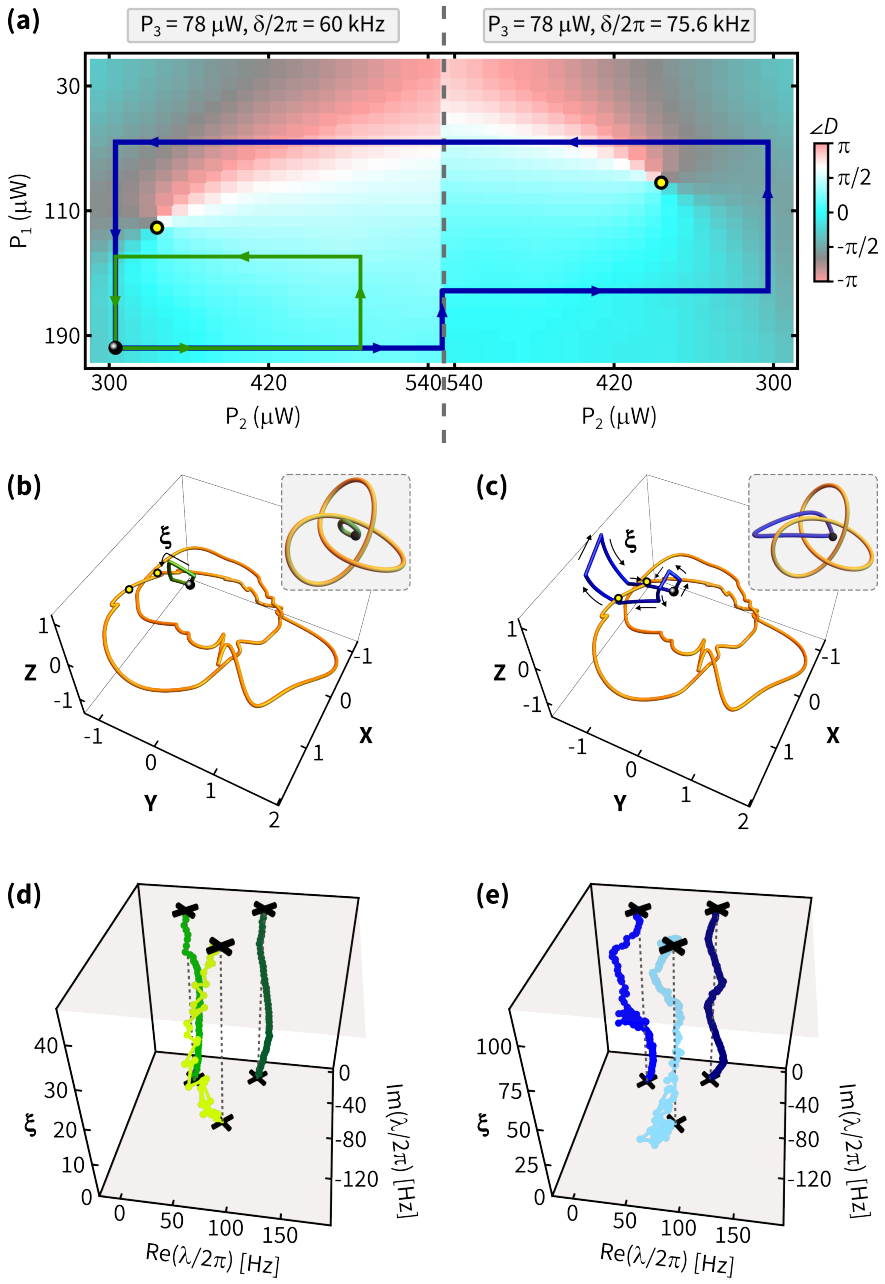

Figure 3.14: Equivalent eigenvalue braids from "different" loops. (a) The 2D control space $\mathcal{B}^{(1)}$. Color scale: $\angle D$. Yellow circles: phase-vortices $\angle D$, which corresponds to EP_2s. Green and blue curves: control loops. Black disk: the loops' common basepoint. A view of $\mathcal{B}^{(1)}$ in full control space $\mathcal{L}_3$ is shown in Fig. B.1. **(b)** Standard stereographic projection of hypersurface $\mathcal{S}$. The axes X, Y, Z are defined in Sec. B.2.1. Orange curve: the measured EP_2s. The black disk, green curve, and yellow circles are as in (a). The control loops consist of straight segments in (a) but appear curved in (b) owing to the stereographic projection. Inset: a simplified cartoon of the relationship between the EP_2s and the control loop. **(c)** As in (b), but for the blue control loop. **(d)** The eigenvalue spectrum $\boldsymbol{\lambda}$ as a function of position along the green control loop. ξ indexes the measurements of $\boldsymbol{\lambda}$ along the control loop. **(e)** As in (d), but for the blue control loop. Although the loops are not homotopic in $\overline{\mathcal{B}}^{(1)}$, they are homotopic in $\mathcal{G}_3$, and so produce isotopic braids.

by its homotopy class in any particular 2D subspace.

Case II: Encircling the same EP_2 degeneracies

Another important feature of 2D control spaces is that control loops may encircle the same EP_2 points and yet give rise to distinct eigenvalue braids [131]. This scenario is demonstrated in Fig. 3.15(a), which shows our second example of a 2D control space $\mathcal{B}^{(2)}$. Here, the two loops (red and blue) share a common basepoint and encircle the same EP_2 points. Nevertheless, they are not homotopic in either $\bar{\mathcal{B}}^{(2)}$ or $\mathcal{G}_3$ as shown in Figs. 3.15(b,c). Consequently, the braids they produce are not isotopic, as illustrated in Fig. 3.15(d,e).

Case III: Role of the basepoint

In this section, we investigate the role of the control loops' basepoints in determining their homotopy equivalence. To do so, we use the data shown in Fig. 3.16(a), which depicts a third 2D control space $\mathcal{B}^{(3)}$, along with two loops. These loops are homotopic if their basepoint is the white circle; however, they are non-homotopic if their basepoint is the black circle. This also holds if the loops are viewed in $\mathcal{L}_3$, as shown in Figs. 3.16(b,c). As a result, the loops generate isotopic braids when based at the white point (Fig. 3.16(d,e)) and non-isotopic braids when based at the black point (Fig. 3.16(f,g)).

Discussion

Through the examples above, we have considered two complementary ways of describing the topological features that arise when the spectrum of a non-Hermitian system is tuned. The first describes tuning all of the system's control parameters [43], while the second considers with two control parameters [131]. The former offers ease of visualization and corresponds to many actal experiments, but may mask the features that determine which control loops are topologically distinct from each other. The latter provides a clear picture of topological equivalence but can be more challenging to visualize.

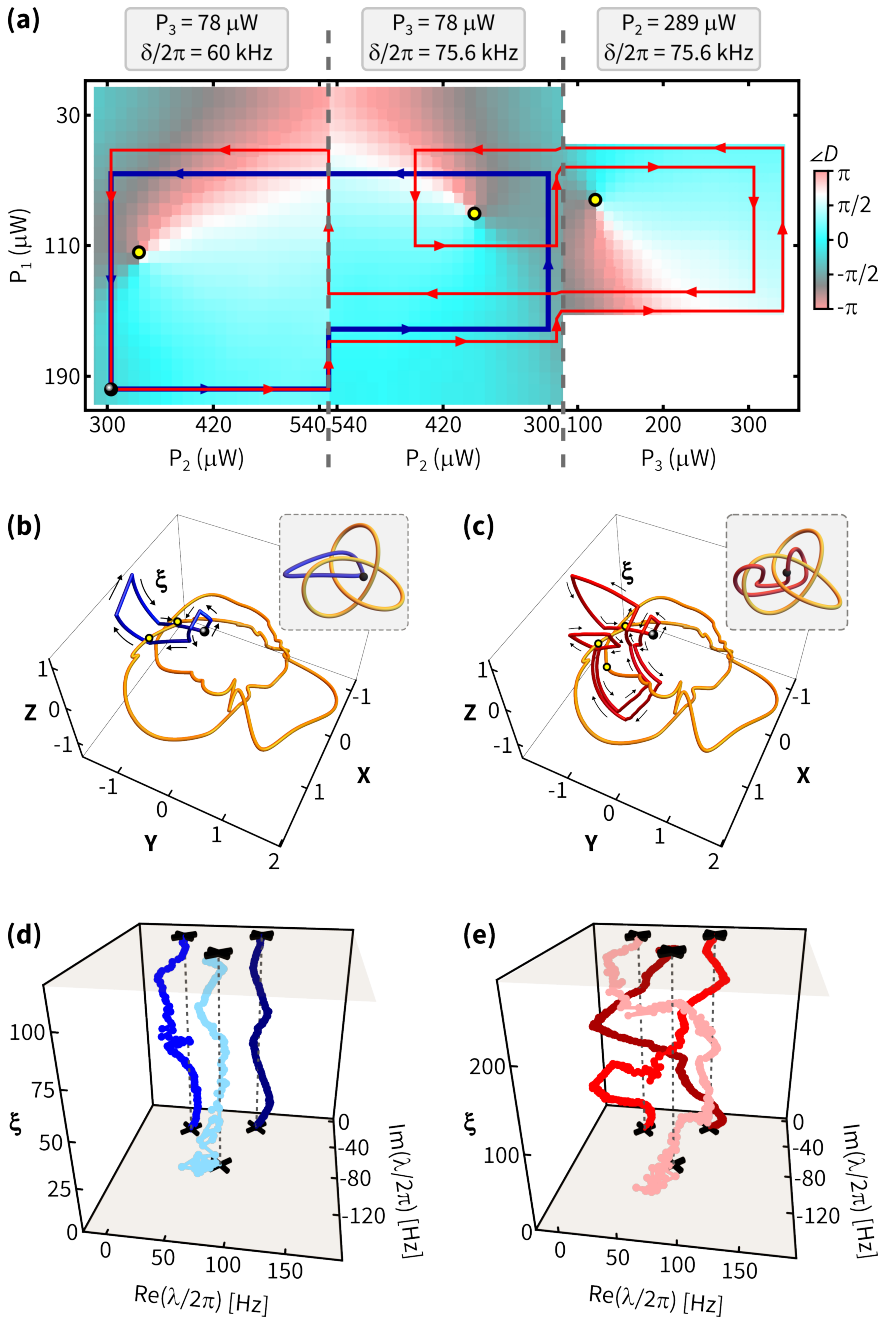

Figure 3.15: Different braids by encircling the "same" EP_2 points. (a) The 2D control space $\mathcal{B}^{(2)}$. Color scale: $\angle D$. Yellow circles: phase-vortices $\angle D$, which corresponds to EP_2s. Blue and red curves: control loops. Black disk: the loops' common basepoint. A view of $\mathcal{B}^{(2)}$ in full control space $\mathcal{L}_3$ is shown in Fig. B.1. **(b)** Standard stereographic projection of hypersurface $\mathcal{S}$. Orange curve: the measured EP_2s. The black disk, blue curve, and yellow circles are as in (a). Inset: a simplified cartoon of the relationship between the EP_2s and the control loop. **(c)** As in (b), but for the red control loop. **(d)** The eigenvalue spectrum $\boldsymbol{\lambda}$ as a function of position along the blue control loop. ξ indexes the measurements of $\boldsymbol{\lambda}$ along the control loop. **(e)** As in (d), but for the red control loop. The braids produced by the two loops are not isotopic and do not produce the same permutation, even though they encircle the same EP_2s in $\mathcal{B}^{(2)}$.

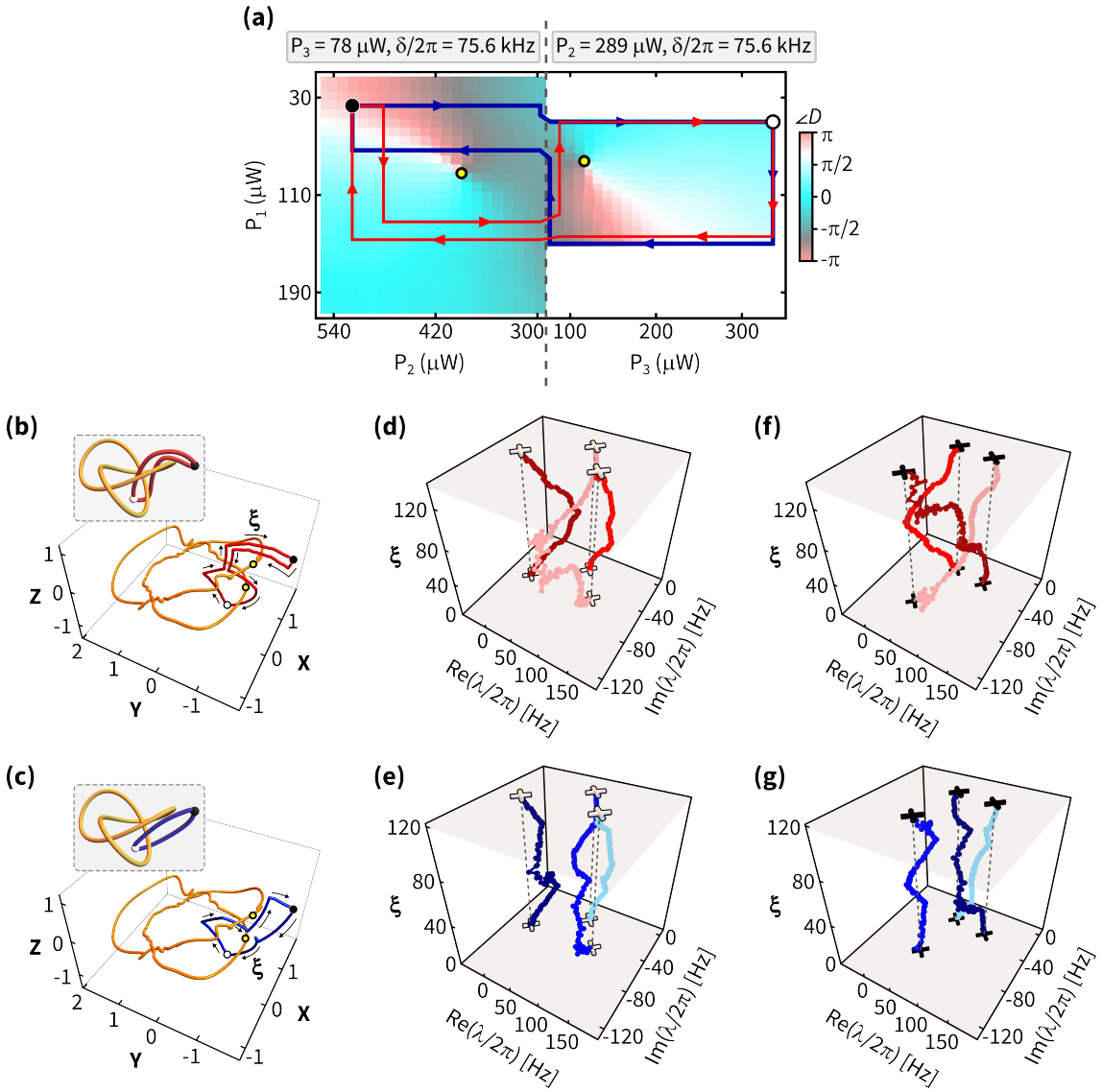

Figure 3.16: Measuring the basepoint dependence of homotopy equivalence. **(a)** The 2D control space $\mathcal{B}^{(3)}$. Color scale: $\angle D$. Orange circles: phase-vortices $\angle D$, which corresponds to EP_2s. Blue and red curves: control loops. Black and white disk: two choices for the loops' basepoint. A view of $\mathcal{B}^{(3)}$ in full control space $\mathcal{L}_3$ is shown in Fig. B.1. **(b)** Standard stereographic projection of hypersurface $\mathcal{S}$. Yellow curve: the measured EP_2s. The black disk, white disk, red curve, and yellow circles are as in (a). Inset: a simplified cartoon of the relationship between the EP_2s and the control loop. **(c)** As in (b), but for the blue control loop. **(d)** The eigenvalue spectrum $\boldsymbol{\lambda}$ as a function of position along the red control loop, using the white basepoint. ξ indexes the measurements of $\boldsymbol{\lambda}$ along the control loop. **(e)** As in (d), but for the blue control loop. **(f)** As in (d), but for the black basepoint. **(g)** As in (e), but for the black basepoint. When the two control loops shown in (a) are based at the white point, they are homotopic and so produce isotopic braids; however, the same loops based at the black point are not homotopic and produce non-isotopic braids.

Chapter 4

A new membrane-in-the-middle platform

In this chapter, we describe the experimental apparatus, that enables majority of the work reported in this thesis. We begin by highlighting the key features of the Membrane-in-the-middle (MIM) platform in Sec. 4.1, which readily casts it into an arbitrarily tunable non-Hermitian system. We then describe the design and construction of a new MIM system, specifically designed to study non-Hermitian physics. In Secs. 4.2 and 4.3, we individually characterize its two main ingredients: the Fabry-Perot optical cavity and the membrane, respectively. In Sec. 4.4, we integrate the membrane inside the optical cavity and characterize the resulting MIM system. We then benchmark it as a tunable and robust non-Hermitian system in Sec. 4.5. In Sec. 4.6 we describe the optical and electrical setups that are used to probe, control and stabilize the experimental apparatus. Additional technical details regarding this chapter can be found in Appendix C.

4.1 MIM design and construction

As motivated in Chapters 1 and 2, the MIM platform is an attractive candidate for studying arbitrarily tunable non-Hermitian systems with several naturally occurring degeneracies. In particular, the cryogenic MIM system in the Harris lab [93, 94] was a robust and prolific non-Hermitian experimental system with full static and real time control over system's dynamical matrix (H), eigenvalues ($\boldsymbol{\lambda}$) and eigenvectors ($\mathbf{u}$) [32, 43, 61, 91, 94, 95, 188, 192], via the dynamical back-action (DBA) effect of cavity optomechanics [175]. These achievements become even more admirable by noting the fact that they were all done in a single cool-down of the cryostat whose duration was 8 years (2014-2021). However, even with such a palmarès[1], it may come as a surprise that the cryogenic system was never designed for non-Hermitian physics but rather for studying quantum behavior of massive objects [81] (a detailed historical account is in Refs. [94, 95]). In addition, the results described in Refs. [43, 91, 95] (and adapted in Chapter 3) came at a certain cost, notably they required $\sim$100 days of non-stop data acquisition. While that is a testament to the system's robustness and long-term stability, it is natural to expect a faster turnaround.

In the following sections, we describe the design and construction of a new room-temperature MIM system that seeks to preserve the tunability, robustness and long-term stability of the previous system while incorporating the necessary and some desirable upgrades. (see also Sec. 8.2 of Ref. [95])

4.1.1 Design considerations

Below is a list of features we envisioned to incorporate in the new system.

Room-temperature operation

Non-Hermitian physics explored in the previous system is purely classical physics of few coupled Harmonic oscillators in a cryogenic environment (Sec. 3.1.1). This task maybe accomplished with a simpler and cost-effective room-temperature operation [203]. Any

[1]Palmarès (pronounced: pahl-mah-rays) is a French word meaning a compiled list of accolades.

room-temperature experiment will suffer from amplified thermal effects compared to its cryogenic counterpart. However, with appropriate monitoring and stabilization, one may expect similar performance from a MIM system operated at room-temperature.

Telecom wavelength and full fiber-optic based operation

Technological advances have put fiber-optic operations at telecom wavelength at the forefront. Incorporating all-fiber based 1550 nm light would represent a significant upgrade. These include more efficient, significantly cheaper and readily available fiber-optic components. Compared to their free-space counterparts, they have a much smaller footprint on an optical table which simplifies their control, improves robustness and require almost no optical alignment.

A "faster" MIM system

We would like a 100x speed-up of our system which would enable us to reproduce our previous work [43, 91] in a $\sim$1 day. To better understand the situation, we may note that for the previous system each datapoint corresponding to a measurement of the set of eigenvalues (Sec. 3.1.3), required $\sim$2 minutes of experimentation: half of it was spent for setting desired control parameters and the other half for mechanical modes' spectroscopy. While, using telecom wavelength optics would remedy the first part, and could already result in $>$10x speed-up, the second part requires a closer examination of the mechanical spectroscopy. The time-scale of such a measurement scales inversely with the normal modes' damping rate. If one were to simply increase the overall damping rate by a factor of 10, the susceptibility measurements would be 10x faster, thereby resulting in the desired speed-up. This can be achieved by increasing the DBA effect to produce larger optical damping. Detailed simulations were performed to obtain new system designs that would enable this speed-up (see Table 4.1). However, loosely speaking this translated to scaling down the system size, especially the optical cavity by a factor of $\sim$10. This scaling increased the single-photon coupling rate (g_0), which sets the overall magnitude of DBA, by a significant amount.

A "simpler" MIM system

A key feature of the previous system was the use of two independent optical modes of the Fabry-Perot optical cavity (both $\mathrm{TEM}_{0,0}$, but differ in their longitudinal index). One of them was used solely for the control of membrane motion, while the other for actuating and probing the membrane motion. This was accomplished using two independent laser systems whose frequencies were tethered with a Phase-Locked loop (PLL) and required precise control ($\sim$10 nm) of the membrane's position inside the cavity. This scheme was ingenious but a formidable task in practice [93–95, 188]. A simpler scheme with a single laser system is more desirable, with access to arbitrary optical modes ($\mathrm{TEM}_{\mathrm{m,n}}$) using polarization control and frequency modulation techniques. We also evaluated the feasibility of working with nearly degenerate membrane modes (as opposed to ones that required a Floquet theory description) and considered alternatives to a single square membrane system.

Preserve arbitrary tunability of the previous generation

The key feature enabling arbitrary tunability of the previous system was the ability to span a large portion of the complex plane of eigenvalues ($\boldsymbol{\lambda}$) using DBA, which was tuned via its control parameters. This was made possible partly because the system was comfortably in the resolved sideband regime of cavity optomechanics [175] i.e., $\kappa/\omega_m < 1$ where κ is the optical cavity linewidth and ω_m is membrane mode's frequency. This feature is illustrated in Sec. 2.3.1.1 and in Refs. [94, 189]. The other part came from the fact the system was well-behaved and stable to a wide-range of laser power and (red) detuning from cavity resonance. We would simply like to adapt this feature to the new system.

With the above considerations in mind, we performed simulations and obtained several candidates that incorporated the desired features and would crucially provide $\sim$10x speed-up in spectroscopy [189, 204]. The speed-up in spectroscopy is estimated as the ratio of the membrane modes' damping rate at EP_3 for the simulated system to that of the previous generation. The key specifications of a choice candidate are given in Table 4.1, and they are compared to those of the previous system (utilized in [43, 91, 95] and in Chapter 3). We note that the values for the previous generation system are either

measured experimentally or known a priori. We also provide the expected specifications for the actual system that was constructed and utilized for the majority of the work done in this thesis (Chapters 5, 6 and 7).

	MIM System		
Parameter	**Previous generation**	**Simulated**	**Actual**
λ (nm)	1064	1550	1550
L_{c} (mm)	37	3	7
$\mathcal{F}$	23000	40000	12320
$\kappa/2\pi$ (MHz)	0.18	1.25	1.74
a_m (mm)	1	0.5	0.5
t_m (nm)	50	136.9	150
$\omega_{5,5}/2\pi$ (MHz)	–	4.08	4.08
$\kappa/\omega_{5,5}$	–	0.31	0.43
$g_{0,[5,5]}/2\pi$ (Hz)	–	28.6	12.3
$\gamma_{EP_3}/2\pi$ (Hz)	102	1734	765
spectroscopy speed-up*	–	17x	7.5x

*estimated

Table 4.1: Comparing simulated MIM systems with the previous generation. λ: operating wavelength of lasers, L_c: optical cavity length, $\mathcal{F}$: optical cavity finesse, κ: optical cavity linewidth, a_m: square membrane side length, t_m: membrane thickness, $\omega_{5,5}$: frequency of the triply degenerate membrane mode, $g_{0,[5,5]}$: maximum single photon coupling rate of the triply degenerate membrane mode (assuming unity spatial overlap of the membrane mode to the optical mode), $\gamma_{EP_3}/2\pi$: membrane modes' damping rate at EP_3. We note that all systems here feature a free-space MIM cavity, and both the simulated and the actual system are intended for a room-temperature operation.

4.1.2 A new room-temperature MIM system

In this section, we describe the design and construction of the new MIM system that operates at room-temperature and high vacuum conditions. Here we specifically focus on the mechanical construction, vibration isolation and establishing vacuum.

4.1.2.1 Mechanical design and vibration isolation

The mechanical design of the system is illustrated in Fig. 4.1(a). The MIM cavity is fixed to the top copper plate[1] while sandwiching a thermo-electric cooler (TEC). This assembly is kinematically mounted [205] and thermally anchored to the middle copper plate[2]. Kinematic mounting is accomplished by housing three Viton balls[3] between sockets and vee-grooves in the middle and the top plate, respectively (see Fig. 4.1(b, c)). The middle copper plate is also connected to a heat-sink for heat dissipation. This assembly is again kinematically mounted on a stainless-steel puck[4] which in turn is kinematically mounted on a modified stainless-steel ConFlat (CF) vacuum flange[5]. The entire assembly is then enclosed in a vacuum chamber (Sec. 4.1.2.2) and sits on top of a custom aluminum mount[6] fixed to an optical breadboard[7]. The optical breadboard rests on a uniformly spaced 7×5 grid of 1" thick sorbothane pieces[8] with lateral dimensions: 2"×1.5", placed on an optical table-top[9]. The sorbothane dimensions result in a shape-factor of 0.43 (recommended: 0.3 - 1) and the estimated load per piece is ∼7 lb[10] (recommended: 3.7-8.6 lb) . The table-top rests on pneumatically floated supports. For acoustic noise isolation, a layer of sound-absorbing foam was glued to the underside of the optical breadboard. The entire assembly and all free-space optics were also enclosed in a box[11] with similar acoustic noise isolation.

[1] Oxygen-free high conductivity (OFHC) copper, thickness: 0.5", diameter: 4"
[2] OFHC copper, thickness: 1", diameter: 4"
[3] separated by 120°, diameter: 0.38"
[4] SS316, thickness: 2.6", diameter: 4"
[5] LDS 800-000
[6] thickness: 1", diameter: 5"
[7] THORLABS MB2448
[8] Durometer 0300
[9] TMC/ Ametek, 4 ft × 6 ft
[10] Shape factor: Ratio of loaded area (top surface: 3 sq. in.) to the exposed area (four vertical surfaces: 7 sq. in.). The total weight of the assembly is ∼250 lb.
[11] THORLABS XE25C series

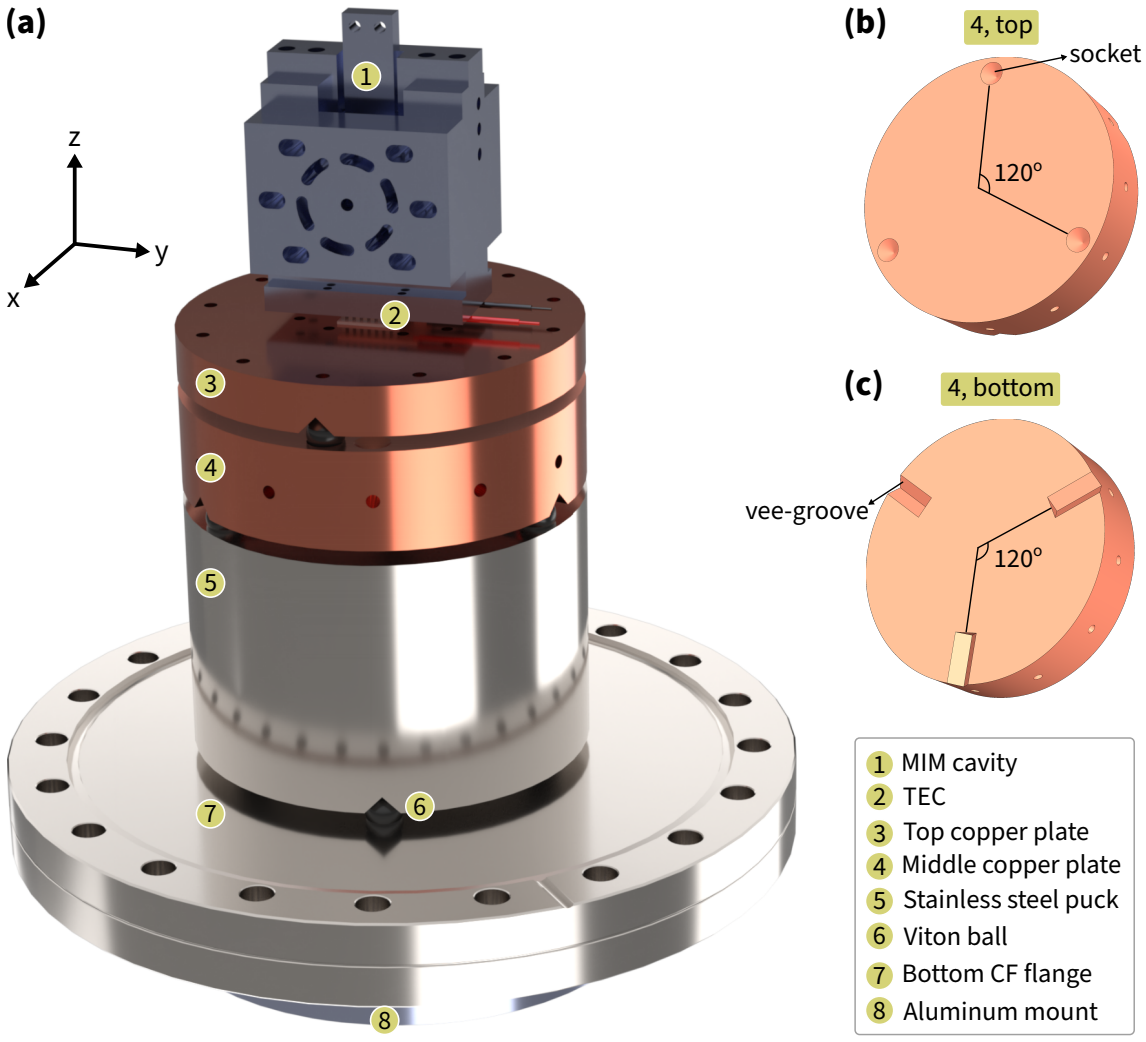

Figure 4.1: Mechanical design of the room-temperature MIM system. (a) Rendering of the MIM system design (to scale) with its components identified in the legend (bottom-right). Not shown: thermal anchoring between top and middle copper plate, the vacuum chamber and the optical breadboard. **(b,c)** Kinematic mount socket and vee-grooves for the top and bottom plane of middle copper plate, respectively. All kinematic mounts shown here have the same design.

The above design combined with the fact that our new lab was constructed atop bedrock, provided sufficient isolation from seismic noise and vibrations. Extra attention was given to cable management and instruments with fans to minimize vibration transduction and periodically topping-up the nitrogen gas supply, to float the optical table continually.

4.1.2.2 Vacuum system

A simplified schematic of the vacuum system is shown in Fig. 4.2, as seen from the top. The entire assembly shown in Fig. 4.1 is housed inside a stainless steel cube[1]. Its side faces A and C have an anti-reflection (AR) coated window[2] for optical access. Face C also has a custom CF flange with 9 pin sub-D feed-through[3] that allows for temperature control. Face B allows for connecting pumps. The initial pump down from atmosphere was carried with a Turbo molecular pump (TMP) backed with a roughing pump. Extra care was taken while opening the valve for this pump down as a sudden drop in chamber pressure could be fatal for the membrane inside the MIM cavity. Once the pressure read by the TMP gauge went below 5×10^{-5} mBar, we opened the gate valve to the Ion pump[4]. At this pressure, the Ion pump drew a significant amount of current ($\sim$15 mA). Within 5 minutes, the current started reducing, and correspondingly the pressure read by the Ion pump gauge. At this point, the TMP was no longer pumping our system, so we closed the TMP valve and crucially disconnected it from the system, to cut-off its vibration. We then performed a standard leak-check of our vacuum system and it was deemed successful. We achieved a pressure below 8×10^{-8} mBar within a week and $< 6 \times 10^{-8}$ mBar after a month of pumping, as read by the pressure gauge[5] connected on face D, while the Ion pump gauge read $< 2.5 \times 10^{-8}$ mBar, while drawing 10 μA current. We note that these pressures are well below the viscous damping limit of Silicon Nitride membranes (see Fig.2.6 of Ref. [206]), which represents the most stringent vacuum requirement for our system. Finally, on face D we have two more custom CF

[1]Kurt J. Lesker CU6-0800
[2]THORLABS VC234C
[3]Accu-Glass Products, Inc. 9D-275
[4]DUNIWAY 30 L/S diode Ion pump, DSD-030-5125-M
[5]Inficon, VGC501-MPG400-CF275

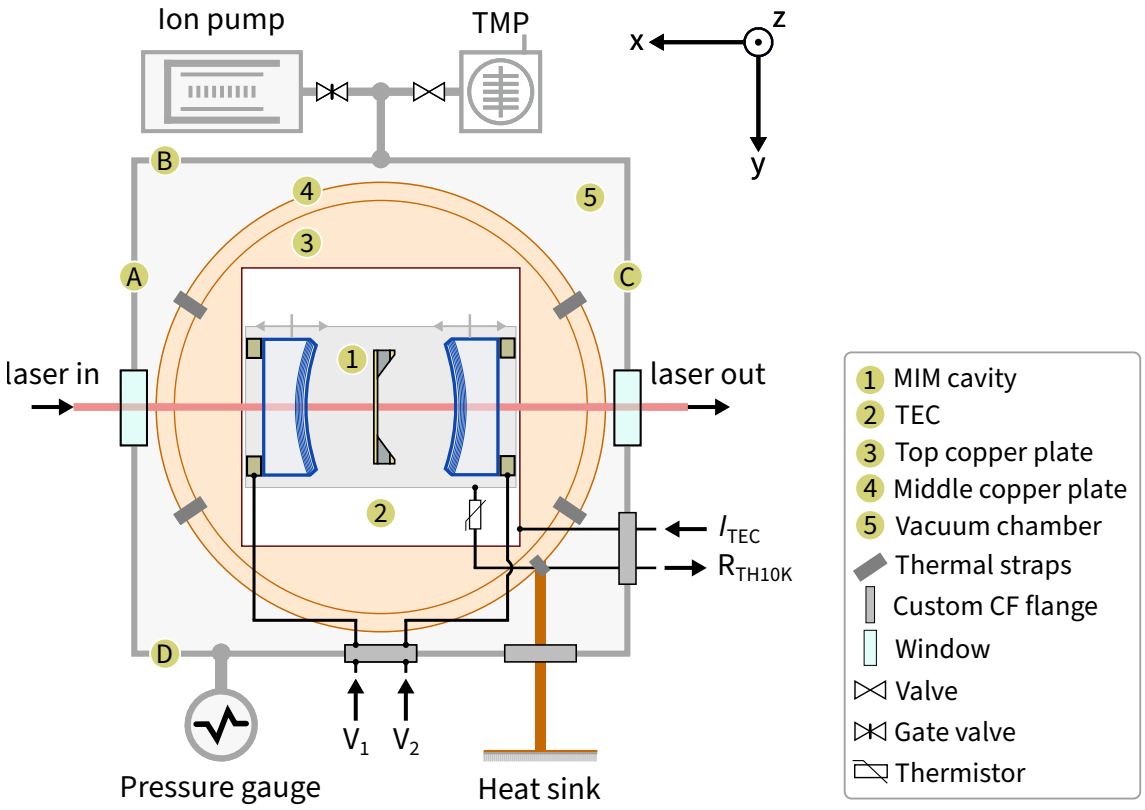

Figure 4.2: Vacuum chamber. The schematic of the vacuum chamber (not to scale) as seen from the top, with its key components labeled or identified in the legend (bottom-right). TMP: Turbo molecular pump, CF: ConFlat, TEC: Thermo-electric cooler, I_{TEC}: feedback current sent to TEC, R_{TH10K}: thermistor resistance to infer MIM cavity temperature, $V_{1,2}$: Voltages sent to cavity mirror piezos. For clarity, the top copper plate's size is artificially reduced compared to the middle copper plate. This arrangement provides a vacuum with pressure $< 6 \times 10^{-8}$ mBar at room-temperature.

flanges: BNC connectors[1] for controlling piezos on MIM cavity mirrors and heat sink feed-through[2] for heat dissipation. The top and bottom of the cube are blanked off by CF flanges[3], with the bottom one being modified as for kinematic mounting (described in Sec. 4.1.2.1).

[1]Accu-Glass Products, Inc. BNC-GS3-275
[2]Kurt J. Lesker EFT0313373
[3]LDS 800-000

4.2 Fabry-Perot cavity

In this section, we describe the design and construction of the Fabry-Perot (FP) optical cavity used in the MIM system. We then discuss mode-matching of the input light to the optical cavity and characterize its properties.

4.2.1 Design and construction

In this section, we discuss the design and the mechanical construction of the the optical cavity. Our design combines tried and tested ideas in the long history of MIM cavities in the Harris lab [78, 80, 207–212] with some key modifications inspired by Refs. [184, 213–216].

The key parameters of the optical cavity are listed in Table 4.1 (third column: **Actual**) and its design is illustrated in Fig. 4.3(a,b). Below we describe its key mechanical design and construction features:

1. The cavity mirrors (CM) were procured from FiveNine optics. They are super polished fused silica substrates and have a diameter: 7.75 mm, thickness: 4 mm, and a curved face with a radius of curvature (ROC) 50 mm. This ROC with cavity length (L_c) of 7 mm, places us comfortably within the stability limits of a Fabry-Perot cavity.

$$0 \leq \left(1 - \frac{L_\mathrm{c}}{\mathrm{ROC}}\right) . \left(1 - \frac{L_\mathrm{c}}{\mathrm{ROC}}\right) \sim 0.74 \leq 1. \tag{4.1}$$

where the optical cavity is formed by nominally identical CMs. The CM flat face is AR coated for $<0.1\%$ power reflection in the 1540-1560 nm wavelength range while the curved side is coated for 99.96% - 99.98% power reflection at 1550 nm with <5 ppm (parts per million) of combined absorption and scattering losses. Fig. 4.3(c) shows an attempt at measuring these mirror coating properties[1]. The CM is glued to its mount (in the appropriately sized recess, see part ② in Fig. 4.3(a)), using epoxy[2].

2. The CM mounts, adapters, and spacers are all machined out of invar, for its excep-

[1] However, this specific mirror wasn't used for the actual cavity.
[2] Stycast 2850 FT with Catalyst 9

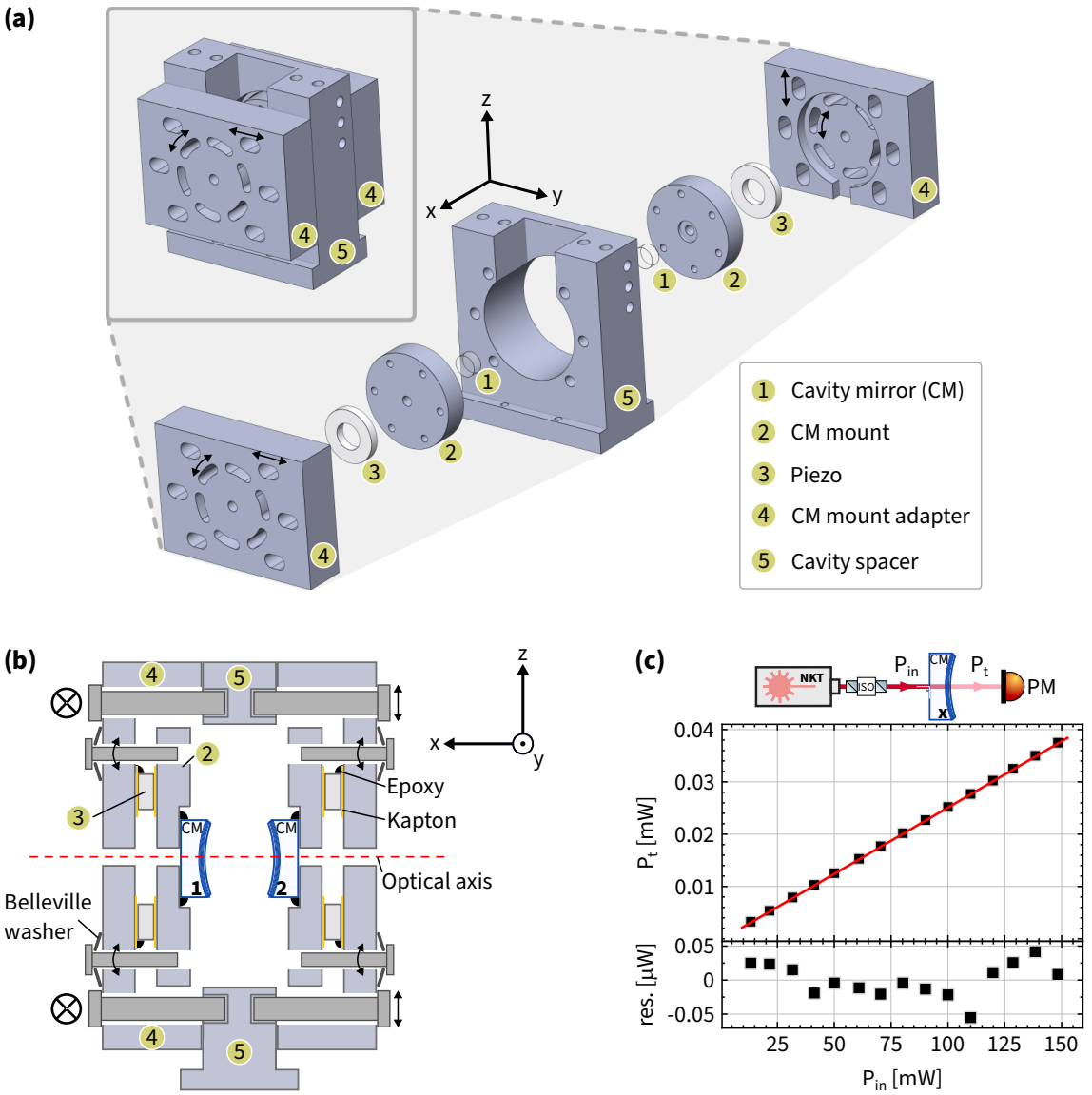

Figure 4.3: Cavity design. (a) Rendering of the optical cavity design (to scale) with its components highlighted in the exploded version. The components are identified in the legend (bottom-right). The alignment degrees of freedom are indicated with black arrows. Not shown: connecting screws, epoxy joints and Belleville washers. **(b)** A cut-out schematic (not to scale) showing the side-view of the optical cavity, which illustrates its parts including the alignment degrees of freedom, screw connections, epoxy joints and the Belleville washers. **(c)** Top panel: Schematic of the setup used for characterizing mirror coating properties. ISO: isolator, PM: power monitor. Middle panel: Transmitted power (P_{t}) versus input laser power (P_{in}) normally incident on a CM. Data (black squares) is fit to straight line (red) passing through the origin. Bottom-panel: fit residuals corresponding to the measurement and fit in the middle panel. We note that this cavity mirror is not used in the experiments described in this thesis

tionally low thermal expansion. Since we intend to operate at room-temperature, the design wasn't constrained to be strictly monolithic. These parts were machined at the Yale machine shop with a specified machining tolerance of 0.0254 mm (0.001"). Vented stainless-steel screws were used to connect these parts.

3. As illustrated in Fig. 4.3(a), the CM holders and adapters allow for rotational (up to 30°) and horizontal/vertical (up to 2.54 mm or 0.1") degrees of freedom, respectively. We also note the use of Belleville washers (Fig. 4.3 (b)) that allow for tip and tilt degrees of freedom. These allow for flexibility in the initial alignment of the bare optical cavity (see Sec. 4.2.2).

4. We intended the optical cavity to have both CMs movable (and the membrane fixed, see Sec. 4.4). This is a departure from the historical free-space MIM cavity designs in the Harris lab. The CM positions are tuned by nominally identical piezos[1] sandwiched between two layers of Kapton, for electrical insulation, and subsequently clamped between the CM mount and its adapter. The piezos have an unloaded travel range of 2 μm and are tuned using dedicated piezo drivers[2]. The driver can produce DC voltage in situ, accepts external voltage modulation and houses a 10× voltage amplifier. Care was taken to provide clean power supply to the piezo driver and extra precautions were taken to **never** send negative voltage to the piezos and their drivers.

4.2.2 Mode-matching and optical alignment

We follow a standard recipe of mode-matching propagating Gaussian beams to our optical cavity [217], as illustrated in Fig. 4.4(a). The incoming light from a polarization maintaining fiber (PMF)[3] exits a collimator (col)[4] (independently characterized for its waist (w_0) or Rayleigh range (x_R), and focusing distance (x_d, using a beam profiler[5]), Fig. 4.4(b)), bounces off of two plane mirrors (M1 and M2)[6] on tip and tilt adjustable mounts

[1]Physik Instrumente PD160.3x
[2]Physik Instrumente E-836.1G
[3]THORLABS PM1550-XP
[4]THORLABS CFC2-C
[5]DataRay WinCamD-LCM
[6]THORLABS P01

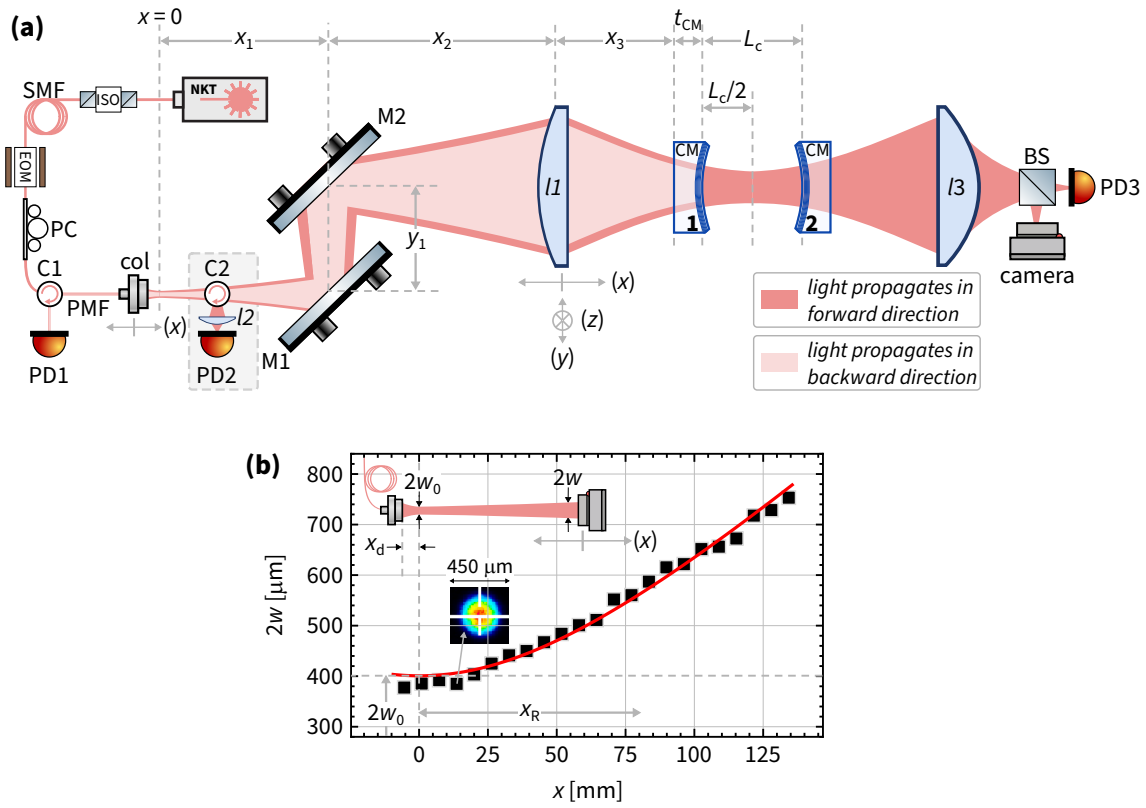

Figure 4.4: Mode-matching. (a) Schematic of the mode-matching experimental setup and Gaussian beam propagation are shown (not to scale). The reflected beam's diameter is artificially reduced for clarity. Gray box: NKT laser, ISO: optical isolator, SMF: single-mode fiber, EOM: electro-optic modulator, PC: polarization control, C1: fiber-optic circulator, PMF: polarization maintaining fiber, col: collimator, C2: free-space optical circulator, PD: photo-detector, l: plano-convex lens, M: plane mirror on tip-tilt mount, CM: cavity mirror, BS: beam-splitter, t_{CM}: cavity mirror thickness, L_{c}: cavity length. Key distances between optical elements are indicated. Optical elements on translation stages are flanked by arrows indicating the direction of motion. **(b)** Beam diameter ($2w$) versus distance (x) from the collimator measured using a beam profiler, with data (black squares) and fit (red curve). Inset: schematic of the measurement setup and image of the beam profile for a data point. Key parameters: beam-waist (w_0), Rayleigh range (x_R) and focussing distance (x_d) are indicated.

and thereafter gets focused by a plano-convex lens($l1$)[1] into the cavity. Optimal mode-matching is achieved when the incoming beam's waist size and location are matched to that of the normal mode of the cavity (henceforth referred to as "cavity-mode"). This constraints the incoming beam to have a specific diameter and a phase-front curvature equal to the radius of curvature (ROC) of the input cavity mirror (here CM1), at CM1. The setup here satisfies these requirements by specifying distances ($x_1 + y_1 + x_2$) and x_3 for a given focal length of the convex lens and collimator characteristics: $\{x_R, x_d\}$. A numerical routine for solving these distances is provided in Sec. C.1.

[1]THORLABS N-BK7 C-coated

In practice, mode-matching, input beam alignment, and alignment of detectors are simultaneously at play when setting up a high-finesse optical cavity, and it is a useful strategy to isolate them, as much as possible. While there are various recipes for aligning a high-finesse optical cavity, a step-by-step description of our recipe is given below. The author also found the discussion in Refs. [217, 218] useful.

1. We start by positioning the collimator and $l1$ on x-translation stages as suggested by the numerical routine. Other optical elements are on fixed posts or are fiber-coupled. We then mode-match and align to maximize the retroreflection from the curved surface of the input mirror (CM1). This is accomplished by iteratively tweaking the tip and tilt alignment of M1 and M2, and x-positions of the collimator and $l1$, while simultaneously monitoring the retroreflected light at a fiber-coupled photo-detector (PD1). This is a useful proxy that tunes the input beam's profile to be appropriate for the optical cavity (as discussed above) and its alignment, such that it retraces itself back into the collimator. The retroreflection can be maximized to unity w.r.t. the input light (modulo the losses in optical components). Note that circulator 2 (C2) is absent for this step.

2. The next step is to scan the cavity length by modulating the piezo on CM1 by >2 expected free-spectral range (FSR) of the optical cavity and monitor the reflected signal on PD1. In the ray optics picture, a cavity mode is normally incident on both cavity mirrors and forms a cavity axis. As our cavity geometry isn't very stringent (for e.g. in contrast to a spherical cavity), with reasonable machining tolerance the input beam can be expected to be collinear with a finite range of cavity axes. Regardless, if there is no coupling as indicated by no dips in reflection, we tweak the tip and tilt of CM2 by adjusting the screws on Belleville washers (see Sec. 4.2.1), in an attempt to have some cavity axis be collinear with the input beam. Once we have some periodically spaced reflection dips, we align a free-space photo-detector (PD3) to optimally measure the corresponding transmitted signal and image the cavity modes with a camera. Note that C2 is absent for this step.

3. We now optimize the coupling of the input beam to the $\mathrm{TEM}_{0,0}$ cavity mode. This

is accomplished by walking the input beam using M1 and M2 in tandem while simultaneously monitoring the reflected signal on free-space photo-detector PD2 (via C2[1]) and the transmitted signal. The shift from PD1 to PD2 is made to simplify alignment constraints and subsequent analysis for mode-matching [218]. Ideally, the equal reflectivity of CM1 and CM2 specify a complete extinction (transmission) of reflected (transmitted) light when a perfectly aligned and mode-matched input laser is tuned onto the cavity resonance. However in practice, finite losses in the cavity mirrors prevent such a case. Our proxy for optimal alignment involved maximizing the transmission peak at resonance while simultaneously minimizing those for other cavity modes ($\mathrm{TEM}_{\mathrm{m}\neq 0,\mathrm{n}\neq 0}$). This exercise resulted in reducing transmission peak value for all detected $\mathrm{TEM}_{\mathrm{m}\neq 0,\mathrm{n}\neq 0}$ modes to $<0.5\%$ of the $\mathrm{TEM}_{0,0}$ mode. We subsequently aligned PD2 to optimally detect the reflected signal. This completes the full-exercise of mode-matching and aligning the laser to the cavity and the corresponding detectors.

In addition to these steps, it was found that tweaking the y-z position[2] of $l1$ provided a simple and reliable knob to supplement beam alignment procedure. We note that tip and tilt of M1 and M2 along with a well-defined cavity-axis, provide all degrees of freedom required for beam alignment. The y-z tweaking of $l1$ doesn't add anything new but is preferred for its convenience in our setup. We also found that the x-position of the collimator and $l1$ had $\sim$1 cm range, which provided $>85\%$ mode-matching efficiency. The mode-matching efficiency is quantified in Sec. 4.2.3.3.

4.2.3 Bare cavity characterization

In this section, we characterize the bare optical cavity (i.e., without the membrane inside it). In particular, we characterize for the following parameters: cavity linewidth (κ), cavity length (L_{c}), mode-matching efficiency for a given input (ϵ) and coupling rate of the input mirror (κ_{in}). We note that the bare-cavity characterization was done by maximally coupling to the $\mathrm{TEM}_{0,0}$ modes of the cavity, and in ambient conditions, without any thermal stabilization or vibration isolation, unlike what we described previously in Sec. 4.1.2.

[1] Ascentta,Inc. FSC-3-PD-S-N-15-20-01
[2] THORLABS LM1XY

4.2.3.1 Cavity linewidth

There are several methods to measure a cavity linewidth (κ), and we tried three of them. They are described below, illustrated in Fig. 4.5(a-e) and their results are reported in Table 4.2.

1. Fixed frequency modulation sidebands

In this method, we frequency modulate the input laser using an EOM[1] (RF drive: 2.5 V_{pp} at $f_{\mathrm{EOM}} = 25$ MHz) and monitor the transmitted signal of the cavity while "slowly"[2] scanning its length (via CM1) across a $\mathrm{TEM}_{0,0}$ resonance. Such frequency modulation generates two sidebands symmetrically around the carrier (the main peak) at f_{EOM} which calibrates the time axis to frequency units. The transmission signal is processed by subtracting a constant detection background (independently measured) and then fitting to a sum of three (real) Lorentzians with independent amplitudes, independent κs (in time units) and unconstrained peak locations (in time units) as fit parameters. We then extract nine estimates for κ (in frequency units) per measurement[3]. An exemplary measurement and corresponding fit are shown in Fig. 4.5(a). Three separate measurements were made and the final result is reported as the mean and standard deviation of the 27 extracted values of κ.

2. Swept frequency modulation sideband

For this method, the laser beam is modulated via the EOM driven at 2.5 V_{pp} while modulating the drive frequency linearly over a range $f_{\mathrm{dev}} = 70$ MHz, at a rate $f_s = 12$ kHz, which results in sweeping[4] both of the frequency modulation sidebands over a frequency range f_{dev}, and at a rate f_s. For a nominally fixed cavity length, we ensured only one of the sidebands is resonant with the cavity and recorded the corresponding transmitted signal of the cavity. The transmission signal is processed by subtracting a constant detection background (independently measured), as in Method **1**. and then fitting to a (real) Lorentzian with amplitude and κ as fit parameters. An exemplary measurement and corresponding fit are shown in Fig. 4.5(b). The final result is

[1] THORLABS LN65S-FC
[2] Time taken to scan over κ (T_s): ∼10 µs, expected cavity ringdown time ($1/\kappa$): ∼90 ns, $T_s >> 1/\kappa$.
[3] Ratio of three κ-s (in time units) and three sideband calibrations have nine possibilities.
[4] This is also a "slow" sweep as T_s given by $(\kappa/f_{\mathrm{dev}}) \times f_s \sim 2$ µs $>> 1/\kappa$.

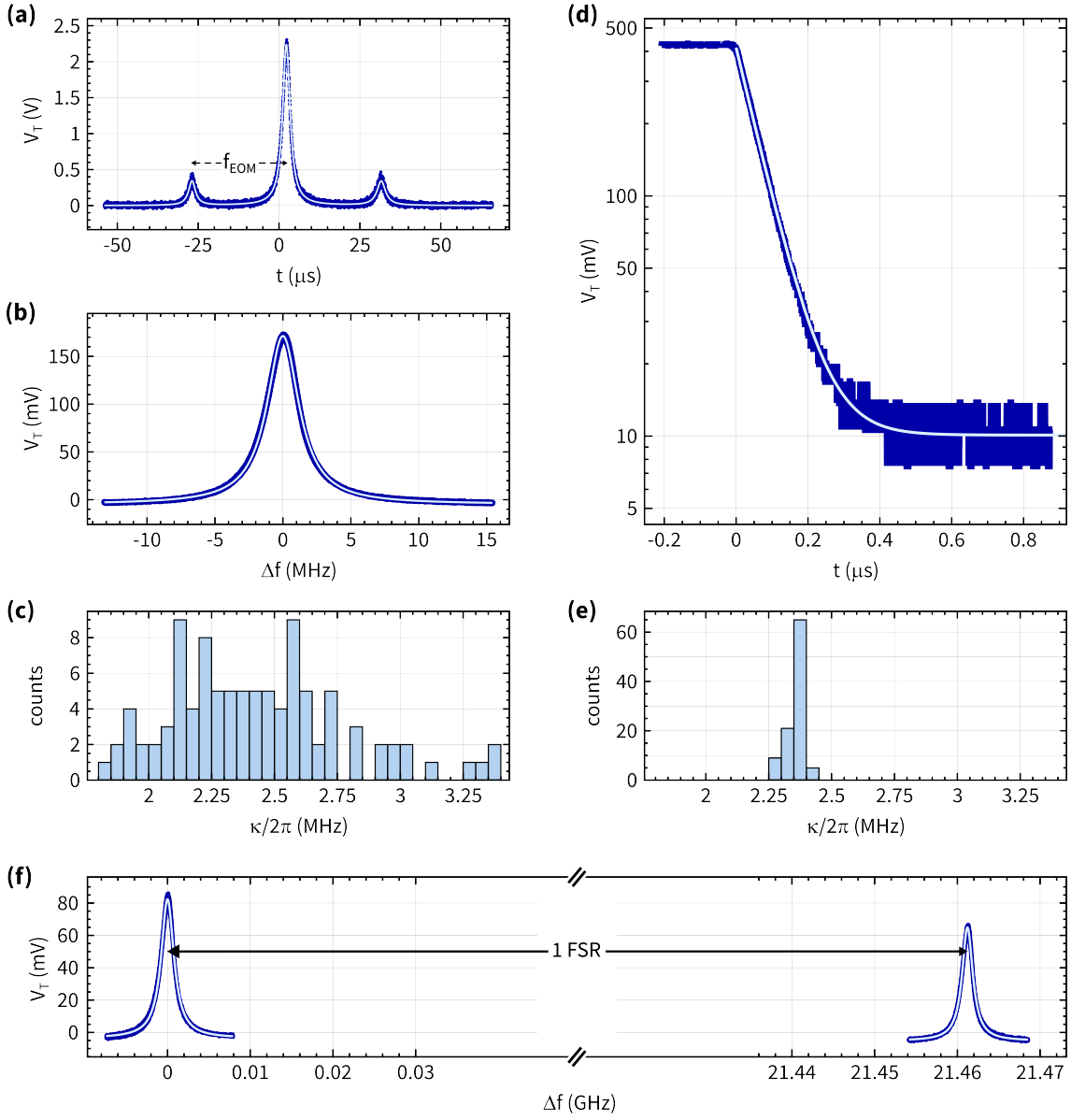

Figure 4.5: Bare cavity characterization - part I. (a) Transmitted signal ($\mathrm{V_T}$) versus time (t) for cavity linewidth (κ) measurement using Method **1**. with data (dark blue points) and fit (light blue curve). **(b)** $\mathrm{V_T}$ versus sideband detuning ($\Delta\mathrm{f}$) for κ measurement using Method **2**. with data (dark blue points) and fit (light blue curve). **(c)** Histogram of fitted κ from 100 individual measurements as (b), with 50 kHz bin-size. **(d)** $\mathrm{V_T(t)}$ for κ measurement using Method **3**. with data (dark blue curve: points joined by straight lines) and fit (light blue curve). **(e)** Histogram of fitted κ from 100 individual measurements as (d), with 50 kHz bin-size (same as (c)). **(f)** $\mathrm{V_T}(\Delta\mathrm{f})$ for free-spectral range (FSR) measurement using two adjacent $\mathrm{TEM_{0,0}}$ modes of the optical cavity. Data : dark blue points, fit: light blue curve. The separation between the two resonances provides the FSR and subsequently the cavity length (L_c).

estimated as the mean and the standard deviation of fit values of κ obtained from 100 independent sweep measurements and also shown in Fig. 4.5(c), as a histogram.

3. Ringdown

For this method, we modulate the input laser at a fixed frequency using the EOM (same RF drive as in Method **1**.) and Pound-Drevor-Hall (PDH) [219] lock the laser to the $\mathrm{TEM}_{0,0}$ resonance corresponding to one of the frequency modulation sidebands[1]. Subsequently, we toggled the RF drive on and off using a switch[2] gated with a TTL signal, and monitored the transmitted signal of the cavity. The ringdown part of the transmitted signal that is $\leq 95\%$ of the maximum[3], is fit to a sum of a decaying exponential ($Ae^{-\kappa t}$, with A and κ as fit parameters) and a constant offset (due to detection background). An exemplary measurement and corresponding fit are shown in Fig. 4.5(d). The final result is estimated as the mean and the standard deviation of fit values of κ obtained from 100 independent ringdown measurements and are shown in Fig. 4.5(e), as a histogram.

Method	Estimated $\kappa/2\pi$ (MHz)	Sample size
1.	2.43 $\pm$ 0.32	27
2.	2.43 $\pm$ 0.35	100
3.	2.36 $\pm$ 0.033	100

Table 4.2: Summary of κ measurements. Method **1**.: Fixed frequency modulation sidebands, Method **2**.: Swept frequency modulation sideband, Method **3**.: Ringdown. Estimated value is reported as mean $\pm$ one standard deviation. Sample size is given by 9$\times$number of measurements for Method 1 and number of measurements for Methods 2 and 3.

As shown in Table 4.2, the ringdown measurements estimate κ $\sim$10$\times$ more precisely than their sweep counterparts. We ascribe the inflated imprecision of sweeps to the fact that they are literally slow measurements made using a free-running laser, and thus suffer more from the lack of thermal stabilization and vibration isolation of the system. In comparison, ringdowns are faster and measured with a frequency locked laser.

[1]PDH locking was done seamlessly using the "Laser lock Box" module of Moku:Lab [220].
[2]Minicircuits ZASWA-2-50DRA+
[3]The slowest element of this experimental setup (excluding the optical cavity) was the RF switch with a 5 ns delay time. The 95% level provided enough time for all unintended transients to settle.

4.2.3.2 Cavity length

The cavity length (L_{c}) is estimated by measuring the free-spectral range (FSR) of the optical cavity and using the relation FSR $= c/2L_{\mathrm{c}}$, where c is the speed of light in vacuum.

For this measurement, we tuned the laser wavelength approximately on resonance with a $\mathrm{TEM}_{0,0}$ mode (at 1550.142 nm)[1]. We then scanned the laser frequency using the EOM (as in Method **2**. of κ measurements) for its precise location and also recorded the transmitted signal of the cavity. We then decreased the laser wavelength (in 0.001 nm steps[2]) by 0.172 nm, the expected the FSR for $L_{\mathrm{c}} = 7$ mm, in order to approximately locate the next $\mathrm{TEM}_{0,0}$ mode. We repeated the same exercise as above for precisely locating the mode and recorded the corresponding transmitted signal. The resonance frequencies of both modes were estimated by combing their approximate resonance wavelengths and fitting the transmitted signal for the remainder. The difference in their resonance frequencies (FSR) is measured to be 21.461 GHz. The biggest source of uncertainty was the least count for wavelength tuning. This resulted in an uncertainty in FSR of 0.250 GHz. Consequently L_{c} is estimated to be 6.999 mm with 1.17% uncertainty. The two $\mathrm{TEM}_{0,0}$ resonances measured for estimating FSR are shown in Fig. 4.5(f) with corresponding fits.

4.2.3.3 Mode-matching efficiency and input coupling rate

In this section, we describe measurements that quantify mode-matching efficiency (ϵ) and the input coupling rate (κ_{in}). These measurements follow the prescription in Refs. [221] and [216], which involves probing the cavity from both directions independently, and monitoring the corresponding reflected and transmitted signals of the cavity near a resonance. The four signals (two reflections and two transmissions, one for each direction) and the knowledge of cavity finesse ($\mathcal{F}$) are enough to solve for: two mode-matching efficiencies, two input coupling rate (one for each direction) and the combined losses of the cavity mirrors (for e.g. due to scattering or absorption of light). κ_{in} can also be characterized using a heterodyne measurement of the reflected signal as in

[1] As read by the laser controller - Graphik software from NKT lasers.
[2] This is the least count for wavelength tuning via the laser controller.

[222, 223]. However, it was not clear to the author how to distinguish $\kappa_{\rm in}$ from ϵ in these measurements and hence was not pursued any further.

To implement this measurement, we first probed the cavity with a fixed wavelength laser input via CM1, "slowly" scanned its length (via CM2) across a $\mathrm{TEM}_{0,0}$ resonance and recorded the corresponding reflected and transmitted signals of the cavity as shown in Fig. 4.6(a,b), respectively. Both the reflected (R_1) and the transmitted (T_1) signals are normalized to the input power that is measured independently, beforehand. While holding everything else nominally fixed, we flipped the cavity, probed it via CM2, "slowly" scanned its length (via CM1) across the same $\mathrm{TEM}_{0,0}$ resonance as above, and recorded the corresponding reflected and transmitted signals as shown in Fig. 4.6(c,d). As in the previous case, the reflected (R_2) and transmitted (T_2) signals are normalized to the independently measured input power. The cavity finesse ($\mathcal{F}$) is estimated using $\mathcal{F} = \mathrm{FSR}/(\kappa/2\pi)$. We use the value of FSR from Sec. 4.2.3.2 and κ from Method **3**. of Sec. 4.2.3.1, and obtain $\mathcal{F} = 9093.64$.

The relation between measured parameters (reflections, transmission and cavity finesse) and unknown variables (mode matching efficiencies, input coupling rates and total loss) is given by the following set of equations:

$$\mathcal{F} = \frac{2\pi}{\mathcal{T}_1 + \mathcal{T}_2 + L} \tag{4.2}$$

$$\frac{\mathrm{T}_1}{\epsilon_1} = \frac{4\mathcal{T}_1\mathcal{T}_2}{(\mathcal{T}_1 + \mathcal{T}_2 + L)^2} \tag{4.3}$$

$$\frac{\mathrm{R}_1 - 1}{\epsilon_1} + 1 = \frac{(L - \mathcal{T}_1 + \mathcal{T}_2)^2}{(\mathcal{T}_1 + \mathcal{T}_2 + L)^2} \tag{4.4}$$

$$\frac{\mathrm{T}_2}{\epsilon_2} = \frac{4\mathcal{T}_1\mathcal{T}_2}{(\mathcal{T}_1 + \mathcal{T}_2 + L)^2} \tag{4.5}$$

$$\frac{\mathrm{R}_2 - 1}{\epsilon_2} + 1 = \frac{(L + \mathcal{T}_1 - \mathcal{T}_2)^2}{(\mathcal{T}_1 + \mathcal{T}_2 + L)^2} \tag{4.6}$$

where $\epsilon_{1,2}$ denote mode-matching efficiencies when probing via CM1 and CM2, respectively. $\mathcal{T}_{1,2}$ denote the transmittance of CM1 and CM2, respectively and L represents the combined losses of CM1 and CM2. The values of $\{\mathrm{R}_1, \mathrm{R}_2, \mathrm{T}_1, \mathrm{T}_2, \mathcal{F}\}$ are known

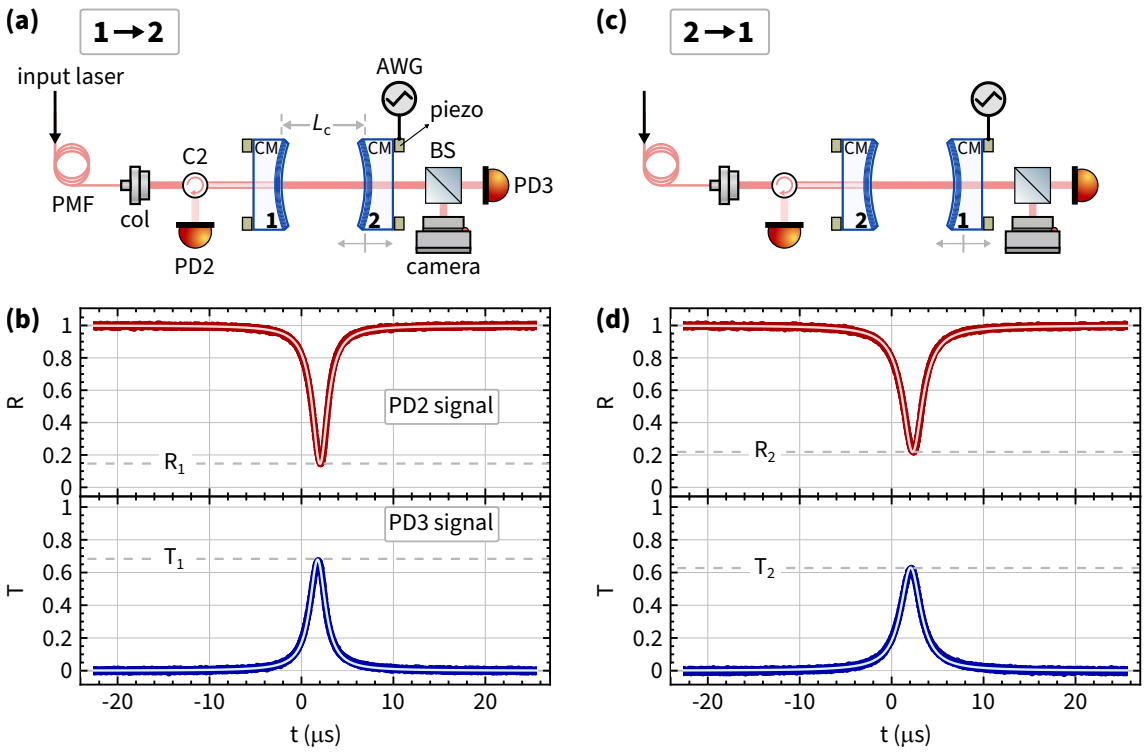

Figure 4.6: Bare cavity characterization - part II. (a) Experimental schematic for probing the optical cavity via CM1 and scanning its length (via CM2) across a $\mathrm{TEM}_{0,0}$ resonance. **(b)** Reflected (top panel) and transmitted (bottom panel) signals normalized to input power corresponding to (a). **(c)** Same as (a) except we probe the cavity via CM2 and scan its length using CM1, across the (same) $\mathrm{TEM}_{0,0}$ resonance. **(d)** Reflected (top panel) and transmitted (bottom panel) signals normalized to input power corresponding to (c). For this measurement, the laser wavelength λ is fixed.

from measurements as described above. Each of these equations has a simple physical description: Eq. (4.2) relates the cavity finesse and the CM transmittance and losses, in the high-finesse limit. Eq. (4.3) and (4.5) relate the transmitted power normalized to the mode-matched input power and CM transmittance and losses, when probing via CM1 and CM2, respectively. Eqs. (4.4) and (4.6) relate the difference of the mode-matched reflected and unmatched input power, normalized to the mode-matched input power and CM transmittance and losses, when probing via CM1 and CM2, respectively.

Eqs. (4.2) to (4.6) represent five equations for five variables $\{\epsilon_1, \epsilon_2, \mathcal{T}_1, \mathcal{T}_2, L\}$, and are straightforward to solve. We note that taking the ratio of Eqs. {(4.3), (4.4)} and {(4.5), (4.6)} may reduce it to a simpler problem of three equations and three variables $\{\mathcal{T}_1, \mathcal{T}_2, L\}$. We would like to point out that Ref. [216] (its Eq. (3.5)) and references therein missed the $()^2$ factor in the denominator of Eqs. (4.3) and (4.5). Finally, the

input coupling rates $\kappa_{\mathrm{in},\{1,2\}}$ are related to $\mathcal{T}_{1,2}$ and L as $\kappa_{\mathrm{in},\{1,2\}}/\kappa = \mathcal{T}_{1,2}/(\mathcal{T}_1+\mathcal{T}_2+L)$.

Solving these equations for our measurement results in: $\epsilon_1 = 0.86$, $\epsilon_2 = 0.80$, $\mathcal{T}_1 =$ 318.28 ppm, $\mathcal{T}_2 =$ 295.68 ppm and $L =$ 76.98 ppm. The corresponding input coupling rates are: $\kappa_{\mathrm{in},1}/\kappa = 0.46$ and $\kappa_{\mathrm{in},2}/\kappa = 0.43$. We note that the mirror coating company specifies $\mathcal{T} =$ 250 ppm and $L \leq$ 10 ppm (or $\leq$ 5 ppm per cavity mirror). Independent measurement of $\mathcal{T}$ for an independent mirror from the same coating batch corroborates at least one specification (see Fig. 4.3(c)). The inflated value of measured L is simply attributed to the unfortunate fact that we did not clean the mirrors, and |no| extra care was taken during bare cavity characterization, to ensure their cleanliness.

Moving forward, we flipped the cavity back to CM1 being the input mirror, for the rest of this thesis.

4.3 Membrane

In this section, we describe the membrane, its mounting and characterize its mechanical modes, that are used in this thesis

We use a high-tensile stressed ($\sim$1 TPa) stoichiometric silicon-nitride ($\mathrm{Si_3N_4}$) membrane with specified dimensions: 0.5 mm (length)$\times$0.5 mm (width)$\times$150 nm (thickness) and supported by a silicon frame[1]. It was manufactured by NORCADA[2] in a custom fabrication run, back in 2011 and the fabrication technique is elucidated in Refs. [222, 224]. Fig. 4.7(b) shows a picture of a membrane from the same batch and part number.

Without any modifications, these membrane have remarkable mechanical and optical properties [225]. The mechanical modes of interest resemble the vibrations of a tightly stretched drum head. Their mechanical quality factors (Q) at room-temperature (T_{room}) have been demonstrated to exceed 10^6 and $\mathrm{Q} \times f > k_{\mathrm{B}} T_{\mathrm{room}}/h$, a pre-requisite for observing quantum effects at room-temperature, where f is the resonance frequency of the mechanical mode of interest and h is the Planck's constant. They have low optical absorption ($<$100 ppm) at infrared and telecom wavelengths, which makes them suitable for integration with high-finesse optical cavities resonant at these wavelengths. Many of these properties were first demonstrated in the Harris lab and have been compiled in previous Harris lab theses such as Ref. [222] and elsewhere [206, 224].

With the final aim of integrating a membrane with our optical cavity, the membrane frame is epoxied[3] to a holder made out of Invar as illustrated in Fig. 4.7(a). While there exists a large body of work devoted to efficient mounting and clamping of membranes to achieve record Q-factors [226–232], for our purposes, we followed a simple recipe of using the least amount of epoxy that would provide a reliable mechanical connection while keeping the mechanical Q-factors nominally high. Hence, despite conventional wisdom, only one corner of the membrane frame was epoxied to the holder and one such epoxy joint is pictured in Fig. 4.7(c,d). We ascribe our choice to the expected absence of thermal cycling in a room-temperature system. In practice, we found our procedure

[1] 5 mm (length) $\times$ 5 mm (width) $\times$ 200 µm (thickness)
[2] Part number: NX5050CDS
[3] Stycast 2850 FT with Catalyst 23LV

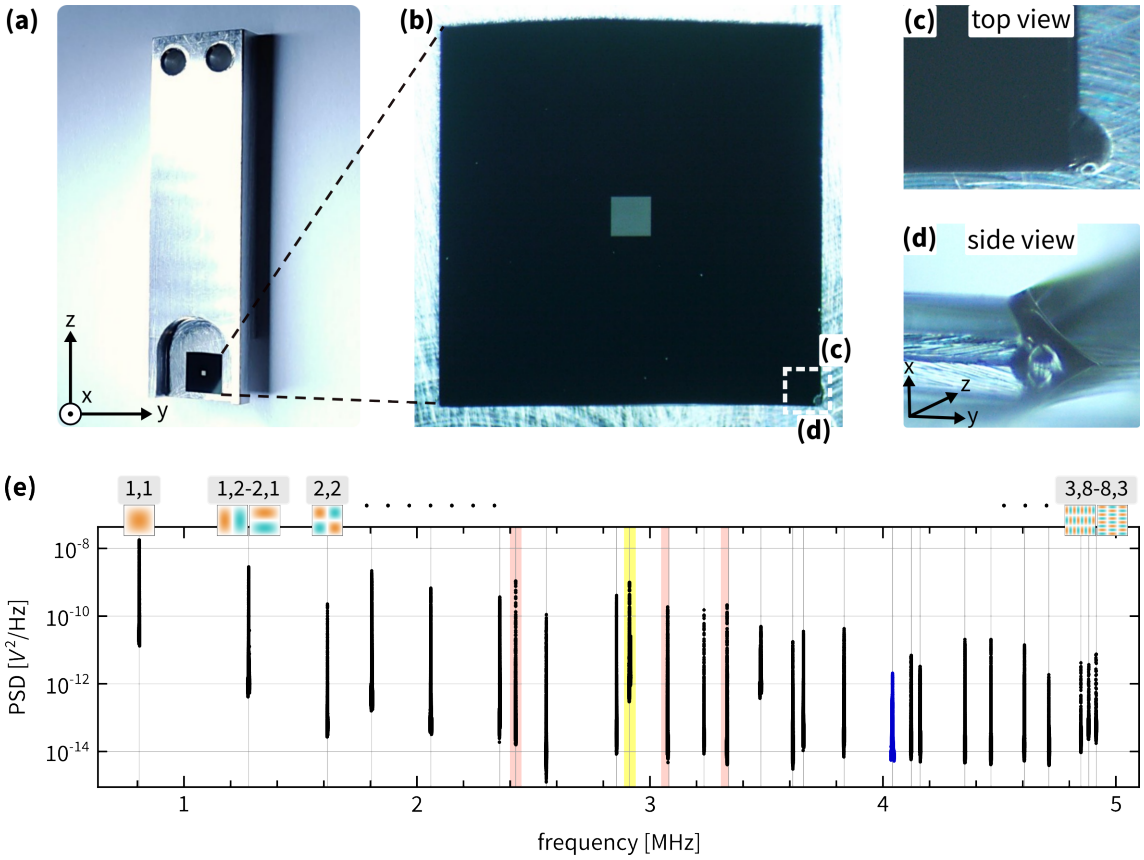

Figure 4.7: The membrane, its mounting and its modes. **(a)** A silicon-nitride membrane (small white square) in the middle of a silicon frame (black square), epoxied on a invar membrane mount (gray-silver).**(b)** A zoom-in to the membrane (gray square) in the middle of the frame (black square). **(c-d)** A top (side) view zoom-in to the epoxy joint connecting the frame to the holder. We note that this membrane is not used in the experiments described in this thesis. **(e)** Spectra of Brownian motion measured near expected drumhead mode resonances. Data (black dots) are flanked by gray vertical line representing the expected location of the mode. The modes (1,1), (2,1);(1,2), (2,2) and (8,3);(8,3) are identified with their corresponding spatial profile. Sec. C.2 shows a detailed illustration and identification of these modes.

to be repeatable with mechanical Q$>10^6$ for the triply degenerate drumhead modes: (7,1);(5,5);(1,7) for the epoxied membrane.

4.3.1 Membrane characterization

In this section, we characterize the drumhead mechanical modes of the square membrane for their resonance frequencies and damping rates. We note that the very first characterization of these modes were done inside the optical cavity, which was probed with resonant 1550 nm light. Thus, from the outset, we are not probing the bare membrane modes

(i.e., in absence of DBA due to radiation pressure and photothermal effect), despite our best intentions.

The drumhead modes of a square membrane have a particularly simple form. Their motion $x_{i,j}(y,z,t)$ can be described by [222, 224]:

$$x_{i,j}(y,z,t) = x_{ij,0}\,\sin\left(\frac{i\pi y}{a_m}\right)\,\sin\left(\frac{j\pi z}{a_m}\right)\cos\left(2\pi f_{ij}t + \phi_{ij,0}\right) \tag{4.7}$$

where (y,z) are the two coordinates along the length and the width of the membrane, with one of its corners as the origin, t denotes time and $\{x_{ij,0}, \phi_{ij,0}\}$ are initial amplitude and initial phase, respectively. The square membrane has a side length a_m with drumhead modes indexed by (i,j) and resonance frequency f_{ij} given by:

$$f_{ij} = \sqrt{\frac{\sigma(i^2+j^2)}{4\rho {a_m}^2}} \tag{4.8}$$

where (σ, ρ) specify the uniform tensile stress and density of the membrane. For this membrane, we expect $\sigma \sim$ 0.9 TPa and $\rho \sim$ 2700 kg/m^3 [211]. This sets the fundamental mode's ($i = 1$, $j = 1$) resonance at $f_{1,1} \sim$ 0.816 MHz. Furthermore from Eq. (4.8), it is immediately seen that $f_{ij} = f_{ji}$. Thus, for $i \neq j$ we expect naturally occurring double degeneracies (doublets) for a square membrane, reflecting its geometric symmetry [233]. We also note that any degeneracy of order >2 is classified as "accidental". They do not arise due to geometric symmetry and merely reflect some number theory coincidences. For completeness, we note the first two triple degeneracies (triplets): (7,1);(5,5);(1,7) and (14,2);(10,10);(2,14) and the first two quadruple degeneracies (quadruplets): (8,1);(7,4);(4,7);(1,8) and (9,2);(7,6);(6,7);(2,9). A curious reader may refer to Ref. [233] for an extended discussion of geometric and accidental degeneracies[1].

The Brownian motion of the first 52 drumhead modes are illustrated in Fig. 4.7(e). The measurement was done with a probe beam, locked to the $\mathrm{TEM}_{0,0}$ cavity mode, with power $P_{\mathrm{probe}} = 7$ μW and a small detuning from cavity resonance $\Delta_0/2\pi =$ -23 kHz

[1] Topped off with an example of a 48-fold degeneracy.

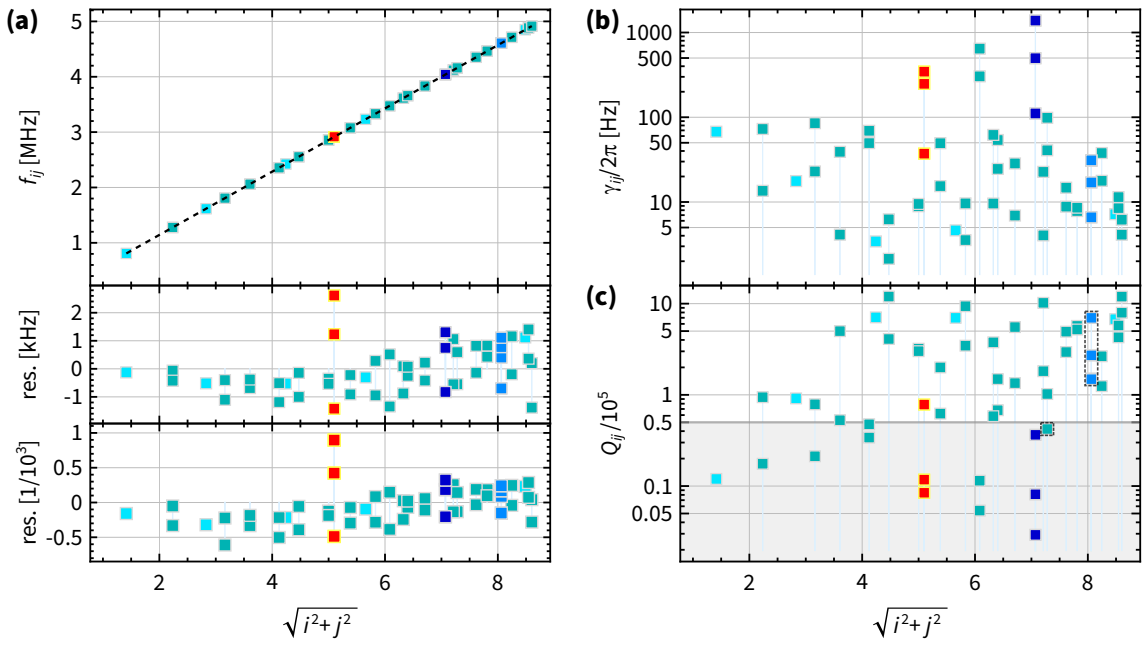

Figure 4.8: Characterization of membrane modes. **(a)** Mode frequency (f_{ij}) versus $\sqrt{i^2+j^2}$. Top panel: data (squares), fit (dashed black line); middle (bottom) panel: fit residuals (res.) versus $\sqrt{i^2+j^2}$ in frequency (relative) units. We note that modes: (1,5), (5,1) (red squares) and (1,7), (7,1), (5,5) (dark blue squares) are excluded from the fit but included in the residual plots to highlight their compromised nature. **(b)** Top panel: Mode damping rate (γ_{ij}) vs $\sqrt{i^2+j^2}$ with data as squares. Bottom panel: quality factor (Q_{ij}) extracted from the ratio of mode frequency and damping. Horizontal line demarcates Q = 50,000. All modes with Q < 50,000 have at least one of their indices as 1, barring two exceptions highlighted with dashed black rectangle. In panels (a: middle and bottom) and (b,c), nominally degenerate modes are connected by vertical lines from the x-axis.

$\sim -\kappa/100$.[1] A detailed illustration and identification of these modes are shown in Sec. C.2. These Brownian spectra are subsequently fit to the squared modulus of the sum of N Lorentzians and a constant offset representing the detection background, following Ref. [192]. Here N denotes the order of degeneracy. While the choice of the fit function assumes some interesting properties of the modes' interaction with the thermal bath [234, 235], its justification is beyond the scope of this thesis. The fit returns the peak positions and the widths of the Lorentzians which correspond to the modes' resonance frequencies (f_{ij}) and energy damping rates (γ_{ij}), respectively. The mechanical Q-factor is evaluated as $Q_{ij} = 2\pi f_{ij}/\gamma_{ij}$. These parameters are illustrated in Fig. 4.8 as a function of a single parameter $\sqrt{i^2+j^2}$. While this method is helpful in some ways, it cannot distinguish between (i,j) and (j,i) modes. This happens to coincide with the fact that

[1] In this configuration, we expect an nominal optical spring shift of ∼20 Hz, almost entirely due to photothermal effect. See Sec. 4.4.3.1 for more details.

at present, our measurement apparatus is not set up to distinguish between (i, j) and (j, i) modes, either.

The resonance frequencies in Fig. 4.8(a) are fit to $\frac{f_0}{\sqrt{2}}\sqrt{i^2+j^2}$, with f_0 as a fit parameter. The fit provides $f_0 =$ 808130 $\pm$ 23 Hz, which is an estimate of the factor $\sqrt{\sigma/2\rho{a_m}^2}$. The error in f_0 is the fit error given by the square-root of the diagonal element in the covariance matrix [236]. The fit residuals maybe interpreted as the membrane being a square or its stress being uniform (or a combination of both) to $\sim$1 part in 1000. However, we note that the probe beam's radiation pressure backaction and photothermal effect (see Sec. 4.4.3) will complicate any efforts to isolate bare frequencies[1]. We also note a few outliers in this dataset that were not included in the previous fit. The first one is the (5,1);(1,5) doublet, as the spectra near its expected location has three peaks unlike other measured doublets. The second outlier is the triplet (7,1);(5,5);(1,7), as it was not measured in the same data run as all other modes[2]. The inclusion of said outliers in the plot of fit residuals is solely to highlight their compromised nature.

The damping rates and especially the Q-factors provide some interesting observations. As discussed above the probe beam's radiation pressure backaction may complicate efforts to isolate bare parameter values. However, we rely on the fact that the probe beam's detuning from the cavity resonance is small, which reduces radiation pressure backaction, and as will be shown in Sec. 4.4.3.1, the photothermal effect does not induce any damping/amplification. Hence, these observations (along with similar data over time, not shown here) hold some weight. We observe that almost all modes with Q$<$50,000, have at least one of their indices as 1 and are identified in 4.8(c). However, there are two exceptions to this empirical observation[3]: one of (7,2); (2,7) has its Q$<$50,000, and the first quadruplet which involves (1,8);(8,1) have all of their Q$>$50,000. This happens to be our first observation of consistently low mechanical-Qs for a set of modes including the triplet, which is rather untimely and contributed to our decision to in not proceed with the initially planned experiments involving the triplet (7,1);(5,5);(1,7).

[1] Even though one may claim that the radiation pressure backaction can be made 0 by setting $\Delta_0 = 0$, the photothermal effect on frequency is maximum at $\Delta_0 = 0$, thus perturbing the bare-frequencies.
[2] The measurement of (7,1);(5,5);(1,7) modes precedes others by $\sim$14 months.
[3] Q = 50,000 is not a special value., but rather selected to highlight an empirical observation.

4.3.1.1 Characterizing the nominally degenerate membrane modes

It can be a fun exercise (with possible utility) to systematically quantify the non-square-ness or the fractional anisotropic stress in the membrane, using the present data, and crucially ignoring the probe beam's photothermal effect. This can be done by considering a rectangular membrane with anisotropic stresses along axes parallel to its sides. It is straightforward to obtain an equivalent expression for its resonance frequencies f'_{ij} [222, 224]:

$$f'_{ij} = \sqrt{\frac{1}{4\rho}\left(\frac{\sigma_y}{{a_m}^2}i^2 + \frac{\sigma_z}{{b_m}^2}j^2\right)} \tag{4.9}$$

where $\{a_m, \sigma_y\}(\{b_m, \sigma_z\})$ denote the side length and tensile stress, respectively along $y(z)$ direction. Eq. (4.9) can be re-written in a more suggestive form with the following substitutions: $\sigma_y = \sigma, \sigma_z = s\sigma, b_m = \alpha a_m$ and $\{s, \alpha\} > 0$, and we have

$$f'_{ij} = f'_{11}\frac{\sqrt{i^2 + \frac{s}{\alpha^2}j^2}}{\sqrt{1+\frac{s}{\alpha^2}}} \tag{4.10}$$

where we replaced $\sqrt{\frac{\sigma}{4\rho{a_m}^2}}$ with $\frac{f'_{11}}{\sqrt{1+\frac{s}{\alpha^2}}}$.

In Eq. (4.10), the anisotropy in stress and the non-square-ness appear in a linearly dependent fashion (s/α^2) and without further specifications (our case), they cannot be isolated. Nevertheless, we can perturbatively estimate their combined effect $s/\alpha^2 = r$, for an almost uniformly stressed square membrane. In this limit, we Taylor expand $r \to 1+\delta r$ with $|\delta r| << 1$ and up to $\mathcal{O}(\delta r)$ we have:

$$f'_{ij} = \frac{f'_{11}}{\sqrt{2}}\sqrt{i^2+j^2} + \left(\frac{f'_{11}}{\sqrt{2}}\sqrt{i^2+j^2})\right)\left(\frac{j^2}{2(i^2+j^2)} - \frac{1}{4}\right)\delta r \tag{4.11}$$

We now recall our inability to distinguish between (i, j) and (j, i) modes and in order to make further progress, we convert $f'_{i,j}$ into a quantity agnostic to the mode indices. This is done by evaluating $|f'_{i,j} - f'_{j,i}| \equiv \Delta f'_{i,j}$, which is given by:

$$\Delta f'_{ij} = \frac{f'_{11}\delta r}{\sqrt{2}}\left(\frac{|j^2 - i^2|}{2\sqrt{i^2+j^2}}\right) \tag{4.12}$$

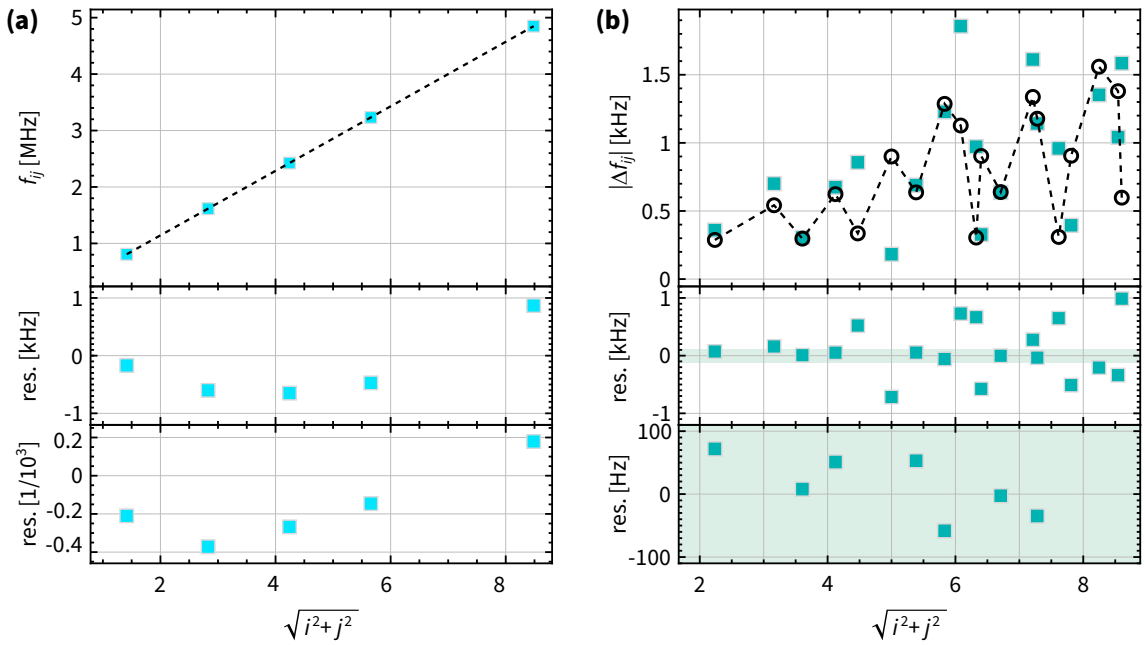

Figure 4.9: Characterizing the degeneracy breaking of doublets. **(a)** Mode frequency f_{ij} versus $\sqrt{i^2+j^2}$ for singlets i.e., $i=j$. Top panel: data (cyan squares), fit (dashed black line), middle (bottom) panel: fit residuals (res.) versus $\sqrt{i^2+j^2}$ in frequency (relative) units. **(b)** Absolute non-degeneracy of doublets $\Delta f'_{ij}$ vs $\sqrt{i^2+j^2}$. Top panel: data (teal squares), fit (black circles connected by straight lines), middle panel: fit residuals (res.) versus $\sqrt{i^2+j^2}$ in frequency units. Small residuals are highlighted with a teal band and zoomed into in the bottom panel.

Notice that f'_{11} and δr appear in a linearly dependent fashion in Eq. (4.12). However, we can isolate them this time around. The resonance frequency of singlets i.e., $i=j$, are independent of δr (eqn. (4.11)), and thus can be fit to provide f'_{11}. We then fit the absolute non-degeneracy of doublets to Eq. (4.12) with δr as a fit parameter and a fixed value of f'_{11} as obtained by analyzing the singlets. This analysis is illustrated in Fig. 4.9. The fit to singlets provided $f'_{11} = 808172 \pm 82$ Hz. The analysis of non-degeneracy of the doublets used the above value of f'_{11} and resulted in $\delta r = 0.00075 \pm 0.00009$. The error in these parameters are the fit errors [236].

4.4 Membrane in the middle of a Fabry-Perot cavity

In this section, we integrate the membrane with the optical cavity. We describe the system design with the necessary alignment procedure, and then characterize the combined system on two main fronts: the backaction of the membrane on the cavity and the backaction of the cavity on the membrane.

4.4.1 Integrating the membrane with the Fabry-Perot cavity

In this section, we describe the integration of the membrane with the optical cavity. The starting point of this exercise is a mode-matched bare optical cavity ($>85\%$ efficiency for $\mathrm{TEM}_{0,0}$ mode), with appropriately aligned optics. The task at hand is to align the membrane in the middle of the optical cavity, such that we have *similarly* a mode-matched and well-aligned $\mathrm{TEM}_{0,0}$ cavity mode for the resulting system.

To accomplish this task, we once again fall back on the rich history of MIM systems in the Harris lab. The author found Refs. [80, 207, 208] particularly useful as well as those from Cindy Regal's group [216]. As discussed in Sec. 4.2.2, for a bare optical cavity with our specifications, generically there exist a range accessible cavity axes. Aligning the input laser beam to any one of these cavity axes would do the job. However, the introduction of a third element (here, the membrane) places stringent requirements on alignment. In particular, the membrane has to be interferometrically aligned to retrieve the cavity modes [207, 216] and the cavity modes' are interferometrically sensitive to the membrane's position along the cavity axis, and its tip and tilt angles [80, 208]. The steps taken to introduce and align the membrane to the cavity and subsequently retrieve the cavity modes are described below. Its mechanical design and the experimental setup are illustrated in Fig. 4.10(a) and (b), respectively.

1. The membrane holder adapter (part ⑥) is connected to the cavity spacer (part ⑤) via vented screws. Its recessed face on the front side is designed to be positioned in the middle of the cavity (which is also the expected position of the cavity waist), up to machining tolerance. The membrane (part ⑧) epoxied to membrane holder (part

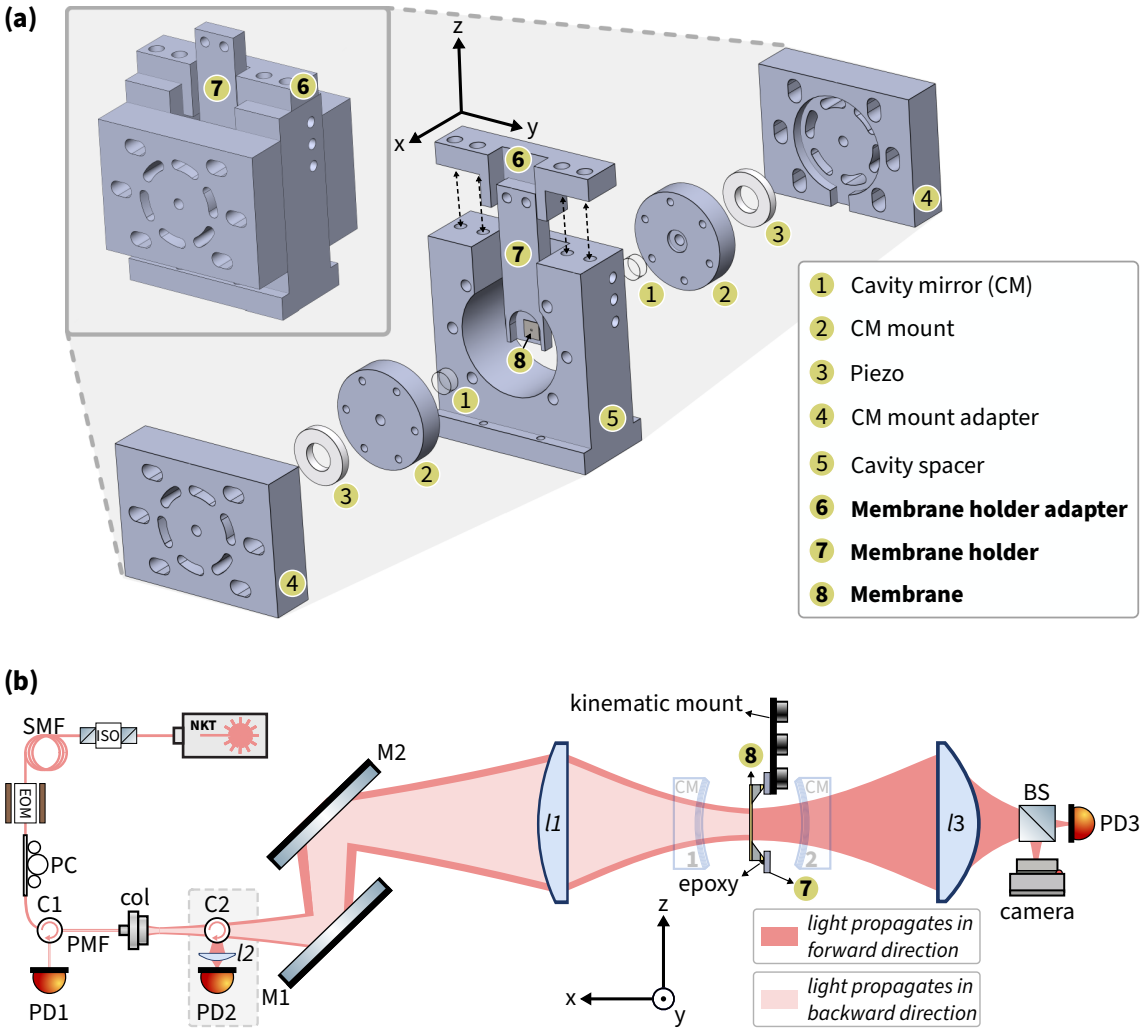

Figure 4.10: MIM cavity design and membrane alignment. (a) Rendering of the MIM cavity design (to scale) with its components highlighted in the exploded version. Many of the components are same from Fig. 4.3(a). They are all identified in the legend (bottom-right), with the new additions highlighted in **bold**. The connections between cavity spacer ⑤ and membrane holder adapter ⑥ are indicated with dashed black arrows. Not shown: connecting screws and epoxy joints. **(b)** Schematic of the membrane alignment setup, as an extension of the mode-matching setup (Fig. 4.4(a)). The membrane via the membrane mount is attached to a kinematic mirror mount that allows for fine translation in x-direction, tip and tilt degrees of freedom. All other optical elements and alignments are held fixed. Not shown: translation stages used for coarse motion in x, y and z-direction.

⑦) is attached to a set of three translation stages[1] for coarse linear motion, and a kinematic mount[2] with three manual actuators[3] for fine translation along x-direction, and tip and tilt degrees of freedom. The kinematic mount actuators are specified with a travel sensitivity of 0.56 μm for a 1° turn. At the very end, the membrane holder would be epoxied to the adapter.

2. The membrane is brought vertically above the bare optical cavity and approximately at the x-position where we expect the waist of the cavity (midway between the two CMs). The bare optical cavity supported on four optical posts is then temporarily removed from the optical path, while the posts retain its position[4]. Subsequently, we lower the membrane down to the optical axis (z-translation).

3. At this point, it is helpful to have an additional visible laser beam for alignment. We used a He-Ne laser that was made collinear to the 1550 nm beam (up to a propagation distance of ∼10 m)[5], and coarsely located the center[6] of the membrane (along y and z) using a camera. We then tweaked the x-position, and tip and tilt angles via the kinematic mount to retroreflect the 1550 nm light, such that the signal on PD2 was maximized. This step is meant to improve the membrane's x-position to be closer to the cavity waist and coarsely align the tip and tilt angles to be interferometrically aligned to the cavity axis. Subsequently, we verified the centering of the membrane by monitoring the transmitted 1550 nm light as detected on PD3. The transmitted light is expected to be constant when the light is incident on the membrane and to fall sharply at the edges. We approximated the center of the membrane being midway between two edges, which matched with the result from the He-Ne beam alignment exercise. The final positions of all translations, tip and tilt actuators were noted. The x-position was then offset (towards CM1) by a known amount using the kinematic mount. This is to ensure that the membrane holder does not run into anything when

[1]THORLABS PT1
[2]Newport ULTIMA U100-AC3K
[3]Newport AJS127-0.5K
[4]An improvement for a future design may involve just the requisite number (three) of posts/points of contact, with kinematic mounting to simplify optics alignment.
[5]This is roughly two-thirds the size of our lab, in the longer direction.
[6]The cavity mode centered on the membrane is a favorable location as deemed by simulations (Sec. 4.1.1).

being lowered inside the optical cavity, in the following steps.

4. The membrane is then moved vertically up and away from the optical axis. The bare optical cavity is brought back and its position manually adjusted to retrieve the cavity mode[1], with the same specifications as before.

5. The membrane is lowered again, this time inside the optical cavity, up to the vertical position marked in step **3**. Note that the x-position is currently offset from the cavity waist. We finely tune the x-position of the holder (part ⑦) towards the adapter (part ⑥), with extra care so as to not bump into any parts of the optical cavity. Once a contact is made, we stop and back-off by $\sim 1/8$ of a turn to have some room for the final alignment of the membrane.

6. Due to the stringent constraints of alignment as discussed above, it can be expected to have no transmitted light from the MIM cavity without further fine-tuning. Regardless, we fine-tune the tip and tilt angle to obtain some transmission signal from the $\mathrm{TEM}_{0,0}$ resonance (while scanning the cavity length via CM2). We verify its quality by simultaneously monitoring the transmission signal on PD3 and the camera, while tuning the x-position over a few microns. The optical properties of the MIM cavity are expected to have a periodicity of half the laser wavelength ($\lambda = 1550$ nm) and here we use it as a diagnostic (a detailed study is carried out in Sec. 4.4.2). If the membrane is tilted, $\mathrm{TEM}_{0,0}$ mode would hybridize with other modes in the direction of tilt [208, 216] and is indicated by abrupt changes in the transmitted signal and its image[2]. With subsequent tip and tilt fine-tuning it is possible to obtain a transmitted beam whose profile is indistinguishable (by eye) from an un-hybridized $\mathrm{TEM}_{0,0}$ mode for a range of x-tuning comparable to λ. This step completes the final membrane alignment.

7. The final task is to get the membrane holder back in contact with the adapter and epoxy them together. As before, we tune the x-position with extreme care to get some contact between the two parts. For possibly the only time, the backlash of the actuators is helpful as it provides some small but helpful recess from the contact

[1] The exercise of flipping the cavity and retrieving cavity modes (Sec. 4.2.3.3) involved the same process.
[2] A curious reader is referred to Refs. [80, 208] for a detailed and exhaustive study of membrane's backaction on the cavity for the MIM system.

point. We subsequently apply epoxy, in and around the recess from the contact point and wait for a day for the epoxy to cure.

4.4.2 MIM characterization: Part I

In this section, we characterize the MIM system by measuring the membrane's backaction on the optical cavity.

The usual recipe to characterize the membrane's backaction is by performing spectroscopy of cavity modes as a function of input laser detuning ($\delta f_{\rm L}$) and the membrane displacement (δx_m) along the cavity (x) axis, while the cavity length ($L_{\rm c}$) stays fixed. However for our system, the membrane's position is fixed, while the cavity mirrors' (CM) positions can be tuned using piezo. Since it is the relative displacement of the membrane w.r.t. the cavity that detunes the cavity modes, an equivalent control knob to δx_m would be to displace both cavity mirrors by equally while the membrane stays fixed.

Furthermore our laser's[1] fine frequency tuning range is restricted to $\sim$3 GHz $<$ 1 free-spectral range (FSR $\sim$21.5 GHz, Sec. 4.2.3.2). This necessitated other ways of tuning the laser or using CM-s, in order to scan at least over two FSRs. With these considerations, we settled on the scheme described below and is illustrated in Fig. 4.11(a).

1. Statically step the position of CM2 by applying discrete DC voltages to the corresponding piezo.

2. Tune CM1 to scan $L_{\rm c}$ over $>$2 FSRs and measure corresponding reflected and/or transmitted signal. The tuning was done by sending a triangular voltage ramp (0-10-0 V at 7 Hz) to the corresponding piezo.

3. Fixed parameters: laser wavelength (λ) and membrane position (x_m)

4. A spectroscopy measurement comprised of setting a particular CM2 position, scanning the cavity via CM1, and recording corresponding reflected and transmitted signals.

Fig. 4.11(b) shows the result of cavity spectroscopy as a function of CM1 and CM2 positions as a colormap. The entire measurement consisted of setting 151 distinct CM2

[1]NKT Koheras Adjustik K82-152-23, with coarse frequency tuning range of $\sim$50 GHz.

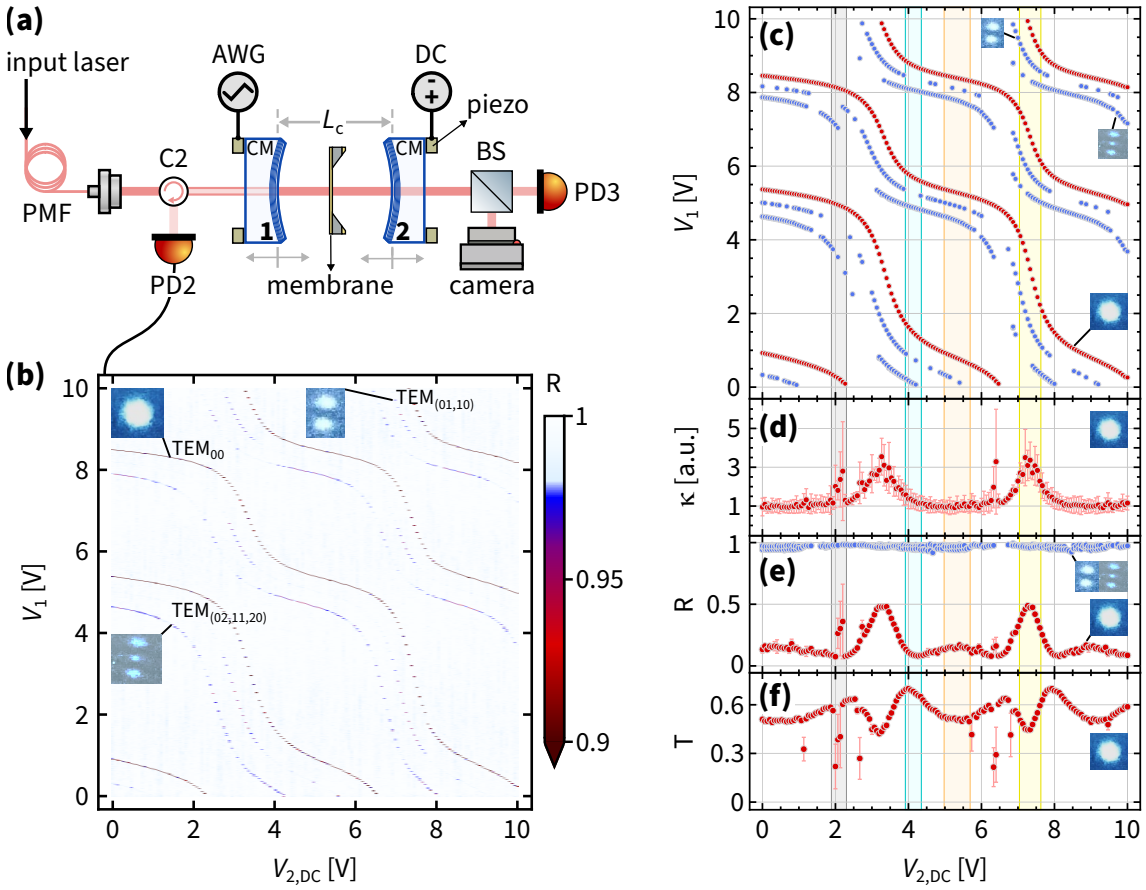

Figure 4.11: Spectroscopy of MIM cavity. (a) Schematic of experimental setup. **(b)** Reflected signal of the MIM cavity versus CM1 (via V_1) and CM2 (via $V_{2,\mathrm{DC}}$) positions, plotted as a colormap. The cavity modes are labeled and their images (inset) are shown. **(c-f)** Resonance location, linewidth (κ), resonant reflection (R) and resonant transmission (T) of cavity modes versus CM1 and CM2 positions, obtained via fitting reflected signal (b), except for (f). To obtain (f), a separate dataset of transmitted signal versus CM1 and CM2 positions was acquired. Red circles: $\mathrm{TEM}_{0,0}$ mode, blue circles: $\mathrm{TEM}_{\mathrm{m}\neq 0,\mathrm{n}\neq 0}$ modes. Inset: images of cavity modes. Some notable locations are identified. Gray: $\mathrm{TEM}_{0,0}$ mode undergoing avoided crossing with a higher order transverse cavity mode; teal: negligible linear coupling between $\mathrm{TEM}_{0,0}$ mode and the membrane, with minimum (maximum) R(T); orange: maximum linear coupling between $\mathrm{TEM}_{0,0}$ mode and the membrane with small κ and yellow: maximum linear coupling between $\mathrm{TEM}_{0,0}$ mode and the membrane with large κ and maximum (minimum) R(T). For all these measurements the laser wavelength λ and membrane position (x_m) are nominally fixed.

positions. We note that the measurement was carried out by maximally coupling into the $\mathrm{TEM}_{0,0}$ mode. Further analysis of this data involved its fitting, to identify and characterize various cavity resonances. They are illustrated in Figs. 4.11(c-f) which show the resonance location, linewidth, normalized reflection and transmission as function of CM1 and CM2 positions, respectively. The measurements highlight several well-known optical properties of MIM systems [78–80, 208], most notably the periodic behavior of various quantities. We also highlight some notable features of the spectroscopy such as positions where the linear coupling coefficient is maximal or minimal, and of avoided-crossings. While these features are already well-studied, Figs. 4.11(c-f) represents a road-map for where the final mirror positions (or the static wavelength) should be set. This road map is of utility for system debugging and nominal operation.

A key feature of our measurement scheme is the fact that two CM displacements $(\delta x_{\mathrm{CM1}}, \delta x_{\mathrm{CM2}})$ are linear combinations of $(\delta f_{\mathrm{L}}, \delta x_m)$. This is seen by noting that a relative change in CM positions is equivalent to tuning λ, while the common translation is equivalent to δx_m (as discussed before). This is highlighted in the fact that the cavity resonances are sloping downwards in Fig. 4.11(b,c), with longitudinal cavity modes spaced by an FSR in the perpendicular direction. To make this relation clear (to first order), we isolate the longest contiguous $\mathrm{TEM}_{0,0}$ resonance locations and fit them to a straight line, as in Fig. 4.12(a). The slope of the line identifies the angle between $(x_{\mathrm{CM1}}, x_{\mathrm{CM2}})$ and (f_{L}, x_m) planes. If the two piezos on CM-s produced the same displacement per unit voltage, the angle is simply 45°. For our setup, the dissimilar piezo strokes result in an angle of 42.6°, as given by the fit. Fig. 4.12(b) illustrates the same spectroscopy data by rotating it counter-clockwise by the slope of the fitted line (i.e., by 42.6°). We then use the fact that the optical properties of a MIM system are $\lambda/2$ periodic and obtain an estimated δx_m, while the bare cavity FSR provides an estimate of δf_{L}. This information is sufficient to transform Fig. 4.12(b) to (c-top panel), which is a more traditional looking cavity spectroscopy for a MIM system. We subsequently take the numerical derivative of this data w.r.t. δx_m to obtain $G = \dfrac{\partial \omega_{\mathrm{c}}}{\partial x_m}$, where ω_{c} is the cavity resonance frequency. The estimated G is shown in the bottom panel of Fig. 4.12(c), and its maximum absolute value matches the theoretical expectation. We also note in passing that our MIM system with a fixed membrane position and both movable mirrors isn't unique and similar systems

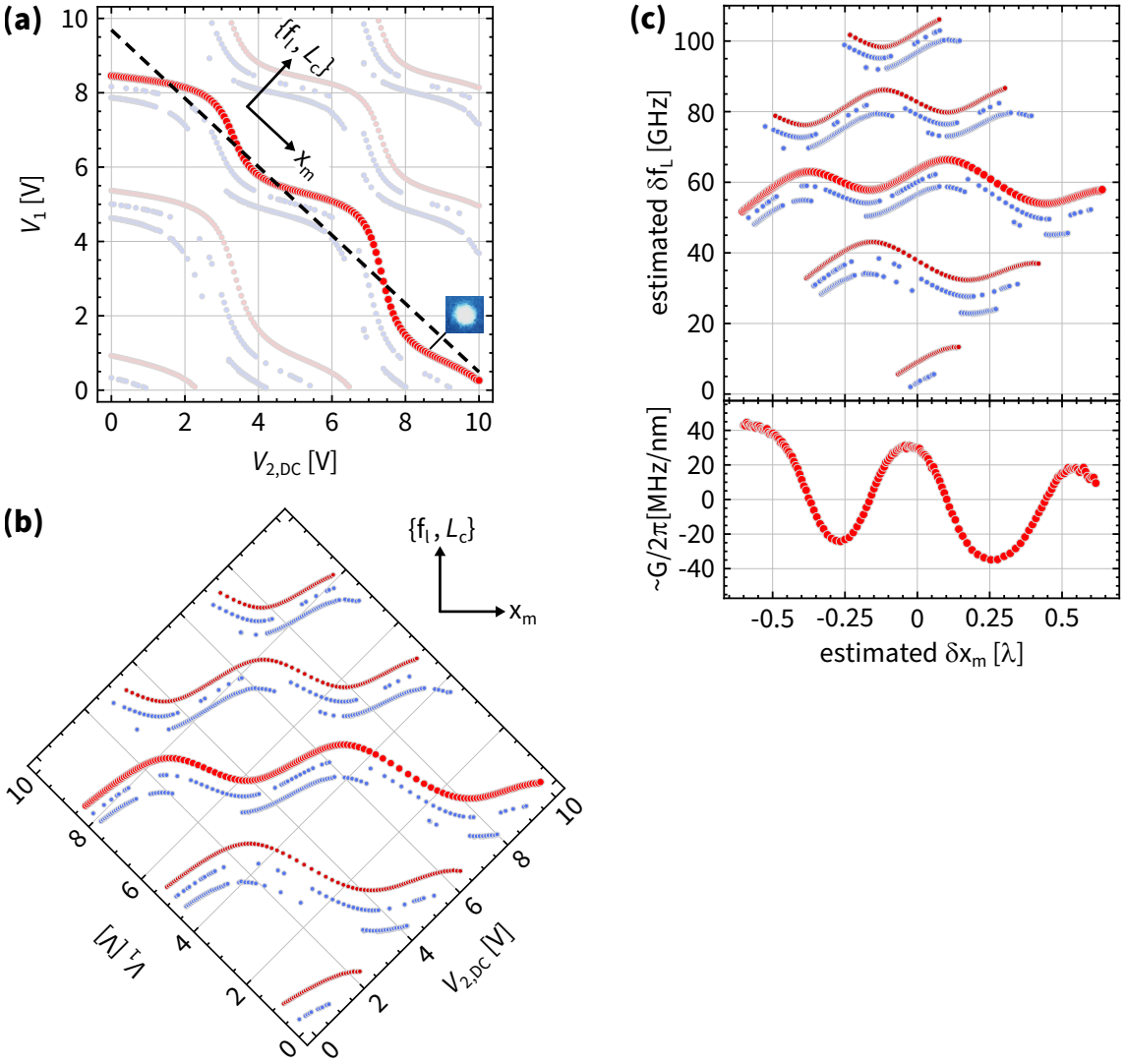

Figure 4.12: Alternate views and analysis of MIM cavity spectroscopy. **(a)** Cavity resonances versus CM1 and CM2 positions, same as 4.12(c). The longest contiguous $\mathrm{TEM}_{0,0}$ resonance locations are identified (bright-red circles) and fit to a straight line (dashed-black). The fit identifies the angle between $(V_1, V_{2,\mathrm{DC}})$ plane and $(f_\mathrm{L}/L_\mathrm{c}, x_m)$ plane. **(b)** Same as (a) but rotated counter-clockwise by the slope of the fitted line in (a). **(c)** Top panel: Cavity resonance versus estimated f_L and estimated x_m. Bottom panel: estimated G for longest contiguous $\mathrm{TEM}_{0,0}$ resonance as in (a) versus estimated x_m. Note that the estimated G shows a pronounced linear trend, which may be resolved by updating our analysis technique i.e., replace the linear fit in panel (a) with a quadratic fit. However, we do not attempt such an analysis mainly because there are more precise ways to measure G via g_0, as shown in Sec. 4.4.3. For panels (a, b, c-top panel), bright red circles: longest contiguous $\mathrm{TEM}_{0,0}$ resonances, smaller red circles: other $\mathrm{TEM}_{0,0}$ modes and blue circles: $\mathrm{TEM}_{\mathrm{m}\neq 0,\mathrm{n}\neq 0}$ modes.

are used elsewhere [237–239].

This concludes our characterization of the membrane's backaction on the optical cavity. As the work in this thesis is primarily focused on tuning membrane modes using the $\mathrm{TEM}_{0,0}$ mode's backaction, we tune the CM positions and λ to achieve the largest value of G and small κ (orange region of 4.11(c)). In particular, to reduce noise sources, we disconnect the CM2 piezo ($V_{2,\mathrm{DC}} = 0$), and obtained large G and small κ at $\lambda =$ 1549.948 nm and CM1 position corresponding to $V_{1,\mathrm{DC}} = 28.5$ V, set directly on the piezo driver and subsequently low pass filtered with 0.7 Hz bandwidth. For the rest of this thesis, $\mathrm{TEM}_{0,0}$ mode is the cavity resonance of interest, unless specified otherwise.

4.4.3 MIM characterization: Part II

In this section, we characterize the MIM system by measuring the optical cavity's dynamical backaction (DBA) on individual membrane modes, due to radiation pressure [173, 175]. The radiation pressure backaction forms the basis of all the work described in this thesis and its theoretical underpinnings appear in Sec. 2.3.

For this characterization, we parametrically tune the laser drive addressing the optical cavity (thereby tuning DBA) and perform spectroscopy of the membrane modes. The DBA is predicted to tune the mechanical mode's resonance frequency (optical-spring) and damping rate (optical-damping). The laser drive is parametrized by two control knobs: its power (P) and its detuning (Δ) from the cavity resonance. The contribution of each control knob is described in Sec. 2.3.

Here we characterize DBA for three distinct mechanical modes: (3,3), (5,2)[1] and (5,3)[1]. For this measurement, the optical cavity is driven with the first control laser tone (Sec. 4.6.1.2) with power $P_1 = 17$ μW while varying its detuning from cavity resonance, Δ_1 over a $\sim 4\kappa$ range. At each value of Δ_1, we perform a mechanical susceptibility measurement for each mechanical mode, and fit it to a complex-Lorentzian to obtain the shift[2] in resonance frequency ($\delta\omega_\mathrm{i}$) and the energy damping rate (γ_i). This characterization is illustrated in Fig. 4.13.

[1] We independently verified (Sec. C.3) that their nominally degenerate partners aren't readily tunable by DBA with current system configuration.

[2] Shift measured from bare resonance frequency ${\omega_\mathrm{i}}^{(0)}$, i.e. in absence of DBA.

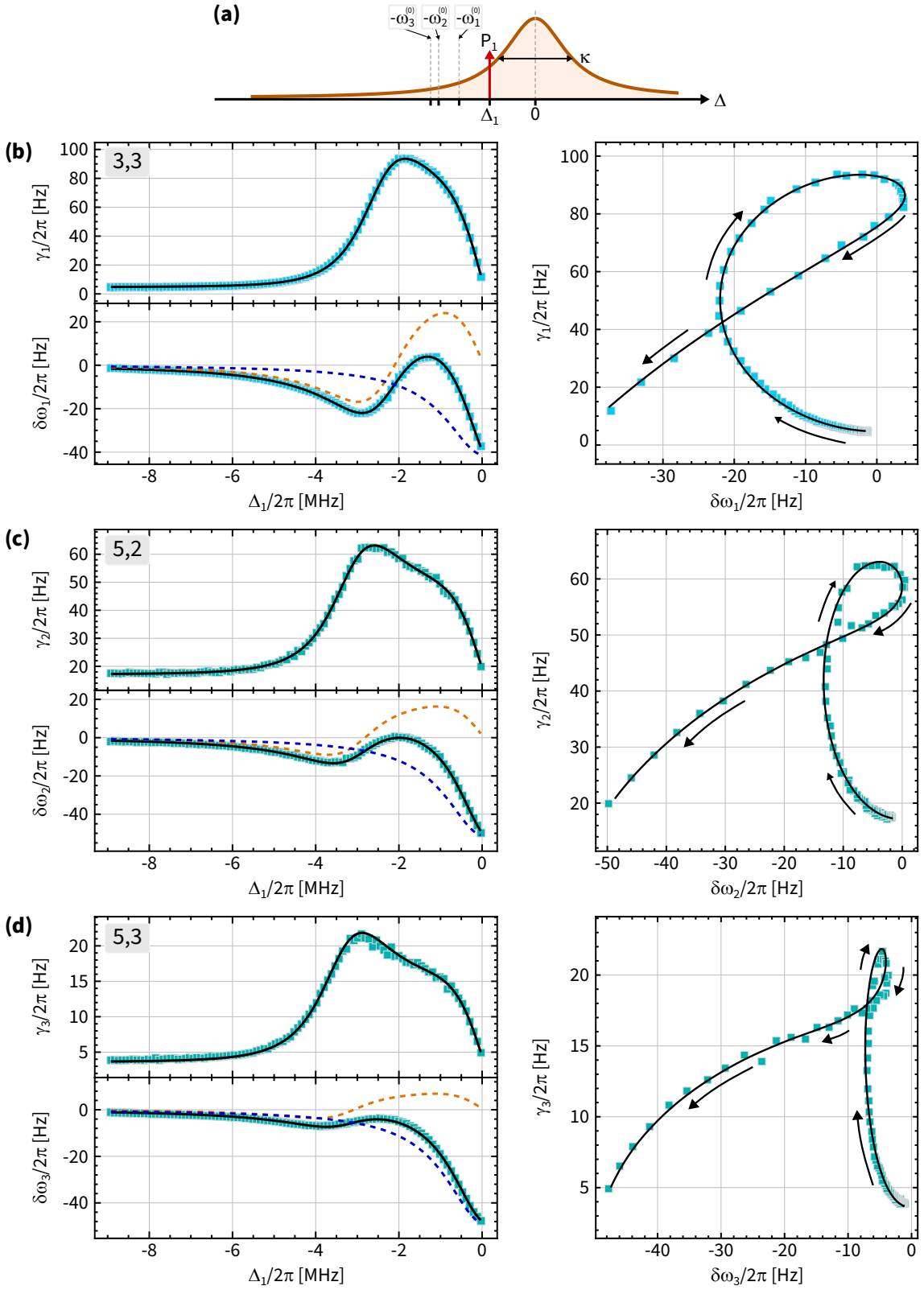

Figure 4.13: DBA characterization. (a) Optical spectrum. Orange: cavity mode; red arrow: control tone, its power P_1 and detuning Δ_1 from cavity resonance. The detuning (Δ) axis is to scale.

Figure 4.13: DBA characterization. *continued from previous page*
(b) DBA characterization (3,3) mode. Left top (bottom) panel: modes' damping (shift in frequency) versus Δ_1, and right panel: parametric plot of damping versus shift in frequency, black arrows indicate the direction of increasing Δ_1. For all panels, data: blue squares, fit to DBA: black curve. DBA includes only radiation pressure for damping, while it includes both radiation pressure (dashed-orange) and photothermal effect (dashed-blue) for shift in frequency. **(c)** Same as (b) but for (5,2) mode. **(d)** Same as (b) but for (5,3) mode. For all measurements $P_1 = 17$ μW.

The values of ($\delta\omega_{\rm i}$,$\gamma_{\rm i}$) can be conveniently fit to the expected radiation pressure DBA with several system parameters as fit parameters. However, we observed an additional source of spring shift that is linearly proportional to the number of intracavity photons ($n_{\rm cav}$). We label this effect as photothermal and characterize it further in Sec. 4.4.3.1. For the present characterization, the $\gamma_{\rm i}(P_1, \Delta_1)$ were fit to expected radiation pressure DBA (further justification in Sec. 4.4.3.1) while the $\delta\omega_{\rm i}(P_1, \Delta_1)$ were fit to a sum of radiation pressure and photothermal effect, which captures the data well. These fits used (κ, $g_{\rm i}$, $A_{\rm i}$, $\Delta_{\rm o}$) as fit parameters, where $g_{\rm i}$ ($A_{\rm i}$) are the single-photon optomechanical (photothermal) coupling rate for each mechanical mode and $\Delta_{\rm o}$ represents a detuning offset of the control laser tone from the cavity resonance. We provide further details about $\Delta_{\rm o}$ in Sec. 4.6.2.2, and for all subsequent discussions, Δ implicitly includes this offset as $\Delta_{\rm actual} = \Delta_{\rm set} + \Delta_{\rm o}$. The values of all fit parameters are given in Table 4.3. Other system parameters required for this analysis were known a-priori or independently characterized, and are given as fixed parameters in Table 4.4. In Sec. 4.6.3, we demonstrate the robustness and long-term stability of these fit and fixed parameters.

Similar measurements of DBA were performed for other membrane modes. In particular, we found that the triplet (7,1);(5,5);(1,7) had negligible optomechanical coupling. We thus postponed replicating and expanding on Chapter 3 with this triplet. Instead, we reverted back to experiments that involve two membrane modes, which are nominally non-degenerate and in particular, we use the pairs consisting of (3,3), (5,2) and (3,3), (5,3) modes for the work described in Chapters 5, 6 and 7.

Parameter	Best fit value	Fit error
$\kappa/2\pi$ (MHz)	2.250	0.003
$g_1/2\pi$ (Hz)	4.416	0.003
$g_2/2\pi$ (Hz)	3.942	0.005
$g_3/2\pi$ (Hz)	2.676	0.008
$A_1/2\pi$ (μHz)	-3.176	0.009
$A_2/2\pi$ (μHz)	-3.955	0.010
$A_3/2\pi$ (μHz)	-3.732	0.010
$\Delta_o/2\pi$ (kHz)	-44	1

Table 4.3: Fit parameters of DBA characterization. For optomechanical (g) and photothermal (A) coupling rates, the subscript denotes the mechanical mode: 1→(3,3), 2→(5,2), 3→(5,3). The fit errors are reported as one standard deviation.

Parameter	Value	Source
λ (nm)	1549.948	Laser controller
ϵ	0.85	Cavity spectroscopy
κ_{in}/κ	0.41	Cavity spectroscopy
${\omega_1}^{(0)}/2\pi$ (MHz)	2.423859	Bare Brownian
${\omega_2}^{(0)}/2\pi$ (MHz)	3.076347	Bare Brownian
${\omega_3}^{(0)}/2\pi$ (MHz)	3.331049	Bare Brownian
${\gamma_1}^{(0)}/2\pi$ (Hz)	4.4	Bare Brownian
${\gamma_2}^{(0)}/2\pi$ (Hz)	17.3	Bare Brownian
${\gamma_3}^{(0)}/2\pi$ (Hz)	3.4	Bare Brownian

Table 4.4: Fixed parameters of DBA characterization. For bare resonance frequencies ($\omega^{(0)}$) and energy damping rates ($\gamma^{(0)}$), the subscript denotes the mechanical mode: 1→(3,3), 2→(5,2), 3→(5,3).

4.4.3.1 Characterization of photothermal effect

The additional spring shift observed in the previous section can be ascribed to heating of the membrane by laser tones, and the corresponding change in its mechanical properties. In this section, we describe measurements that provide further insights into the photothermal effect, verify its static features, and characterize its dynamical features.

We perform ringdown spectroscopy of the mechanical modes (3,3), (5,2) and (5,3) as a function of n_{cav}. For these measurements, n_{cav} is tuned by P_1 with fixed $\Delta_1 \sim 0$. This isolates the photothermal effect from radiation pressure, as the latter is expected to vanish at $\Delta = 0$. The timing sequence of the experiment is illustrated in Fig. 4.14(a). For time $t < 0$, the mechanical drive and the control tone are on. This prepares the membrane's modes in a coherent state with its frequency ω_{i} and damping rate γ_{i} predicted by the sum of radiation pressure and photothermal effect. At $t = 0$, the mechanical drive and the control tone are turned off, and ringdown begins. For $t > 0$, the magnitude ($|V|$) and the frequency ($\delta\omega$)[1] of the corresponding heterodyne signal are shown in Fig. 4.14(b, d, f) for modes (3,3), (5,2) and (5,3), respectively. If the photothermal effect were to be zero, the magnitude and the frequency would be an exponentially decaying and constant function of time, respectively. The exponentially decaying magnitude is characterized by bare-damping rate, while the constant frequency is given by the difference between the demodulation frequency compared to the bare resonance frequency. The measurements highlight several intriguing features, and are described below.

Photothermal effect induced damping

$|V|$ appears to decay exponentially with no dependence on n_{cav} at $t = 0$, as shown in the top panel of Fig. 4.14(b,d,f). To further verify these observations, we fit these datasets to $\sqrt{(ae^{-\gamma_{\mathrm{i}}t/2})^2 + b^2}$, with $(a, \gamma_{\mathrm{i}}, b)$ as fit parameters, where a is the initial amplitude, γ_{i} is the energy damping rate and b is a constant offset representing background due to detection and thermal motion of the modes. The fits capture the data well, highlighting a lack of additional transient behavior.

For a systematic comparison, we also measured bare ringdowns i.e., for $P_1 = 0$ in-

[1]Obtained by taking the time derivative of the phase of the heterodyne signal.

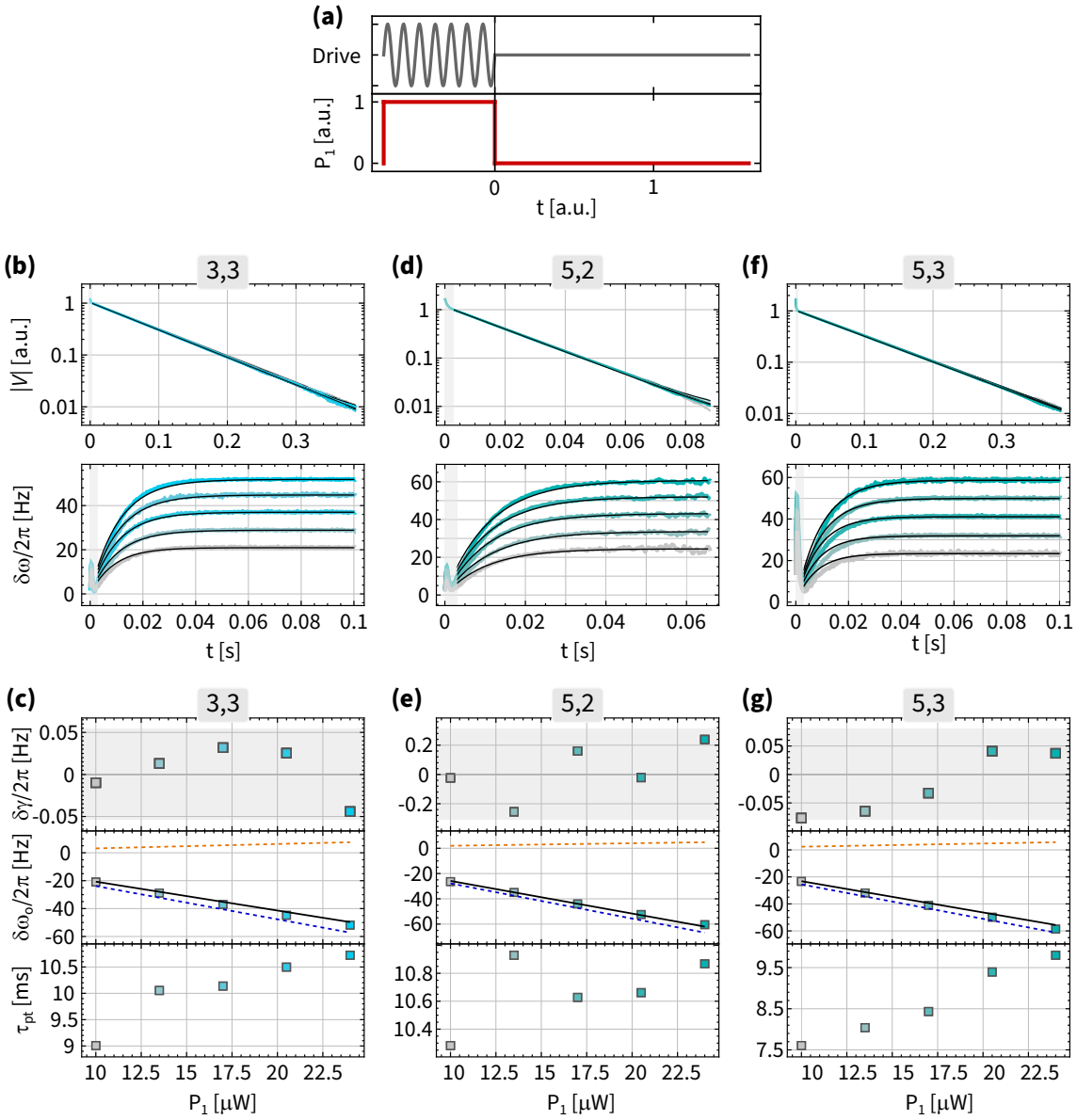

Figure 4.14: Photothermal effect characterization. **(a)** The timing sequence of the experiment. Top panel: the initial drive to the mechanical modes, Bottom panel: power (P_1) of the control tone. Ringdown begins when the mechanical drive is turned off at $t = 0$. **(b)** Ringdown signal (V) versus time (t) for (3,3) mode. Top panel: $|V(\mathrm{t})|$, bottom panel: $\delta\omega(\mathrm{t}) = \partial_\mathrm{t}\angle V(\mathrm{t})$. Data: Thick gray to cyan curves. They correspond to $P_1 = \{10, 13.5, 17, 20.5, 24\}$ μW, respectively. Fit: Thin black curves. For this measurement, $\Delta_1/2\pi$ = -0.076 MHz. **(c)** Fit parameters versus P_1 for (3,3) mode. (Top panel) squares: $\delta\gamma \equiv \gamma - \gamma_\mathrm{bare}$ and gray region: scatter in γ_bare. (Middle panel) squares: $\delta\omega_\mathrm{o}$, black curve: predicted $\delta\omega_\mathrm{o}$ (not a fit) using system parameters in Table 4.3 and 4.4, dashed blue curve: photothermal contribution to $\delta\omega_\mathrm{o}$ and dashed orange curve: radiation pressure contribution to $\delta\omega_\mathrm{o}$. (Bottom panel) squares: τ_pt. **(d, e)** Same as (b, c), respectively but for (5,2) mode. **(f, g)** Same as (b, c), repectively but (5,3) mode and $\Delta_1/2\pi$ = -0.331 MHz.

terleaved with $P_1 \neq 0$ measurements. The difference between fitted γ_i and bare γ_i are shown in the top panel of Fig. 4.14(c, e, g) for modes (3,3), (5,2) and (5,3), respectively, and they lie within the bounds of scatter in bare γ_i measurements. Here, the scatter is quantified by one standard deviation of all bare γ_i measurements. These results support the conclusion that photothermal effect does not impact the damping at the current level of measurements and data analysis.

Photothermal effect induced spring shift

The measurements of $\delta\omega$ as shown in the bottom panel Fig. 4.14(b,d,f), suggests a transient behavior of the photothermal effect on a few milliseconds time-scale[1], with a dependence on n_cav at $t = 0$. At large times, $\delta\omega$ settles to a non-zero $\sim$constant value, which reflects the fact that we used predicted values of $\omega_\mathrm{i}/2\pi$ as the demodulation frequency for these ringdown measurements, while the mechanical mode's frequency settles to its bare value (i.e., in the absence of control tones), over time.

We fit these datasets to a phenomenological model given by $\delta\omega_\mathrm{o}(1 - e^{-t/\tau_\mathrm{pt}})$ where $\delta\omega_\mathrm{o}$ is the expected spring shift predicted by the sum of radiation pressure and photothermal effect and τ_pt is the photothermal time-scale. The fit captures the data reasonably well. Fitted $\delta\omega_\mathrm{o}$ is shown in the middle panel of Fig. 4.14(c, e, g) for modes (3,3), (5,2) and (5,3), respectively, which shows a linear dependence on n_cav. Also shown are the predicted values of $\delta\omega_\mathrm{i}$ as the sum of radiation pressure and photothermal effect using system parameters given in Tables 4.3 and 4.4 (i.e., not a fit). The fitted τ_pt are shown in the bottom panel of Fig. 4.14(c, e, g) for modes (3,3), (5,2) and (5,3), respectively. This time-scale is neither small ($<$0.1 ms) nor large ($>$1 s), but the rather just the right amount to unnecessarily interfere with our experiments involving the real time dynamics (10-100 ms) of coupled mechanical modes.

While our phenomenological model captures the photothermal effect reasonably, we are unable to pinpoint its origin. There are similar room-temperature MIM systems, for example Ref. [240] (its Fig. 2), which shows purely radiation pressure effects. This leads to

[1]Added for clarity: Radiation pressure backaction also has a transient behavior, with a time-scale $\sim 1/\kappa \sim 100$ ns. However, it is much faster than the data sampling rate (here 3 kHz), and hence we are insensitive to its transient.

the hypothesis that ours is a special case. Going forward, the static photothermal spring shift is incorporated in the full-system model used for theoretical predictions. However, its dynamical aspect is a bane and appropriate steps are taken to circumvent it.

4.5 Benchmarking a tunable non-Hermitian system

In this section, we describe several measurements that benchmark our system as a tunable and robust platform to study non-Hermitian physics. We specifically focus on measurements that set the stage for the work described in Chapters 5, 6 and 7. These measurements include spectroscopy and real time dynamics of Floquet-coupled membrane modes. We subsequently introduce one of the new control knobs that tunes the overall dissipation of the membrane modes, and which single-handedly made the work in Chapters 6 and 7 possible. Finally, we evaluate the robustness and long-term stability of our system via spectroscopy near an EP_2.

4.5.1 Characterizing Floquet-coupled membrane modes: Part I

In this section, we characterize Floquet-coupled membrane modes by performing spectroscopy as a function of statically tuned control parameters. As described in Chapter 2 and elsewhere [61, 94], two nominally non-degenerate membrane modes (i.e., $\sqrt{i^2+j^2} \neq \sqrt{m^2+n^2}$ where $(i,j);(m,n)$ index the membrane modes) can be coupled by driving the optical cavity with two laser tones whose relative detuning is comparable to the modes' frequency non-degeneracy. The laser tones' powers, relative detuning and their common detuning from the cavity provide four independent control knobs to tune DBA, thereby tuning the dynamical matrix (H) that governs the membrane modes' motion, its eigenvalues ($\boldsymbol{\lambda}$) and eigenvectors ($\mathbf{u}$).

Here, we characterize the static properties of H via measurements of $(\boldsymbol{\lambda}, \mathbf{u})$ for two pairs of non-degenerate membrane modes: **(1)**: (3,3) and (5,2) and **(2)**: (3,3) and (5,3), Floquet-coupled via two laser tone drives to the optical cavity. For each pair, the corresponding laser tones are parameterized by their powers (P_1, P_2) and detunings (Δ_1, Δ_2) from the cavity resonance. The detunings are constrained by Eqs. (4.13) and (4.14) for pairs **(1)** and **(2)**, respectively.

$$\Delta_1 = -{\omega_1}^{(0)} + \delta, \Delta_2 = -{\omega_2}^{(0)} + \delta + \eta \tag{4.13}$$

$$\Delta_1 = -{\omega_1}^{(0)} + \delta, \Delta_2 = -{\omega_3}^{(0)} + \delta + \eta \tag{4.14}$$

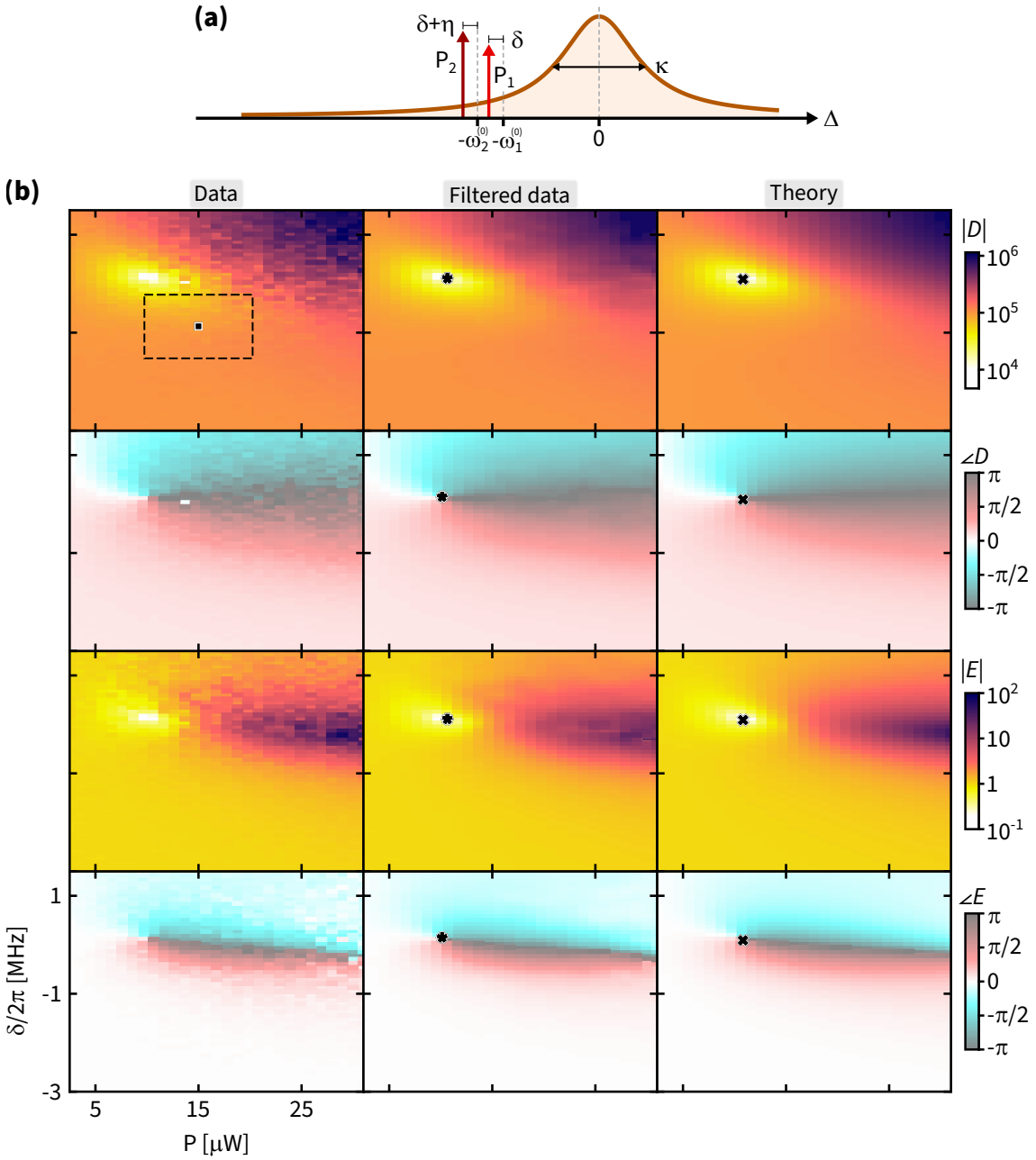

Figure 4.15: Spectroscopy of Floquet-coupled (3,3) and (5,2) modes. **(a)** Optical spectrum. Orange: cavity mode; vertical arrows: control tones. Each control tones' power and detuning are indicated. The detuning (Δ) axis is to scale. **(b)** $D(\delta, P)$ and $E(\delta, P)$. For these measurements $P_1 = P_2 = P$ and $\eta/2\pi$ = -50 Hz. Left column: data, dashed rectangle and black square: control space for Geometric phase measurements in Chapter 5; middle column: filtered data, black star: experimentally predicted EP_2 location; right column: fit, black cross: theoretically predicted EP_2 location. First row: $|D|$ (units: $(2\pi \times \mathrm{Hz})^2$), second row: $\angle D$ (units: radians), third row: $|E|$ and fourth row: $\angle E$ (units: radians).

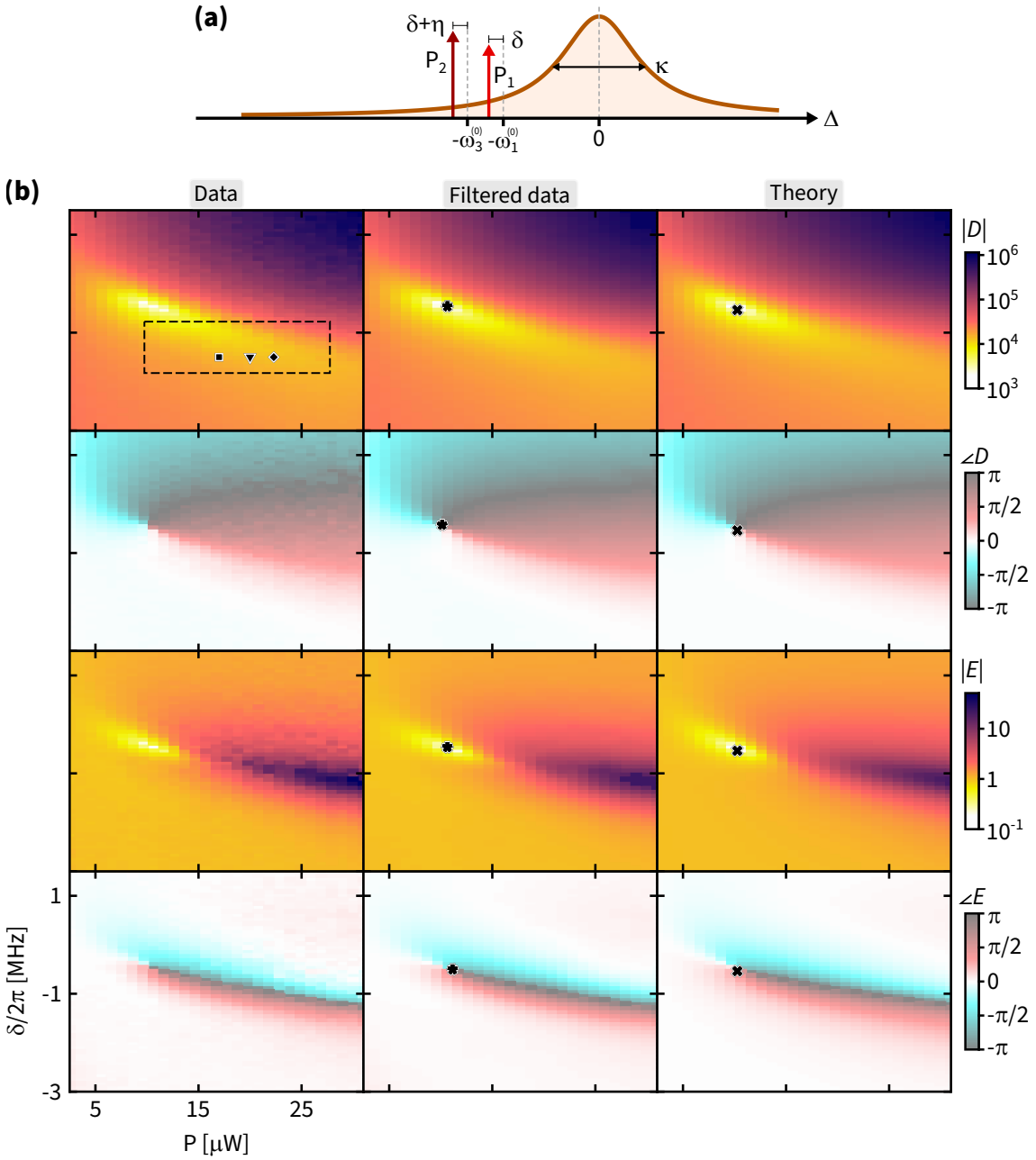

Figure 4.16: Spectroscopy of Floquet-coupled (3,3) and (5,3) modes. **(a)** Optical spectrum. Orange: cavity mode; vertical arrows: control tones. Each control tones' power and detuning are indicated. The detuning (Δ) axis is to scale. **(b)** $D(\delta, P)$ and $E(\delta, P)$. For these measurements $P_1 = P_2 = P$ and $\eta/2\pi$ = -27.5 Hz. Left column: data, dashed rectangle and black symbols: control space for Geometric phase measurements in Chapter 5; middle column: filtered data, black star: experimentally predicted EP_2 location; right column: fit, black cross: theoretically predicted EP_2 location. First row: $|D|$ (units: $(2\pi \times \mathrm{Hz})^2$), second row: $\angle D$ (units: radians), third row: $|E|$ and fourth row: $\angle E$ (units: radians).

where ${\omega_1}^{(0)}, {\omega_2}^{(0)}$ and ${\omega_3}^{(0)}$ denote the bare resonance frequency of (3,3), (5,2) and (5,3) modes, respectively. δ and η denote the common and relative detuning parameters. As discussed in Chapter 2, qualitatively this arrangements provides a frame of reference $\mathcal{R}$ where a pair of membrane modes originally separated by $|{\omega_1}^{(0)} - {\omega_j}^{(0)}|$ in absence of control tones and $j \in \{2, 3\}$, are now effectively separated by $\sim \eta$, and tuning the control parameters provides tunable optical spring, optical damping and Floquet-coupling.

For these measurements, we statically tune control parameters ($\delta, P_1 = P_2 = P$) on a 2D-sheet in a discretized manner, while holding η fixed. Fixing η fixes $\mathcal{R}$, which simplifies the interpretation of these measurements. For each point of such a 2D-sheet, we measure two copies of the mechanical susceptibility: one at ${\omega_1}^{(0)}$ and other at ${\omega_j}^{(0)}$ for $j \in \{2, 3\}$ and fit them to a sum of two complex Lorentzians plus a constant offset (to account for background due to the mechanical drive). Constraints on this fit are provided by the unordered complex eigenvalues (λ_+, λ_-) and the complex eigenvector parameter s_{12}, where $\lambda_i = \omega_i - i\gamma_i/2$; $\omega_i(\gamma_i)$ is the peak position (width) of the Lorentzian corresponding to mode $i \in \{+, -\}$ and s_{12} represents the constrained complex heights of the four Lorentzians (two for each measurement). These parameters are converted into order-agnostic quantities such as discriminant $D = (\lambda_+ - \lambda_+ -)^2$, trace $\mathcal{T} = \lambda_+ + \lambda_-$ and the eigenvector indicator $E = (2s_{12} - 1)^{-2}$. Figs. 4.15 and 4.16 (b - first column) illustrate these measurements for mode pairs **1** and **2**, respectively. These measurements are subsequently analyzed to algorithmically identify the point at which the 2D-plane of control parameters intersects the $\mathcal{EP}_2$ subspace i.e., the eigenvalues and the eigenvectors become degenerate, and correspondingly, D and E vanish. We refer to this point of intersection as EP_2, which is located as a minima in $|D|$ and $|E|$ and a 2π winding in $\angle D$ and $\angle E$. This analysis is illustrated in Figs. 4.15 and 4.16 (b - second column).

To put these measurements on a firm theoretical footing, we fit and compare them to the optomechanical model in Chapter 2 with several system parameters as fit parameters. This is done by observing that D and $\mathcal{T}$ are simple functions of H given by:

$$D = \mathcal{T}^2 - 4\mathrm{Det}(H), \mathcal{T} = \mathrm{Tr}(H) \tag{4.15}$$

where Det and Tr denote the determinant and trace of a matrix, and D is the discriminant

of a matrix's characteristic polynomial. Using the above relations, we fit the measured $D(P,\delta)$ and $\mathcal{T}(P,\delta)$ for mode pair **1** to obtain $(\kappa, g_1, g_2, A_1, A_2, \Delta_0)$ and mode pair **2** modes to obtain $(\kappa, g_1, g_3, A_1, A_3, \Delta_0)$. The fit parameters are listed in Table 4.5 and the fits are illustrated in Figs. 4.15 and 4.16 (b - third column) for mode pairs **1** and **2**, respectively. A detailed examination of these fits is in Sec. C.4.

These and similar measurements over time highlight some key aspects: **(1)** We are able to tune our system to and around EP_2, a precursor to the goal of tuning the system in the $\mathcal{EP}_2$ subspace (Chapter 7). **(2)** The agreement with the optomechanical model will allow us to predict the system's behavior when undergoing real time dynamics. In particular, we emphasize that fits to such spectroscopy measurements provide the relevant system parameters, which produce all theory curves and estimates shown in Chapters 5-7 (i.e., they are not fits). **(3)** While these spectroscopy measurements are not specifically geared towards our original goal of replicating the results of Chapter 3 in a short amount of time, we note that the measurements shown in Figs. 4.15 and 4.16 each took ∼8 hours to acquire. A similarly sized dataset in the old system would have taken ∼2.5 days (at ∼600 spectroscopy measurements/day).

4.5.2 Characterizing Floquet-coupled membrane modes: Part II

In this section, we measure the real time dynamics of the Floquet-coupled membrane modes. These measurements also test our strategy of simulating the system's real time dynamical behavior a priori using the optomechanical model with the parameter values given by fits to spectroscopy (see Sec. 4.5.1), and subsequently comparing them with actual measurements. For these measurements, we used Floquet-coupled (3,3) and (5,2) membrane modes, tuned by varying control parameters $(\delta, P_1 = P_2 = P)$ in real time around control loop CL that encircles an EP_2, with a fixed starting point $(s = 0 = 1)$. As in Sec. 4.5.1, we hold η fixed, which fixes $\mathcal{R}$. We note that we chose the same 2D-plane of control parameters as in Fig. 4.15. The 2D control plane with the control loop CL, its starting point and the EP_2 are illustrated in Fig. 4.17(a)

As a rule of thumb, prior to measuring any real time dynamics, we confirm the static properties of CL, such as the eigenvalues (λ_1, λ_2) along it. We perform spectroscopy as

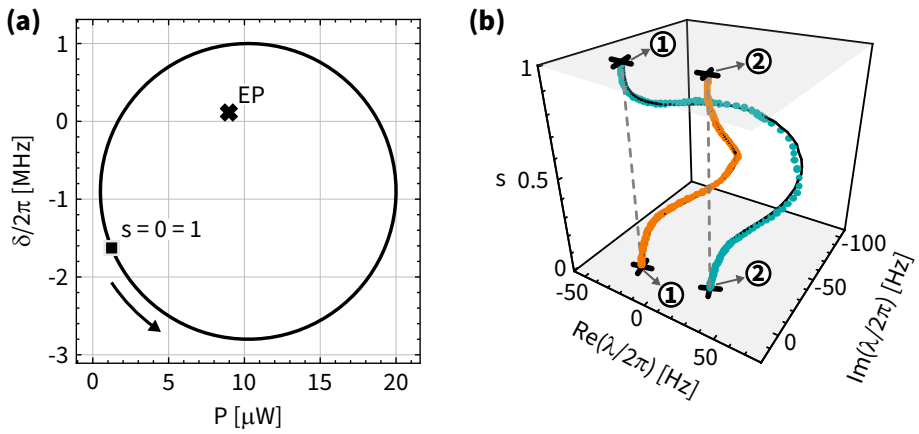

Figure 4.17: Static eigenvalue braiding of Floquet-coupled (3,3) and (5,2) modes. (a) The 2D control space $\delta \times P$. Cross: theoretically estimated EP_2 location, curve: the control loop that encircles the EP_2, square: starting and ending point of the loop indexed by $s = 0 = 1$, the arrow denotes the direction of loop used for measuring the eigenvalue braid in (b). **(b)** Eigenvalue braid corresponding to the control loop in (a). Data: orange (dark cyan) points for braid strand corresponding to $\lambda_1(\lambda_2)$, theory prediction: black curve. s indexes the measurement of $\boldsymbol{\lambda}$ along the control loop. As the control loop encircles the EP_2, the eigenvalue braid strands swap. For this measurement: $P_1 = P_2 = P$, $\eta/2\pi$ = -50 Hz and we used Floquet-coupled (3,3) and (5,2) modes.

in Sec. 4.5.1 by tuning $(\delta, P_1 = P_2 = P)$ at 100 points along CL in counter-clockwise sense, and verify that the eigenvalue braid strands indeed swap, as expected for a control loop encircling an EP_2. This eigenvalue braid is illustrated in Fig. 4.17(b).

We now measure the effect of traversing CL in real time, as a function of traversal duration (or loop-time, T), for various choices of initial state and direction of traversal (or loop-direction). For these measurements, we apply a mechanical drive to initialize in either $\sim (1,0)^{\mathrm{T}}$ or $\sim (0,1)^{\mathrm{T}}$, corresponding to mode ① or ② in $\mathcal{R}$, respectively. At time $t = 0$, we stop the drive and vary the control parameters around CL in a duration T, as illustrated in Fig. 4.5.2(a). The heterodyne signals for $t > T$ are fit and analyzed by following the procedure outlined in Refs. [32, 61, 94, 188], a "Transfer efficiency" is obtained as a function of T. Transfer efficiency quantifies the fraction of the energy transferred from mode ⓘ to ⓙ at the end of CL of duration T. The Transfer efficiency corresponding to two distinct initialization and two loop-directions as function of T are illustrated in Fig. 4.18. Also illustrated are the no-free-parameter theory prediction corresponding to these measurements. Their agreement validates our strategy.

We note in passing that the specific choice of CL was chosen to simplify these

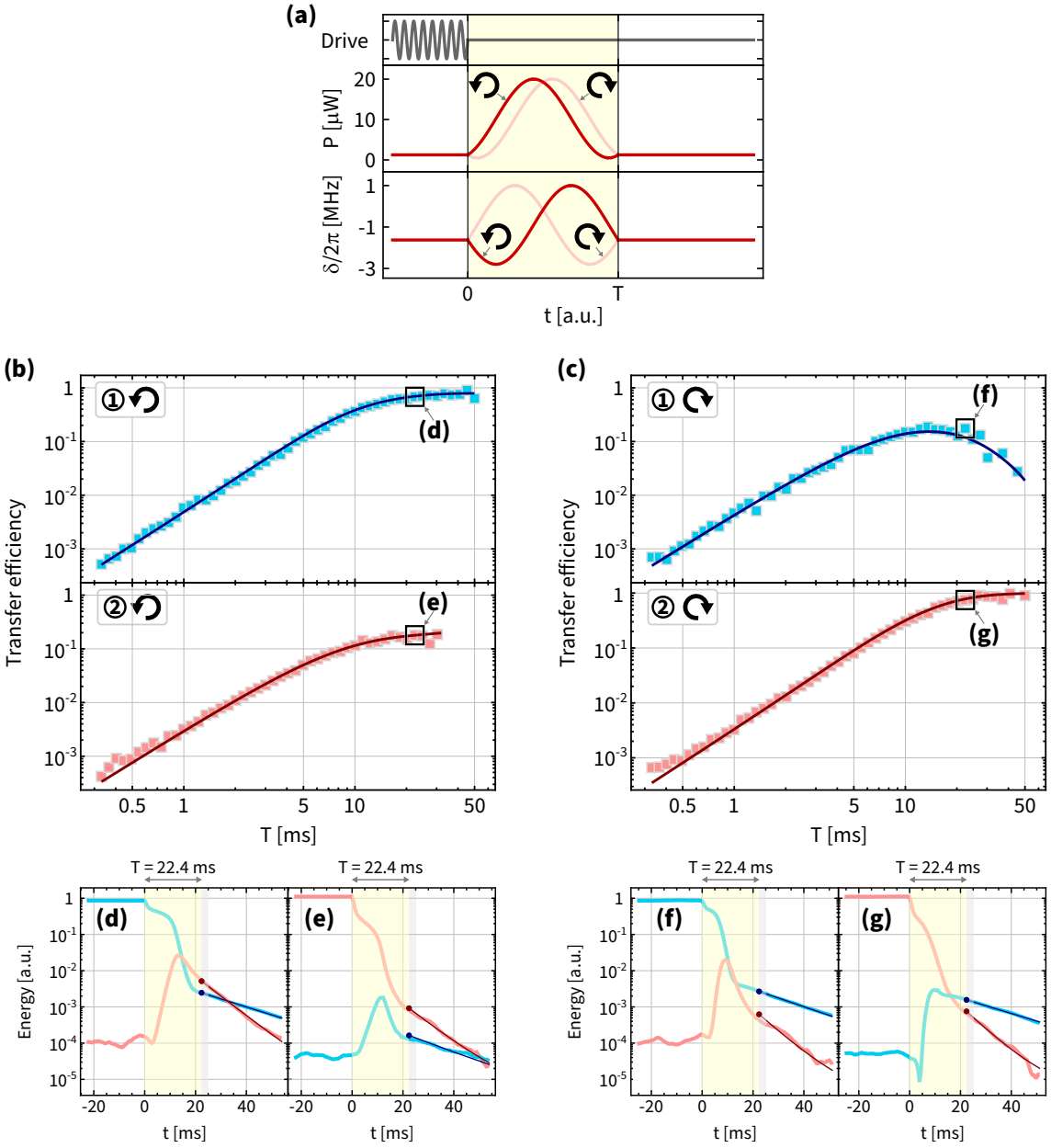

Figure 4.18: Real time dynamics of Floquet-coupled (3,3) and (5,2) modes. **(a)** The timing sequence of the experiment. Top panel: mechanical drive that prepares the initial state to either ① or ②, middle (bottom) panel: $P(t)$ ($\delta(t)$). Arrow markers indicate loop direction. The loop duration ($0 < t < T$) is yellow. **(b)** Transfer efficiency versus T for counter-clockwise control loop direction. Top (bottom) panel: Initial state is ① (②), data: blue (red) squares, theory: blue (red) curve without any fit parameters. Exemplary data points at nominally large T are highlighted, as (d) and (e). **(c)** Same as (b) but with clockwise control loop direction. **(d)** Energy versus t: for counter-clockwise loop direction, loop duration $T = 22.4$ ms and mode ① as initial state. Data (theory prediction): blue (dark blue) curve for mode ①, red (dark red) curve mode ②. The loop duration ($0 < t < T$) is yellow and the LIA 95% settling time is gray. **(e)** Same as (d) but for mode ② as initial state. **(f)** Same as (d) but for clockwise control loop direction. **(g)** Same as (f) but for mode ② as initial state. For this measurement: $P_1 = P_2 = P$, $\eta/2\pi$ = -50 Hz and we used Floquet-coupled (3,3) and (5,2) modes.

measurements. Its starting point being close to $P \sim 0$ enabled us to prepare the initial state close to $(1,0)^{\mathrm{T}}$ or $(0,1)^{\mathrm{T}}$, simply with a sinusoidal mechanical drive at frequencies ${\omega_1}^{(0)} + \mathrm{Re}(\lambda_1(s=0))$ and ${\omega_2}^{(0)} + \mathrm{Re}(\lambda_2(s=0))$, respectively[1]. Here ${\omega_{1,2}}^{(0)}$ denote the bare frequencies of (3,3) and (5,2), respectively. As we will see in Chapter 7, preparing a desired initial state isn't as straightforward.

4.5.3 Introducing the blue-detuned control tone

All DBA measurements described until now have used only red-detuned control laser tones, which result in DBA induced damping rate of $\gtrsim 2\pi\times$10 Hz, for all three mechanical modes: (3,3), (5,2) and (5,3), for typical control parameters. This puts a practical upper limit on the duration of control loops at ∼50 ms (as in 4.5.2), before the mechanical modes' coherent amplitude decays below the level of thermal fluctuations. With appropriate analysis, we can still isolate coherent signals at the level of thermal fluctuations, and are able to squeeze out extra ∼10 ms of loop duration. However, given our system parameters, several aspects of our work would be simplified if control loops could access loop durations >100 ms (such as in Chapter 7). This necessitated reducing the mechanical modes' overall damping rate, more specifically for the least-damped mode.

A blue-detuned control tone results in DBA induced anti-damping [175], and if used together with the red-detuned control tones, can provide the desired overall damping rates. In order to characterize our system in presence of the blue-detuned control tone, we performed spectroscopy of mechanical modes via ringdown measurements, as a function of blue-detuned control tone's power (P_4) and its detuning from cavity resonance (Δ_4), while shining enough red-detuned laser tones to ensure that the system is damped overall. We note some changes in spectroscopy compared to Sec. 4.5.1. Firstly, the switch from driven susceptibility measurements to ringdowns was out of precaution, as we did not want the mechanical drive tone and the blue-detuned tone to simultaneously co-exist inside the cavity. Secondly, the photothermal transient (Sec. 4.4.3.1) is an unwanted effect in ringdown measurements. It can be avoided by keeping the number of intracavity photons constant - over a measurement sequence. This is achieved using another control

[1] Indeed any such loop whose starting point has small DBA (i.e., small power or large detuning from the cavity resonance) would provide such a simplification.

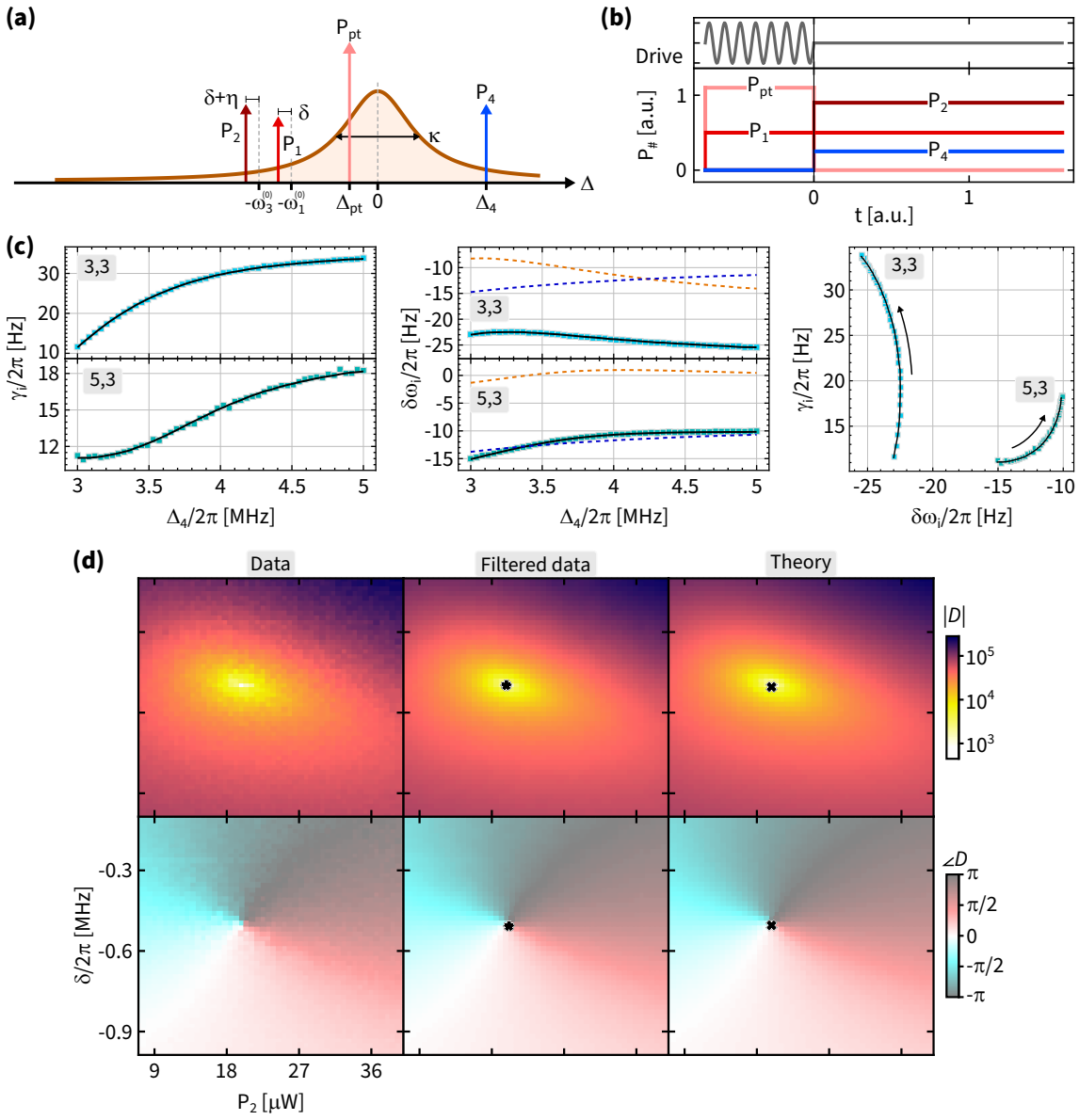

Figure 4.19: Characterizing the blue-detuned control tone. (a) Optical spectrum. Orange: cavity mode; vertical arrows: all control tones. Each control tones' power and detuning are indicated. The detuning (Δ) axis is to scale. **(b)** The timing sequence of spectroscopy measurements via ringdowns. Top panel: the initial drive to the mechanical modes, Bottom panel: power of all control tones. Ringdown begins when the mechanical drive is turned off at $t = 0$. **(c)** DBA verification for the blue detuned control tone for (3,3) and (5,3) modes. Left (middle) panel: modes' damping (shift in frequency) versus Δ_4, and right panel: parametric plot of damping versus shift in frequency, black arrow indicates the direction of increasing Δ_4. For all panels, data: blue squares, fit to DBA: black curve. DBA includes only radiation pressure for damping, while it includes both radiation pressure (dashed-orange) and photothermal effect (dashed-blue) for shift in frequency. **(d)** $D(\delta, P_2)$. Left column: data; middle column: filtered data, black star: experimentally predicted EP_2 location; right column: fit, black cross: theoretically predicted EP_2 location. Top row: $|D|$ (units: $(2\pi \times \mathrm{Hz})^2$), bottom row: $\angle D$ (units: radians).

tone at a fixed red-detuning $\Delta_{\rm pt}$ from the cavity resonance and tuning its power $P_{\rm pt}$ based on other control tones.

The control tones used for this characterization are shown in Fig. 4.19(a). Fig. 4.19(b) illustrates the timing sequence of a ringdown measurement. For time t <0, the mechanical drive is on along with the photothermal control tone $(\Delta_{\rm pt}, P_{\rm pt})$. At $t = 0$, the mechanical drive and the photothermal tone are turned off, simultaneously two red (tone 1,2: $(\Delta_{1,2}, P_{1,2})$) and a blue (Δ_4, P_4) control tone are turned on and ringdown begins. Here, $\Delta_{1,2}$ are tethered together as in Sec. 4.5.1 via $({\omega_{1,2}}^{(0)}, \delta, \eta)$ to produce Floquet coupling. For this arrangement, the value of $P_{\rm pt}$ is found by solving for:

$$n_{\rm cav}(\Delta_{\rm pt}, P_{\rm pt}) = n_{\rm cav}(\Delta_1, P_1) + n_{\rm cav}(\Delta_2, P_2) + n_{\rm cav}(\Delta_4, P_4) \tag{4.16}$$

where $n_{\rm cav}$, represents the intracavity photon number.

For these measurements, we used the (3,3) and (5,3) mechanical modes. Heterodyne signals for $t > 0$ are fit to the expected form (i.e. sum of two decaying sinusoids) to extract the eigenvalues $(\lambda_\pm)$. Fitted $\lambda_\pm$ are shown in Fig. 4.19(c) for control parameters: P_1 = 20 μW, P_2 = 0, P_4 = 10 μW, $\Delta_1/2\pi$ = -3.174 MHz and $\Delta_4/2\pi$ is varied from +3 to +5 MHz, in 50 steps. Fitting $\lambda_\pm$ to the optomechanical model provides consistent system parameters as in Sec. 4.4.3 and verifies the expected DBA of the blue-detuned control tone (see Table 4.5). Subsequently, we performed spectroscopy over a 2D plane of control parameters as shown in Fig. 4.19 similar to 4.5.1. While we are yet to furnish a foolproof E for ringdowns, we find $\lambda_\pm$ and corresponding D are more precise compared to susceptibility measurements. For this sheet, P_1 = 30 μW, $\eta/2\pi$ = -45 Hz, P_4 = 33.5 μW, $\Delta_4/2\pi$ = +3.5 MHz and (δ, P_2) were tuned on a 50×50 rectangular grid with corners (-0.987 MHz, 7 μW) and (-0.1 MHz, 40 μW). The parameters obtained by fitting this sheet are consistent with previous measurements, and are listed in Table 4.5. A detailed view of the corresponding fit is provided in Sec. C.4.

This happens to be the very first instance of successfully tuning a MIM system with a blue-detuned tone, in the Harris lab. While reduction of damping rates was the sole focus, the blue-detuned tone opened unexplored avenues in the parameter space which

	Measurement as shown in:			
Fit Parameter	**Fig. 4.15**	**Fig. 4.16**	**Fig. 4.19(c)**	**Fig. 4.19(d)**
$\kappa/2\pi$ (MHz)	2.38 ± 0.02	2.33 ± 0.02	2.19 ± 0.02	2.301 ± 0.002
$g_1/2\pi$ (Hz)	4.39 ± 0.01	4.43 ± 0.01	4.19 ± 0.02	4.519 ± 0.003
$g_2/2\pi$ (Hz)	3.88 ± 0.01	-	-	-
$g_3/2\pi$ (Hz)	-	2.65 ± 0.01	2.35 ± 0.01	2.619 ± 0.001
$A_1/2\pi$ (μHz)	-2.57 ± 0.07	-3.01 ± 0.06	-5.75 ± 0.16	-3.55 ± 0.01
$A_2/2\pi$ (μHz)	-4.07 ± 0.07	-	-	-
$A_3/2\pi$ (μHz)	-	-3.63 ± 0.06	5.37 ± 0.10	-4.35 ± 0.01
$\Delta_o/2\pi$ (kHz)	-37 ± 3	-54 ± 2	-61 ± 7	-7 ± 0.5
Specifications				
Floquet-coupled	Yes	Yes	No	Yes
Blue tone	off	off	on	on
Method	S	S	R	R
DAq speed-up	7.5x	7.5x	5x	5x

Table 4.5: Summary of spectroscopy measurements. For optomechanical (g) and photothermal (A) coupling rates, the subscript denotes the mechanical mode: 1→(3,3), 2→(5,2), 3→(5,3). The values of the fit parameters are reported as fit value ± fit error reported as one standard deviation. For method, 'S' denotes mechanical susceptibility measurements and 'R' denotes ringdowns. Data acquisition (DAq) speed-up is estimated by comparing total time elapsed for these measurements and estimated time for the old system for the same dataset @ ∼600 spectroscopy measurements/day.

allowed us to uncover a qualitatively new phenomena as described in Chapter 6.

4.5.4 Evaluating system stability near an EP_2

Robustness and long-term stability of our system and control parameters are key features that enable the measurements in this thesis. Here we demonstrate a facet of these features by performing spectroscopy on a 2D plane that intersects the degenerate ($\mathcal{EP}_2$) subspace at a point (EP_2), and tracking this EP_2, over a period time.

Spectroscopy was done via ringdown measurements of mechanical modes: (3,3) and (5,3), over a sheet of δ and $P_1 = P_2 = P$ with fixed values of $\eta/2\pi = -50$ Hz and blue-detuned tone's parameters: $P_4 = 35$ μW and $\Delta_4/2\pi = +3.5$ MHz. As in Sec. 4.5.3, ringdown measurements were fit to determine $\lambda_\pm$, and subsequently converted to D. The EP_2 was located via $\angle D$. Fig. 4.20 illustrates the result of several such sheets that feature this EP_2 (inferred via filtered $\angle D$), measured intermittently over a period of 20 days[1]. Typically, two types of $\delta \times P$ sheets were measured: large range and large step-size of (δ, P) as in Fig. 4.20(a), for approximately locating the EP_2 and small range and small step-size of (δ, P) as in Fig. 4.20(b, c), for precisely locating the EP_2.

EP_2 locations for all sheets measured over 20 days are collated in Fig. 4.20(d). Its (δ, P) coordinate is consistently located within a step-size of (δ, P) for the large (δ, P) range sheet. The error bars on $EP_2(\delta, P)$ coordinates are given by the step-size of the $\delta \times P$ sheet. Also shown are measured P_1 and P_2 (top panel) as black and dark-red disks, respectively, which are virtually indistinguishable from each other, and from their target values.

This result was a key step towards performing real time dynamics in $\mathcal{EP}_2$, as described in Chapter 7. In particular, they indicated that our control parameters and system parameters are robust and stable enough to reliably tune to a selected EP_2, over a long period of time. In a later section (Sec. 7.3.1), we will revisit this subject again, while performing measurements of real time dynamics in $\mathcal{EP}_2$, for over a long period of time.

[1] March 11, 2024 - March 31, 2024

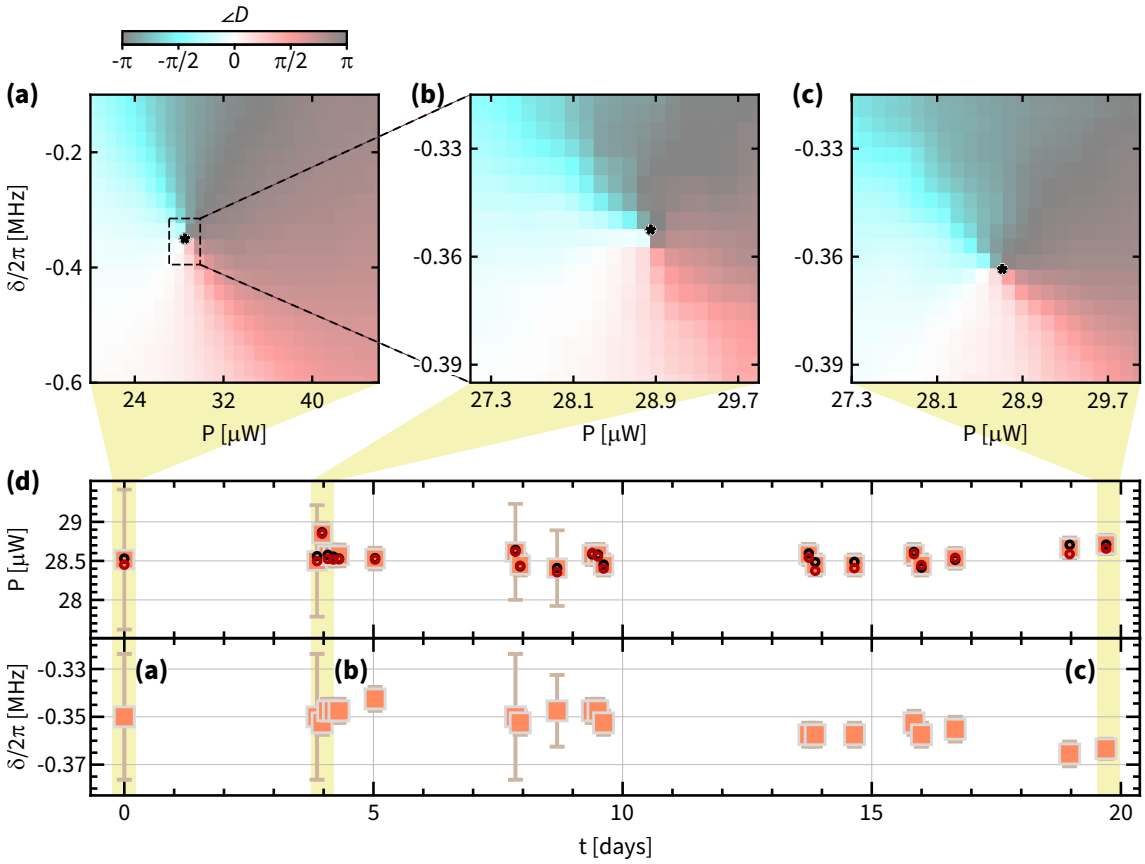

Figure 4.20: Spectroscopy near EP_2 over time. **(a)** Filtered $\angle D(\delta, P)$ for the first large range and step-size sheet. Dashed box: (δ, P) range for small range and step-size sheet in (b). **(b)** Filtered $\angle D(\delta, P)$ for the first small range and step-size sheet. **(c)** Filtered $\angle D(\delta, P)$ for the last small range and step-size sheet. For each sheet shown in (a-c), the black star denotes the predicted EP_2 location. **(d)** Predicted EP_2 location versus time. Top panel - Light Red square: set P, black disk: measured P_1, dark-red disk: measured P_2. Bottom panel - Orange squares δ. Light-yellow bars highlight the sheet measurements in (a-c).

4.6 System control and stabilization

In this section, we describe the optical and the electrical setups that are used to probe, control and stabilize the experimental apparatus and its parameters. We then provide a compilation of measurements that illustrate the robustness and long-term stability of the system and the control parameters.

4.6.1 Optical and electrical setups

This section details the optical and electrical setups used for interrogating and controlling the system.

4.6.1.1 Actuation and detection

The system is addressed using a single NKT laser operating at ∼1550 nm. A portion of the light from the laser is routed to the probe and the local-oscillator (LO) paths. Here we describe how we generate and the tune the laser tones that drive and detect the membrane motion, and lock it to the MIM cavity resonance. The schematic of the optical and electrical setups are illustrated in Fig. 4.21.

Probe

The light in the probe path is frequency shifted by +83 MHz, using a polarization-maintaining (PM) fiber acousto-optic modulator (AOM)[1], driven by function generator FG1[2]. This tone (probe tone) is locked to the cavity resonance using the standard Pound-Drevor-Hall (PDH) technique with frequency modulation (FM) sidebands at ±32.5 MHz. The FM sidebands are created by driving an electro-optic modulator (EOM)[3] with the RF output of a laser lock box[4]. Sec. 4.6.2.2 provides additional details about PDH locking.

The probe tone is also intensity modulated at the membrane modes' resonance frequency (f_m). This is accomplished by amplitude-modulating (AM) the RF tone of FG1.

[1]Gooch and Housego FiberQ
[2]RIGOL DG4162
[3]THORLABS LN65S-FC
[4]Liquid Instruments Moku:Lab

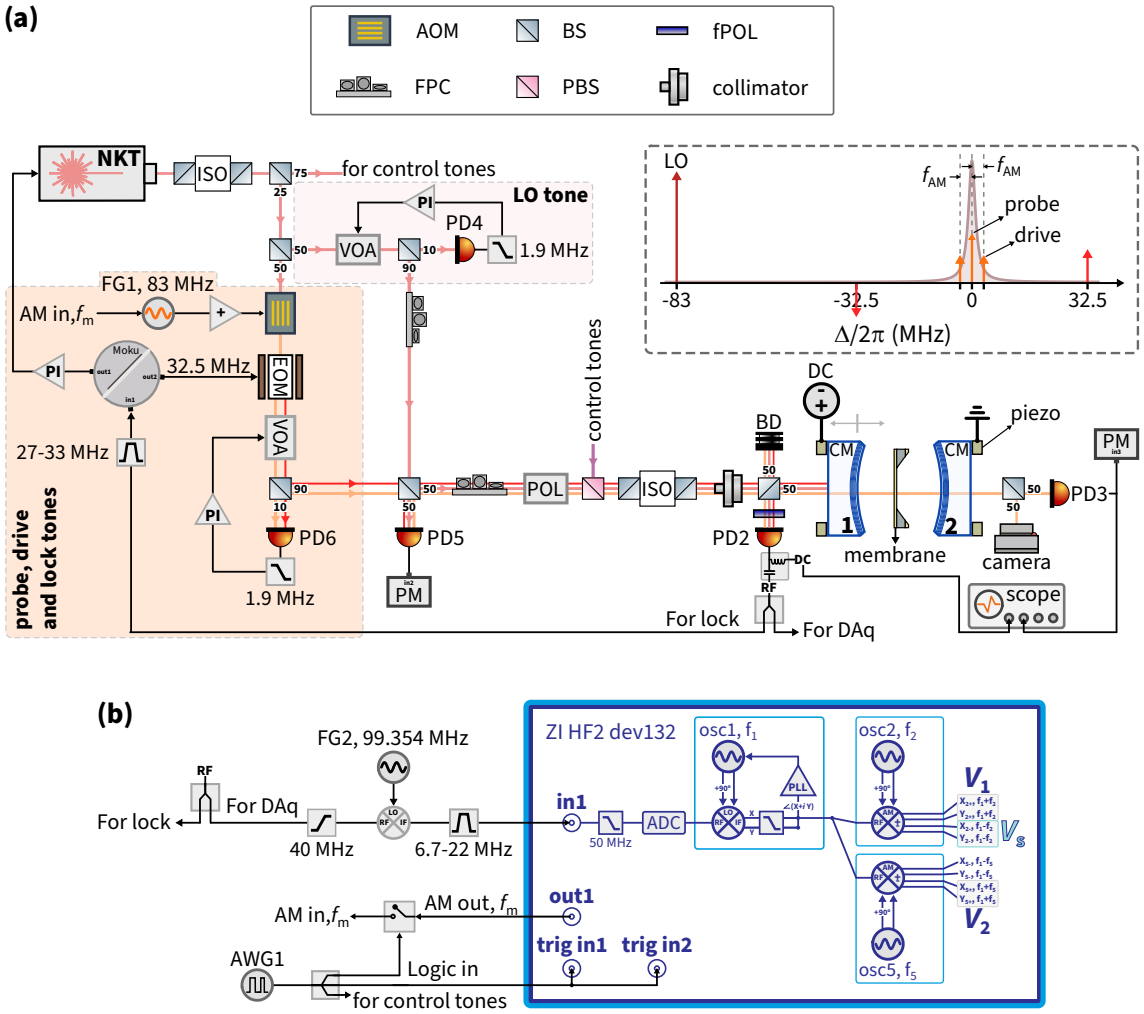

Figure 4.21: Optical and electrical setup I. (a) Setup to generate probe, lock, drive and LO tones. ISO: isolator, VOA: variable optical attenuator, PD: photo-detector, PI: proportional-integral, BS: beam splitter, PBS: polarizing beam splitter, AOM: acousto-optic modulator, EOM: electro-optic modulator, POL: polarizer, fPOL: free-space polarizer, FPS: fiber polarization controller, PM: power monitor, FG: function generator, AM: amplitude modulation, BD: beam dump, CM: cavity mirror. Black lines: electrical paths, colored lines: optical paths. Inset: Frequency space diagram showing optical tones (vertical arrows) and MIM cavity resonance (filled mauve curve). Dark red: LO, orange: probe tone and its AM sidebands (used to drive the membrane modes), red: probe tone's FM sidebands, used for the PDH lock. **(b)** RF detection setup. AWG: arbitrary waveform generator, ADC: analog-to-digital converter, PLL: phase locked loop. Black lines: electrical paths. Demodulated signals used in thesis: $V_1 = X_{2+} + iY_{2+}$ for Brownian measurements, V_1 and $V_2 = X_{5+} + iY_{5+}$ and ringdown measurements and $V_s = X_{2-} + iY_{2-}$ for driven susceptibility measurements.

The modulation is sourced externally, from the output of a lock-in amplifier (LIA)[1] and the modulation depth is set by the output amplitude of the LIA. It is this intensity modulation that modulates the radiation pressure inside the MIM cavity, which drives the membranes modes and thus enabling susceptibility and ringdown measurements.

Low-frequency power fluctuations of all the tones in the probe path are stabilized by monitoring their combined power and sending it to the input of a PID controller[2], which tunes an optical attenuator (VOA)[3] with a bandwidth (BW) $<$1 kHz.

Local oscillator (LO)

The light in this path is un-shifted from the laser frequency and serves as the local-oscillator (LO) for the heterodyne measurement of the membrane's motion. Its low-frequency power fluctuations are stabilized in the same way as the laser tones in the probe path[4].

The probe tone, along with its AM and FM sidebands, are combined with the LO tone by matching and optimizing their polarization via fiber paddle tensioners[5]. The combined beams are passed through an in-line polarizer(ILP)[6] to the slow-axis input of the polarizing fiber beam splitter (PBS)[7]. The output of the PBS is sent through a collimator[8], which is mode-matched to the MIM cavity (Sec. 4.2.2).

Heterodyne detection

The reflected light from the cavity is routed to a free-space fast photo-detector (PD2)[9] via a beam-splitter[10] and a polarizer[11], which isolates the probe, its sidebands and LO from other (control) laser tones. The electrical signal from PD2 is split, filtered, and sent

[1]Zurich Instruments HF2LI dev132
[2]New Focus LB10005
[3]THORLABS V1550A
[4]However, for the LO, we tune a PM VOA (THORLABS V1550PA).
[5]THORLABS FPC032
[6]THORLABS ILP1550PM-APC
[7]THORLABS PFC1550A
[8]THORLABS CFC2A-C
[9]THORLABS PDA10CF, 150 MHz bandwidth
[10]THORLABS BS015
[11]LPNIR050-MP2

into various detectors. Here we focus only on detecting the membrane motion.

Membrane motion at a frequency f_m imparts phase modulation sidebands on the probe tone, at the same frequency f_m. The intensity beat-notes between the probe, its motional phase modulation sidebands and the LO tone are detected by PD2, which converts them to electrical signals at 83 MHz and 83 MHz $\pm f_m$[1]. These signals are mixed down to 16.354 MHz and 16.354 MHz $\pm f_m$ by mixing an RF tone at 99.354 MHz produced by FG2[2]. These signals are band-pass filtered and sent to the LIA input, where two important tasks are undertaken.

1. One of the oscillators of the LIA is dedicated for a phase-locked-loop (PLL) procedure which tracks the frequency fluctuations of the signal at 16.354 MHz. It is this step that subsequently allows for phase sensitive detection of membrane motion. The PLL has bandwidth of 0.5-1 kHz, and is accomplished seamlessly using the PLL tool of the LIA. By construction, the PLL also tracks the 16.354 MHz part of 16.354 MHz $\pm f_m$ signals.

2. The signal corresponding to the membrane motion is isolated from the PLL-ed signals at 16.354 MHz $\pm f_m$. This is accomplished by using the AM modulation option of the LIA, which simultaneously and phase-coherently demodulates two signals oscillating at $f_{\rm carrier} \pm f_{\rm mod}$, by setting $f_{\rm carrier}$ = 16.354 MHz, and $f_{\rm mod} = f_m$. Here, we use two additional oscillators of the LIA, that are phase-coherently tethered to the PLL oscillator, above.

In this manner, we end up with two redundant in-phase and quadrature signals at 16.354 MHz $\pm f_m$ for membrane modes' motion at f_m. For the work described in this thesis, we use the signal at 16.354 MHz $+f_m$ (upper sideband: USB) for Brownian and ringdown measurements, and the signal at 16.354 MHz $-f_m$ (lower sideband: LSB) for susceptibility measurements. A thorough characterization of this detection scheme is provided in Ref. [222], with additional details in the LIA user manual [241].

[1]Other beat-notes at f_m are filtered by a 40 MHz high-pass filter.
[2]Vaunix LMS-451D-13

4.6.1.2 Tuning control parameters

In this section, we describe the generation and control of the laser tones that tune the DBA parameters statically and in real time. The remaining portion of the laser light is routed to the control path and subsequently tuned as described below. Its optical and electrical setup is schematically illustrated in Fig. 4.22.

The light in the control path starts out with a power stabilization similar to the probe and the LO tones. It is then polarization controlled with a fiber paddle tensioner and ILP in series to optimize the input to a PM AOM[1]. The AOM is driven with individual RF tones $\sim$80 MHz, which up-shifts the laser tones near the cavity resonance. In the final trim of our experiments, we send four separate RF tones to the AOM via FG3, FG4, FG5 and FG6, which correspond to control laser tones $(\Delta_1(t), P_1, \theta_{12}(t))$, $(\Delta_2(2), P_2(t))$, $(\Delta_{\rm pt}, P_{\rm pt})$ and (Δ_4, P_4), respectively. The first two tones are red-detuned w.r.t. the cavity resonance, and specifically provide tunable Floquet-coupling between membrane modes (i, j) and (m, n), by constraining their relative detuning $|\Delta_1 - \Delta_2| \sim 2\pi|f_{ij} - f_{mn}|$. These control tones are amenable to static and real time tuning by phase, frequency and amplitude modulating their RF signals with respective arbitrary waveform generators (AWG). The third tone is located at a small red-detuning (-1 MHz $< \Delta_{\rm pt} <$ 0) and is tuned statically (i.e., DC tuning, and not in real time) to specifically circumvent photothermal transient in experiments involving ringdowns. The last tone is blue-detuned w.r.t. the cavity and is tuned statically to specifically reduce overall damping of the mechanical modes. For all experiments involving ringdowns and measuring real time dynamics, the control tones and the mechanical drive are logic-gated by a fast microwave switch[2], toggled with a TTL signal from AWG1.

These control tones are subsequently polarization-optimized with another pair of fiber paddle tensioners and ILP in series, and sent to the fast-axis (second) input of the PBS, and subsequently to the collimator. This allows the control tones to be nominally orthogonal to the probe and LO tones, and address the orthogonal partner of the cavity resonance we locked to. To the best of our abilities, we could not measure any birefringence-induced

[1] Gooch and Housego FiberQ
[2] Minicircuits ZASWA-2-50DRA+

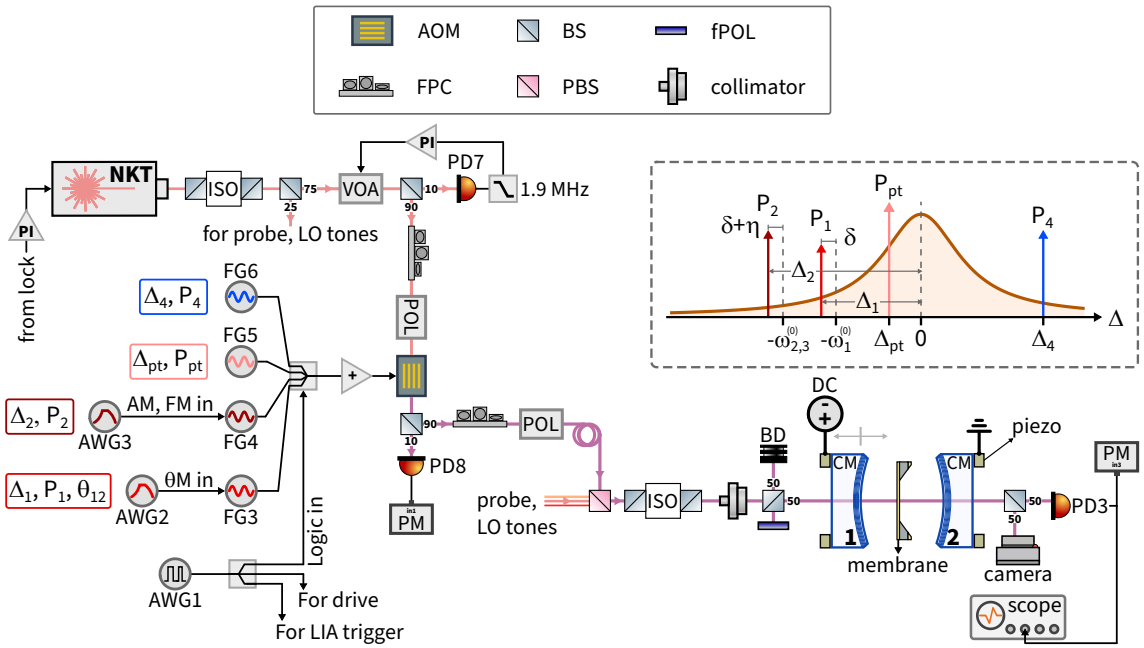

Figure 4.22: Optical and electrical setup II. Setup to generate all four control tones: $(\Delta_1, P_1, \theta_{12})$, (Δ_2, P_2), $(\Delta_{\rm pt}, P_{\rm pt})$ and (Δ_4, P_4). LIA: lock-in amplifier. All other parts are described in Fig. 4.21. Inset: Frequency space diagram showing all control tones (labeled vertical arrows) and MIM cavity resonance (filled mauve curve).

polarization splitting of the cavity modes via cavity spectroscopy or DBA measurements, and we thus assume that both cavity modes are degenerate throughout this thesis. We note that maintaining orthogonal polarization of control and probe+LO tones is of key necessity as:

1. Polarization non-orthogonality of the probe and the control tones will produce unwanted intensity beat-notes between which may spuriously drive the membrane modes in exactly the same way as amplitude modulating the probe tone.

2. Polarization non-orthogonality of the LO and the control tones prevents unwanted intensity beat-notes between which contaminate the heterodyne signal.

While extra precautions were taken to address this issue, we had to resort to several kludges[1] to get a less-compromised final result (i.e., with no detectable spurious driving of membrane modes of interest and no detectable contamination of the heterodyne signal

[1]Notable ones include generically favoring small control powers, specifically avoiding detunings that coincide with membrane mode resonances, and misaligning PD2 to empirically reduce overall levels control and LO beat-note.

at frequencies of interest). However, at the time of finishing the work described in this thesis, we had not solved these issues completely. We anticipate that future technological improvements in polarization sensitive fiber-optics would remedy these issues more simply.

4.6.2 Feedback and stabilization

In this section, we detail various feedback techniques used to stabilize the system and control parameters.

4.6.2.1 Thermal stabilization

Thermal stability is a crucial aspect of our system. Several active and passive methods are employed to thermally stabilize various parts of the experiment and are described below.

The MIM cavity is actively stabilized by feedback via a TEC[1], shown in Figs. 4.1 and 4.2, tuned by temperature controller[2]. This configuration is specified to provide temperature stabilization of $\sim$1 mK over a day. Typical temperature of the MIM cavity is shown in Fig. 4.23(top panel), as read off by an independent thermistor[3] (shown in Fig. 4.2), and its performance is as expected. We note that this feedback uses proportional (P) and differential (D) gains, and no integral (I) gain. We attribute this to the slow thermal time-scales of the system. The system is further (passively) stabilized by three layers of enclosures. The largest enclosure contains the entire experiment on the optical table and an air-conditioner[4] is operated inside it, which reduces the impact of room-temperature drifts. Our new lab is specified to be temperature stabilized to $\sim$1 K. However, this specification is not always met.

In addition to the MIM cavity, the polarization-sensitive fiber-optics are actively temperature stabilized. Changes in temperature vary the stress in the fibers thereby changing their birefringence and hence the polarization of the output light w.r.t. input polarization. Maintaining polarization of laser tones is crucial for our experiments and thus all

[1]THORLABS TECL4
[2]THORLABS TED200C
[3]THORLABS TH10K
[4]RolliBot COOL100H

polarization-sensitive fiber-optics are installed on a common optical breadboard which is actively stabilized and monitored, in the same manner as the MIM cavity and then enclosed in an insulating box. The typical temperature of this optical breadboard is shown in Fig. 4.23(second panel), for the same duration as the MIM cavity. All other optics are enclosed in insulating boxes for passive thermal stabilization.

4.6.2.2 Laser frequency stabilization

We use the standard Pound-Drevor-Hall (PDH) technique [219] to lock the laser's frequency to a cavity resonance. This is accomplished by using Moku:Lab and its "Laser-lock box" module [220]. We briefly sketch the steps taken, below:

1. Frequency modulate the probe beam at frequency $f_{\rm lock} = 32.5$ MHz by driving the EOM (RF drive amplitude: 1 $V_{\rm pp}$), using output 2 of Moku:Lab (see Fig. 4.21(a)).

2. Detect the reflected signal of the MIM cavity at frequency $f_{\rm lock}$. This signal is amplified (or attenuated, as needed) and mixed-down to DC by Moku:Lab's internal local oscillator (ILO). By adjusting the phase of ILO, the well-known PDH error-signal is generated (see Fig.7 of Ref. [219]).

3. Set various locking parameters: lock bandwidth (here 1 kHz), lock set-point, proportional (P) and integral (I) gains to generate the feedback signal. The lock set-point directly translates to detuning the probe w.r.t. the cavity resonance (Δ_0) and is tuned by applying a DC offset to the PDH error signal. We note that no differential (D) gain was applied to the feedback signal as applying it produced no noticeable improvement in the quality of the feedback.

4. Send the feedback signal from Moku:Lab output 1 to the piezo driver of the laser (see Fig. 4.21(a)) for locking the laser to the MIM cavity.

The above feedback, along with temperature stabilization of the MIM cavity, has resulted in locking the laser to the cavity for arbitrarily long times, with a nearly constant probe detuning (panel four of Fig. 4.23), which translates to the robustness and reliability of control tones' detuning.

4.6.2.3 Feedback and stabilization of control powers

Similar to control tones' detuning, robustness and reliability of its power is crucial for the measurements described in the thesis. For each control power P_{desired} we wish to apply, we perform three independent steps to achieve its stabilization, as described below.

1. The first layer of control power feedback utilizes the VOA and PI-feedback circuit in Fig. 4.22 to stabilize the laser power input to the control AOM portion of the optical setup.

2. The second step ensures that we can reliably apply the first control tone $\{\Delta_1/2\pi = -3$ MHz$, P_1 = 10$ μW$\}$, as read by PD3 in Fig. 4.22. Appropriate steps are taken to isolate the control power from the probe and the LO powers that are also being simultaneously measured by PD3. The corresponding tap reading V_τ is compared to $V_{\tau 0}$ (Sec. C.5) to obtain $\tau = V_{\tau 0}/V_\tau$. In the ideal scenario, $\tau = 1$, while any deviation from it is taken as a proportional error. Subsequently all control powers that we wish to apply are rescaled as τP_{desired}.

3. The next step is to tap measure τP_{desired} using PD8 in Fig. 4.22. The tap value $P_{\text{tap},1}$ is then utilized to obtain $P_{\text{new}} = \tau P_{\text{desired}} \dfrac{\tau P_{\text{desired}}}{P_{\text{tap},1}}$ and $\delta P = |(P_{\text{new}} - P_{\text{desired}})/P_{\text{desired}}|$. In the ideal scenario, $\tau = 1, P_{\text{new}} = P_{\text{desired}} = P_{\text{tap},1}$ and $\delta P = 0$. Note that P_{new} obtained by taking the deviation of $P_{\text{tap},1}$ from τP_{desired}, proportionately. As a hard limit we enforce $|\delta P| < 0.5$, beyond which the experiment is halted for manual intervention. The final part of this step is to tap measure control powers corresponding to P_{new}.

We have empirically found that this layered approach to control power stabilization provides the desired precision and robustness. In particular, it solves a critical issue that plagues our setup i.e., temperature fluctuations of the lab causing fluctuations in polarization of light in optical fibers, which get translated to fluctuations in power. Fig. 4.23(bottom panel) illustrates this stabilization by way of tap measured P_{new} alongside $P_{\text{desired}} = 17$ μW.

4.6.3 Evaluating system stability via its parameters

In this section, we illustrate measurements of system and control parameters, performed over $\sim$1 month to benchmark the robustness and long-term stability of the new MIM system. These measurements involved DBA characterizations[1] as in Sec. 4.4.3 and system monitoring[2] as stop-gaps between other measurements. The timeline of these measurements fully overlap with those described in Chapter 7 and their results are illustrated in Figs. 4.23, 4.24 and 4.25 and listed in Table4.6.

These results highlight that the system is indeed robust and stable, and that appropriate monitoring makes it possible to track the system parameters that drift over time.

[1]September 08, 2024 - October 04, 2024
[2]October 06, 2024 - October 07, 2024

Parameter	Value	Sample size
${\omega_1}^{(0)}/2\pi$ (Hz)	2423438 ± 7	30
${\omega_2}^{(0)}/2\pi$ (Hz)	3075815 ± 9	22
${\omega_3}^{(0)}/2\pi$ (Hz)	3330469 ± 8	8
${\gamma_1}^{(0)}/2\pi$ (Hz)	4.32 ± 0.27	30
${\gamma_2}^{(0)}/2\pi$ (Hz)	16.50 ± 0.16	22
${\gamma_3}^{(0)}/2\pi$ (Hz)	3.30 ± 0.20	8
$\kappa/2\pi$ (MHz)	2.256 ± 0.037	30
$g_1/2\pi$ (Hz)	4.896 ± 0.018	30
$g_2/2\pi$ (Hz)	4.146 ± 0.023	22
$g_3/2\pi$ (Hz)	2.751 ± 0.006	8
$A_1/2\pi$ (μHz)	-2.804 ± 0.109	30
$A_2/2\pi$ (μHz)	-3.804 ± 0.028	22
$A_3/2\pi$ (μHz)	-3.411 ± 0.021	8
$\Delta_o/2\pi$ (MHz)	-0.060 ± 0.006	30
P_1 (μW)	16.989 ± 0.004	>1200

Table 4.6: System and control parameters measured over ∼1 month. Fixed $(\omega^{(0)}, \gamma^{(0)})$, fit (κ, g, A, Δ_0) and control (P_1) parameters corresponding to DBA characterizations done for ∼1 month, alongside data acquisition of Chapter 7. Each value is reported as the mean ± one standard deviation over the sample size. For bare resonance frequencies, energy damping rates, single photon optomechanical coupling and single photon photothermal coupling, the subscript denotes the mechanical mode: 1→(3,3), 2→(5,2), 3→(5,3).

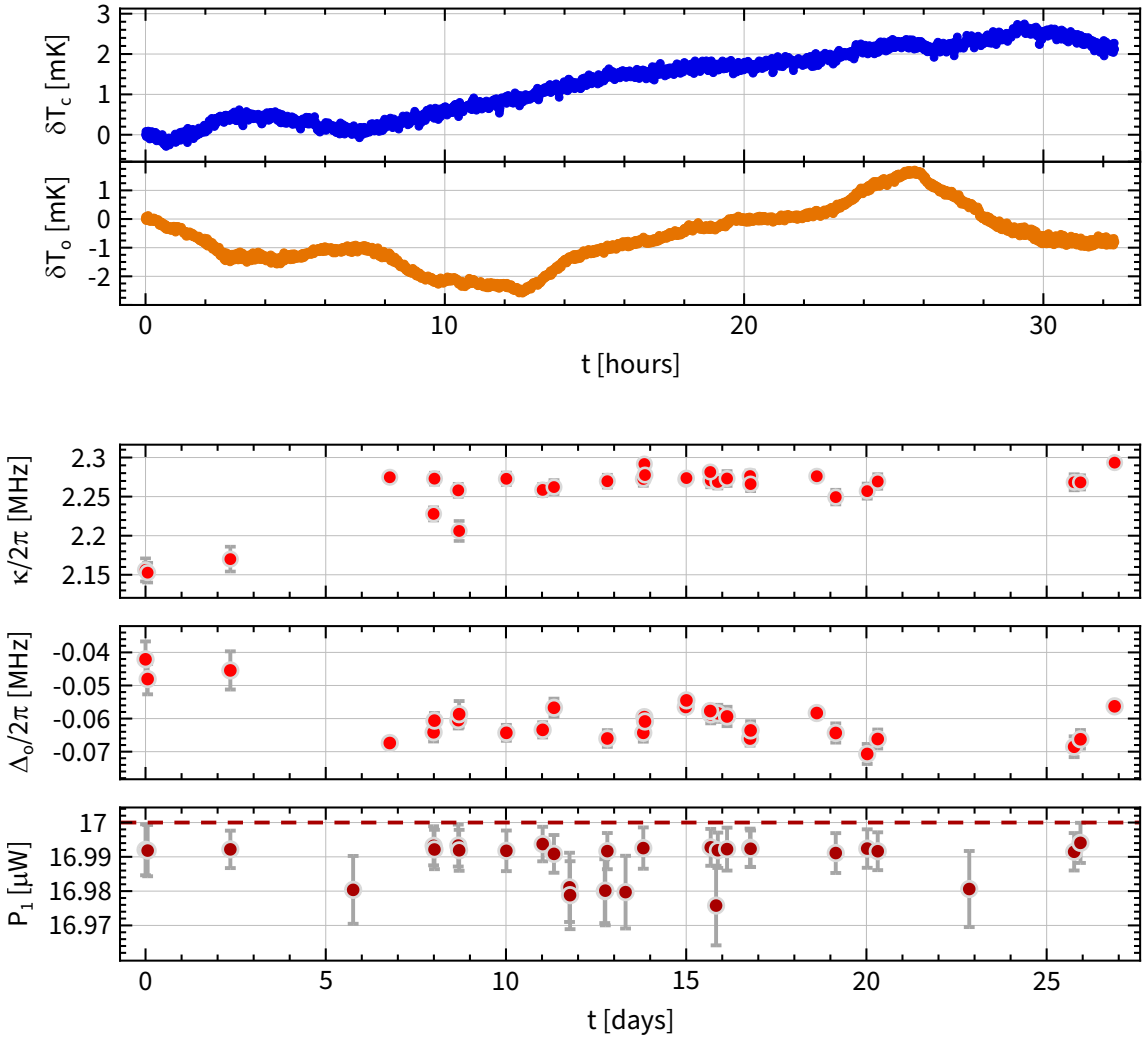

Figure 4.23: System and control parameters over time - part I. **Panel 1 and 2**: deviation in cavity temperature (δT_{c}) and in optical breadboard temperature (δT_{o}) that houses polarization sensitive fiber optic components, measured during a stop-gap period for other measurements. Data: blue and orange points, respectively. **Panel 3 and 4**: cavity linewidth (κ) and probe detuning offset (Δ_0) inferred from DBA characterizations as in Sec. 4.4.3. Fit values and their errors: red disks and gray fences, respectively. **Panel 5**: Control power P_1 used for DBA characterizations. Target value: dark red dashed line, measured value: dark red disks show mean of >40 individual measurements for every DBA characterization with gray fences indicating their one standard deviation.

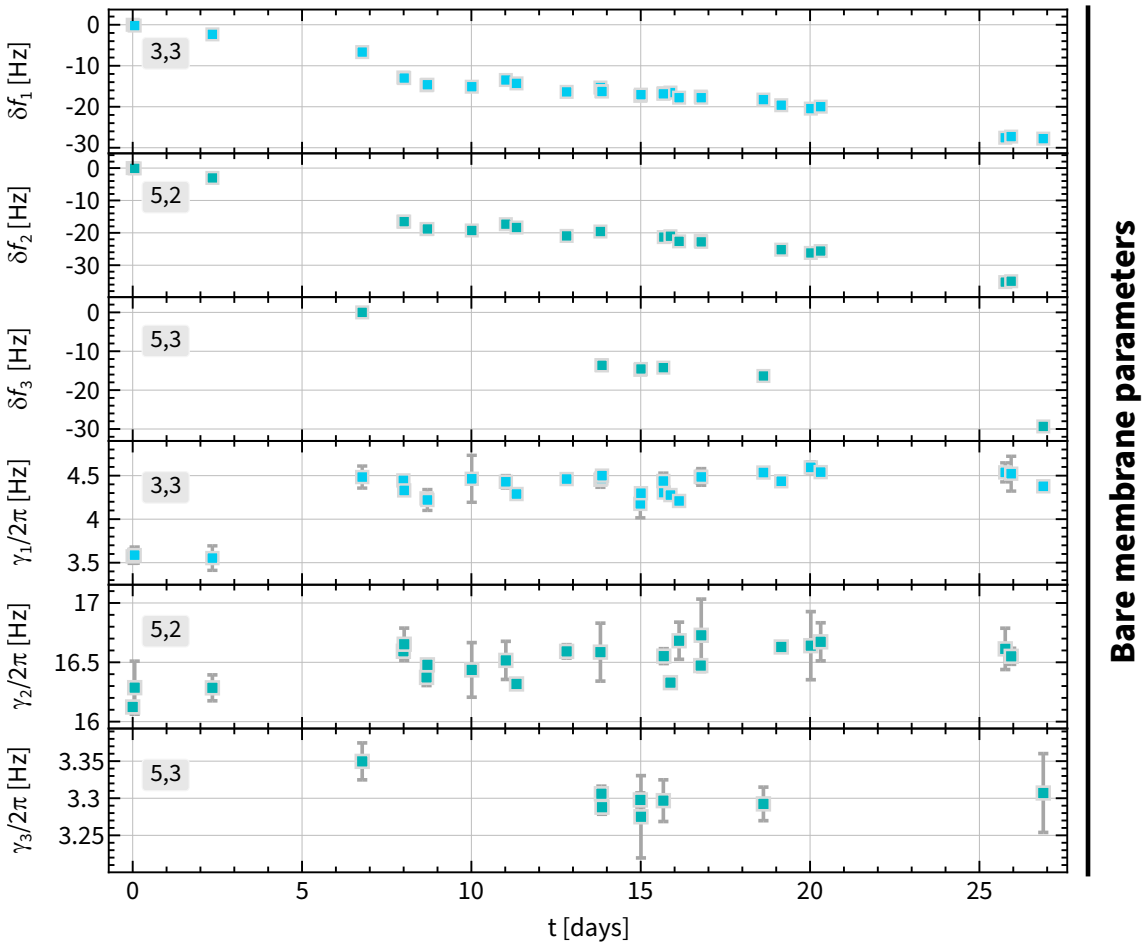

Figure 4.24: System and control parameters over time - part II. **Panel 1**: Deviation in bare resonance frequency (δf_1) of (3,3) mode inferred from bare-ringdown measurements performed intermittently for each DBA characterization. Blue squares indicated mean of 3 measurements every DBA characterization and gray fences indicate one standard deviation. **Panel 2**: Same as Panel 1 but for (5,2) mode, (δf_2). **Panel 3**: Same as Panel 1 but for (5,3) mode, (δf_3). **Panel 4**: Bare energy damping rate (γ_1) of (3,3) mode inferred from bare-ringdown measurements performed intermittently for each DBA characterization. Blue squares indicated mean of 3 measurements every DBA characterization and gray fences indicate one standard deviation. **Panel 5**: Same as Panel 4 but for (5,2) mode, (γ_2). **Panel 6**: Same as Panel 5 but for (5,3) mode, (γ_3). For bare resonance frequencies (δf) and energy damping rates (γ), the subscript denotes the mechanical mode: 1→(3,3), 2→(5,2), 3→(5,3).

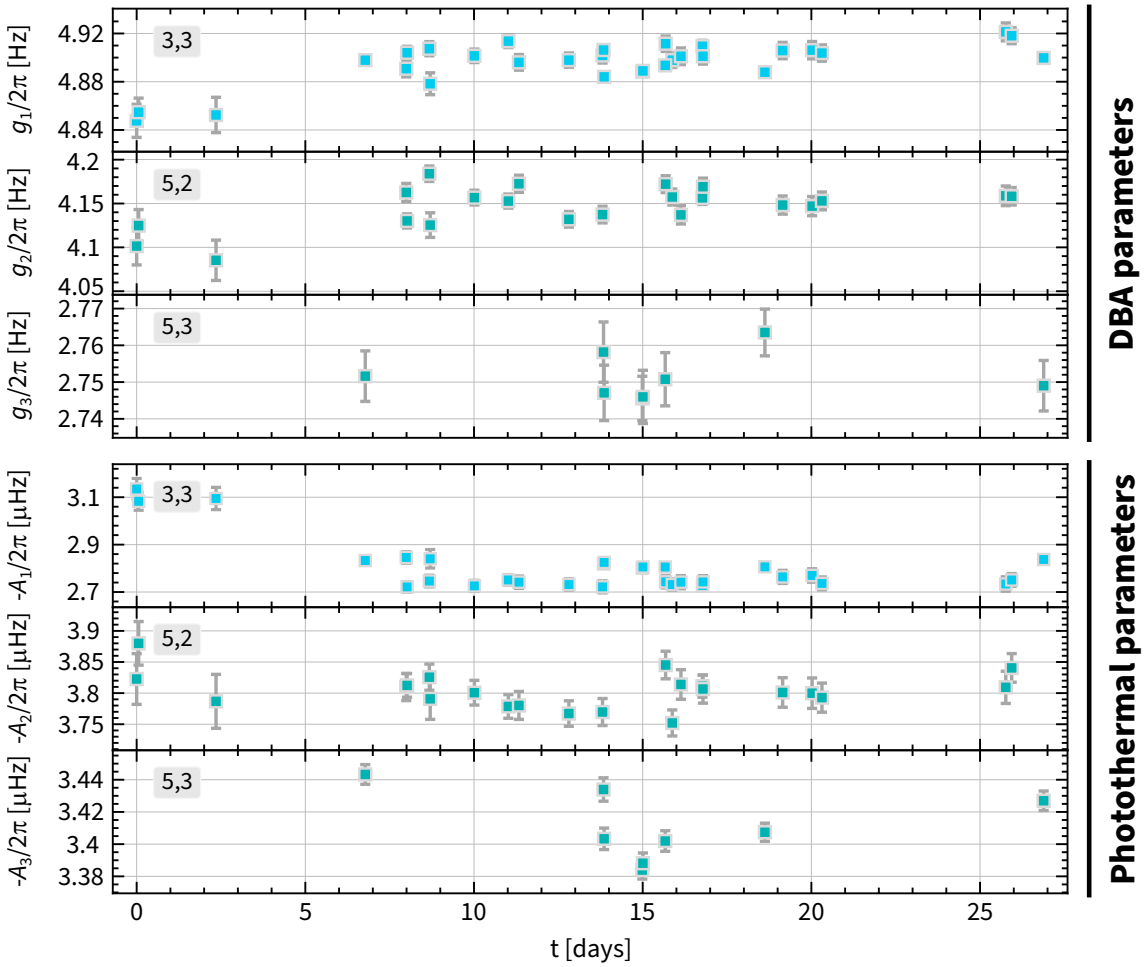

Figure 4.25: System and control parameters over time - part III. **Panel 1**: Optomechanical coupling rate (g_1) of (3,3) mode inferred from DBA characterizations. Fit values and their errors: blue squares and gray fences, respectively. **Panel 2**: Same as Panel 1 but for (5,2) mode, (g_2). **Panel 3**: Same as Panel 1 but for (5,3) mode, (g_3). **Panel 4**: Photothermal coupling rate (A_1) of (3,3) mode inferred from DBA characterizations. Fit values and their errors: blue squares and gray fences, respectively. **Panel 5**: Same as Panel 4 but for (5,2) mode, (A_2). **Panel 6**: Same as Panel 5 but for (5,3) mode, (A_3). For Optomechanical (g) and Photothermal (A) coupling rates, the subscript denotes the mechanical mode: 1→(3,3), 2→(5,2), 3→(5,3).

Chapter 5

Complex geometric phase of non-Hermitian systems

In this chapter, we describe experiments using the new MIM platform (Chapter 4) that enable the measurement of the most general complex geometric phase ϕ_B of a non-degenerate $N = 2$-mode non-Hermitian system comprised. These measurements are made for arbitrary control paths in parameter space, using adiabatic protocols suitable for non-Hermitian systems (Sec. 2.2). Since all the necessary ingredients are already detailed in Chapters 2 and 4, we waste no time to assemble them, and jump directly into a discussion about measuring ϕ_B (Sec. 5.1). We then demonstrate the geometric character of ϕ_B by: **(a)** varying the manner in which we traverse a control path (Sec. 5.2.1), **(b)** varying the shape of the control path (Sec. 5.2.2), and **(c)** repeating a control path multiple times (Sec. 5.2.3). The imaginary part of complex ϕ_B is well-defined for open control paths (i.e. for control non-loops) and we experimentally demonstrate it in Sec. 5.3. In Sec. 5.4, we shed more light on adiabatic evolution in non-Hermitian systems via measurements and numerical simulations. These insights are possibly beyond the purview of the non-Hermitian adiabatic theorem [11, 88]. Additional technical details for these measurements and their analyses are given in D.

5.1 Measuring ϕ_B

In this section, we describe our protocol for measuring the geometric phase ϕ_B. To focus the discussion, we consider a system of two mechanical oscillators: the (3,3) and the (5,3) mode of the membrane (Sec. 4.3) that are tunably coupled to each other via optomechanical interactions with the optical cavity (Sec. 4.4.3), which is driven by several control laser tones (Sec. 4.6.1.2). Specifically, we tune the system in real time along a specific control path for duration T, and perform various measurements to determine ϕ_B. The membrane modes' bare eigenvalues (i.e., in the absence of any optomechanical effects due to the control laser tones) are: $\lambda_1^{(0)} \equiv \omega_1^{(0)} - i\gamma_1^{(0)}/2 = 2\pi \times (2{,}423{,}969 - 1.8i)$ Hz and $\lambda_3^{(0)} \equiv \omega_3^{(0)} - i\gamma_3^{(0)}/2 = 2\pi \times (3{,}331{,}064 - 1.7i)$ Hz.

The protocol begins with a suitable choice of a control path. It is realized by control parameters $\vec{X} \equiv \{P_1, P_2, \delta, \eta, \theta_{12}\}$, where $P_{1,2}$, δ and η are the individual powers, common and differential detuning of two red-detuned (w.r.t. optical cavity resonance) laser tones. They provide tunable optical spring, optical damping and Floquet-coupling (Sec. 2.3.2) for the membrane modes. The detuning of each tone from the optical cavity resonance is given in Eq. (4.14). θ_{12} is the phase of the intracavity intensity beat-note of the two red-detuned laser tones. In a frame rotating with the beat-note, the non-Hermitian dynamical matrix H (Eq. (2.81)) that governs the motion of the membrane modes (Eq. (2.80)), depends on time solely via $\vec{X}(t)$.

For these measurements, we chose a "simple" control loop (see Sec. 2.2.3.1). This is accomplished by holding the parameters $\{P_1, P_2, \delta, \eta\}$ fixed, while varying $\theta_{12} = 2\pi s$ with $0 \leq s = t/T \leq 1$, in real time. This is a loop because θ_{12} is defined modulo 2π, such that $\vec{X}(t=0) = \vec{X}(t=T)$. Furthermore, this choice of loop satisfies the requirements for adiabatic evolution for non-Hermitian systems. Specifically for this control loop, **(a)** the eigensystem remains strictly non-degenerate throughout this control loop (if it were so at the starting point of the control loop), and **(b)** there exists a unique least-dissipative eigenvector throughout this control loop that is amenable to adiabatic evolution [11, 88] in the large-T limit. This is accomplished simply by choosing $\{P_1, P_2, \delta, \eta\}$ such that the system is non-degenerate and recalling that the system's

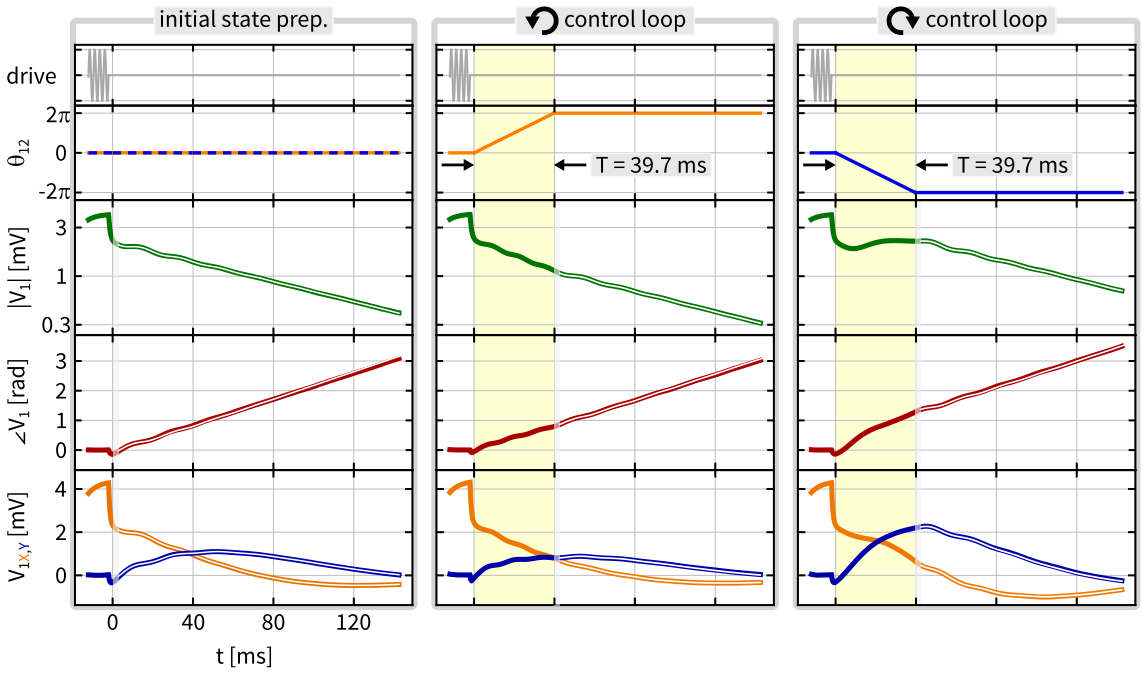

Figure 5.1: Preparation of the initial state vector $\vec{c}^{(a)}(0)$, and its evolution to $\vec{c}^{(a)}(T)$ along a control loop. First column: measurements for $\vec{c}^{(a)}(0)$ i.e, with no control loop. **Second column**: measurements for $\vec{c}^{(a)}(T)$ for a "simple" control loop in "forward" direction. **Third column**: measurements for $\vec{c}^{(a)}(T)$ for a "simple" control loop in "backward" direction. For all columns, gray curves: a schematic of the driving force applied to the membrane, which is switched off at $t = 0$. Orange curve in second column: a plot of the beat-note phase $\theta_{12}(t)$, for the control loop in the "forward" direction. Blue curve in second column: a plot of the beat-note phase $\theta_{12}(t)$, for the control loop in the "backward" direction. Solid green, red, dark-orange and dark-blue curves: the magnitude, the phase, the in-phase and the quadrature part of the heterodyne signal, respectively and for measurements shown in each column. Corresponding to each measurement, the solid white curve is a fit to the evolution at constant H (see Sec. D.2). For this measurement, we used the (3,3) and the (5,3) membrane modes with other control parameters: $P_{1,2} = P =$ 23.45 μW, $\delta/2\pi = -0.989$ MHz, $\eta/2\pi = -50$ Hz for the red-detuned laser tones and $P_4 =$ 25 μW, $\Delta_4/2\pi = +3.5$ MHz for the blue-detuned laser tone.

eigenvalues are independent of θ_{12} (Secs. 2.3.2 and Eq. (2.17)). For these measurements, $P_{1,2} = P =$ 23.45 μW, $\delta/2\pi = -0.989$ MHz, $\eta/2\pi = -50$ Hz. Additionally for this particular measurement, we apply a blue-detuned control tone during the control loop with its power $P_4 =$ 25 μW and detuning from cavity resonance $\Delta_4/2\pi = +3.5$ MHz, to reduce damping of the membrane modes (see Sec. 5.2.3).

To measure the geometric phase associated with a control loop, we determine the propagator matrix $U(T)$ that fully characterizes the modes' evolution during the loop (Sec. D.3). The procedure is sketched in Figs. 5.1 and 5.2, with corresponding data in Figs. 5.3 and 5.4. In the first step, the membrane is driven at frequency $\omega_d \approx \omega_1^{(0)}$ $\left(\omega_2^{(0)}\right)$

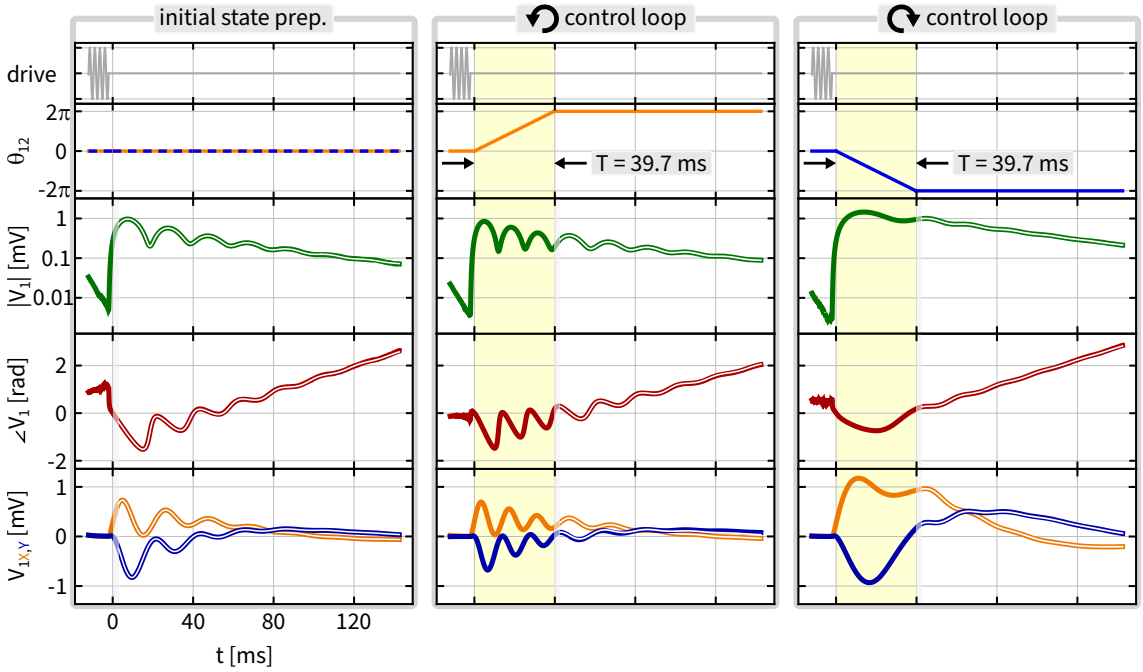

Figure 5.2: Preparation of the initial state vector $\vec{c}^{(b)}(0)$, and its evolution to $\vec{c}^{(b)}(T)$ along a control loop. First column: measurements for $\vec{c}^{(b)}(0)$ i.e, with no control loop. **Second column**: measurements for $\vec{c}^{(b)}(T)$ for a "simple" control loop in "forward" direction. **Third column**: measurements for $\vec{c}^{(b)}(T)$ for a "simple" control loop in "backward" direction. For all columns, gray curves: a schematic of the driving force applied to the membrane, which is switched off at $t = 0$. Orange curve in second column: a plot of the beat-note phase $\theta_{12}(t)$, for the control loop in the "forward" direction. Blue curve in second column: a plot of the beat-note phase $\theta_{12}(t)$, for the control loop in the "backward" direction. Solid green, red, dark-orange and dark-blue curves: the magnitude, the phase, the in-phase and the quadrature part of the heterodyne signal, respectively and for measurements shown in each column. Corresponding to each measurement, the solid white curve is a fit to the evolution at constant H (see Sec. D.2). For this measurement, we used the same membrane modes and the same other control parameters as in Fig. 5.1.

until it reaches its steady state $\vec{c}^{(a)}(0)$ $\left(\vec{c}^{(b)}(0)\right)$. The drive is then turned off at $t = 0$ and the subsequent motion of the membrane is recorded and fit (Sec. D.1) to determine $\vec{c}^{(a)}(0)$ $\left(\vec{c}^{(b)}(0)\right)$. This is illustrated in the first column of Figs. 5.1 and 5.2 for $\vec{c}^{(a)}(0)$ and $\vec{c}^{(b)}(0)$, respectively. In the second step, the membrane is initialized in the same way, but immediately after the drive is turned off (at $t = 0$), the control parameters $\{P_1, P_2, \delta, \eta\}$ are dialed to their respective fixed values and turned on, while a time-dependent phase shift is applied to one of the laser tones such that $\theta_{12}(t) = 2\pi t/T$. For $t > T$, θ_{12} is held constant at 2π. The subsequent motion of the membrane is recorded and fit (Sec. D.1) to determine $\vec{c}^{(a)}(T)$ $\left(\vec{c}^{(b)}(T)\right)$. This is illustrated in the second column of Figs. 5.1 and 5.2 for $\vec{c}^{(a)}(T)$ and $\vec{c}^{(b)}(T)$, respectively.

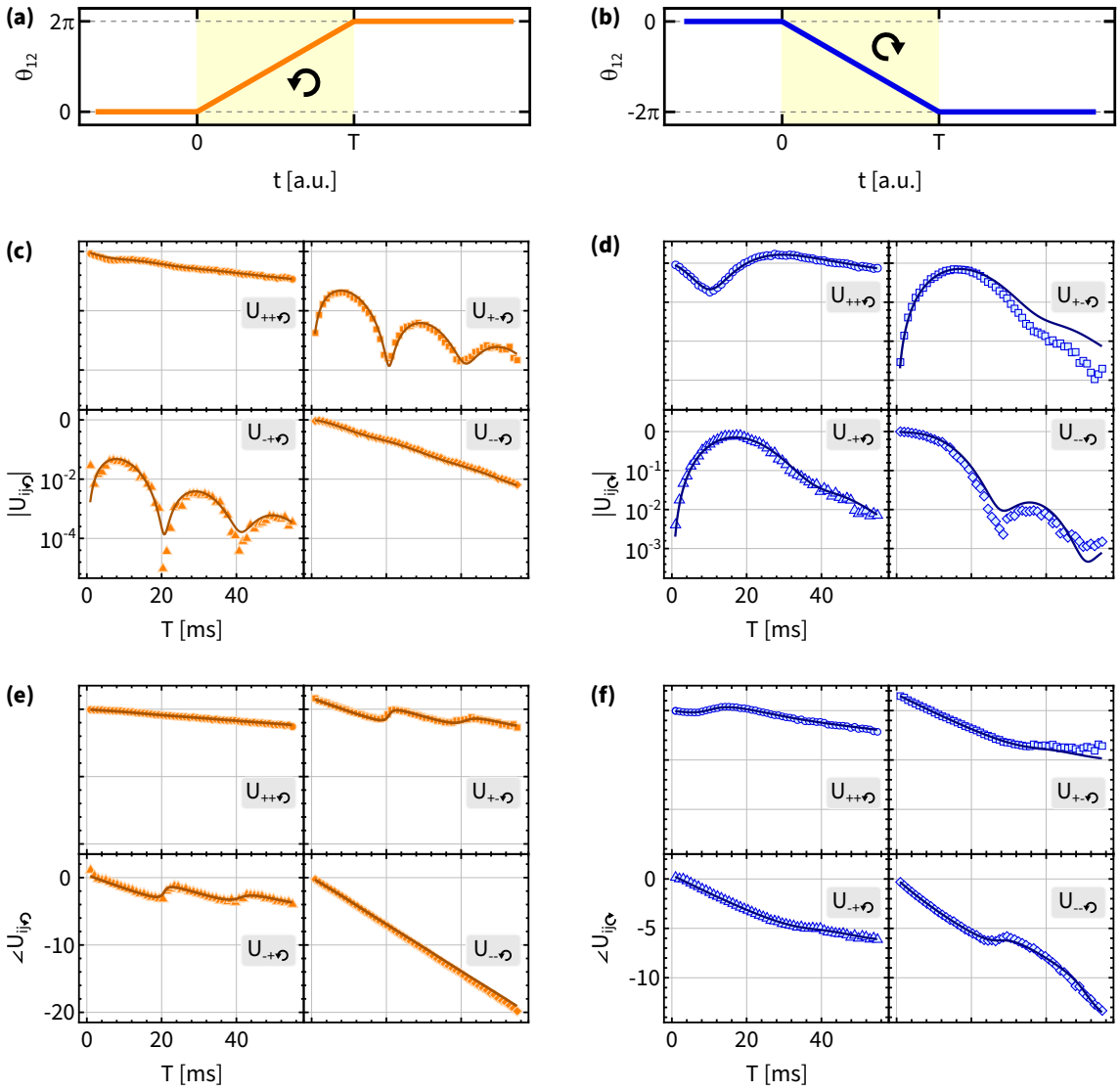

Figure 5.3: Measurement of the propagator matrix $U(T)$. (a) The beat-note phase $\theta_{12}(t)$, for a "simple" control loop in the "forward" direction. **(b)** The beat-note phase $\theta_{12}(t)$, for the "simple" control loop in the "backward" direction. **(c)** Magnitude of each element of the propagator U versus the loop duration T for control loop in "forward" direction. **(d)** Magnitude of each element of the propagator U versus the loop duration T for control loop in "backward" direction. **(e)** Complex argument of each element of the propagator U versus the loop duration T for control loop in "forward" direction. **(f)** Argument of each element of the propagator U versus the loop duration T for control loop in "backward" direction. In each panel, symbols represent data while solid curves represent the no-free-parameter theory prediction. For this measurement, we used the same membrane modes and the same other control parameters as in Figs. 5.1 and 5.2.

For a particular control loop duration T_0, the set of initial states $\{\vec{c}^{(a)}(0), \vec{c}^{(b)}(0)\}$ and final states $\{\vec{c}^{(a)}(T_0), \vec{c}^{(b)}(T_0)\}$ together determine $U(T_0)$ (Sec. D.1). We repeat the above sequence of measurements as a function of T to obtain $U(T)$. Fig. 5.3(c,e) shows the complex-valued $U(T)$, where each panel represents an element of U expressed in the basis of $\vec{\mathrm{v}}_\pm$: the least-dissipative eigenvector and the more-dissipative eigenmode of $H(0)$, respectively[1]. Additionally, the system's overall damping is evident in the decay of all four elements of U with increasing T.

For large T, U_{++} dominates the other elements of U, reflecting the fact that for a non-Hermitian system the adiabatic theorem applies only to a state if it is the least-dissipative eigenmode of H throughout the control loop [11, 88]. A given control loop possesses such a state if it does not cross a "gain/loss boundary" i.e., where $\mathrm{Im}(\lambda_+) = \mathrm{Im}(\lambda_-)$. This condition is met by the control loop under investigation here, and all other control loops discussed in this Chapter and in Chapter 6. At large T, for the least-dissipative state, the complex phase $\phi(T)$ defined via $U_{++}(T) = e^{-i\phi(T)}$ is predicted to be

$$\phi(T) = q_D T - \phi_B + \frac{q_1}{T} + \frac{q_2}{T^2} + ... \tag{5.1}$$

where the q_i are the complex constants (Sec. A.3.1 and Refs. [11, 27, 88]). The first term of Eq. (5.1): $q_D T = \phi_D$ is the well-known linear dynamical phase. For a "simple" control loop, $q_D = \lambda_+$, while for "non-simple" control loops $q_D = \int_0^1 \lambda_+(s) ds$. In practice, Eq. (5.1) is expected to hold when the adiabaticity condition $T \gtrsim T_{\mathrm{ad}}$ is satisfied, where T_{ad} is the largest value of $1/|\lambda_+(s) - \lambda_-(s)|$, with $0 \leq s \leq 1$ (i.e., along a control loop).

Fig. 5.4(b) shows $\phi(T)$ as determined from $U_{++}(T)$. For large T, the phase of the motion evolves roughly linearly with T as shown in $\mathrm{Re}(\phi)$ (upper panel), while the amplitude of the motion decays roughly exponentially with T as shown in $\mathrm{Im}(\phi)$ (lower panel). Both reflect the fact that ϕ_D dominates $\phi(T)$ for large T.

To empirically isolate ϕ_B, we also perform measurements for a control loop that is identical to the one described above except that $\theta_{12}(t) = -2\pi t/T$. Loosely speaking, this corresponds to traversing the same loop in the opposite sense; however, formally these loops are inequivalent. For simplicity of notation, we denote the control loop for

[1]Specifically, $\vec{\mathrm{v}}_\pm$ are the right eigenvectors of $H(0)$ and it is implied throughout this chapter.

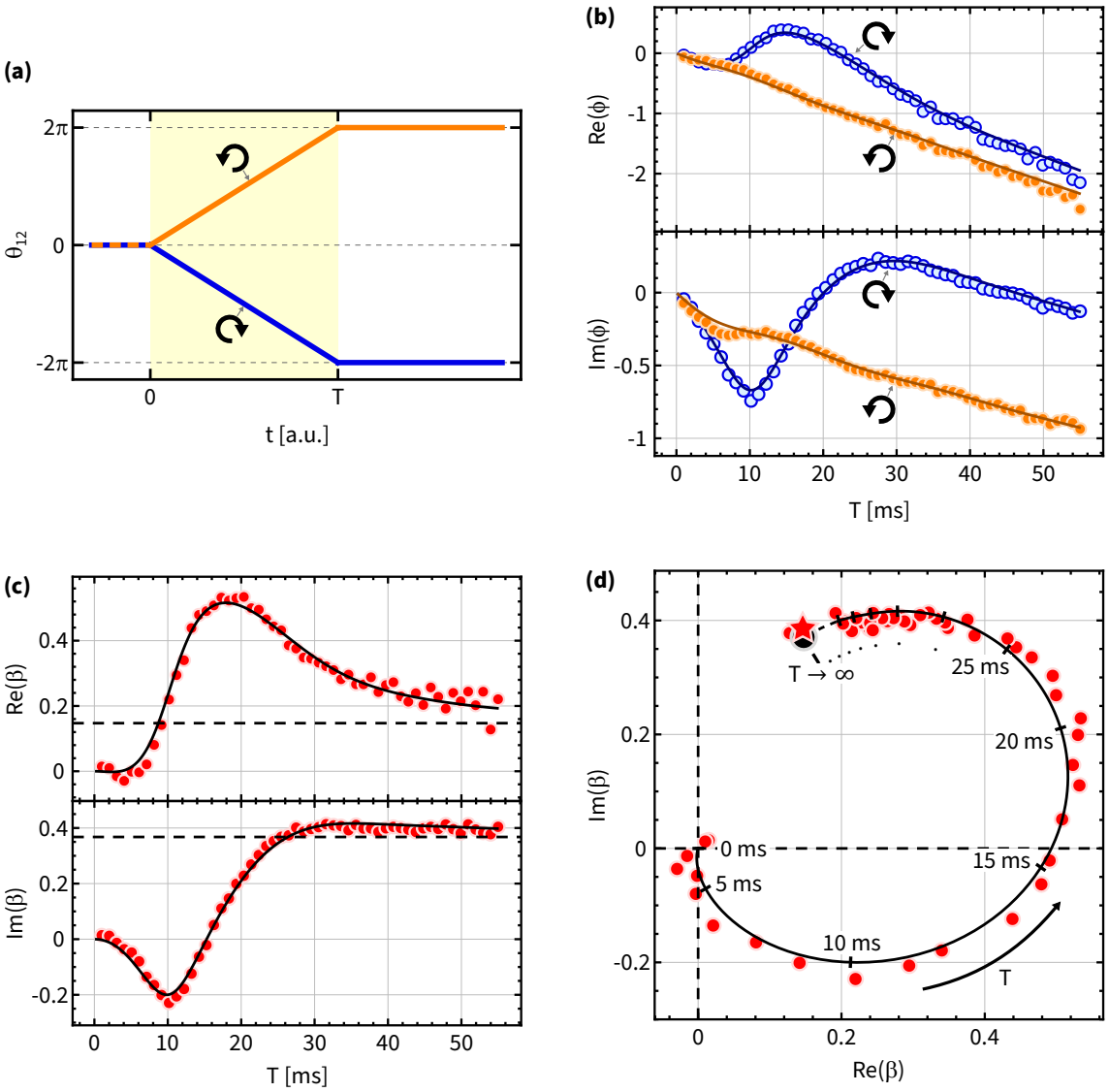

Figure 5.4: Measurement of $\beta(T)$. **(a)** The beat-note phase $\theta_{12}(t)$. Orange and blue curves: "simple" control loop in "forward" and "backward" direction, respectively. **(b)** $\phi = i\,\mathrm{Log}(U_{++})$ versus the loop duration T. Orange and blue symbols: data corresponding to control loop in "forward" and "backward" direction, respectively. Corresponding solid lines represent the no-free-parameter theory prediction. Top panel: $\mathrm{Re}(\phi(T))$ and bottom panel: $\mathrm{Im}(\phi(T))$. **(c)** $\beta = (\phi_{\circlearrowright} - \phi_{\circlearrowleft})/2$ versus the loop duration T. Data are shown as red symbols, while the solid black curve represents the no-free-parameter theory prediction of $\beta(T)$. Dashed line represents no-free-parameter theory prediction of ϕ_B. Top panel: $\mathrm{Re}(\beta(T))$ and $\mathrm{Re}(\phi_B)$. Bottom panel: $\mathrm{Im}(\beta(T))$ and $\mathrm{Im}(\phi_B)$. **(d)** Parametric plot $\beta(T)$. Data are shown as red symbols, while the solid black curve represents the no-free-parameter theory prediction of $\beta(T)$. Red star: estimated value of ϕ_B (see Sec. D.4) Black disk: no-free-parameter theory prediction of ϕ_B. For this measurement, we used the same membrane modes and the same other control parameters as in Figs. 5.1-5.3.

which $\theta_{12}(t) = 2\pi t/T$ with $\mathcal{C}_{\circlearrowleft}$ and label it as the control loop in the "forward" direction. The control loop for which $\theta_{12}(t) = -2\pi t/T$, we denote it with $\mathcal{C}_{\circlearrowright}$ and label it as the control loop in the "backward" direction. For a pair of such loops, the odd-order terms in Eq. (5.1), i.e., $T, 1/T$ are identical (e.g., $q_{D,\circlearrowleft} = q_{D,\circlearrowright}$ and $q_{1,\circlearrowleft} = q_{1,\circlearrowright}$) while the even-order terms in $T, 1/T$ differ by a sign (e.g, $\phi_{B,\circlearrowleft} = -\phi_{B,\circlearrowright}$ and $q_{2,\circlearrowleft} = -q_{2,\circlearrowright}$). See also Secs. A.3.1 and D.4. The measurement protocol and the ringdowns that determine the state vectors $\vec{c}^{(a)}(T)$ and $\vec{c}^{(b)}(T)$ at the end of $\mathcal{C}_{\circlearrowright}$, are illustrated in the third column of Figs. 5.1 and 5.2, respectively. Fig. 5.3(d,f) shows the measured $U_{\circlearrowright}(T)$.

Consistent with the prediction of Eq. (5.1) for $\mathcal{C}_{\circlearrowleft}$ and $\mathcal{C}_{\circlearrowright}$ respectively, $\phi_{\circlearrowleft}(T)$ and $\phi_{\circlearrowright}(T)$ show similar trends at large T but are clearly offset from each other (Fig. 5.4(b)). This is explicitly demonstrated in Fig. 5.4(c) which shows $\beta(T) = (\phi_{\circlearrowright}(T) - \phi_{\circlearrowleft}(T))/2$, and approaches $\phi_{B,\circlearrowleft}$, the complex geometric phase of $\mathcal{C}_{\circlearrowleft}$, for large T. All of these measurements shown in Figs. 5.3 and 5.4 are well-corroborated with no-free-parameter theory predictions, which are shown as solid and dashed curves. Finally, Fig. 5.4(d) shows the estimated value of $\phi_{B,\circlearrowleft} \equiv \phi_B$ (our convention herein) estimated from measured $\beta(T)$: red star (see Sec. D.4), which agrees well with the no-free-parameter theory prediction of ϕ_B: black disk. This concludes our discussion of measuring ϕ_B for a particular pair of control loops: $\mathcal{C}_{\circlearrowleft,\circlearrowright}$, and all subsequent measurements of ϕ_B are subject to this protocol.

5.2 Geometric character of ϕ_B

In this section, we describe measurements that demonstrate the geometric character ϕ_B. These include measurements where we: **(a)** vary the manner in which we traverse a control path (Sec. 5.2.1), **(b)** vary the shape of the control path (Sec. 5.2.2), and **(c)** repeat a control path multiple times (Sec. 5.2.3).

5.2.1 Part I: Varying the manner of control path traversal

In order to vary the manner in which we traverse a control path, we apply a minor modification to the "simple" control loop, as given below:

1. Similar to "simple" control loops, hold control parameters $\{P_1, P_2, \delta, \eta\}$ fixed.

2. Contrary to "simple" control loops, vary the beat-note phase $\theta_{12}(t)$ with a different functional form i.e., not a linear ramp $\theta_{12}(t) = \pm 2\pi t/T$.

Intuitively, such loops correspond to rigidly rotating the two three-vectors $\mathbf{B}_{\mathrm{Re,Im}}$ once around the z-axis but at a variable rate (See Sec. 2.2.3.1), contrary to the "simple" control loop which has a constant rate of rotation. For these measurements, we chose five functional forms of $\theta_{12}(t)$ that vary from 0 to $\pm 2\pi$, as $0 \leq t \leq T$:

(a) $\theta_{12}(t) = \pm 2\pi (t/T)^2$

(b) $\theta_{12}(t) = \pm 2\pi \sqrt{t/T}$

(c) $\theta_{12}(t) = \pm 2\pi \mathrm{Sin}(\pi t/2T)$

(d) $\theta_{12}(t) = \pm 2\pi \left(6(t/T)^5 - 15(t/T)^4 + 10(t/T)^3\right)$

(e) $\theta_{12}(t) = \pm 2\pi \left(t/T + \mathrm{Sin}(\pi t/T)^2/4\right)$

These functions are shown in the first column of the corresponding panels in Fig. 5.5(a-e), alongside the linear ramp for the "simple" control loop. Measurements of $\beta(T)$ and ϕ_B were carried out in the same manner as described in Secs. 5.1 and D.1. These measurements used the (3,3) and the (5,3) membrane modes with other control parameters: $P_{1,2} = P = $ 21 μW, $\delta/2\pi = -1.6$ MHz, $\eta/2 = -27.5$ Hz. The measurements are

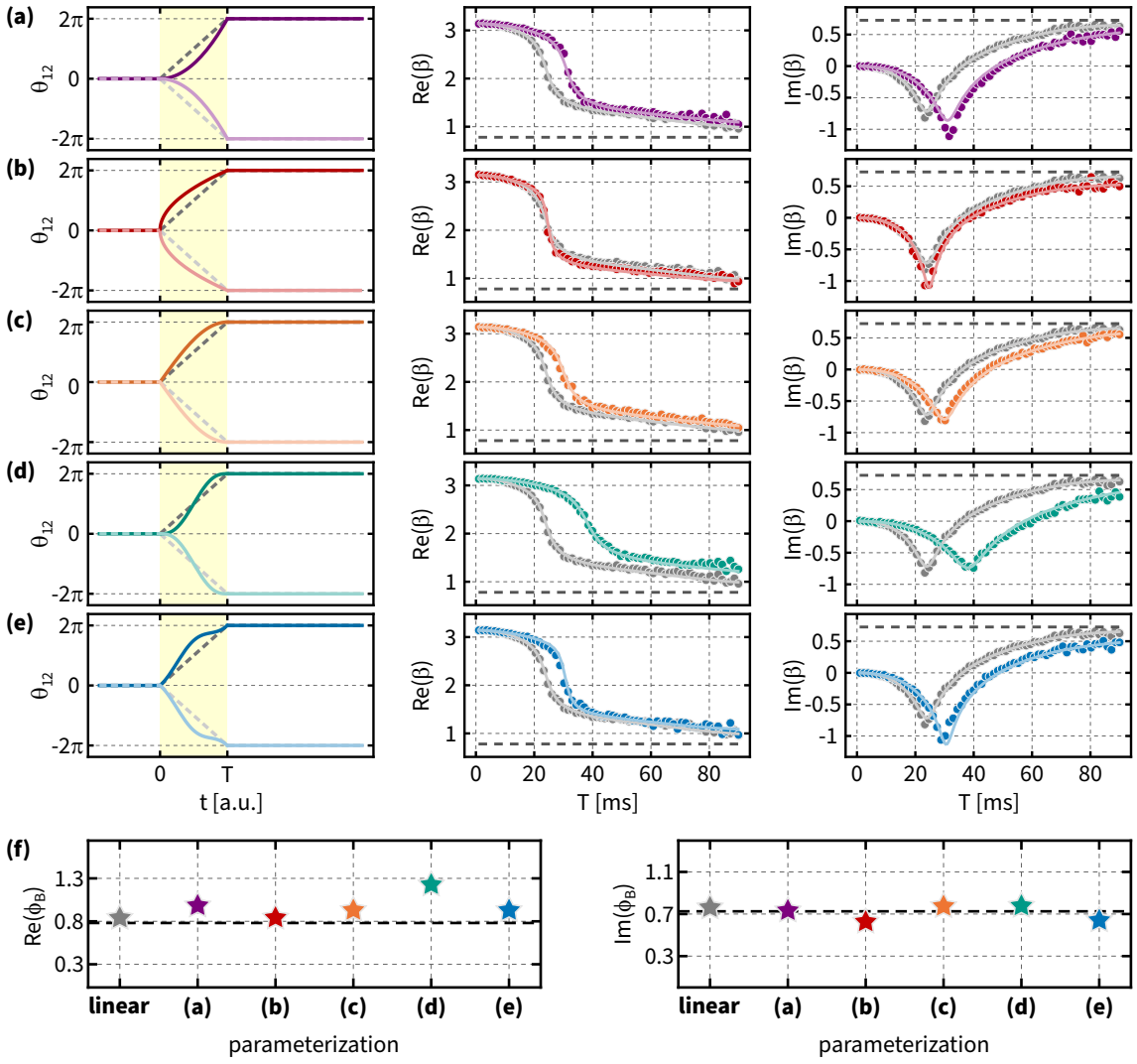

Figure 5.5: Geometric character of ϕ_B - part I. (a-e) First column: solid curves show the five $\theta_{12}(t)$ described in Sec. 5.2.1. For comparison, the dashed gray line shows the "linear ramp" $\theta_{12}(t) = \pm 2\pi t/T$ constituting a pair of "simple" control loops. Second column: Colored disks show measured $\mathrm{Re}(\beta(T))$ for the corresponding $\theta_{12}(t)$, along with the no-free-parameter theory prediction shown as solid curves. The dashed line shows the no-free-parameter theory prediction of $\mathrm{Re}(\phi_B)$. For comparison, the corresponding results for the linear ramp are shown as gray disks for data and gray solid curve for the no-free-parameter theory prediction. Third column: same as the second column, but showing $\mathrm{Im}(\beta(T))$ and $\mathrm{Im}(\phi_B)$. **(f)** The real (left) and the imaginary (right) components of ϕ_B, extracted via asymptote analysis of $\beta(T)$ for each $\theta_{12}(t)$ (Sec. D.4). The horizontal axis indicates various $\theta_{12}(t)$. Dashed line: no-free-parameter theory prediction of $\mathrm{Re}(\phi_B)$. For these measurements, we used the (3,3) and the (5,3) membrane modes with other control parameters: $P_{1,2} = P = $ 21 μW, $\delta/2\pi = -1.6$ MHz, $\eta/2 = -27.5$ Hz.

illustrated in the second and the third columns of Fig. 5.5(a-e) and Fig. 5.5(f).

These measurements demonstrate that:

1. The manner in which β evolves as function of loop duration T and approaches ϕ_B, does depend on the functional form of $\theta_{12}(t)$. This is shown in the second and the third columns of Fig. 5.5(a-e).

2. ϕ_B is predicted to be independent of $\theta_{12}(t)$. This is shown explicitly in Fig. 5.5(f), which plots the estimated ϕ_B via asymptote analysis of $\beta(T)$ (Sec. D.4). The no-free-parameter theory prediction of ϕ_B is plotted along with the measurements, and they match favorably.

This exercise demonstrates of one of the key features of geometric phase: it is determined entirely by the shape of the control loop (here, it is determined by the fixed values of $\{P_1, P_2, \delta, \eta\}$ and $0 \leq \theta_{12} \leq 2\pi$), and does not depend on the manner in which the control loop is traversed (here, it is the time-dependence of θ_{12}).

5.2.2 Part II: Varying the shape of the control path

To study the effect of the shape of a control loop, we consider two examples below. The first example (Sec. 5.2.2.1) continues with "simple" control loops where we use the same $\theta_{12}(t) = \pm 2\pi t/T$ but with different values of the other control parameters: $\{P_1, P_2, \delta, \eta, P_4, \Delta_4\}$. Intuitively, this amounts to using $\mathbf{B}_{\mathrm{Re,Im}}$ with different lengths and orientations, while continuing to rotate them around the z-axis at a constant rate. The second example (Sec. 5.2.2) represents a more general set of control loops as illustrated in Fig. 2.6(a) where its time dependence is encoded in additional control parameters (i.e., beyond $\theta_{12}(t)$).

5.2.2.1 "Simple" control loops

For these measurements, we systematically varied control parameters: $\{P_1, P_2, \delta, \eta\}$ and employed two distinct pairs of membrane modes: (3,3); (5,3) and (3,3); (5,2) to study a wide range of "simple" control loop shapes. Measurements of $\beta(T)$ and ϕ_B were carried out in the same manner as described in Secs. 5.1 and D.1. Some exemplary measurements

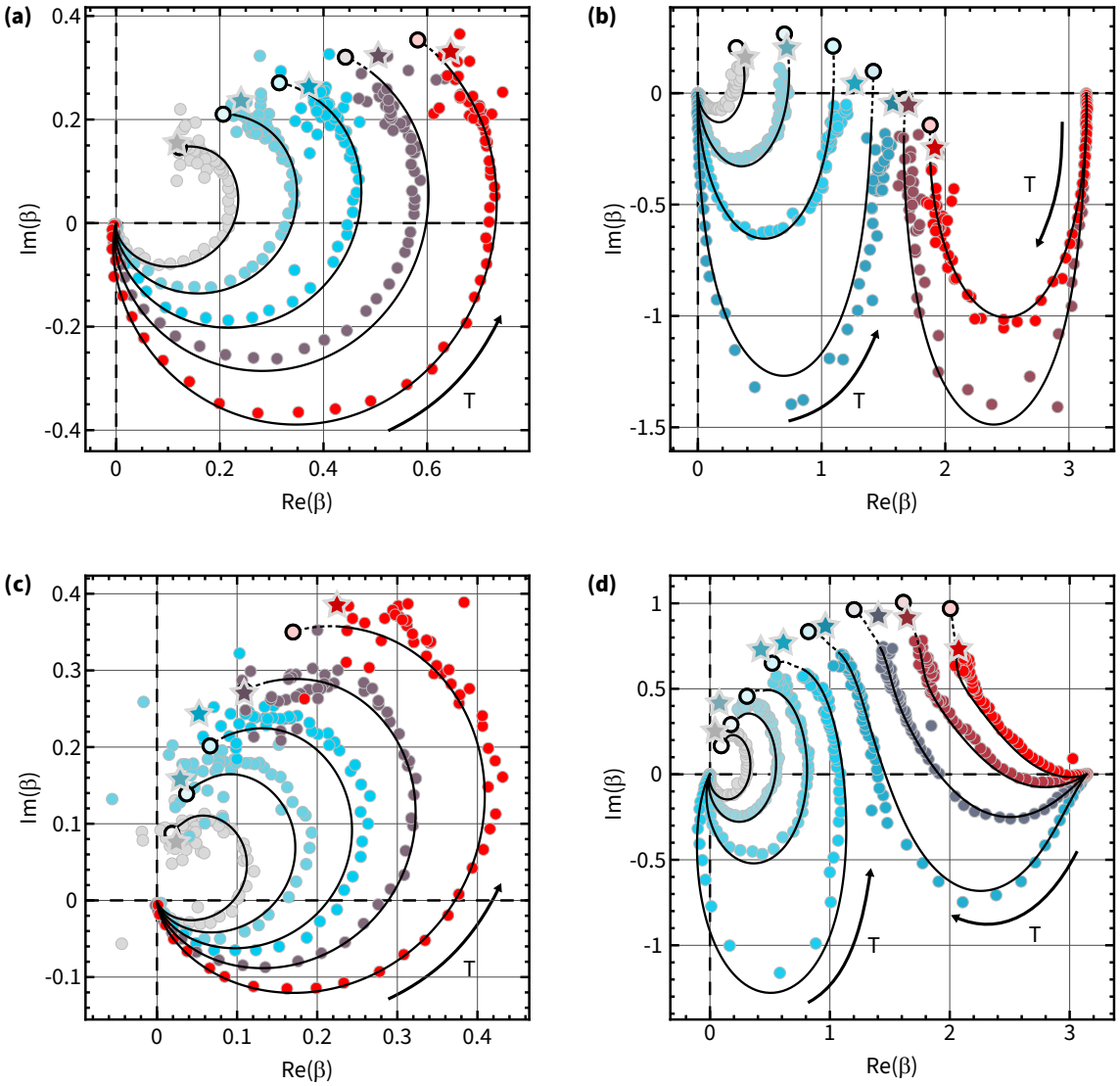

Figure 5.6: Geometric character of ϕ_B - part IIA. (a) Parametric plot of $\beta(T)$ and ϕ_B corresponding to a variety of "simple" control loops. Data nearest to origin corresponds to $T = 0$. Points: data for $\beta(T)$, curves: no-free-parameter theory estimate of $\beta(T)$ (solid for the range of T corresponding to data; dashed for T beyond the measured range), stars: estimated ϕ_B via asymptote analysis of measured $\beta(T)$ (Sec. D.4), disks: no-free-parameter theory estimate of ϕ_B. For these measurements, we used the (3,3) and the (5,2) membrane modes, with other control parameters: $\delta/2\pi = -1$ MHz, $\eta/2\pi = -50$ Hz and $P_{1,2} = P =$ (10, 12,5, 15, 17.5, 20)μW (gray,....,red). **(b)** Same as (a) except, data nearest to origin and $\{\pi, 0\}$ correspond to $T = 0$, $\delta/2\pi = -0.75$ MHz, $\eta/2\pi = -20$ Hz and $P_{1,2} = P =$ (5, 7.5, 10, 12,5, 15, 17.5)μW (gray,....,red). **(c)** Same as (a) except $\delta/2\pi = -0.75$ MHz, $\eta/2\pi = -90$ Hz and $P_{1,2} = P =$ (10, 12,5, 15, 17.5, 20)μW (gray,....,red). **(d)** Same as (a) except we used the (3,3) and the (5,3) membrane modes, data nearest to origin and $\{\pi, 0\}$ correspond to $T = 0$, $\delta/2\pi = -1.4$ MHz, $\eta/2\pi = -27.5$ Hz and $P_{1,2} = P =$ (10, 12,5, 15, 17.5, 20, 22.5, 25, 27.5)μW (gray,....,red).

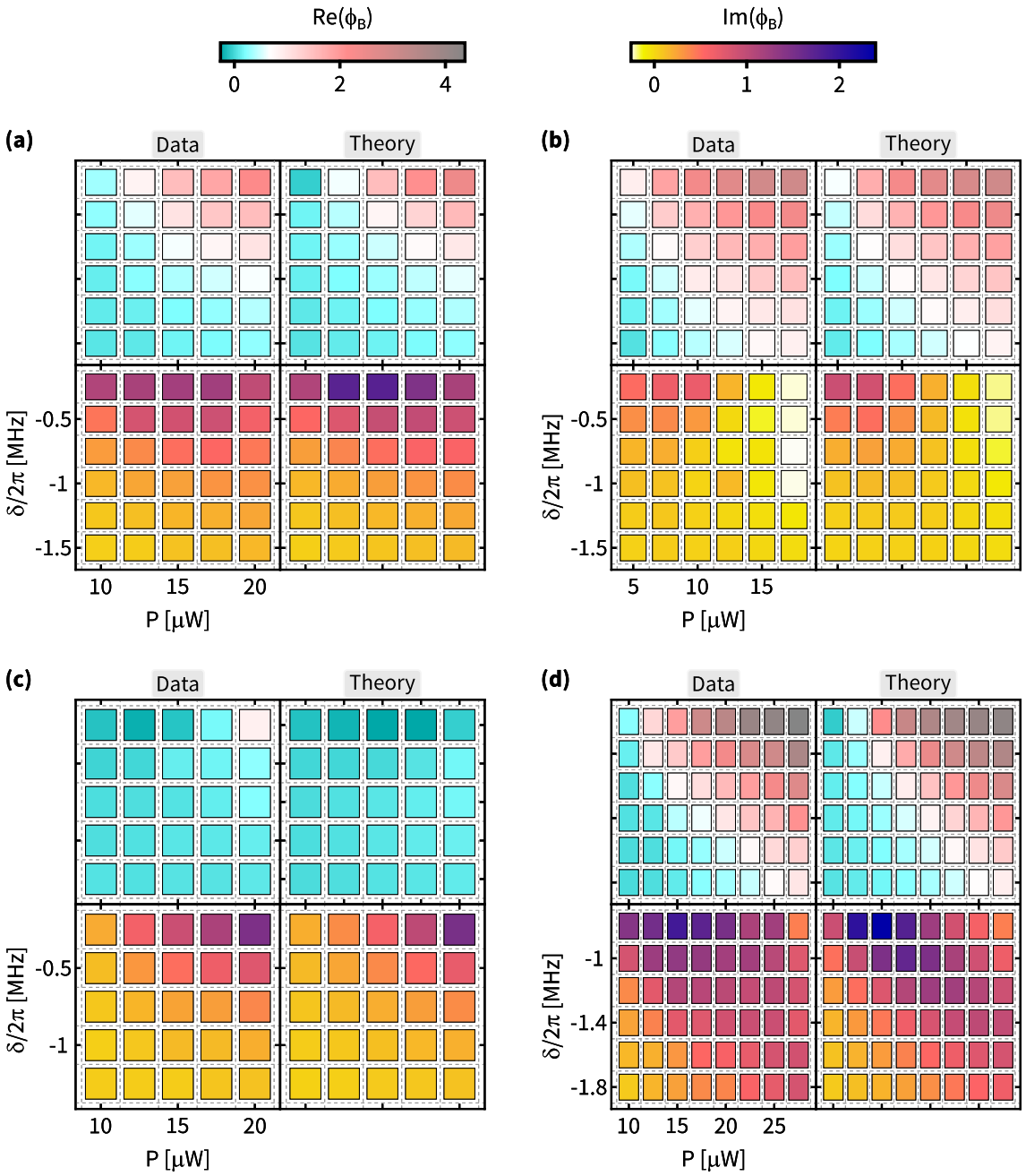

Figure 5.7: Geometric character of ϕ_B - part IIB. For all panels: the left column labeled 'Data' shows the estimated value of ϕ_B via asymptote analysis of $\beta(T)$ (Sec. D.4), measured for several "simple" control loops. They are shown as a color scale and as a function of $\{P_{1,2} = P, \delta\}$. The corresponding right column labeled 'Theory' shows no-free-parameter theory prediction of ϕ_B. Top (bottom) row shows real (imaginary) part of ϕ_B. All panels follow the same color scale as indicated at the top. For panels **(a-c)**, (3,3) and (5,2) membrane modes were used. For panel **(d)**, (3,3) and (5,3) membrane modes were used. Control parameter $\eta/2\pi$ is -50 Hz for **(a)**, -20 Hz for **(b)**, -90 Hz for **(c)** and -27.5 Hz for **(d)**. We note that for panels (b) and (c), ϕ_B is almost exclusively real and imaginary, respectively.

of $\beta(T)$ and corresponding ϕ_B via asymptote analysis (Sec. D.4) are shown as polar plots in Fig. 5.6. For these measurements, we varied $P_{1,2}$ at a fixed value of $\{\delta, \eta\}$. The no-free-parameter theory prediction of $\beta(T)$ and ϕ_B are shown alongside, and they match favorably with the measurements. Fig. 5.7(left column labeled as 'Data' in each panel) shows ϕ_B estimated from $\beta(T)$ over a wider range of $\{P, \delta\}$ with four choices of η, and for two distinct pairs of membrane modes. The right column labeled as 'Theory' shows the no-free-parameter theory estimates and they are in good agreement with the measured values.

5.2.2.2 "Non-Simple" control loops

In this section we describe measurements that use "non-simple" control loops, by which we mean loops that involve varying the control tones' powers and detunings (in addition to their beat-note phase θ_{12}). For this study, we consider three distinct family of control loops which can be parameterized as: $\vec{X}(s) = (P_1, P_2(s), \delta(s), \eta, \theta_{12}(s))$. They are defined as follows:

Control loop family (i)

$$\vec{X}_1(s) = \left(P_1, P_{2,0} + P_{2,1}\mathrm{Sin}(2\pi s), \left(\frac{\delta_0 + \delta_1}{2}\right) + \left(\frac{\delta_0 - \delta_1}{2}\right)\mathrm{Cos}(2\pi s), \eta, 2\pi s\right)$$

where $s = \pm t/T, t \in [0, T]$, and the control parameters are: $P_1 =$ 15 μW, $\eta/2\pi =$ $-$50 Hz, $P_{2,0} =$ 15 μW, $P_{2,1} =$ 5 μW, $\delta_0/2\pi = -1.5$ MHz and δ_1 is varied as $\{-1.5$, -1.25, -1, -0.75, -0.5, $-0.25\}$ MHz. Membrane modes (3,3) and (5,2) were employed for these measurements.

Control loop family (ii)

$$\vec{X}_2(s) = \left(P_1, P_{2,0}+P_{2,1}\mathrm{Sin}(2\pi s), \left(\frac{\delta_0 + \delta_1}{2}\right)+\left(\frac{\delta_0 - \delta_1}{2}\right)\mathrm{Cos}(2\pi s), \eta, \theta_{12,\mathrm{m}}\,\mathrm{Sin}(\pi s)^2\right)$$

where $s = \pm t/T, t \in [0, T]$, and the control parameters are: $P_1 =$ 15 μW, $\eta/2\pi =$ $-$50 Hz, $P_{2,0} =$ 15 μW, $P_{2,1} =$ 5 μW, $\delta_0/2\pi = -1.5$ MHz, $\delta_1 = -0.25$ MHz and $\theta_{12,\mathrm{m}}$ is varied as $\{0, 2\pi/5, 4\pi/5, 6\pi/5, 8\pi/5, 2\pi\}$. Membrane modes (3,3) and (5,2) were employed for these measurements. These control loops differ qualitatively from all others

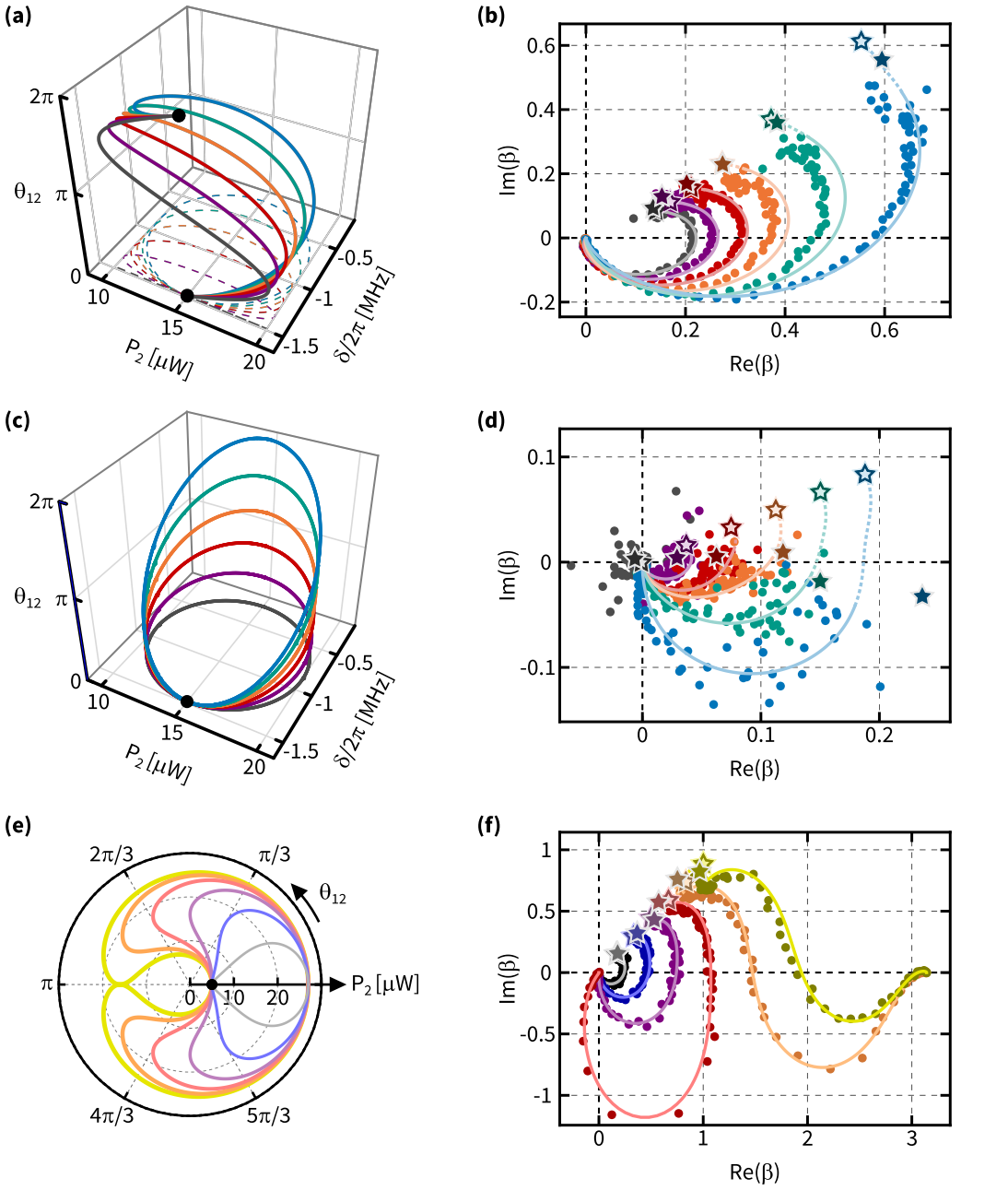

Figure 5.8: Geometric character of ϕ_B - part IIC. (a) Control loops from family **(i)** (Sec. 5.2.2.2), plotted in the 3D space of the parameters P_2, δ, θ_{12}. The solid lines are the actual loop, and the dashed lines show the loop projected onto the (P_2, δ) plane. Black dots are the start/stop point. **(b)** $\beta(T)$ and ϕ_B for loops in (a). Points: data for $\beta(T)$, curves: no-free-parameter theory estimate of $\beta(T)$ (solid for the range of T corresponding to data; dashed for T beyond the measured range), solid stars: estimated ϕ_B via asymptote analysis of measured $\beta(T)$ (Sec. D.4), open stars: no-free-parameter theory estimate of ϕ_B. The colors in (b) correspond to the loops in (a). **(c)** Same as (a) but for control loops from family **(ii)** (Sec. 5.2.2.2). These control loops are our first example where θ_{12} does not wind by 2π when the control loop is completed. **(d)** Same as (b) but for control loops in (c). **(e)** Control loops from family **(iii)** (Sec. 5.2.2.2), plotted in (P_2, θ_{12}) plane. These control loops are our second example where θ_{12} does not wind by 2π when the control loop is completed. **(f)** Same as (b) but for control loops in (e).

that we have described up until now. They are our first example where θ_{12} does not wind by 2π when the control loop is completed.

Control loop family (iii)

$$\vec{X}_3(s) = \left(P_1, P_{2,0} + P_{2,1} \left| \mathrm{Sin}(\pi s) + \frac{\mathrm{Sin}(2\pi s)^2}{4} \right|, \delta, \eta, \theta_{12,\mathrm{m}}\ \mathrm{Sin}\left(2\pi s + \frac{\mathrm{Sin}(2\pi s)}{2} \right) \right)$$

where $s = \pm t/T, t \in [0, T]$, and the control parameters are: $P_1 =$ 21 μW, $\delta/2\pi =$ $-$0.95 MHz, $\eta/2\pi = -30$ Hz, $P_{2,0} =$ 5 μW, $P_{2,1} =$ 22 μW and $\theta_{12,\mathrm{m}}$ is varied as $\{\pi/6, \pi/3, \pi/2, 2\pi/3, 5\pi/6, \pi\}$. Membrane modes (3,3) and (5,3) were employed for these measurements. These control loops are our second example where θ_{12} does not wind by 2π when it is completed. In addition, we applied a blue-detuned tone during the control loop with its $P_4 =$ 20 μW and $\Delta_4/2\pi = +3.5$ MHz to provide modest anti-damping.

Crucially for all three families of control loops described here, we ensured the existence of a unique least-dissipative eigenvector for the entirety of each control loop, and hence the adiabatic theorem applies to it for large T. Measurements of $\beta(T)$ and ϕ_B were carried out in the same manner as described in Secs. 5.1 and D.1. The control loops from family **(i,ii,iii)** are shown in Fig. 5.8(a,c,e), respectively. The corresponding measurements of $\beta(T)$ and estimated ϕ_B via asymptote analysis of $\beta(T)$ (Sec. D.4) are shown as a polar plot in Fig. 5.8(b,d,f), respectively. They are plotted along with the no-free-parameter theory prediction, and are in good agreement with each other.

5.2.3 Part III: Multiple repetitions of a control path

Repeating a control path is a straightforward affair. For this example, we chose the "simple" control loop illustrated in Sec. 5.1 and simply modified $\theta_{12}(t)$ to $\pm 2\pi n t/T \bmod 2\pi$. Intuitively, these loops correspond to rigidly rotating $\mathbf{B}_{\mathrm{Re,Im}}$ around the z-axis multiple (n) times, at a constant rate. However, formally they correspond to inequivalent loops. The corresponding measurements of $\beta(T)$ and ϕ_B were carried out in the same manner as described in Secs. 5.1 and D.1. Fig. 5.9 illustrates the control loops and corresponding measurements of $\beta(T)$ and ϕ_B for $n = \{0, 1, 2, 3, 4, 5\}$.

The measurements of $\beta(T)$ are shown in Fig. 5.9(b-d). For $n \geq 1$, they indicate a trend that increases roughly linearly with n for large T. This is better quantified in Fig. 5.9(e) where we show β/n as a function of T/n. For $n = 0$, we obtain the expected: $\beta(T) \sim 0$ for all T. This seemingly innocuous measurement of $n = 0$ case is of utility beyond simply corroborating our expectations. In particular, it being $\sim$0 signifies an absence of any systematic errors in our experimental protocol and its scatter around zero can be used to quantify the error in estimating ϕ_B[1]. Finally, via asymptote analysis of $\beta(T)$ (Sec. D.4), we obtain ϕ_B as shown in Fig. 5.9(f,g). They corroborate: $\phi_{B,n} = n\phi_{B,1}$ as in Eq. (2.22), where the additional subscript indicates the number of repetitions of a control loop. In all these cases, the measurements are in good agreement to the no-free-parameter theory predictions.

To conclude this section, we note a technical point. A systematic and straightforward study of this example (see Fig. 5.9(e-g)) was made possible by constraining the maximum duration of a control loop repeated n-times as $T_{\max,n} = nT_{\max,1}$ for $n \geq 1$. Such loop durations are longer than our usual measurements (see Secs. 5.1, 5.2.1, 5.2.2 and 5.3), and they necessitated a sufficiently long ringdown time of membrane modes' amplitude. This was accomplished via the use of a blue-detuned control tone during the control loop. Its parameters are specified in Sec. 5.1 and its optomechanical effects are characterized in Sec. 4.5.3. As will be shown in Chapters 6 and 7, it is this technique that single-handedly made the work therein possible.

[1]However, we do not quantify the error in estimating ϕ_B, systematically, in this chapter or in Chapter 6.

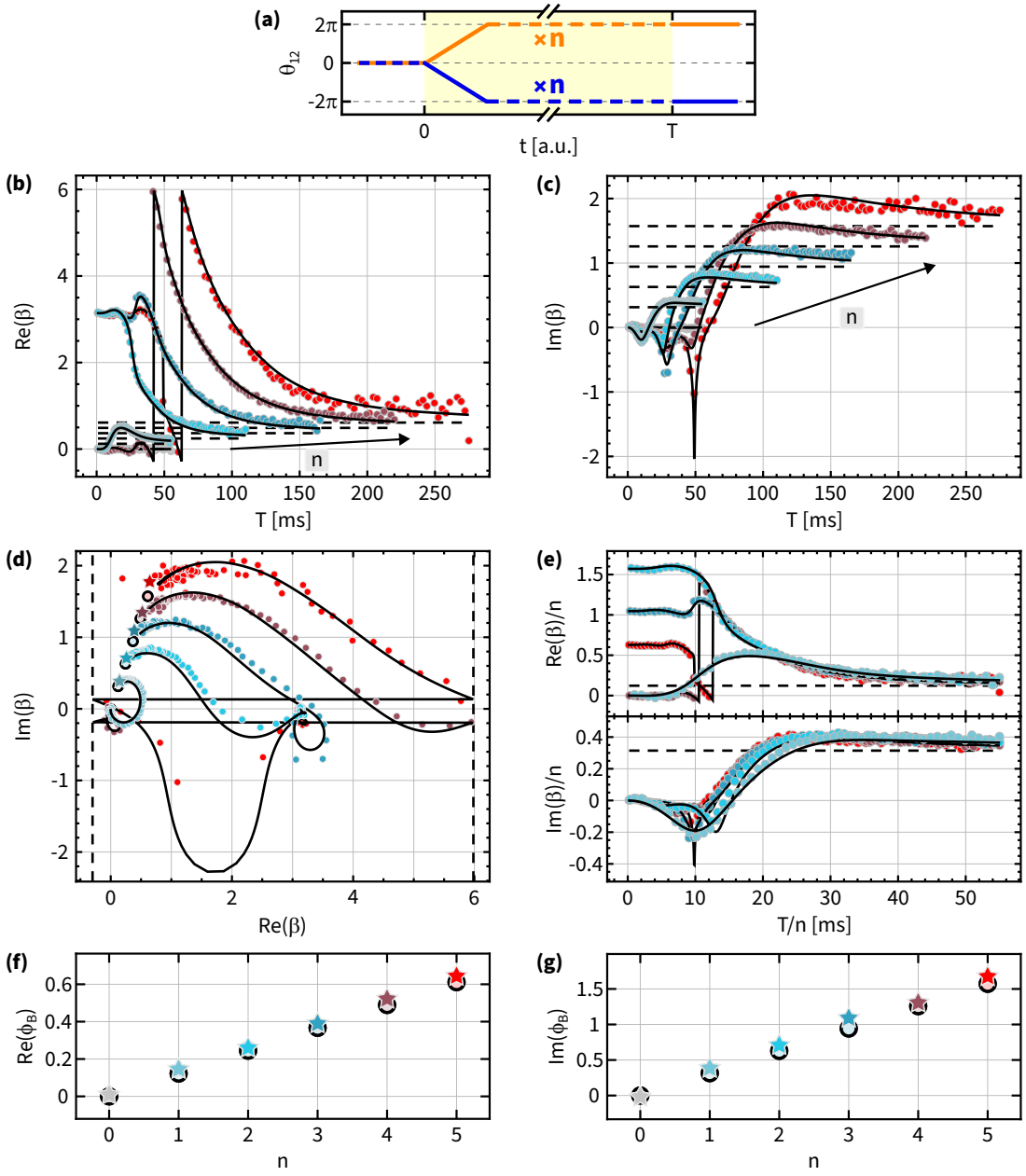

Figure 5.9: Geometric character of ϕ_B - part III. (a) Control paths in which θ_{12} is ramped from 0 to $\pm 2\pi n \bmod 2\pi$, for $n = \{0, 1, 2, 3, 4, 5\}$. Orange (blue) curves: correspond to control loops in "forward" ("backward") direction. **(b-c)** Corresponding $\mathrm{Re}/\mathrm{Im}(\beta(T))$, respectively. Colored points (gray to red for $n = 0$ to 5): data, solid black lines: no-free-parameter theory expectation for each n. Dashed black lines: no-free-parameter theory expectation of $\mathrm{Re}/\mathrm{Im}(\phi_B)$ for each n. **(d)** Polar plot of $\beta(T)$ and ϕ_B. Colored points (gray to red): data corresponding to $\beta(T)$, solid black curve: no-free-parameter theory expectation of $\beta(T)$ for each n, colored stars (gray to red): estimated ϕ_B from $\beta(T)$ data via asymptote analysis (Sec. D.4), colored disks (gray to red): no-free-parameter theory expectation of ϕ_B. **(e)** β/n versus T/n for $1 \leq n \leq 5$. Colored points: data, black solid lines: no-free-parameter theory expectation. The dashed black line indicates ϕ_B for $n = 1$. Top (bottom) panel: real (imaginary) part of $\beta(T/n)/n$. **(f-g)** $\mathrm{Re}/\mathrm{Im}(\phi_B)$ versus n, respectively. Stars: estimated ϕ_B, disks: no-free-parameter theory expectation of ϕ_B. For this measurement, we used the same membrane modes and the same other control parameters as in Figs. 5.1-5.4.

5.3 Imaginary geometric phase for open control paths

In section 2.2.3.4, we showed that the imaginary part of the Berry connection is gauge invariant, from which it follows that the imaginary part of the geometric phase is also gauge independent, regardless of whether or not the path is closed [159]. In this section, we supplement this discussion with experimental measurements of the geometric phase for open control paths.

We recall that the (real) phase of an oscillator is only defined relative to a reference or gauge, which may vary within the space of control parameters. As a result, the accumulated phase has a gauge-invariant definition only if the control path is a loop. In contrast, an oscillator's amplitude does not depend on a gauge choice, and so $\mathrm{Im}(\phi_B)$ is well defined even when the control path is not a loop.

Fig. 5.10 shows measurements of $\mathrm{Im}(\phi_B)$ for a family of control paths, some of which are not loops. They are realized by fixing $P_1 = P_2 = P, \delta$ and η, while ramping θ_{12} from 0 to $\pm 2\pi(Nt/5T)$ for $N = 0, 1, 2, 3, 4, 5$ (Fig. 5.10(a)), resulting in open control paths for $1 \leq N \leq 4$. The left panel of Fig. 5.10(b-e) shows $\mathrm{Im}(\beta(T))$ for each N (data and no-free-parameter theory prediction), while the corresponding right panel shows $\mathrm{Im}(\phi_B)$ determined via asymptote analysis of $\beta(T)$ as described in Sec. D.4. Lastly, the agreement between data and theory remains in good shape.

There are works discussing real geometric phase being well-defined for open control paths [140, 242–247]. However, we do not explicitly study it in this thesis, and leave it for a later endeavor.

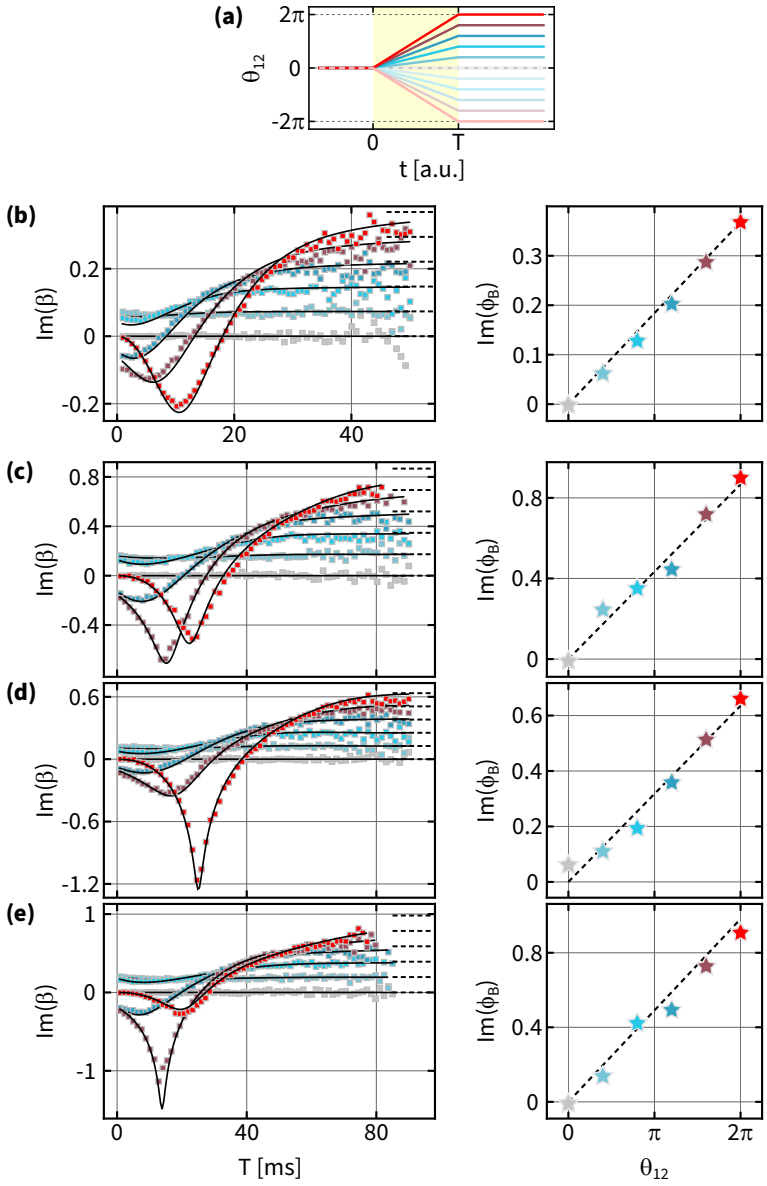

Figure 5.10: Imaginary geometric phase of open control paths. (a) Control paths in which θ_{12} is ramped from 0 to $\pm 2\pi(N/5)$, for $N = 0, 1, 2, 3, 4, 5$ (gray,....,red). Dark (pale) curves: correspond to control loops in "forward" ("backward") direction. **(b)** Left panel shows $\mathrm{Im}(\beta(T))$: measured (disks) and no-free-parameter theory prediction (solid curves) for each N; dashed lines: no-free-parameter theory prediction of $\mathrm{Im}(\phi_B)$ for each N. Right panel for ϕ_B. Stars: measured $\mathrm{Im}(\phi_B)$; dashed line: no-free-parameter theory prediction of $\mathrm{Im}(\phi_B)$. For this measurement, we used the (3,3) and the (5,2) membrane modes, and other control parameters: $P_{1,2} = P =$ 15 μW, $\delta/2\pi = -0.87$ MHz, $\eta/2\pi = -50$ Hz. This control parameter is marked as a square marker in Fig. 4.15(b). **(c-e)** Same as (b) except we used the (3,3) and the (5,3) membrane modes, and other control parameters: $\delta/2\pi = -1.5$ MHz, $\eta/2\pi = -27.5$ Hz and $P_{1,2} = P = (17, 20, 23)$μW for panels (c, d, e), respectively. These control parameters are marked as a square, down-triangle and diamond marker, respectively in Fig. 4.16(b).

5.4 Further insights into non-Hermitian adiabatic evolution

In this section, we report additional measurements and corresponding numerical simulations that may provide new insights on adiabatic evolution in non-Hermitian systems. This study continues with the same "simple" control loop as in Sec. 5.1 and supplement our discussion in Sec. 2.2.3.1 around Fig. 2.6(e).

For this study, we focus on additional complex-phases that are borne out of adiabatic evolution, and that may have a constant asymptote (or a T^0-part) without any additional intensive processing. This is inspired by our example shown in Fig. 2.6(d,e-bottom panel). More concretely, here we investigate the quantity $\beta_{ij}(T)$ given by:

$$\beta_{ij}(T) = -\frac{i}{2}\mathrm{Log}\left(\frac{U_{ij,\circlearrowleft}}{U_{ij,\circlearrowright}}\right) \tag{5.2}$$

where $i,j \in \{+,-\}$ and $\beta_{++} \equiv \beta$ as studied in Secs. 5.1 and D.1. Combining the measurements as shown in Fig. 5.3 as per Eq. (5.2), we obtain Fig. 5.11(a,b). They show real and imaginary parts of $\beta_{ij}(T)$, respectively. The data (shown as red symbols) agree well with the corresponding no-free-parameter theory estimates (solid black). However, it is unclear from this exercise if any of $\beta_{ij}(T)$ (other that $\beta_{++}(T)$) asymptote to a constant (T^0-part).

In hindsight, it could have been useful to acquire data for a longer control loop duration which may provide more insights. However, the reliable agreement between data and theory motivates us to simply extrapolate the theory curve for a longer loop duration. This exercise is illustrated in Fig. 5.11(c,d). They show real and imaginary parts of $\beta_{ij}(T)$ for loop durations extended by 20x of the measured value, respectively. The constant asymptote is visually evident in all $\beta_{ij}(T)$. The explicit value of these asymptotes (other than that of $\beta_{++}(T)$ which asymptotes to ϕ_B) are yet to be calculated, and we relegate them for a future work. However, a more useful task would be to isolate the physical origin of such behavior as well as finding the characteristic time scale for which $\{\beta_{+-}(T), \beta_{-+}(T), \beta_{--}(T)\}$ converge to their corresponding asymptotes. See also the

second entry of Sec. 8.1. This concludes the discussion of one of our new insights into Adiabatic evolution in non-Hermitian systems.

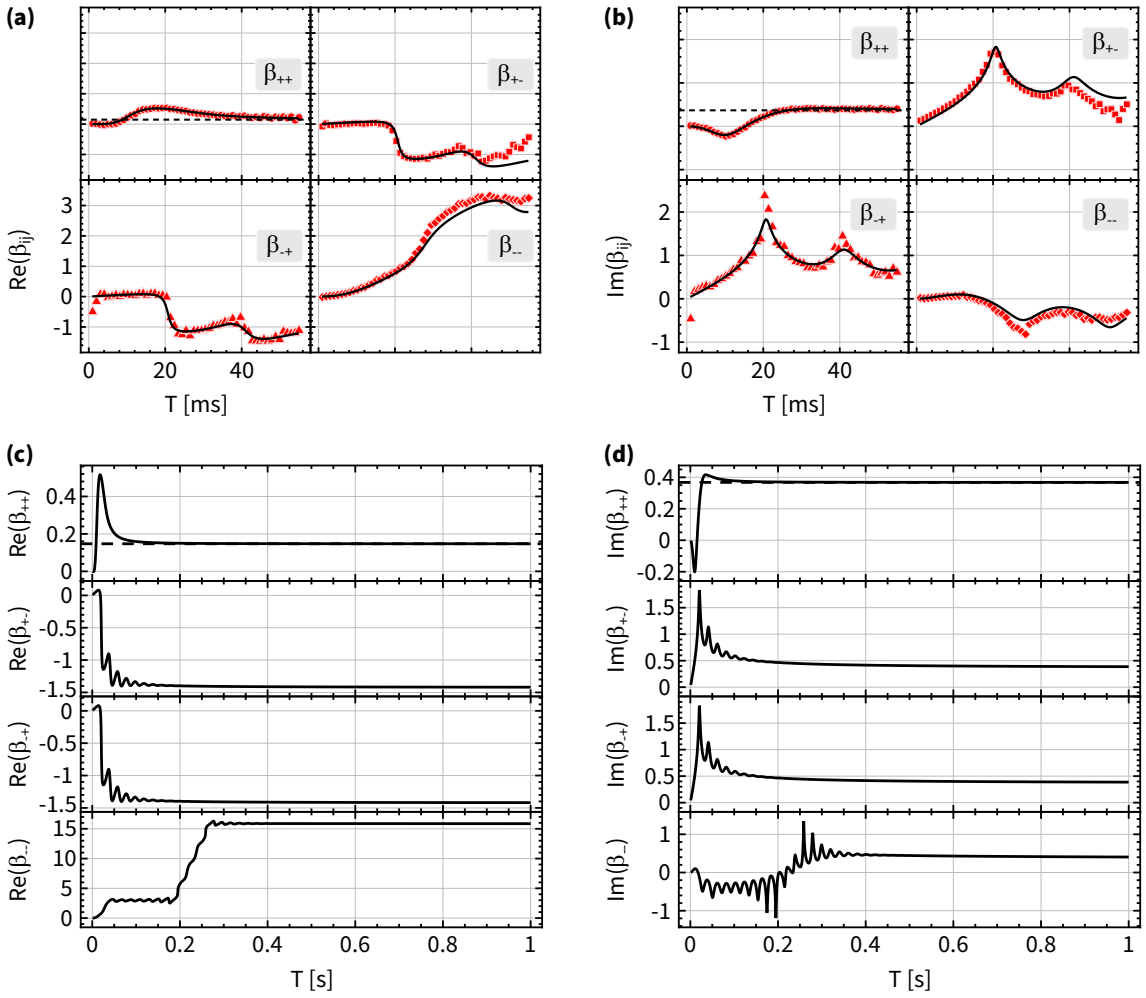

Figure 5.11: Measurement and numerical simulation of $\boldsymbol{\beta_{ij}(T)}$. **(a)** $\mathrm{Re}(\beta_{ij}(T))$ obtained from U_{ij} measurements along "forward" and "backward" control loops, for $i, j \in \{+, -\}$ (see Fig. 5.3). Red symbols: data, solid black lines: no-free-parameter theory estimates and dashed black line: asymptote of $\beta_{++}(T) \equiv \beta(T)$: $\mathrm{Re}(\phi_B)$. **(b)** Same as a but for $\mathrm{Im}(\beta_{ij}(T))$. **(c)** Same as (a) but we only show the no-free-parameter theory estimates for 20x longer loop duration. **(d)** Same as (c) but for $\mathrm{Im}(\beta_{ij}(T))$. In both (c) and (d), all $\beta_{ij}(T))$ visually asymptote to a constant value $(\beta_{++}(T)) \equiv \beta$ asymptotes to ϕ_B). For these measurements and this exercise, we used the same membrane modes and the same other control parameters as in Figs. 5.1-5.4 and 5.9.

Chapter 6

A geometric amplifier

In this chapter, we describe a novel form of amplification via the non-Hermitian geometric phase. Following-up on its teaser given in Sec. 2.2.3.5, we begin with a platform-agnostic definition of the geometric amplifier (Sec. 6.1). We then show via numerical simulations that this amplification does not require fine-tuning, but rather arises generically in non-Hermitian systems and from the geometric character of their dynamics (Sec. 6.2). In Sec. 6.3, we experimentally demonstrate the geometric amplifier using the new MIM platform (Chapter 4) and its non-Hermitian geometric phase (Chapter 5). In particular, we illustrate measurements of the geometric amplifier for two distinct families of control loops. We conclude this chapter with further insights into this topic in Sec. 6.4, including a brief comparison to the parametric amplifier, and some additional features in the geometric amplifier measurements.

6.1 Defining SSGG

In this section, we provide a concrete and platform-independent definition of geometric amplification. In particular, we focus on the flow of energy into or out of a non-Hermitian system, and describe it terms of its complex geometric phase. This analysis reveals an important result (Secs. 6.2 and 6.3): a collection of linear but lossy elements can produce continuous gain if the elements' parameters are varied "slowly", and we refer to this mechanism as steady-state geometric gain (SSGG).

To focus the discussion, we consider systems that consist of two harmonic modes whose parameters are repeatedly tuned around a control loop $\mathcal{C}_{\mathrm{amp}}$, with each traversal using the same time dependence $s(t/T)$, and the same duration T. The following four conditions define SSGG:

(1) There is a least-dissipative eigenvector[1] for the entirety of $\mathcal{C}_{\mathrm{amp}}$.

(2) When the system is prepared in this least-dissipative eigenvector, its state after a single traversal of $\mathcal{C}_{\mathrm{amp}}$ using $s(t/T)$ in a duration T is well-approximated by the initial state multiplied by $e^{-i\phi(T)}$, where the complex phase $\phi(T)$ is given by Eq. (5.1).

(3) For each such traversal, this mode's dynamical phase contributes loss. Specifically, the linear dynamical phase $\mathrm{Im}(\phi_D) < 0$.

(4) For each traversal, this mode's total gain $\mathrm{Im}(\phi(T))$ lies in the region $\mathbf{\Gamma}$, which is bounded by:

- **(a)** $T > T_{\mathrm{ad}}$
- **(b)** $\mathrm{Im}(\phi(T)) > 0$
- **(c)** $\mathrm{Im}(\phi(T)) < -\mathrm{Im}(\phi_B)$
- **(d)** $\mathrm{Im}(\phi(T)) < \mathrm{Im}(\phi_D) - 2\mathrm{Im}(\phi_B)$

We now elaborate upon each of these conditions.

[1] Throughout this chapter, the phrase 'least-dissipative eigenvector' implies the least-dissipative right eigenvector.

When condition (1) is met, the adiabatic theorem [11, 88] guarantees that condition (2) is also met for sufficiently large T. We take $T > T_{\mathrm{ad}}$ as the threshold for this condition where $T_{\mathrm{ad}} = \max_{\mathcal{C}_{\mathrm{amp}}}(1/|\lambda_+(s) - \lambda_-(s)|)$.

Condition (3) requires that the system's dynamical phase contributes loss. This condition is included because otherwise the system can serve as steady-state amplifier without the geometric phase (i.e., just by using large T and relying on the dynamical phase).

Condition (4) identifies the features that $\mathrm{Im}(\phi(T))$ must exhibit upon a single traversal of $\mathcal{C}_{\mathrm{amp}}$ using the time dependence s and duration T, for the system's gain to be attributed to the geometric phase. Each of its sub-conditions has a straightforward physical interpretation.

- Condition (4a) ensures that the system's dynamics are compatible with the notion of adiabaticity, and hence are described by Eq. (5.1).
- Condition (4b) ensures that the mode experiences net gain upon each traversal of $\mathcal{C}_{\mathrm{amp}}$.
- Condition (4c) ensures that the net gain can be attributed to the geometric gain. Specifically, it requires that the net gain would be negative without the contribution from the geometric gain.
- Condition (4d) also ensures that the net gain can be attributed to the geometric gain. Specifically, it requires that the geometric gain accounts for the majority of the difference between the dynamical loss $\mathrm{Im}(\phi_D)$ and the net gain. This ensures that the net gain is not attributable to the higher-order terms i.e., $\mathcal{O}(1/T)$ in Eq. (5.1).

For a given $\mathcal{C}_{\mathrm{amp}}$ and $s(t/T)$, the conditions (4a - 4d) can be visualized by noting that they each bisect the plane spanned by $\mathrm{Im}(\phi(T))$ and T. Together they define a region $\mathbf{\Gamma}$ with the following interpretation: for this $\mathcal{C}_{\mathrm{amp}}$ and $s(t/T)$, SSGG results iff T is chosen such that $\mathrm{Im}(\phi(T))$ lies within the $\mathbf{\Gamma}$. Fig. 6.1 illustrates the region $\mathbf{\Gamma}$.

We conclude this discussion with a quick reminder (Sec. 2.2.3.5) of how one may

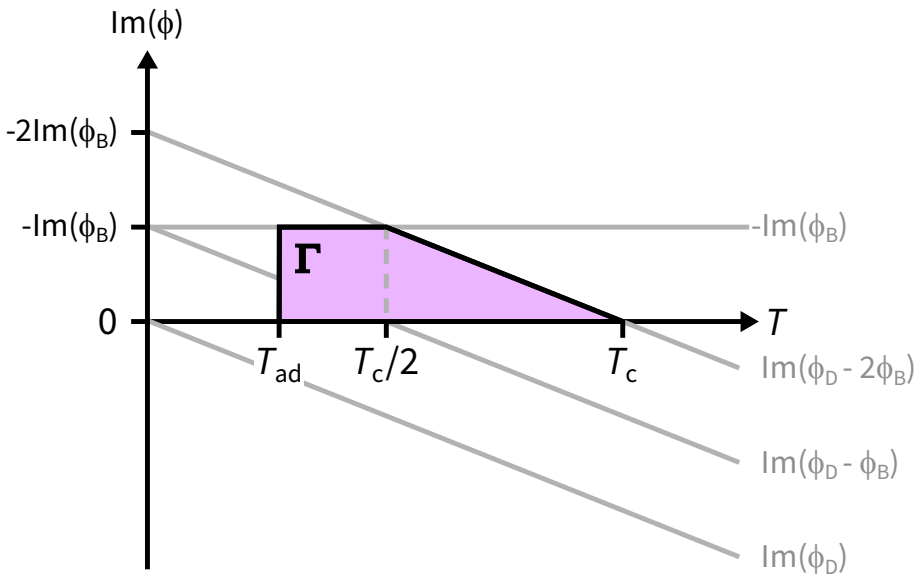

Figure 6.1: Conditions for achieving SSGG. For a given control loop $\mathcal{C}_{\rm amp}$, its time dependence $s(t/T)$ and its duration T, SSGG occurs iff $\mathrm{Im}(\phi(T))$ lies in the pink shaded region $\mathbf{\Gamma}$. ϕ_D: the linear dynamical phase, ϕ_B: the geometric phase, $T_{\rm ad} = \max_{\mathcal{C}_{\rm amp}}(1/|\lambda_+(s) - \lambda_-(s)|)$, the threshold time duration for adiabatic theorem to hold, T_c: solution to $\mathrm{Im}(\phi_D - 2\phi_B) = 0$, the largest duration for which SSGG may occur, with corresponding gain = 0 dB.

extend SSGG to arbitrarily large times. Consider the range for which gain results if $\mathcal{C}_{\rm amp}$ is traversed once with a particular $s(t/T)$. To extend this gain in definitely, one may simply repeat $\mathcal{C}_{\rm amp}$ multiple $(n > 1)$ times with the same $s(t/T)$ and T. Using the result in Sec. A.3.1, we expect the time over which gain is maintained to be $T^{(n)} = nT^{(1)}$. We note that this prediction does not contradict the fact that the linear dynamical phase (which is of $\mathcal{O}(T^1)$) dominates the geometric phase (of $\mathcal{O}(T^0)$), at large T. This is because the prediction applies to a given $\mathcal{C}_{\rm amp}$, and each choice of n formally corresponds to a distinct control loop. Since there is no limit to how large n maybe, $T^{(n)} = nT^{(1)}$ can be arbitrarily large i.e., in the steady state. However, see Sec. 6.4.2.2 for a possible practical upper limit on the duration for which SSGG may occur.

6.2 Identifying control loops that produce SSGG

In this section, we identify families of control loops that produce SSGG via analytical calculations and numerical simulations. To emphasize the broad applicability of SSGG, we simulate a generic two-mode non-Hermitian system, rather than any specific realization[1].

Conditions (1-3) for SSGG (Sec. 6.1) depend only on the static properties of the system. For example, its eigenvalues $\boldsymbol{\lambda}$ at each value of s. As a result, for a given system, a control loop $\mathcal{C}_{\mathrm{amp}}$ and its traversal $s(t/T)$, it is straightforward to determine whether these conditions are satisfied.

In contrast, condition (4) depends on the real time dynamics of the system governed by Eq. (2.80). For a specific $\mathcal{C}_{\mathrm{amp}}$ and $s(t/T)$, numerical integration of Eq. (2.80) as a function of loop duration T can be used to determine if $\mathrm{Im}(\phi(T))$ passes through the region $\boldsymbol{\Gamma}$. This approach was used in Secs. 6.2.2 and 6.3. However, in addition to explicit numerical integration, it would be helpful to also have a simple criteria that could be used to identify a pair of $\{\mathcal{C}_{\mathrm{amp}}, s(t/T)\}$ that can produce SSGG. As a practical matter, this would facilitate the design of SSGG devices. More abstractly, it could also provide a useful measure of how common such loops are.

We are not aware of any simple criteria that determines whether an arbitrary pair of $\{\mathcal{C}_{\mathrm{amp}}, s(t/T)\}$ can meet condition (4). However, we can instead consider particular families of loops that are parameterized by a few variables, and determine the range of these variables that satisfy condition (4). This exercise is shown in Secs. 6.2.1 and 6.2.2, and we find that in both cases a wide range of loops satisfy condition (4).

[1]This discussion can be directly translated into the MIM platform of Chapters 3 and 4 via Eq. (2.83). See Sec. 2.3.2.1 for further details.

6.2.1 SSGG with "simple" control loops

The first family of loops we consider are the "simple" control loops from Sec. 2.2.3.1. For simplicity we re-write their parameterization here (similar to Eq. (2.14)).

$$H(t) = \begin{bmatrix} \mathcal{T} + L & Me^{-2\pi it/T} \\ Ne^{2\pi it/T} & \mathcal{T} - L \end{bmatrix} \tag{6.1}$$

where $\{\mathcal{T}, L, M, N\}$ are complex constants. For this $H(t)$, its eigenvalues are time-independent and are given by $\lambda_\pm = \mathcal{T} \pm \lambda_0$ where $\lambda_0 = \sqrt{L^2 + MN}$. Since we are interested only in the unique least-dissipative eigenvector, we take $\mathrm{Im}(\lambda_0) > 0$. In this discussion, the trace of $H(t)$ (i.e., $2\mathcal{T}$) plays an important role, as its imaginary part contributes to the system's loss. In particular, to $\mathrm{Im}(\phi_D)$.

The real time evolution of the least-dissipative eigenvector under $H(t)$ (Eq. (6.1)) can be solved analytically. The resulting $\phi(T)$ is given by:

$$\phi(T) = \mathcal{T}T + \sqrt{\lambda_0^2 T^2 - 2\pi LT + \pi^2} - \pi \tag{6.2}$$

In the limit of $T \to \infty$, $\phi(T) \to \phi_D - \phi_B$, where $\phi_D = q_D T = (\mathcal{T} + \lambda_0)T$ and $\phi_B = \pi\left(\frac{L}{\lambda_0} + 1\right)$.

These loops always meet condition (1), and always meet condition (2) in the large-T limit. Meeting condition (3) amounts to constraining $\mathrm{Im}(\mathcal{T} + \lambda_0) < 0$. As a result, identifying the loops that can produce SSGG amounts to finding the values of $\mathcal{T}, \lambda_0$ and L that meet condition (4).

Condition (4) requires that the function $\mathrm{Im}(\phi(T))$ passes through the region $\mathbf{\Gamma}$, which in turn requires that $\mathrm{Im}(\phi(T))$ intersects (non-tangentially) at least one of the boundaries of $\mathbf{\Gamma}$. In the sections below, we derive analytic expressions or numerically evaluate for loops that intersect each of the boundaries of $\mathbf{\Gamma}$.

6.2.1.1 Intersecting the lower boundary of $\mathbf{\Gamma}$

$\mathrm{Im}(\phi(T))$ intersects the lower boundary of $\mathbf{\Gamma}$ if there is a loop duration T_* such that the following two conditions hold:

$$\textbf{(a)}\ T_{\mathrm{ad}} < T_* < T_c$$

$$\textbf{(b)}\ \mathrm{Im}(\phi(T_*)) = 0$$

where $T_{\mathrm{ad}} = 1/2|\lambda_0|$ and $T_c = 2\mathrm{Im}(\phi_B)/\mathrm{Im}(q_D)$.

Considering condition (b) first, we rewrite it as:

$$\mathrm{Im}(\phi(T_*)) = 0 \tag{6.3}$$

$$\Rightarrow \mathrm{Im}\left(\mathcal{T}T_* + \sqrt{\lambda_0^2 T_*^2 - 2\pi L T_* + \pi^2} - \pi\right) = 0 \tag{6.4}$$

$$\Rightarrow \mathrm{Im}\left(\sqrt{\lambda_0^2 T_*^2 - 2\pi L T_* + \pi^2}\right) = \mathrm{Im}(-\mathcal{T}T_*) \tag{6.5}$$

$$\Rightarrow \sqrt{\lambda_0^2 T_*^2 - 2\pi L T_* + \pi^2} = -\mathcal{T}T_* + r \tag{6.6}$$

where r is a real number. Squaring both sides of Eq. (6.6) gives:

$$\lambda_0^2 T_*^2 - 2\pi L T_* + \pi^2 = \mathcal{T}^2 T_*^2 - 2\mathcal{T}T_* r + r^2 \tag{6.7}$$

The imaginary part of Eq. (6.7) is:

$$T_*^2 \mathrm{Im}(\lambda_0^2 - \mathcal{T}^2) - 2\pi T_* \mathrm{Im}(L) + 2T_* r \mathrm{Im}(\mathcal{T}) = 0 \tag{6.8}$$

For any value of r, one solution of this equation is $T_* = 0$ (which obviously a solution of Eq. (6.3)). For $T_* \neq 0$ and $\mathrm{Im}(\mathcal{T}) \neq 0$, we have:

$$r = \frac{T_* \mathrm{Im}(\mathcal{T}^2 - \lambda_0^2) + 2\pi \mathrm{Im}(L)}{2\mathrm{Im}(\mathcal{T})} = \frac{T_*(\mathcal{T}_{\mathrm{r}}\mathcal{T}_{\mathrm{i}} - \lambda_{\mathrm{r}}\lambda_{\mathrm{i}}) + \pi L_{\mathrm{i}}}{\mathcal{T}_{\mathrm{i}}} \tag{6.9}$$

where we substituted $\mathcal{T} = \mathcal{T}_{\mathrm{r}} + i\mathcal{T}_{\mathrm{i}}$, $\lambda_0 = \lambda_{\mathrm{r}} + i\lambda_{\mathrm{i}}$ and $L = L_{\mathrm{r}} + iL_{\mathrm{i}}$. Inserting this r into

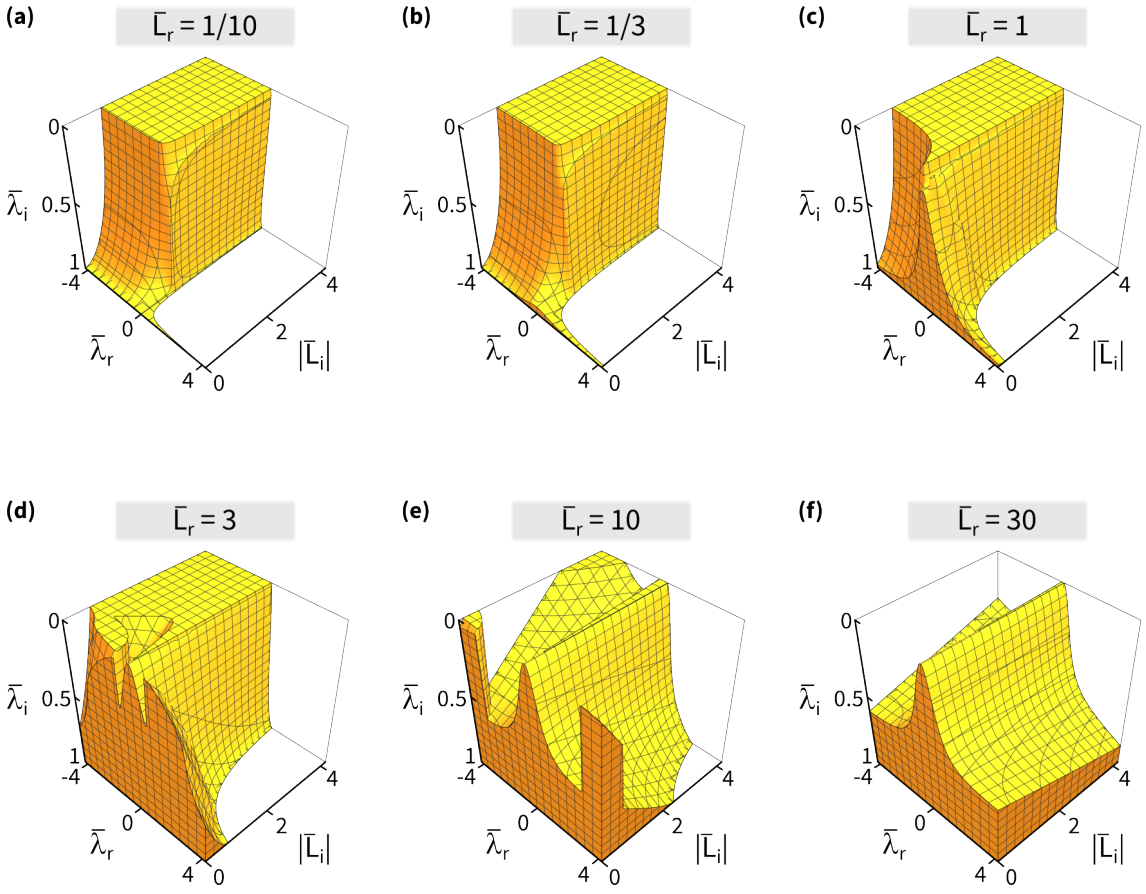

Figure 6.2: Range of "simple" control loops that result in SSGG - part I. (a) Golden region: The range of $\{\overline{\lambda}_{\rm i}, \overline{\lambda}_{\rm r}, |\overline{L}_{\rm i}|\}$ with $\overline{L}_{\rm r} = 1/10$, that can produce SSGG when $\mathrm{Im}(\phi(T))$ intersects the lower boundary of $\mathbf{\Gamma}$ (Sec. 6.2.1.1). The over-bar denotes normalization by $\mathcal{T}_{\rm i}$. **(b-f)** Same as (a) but for $\overline{L}_{\rm r} = \{1/3, 1, 3, 10, 30\}$, respectively. For this analysis, we found that $\{\overline{L}_{\rm i}, \overline{\lambda}_{\rm r}\} \rightarrow \{-\overline{L}_{\rm i}, -\overline{\lambda}_{\rm r}\}$ leaves the SSGG region unchanged.

the real part of Eq. (6.7) and performing some algebraic simplification results in:

$$(\mathcal{T}_{\rm i}^2 - \lambda_{\rm i}^2)(\mathcal{T}_{\rm i}^2 + \lambda_{\rm r}^2)T_*^2 + 2\pi(L_{\rm i}\lambda_{\rm r}\lambda_{\rm i} - \mathcal{T}_{\rm i}^2 L_{\rm r})T_* + \pi^2(\mathcal{T}_{\rm i}^2 - L_{\rm i}^2) \tag{6.10}$$

This is a quadratic equation in T_* with all real coefficients. Its roots $T_\pm$ are guaranteed to be real if its discriminant is positive. This constraint is given by:

$$(L_{\rm i}\lambda_{\rm r}\lambda_{\rm i} - \mathcal{T}_{\rm i}^2 L_{\rm r})^2 - (\mathcal{T}_{\rm i}^2 - \lambda_{\rm i}^2)(\mathcal{T}_{\rm i}^2 + \lambda_{\rm r}^2)(\mathcal{T}_{\rm i}^2 - L_{\rm i}^2) > 0 \tag{6.11}$$

Thus, condition (b) is satisfied for $T_* = T_\pm$ together with the constraint given by Eq. (6.11). To produce SSGG, a loop must satisfy condition (a), which amounts to the requirement that either $T_{\rm ad} < T_- < T_c$ or $T_{\rm ad} < T_+ < T_c$. These two conditions define the range of the five parameters $\{\mathcal{T}_{\rm i}, \lambda_{\rm r}, \lambda_{\rm i}, L_{\rm r}, L_{\rm i}\}$ over which SSGG occurs. We note that $\mathcal{T}_{\rm r}$ does not appear in any of these expressions. This range is shown in Fig. 6.2, from which it is clear that SSGG can be produced by a wide range of "simple" control loops even when we just consider intersecting the lower boundary of $\mathbf{\Gamma}$.

6.2.1.2 Intersecting the left boundary of $\mathbf{\Gamma}$

$\mathrm{Im}(\phi(T))$ intersects the left boundary of $\mathbf{\Gamma}$ i.e. at $T = T_{\rm ad}$ if it satisfies the following condition:

$$\textbf{(a)}\ \ 0 < \mathrm{Im}(\phi(T_{\rm ad})) < -\mathrm{Im}(\phi_B)$$

where $T_{\rm ad}$ is the same as in Sec. 6.2.1.1 and $\phi_B = \pi\,(L/\lambda_0 + 1)$.

This condition is straightforward to numerically evaluate and similar to the previous case (Sec. 6.2.1.1), it defines a range of the five parameters $\{\mathcal{T}_{\rm i}, \lambda_{\rm r}, \lambda_{\rm i}, L_{\rm r}, L_{\rm i}\}$ over which SSGG occurs. We note that similar to Sec. 6.2.1.1, $\mathcal{T}_{\rm r}$ does not appear this evaluation. This range is shown in Fig. 6.3, which supplements the range of "simple" control loops that produce SSGG.

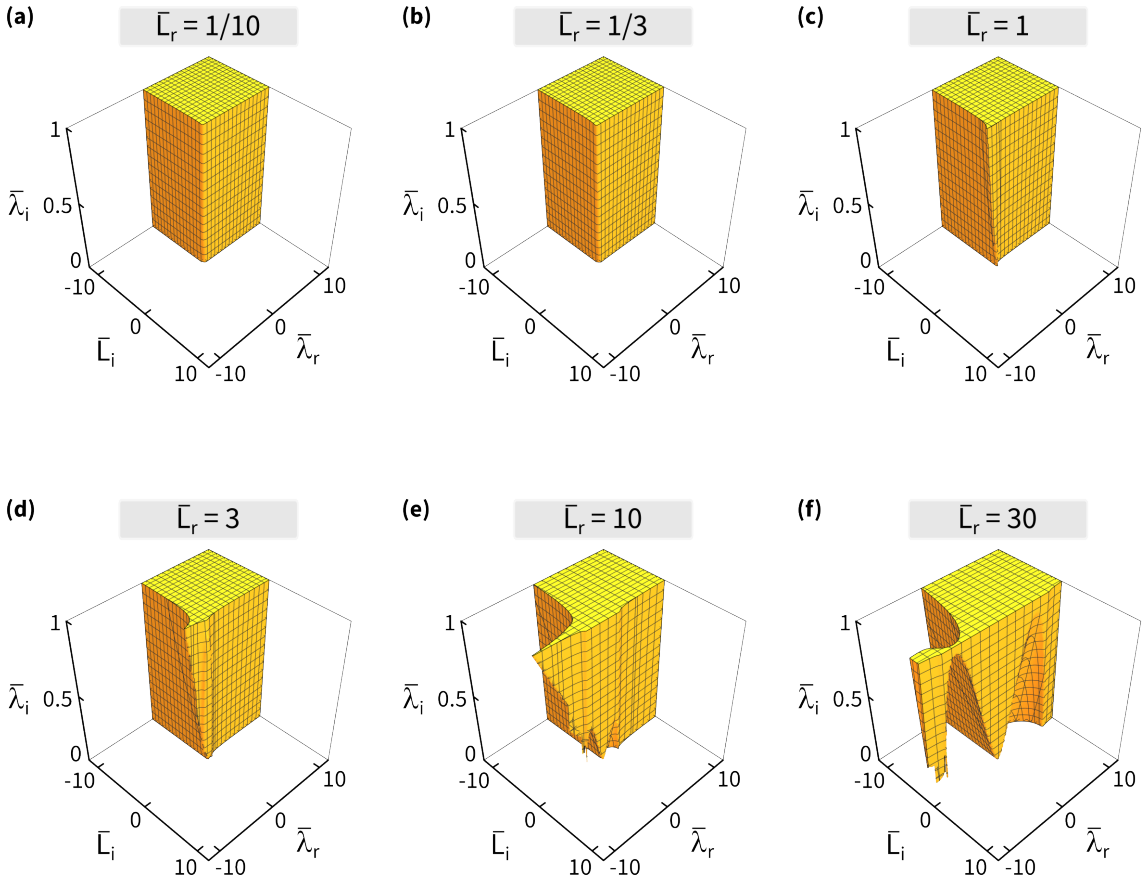

Figure 6.3: Range of "simple" control loops that result in SSGG - part II. (a) Golden region: The range of $\{\overline{\lambda}_{\rm i}, \overline{\lambda}_{\rm r}, |\overline{L}_{\rm i}|\}$ with $\overline{L}_{\rm r} = 1/10$, that can produce SSGG when $\mathrm{Im}(\phi(T))$ intersects the left boundary of $\mathbf{\Gamma}$ (Sec. 6.2.1.2). The over-bar denotes normalization by $\mathcal{T}_{\rm i}$. **(b-f)** Same as (a) but for $\overline{L}_{\rm r} = \{1/3,\ 1,\ 3,\ 10,\ 30\}$, respectively.

6.2.1.3 Intersecting the upper boundary of $\mathbf{\Gamma}$

$\mathrm{Im}(\phi(T))$ intersects the upper boundary of $\mathbf{\Gamma}$ if there is a loop duration T_* such that the following two conditions hold:

$$\textbf{(a)}\ \ T_{\mathrm{ad}} < T_* < T_c/2$$

$$\textbf{(b)}\ \ \mathrm{Im}(\phi(T_*)) = -\mathrm{Im}(\phi_B)$$

where T_{ad}, T_c are the same as in Sec. 6.2.1.1 and $\phi_B = \pi\,(L/\lambda_0 + 1)$.

To obtain an analytic expression for this case, we repeat the procedure outlined in Sec. 6.2.1.1. Considering condition (b) first, we rewrite it as:

$$\mathrm{Im}(\phi(T_*)) = -\mathrm{Im}(\phi_B) \tag{6.12}$$

$$\Rightarrow \mathrm{Im}\left(\mathcal{T}T_* + \sqrt{\lambda_0^2 T_*^2 - 2\pi L T_* + \pi^2} - \pi\right) = -\mathrm{Im}(\phi_B) \tag{6.13}$$

$$\Rightarrow \mathrm{Im}\left(\sqrt{\lambda_0^2 T_*^2 - 2\pi L T_* + \pi^2}\right) = \mathrm{Im}(-\mathcal{T}T_* - \phi_B) \tag{6.14}$$

$$\Rightarrow \sqrt{\lambda_0^2 T_*^2 - 2\pi L T_* + \pi^2} = -\mathcal{T}T_* - \phi_B + r \tag{6.15}$$

where r is a real number. Squaring both sides of Eq. (6.15) gives:

$$\lambda_0^2 T_*^2 - 2\pi L T_* + \pi^2 = (\mathcal{T}T_* + \phi_B)^2 - 2(\mathcal{T}T_* + \phi_B)r + r^2 \tag{6.16}$$

The imaginary part of Eq. (6.16) is:

$$\mathrm{Im}((\mathcal{T}T_* + \phi_B)^2) - T_*^2\mathrm{Im}(\lambda_0^2) + 2\pi T_*\mathrm{Im}(L) - 2r\mathrm{Im}(\mathcal{T}T_* + \phi_B) = 0 \tag{6.17}$$

For $\{T_*, \mathrm{Im}(\mathcal{T}), \mathrm{Im}(\phi_B)\} \neq 0$, we have:

$$\begin{aligned} r &= \frac{\mathrm{Im}((\mathcal{T}T_* + \phi_B)^2) - T_*^2\mathrm{Im}(\lambda_0^2) + 2\pi T_*\mathrm{Im}(L)}{2\mathrm{Im}(\mathcal{T}T_* + \phi_B)} \\ &= \mathcal{T}_{\mathrm{r}}T_* + \phi_{B,\mathrm{r}} - T_*\left(\frac{\lambda_{\mathrm{r}}\lambda_{\mathrm{i}}T_* - \pi L_{\mathrm{i}}}{\mathcal{T}_{\mathrm{i}}T_* + \phi_{B,\mathrm{i}}}\right) \end{aligned} \tag{6.18}$$

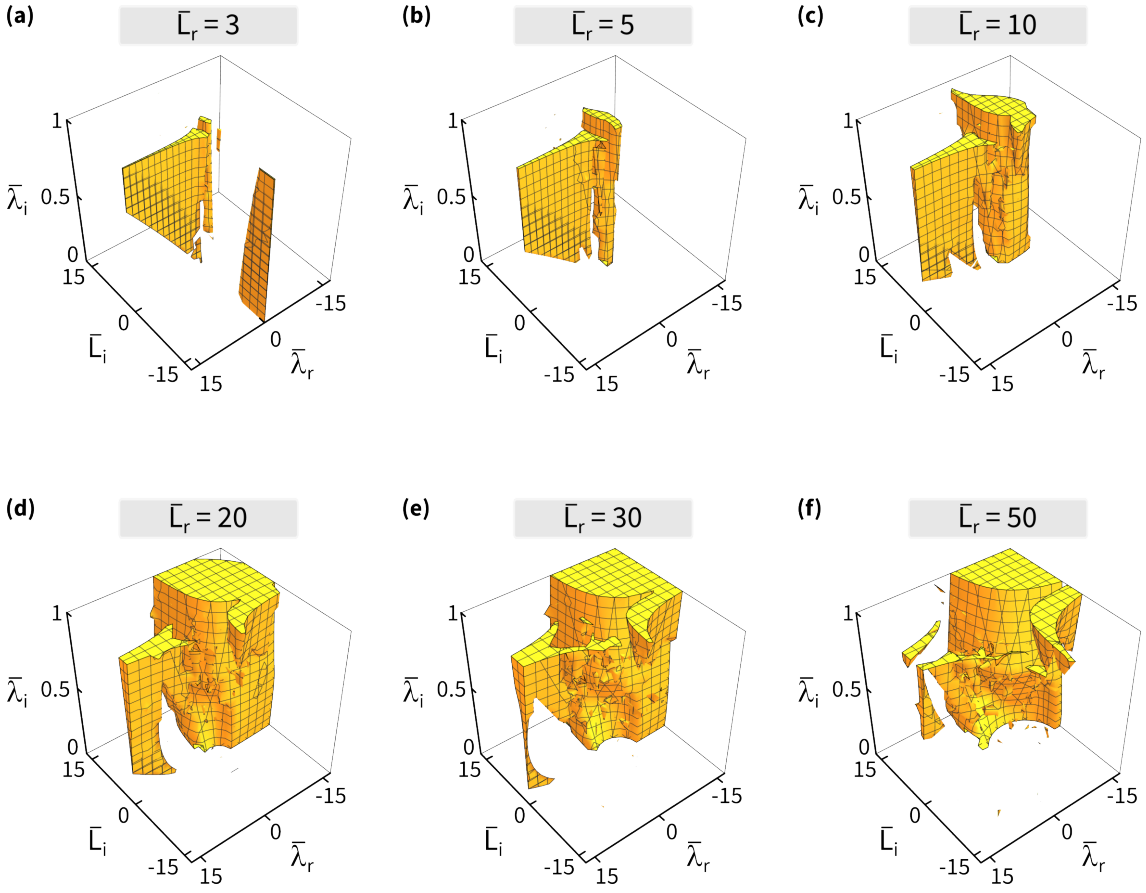

Figure 6.4: Range of "simple" control loops that result in SSGG - part III. (a) Golden region: The range of $\{\overline{\lambda}_{\rm i}, \overline{\lambda}_{\rm r}, |\overline{L}_{\rm i}|\}$ with $\overline{L}_{\rm r} = 3$, that can produce SSGG when $\mathrm{Im}(\phi(T))$ intersects the upper boundary of $\mathbf{\Gamma}$ (Sec. 6.2.1.3). The over-bar denotes normalization by $\mathcal{T}_{\rm i}$. **(b-f)** Same as (a) but for $\overline{L}_{\rm r} = \{5, 10, 20, 30, 50\}$, respectively.

where we substituted $\mathcal{T} = \mathcal{T}_\mathrm{r} + i\mathcal{T}_\mathrm{i}, \lambda_0 = \lambda_\mathrm{r} + i\lambda_\mathrm{i}$ and $L = L_\mathrm{r} + iL_\mathrm{i}, \phi_B = \phi_{B,\mathrm{r}} + i\phi_{B,\mathrm{i}}$. Inserting this r into the real part of Eq. (6.16) and performing some algebraic simplification results in a quartic equation:

$$(\mathcal{T}_\mathrm{i}T_* + \phi_{B,\mathrm{i}})^4 - (\lambda_\mathrm{r}^2 - \lambda_\mathrm{i}^2)(\mathcal{T}_\mathrm{i}T_* + \phi_{B,\mathrm{i}})^2T_*^2 - 2\pi L_\mathrm{r}T_*(\mathcal{T}_\mathrm{i}T_* + \phi_{B,\mathrm{i}})^2 \\ -T_*^2(\lambda_\mathrm{r}\lambda_\mathrm{i}T_* - \pi L_\mathrm{i})^2 + \pi^2(\mathcal{T}_\mathrm{i}T_* + \phi_{B,\mathrm{i}})^2 = 0 \tag{6.19}$$

and curiously, this expression is devoid of $\mathcal{T}_\mathrm{r}$, as in the previous cases and $\phi_{B,\mathrm{r}}$.

Condition (b) is therefore satisfied by the real roots of Eq. (6.19). If these real roots satisfy condition (a), they define the range of the five parameters $\{\mathcal{T}_\mathrm{i}, \lambda_\mathrm{r}, \lambda_\mathrm{i}, L_\mathrm{r}, L_\mathrm{i}\}$ over which SSGG occurs. This range is shown in Fig. 6.4, and they continue to supplement the range of "simple" control loops that produce SSGG.

6.2.1.4 Intersecting the right boundary of $\mathbf{\Gamma}$

$\mathrm{Im}(\phi(T))$ intersects the right boundary of $\mathbf{\Gamma}$ if there is a loop duration T_* such that the following two conditions hold:

(a) $\max(T_\mathrm{ad}, T_c/2) < T_* < T_c$

(b) $\mathrm{Im}(\phi(T_*)) = \mathrm{Im}(\phi_D - 2\phi_B)$

where T_ad, T_c and ϕ_B are the same as in Sec. 6.2.1.1.

To obtain an analytic expression for this case, we adapt the procedure outlined in Sec. 6.2.1.1. Considering condition (b) first, we rewrite it as:

$$\mathrm{Im}(\phi(T_*)) = \mathrm{Im}(\phi_D - 2\phi_B) \tag{6.20}$$

$$\Rightarrow \mathrm{Im}\left(\mathcal{T}T_* + \sqrt{\lambda_0^2T_*^2 - 2\pi LT_* + \pi^2} - \pi\right) = \mathrm{Im}(\mathcal{T}T_* - 2\phi_B) \tag{6.21}$$

$$\Rightarrow \sqrt{\lambda_0^2T_*^2 - 2\pi LT_* + \pi^2} = -2\phi_B + r \tag{6.22}$$

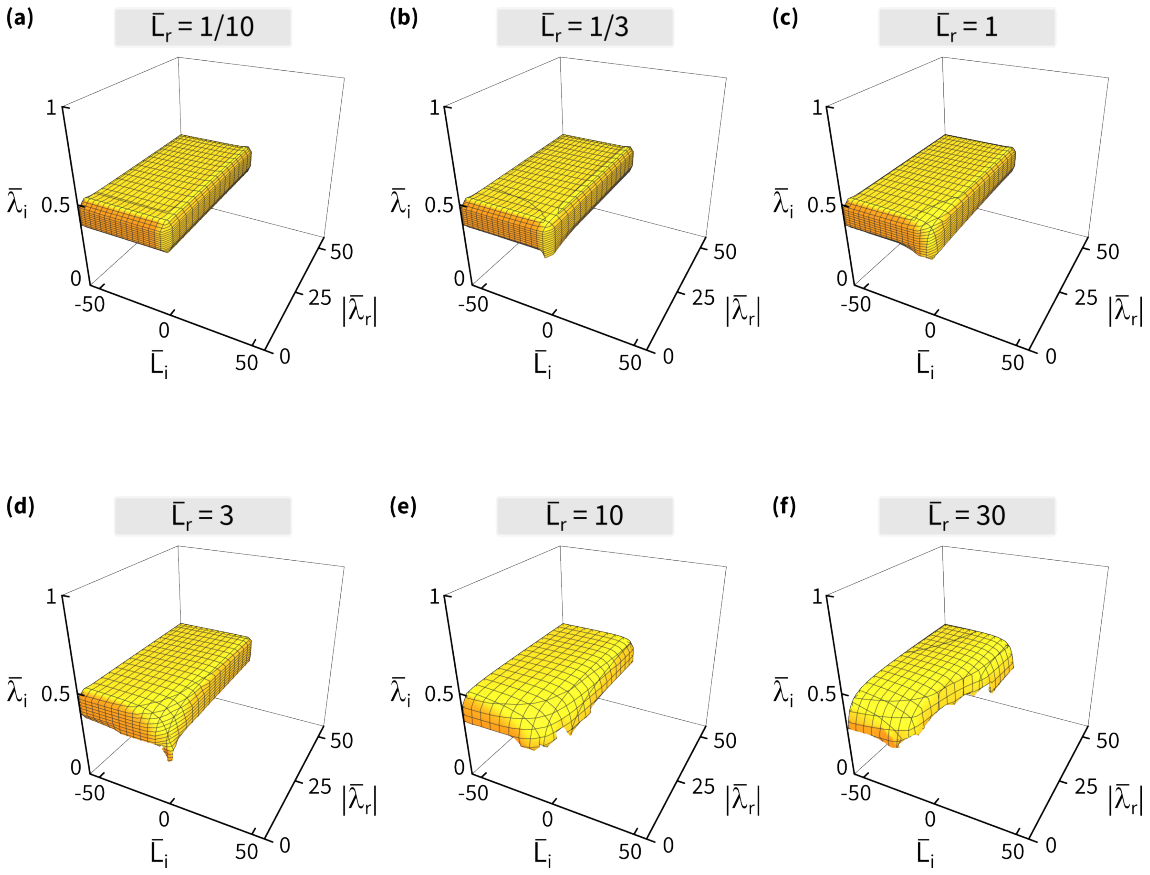

Figure 6.5: Range of "simple" control loops that result in SSGG - part IV. (a) Golden region: The range of $\{\overline{\lambda}_{\rm i}, \overline{\lambda}_{\rm r}, |\overline{L}_{\rm i}|\}$ with $\overline{L}_{\rm r} = 1/10$, that can produce SSGG when $\mathrm{Im}(\phi(T))$ intersects the right boundary of $\mathbf{\Gamma}$ (Sec. 6.2.1.4). The over-bar denotes normalization by $\mathcal{T}_{\rm i}$. **(b-f)** Same as (a) but for $\overline{L}_{\rm r} = \{1/3,\ 1,\ 3,\ 10,\ 30\}$, respectively. For this analysis, we found that $\{\overline{L}_{\rm i}, \overline{\lambda}_{\rm r}\} \rightarrow \{-\overline{L}_{\rm i}, -\overline{\lambda}_{\rm r}\}$ leaves the SSGG region unchanged.

where r is a real number. Squaring both sides of Eq. (6.15) gives:

$$\lambda_0^2 T_*^2 - 2\pi L T_* + \pi^2 = 4\phi_B^2 - 4r\phi_B + r^2 \tag{6.23}$$

The imaginary part of Eq. (6.23) is:

$$T_*^2 \mathrm{Im}(\lambda_0^2) - 2\pi T_* \mathrm{Im}(L) - 4\mathrm{Im}(\phi_B^2) + 4r\mathrm{Im}(\phi_B) = 0 \tag{6.24}$$

For $\{T_*, \mathrm{Im}(\phi_B)\} \neq 0$, we have:

$$\begin{aligned} r &= \frac{2\pi T_* \mathrm{Im}(L) + 4\mathrm{Im}(\phi_B^2) - T_*^2 \mathrm{Im}(\lambda_0^2)}{4\mathrm{Im}(\phi_B)} \\ &= 2\phi_{B,\mathrm{r}} + T_* \left(\frac{\pi L_\mathrm{i} - \lambda_\mathrm{r} \lambda_\mathrm{i} T_*}{2\phi_{B,\mathrm{i}}} \right) \end{aligned} \tag{6.25}$$

where we substituted $\lambda_0 = \lambda_\mathrm{r} + i\lambda_\mathrm{i}$ and $L = L_\mathrm{r} + iL_\mathrm{i}, \phi_B = \phi_{B,\mathrm{r}} + i\phi_{B,\mathrm{i}}$. Inserting this r into the real part of Eq. (6.23) and performing some algebraic simplification, we get a quartic equation:

$$4\phi_{B,\mathrm{i}}^2(\lambda_\mathrm{r}^2 - \lambda_\mathrm{i}^2)T_*^2 - (\pi L_\mathrm{i} T_* - \lambda_\mathrm{r}\lambda_\mathrm{i} T_*^2)^2 - 8\pi\phi_{B,\mathrm{i}}^2 L_\mathrm{r} T_* + 4\pi^2 \phi_{B,\mathrm{i}}^2 + 16\phi_{B,\mathrm{i}}^4 = 0 \tag{6.26}$$

where we note that $\mathcal{T}$ does not appear in any of these expressions, while Eq. (6.26) is devoid of $\phi_{B,\mathrm{r}}$.

Condition (b) is satisfied by the real roots of Eq. (6.26). If these real roots satisfy condition (a), they define the range of the five parameters $\{\mathcal{T}_\mathrm{i}, \lambda_\mathrm{r}, \lambda_\mathrm{i}, L_\mathrm{r}, L_\mathrm{i}\}$ over which SSGG occurs. This range is shown in Fig. 6.5, and they add on to the range of "simple" control loops that produce SSGG.

In conclusion, the full range of "simple" control loops that produce SSGG is given by the union of individual regions from each case, and as such they are fairly abundant. The union of these regions is explicitly shown in Fig. 6.6. An experimental demonstration of SSGG using a similar control loop is illustrated in Sec. 6.3.1.

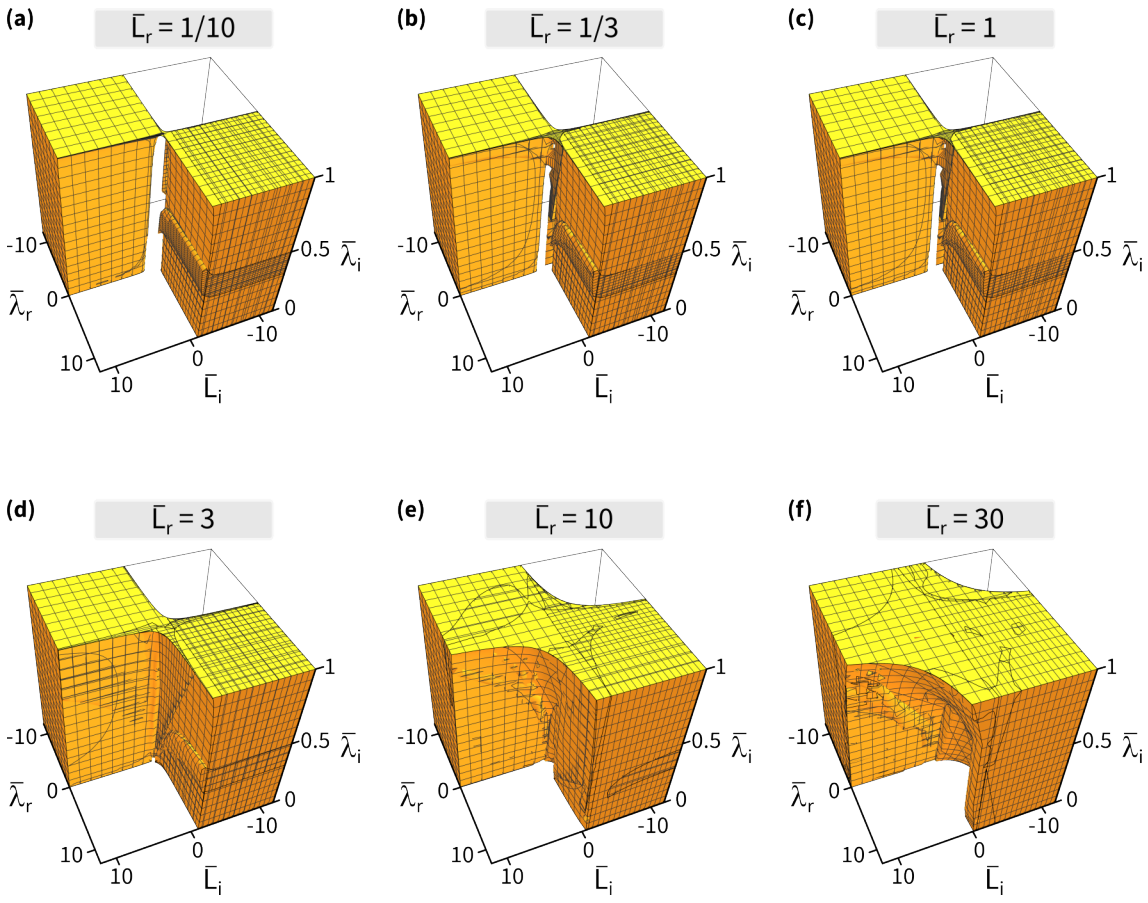

Figure 6.6: Union of all "simple" control loop ranges that result in SSGG. (a) Golden region: The range of $\{\overline{\lambda}_{\rm i}, \overline{\lambda}_{\rm r}, \overline{L}_{\rm i}\}$ with $\overline{L}_{\rm r} = 1/10$, that can produce SSGG, when all four cases discussed for "simple" control loops in Sec. 6.2.1 are combined together. The over-bar denotes normalization by $\mathcal{T}_{\rm i}$. **(b-f)** Same as (a) but for $\overline{L}_{\rm r} = \{1/3, 1, 3, 10, 30\}$, respectively.

6.2.2 SSGG with "non-simple" control loops

In this section, we identify a family of "non-simple" control loops that produce SSGG. These control loops are parameterized via

$$H = \mathbf{B}.\vec{\sigma} + (\mathcal{T}/2)\ \mathbb{I} \tag{6.27}$$

with

$$\begin{aligned} \mathcal{T} &= 0 - 10i \\ [\mathbf{B}.\mathbf{x}]\,(s) &= -a\left(1 + \tfrac{20}{23}i\right)\sqrt{1 + 6f_1(s)}\mathrm{Cos}(f_2(s)) \\ [\mathbf{B}.\mathbf{y}]\,(s) &= -b\left(1 + \tfrac{20}{23}i\right)\sqrt{1 + 6f_1(s)}\mathrm{Sin}(f_2(s)) \\ [\mathbf{B}.\mathbf{z}]\,(s) &= -c\left(1 + \tfrac{1}{6}i\right)f_1(s) + 27 + \tfrac{3}{20}i \end{aligned} \tag{6.28}$$

and

$$f_1(s) = \mathrm{Sin}\left(\pi s + \tfrac{1}{4}\mathrm{Sin}\left(2\pi s\right)\right)^2,\ f_2(s) = \tfrac{2\pi}{3}\mathrm{Sin}\left(2\pi s + \tfrac{1}{2}\mathrm{Sin}\left(2\pi s\right)\right) \tag{6.29}$$

where $\{a, b, c\}$ are real-valued parameters that set the lengths of the three complex components of $\mathbf{B}$. These "non-simple" control loops qualitatively differ from their "simple" counter parts as in this case, $\mathbf{B}$ does not make a full rotation around the z-axis at the end of the control loop. Such "non-simple" control loops have been previously investigated in Sec. 5.2.2.2 (control loop family iii) and illustrated in Fig. 5.8(e,f). An example of one such loop in shown in Fig. 6.7(a).

To identify control loops that produce SSGG, we calculated their static properties, numerically integrated Eq. (2.80) as a function of loop duration T and checked if the calculated $\mathrm{Im}(\phi(T))$ passes through the region $\mathbf{\Gamma}$ (Sec. 6.1), for various $\{a, b, c\}$. A typical example of $\mathrm{Im}(\phi(T))$ resulting from one such solution is shown in Fig. 6.7(b). For this example, $\{a, b, c\} = \{5, 5, 5\}$ and $\mathrm{Im}(\phi(T))$ lies with $\mathbf{\Gamma}$ for $0.185 \leq T \leq 0.459$.

Fig. 6.7(c,d) illustrate the result of performing this analysis for values of $\{a, b, c\}$ ranging from -10 to 10, in increments of 0.2. Each value of $\{a, b, c\}$ that satisfies Conditions

(1-4) (Sec. 6.1) and hence, for which $\mathrm{Im}(\phi(T))$ passes through $\mathbf{\Gamma}$ is represented by the golden region. As with the "simple" control loops considered in Sec. 6.2.1, SSGG occurs over a substantial range of this "non-simple" control loop parameters. An experimental demonstration of SSGG using one such control loop is illustrated in Sec. 6.3.2.

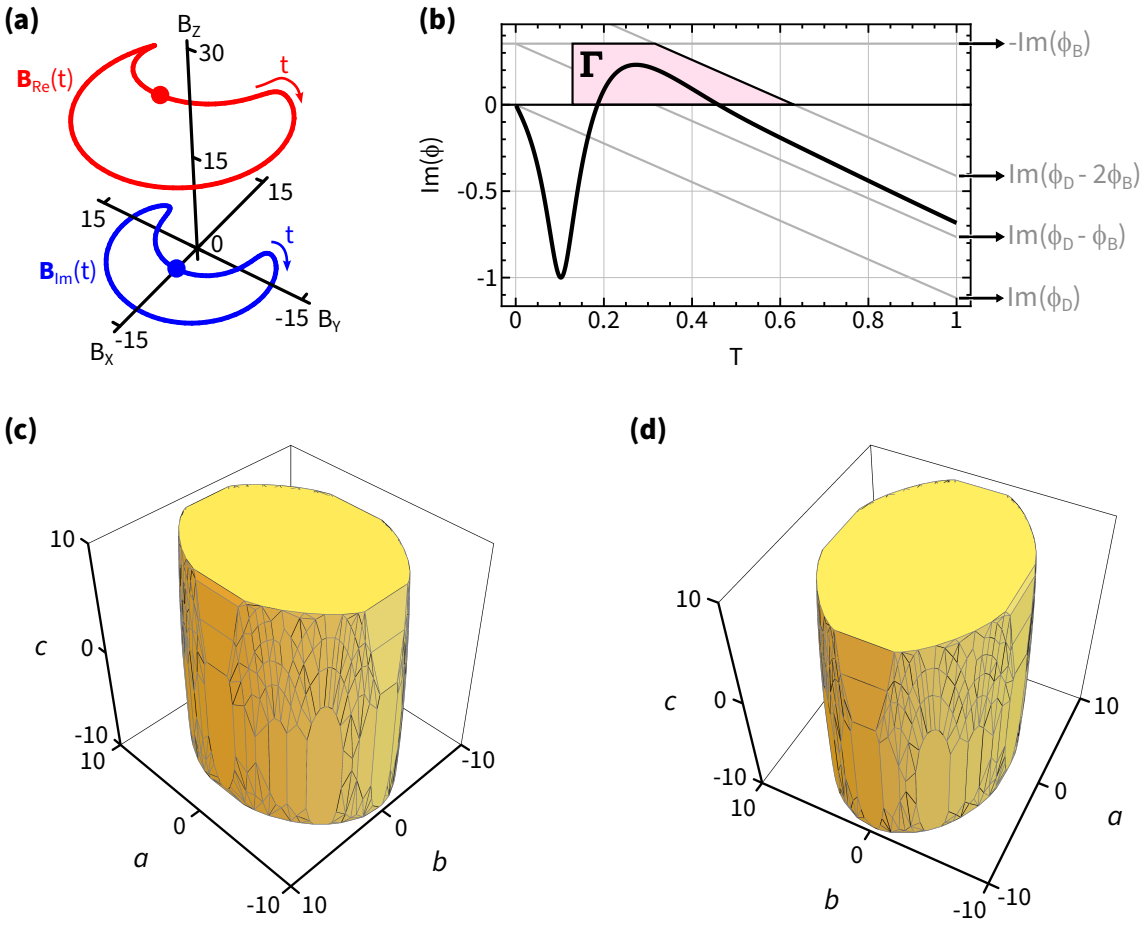

Figure 6.7: Range of a class of "non-simple" control loops that result in SSGG. (a) A "non-simple" control loop parameterized by Eqs.(6.27)-(6.29) with $\{a, b, c\} = \{5, 5, 5\}$. Circles: the starting and the stopping point of the loop, at $t = 0, T$, respectively; red and blue curves: $\mathbf{B}_{\mathrm{Re,Im}}$, respectively; arrows are a guide to the eye. **(b)** For the same choice $\{a, b, c\}$ as in panel (a), black curve: $\mathrm{Im}(\phi(T))$, pink: the region $\mathbf{\Gamma}$. For these parameters, $T_{\mathrm{ad}} = 0.185$ and $T_c = 0.459$. **(c)** Golden region: The range of $\{a, b, c\}$ that can produce SSGG (Sec. 6.1). All points that satisfy the conditions that result in SSGG are visually inspected for features such as "voids", by plotting them independently in the 3D parameter space spanned by $\{a, b, c\}$ using Ref. [248]. No systematic voids were discovered, and subsequently in order to improve visualization, they are represented as a planar convex hull [249]. **(d)** Same as (c) but with a different view.

6.3 Measuring SSGG

In this section, we experimentally demonstrate SSGG for two distinct families of control loops, $\mathcal{C}_{\rm amp}$. These measurements are carried out in the same manner as those described in Chapter 5 and they both employ "non-simple" control loops (Sec. 5.2.2.2). These control loops can be parameterized as: $\vec{X}(s) = (P_1, P_2(s), \delta(s), \eta, \theta_{12}(s))$, with a modest helping of a blue-detuned control tone to provide some anti-damping. This setup allows us to make the loss small enough (though non-zero) for SSGG to fully compensate it.

6.3.1 Control loop family I

The first family of $\mathcal{C}_{\rm amp}$ is given by:

$$\vec{X}_{\rm I}(s) = \Big(P_1, P_{2,0} + P_{2,1}{\rm Sin}(2\pi s)^2, \delta, \eta, 2\pi s\Big)$$

where $s = \pm t/T, t \in [0, T]$, and the control parameters are: $P_1 =$ 21 μW, $\delta/2\pi =$ -1.007 MHz, $\eta/2\pi = -50$ Hz, $P_{2,0} =$ 15 μW and $P_{2,1} =$ 20 μW. The additional blue-detuned tone applied during the control loop had $P_4 =$ 25 μW and $\Delta_4/2\pi =$ $+3.5$ MHz. Membrane modes (3,3) and (5,3) were used for these measurements. Fig. 6.9(a) illustrates this control loop in terms of the two three-vectors $\mathbf{B}_{\rm Re,Im}$.

Prior to any real time dynamics measurements of SSGG, we explicitly verified the existence of a unique least-dissipative eigenvector for the entirety of the control loop $\mathcal{C}_{\rm amp}$ (condition (1) for SSGG, Sec. 6.1) by performing mechanical spectroscopy measurement along it and obtaining $\boldsymbol{\lambda}$[1]. This is shown in Fig. 6.8, and its panels (c,d) explicitly verify condition (1) for SSGG. It also confirms: ${\rm Im}(\phi_D) = T\int_0^1 {\rm Im}(\lambda_+(s))ds < 0$ (condition (3) for SSGG, Sec. 6.1) as ${\rm Im}(\lambda_+(s)) < 0$ for $0 \leq s \leq 1$. The measurements of $\boldsymbol{\lambda}$ are plotted along with the no-free-parameter theory prediction (solid black curves), and they are in good agreement.

The timing sequence for the real time dynamics measurements is shown in Fig. 6.9(b). Fig. 6.9(c) shows the gain i.e., ${\rm Im}(\phi)$ corresponding to the least-dissipative normal mode

[1]Quick reminder that the eigenvalues $\boldsymbol{\lambda}$ are independent of the beat-note phase θ_{12}.

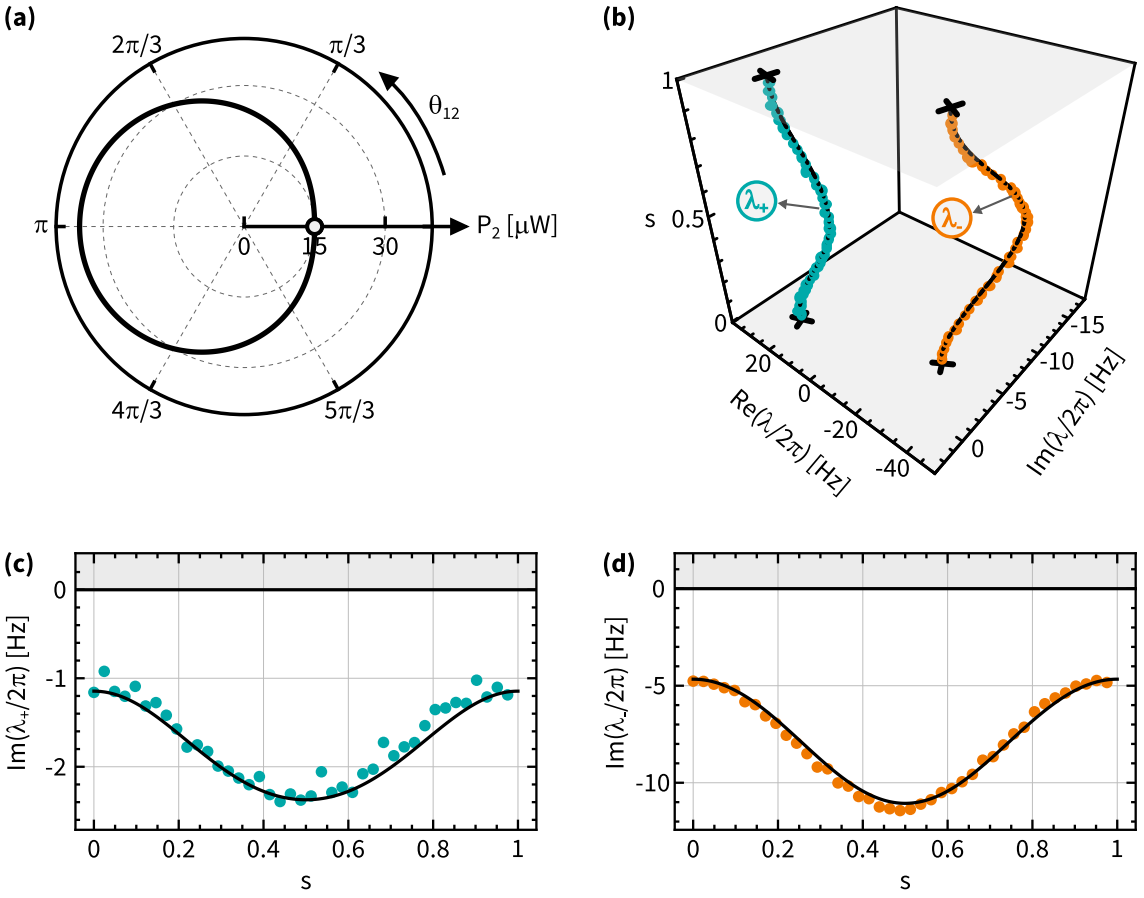

Figure 6.8: Verifying conditions for achieving SSGG: for Control loop family I. (a) Control loop $\mathcal{C}_{\text{amp}}$ from family I (Sec. 6.3.1) plotted in (P_2, θ_{12}) plane, shown as solid black curve. White disk indicates the starting $(s = 0)$ and the ending $(s = 1)$ point of $\mathcal{C}_{\text{amp}}$. **(b)** Eigenvalues $\boldsymbol{\lambda}$ corresponding to a single traversal of $\mathcal{C}_{\text{amp}}$ in (a), as a function of $0 \leq s \leq 1$. Cyan (orange) points: measurement corresponding to $\lambda_+(\lambda_-)$ when P_2 is varied along $\mathcal{C}_{\text{amp}}$, while θ_{12} is held fixed. Recall that $\boldsymbol{\lambda}$ is independent of θ_{12}. Black curves: no-free-parameter theory prediction of $\boldsymbol{\lambda}$. The black crosses show $\boldsymbol{\lambda}$ at the basepoint $s = 0 = 1$. **(c,d)** Same as (b), but showing only $\text{Im}(\lambda_+)$ and $\text{Im}(\lambda_-)$ versus $0 \leq s \leq 1$ along $\mathcal{C}_{\text{amp}}$, respectively. For all s, we have a unique least-dissipative eigenvector and it is damped ($\text{Im}(\lambda_+(s)) < 0$ for $s \in [0, 1]$) for the entirety of $\mathcal{C}_{\text{amp}}$, thereby verifying conditions (1) and (3) for SSGG (Sec. 6.1). For these measurements, we used the (3,3) and the (5,3) membrane modes with fixed control parameters during $\mathcal{C}_{\text{amp},n}$: $P_1 =$ 21 μW, $\delta/2\pi = -1.007$ MHz, $\eta/2\pi = -50$ Hz for the red-detuned laser tones and $P_4 =$ 25 μW, $\Delta_4/2\pi = +3.5$ MHz for the blue-detuned laser tone.

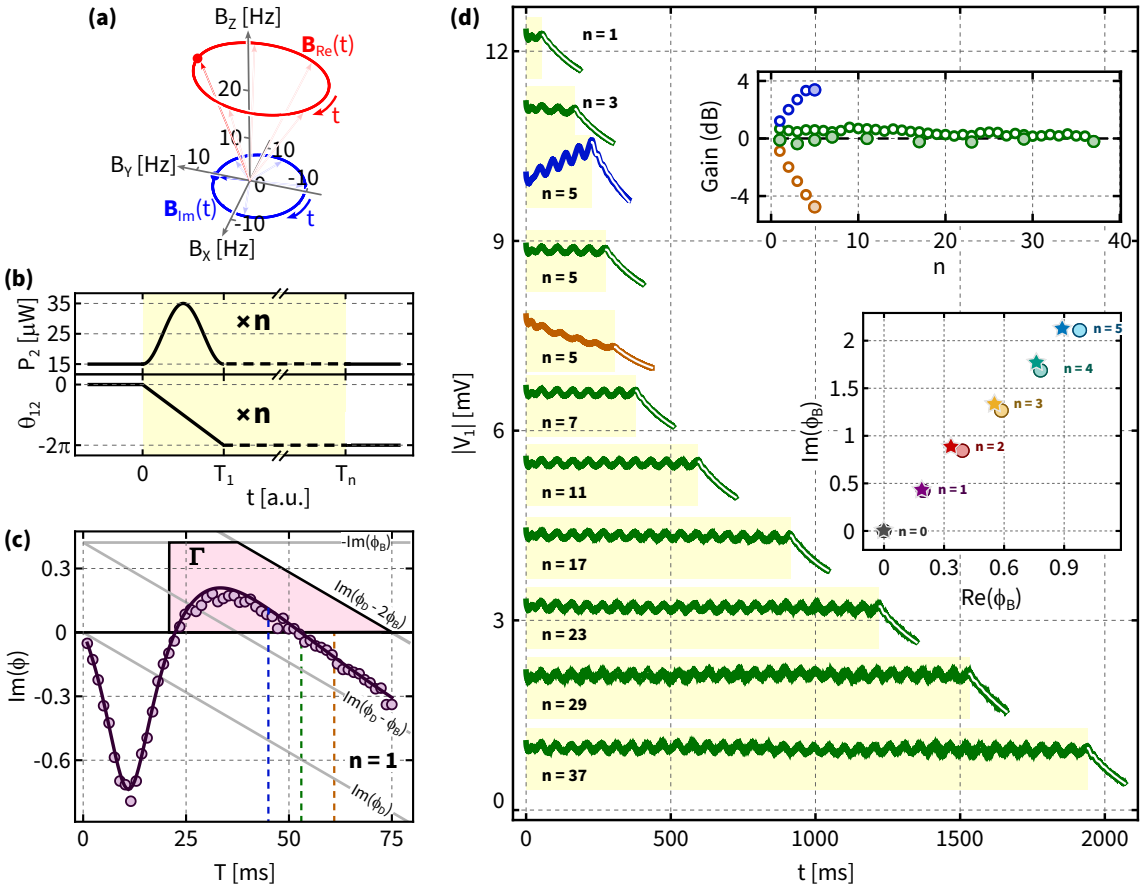

Figure 6.9: SSGG for Control loop family I. (a) The control loop $\mathcal{C}_{\mathrm{amp},1}$ visualized as two three-vectors $\mathbf{B}_{\mathrm{Re,Im}}$. **(b)** $P_2(t)$ and $\theta_{12}(t)$ during $\mathcal{C}_{\mathrm{amp},n}$. **(c)** The least-dissipative normal mode's gain $\mathrm{Im}(\phi)$ when $\mathcal{C}_{\mathrm{amp},1}$ is traversed once in duration T. Disks: data; black curve: no-free-parameter theory prediction; pink shaded area: the region $\mathbf{\Gamma}$ that results in SSGG. Blue, green and orange dashed vertical lines: values of T used in (d). **(d)** Green curves: the amplitude of the mode's motion during loops $\mathcal{C}_{\mathrm{amp},n}$ for $T = 52$ ms; blue and orange curves: the amplitude of the mode's motion during loops $\mathcal{C}_{\mathrm{amp},n}$ for $T = 45$ ms and 61 ms, respectively. Each curve is vertically offset by 1 mV, so that $|V_1| = 0$ corresponds to the bottom of the yellow band. White curves: fit to ringdown data (Sec. D.2). Upper inset: a summary of the gain resulting from these loops. Filled circles: the gain from each $\mathcal{C}_{\mathrm{amp},n}$ in the main panel; green hollow circles: the gain after each circuit of the $n = 37$ loop; blue and orange hollow circles: the gain after each circuit of the $n = 5$ loop with $T = 45$ ms and 61 ms, respectively. Lower inset: ϕ_B for $\mathcal{C}_{\mathrm{amp},n}$. Stars: measured and disks: no-free-parameter theory prediction. For this measurement, we used the same membrane modes and the same other control parameters as in Fig. 6.8.

when it is transported along $\mathcal{C}_{\rm amp}$ for duration T. Despite the loss contributed by $\mathrm{Im}(\phi_D)$ (lowest gray line), the mode experiences a net gain for 22 ms $< T <$ 52 ms. For this example, $\mathrm{Im}(\phi(T)) > 0$ lies entirely within $\mathbf{\Gamma}$ (pink region in Fig. 6.9(c)), and thus is attributable to the geometric gain (condition (4) for SSGG, Sec. 6.1).

As expected, $\mathrm{Im}(\phi_D)$ dominates for large T, and results in net loss for $T >$ 52 ms. However as discussed in Secs. 2.2.3.5 and 6.1, net gain at arbitrarily large times (i.e., in the steady state) can be achieved simply by repeating $\mathcal{C}_{\rm amp}$ multiple times. This is demonstrated in Fig. 6.9(d), which shows the mode's amplitude of motion while $\mathcal{C}_{\rm amp}$ is repeated for $n = 37$ times (corresponding $T \sim 2$ s). The amplitude varies periodically, but returns to its initial value at the end of each repetition of $\mathcal{C}_{\rm amp}$. This "break-even" condition occurs because $\mathcal{C}_{\rm amp}$ of duration $T =$ 52 ms is chosen to provide a near-exact balance between the dynamical loss and the gain produced by traversing it (dashed vertical green line in Fig. 6.9(c)). For smaller (larger) values of T (dashed blue and orange vertical line in Fig. 6.9(c), respectively), each repetition of $\mathcal{C}_{\rm amp}$ results in net gain (loss).

The measured mode's motion corresponding to choosing T as a multiple of "break-even", net gain and net loss $\mathcal{C}_{\rm amp}$ durations (formally $\mathcal{C}_{{\rm amp},n}$) are illustrated in Fig. 6.9(d), as green, blue and orange curves, respectively. The gain obtained by traversing each $\mathcal{C}_{{\rm amp},n}$ are plotted in the top-inset of Fig. 6.9(d). The bottom-inset of Fig. 6.9(d) shows the geometric phase $\phi_{B,{\rm amp},n}$ for $\mathcal{C}_{{\rm amp},n}$ for $n \in \{0,1,2,3,4,5\}$. The agreement between the measurements (stars) with the no-free-parameter theory predictions of $\phi_{B,{\rm amp},n} = n\phi_{B,{\rm amp},1}$ (disks) indicates a facet of the fact that mode's motion is phase-coherent during the real time operations used in Fig. 6.9(c,d).

6.3.2 Control loop family II

The second family of $\mathcal{C}_{\rm amp}$ is given by:

$$\vec{X}_{\rm II}(s) = \left(P_1, P_{2,0} + P_{2,1} \left| \mathrm{Sin}(\pi s) + \frac{\mathrm{Sin}(2\pi s)^2}{4} \right|, \delta, \eta, \theta_{12,\rm m}\ \mathrm{Sin}\left(2\pi s + \frac{\mathrm{Sin}(2\pi s)}{2} \right) \right)$$

where $s = \pm t/T, t \in [0, T]$, and the control parameters are: $P_1 =$ 26 μW, $\delta/2\pi =$ -0.911 MHz, $\eta/2\pi = -50$ Hz, $P_{2,0} =$ 5 μW, $P_{2,1} =$ 30 μW and $\theta_{12,\mathrm{m}} = 2\pi/3$. The additional blue-detuned tone applied during the control loop had $P_4 =$ 28 μW, $\Delta_4/2\pi =$ $+3.38$ MHz, and we continued using membrane modes (3,3) and (5,3). Fig. 6.11(a) illustrates this control loop in terms of the two three-vectors $\mathbf{B}_{\mathrm{Re,Im}}$. In addition, we note that this family $\mathcal{C}_{\mathrm{amp}}$ is qualitatively distinct from the first family (Sec. 6.3.1) as in this case θ_{12} does not wind by 2π when it is completed. Additional measurements of ϕ_B for this family of control loops are described in Sec. 5.2.2.2 (control loop family iii) and illustrated in Fig. 5.8(e,f).

As in the previous case (Sec. 6.3.1), the first step is to explicitly verify conditions (1) and (3) for SSGG (Sec. 6.1) by measuring $\boldsymbol{\lambda}$ along $\mathcal{C}_{\mathrm{amp}}$ via mechanical spectroscopy. The verification is illustrated in Fig. 6.10, and the measurements (points in panels (b-d)) continue to be in good agreement with the no-free-parameter theory prediction (solid black curves).

Similar to the previous case (Sec. 6.3.1), the real time dynamics measurements are shown in Fig. 6.11. For this case, the least-dissipative eigenvector experiences net gain for 32 ms $< T <$ 58 ms. In particular, the corresponding $\mathrm{Im}(\phi(T))$ lies entirely within $\boldsymbol{\Gamma}$ and so is attributable to the geometric gain (condition (4) for SSGG, Sec. 6.1). As before, we sustain, amplify or controllably de-amplify the mode's motion for arbitrarily large times, by simply repeating this $\mathcal{C}_{\mathrm{amp}}$ for n-times. This is done by choosing T for a single traversal of $\mathcal{C}_{\mathrm{amp}}$ indicated by dashed green, blue and orange vertical lines, respectively in Fig. 6.11(c). This is demonstrated in Fig. 6.11(d) for a variety of n values with maximum $n = 37$ corresponding to $T >$ 2 s. The upper-panel in Fig. 6.11(d) is a record of the gains obtained from these measurements while the bottom-panel shows good agreement between the measured $\phi_{B,\mathrm{amp},n}$ (stars) with no-free-parameter theory prediction (disks) for $n \in \{0, 1, 2, 3, 4, 5\}$, and provides evidence of phase-coherence of the mode's motion during real time traversal of $\mathcal{C}_{\mathrm{amp}}$.

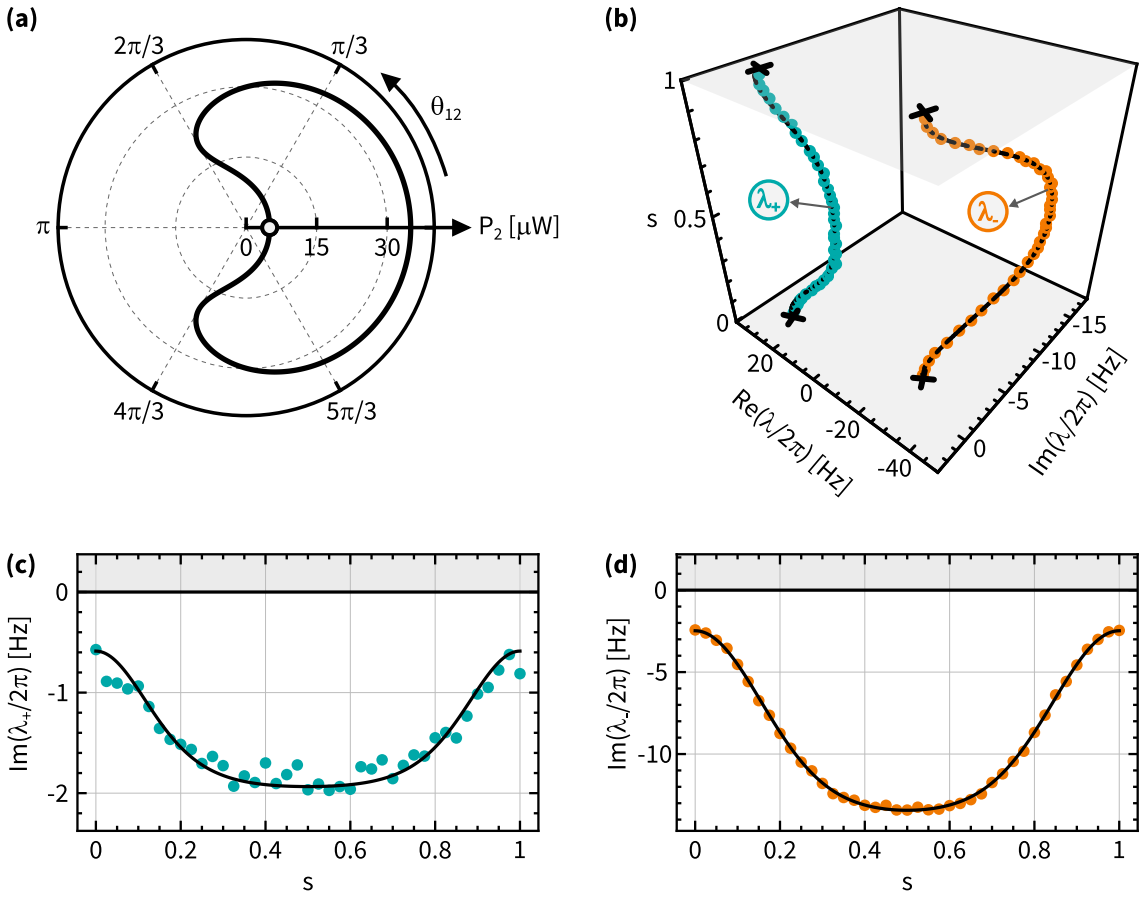

Figure 6.10: Verifying conditions for achieving SSGG: for Control loop family II. (a) Control loop $\mathcal{C}_{\text{amp}}$ from family II (Sec. 6.3.2) plotted in (P_2, θ_{12}) plane, shown as solid black curve. White disk indicates the starting $(s = 0)$ and the ending $(s = 1)$ point of $\mathcal{C}_{\text{amp}}$. Note that for this $\mathcal{C}_{\text{amp}}$, θ_{12} does not wind by 2π when it is completed. **(b)** Eigenvalues $\boldsymbol{\lambda}$ corresponding to a single traversal of $\mathcal{C}_{\text{amp}}$ in (a), as a function of $0 \leq s \leq 1$. Cyan (orange) points: measurement corresponding to $\lambda_+(\lambda_-)$ when P_2 is varied along $\mathcal{C}_{\text{amp}}$, while θ_{12} is held fixed. Recall that $\boldsymbol{\lambda}$ is independent of θ_{12}. Black curves: no-free-parameter theory prediction of $\boldsymbol{\lambda}$. The black crosses show $\boldsymbol{\lambda}$ at the basepoint $s = 0 = 1$. **(c,d)** Same as (b), but showing only $\text{Im}(\lambda_+)$ and $\text{Im}(\lambda_-)$ versus $0 \leq s \leq 1$ along $\mathcal{C}_{\text{amp}}$, respectively. For all s, we have a unique least-dissipative eigenvector and it is damped ($\text{Im}(\lambda_+(s)) < 0$ for $s \in [0, 1]$) for the entirety of $\mathcal{C}_{\text{amp}}$, thereby verifying conditions (1) and (3) for SSGG (Sec. 6.1). For these measurements, we used the (3,3) and the (5,3) membrane modes with fixed control parameters during $\mathcal{C}_{\text{amp},n}$: $P_1 = 26$ μW, $\delta/2\pi = -0.911$ MHz, $\eta/2\pi = -50$ Hz for the red-detuned laser tones and $P_4 = 28$ μW, $\Delta_4/2\pi = +3.38$ MHz for the blue-detuned laser tone.

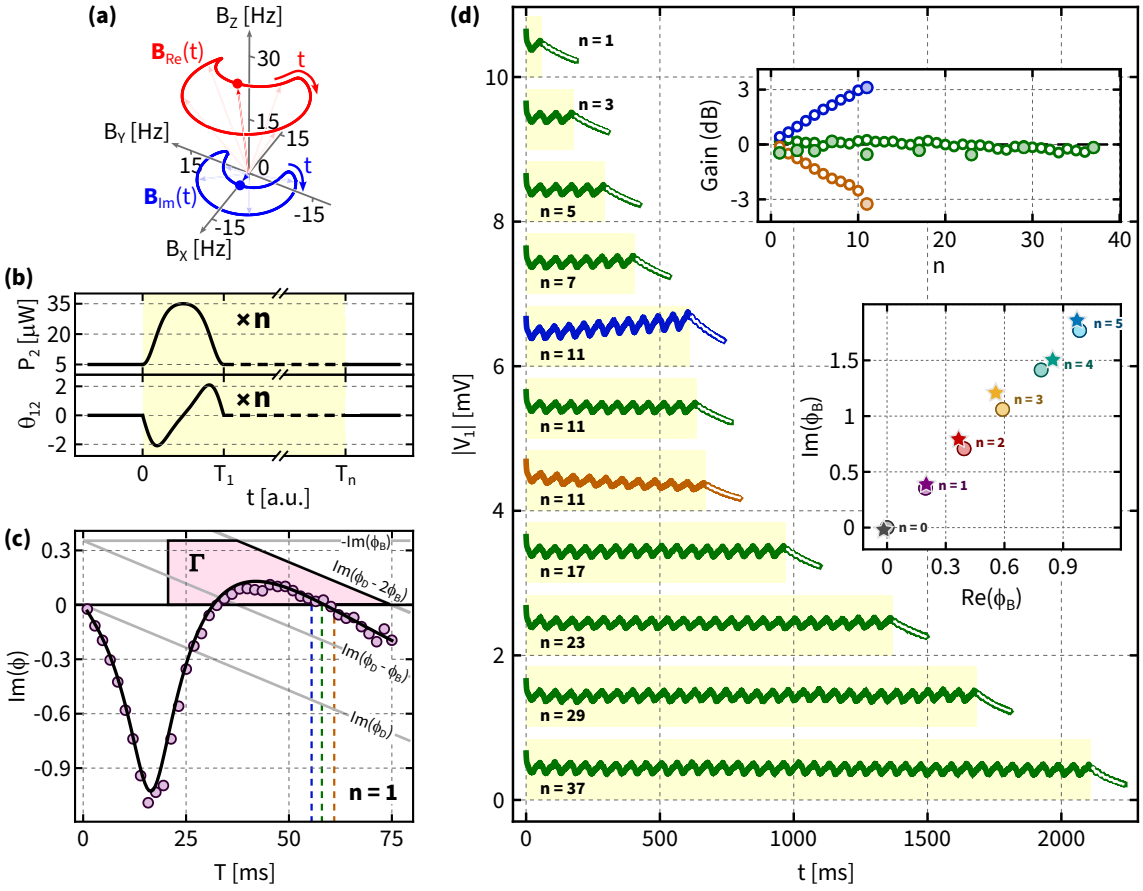

Figure 6.11: SSGG for Control loop family II. (a) The control loop $\mathcal{C}_{\mathrm{amp},1}$ visualized as two three-vectors $\mathbf{B}_{\mathrm{Re,Im}}$. **(b)** $P_2(t)$ and $\theta_{12}(t)$ during $\mathcal{C}_{\mathrm{amp},n}$. **(c)** The least-dissipative normal mode's gain $\mathrm{Im}(\phi)$ when $\mathcal{C}_{\mathrm{amp},1}$ is traversed once in duration T. Disks: data; black curve: no-free-parameter theory prediction; pink shaded area: the region $\mathbf{\Gamma}$ that results in SSGG. Blue, green and orange dashed vertical lines: values of T used in (d). **(d)** Green curves: the amplitude of the mode's motion during loops $\mathcal{C}_{\mathrm{amp},n}$ for $T = 58$ ms; blue and orange curves: the amplitude of the mode's motion during loops $\mathcal{C}_{\mathrm{amp},n}$ for $T = 55.5$ ms and 61 ms, respectively. Each curve is vertically offset by 1 mV, so that $|V_1| = 0$ corresponds to the bottom of the yellow band. White curves: fit to ringdown data (Sec. D.2). Upper inset: a summary of the gain resulting from these loops. Filled circles: the gain from each $\mathcal{C}_{\mathrm{amp},n}$ in the main panel; green hollow circles: the gain after each circuit of the $n = 37$ loop; blue and orange hollow circles: the gain after each circuit of the $n = 11$ loop with $T = 55.5$ ms and 61 ms, respectively. Lower inset: ϕ_B for $\mathcal{C}_{\mathrm{amp},n}$. Stars: measured and disks: no-free-parameter theory prediction. For this measurement, we used the same membrane modes and the same other control parameters as in Figs. 6.10.

6.4 Further remarks on SSGG

In this section, we provide further insights into SSGG. These include: (a) a specific comparison to parametric amplification (Sec. 6.4.1), (b) data on the phase-coherence of motion undergoing SSGG (Sec. 6.4.2), and (c) an illustration of mode's motion being driven into non-linearity using SSGG (Sec. 6.4.3).

6.4.1 Comparison to a parametric amplifier

As a specific comparison, conventional parametric amplification (PA) and SSGG both add gain to a mode by modulating the system's parameters. However, the modulation frequency required for SSGG is lower than that of PA by a factor $\sim Q$ (the mode's quality factor). This is because the typical modulation rate required for SSGG is $\sim \gamma$ (the mode's intrinsic decay rate), while PA operates by non-adiabatically modulating parameters at rates comparable to the mode's oscillation frequency. See also Ref. [250].

In addition to this important practical difference, these schemes differ fundamentally as follows: **(i)** PA does not involve geometric phase or non-Hermiticity; **(ii)** SSGG is insensitive to the phase of the (input) signal it amplifies i.e., it is phase-insensitive while PA is generically phase-sensitive; and **(iii)** SSGG requires at least two modes for its implementation, while PA requires just one.

6.4.2 Additional analysis and views of SSGG data

In this section, we illustrate additional analysis of the SSGG data. This includes analysis of geometric phase ϕ_B for control loops $\mathcal{C}_{\mathrm{amp},n}$ that produce SSGG (similar to Sec. 5.2.3 and Fig. 5.9), and additional views of data shown in panel (d) of Figs. 6.3.1 and 6.3.2 that provide tangible evidence of phase-coherence of mechanical motion undergoing SSGG.

6.4.2.1 Measuring ϕ_B for loops that produce SSGG

Measurement of ϕ_B for $\mathcal{C}_{\mathrm{amp},n}$ is carried out in the same manner as described in Secs. 5.1 and D.1. As a quick reminder, we vary system parameters along $\mathcal{C}_{\mathrm{amp},n}$ (denoted by $\circlearrowleft$), and its time-reversed version (denoted by $\circlearrowright$), and measure the propagator matrix U

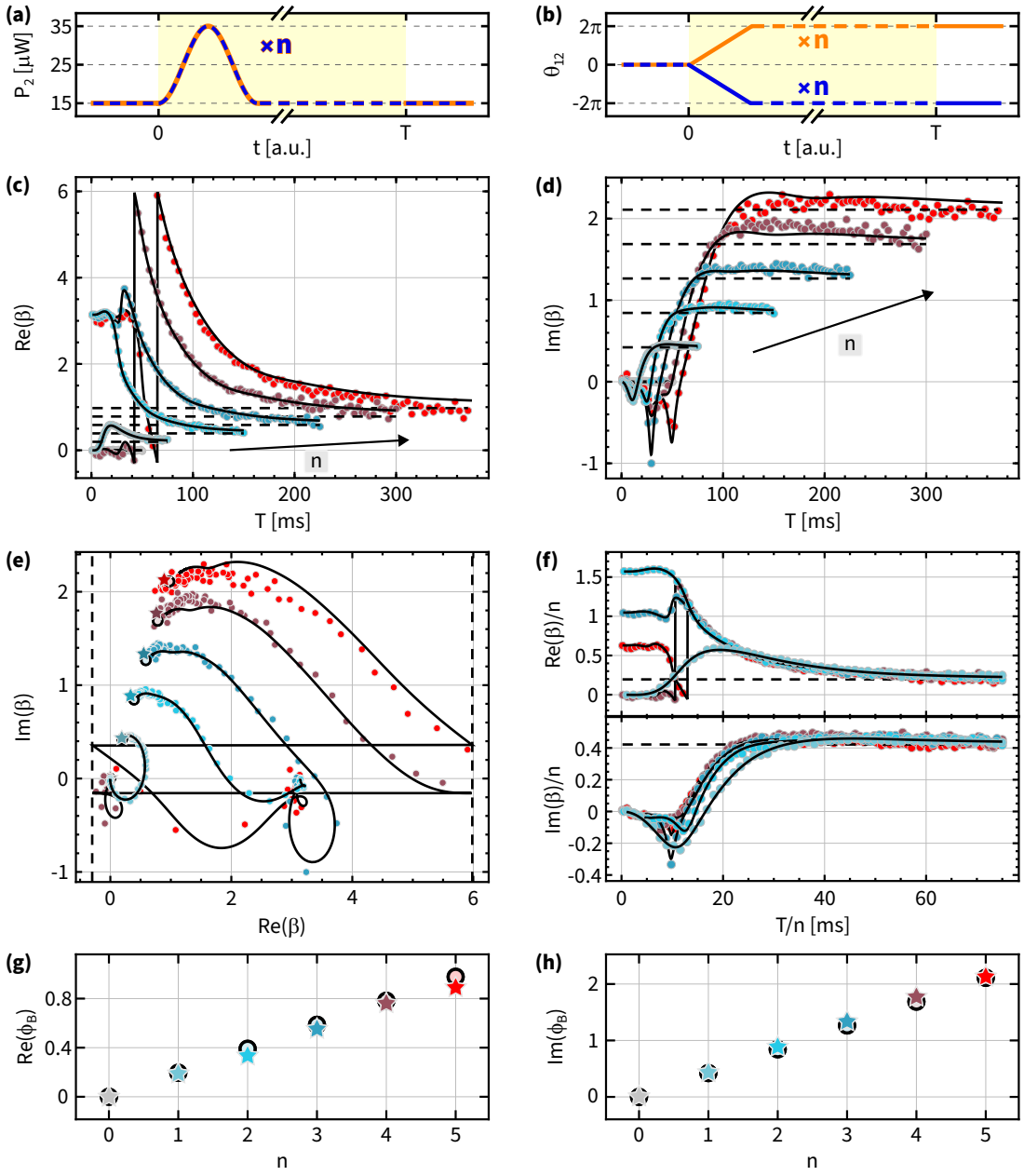

Figure 6.12: Geometric phase of Control loops that produce SSGG - family I. (a-b) Control paths $\mathcal{C}_{\mathrm{amp},n}$ in which P_2 and θ_{12} varied, for $n = 0, 1, 2, 3, 4, 5$. Orange (blue) curves: correspond to $\mathcal{C}_{\mathrm{amp},n}$ in $\circlearrowright$ ($\circlearrowleft$) sense. **(c-d)** Corresponding $\mathrm{Re/Im}(\beta(T))$, respectively. Colored points (gray to red for $n = 0$ to 5): data, solid black lines: no-free-parameter theory expectation for each n. Dashed black lines: no-free-parameter theory expectation of $\mathrm{Re/Im}(\phi_B)$ for each n. **(e)** Polar plot of $\beta(T)$ and ϕ_B. Colored points (gray to red): data corresponding to $\beta(T)$, solid black curve: no-free-parameter theory expectation of $\beta(T)$ for each n, colored stars (gray to red): estimated ϕ_B from $\beta(T)$ data via asymptote analysis (Sec. D.4), colored disks (gray to red): no-free-parameter theory expectation of ϕ_B. **(f)** β/n versus T/n for $1 \leq n \leq 5$. Colored points: data, black solid lines: no-free-parameter theory expectation. The dashed black line indicates ϕ_B for $n = 1$. Top (bottom) panel: real (imaginary) part of $\beta(T/n)/n$. **(g-h)** $\mathrm{Re/Im}(\phi_B)$ versus n, respectively. Stars: estimated ϕ_B, disks: no-free-parameter theory expectation of ϕ_B. For this measurement, we used the same membrane modes and the same other control parameters as in Figs. 6.8 and 6.9.

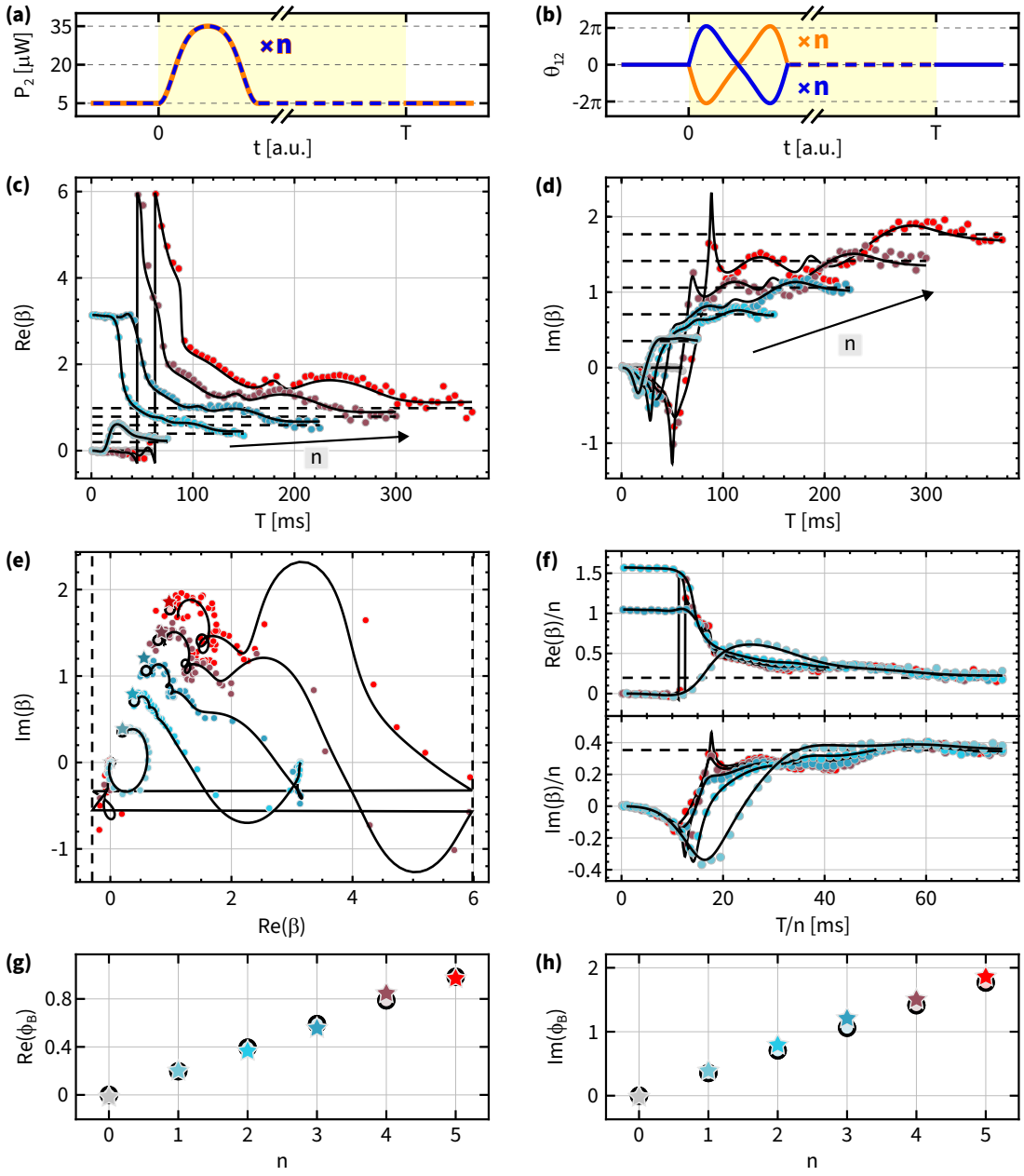

Figure 6.13: Geometric phase of Control loops that produce SSGG - family II. (a-b) Control paths $\mathcal{C}_{\text{amp},n}$ in which P_2 and θ_{12} varied, for $n = 0, 1, 2, 3, 4, 5$. Orange (blue) curves: correspond to $\mathcal{C}_{\text{amp},n}$ in $\circlearrowleft$ ($\circlearrowright$) sense. **(c-d)** Corresponding $\text{Re}/\text{Im}(\beta(T))$, respectively. Colored points (gray to red for $n = 0$ to 5): data, solid black lines: no-free-parameter theory expectation for each n. Dashed black lines: no-free-parameter theory expectation of $\text{Re}/\text{Im}(\phi_B)$ for each n. **(e)** Polar plot of $\beta(T)$ and ϕ_B. Colored points (gray to red): data corresponding to $\beta(T)$, solid black curve: no-free-parameter theory expectation of $\beta(T)$ for each n, colored stars (gray to red): estimated ϕ_B from $\beta(T)$ data via asymptote analysis (Sec. D.4), colored disks (gray to red): no-free-parameter theory expectation of ϕ_B. **(f)** β/n versus T/n for $1 \leq n \leq 5$. Colored points: data, black solid lines: no-free-parameter theory expectation. The dashed black line indicates ϕ_B for $n = 1$. Top (bottom) panel: real (imaginary) part of $\beta(T/n)/n$. **(g-h)** $\text{Re}/\text{Im}(\phi_B)$ versus n, respectively. Stars: estimated ϕ_B, disks: no-free-parameter theory expectation of ϕ_B. For this measurement, we used the same membrane modes and the same other control parameters as in Figs. 6.10 and 6.11.

as a function of loop duration T, for both cases. Subsequently, we use the $U_{++}(T)$ data (the matrix element of $U(T)$ that captures the evolution of the least-dissipative state at large T) for both of these loops to calculate $\beta(T) = -i\,\mathrm{Log}(U_{++,\circlearrowleft}/U_{++,\circlearrowright})/2$, which is then used for estimating ϕ_B via asymptote analysis (Sec. D.4).

Figs. 6.12 and 6.13 show measurements of $\beta(T)$ for $\mathcal{C}_{\mathrm{amp},n}$ from the first (Sec. 6.3.1) and the second (Sec. 6.3.2) family of loops, respectively with $n \in \{0, 1, 2, 3, 4, 5\}$, and they are in good agreement with the respective no-free-parameter theory prediction. This exercise illustrates a facet of the fact that the mechanical motion is phase-coherent when undergoing SSGG. We note in passing that β for the second family of SSGG producing loops (precisely for $n \in \{2, 3, 4, 5\}$) have additional features in intermediate loop durations which we hand-wavingly attribute to the non-trivial shape of the control loop.

6.4.2.2 Phase-coherence of mechanical motion undergoing SSGG

More tangible evidence of the phase-coherence of mechanical motion undergoing SSGG comes from inspecting the individual data traces (see Sec.E). These individual traces are "complex averaged" (Sec. D.1) to produce each trace in panel (d) of Figs. 6.9 and 6.11. For each complex averaged trace shown in panel (d) of Fig. 6.9 (Fig. 6.11), Figs. E.1-E.4 (Figs. E.5-E.8) illustrate the corresponding individual traces showing the amplitude as well as the phase of the mechanical motion. From visual inspection, we note that the variance in phase of the individual traces increases with the increasing duration of $\mathcal{C}_{\mathrm{amp},n}$, indicating a deterioration of phase-coherence. While we have not attempted any further analysis, the author conjectures that these datasets may be utilized to probe the phase-coherence time-scale of these mechanical oscillators, which in turn may put a practical upper limit on the duration of $\mathcal{C}_{\mathrm{amp},n}$. Loosely speaking, this is a linear and phase-insensitive process and thereby the phase will diffuse [251–254]. We relegate further discussion of this topic for a future work.

6.4.3 Driving a mechanical oscillator into nonlinearity regime using SSGG

So far, our discussions have focused on mechanical modes behaving as linear harmonic oscillators. This is indeed a good approximation, given the range of control and mechanical drive (Sec. 4.6.1.1) parameters we access in our experiments (see also Ref. [207, 225]). In this section and for the first time in this thesis, we unveil a behavior of mechanical modes that are not explained by a model involving linear harmonic oscillators. We attribute this behavior to mechanical mode's motion reaching amplitude beyond its linear regime.

To focus this discussion, we take the two examples of $\phi(T)$ measurements (Secs. 5.1 and D.1) involving the family of SSGG producing control loops $\mathcal{C}_{\mathrm{amp},n}$ that produces SSGG as described in Sec. 6.3.1. The first example (Fig. 6.14(a)), involves preparing an initial state $\vec{c}^{(a)}(0)$ (which is approximately $\propto (1,0)^{\mathrm{T}}$ - shown in the first column) with a mechanical drive of amplitude $V_{d,1} = 0.25\ V_{pk}$ and its frequency $\omega_d \approx \omega_1^{(0)}$. The initial state is estimated by fitting the ringdown portion of the data (Sec. D.2), and the fit quality corroborates the choice of modeling the system with coupled linear harmonic oscillators. More precisely, the mechanical modes are within their linear regime for this amount of mechanical drive. Subsequently, $\vec{c}^{(a)}(0)$ is evolved along $\mathcal{C}_{\mathrm{amp},4}$ to the final state $\vec{c}^{(a)}(T)$ (second column) for a duration $T = 99.4$ ms. The final state is estimated by fitting the ringdown portion of the data and the fit quality suggests that despite the amplification produced by SSGG, the mechanical motion is still within its linear regime. Fig. 6.14(b) shows $\mathrm{Im}(\phi)$ as a function of T, where the data points (circles) agree well with the no-free-parameter theory prediction (black lines)[1], and they continue to corroborate the choice of modeling the system with coupled linear harmonic oscillators.

A curious behavior emerges when we repeat the above measurements but this time we use a mechanical drive with amplitude $V_{d,2} = 0.7\ V_{pk} \sim 3 \times V_{d,1}$. The new initial state (still approximately $\propto (1,0)^{\mathrm{T}}$; first column - Fig. 6.14(c)), estimated by fitting its ringdown suggests that the system is still within its linear regime. However, when

[1]Quick reminder: $\phi(T)$ requires two linearly independent initial states $\vec{c}^{(a,b)}(0)$, that were evolved along $\mathcal{C}_{\mathrm{amp},4}$ for a duration T to $\vec{c}^{(a,b)}(T)$. See Secs. 5.1 and D.1. The $\vec{c}^{(b)}$ part of this story is coming up shortly!

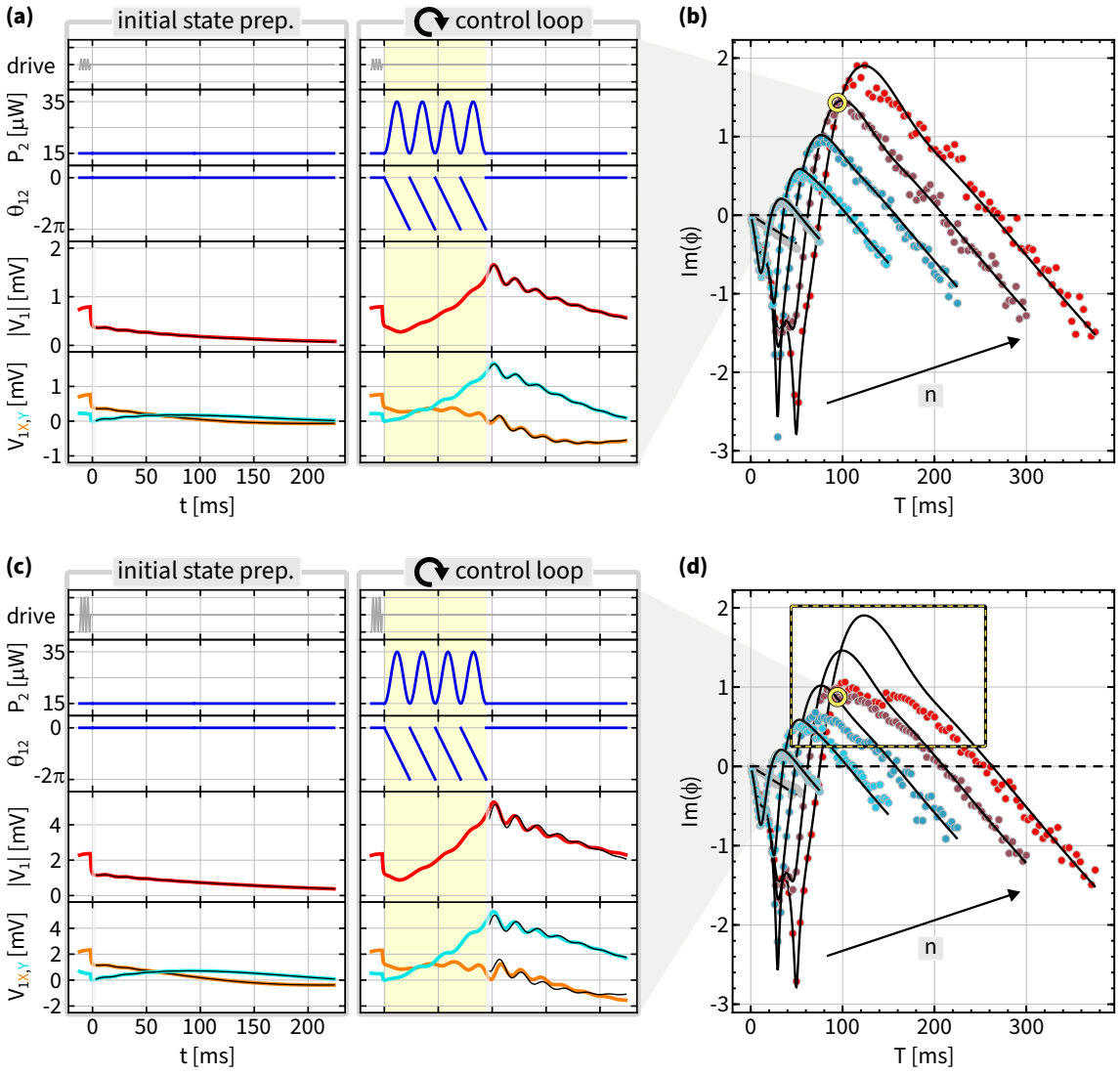

Figure 6.14: Driving the system into non-linearity using SSGG - part I. (a) First column: measurements for $\vec{c}^{(a)}(0) \sim (1,0)^{\mathrm{T}}$ i.e, with no control loop and using an mechanical drive strength $V_{d,1} = 0.25\ V_{pk}$. Second column: measurements for $\vec{c}^{(a)}(T)$ for $\mathcal{C}_{\mathrm{amp},4}$. For both columns, first row: a schematic of the driving force applied to the membrane, which is switched off at $t = 0$; second row: a plot control power $P_2(t)$ and third row: a plot of the beat-note phase $\theta_{12}(t)$, for the respective initialization/control loop. Solid red, orange and cyan curves: the "complex averaged" magnitude, the in-phase and the quadrature part of the heterodyne signal, respectively and for measurements shown in each column. Corresponding to each measurement, the solid black curve is a fit to the evolution at constant H (see Sec. D.2). **(b)** $\mathrm{Im}(\phi(T))$. Colored points (gray to red for $n = 0$ to 5): data, solid black lines: no-free-parameter theory expectation for each n. Yellow circled datapoint corresponds to $\vec{c}^{(a)}$ measurements in (a). **(c,d)** Same as (a,b) respectively, but for a different mechanical drive strength $V_{d,2} = 0.7\ V_{pk} \sim 3 \times V_{d,1}$. In the second column of panel (c), the fit does not capture the ringdown data. In panel (d), the black rectangle encloses a region where the measured $\mathrm{Im}(\phi(T))$ does not match the no-free-parameter theory prediction and shows a apparent saturation behavior. For this measurement, we used the same membrane modes and the same other control parameters as in Figs. 6.8, 6.9 and 6.12.

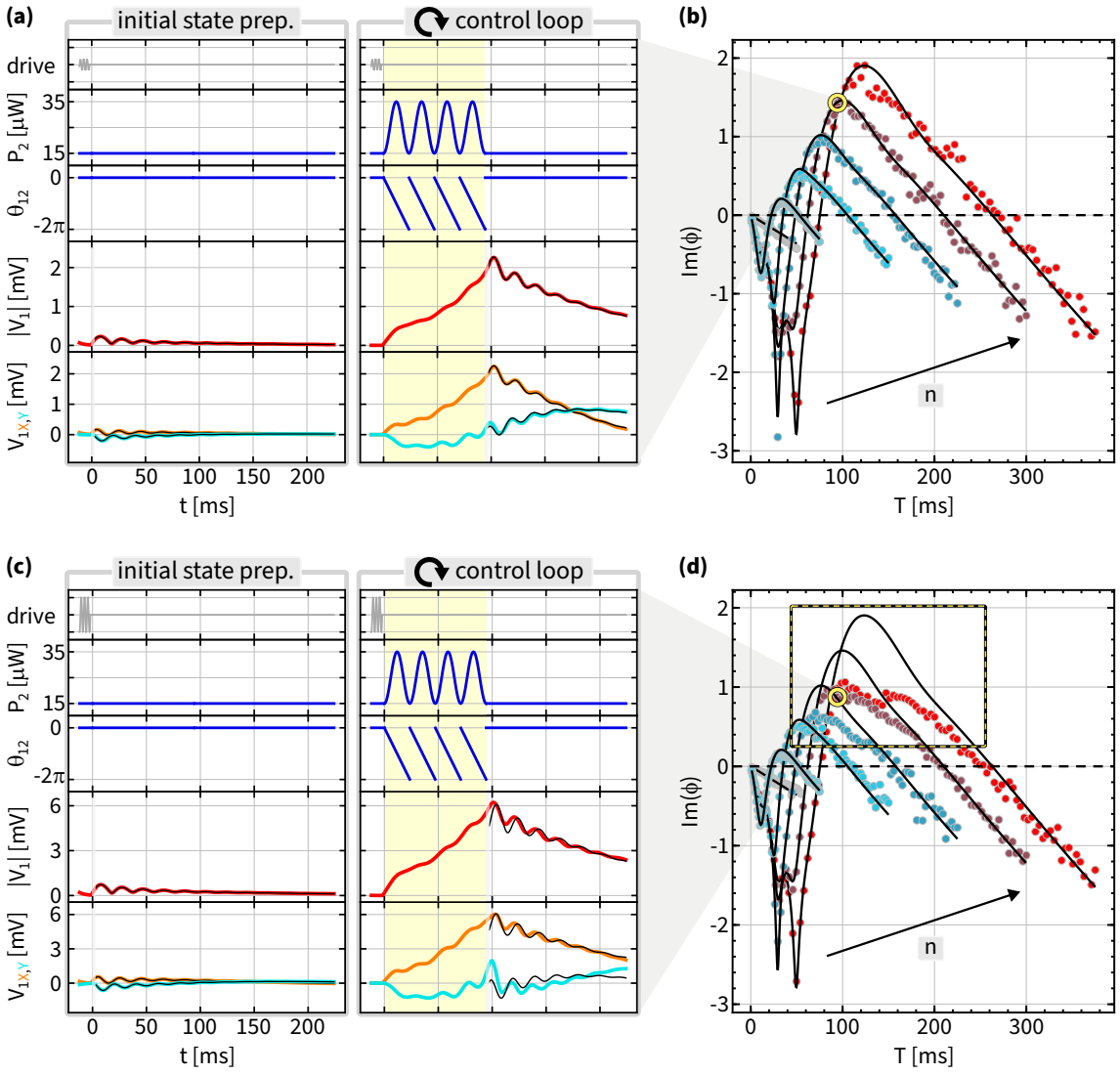

Figure 6.15: Driving the system into non-linearity using SSGG - part II. (a) First column: measurements for $\vec{c}^{(b)}(0) \sim (0,1)^{\mathrm{T}}$ i.e, with no control loop and using an mechanical drive strength $V_{d,1} = 0.25\ V_{pk}$. Second column: measurements for $\vec{c}^{(b)}(T)$ for $\mathcal{C}_{\mathrm{amp},4}$. For both columns, first row: a schematic of the driving force applied to the membrane, which is switched off at $t = 0$; second row: a plot control power $P_2(t)$ and third row: a plot of the beat-note phase $\theta_{12}(t)$, for the respective initialization/control loop. Solid red, orange and cyan curves: the "complex averaged" magnitude, the in-phase and the quadrature part of the heterodyne signal, respectively and for measurements shown in each column. Corresponding to each measurement, the solid black curve is a fit to the evolution at constant H (see Sec. D.2). **(b)** $\mathrm{Im}(\phi(T))$. Colored points (gray to red for $n = 0$ to 5): data, solid black lines: no-free-parameter theory expectation for each n. Yellow circled datapoint corresponds to $\vec{c}^{(b)}$ measurements in (a). **(c,d)** Same as (a,b) respectively, but for a different mechanical drive strength $V_{d,2} = 0.7\ V_{pk} \sim 3 \times V_{d,1}$. In the second column of panel (c), the fit does not capture the ringdown data. In panel (d), the black rectangle encloses a region where the measured $\mathrm{Im}(\phi(T))$ does not match the no-free-parameter theory prediction and shows an apparent saturation behavior. For this measurement, we used the same membrane modes and the same other control parameters as in Figs. 6.8, 6.9, 6.12 and 6.14.

it evolved along $\mathcal{C}_{\mathrm{amp},4}$ to the final state (second column - Fig. 6.14(c)) for the same duration ($T = 99.4$ ms), the fit is unable to capture the details of its ringdown. This is contrary to all previous observations reported in this chapter and in Chapter 5. This is further highlighted in Fig. 6.14(d) via measurements of $\mathrm{Im}(\phi)(T)$ which do not match the theory prediction for the range of T and for $n \in \{3, 4, 5\}$. In particular, we observe an apparent saturation of $\mathrm{Im}(\phi)(T) \sim 0.9$ for $n \in \{4, 5\}$ for 90 ms $\leq T \leq$ 120 ms, contrary to the n-scaling discussed previously (Secs. 2.2.3.1 and A.3.1, among others). Similar behavior is seen when the mechanical drive frequency was chosen to be $\omega_d \approx \omega_2^{(0)}$ such that the initial state $\vec{c}^{(b)}(0)$ is approximately $\propto (0, 1)^{\mathrm{T}}$, for drive amplitudes $V_{d,1}$ and $V_{d,2} \sim 3 \times V_{d,1}$, respectively. This is illustrated in Fig. 6.15 via its panels (a) and (c). Panels (b) and (d) of Fig. 6.15 are the same as the corresponding panels of Fig. 6.14.

In conclusion, these observations suggest that the amplification produced by SSGG is sufficient to place the system in a non-linear regime. We relegate any systematic analysis of this non-linear behavior for a future work.

Chapter 7

Topological and discrete geometric phase of non-Hermitian degeneracies

In this chapter, we provide an experimental demonstration of the topological and discrete geometric phase $\phi_{B,\mathrm{deg}}$ of non-Hermitian degeneracies corresponding to an $N = 2$-mode system, using the new MIM platform (Chapter 4). These measurements are made for a variety of control paths $\mathcal{C}_{\mathrm{deg}}$ that lie entirely in the degenerate subspace (i.e., the system is rendered to be strictly degenerate throughout the control path), and use adiabatic protocols described in Refs. [88, 89] and in Chapter 2 (Secs. 2.2.2.3 and 2.2.4). With these ingredients in place, we start with a discussion about measuring $\phi_{B,\mathrm{deg}}$ (Sec. 7.1). We then demonstrate the topological and discrete nature of $\phi_{B,\mathrm{deg}}$ by measuring it for a variety of $\mathcal{C}_{\mathrm{deg}}$ (Sec. 7.2). In Section 7.3, we turn our attention towards an important question: "How robust is $\phi_{B,\mathrm{deg}}$?". Based on our understanding, robustness of $\phi_{B,\mathrm{deg}}$ has several facets, and we shed light on each of them. In Section 7.4, we highlight a novel $\sqrt{T}$-dynamical phase expected for $\mathcal{C}_{\mathrm{deg}}$. In particular, a careful choice of parameters allows us to re-purpose the machinery of Chapter 6 to demonstrate yet another novel form of amplification: a $\sqrt{T}$-amplifier. Additional technical details for these measurements and their analyses are given in Appendix F.

7.1 Measuring $\phi_{B,\mathrm{deg}}$

In this section, we describe our protocol for measuring $\phi_{B,\mathrm{deg}}$, the geometric phase corresponding to non-Hermitian degeneracies. These measurements are carried out using a system of two mechanical oscillators: the (3,3) and the (5,2) mode of the membrane (Sec. 4.3), which are tunably coupled to each other via optomechanical interactions with the optical cavity (Sec. 4.4.3). The optical cavity is in turn driven by three control laser tones (Sec. 4.6.1.2): two red-detuned control tones that provide tunable optical spring, optical damping and Floquet-coupling (Sec. 2.3.2) and a blue-detuned control tone to reduce damping of the membrane modes (Sec. 4.5.3). The full set of control knobs at our disposal can be represented by $\vec{Z} \equiv \{P_1, P_2, \delta, \eta, \theta_{12}, P_4, \Delta_4\}$, where $P_{1,2}$, δ and η are the individual powers, common and differential detuning of two red-detuned control tones, respectively. θ_{12} is the phase of the intracavity intensity beat-note of the red-detuned laser tones. $\{P_4, \Delta_4\}$ represent the power and the detuning (from cavity resonance) of the blue-detuned control tone, respectively. The specific tuning of these control knobs is described in subsequent sections.

A crucial distinction of this work compared to its predecessors (i.e., Chapters 5 and 6) is that the system is tuned to an EP_2 degeneracy, and the control paths $\mathcal{C}_{\mathrm{deg}}$ lie entirely in the EP_2 degenerate subspace i.e., $\mathcal{EP}_2$ (Sec. 2.2.4), unless mentioned otherwise. We tune the degenerate system along a $\mathcal{C}_{\mathrm{deg}}$ in real time, and measure its corresponding time evolution to determine $\phi_{B,\mathrm{deg}}$. We now describe this measurement protocol below.

7.1.1 Locating EP_2 degeneracy

The protocol begins by locating an EP_2 degeneracy. This is accomplished by performing spectroscopy of the membrane modes via ringdown measurements as a function of control parameters, and extracting the corresponding eigenvalues $(\lambda_{1,2})$. An exemplary measurement of the discriminant $D = (\lambda_+ - \lambda_-)^2$ is shown in Fig. 7.1(a) where we varied control parameters of the two red-detuned tones: $\{P = \sqrt{P_1 P_2}, \delta\}$ on a rectangular grid with fixed control parameters: $\sqrt{P_1/P_2} = 0.4, \eta/2\pi = -30$ Hz for the red-detuned tones, and $P_4 =$ 16.9 μW and $\Delta_4/2\pi = +2.925$ MHz for the blue detuned tone. We

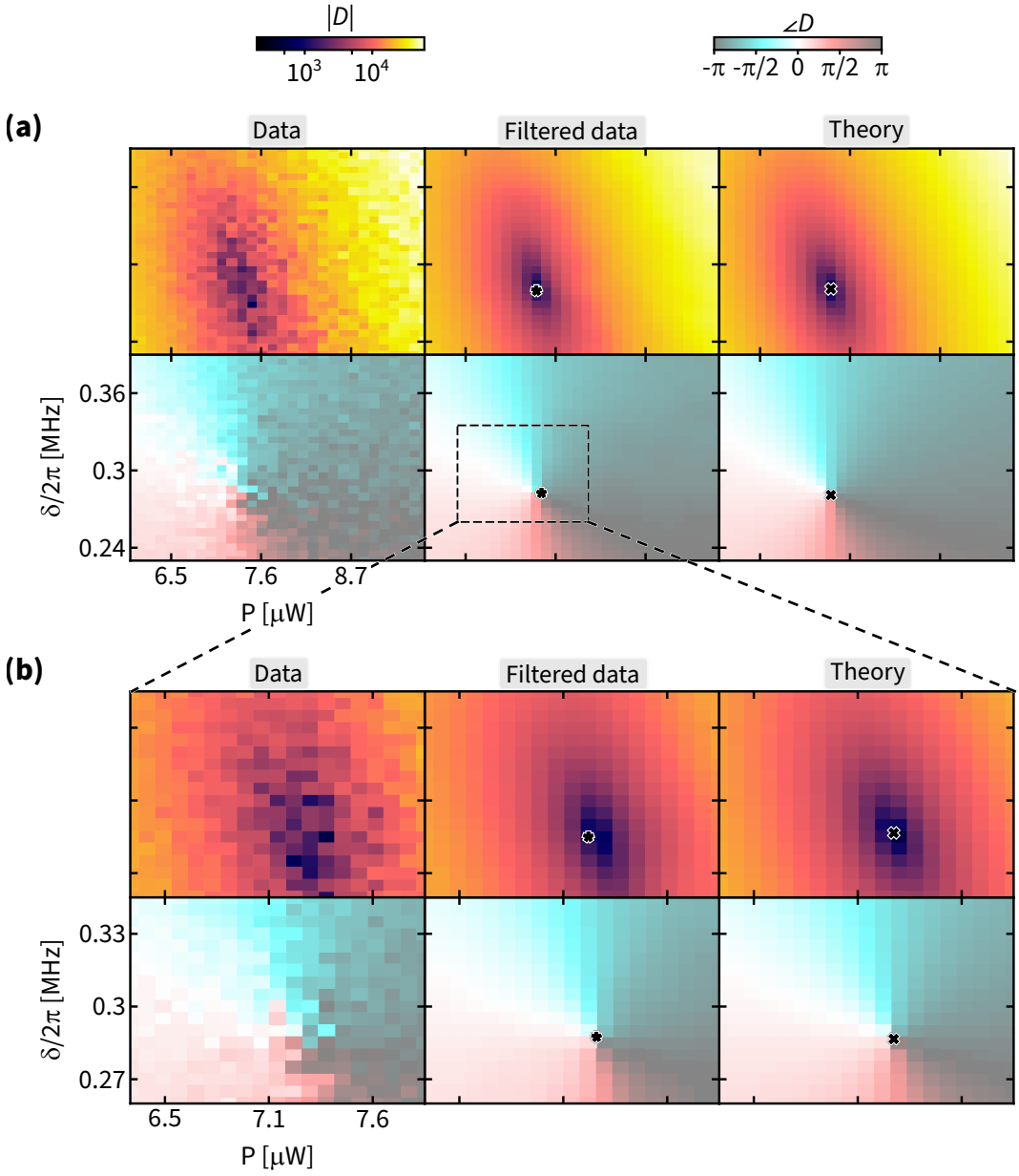

Figure 7.1: Locating EP_2 degeneracy via spectroscopy. **(a)** $D(P, \delta)$ with $P = \sqrt{P_1 P_2}$. Left column: data; middle column: filtered data, black star: experimentally predicted EP_2 location; right column: fit, black cross: theoretically predicted EP_2 location. Dashed rectangle indicates the region in P - δ plane used for a refined search of EP_2 location shown in (b). Top row: $|D|$ (units: $(2\pi \times \text{Hz})^2$), bottom row: $\angle D$ (units: radians). **(b)** Same as (a) but for $\{P, \delta\}$ within the dashed rectangle in bottom-middle panel of (a). Note that both panels use the same color scale for representing D. For this measurement, we used the (3,3) and the (5,2) membrane modes with fixed control parameters: $\sqrt{P_1/P_2} = 0.4, \eta/2\pi = -30$ Hz for the red-detuned laser tones and $P_4 =$ 16.9 μW, $\Delta_4/2\pi = +2.925$ MHz for the blue-detuned laser tone.

recall that the system's eigenvalues are independent of θ_{12} (Secs. 2.3.2 and Eq. (2.17)), and is held fixed to 0 for this and for all subsequent spectroscopy measurements in this chapter. EP_2 is simultaneously located as a minimum of $|D|$ (Sec. B.5.3) and a vortex of the phase of D ($\angle D$, Sec. B.5.4) in the P - δ plane. They are shown as black stars in the second column of Fig. 7.1(a). We have empirically found that vortex of $\angle D$ is a more robust indicator of EP_2 compared to minima of $|D|$. Consequently, EP_2 as identified via the vortex of $\angle D$ gets utilized in the next steps of the protocol.

The experimentally identified EP_2 compares well with the theory prediction (shown as a black cross in the third column of Fig. 7.1(a)). The theory predictions are calculated using system parameters obtained by fitting the spectroscopy data as described in Secs. 4.5.1 and 4.5.3, and exemplary fits are illustrated in Appendix C.4. All subsequent theory predictions in this section are calculated using these system parameters.

Panel (b) of Fig. 7.1 illustrates a more refined search for the EP_2 location, guided by the measurement shown in panel (a). The result of this refined search is our best estimate of the EP_2 location, and it is subsequently utilized for constructing $\mathcal{C}_{\mathrm{deg}}$ (Sec. 7.1.2). For comparison, in panel (b) of Fig. 7.1, the EP_2 is located 1.5x (2.5x) more precisely in P (δ) compared to its panel (a); 26x (16x) more precisely in P (δ) when compared to Fig. 4.15; and 80x more precisely in P when compared to a generic spectroscopy measurement in the older MIM platform (for ex: see Fig. 3.7)[1]. The ability to precisely locate an EP_2 must be complemented by the system's stability to reliably relocate to the same EP_2, thus enabling the work described in this chapter. Spectroscopic verification of this aspect is illustrated in Sec. 4.5.4. The manner in which it gets translated into real time dynamics measurements in $\mathcal{EP}_2$ is illustrated in Sec. 7.3.1.

[1]We note that the new MIM cavity has ∼13x larger linewidth that the older system (∼2.2 MHz versus ∼0.17 MHz) and employs ∼6x larger membrane mode frequencies (∼3 MHz versus ∼0.5 MHz). So putting δ on the same footing requires us to take care of these design considerations. At the end we estimate a ∼25x improvement in precision of δ in determining EP_2 location as given by Fig. 7.1(b) compared to a generic spectroscopy measurement in the older MIM platform. This is given by the product of the ratio of cavity linewidths and the inverse ratio of smallest reliable step-size in δ. In the older system, the smallest reliable step-size in δ was $2\pi \times 10$ KHz.

7.1.2 Constructing $\mathcal{C}_{\mathrm{deg}}$

The EP_2 located above can be succinctly parameterized into a control path $\mathcal{C}_{\mathrm{deg}}$ in $\mathcal{EP}_2$ via control parameters as:

$$\vec{Y}_{EP} \equiv \{P_{EP}, \delta_{EP}, \eta, \theta_{12}, P_4, \Delta_4\} \tag{7.1}$$

where $\{P_{EP}, \delta_{EP}/2\pi\} \equiv \{7.285\ \mu\mathrm{W},\ 0.2872\ \mathrm{MHz}\}$ are coordinates corresponding to the vortex in $\angle(D(P,\delta))$ with $P_{EP} = \sqrt{P_{1,EP}P_{2,EP}}$. In a frame rotating with the intensity beat-note of the two red-detuned control tones, the non-Hermitian dynamical matrix H (Eq. (2.81)) that governs the motion of the membrane modes has the following properties:

(a) It is degenerate and the degeneracy type is indeed EP_2.

(b) It can be expressed as H_{deg} as in Eq. (2.51) via the relations given in Eq. (2.83) and thus spanning $\mathcal{EP}_2$.

(c) In the picture of representing H as a "complex Pauli matrix vector" (Eq. (2.5)), it corresponds to the three-vectors $\mathbf{B}_{\mathrm{Re,Im}}$ being equal in length and perpendicular to each other (henceforth denoted as $\mathbf{B}^{\mathrm{deg}}_{\mathrm{Re,Im}}$), with their common orientation in $\mathbb{R}^3$ fixed by the parameters corresponding to the EP_2.

(d) It depends on time solely via $\vec{Y}_{EP}(t)$.

With the above setup, "simple" control loops $\mathcal{C}_{\mathrm{deg}}$ can be realized by holding the parameters $\{P_{EP}, \delta_{EP}, \eta, P_4, \Delta_4\}$ fixed, while varying $\theta_{12}(s) = -2n\pi s \bmod 2\pi$, in real time for a duration T, with $0 \leq s = t/T \leq 1$ and $n \in \mathbb{N}$. As before, this corresponds to a loop as θ_{12} is defined modulo 2π, such that $\vec{Y}(t=0) = \vec{Y}(t=T)$. Intuitively, it corresponds to rotating $\mathbf{B}^{\mathrm{deg}}_{\mathrm{Re,Im}}$, n-times around the z-axis, at a constant rate (see also Sec. 2.2.4.3). We also recall that in the language of Sec. 2.2.4.1 and Ref. [88, 89], a "simple" $\mathcal{C}_{\mathrm{deg}}$ in $\mathcal{EP}_2$ corresponds to a "straight loop" in $\mathcal{EP}_2$. Below we list some characteristic features of such a $\mathcal{C}_{\mathrm{deg}}$:

(i) The system remains degenerate throughout the control loop, and hence constitutes a control path entirely in $\mathcal{EP}_2$. This is because the system's eigenvalues are inde-

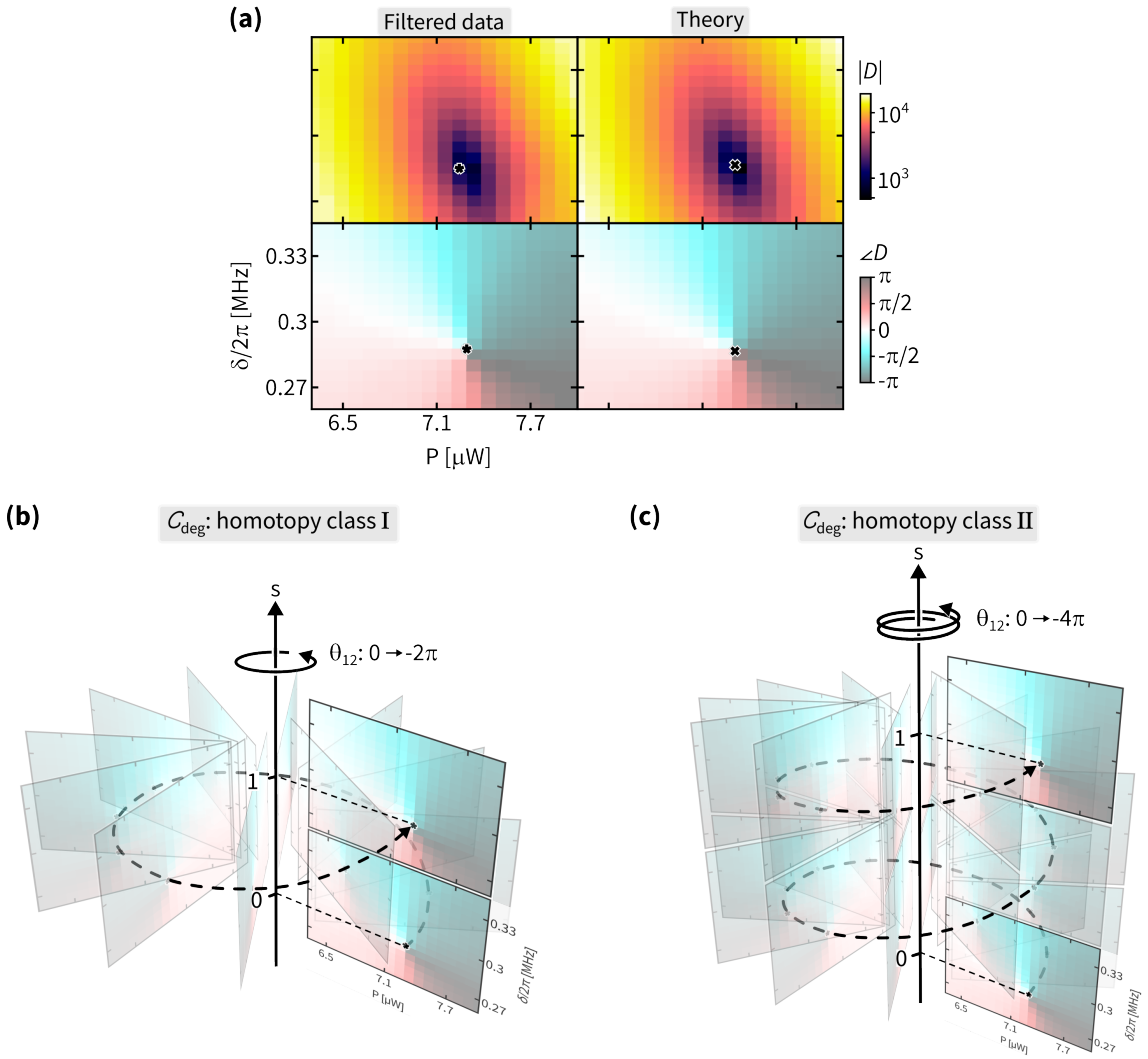

Figure 7.2: Control loops in $\mathcal{EP}_2$. **(a)** $D(P,\delta)$ with $P=\sqrt{P_1P_2}$ for the same 2D sheet shown in Fig. 7.1(b) that is used for locating EP_2 degeneracy, with appropriately scaled colormap for $|D|$. Left column: filtered data, black star: experimentally predicted EP_2 location; right column: fit, black cross: theoretically predicted EP_2 location. **(b)** A schematic illustration of a non-contractible control loop in $\mathcal{EP}_2$ where the control parameters are set to the value corresponding to the black star (experimentally predicted EP_2) and the beat-note phase θ_{12} is varied from 0 to -2π. **(c)** Same as (b) but θ_{12} is varied from 0 to -4π, which corresponds to a contractible control loop in $\mathcal{EP}_2$.

pendent of θ_{12} and as such for a "simple" $\mathcal{C}_{\rm deg}$, they are constant.

(ii) It ensures the strict requirement for the existence of a unique least-dissipative eigenvector of the dynamical matrix that governs evolution along $\mathcal{C}_{\rm deg}$, which is amenable to adiabatic evolution in the large-T limit (see Sec. 2.2.4.3 and Refs. [88, 89]).

(iii) Its homotopy class in $\mathcal{EP}_2$ is determined by $n \mod 2$ where $n \mod 2 = 1\ (0)$ corresponds to a non-contractible (contractible) $\mathcal{C}_{\rm deg}$ in $\mathcal{EP}_2$.

(iv) Intuitively, visualizing such loops as rotating $\mathbf{B}^{\rm deg}_{\rm Re,Im}$, n-times around the z-axis is popularly known as the "Dirac's Belt Trick" [255–259], which very simply demonstrates the doubly connected nature of $\mathrm{SO}(3) \cong \mathbb{RP}^3$ spaces. As described in Sec. 2.2.4.3, the space of $\mathcal{EP}_2 \cong \mathbb{RP}^3 \times \mathbb{R}$.

A schematic illustration of two homotopically distinct $\mathcal{C}_{\rm deg}$ constructed using the EP_2 obtained in Sec. 7.1.1 is shown in Fig. 7.2(b,c).

7.1.3 Measurement of real time dynamics in $\mathcal{EP}_2$

In this section, we describe measurements of real time dynamics when the system is tuned along a $\mathcal{C}_{\rm deg}$ in $\mathcal{EP}_2$. To focus this discussion, we consider a "simple" non-contractible $\mathcal{C}_{\rm deg}$ given by the EP_2 obtained in Sec. 7.1.1 with $\theta(t/T) = -2\pi(t/T)$. This $\mathcal{C}_{\rm deg}$ is shown schematically in Fig. 7.2(b). The corresponding measurement protocol is listed below and schematically illustrated in Fig. 7.3. We note that measurements corresponding to all $\mathcal{C}_{\rm deg}$ accessed in the chapter are carried out in this same fashion.

(1) For a $\mathcal{C}_{\rm deg}$ that will be traversed in real time in a duration T, we prepare the initial state $\vec{x}(0)$ as the least-dissipative right eigenvector[1] ($\vec{u}\,'_+$) of $H'(s=0,T)$. The dynamical matrix $H'(s,T) = J_2 - \mathcal{A}_J(s)/T$ governs the real time evolution of $\vec{x}$ (see Eqs. (2.52), (2.54)). Subsequently, we measure $\vec{x}(0)$.

(2) We then traverse $\mathcal{C}_{\rm deg}$ in real time in duration T and measure the final state $\vec{x}(T)$.

(3) In conjunction with the real time dynamics measurement above, we perform a spec-

[1]From here on, we use the phrase 'least-dissipative eigenvector of H'' or 'least-dissipative eigenvector of the dynamical matrix that governs evolution' to denote $\vec{u}\,'_+$, throughout the chapter. In particular, this phrase is taken to imply that $\vec{u}\,'_+$ is a right eigenvector.

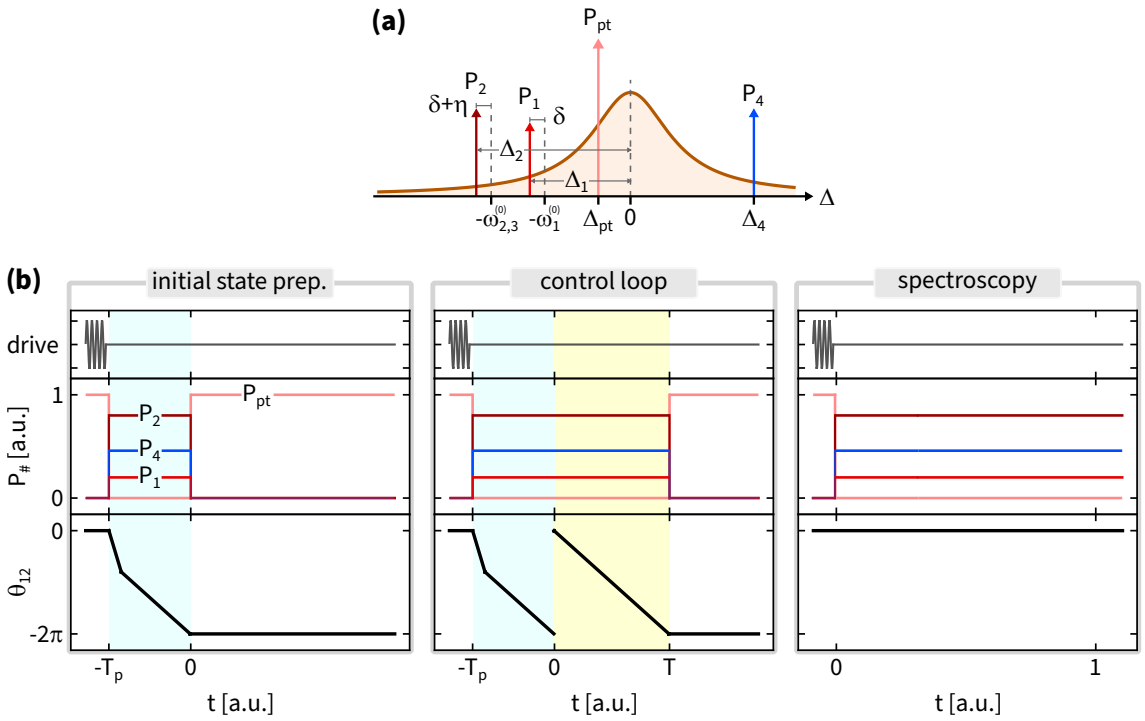

Figure 7.3: Protocol for real time dynamics measurements in $\mathcal{EP}_2$. **(a)** Optical spectrum. Orange: cavity mode; vertical arrows: control tones. Each control tones' power and detuning are indicated. The detuning (Δ) axis is to scale. The two red detuned tones $\{P_1, P_2, \delta, \eta\}$ and the blue detuned tone $\{P_4, \Delta_4\}$ are the control tones used in this work. An auxiliary red-detuned tone $\{P_{\rm pt}, \Delta_{\rm pt}\}$ close to the cavity resonance counteracts detrimental photothermal transients (see Sec. 4.4.3.1). **(b)** The timing sequence of the experiment. **First column:** Initial state preparation. Its duration ($-T_p \leq t < 0$) is shaded in cyan. (Top panel) Dark gray curve: a schematic of the driving force applied to the membrane, which is switched off at $t = -T_p$. (Middle panel) Red, dark-red, blue curves: value of control tones' powers P_1, P_2 and P_4, respectively. They are 0 for $t < -T_p$, $t \geq 0$ and set to the value corresponding to the EP_2 location for $-T_P \leq t < 0$. Light-red curve: value of auxiliary tone's power $P_{\rm pt}$. It is 0 for $-T_p \leq t < 0$ and non-zero (value given by Eq. (4.16)) for $t < -T_p$, $t \geq 0$. (Bottom panel) Black curve: $\theta_{12}(t)$ given by Eq. (7.2). **Second column:** Same as first column but for performing a "simple" non-contractible control loop in $\mathcal{EP}_2$. Its duration ($0 \leq t \leq T$) is shaded in yellow. In the middle panel, P_1, P_2 and P_4 are now on (off) for $-T_p \leq t \leq T$ ($t < -T_p$, $t > T$), and $P_{\rm pt}$ continues to be off (on) when control tones are on (off). $\theta_{12}(-T_p \leq t < 0)$ is given by Eq. (7.2) and $\theta_{12}(0 \leq t \leq T) = -2\pi t/T$. **Third column**: Same as first column but for performing spectroscopy at EP_2. In the top panel, the driving force is switched off at $t = -T_p$. In the middle panel, P_1, P_2 and P_4 are now on (off) for $t \geq 0$ ($t < 0$). θ_{12} is held constant at 0, as it has no role in spectroscopy of eigenvalues.

troscopy measurement of the system's degenerate eigenvalue λ_{EP} and the quantity R at this EP_2. Briefly, the parameter R characterizes the rate at which any state vector of the degenerate system approaches the unique right eigenvector at EP_2 (see Secs. 7.4.1.1 and F.3). These measurements enable us to independently determine the expected dynamical phases that arise when transporting the state vector $\vec{x}(0)$ along $\mathcal{C}_{\rm deg}$, and which persist as $T \to \infty$.

(4) We repeat steps **(1)** and **(2)** as a function of T. For each value of T chosen for step **(1)** and correspondingly **(2)**, we perform step **(3)**.

We now detail each step of this measurement protocol below.

7.1.3.1 Initial state preparation

Motivated by the theoretical prescription as described in Refs. [88, 89] as well as in Secs. 2.2.2.3 (Eq. (2.9)) and 2.2.4, preparing the initial state $\vec{x}(0)$ as the least-dissipative eigenvector ($\vec{u}'_+$) of $H'(s=0,T)$ is a key step that sets the stage for efficiently measuring $\phi_{B,\mathrm{deg}}$. We note that this is another important difference of this work when compared to its predecessors (i.e., Chapters 5 and 6) where we initialized to a pair of linearly independent but arbitrary state vectors. Here we briefly describe the initial state preparation and provide some intuition. Its technical details are relegated to Sec. F.1.

The procedure begins by initializing one of the membrane modes to a large amplitude of motion while leaving the other one un-driven[1]. This is straightforwardly accomplished by turning off all the control tones that mediate coupling between the membrane modes, and mechanically driving one of them for a programmed duration. This prepares the state vector $\vec{x}(t=-T_p)$. In particular, $\vec{x}(t=-T_p)$ is either $\propto (1,0)^{\mathrm{T}}$ or $\propto (0,1)^{\mathrm{T}}$, when expressed in the basis of uncoupled membrane modes i.e., $(1,0)^{\mathrm{T}}$ as the (3,3) mode and $(0,1)^{\mathrm{T}}$ as the (5,2) mode. Subsequently, $\vec{x}(-T_p)$ is transported along $\mathcal{C}_{p,\mathrm{deg}}$ in $\mathcal{EP}_2$ in duration T_p. It is given by $\vec{Y}_{EP}$ (as in Eq. (7.1)) with $\theta_{12}(t)$:

$$\theta_{12}(t) = \begin{cases} \dfrac{-2\pi k_p(t+T_p)}{T_p-(1-k_p)T} & \text{if } \; -T_p \;\leq\; t \;< (k_p-1)T \\ -2\pi \;-\; \dfrac{2\pi t}{T} & \text{if } \; (k_p-1)T \;\leq\; t \;\leq 0 \end{cases} \tag{7.2}$$

where $0 \leq k_p \leq 1$ is a real-valued parameter, and $\{T_p, T\}$ denote the time-duration of $\mathcal{C}_{p,\mathrm{deg}}$ and $\mathcal{C}_{\mathrm{deg}}$, respectively. Empirically, this corresponds to turning on all control tones to the set value of $\vec{Y}_{EP}$ at $t=-T_p$, and then tuning them in real time for a duration T_p via $\theta_{12}(t)$ as given in Eq. (7.2).

[1]The amplitude prepared by mechanically driving the membrane modes is greater than the un-driven motion for e.g. thermal motion, by at least a factor of 100 in all the cases studied in this thesis.

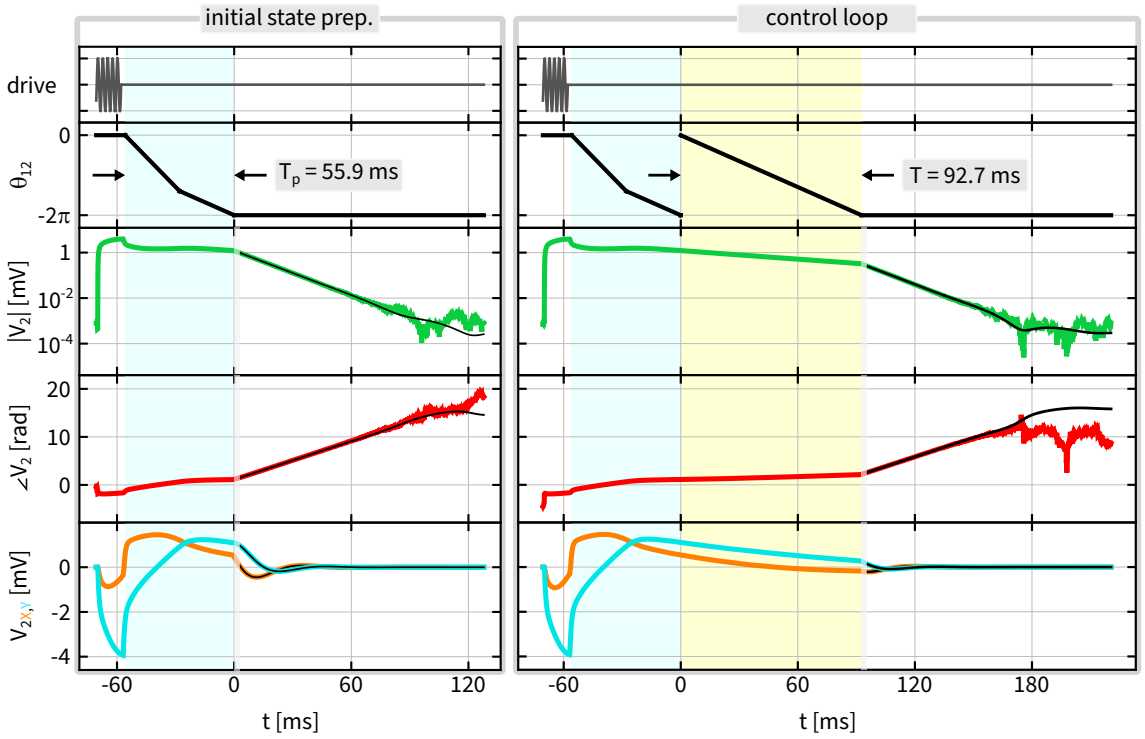

Figure 7.4: Preparing and measuring the initial state vector $\vec{x}(0)$, and its evolution to $\vec{x}(T)$ along a control loop in $\mathcal{EP}_2$: state vector component I. First column: measurements for the first component of $\vec{x}(0)$ obtained by transporting $\vec{x}(-T_p)$ along $\mathcal{C}_{p,\mathrm{deg}}$. **Second column:** measurements for the first component of $\vec{x}(T)$ obtained by transporting $\vec{x}(0)$ along a "simple" non-contractible $\mathcal{C}_{\mathrm{deg}}$. For both columns, dark gray curves: a schematic of the driving force applied to the membrane, which is switched off at $t = -T_p - T_{\mathrm{wait}}$. $T_{\mathrm{wait}} =$ 2 ms is a programmed delay used in these measurements; black curves: $\theta_{12}(t)$ corresponding to $\mathcal{C}_{p,\mathrm{deg}}$ (left column), and $\mathcal{C}_{p,\mathrm{deg}} \,||\, \mathcal{C}_{\mathrm{deg}}$ (right column), where '||' denotes concatenation. Solid green, red, orange and cyan curves: the magnitude, the phase, the in-phase and the quadrature part of the heterodyne signal, respectively and for measurements shown in both columns. Corresponding to each measurement, the solid black curve is a fit to the ringdown evolution which is used to determine $\vec{x}(0)$ (left column) and $\vec{x}(T)$ (right column) as described in Sec. F.3. The duration of initial state preparation, the control loop and the LIA settling are indicated as cyan, yellow and gray shaded regions, respectively. For this measurement, we used the (3,3) and the (5,2) membrane modes with control parameters that tune it to an EP_2 with $\angle R = 0$ (see Secs. 2.2.4.3, 7.1.3 and 7.1.4): $P = \sqrt{P_1 P_2} =$ 7.285 μW, $\sqrt{P_1/P_2} = 0.4, \delta/2\pi =$ 0.2872 MHz, $\eta/2\pi = -30$ Hz for the red-detuned laser tones and $P_4 =$ 16.9 μW, $\Delta_4/2\pi = +2.925$ MHz for the blue-detuned laser tone.

Each segment of θ_{12} shown above performs a specific task to prepare $\vec{x}(0)$. Intuitively, the first leg distills $\vec{x}(-T_p)$ so that it becomes sufficiently equal to the unique least-dissipative eigenvector of $H'(t = (k_p - 1)T, T_p)$, and the second leg subsequently steers it to the unique least-dissipative eigenvector of $H'(t = 0, T)$. The values of k_p and T_p are chosen to prepare the target states in each leg with sufficient accuracy, while ensuring that the decay of the state vector amplitude is minimal.

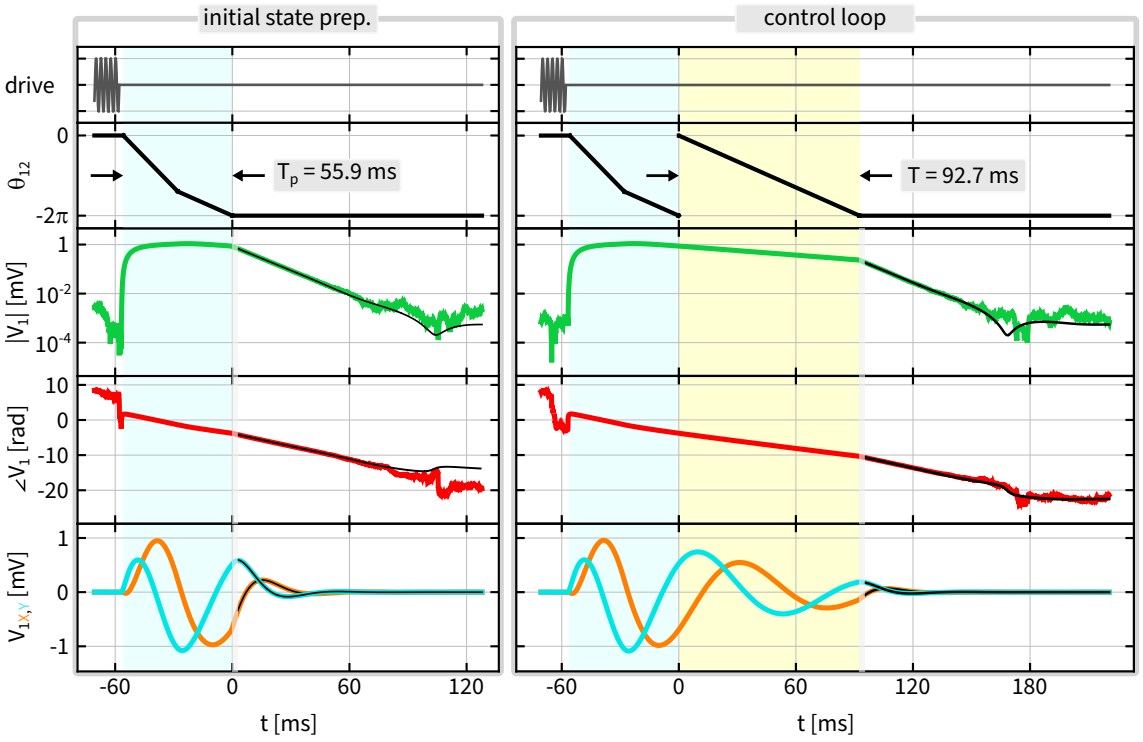

Figure 7.5: Preparing and measuring the initial state vector $\vec{x}(0)$, and its evolution to $\vec{x}(T)$ along a control loop in $\mathcal{EP}_2$: state vector component II. First column: measurements for the second component of $\vec{x}(0)$ obtained by transporting $\vec{x}(-T_p)$ along $\mathcal{C}_{p,\mathrm{deg}}$. **Second column:** measurements for the second component of $\vec{x}(T)$ obtained by transporting $\vec{x}(0)$ along a "simple" non-contractible $\mathcal{C}_{\mathrm{deg}}$. For both columns, dark gray curves: a schematic of the driving force applied to the membrane, which is switched off at $t = -T_p - T_{\mathrm{wait}}$. $T_{\mathrm{wait}} =$ 2 ms is a programmed delay used in these measurements; black curves: $\theta_{12}(t)$ corresponding to $\mathcal{C}_{p,\mathrm{deg}}$ (left column), and $\mathcal{C}_{p,\mathrm{deg}} \,||\, \mathcal{C}_{\mathrm{deg}}$ (right column). Solid green, red, orange and cyan curves: the magnitude, the phase, the in-phase and the quadrature part of the heterodyne signal, respectively and for measurements shown in both columns. Corresponding to each measurement, the solid black curve is a fit to the ringdown evolution which is used to determine $\vec{x}(0)$ (left column) and $\vec{x}(T)$ (right column) as described in Sec. F.3. The duration of initial state preparation, the control loop and the LIA settling are indicated as cyan, yellow and gray shaded regions, respectively. For this measurement, we used the same membrane modes and the control parameters that tune it to the same EP_2 as in Fig. 7.4.

Similar to all previous instances in this thesis, we always work with an intrinsically damped system and as such the initial state vector we have prepared here, must have sufficient amplitude for further processing and experimentation. We provide further details about the initial state preparation protocol in Sec. F.1. We also note that the choice of preparing $\vec{x}(-T_p)$ as $(1,0)^{\mathrm{T}}$ or $(0,1)^{\mathrm{T}}$ does not represent a special constraint. Any other choice of $\vec{x}(-T_p)$, with suitably curated $\mathcal{C}_{p,\mathrm{deg}}$ that can provide the desired $\vec{x}(0)$, is equally valid. However, the present choice is preferred due to the relative ease with which we can perform experiments and subsequent analyses in the basis of uncoupled

membrane modes (see below as well as Secs. 7.1.3.2 and 7.1.4).

Fig. 7.3(b:first column) illustrates this procedure, while the left column of Figs. 7.4 and 7.5 demonstrate initializing the state vector $\vec{x}(-T_p) \propto (1,0)^{\mathrm{T}}$, which is subsequently transported along $\mathcal{C}_{p,\mathrm{deg}}$ to prepare $\vec{x}(0)$. For this measurement: $\{T_p =$ 55.9 ms$, T =$ 92.7 ms$, k_p =$ 0.302$\}$. The prepared $\vec{x}(0)$ is conveniently measured in the basis of uncoupled membrane modes, which is accomplished by turning off all control tones at $t = 0$, and letting the state vector ring down. Fitting this ringdown data provides $\vec{x}(0)$ (Sec. F.3.2). The first panel of Fig. 7.7 shows measured $\vec{x}(0)$ for all T used for traversing $\mathcal{C}_{\mathrm{deg}}$ (see immediately below: Sec. 7.1.3.2).

7.1.3.2 Traversing $\mathcal{C}_{\mathbf{deg}}$ in real time and final state measurement

Transporting $\vec{x}(0)$ along $\mathcal{C}_{\mathrm{deg}}$ is straightforward. It immediately follows the initial state preparation step (Sec. 7.1.3.1) at $t = 0$, and the control tones are tuned in real time for duration T via $\theta_{12}(t) = -2\pi t/T$, in this case. At the end of this procedure, we have $\vec{x}(T)$.

Fig. 7.3(b:second column) illustrates this procedure, while the right column of Figs. 7.4 and 7.5 demonstrate preparing and subsequently transporting $\vec{x}(0)$ along $\mathcal{C}_{\mathrm{deg}}$ to obtain $\vec{x}(T)$. For this measurement, we used the same values of $\{T_p, T, k_p\}$ as in Sec. 7.1.3.1. The resulting $\vec{x}(T)$ is conveniently measured in the basis of uncoupled membrane modes in the same manner as for $\vec{x}(0)$ (Sec. 7.1.3.1). The corresponding ringdown data is fit to obtain $\vec{x}(T)$ (Sec. F.3.2). The second panel of Fig. 7.7 shows measured $\vec{x}(T)$ for a range of T.

7.1.3.3 Spectroscopy at EP_2

Spectroscopy of the system's degenerate eigenvalue λ_{EP} and the quantity R is accomplished via ringdown measurements as described in Secs. 4.5.3 and 7.1.1, with its procedure schematically illustrated in Fig. 7.3(b:third column). Fig. 7.6 shows an exemplary spectroscopy measurement corresponding to real time dynamics measurements in the two previous sections (Sec. 7.1.3.1 and 7.1.3.2). The ringdown data is fit to the expected form near EP_2, as opposed precisely at EP_2. This is simply due to the fact that we

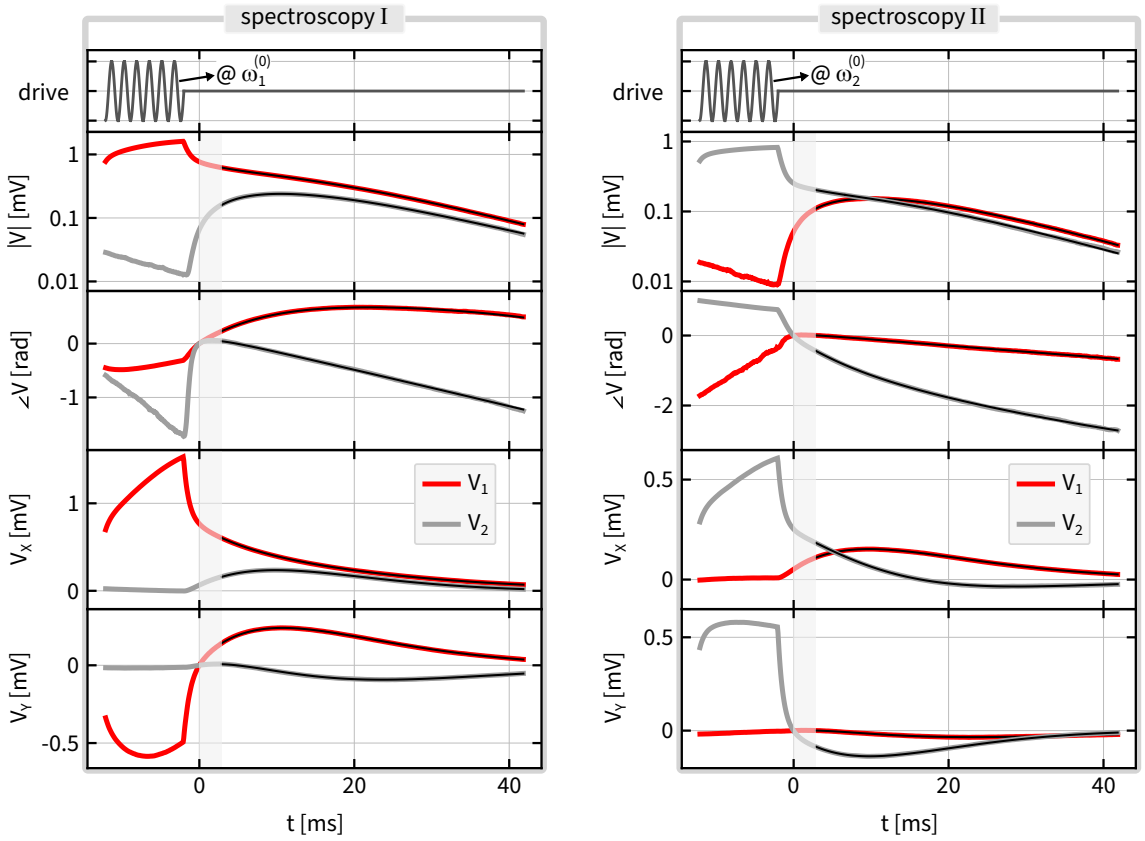

Figure 7.6: Spectroscopy at EP_2. First column: first half of the measurements that determine λ_{EP} and R at EP_2. **Second column:** second half of the measurements that determine λ_{EP} and R at EP_2. For first and second columns, dark gray curves: a schematic of the driving force applied to the membrane near (3,3) and (5,2) membrane modes, respectively, which is switched off at $t = -T_{\mathrm{wait}}$. $T_{\mathrm{wait}} =$ 2 ms is a programmed delay used in these measurements; Second to fifth rows in both columns shows the magnitude, the phase, the in-phase and the quadrature part of the heterodyne signal near (3,3) membrane mode as red curves and (5,2) membrane mode as gray curves, respectively. Corresponding to each measurement, the solid black curve is a fit to the ringdown evolution which is used to determine λ_{EP} and R at EP_2 as described in Sec. F.3. The duration of the LIA settling is indicated as the gray shaded region. For this measurement, we used the same membrane modes and the control parameters that tune it to the same EP_2 as in Figs. 7.4 and 7.5.

can empirically approach an EP_2 with finite precision (see Secs. F.2 and F.3.3). The fit parameters include the system's nearly degenerate eigenvalues $\{\lambda_+, \lambda_-\}$ and nearly degenerate eigenvector components $\{v_1, v_2\}$. The degenerate eigenvalue λ_{EP} is then taken to be

$$\lambda_{EP} = \frac{\lambda_+ + \lambda_-}{2} \tag{7.3}$$

and R at EP_2 is given by

$$R = (\lambda_+ - \lambda_-)\left(\frac{1}{1-k} - \frac{1}{2}\right) \tag{7.4}$$

where $k = v_1 v_2$. The quantity R is detailed in Sec. 7.4.1.1 and Eq. (7.4) is derived in Sec. F.2.2.3.

The third panel of Fig. 7.7 illustrates the result of spectroscopy measurements at this EP_2 that complement the real time dynamics measurements in $\mathcal{EP}_2$ described in Secs. 7.1.3.1 and 7.1.3.2.

Parameter	Measured	Theory
$\lambda_{EP}/2\pi$ (Hz)	$-19.92 \pm 0.24 - (13.65 \pm 0.24)i$	$-20.10 - 14.30i$
$\delta\lambda/2\pi$ (Hz)	$-1.3 \pm 1.6 + (0.0 \pm 1.2)i$	0
$R/2\pi$ (Hz)	$15.15 \pm 0.12 - (0.10 \pm 0.11)i$	15.60

Table 7.1: Spectroscopic properties of the first EP_2 candidate. This EP_2 is located in Sec. 7.1.1 and is utilized in Secs. 7.1, 7.2.1, 7.2.2.1, 7.2.2.2 and 7.3. λ_{EP}: the degenerate eigenvalue at EP_2, $\delta\lambda$: non-degeneracy of eigenvalues, R: parameter that characterizes the rate at which any state vector of the degenerate system approaches the unique right eigenvector at EP_2 (Eq. (7.4)). Measured value is reported as mean $\pm$ one standard deviation. Theoretical values are obtained by fitting the spectroscopy data used for locating this EP_2.

At EP_2, we expect $\lambda_+ = \lambda_-$ and $k = 1$. Measurements of $\delta\lambda = (\lambda_+ - \lambda_-) \approx 0$ and a finite value of $R \approx \delta\lambda/(1-k)$ empirically corroborate this fact. The resulting values of $\{\lambda_{EP}, \delta\lambda, R\}$ are reported as the mean and one standard deviation of all spectroscopy measurements, and are illustrated as such in the third panel of Fig. 7.7. They are summarized in Table 7.1 alongside the corresponding theoretical predictions. Here we remind ourselves that the theory predictions are calculated using system parameters obtained by fitting the spectroscopy data used for locating the EP_2 as described in Sec. 7.1.1. Subsequently, the mean values of $\{\lambda_{EP}, R\}$, i.e., $\{\overline{\lambda}_{EP}, \overline{R}\}$ are utilized to construct two dynamical phases: $\phi_{\mathrm{LD,deg}}(T) = \overline{\lambda}_{EP} T$ - the well-known linear dynamical phase, and $\phi_{\mathrm{sqrt,deg}}(T) = \sqrt{2\pi\overline{R}T}$ (from Eq. (2.58)) - a novel $\sqrt{T}$ phase resulting from real time dynamics in $\mathcal{EP}_2$, respectively. Further intuition and details for $\phi_{\mathrm{sqrt,deg}}$ are provided in Sec. 7.4.1.

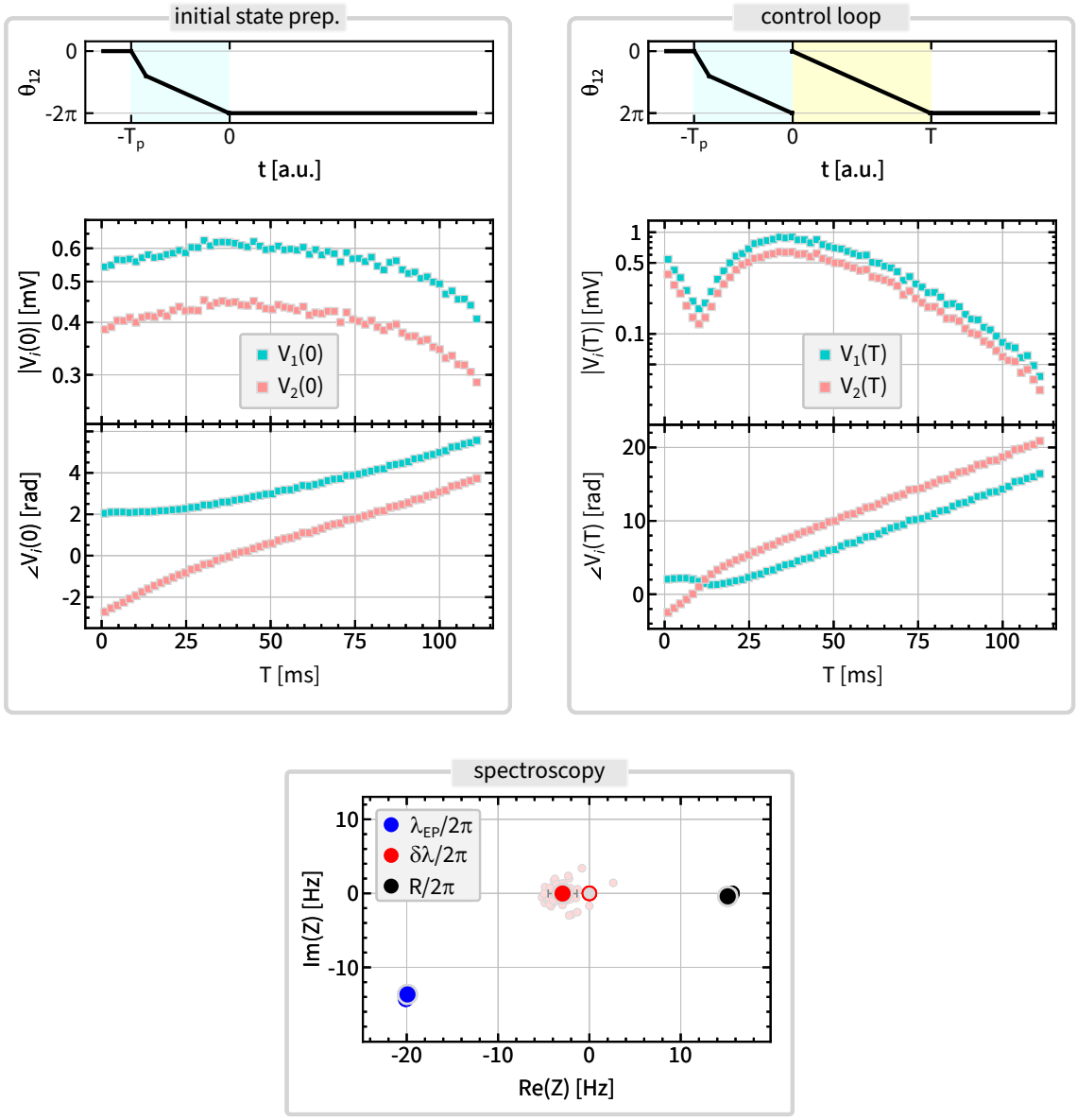

Figure 7.7: Measurement of real time dynamics in $\mathcal{EP}_2$ - part I. Panel I: Black curve (top panel) shows $\theta_{12}(t)$ corresponding to $\mathcal{C}_{p,\mathrm{deg}}$ used for initial state preparation. Measured magnitude (middle panel) and phase (bottom panel) of the heterodyne signal used for determining the initial state $\vec{x}(0)$ for each T used for traversing $\mathcal{C}_{\mathrm{deg}}$. Cyan (pink) squares: the first (second) component of the state vector. **Panel II:** Same as panel I except in top panel, $\theta_{12}(t)$ corresponds to $\mathcal{C}_{p,\mathrm{deg}} \mid\mid \mathcal{C}_{\mathrm{deg}}$; measured heterodyne signal (middle: magnitude and bottom: phase) used for determining the final state $\vec{x}(T)$. **Panel III:** Spectroscopy at EP_2 that complement the measurements in panels I and II. They provide λ_{EP} (blue disk: $\overline{\lambda}_{EP}$) and R (black disk: $\overline{R}$), which independently determine the linear dynamical phase and a novel $\sqrt{T}$ dynamical phase acquired by $\vec{x}(T)$, respectively. Red disk: $\delta\lambda$, which is expected to be 0 at an EP_2. For each quantity, the theoretical prediction is given by a gray disk with same edge color, the individual measurements are represented as smaller disks with a lighter color shade and the gray fences indicate corresponding error bars. For this measurement, we used the same membrane modes and the control parameters that tune it to the same EP_2 as in Figs. 7.4-7.6.

For our present purposes, we note that choosing $\angle R = 0$ is strategic, complemented by its spectroscopic measurements (see Table 7.1 and third panel of Fig. 7.7). As a result of this choice, $\mathrm{Re}(\phi_{\mathrm{sqrt,deg}})$ is expected to vanish. Furthermore, following our discussion of the special case of $\angle R = 0$ in Sec. 2.2.4.3, we expect all real-valued dynamical phases but $\mathrm{Re}(\phi_{\mathrm{LD,deg}})$ to identically vanish for $T \geq \frac{\pi}{2R}$. Consequently, we obtained the following exact result:

$$\mathrm{Re}(\phi_{\mathrm{deg}}(T)) = \mathrm{Re}(\phi_{\mathrm{LD,deg}}(T)) + \phi_{B,\mathrm{deg}},\ \forall\ T \geq \pi/2R \tag{7.5}$$

In what follows (Sec. 7.1.4), the measured $\{\vec{x}(0), \vec{x}(T)\}$ along with λ_{EP} and $\angle R = 0$ are utilized to demonstrate the above exact result, and subsequently the real-valued $\phi_{B,\mathrm{deg}}$ is isolated.

7.1.4 Measuring $\boldsymbol{\phi_{\mathrm{deg}}}$ and isolating $\boldsymbol{\phi_{B,\mathrm{deg}}}$

In this section, we compare the measured final states $\vec{x}(T)$ (Sec. 7.1.3.2) with the corresponding measured initial state $\vec{x}(0)$ (Sec. 7.1.3.1), and extract their relative phase $\phi_{\mathrm{deg}}(T)$. We then isolate $\phi_{B,\mathrm{deg}}$ by removing the independently measured dynamical phases (Sec. 7.1.3.3) from $\phi_{\mathrm{deg}}(T)$. For this discussion, we continue to use the same "simple" non-contractible $\mathcal{C}_{\mathrm{deg}}$ from Sec. 7.1.3, which crucially employs $\angle R = 0$.

The relative phase $\phi_{\mathrm{deg}}(T)$ of $\vec{x}(T)$ compared to $\vec{x}(0)$ is given by

$$\vec{x}(T) = e^{-i\phi_{\mathrm{deg}}(T)}\vec{x}(0) \tag{7.6}$$

$$\Rightarrow \begin{bmatrix} x_1(T) \\ x_2(T) \end{bmatrix} = e^{-i\phi_{\mathrm{deg}}(T)} \begin{bmatrix} x_1(0) \\ x_2(0) \end{bmatrix} \tag{7.7}$$

where in the second step, we expressed the state vectors in the basis of uncoupled membrane modes i.e., $(1,0)^{\mathrm{T}}$ as the (3,3) mode and $(0,1)^{\mathrm{T}}$ as the (5,2) mode. Subsequently, we define:

$$\phi_{\mathrm{deg},1}(T) = i\,\mathrm{Log}(x_1(T)/x_1(0)) \tag{7.8}$$

$$\phi_{\mathrm{deg},2}(T) = i\,\mathrm{Log}(x_2(T)/x_2(0)) \tag{7.9}$$

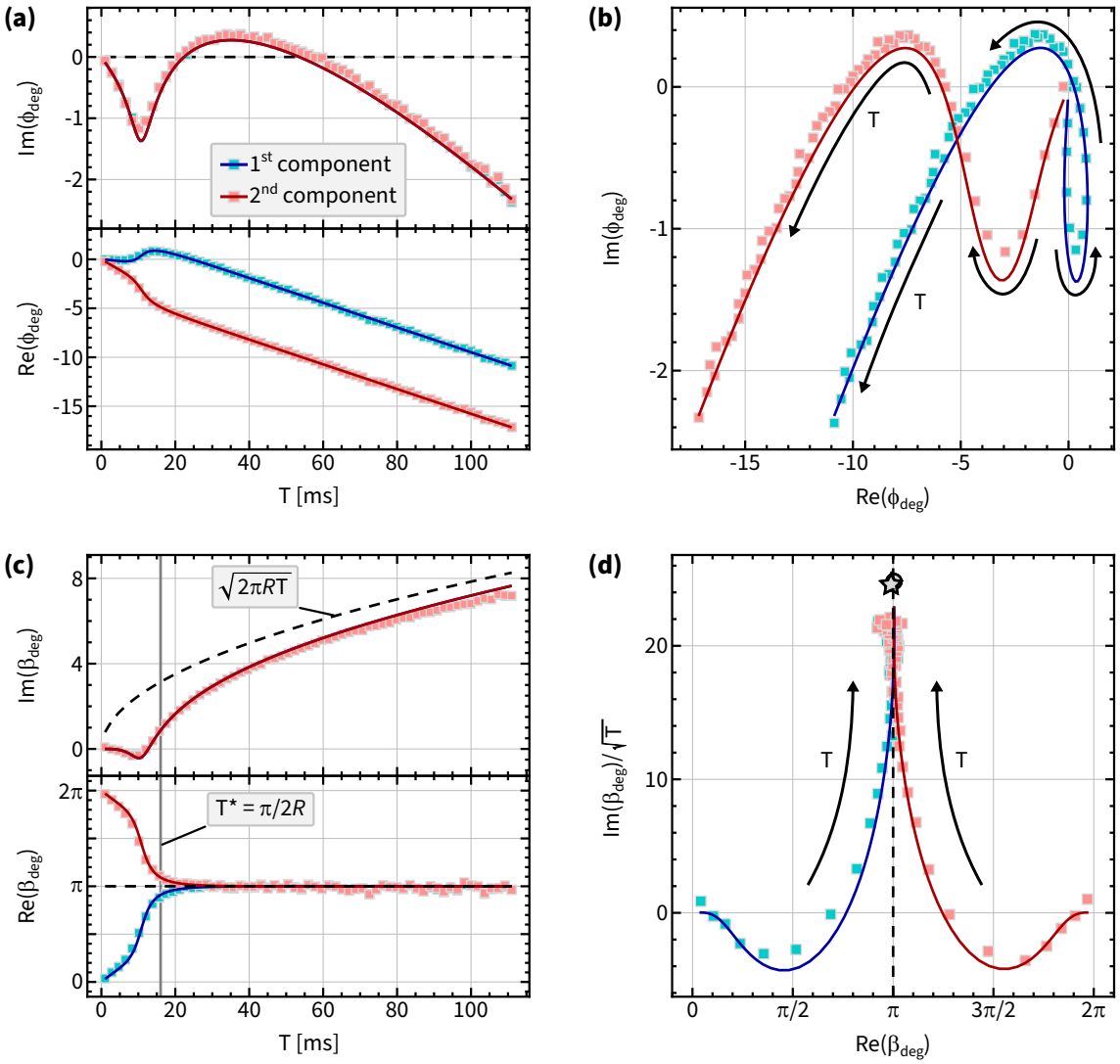

Figure 7.8: Measurement of real time dynamics in $\mathcal{EP}_2$ - part II. (a) $\phi_{\mathrm{deg},j}$ versus duration of $\mathcal{C}_{\mathrm{deg}}$, T, with $j = 1(2)$ denoting quantities corresponding to the first (second) component of the state vector (see Eqs. (7.10) and (7.11)). Cyan and pink squares: data corresponding to $\phi_{\mathrm{deg},1}$ and $\phi_{\mathrm{deg},2}$, while the solid curves represent the corresponding no-free-parameter theory predictions. Top panel: $\mathrm{Im}(\phi_{\mathrm{deg},j}(T))$ and bottom panel: $\mathrm{Re}(\phi_{\mathrm{deg},j}(T))$. Dashed black line in the top panel represents $\mathrm{Im}(\phi_{\mathrm{deg}}) = 0$. **(b)** Same as (a) but illustrating a parametric plot of complex $\phi_{\mathrm{deg},j}(T)$. Curved black arrows indicates increasing T. **(c)** Same as (a) but illustrating $\beta_{\mathrm{deg},\{1,2\}} = \phi_{\mathrm{deg},j} - \phi_{\mathrm{LD,deg}}$ versus T. Top panel: $\mathrm{Im}(\beta_{\mathrm{deg},\{1,2\}}(T))$ and bottom panel: $\mathrm{Re}(\beta_{\mathrm{deg},\{1,2\}}(T))$. Dashed black curves in the top and bottom panel represents $\sqrt{2\pi RT}$ and π, respectively. Gray vertical line denotes $T^* = \pi/2R$ with $\angle R = 0$ (see Sec. 7.1.3). **(d)** Same as (c) but illustrating a parametric plot of $\mathrm{Im}(\beta_{\mathrm{deg},j}(T))/\sqrt{T}$ versus $\mathrm{Re}(\beta_{\mathrm{deg},j}(T))$ for $j \in \{1,2\}$. Gray star: estimated value of $\{\phi_{B,\mathrm{deg}}, \sqrt{2\pi R}\}$ (see Sec. F.4), gray fences around the gray star (not visible): error in estimating $\{\phi_{B,\mathrm{deg}}, \sqrt{2\pi R}\}$ (see Sec. F.4), gray disk: theory prediction: $\{\phi_{B,\mathrm{deg}} = 3.18, \sqrt{2\pi R} = 24.82\ (2\pi\mathrm{Hz})\}$, dashed black line: $\mathrm{Re}(\beta_{\mathrm{deg}}) = \pi$. Curved black arrows indicates increasing T. For this measurement, we used the same membrane modes and the control parameters that tune it to the same EP_2 as in Figs. 7.4-7.7.

They are conveniently re-written as:

$$\phi_{\mathrm{deg},1}(T) = i\,\mathrm{Log}(V_1(T)/V_1(0)) \tag{7.10}$$

$$\phi_{\mathrm{deg},2}(T) = i\,\mathrm{Log}(V_2(T)/V_2(0)) \tag{7.11}$$

where $V_j(t) = \alpha_j x_j(t)$ is the heterodyne signal measured near $\omega_j^{(0)}$: the bare resonance frequency of j^{th} membrane mode with $j \in \{1,2\}$, x_j the motional amplitude, and α_j the motion-to-voltage transduction factor. Since it is the ratio of heterodyne signals that appears in Eqs. (7.10) and (7.11), α_j has no role in $\phi_{\mathrm{deg},j}$, and is left un-measured in these experiments. Fig. 7.8(a,b) illustrates the complex-valued ϕ_{deg} as a function of T. For large T, the phase of the motion evolves linearly with T as shown in $\mathrm{Re}(\phi_{\mathrm{deg},\{1,2\}})$ (lower panel) while the amplitude of the motion displays intriguing features (upper panel: $\mathrm{Im}(\phi_{\mathrm{deg},\{1,2\}})$). Nevertheless, it decays at large T highlighting the overall damping of the system at this EP_2.

To empirically isolate $\phi_{B,\mathrm{deg}}$, we define $\beta_{\mathrm{deg},j}(T) = \phi_{\mathrm{deg},j}(T) - \phi_{\mathrm{LD,deg}}(T)$ for $j \in \{1,2\}$. For our particular choice of $\angle R = 0$, $\mathrm{Re}(\beta_{\mathrm{deg}}(T))$ (defined modulo 2π) is expected to be π for $T \geq T^* = \pi/2R$. This is explicitly demonstrated in the lower panel of Fig. 7.8(c) where $\mathrm{Re}(\beta_{\mathrm{deg},\{1,2\}}(T \geq 2T^*)) \approx \pi$. For the region $T^* \leq T \leq 2T^*$, $\mathrm{Re}(\beta_{\mathrm{deg},\{1,2\}}(T))$ displays a transient behavior consistent with the fact that the fidelity with which the initial state $\vec{x}(0)$ is prepared as the least-dissipative eigenvector of $H'(s=0,T)$ is still not "good enough"; and this interpretation is corroborated by theoretical simulations. We shed more light on this feature in Sec. F.1.2.

The imaginary part of $\beta_{\mathrm{deg},\{1,2\}}(T)$ illustrated in the top panel of Fig. 7.8(c) displays a $\sim \sqrt{T}$ behavior for $T \geq T^*$. This feature agrees with the theoretical prediction. We investigate this novel dynamical phase further in Sec. 7.4.

Fig. 7.8(d) shows a parametric plot of $\mathrm{Im}(\beta_{\mathrm{deg},j}(T))/\sqrt{T}$ versus $\mathrm{Re}(\beta_{\mathrm{deg},j}(T))$ for $j \in \{1,2\}$. Crucially, it also shows the value of $\{\phi_{B,\mathrm{deg}}, \sqrt{2\pi R}\}$ estimated from measured $\beta_{\mathrm{deg},\{1,2\}}$, as a gray star (see Sec. F.4). We estimate $\phi_{B,\mathrm{deg}} = 3.10 \pm 0.08$ which compares favorably to the expected value of π. Additionally, the estimated value of $\sqrt{2\pi R} = 24.59 \pm 0.08$ $(2\pi\mathrm{Hz})$ is in good agreement with the theory prediction of

24.82 $(2\pi\text{Hz})$. This concludes our discussion of measuring $\phi_{B,\mathrm{deg}}$ for this particular $\mathcal{C}_{\mathrm{deg}}$, and all subsequent measurements of $\phi_{B,\mathrm{deg}}$ are subject to this protocol, with possible modifications in analysis techniques indicated therein.

7.2 Topological and geometric character of $\phi_{B,\mathbf{deg}}$

In this section, we describe measurements that demonstrate that $\phi_{B,\mathrm{deg}}$ depends solely on the topology of control paths $\mathcal{C}_{\mathrm{deg}}$ in the degenerate subspace $\mathcal{EP}_2$. These include measurements where we: **(I)** perform "simple" $\mathcal{C}_{\mathrm{deg}}$ that belong to distinct homotopy classes (Sec. 7.2.1), **(II)** vary the shape of $\mathcal{C}_{\mathrm{deg}}$ that belongs to a particular homotopy class (Sec. 7.2.2), and **(III)** vary the manner in which we traverse a $\mathcal{C}_{\mathrm{deg}}$ (Sec. 7.2.3). For clarity, we note that **(I)** and **(II)** probe the topological character of $\phi_{B,\mathrm{deg}}$, while **(III)** probes the geometric character of $\phi_{B,\mathrm{deg}}$.

7.2.1 Part I: Homotopically distinct $\mathcal{C}_{\mathbf{deg}}$

In this section, we reveal via our measurements that $\phi_{B,\mathrm{deg}}$ depends solely on the homotopy class of $\mathcal{C}_{\mathrm{deg}}$ in $\mathcal{EP}_2$. As has been described previously (Sec. 2.2.4.1), the space of $\mathcal{EP}_2 \cong \mathbb{R}\mathrm{P}^3 \times \mathbb{R}$ and consequently all $\mathcal{C}_{\mathrm{deg}}$ belong to one of two homotopy classes.

Homotopy class I: $\mathcal{C}_{\mathrm{deg}}$ is non-contractible; these correspond to an odd winding number (Fig. 7.2(b)).

Homotopy class II: $\mathcal{C}_{\mathrm{deg}}$ is contractible; these correspond to an even winding number (Fig. 7.2(c)).

For this investigation, we continue to utilize the same EP_2 with $\angle R = 0$ as in Sec. 7.1, and consider "simple" $\mathcal{C}_{\mathrm{deg}}$ given by $\vec{Y}_{EP}$ (as in Eq. (7.1)) and $\theta_{12}(s) = -2n\pi s \bmod 2\pi$, varied in real time for a duration T, with $0 \leq s = t/T \leq 1$ and $n \in \mathbb{N}$. Intuitively, it corresponds to rotating $\mathbf{B}^{\mathrm{deg}}_{\mathrm{Re,Im}}$ at a constant rate n-times around the z-axis (see also Secs. 2.2.4.3 and 7.1.2).

Measurements of $\phi_{\mathrm{deg},j}(T)$ for $j \in \{1,2\}$ and dynamical phases $\{\phi_{\mathrm{LD,deg}}, \phi_{\mathrm{sqrt,deg}}\}$ were carried out in the same manner as in Sec. 7.1. However, for this exercise we define $\overline{\beta}_{\mathrm{deg},\{1,2\}}(T) = \phi_{\mathrm{deg},\{1,2\}}(T) - \phi_{\mathrm{LD,deg}}(T)$ such that the range $\mathrm{Re}(\overline{\beta}_{\mathrm{deg},\{1,2\}})$ is no longer constrained to be within $[0, 2\pi]$. Fig. 7.9 illustrates $\theta_{12}(s)$ for various $\mathcal{C}_{\mathrm{deg}}$ and corresponding measurements of $\overline{\beta}_{\mathrm{deg},\{1,2\}}(T)$ for $n = \{1,2,3,4\}$.

$\mathrm{Re}(\overline{\beta}_{\mathrm{deg},1(2)}(T))$ is expected to be $\pm n\pi$ for $T^* \geq n\pi/2R$, and is shown in the top

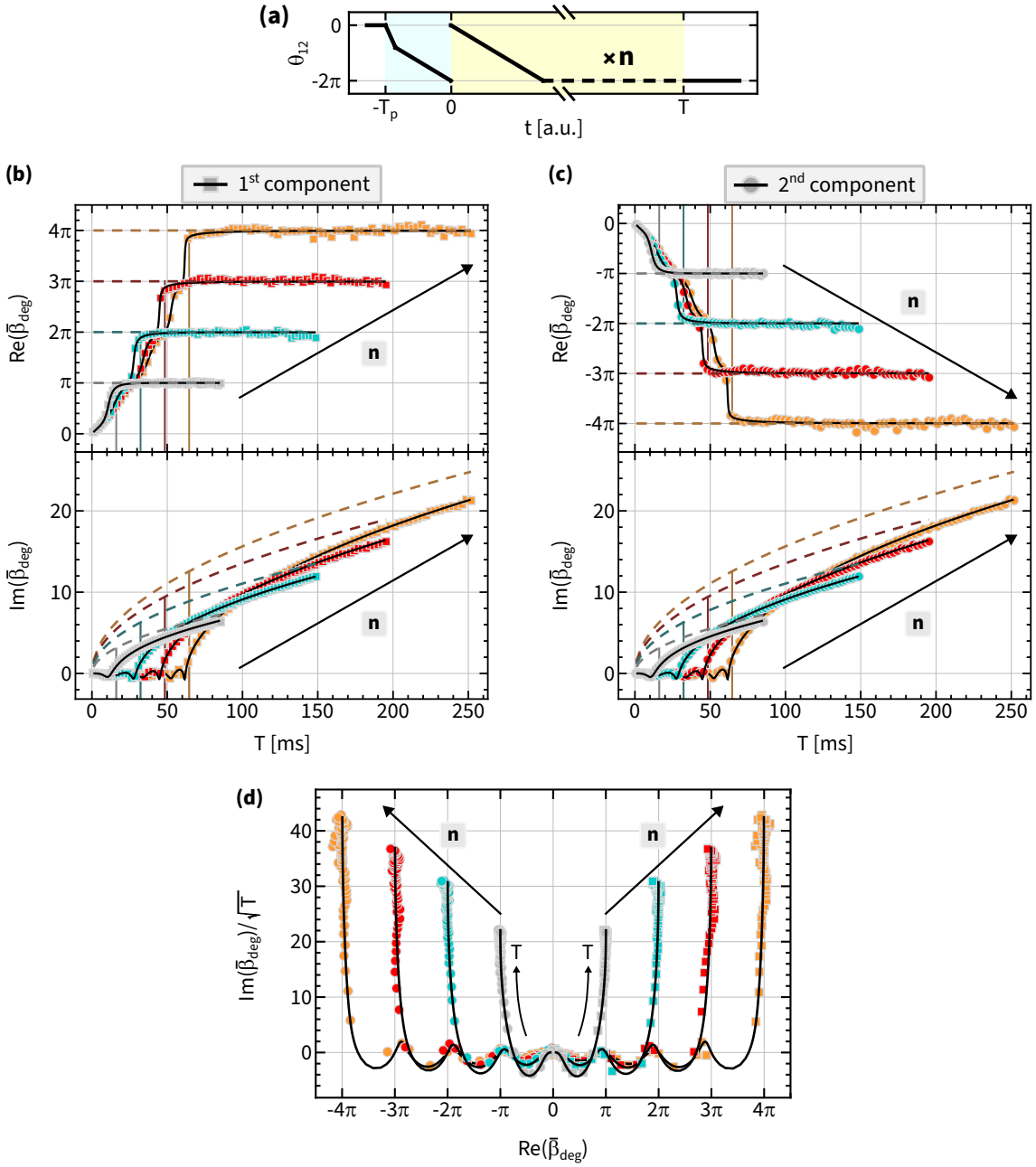

Figure 7.9: Topological character of $\phi_{B,\mathbf{deg}}$ - part IA. (a) $\mathcal{C}_{\mathrm{deg}}$ for which θ_{12} is ramped from 0 to $-2\pi n \mod 2\pi$ for $0 \leq t \leq T$, for $n = \{1, 2, 3, 4\}$. For $-T_p \leq t < 0$, θ_{12} corresponds to $\mathcal{C}_{p,\mathrm{deg}}$ that corresponds to initial state preparation. **(b)** Top (bottom) panel: $\mathrm{Re/Im}(\overline{\beta}_{\mathrm{deg},1}(T))$ corresponding to the first component of the state vector. Gray, cyan, red and orange squares: data corresponding to $n = \{1, 2, 3, 4\}$, respectively. Solid curves: no-free-parameter theory predictions for each n. Dashed lines correspond to $n\pi$ for top panel and $\sqrt{2n\pi RT}$ for the bottom panel. Solid vertical lines indicate $T^* = n\pi/2R$. Straight black arrow indicates increasing n. **(c)** Same as (b) but for $\mathrm{Re/Im}(\overline{\beta}_{\mathrm{deg},2}(T))$ corresponding to the second component of the state vector, and horizontal dashed lines in the top panel correspond to $-n\pi$. **(d)** Same as (b) but a polar plot of $\mathrm{Im}(\overline{\beta}_{\mathrm{deg},1(2)}(T))/\sqrt{T}$ versus $\mathrm{Re}(\overline{\beta}_{\mathrm{deg},1(2)}(T))$. Curved (straight) black arrows indicates increasing $T(n)$. For this measurement, we used the same membrane modes and the control parameters that tune it to the same EP_2 as in Figs. 7.4-7.8.

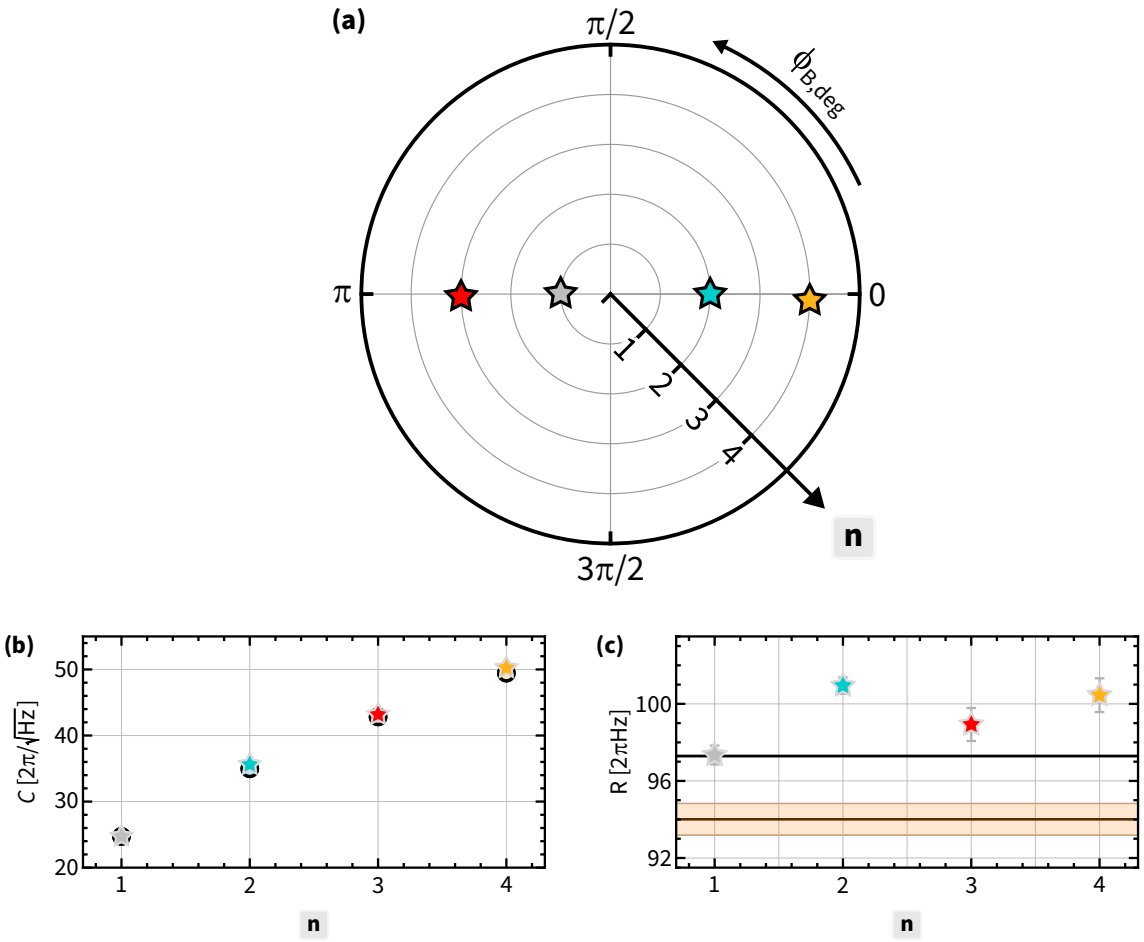

Figure 7.10: Topological character of $\phi_{B,\mathbf{deg}}$ - part IB. (a) Polar plot of $\phi_{B,\mathrm{deg}}$ versus n. Stars: estimated value from data corresponding to $\mathrm{Re}(\overline{\beta}_{\mathrm{deg},\{1,2\}}(T))$ (Sec. F.4). Error bars are smaller than the data symbol. **(b)** The coefficient C versus n that governs $\mathrm{Im}(\overline{\beta}_{\mathrm{deg},\{1,2\}}(T)) \approx \sqrt{CT}$ for large T. Stars: estimated value from corresponding data (Sec. F.4), disks: theory prediction. **(c)** R estimated from $C/2\pi n$ are shown as stars. Black solid line indicates the theory prediction of R while dark-orange solid line flanked by orange shaded region corresponding to mean and standard deviation of $|R|$ obtained from spectroscopy measurement at EP_2. For this measurement, we used the same membrane modes and the control parameters that tune it to the same EP_2 as in Figs. 7.4-7.9.

panels of Fig. 7.9(b,c), respectively. Independently, $\mathrm{Im}(\overline{\beta}_{\mathrm{deg},1(2)}(T))$ is expected to evolve as $\sqrt{2n\pi RT}$ for $T^* \geq n\pi/2R$. This is corroborated by our measurements shown in the bottom panels of Fig. 7.9(b,c) which appear to asymptote to the expected value. Finally, we conclude this initial analysis by showing a parametric plot of $\mathrm{Im}(\overline{\beta}_{\mathrm{deg},1(2)}(T))/\sqrt{T}$ versus $\mathrm{Re}(\overline{\beta}_{\mathrm{deg},1(2)}(T))$ in Fig. 7.9(d).

To isolate $\phi_{B,\mathrm{deg}}$ (always defined modulo 2π), we analyze $\mathrm{Re}(\overline{\beta}_{\mathrm{deg},1(2)})$ as prescribed in Sec. F.4 and the results are illustrated in Fig. 7.10(a). They demonstrate $\phi_{B,\mathrm{deg}} = (n \bmod 2)\pi$. Further analysis of $\mathrm{Im}(\overline{\beta}_{\mathrm{deg},1(2)})$ (Sec. F.4) reveals that it is indeed given by $\sqrt{CT} \equiv \sqrt{2n\pi RT}$ for large T. This analysis is illustrated in Fig. 7.10(b,c).

7.2.2 Part II: Varying the shape of $\mathcal{C}_{\mathrm{deg}}$

To study the effect (or lack thereof) of the shape of $\mathcal{C}_{\mathrm{deg}}$, we consider three examples below. The first example (Sec. 7.2.2.1) continues with "simple" but non-contractible $\mathcal{C}_{\mathrm{deg}}$ that correspond to EP_2 with $\angle R = 0$, but for several distinct EP_2 locations. Intuitively, this corresponds to simply rescaling the lengths of $\mathbf{B}^{\mathrm{deg}}_{\mathrm{Re,Im}}$ while keeping their common orientation in $\mathbb{R}^3$ fixed. The second example (Sec. 7.2.2.2) relaxes the $\angle R = 0$ constraint. Here we consider "simple" non-contractible $\mathcal{C}_{\mathrm{deg}}$ that correspond to EP_2 with constant $\angle R$ that is systematically perturbed from 0. Intuitively, this corresponds to tweaking the common orientation of $\mathbf{B}^{\mathrm{deg}}_{\mathrm{Re,Im}}$ in $\mathbb{R}^3$ from its $\angle R = 0$ orientation. In the final example (Sec. 7.2.2.3), we consider "simple" $\mathcal{C}_{\mathrm{deg}}$ that correspond to EP_2 with arbitrary but constant R. In the picture of $\mathbf{B}^{\mathrm{deg}}_{\mathrm{Re,Im}}$, this corresponds to them having any arbitrary common orientation in $\mathbb{R}^3$.

7.2.2.1 $\mathcal{C}_{\mathrm{deg}}$ with $\angle R = 0$

For these measurements, we systematically located several distinct EP_2 with $\angle R = 0$, subsequently performed "simple" non-contractible $\mathcal{C}_{\mathrm{deg}}$ and measured $\phi_{B,\mathrm{deg}}$, all in the same manner as described in Sec. 7.1. These measurements continue to employ the (3,3) and the (5,2) membrane modes Floquet-coupled using two red-detuned tones $\{P_1, P_2, \delta, \eta, \theta_{12}\}$ and their damping reduced by the blue-detuned tone $\{P_4, \Delta_4\}$. In particular, we stepped the control parameter η to various values and correspondingly

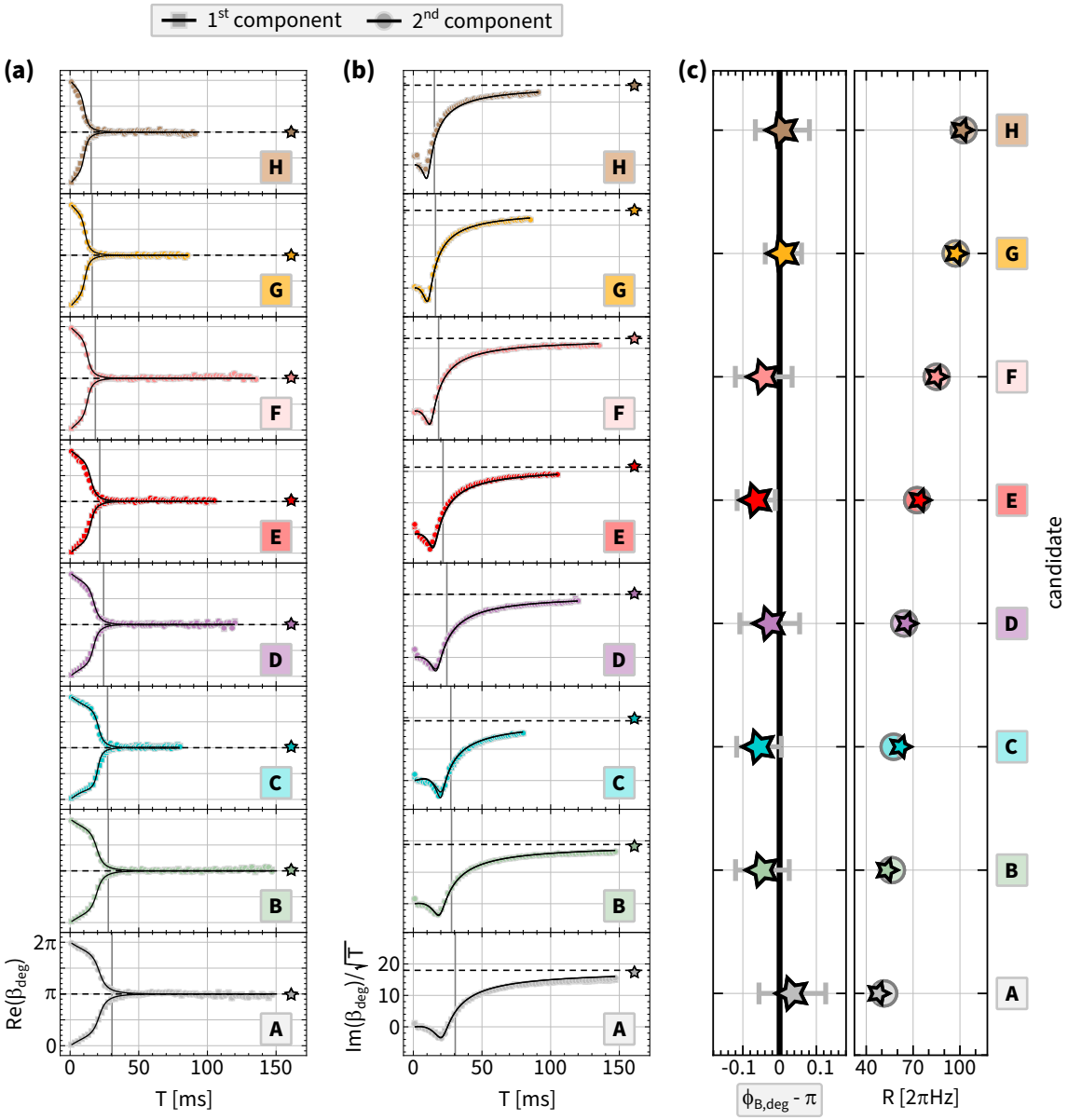

Figure 7.11: Topological character of $\phi_{B,\mathrm{deg}}$ - part IIA(i). (a) $\mathrm{Re}(\beta_{\mathrm{deg}}(T))$ for a variety of "simple" non-contractible $\mathcal{C}_{\mathrm{deg}}$. Bottom to top correspond to candidates A to H. Colored squares and disks: data corresponding to state vector component 1 and 2; solid black curve: corresponding no-free-parameter theory prediction; dashed gray line corresponds to π while the vertical gray line indicates $T^* = \pi/2R$ for each candidate; colored stars: $\phi_{B,\mathrm{deg}}$ estimated from data corresponding to $\mathrm{Re}(\beta_{\mathrm{deg}}(T))$ data (see Sec. F.4). We note that all panels shown here share the same X and Y axes as the bottom-most panel. **(b)** Same as (a) except we illustrate $\mathrm{Im}(\beta_{\mathrm{deg}})(T)/\sqrt{T}$. Dashed gray line: $\sqrt{2\pi R}$ from theory prediction; colored stars: corresponding estimated value of $\sqrt{2\pi R}$ from $\mathrm{Im}(\beta_{\mathrm{deg}})(T)$ data (see Sec. F.4). We note that all panels shown here share the same X and Y axes as the bottom-most panel. **(c)** Left: $(\phi_{B,\mathrm{deg}} - \pi)$ estimated from data corresponding to $\mathrm{Re}(\beta_{\mathrm{deg}})(T)$ for each candidate. Right: R estimated from data corresponding to $\mathrm{Im}(\beta_{\mathrm{deg}})(T)$ for each candidate. For this measurement, we used the (3,3) and the (5,2) membrane modes. Control parameters that tune to corresponding EP_2 for each candidate are listed in Table 7.2.

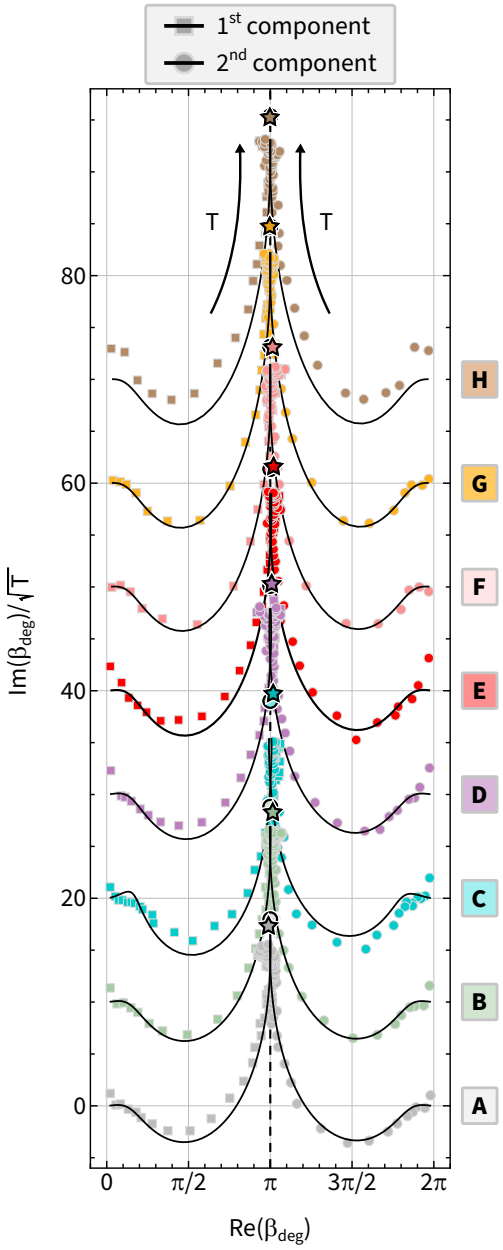

Figure 7.12: Topological character of $\phi_{B,\mathrm{deg}}$ - part IIA(ii). Parametric plot of $\mathrm{Im}(\beta_{\mathrm{deg}}(T))/\sqrt{T}$ versus $\mathrm{Re}(\beta_{\mathrm{deg}}(T))$ for a variety of "simple" non-contractible $\mathcal{C}_{\mathrm{deg}}$. Bottom to top correspond to candidates A to H. Colored squares and disks: data corresponding to state vector component 1 and 2; solid black curve: corresponding no-free-parameter theory prediction; dashed gray line: $\mathrm{Re}(\beta_{\mathrm{deg}}) = \pi$; colored stars: $\{\phi_{B,\mathrm{deg}}, \sqrt{2\pi R}\}$ estimated from β_{deg} data (see Sec. F.4). Curved black arrows indicates increasing T. Each candidate except A is shifted up by 10 units compared to the preceding one. For this measurement, we used the (3,3) and the (5,2) membrane modes. Control parameters that tune to corresponding EP_2 for each candidate are listed in Table 7.2.

	EP_2 coordinates					
Candidate	$P=\sqrt{P_1P_2}$	$\delta/2\pi$	$\sqrt{P_1/P_2}$	$\eta/2\pi$	P_4	$\Delta_4/2\pi$
A	3.84	0.281	1.2	-12	8	2.888
B	4.30	0.275	0.68	-17	8.3	3.031
C	4.28	0.2801	0.75	-19	5.45	2.985
D	4.789	0.2954	0.4	-20	12	3.048
E	5.695	0.2837	0.4	-24	13	2.981
F	6.5	0.289	0.4	-25	16.9	2.964
G	7.285	0.2872	0.4	-30	16.9	2.925
H	8.087	0.2895	0.4	-35	17	2.886

Table 7.2: Coordinates of EP_2 candidates accessed in Sec. 7.2.2.1. The coordinates $P=\sqrt{P_1P_2}$ (units: μW) and δ (units: $2\pi\times$MHz) represent coordinates of the vortex of $\angle D$ obtained from corresponding spectroscopy measurements (see Sec. 7.1.1). Other coordinates $\sqrt{P_1/P_2}$, η ((units: $2\pi\times$Hz)), P_4 (units: μW) and Δ_4 (units: $2\pi\times$MHz) are held fixed to access EP_2 with $\angle R=0$. Note: **(i)** candidate **B** is also studied in Sec. 7.2.3; **(ii)** candidate **G** is also studied in Secs. 7.1, 7.2.1, 7.2.2.2 and 7.3; **(iii)** candidate **F** is also studied in Sec. 7.4.

tweaked $\{P_4,\Delta_4\}$ to locate EP_2 with $\angle R=0$. Intuitively, changing η approximately corresponds to changing the length of $\mathbf{B}^{\mathrm{deg}}_{\mathrm{Re,Im}}$ via changing $|R|$ while tweaking $\{P_4,\Delta_4\}$ maintains its common orientation commensurate with $\angle R=0$. The coordinates and spectroscopic properties of all distinct EP_2 accessed in these measurements are given in Tables 7.2 and 7.4, respectively. Measurements of $\beta_{\mathrm{deg}}(T)$ and $\phi_{B,\mathrm{deg}}$ that correspond to each EP_2 are illustrated in Figs. 7.11 and 7.12. The measurements are supplemented with no-free-parameter theory predictions which continue to be in good agreement. Finally for this example, the measured value $\phi_{B,\mathrm{deg}}\approx\pi$ for all cases corroborates its independence from the shape of non-contractible $\mathcal{C}_{\mathrm{deg}}$.

7.2.2.2 $\mathcal{C}_{\mathbf{deg}}$ with $\angle R$ systematically perturbed from 0

As a simple extension to all previous cases where we access EP_2 with $\angle R=0$, we now relax the $\angle R=0$ condition. For these measurements we continue working with the

Candidate	Parameter	Measured	Theory
A	$\lambda_{EP}/2\pi$ (Hz)	$-5.68 \pm 0.15 - (7.33 \pm 0.12)i$	$-5.40 - 7.77i$
	$\delta\lambda/2\pi$ (Hz)	$-2.1 \pm 0.4 - (1.2 \pm 0.4)i$	0
	$R/2\pi$ (Hz)	$7.88 \pm 0.10 + (0.24 \pm 0.07)i$	8.19
B	$\lambda_{EP}/2\pi$ (Hz)	$-6.67 \pm 0.16 - (9.75 \pm 0.13)i$	$-7.14 - 10.08i$
	$\delta\lambda/2\pi$ (Hz)	$-1.6 \pm 1.4 - (0.3 \pm 0.8)i$	0
	$R/2\pi$ (Hz)	$8.75 \pm 0.09 - (0.02 \pm 0.06)i$	8.98
C	$\lambda_{EP}/2\pi$ (Hz)	$-7.18 \pm 0.24 - (13.08 \pm 0.17)i$	$-6.98 - 13.46i$
	$\delta\lambda/2\pi$ (Hz)	$0.3 \pm 1.9 + (0.4 \pm 1.5)i$	0
	$R/2\pi$ (Hz)	$8.57 \pm 0.11 - (0.13 \pm 0.08)i$	9.16
D	$\lambda_{EP}/2\pi$ (Hz)	$-11.74 \pm 0.22 - (11.59 \pm 0.20)i$	$-12.18 - 11.86i$
	$\delta\lambda/2\pi$ (Hz)	$-0.6 \pm 1.7 + (0.2 \pm 1.5)i$	0
	$R/2\pi$ (Hz)	$9.79 \pm 0.15 - (0.11 \pm 0.16)i$	10.24
E	$\lambda_{EP}/2\pi$ (Hz)	$-14.97 \pm 0.21 - (13.20 \pm 0.19)i$	$-14.82 - 13.22i$
	$\delta\lambda/2\pi$ (Hz)	$0.9 \pm 1.5 + (0.5 \pm 1.7)i$	0
	$R/2\pi$ (Hz)	$11.44 \pm 0.07 - (0.10 \pm 0.11)i$	11.55
F	$\lambda_{EP}/2\pi$ (Hz)	$-17.12 \pm 0.17 - (10.82 \pm 0.19)i$	$-17.33 - 11.19i$
	$\delta\lambda/2\pi$ (Hz)	$-0.9 \pm 1.2 - (0.1 \pm 1.3)i$	0
	$R/2\pi$ (Hz)	$13.73 \pm 0.13 - (0.18 \pm 0.14)i$	13.57
G	$\lambda_{EP}/2\pi$ (Hz)	$-19.92 \pm 0.24 - (13.65 \pm 0.24)i$	$-20.10 - 14.30i$
	$\delta\lambda/2\pi$ (Hz)	$-1.3 \pm 1.6 + (0.0 \pm 1.2)i$	0
	$R/2\pi$ (Hz)	$15.15 \pm 0.12 - (0.10 \pm 0.11)i$	15.60
H	$\lambda_{EP}/2\pi$ (Hz)	$-23.08 \pm 0.32 - (16.58 \pm 0.29)i$	$-23.35 - 16.84i$
	$\delta\lambda/2\pi$ (Hz)	$-0 \pm 1.2 - (0.3 \pm 1.4)i$	0
	$R/2\pi$ (Hz)	$16.70 \pm 0.12 - (0.09 \pm 0.14)i$	16.30

Table 7.3: Spectroscopic properties of EP_2 candidates accessed in Sec. 7.2.2.1. λ_{EP}: the degenerate eigenvalue at EP_2, $\delta\lambda$: non-degeneracy of eigenvalues, R: parameter that characterizes the rate at which any state vector of the degenerate system approaches the unique right eigenvector at EP_2 (Eq. (7.4)). Measured value is reported as mean $\pm$ one standard deviation. Theoretical values are obtained by fitting the spectroscopy data used for locating this EP_2. Note: **(i)** candidate **B** is also studied in Sec. 7.2.3; **(ii)** candidate **G** is also studied in Secs. 7.1, 7.2.1, 7.2.2.2 and 7.3; **(iii)** candidate **F** is also studied in Sec. 7.4.

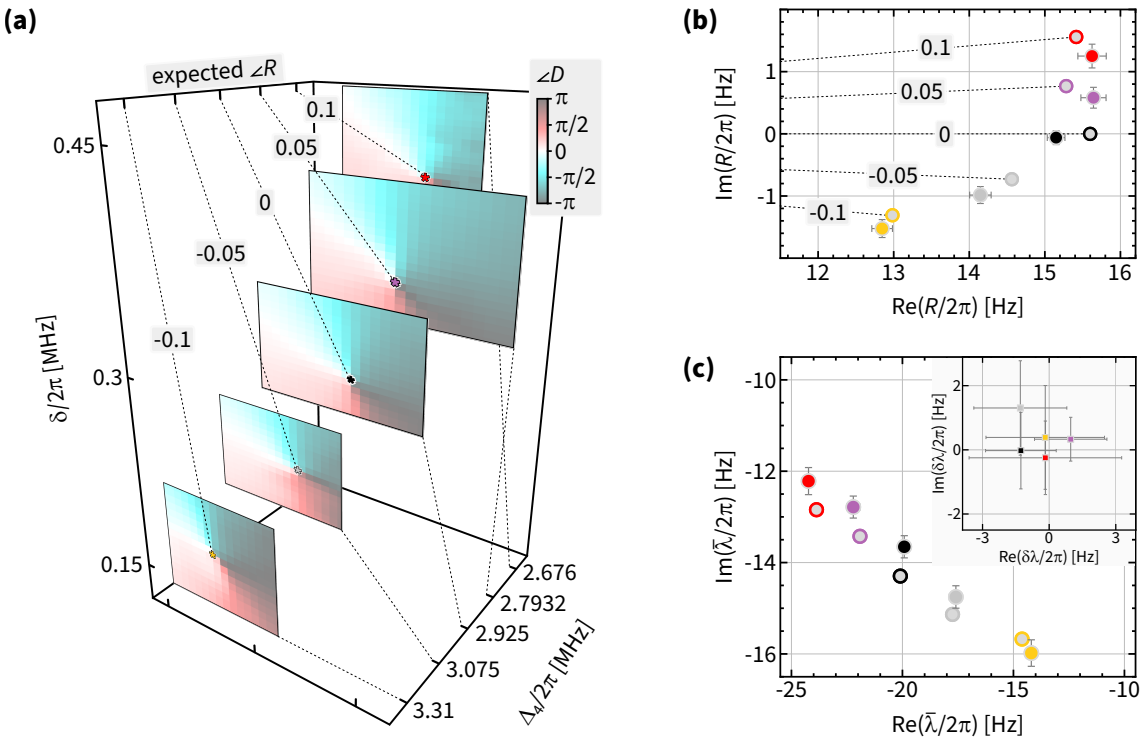

Figure 7.13: Spectroscopically locating EP_2 with a variety of $\angle R$. **(a)** $\angle D(P, \delta, \Delta_4)$ with $P = \sqrt{P_1 P_2}$ for five 2D-sheets that provide EP_2 with distinct $\angle R$. Each sheet shows a color map of measured and filtered $\angle D$ with colored stars as experimentally identified EP_2 location flanked by corresponding $\angle R$ value. Dashed lines connecting the sheet corners indicate the corresponding value of Δ_4. **(b,c)** Spectroscopic properties of identified EP_2 locations. Panel (b) shows R for each EP_2 candidate identified in (a). Data obtained from spectroscopy at EP_2 are as shown as colored disks with gray error bars. Corresponding theory predictions are shown as gray disks with same edge color flanked by expected $\angle R$ values. Panel (c) and its inset shows λ_{EP} and $\delta\lambda$, respectively for each EP_2 candidate identified in (a). Data from spectroscopy at EP_2 is shown as colored disks with gray error bars and corresponding theory prediction as gray disks with same edge color. For this measurement, we used the (3,3) and the (5,2) membrane modes. Control parameters that tune to corresponding EP_2 with distinct $\angle R$ are listed in Table 7.4.

(3,3) and the (5,2) membrane mode. We systematically perturb $\angle R$ by tweaking the detuning of the blue control tone Δ_4 combined with EP_2 search in the $P \times \delta$ plane, while holding other control parameters i.e., $\{\sqrt{P_1/P_2}, \eta, P_4\}$ fixed. The result of this exercise is illustrated in Fig. 7.13 where $\angle R$ corresponding to an EP_2 is stepped over a set values: $\{-0.1, -0.05, 0, 0.05, 0.1\}$. The EP_2 coordinates and its spectroscopic properties are listed in Tables 7.4 and 7.5, respectively. Note that the $\angle R = 0$ dataset corresponds to the first EP_2 candidate we studied in Sec. 7.1 as well as in Secs. 7.2.1, 7.2.2.1 and 7.3.

Following our recipe in Sec. 7.1, we measure $\beta_{\mathrm{deg}}(T)$ for "simple" non-contractible $\mathcal{C}_{\mathrm{deg}}$ constructed using the above EP_2 candidates. Fig. 7.14 (first column) illustrates

	EP_2 coordinates					
$\angle R$	$P=\sqrt{P_1P_2}$	$\delta/2\pi$	$\sqrt{P_1/P_2}$	$\eta/2\pi$	P_4	$\Delta_4/2\pi$
-0.1	6.599	0.165	0.4	-30	16.9	3.31
-0.05	7.103	0.2301	0.4	-30	16.9	3.075
0	7.285	0.2872	0.4	-30	16.9	2.925
0.05	7.375	0.3475	0.4	-30	16.9	2.793
0.1	7.401	0.415	0.4	-30	16.9	2.676

Table 7.4: Coordinates of EP_2 candidates accessed in Sec. 7.2.2.2. The coordinates $P=\sqrt{P_1P_2}$ (units: μW) and δ (units: $2\pi\times$MHz) represent coordinates of the vortex of $\angle D$ obtained from corresponding spectroscopy measurements (see Sec. 7.1.1). Other coordinates $\sqrt{P_1/P_2}$, η ((units: $2\pi\times$Hz)), P_4 (units: μW) and Δ_4 (units: $2\pi\times$MHz) are held fixed to access EP_2 with $\angle R=0$. Note: the candidate corresponding to $\angle R=0$ is also studied in Secs. 7.1, 7.2.1, 7.2.2.1 and 7.3.

$\mathrm{Re}(\beta_{\mathrm{deg}}(T))$ for each of them. For candidates with $\angle R\neq 0$, we observe that at large T, $\mathrm{Re}(\beta_{\mathrm{deg}})$ systematically deviates from π - the expected value of $\phi_{B,\mathrm{deg}}$ for non-contractible $\mathcal{C}_{\mathrm{deg}}$, and as such, they constitute our first example for which $\mathrm{Re}(\beta_{\mathrm{deg}}(T))$ additionally contains the novel-$\sqrt{T}$ dynamical phase. It also highlights that without further processing[1], $\phi_{B,\mathrm{deg}}$ is not directly available from $\mathrm{Re}(\beta_{\mathrm{deg}}(T))$ when $\angle R\neq 0$.

The presence of $\sqrt{T}$ dynamical phase in $\mathrm{Re}(\beta_{\mathrm{deg}}(T))$ does not represent a fundamental impediment, and in order to extract $\phi_{B,\mathrm{deg}}$ we extend our analysis along two independent routes. They are as illustrated in Figs. 7.14 (second column) and 7.15(a), respectively. Succinctly, both methods are expected to isolate the $\sqrt{T}$ dynamical phase given by $\sqrt{2\pi RT}$ from $\beta_{\mathrm{deg}}(T)$, thereby providing $\phi_{B,\mathrm{deg}}$. The first method utilizes the value of R obtained from spectroscopy at EP_2 (see Sec. F.3), while the second method fits the asymptote of complex $\beta_{\mathrm{deg}}(T)$ with $\phi_{B,\mathrm{deg}}$ and R as fit parameters (see Sec. F.4). The result of analyzing the data using the first and the second method are shown in Figs. 7.14(third column) and 7.15(b,c). The estimated $\phi_{B,\mathrm{deg}}$ are both $\approx\pi$.

We note that compared to their $\angle R=0$ counterparts, the $\angle R\neq 0$ candidates have a larger deviation and uncertainty in their estimated $\phi_{B,\mathrm{deg}}$. While the measurements

[1] i.e., beyond the scope of Sec. F.4.1 which is only applicable for $\angle R=0$ cases.

$\angle R$	Parameter	Measured	Theory
-0.1	$\lambda_{EP}/2\pi$ (Hz)	$-14.19 \pm 0.22 - (15.98 \pm 0.29)i$	$-14.61 - 15.67i$
	$\delta\lambda/2\pi$ (Hz)	$-0.2 \pm 2.7 - (0.4 \pm 1.6)i$	0
	$R/2\pi$ (Hz)	$12.85 \pm 0.14 - (1.52 \pm 0.14)i$	$12.98 - 1.31i$
-0.05	$\lambda_{EP}/2\pi$ (Hz)	$-17.59 \pm 0.29 - (14.75 \pm 0.25)i$	$17.74 - 15.14i$
	$\delta\lambda/2\pi$ (Hz)	$-1.3 \pm 2.1 - (1.3 \pm 1.5)i$	0
	$R/2\pi$ (Hz)	$14.15 \pm 0.14 - (0.98 \pm 0.14)i$	$14.56 - 0.73i$
0	$\lambda_{EP}/2\pi$ (Hz)	$-19.92 \pm 0.24 - (13.65 \pm 0.24)i$	$-20.10 - 14.30i$
	$\delta\lambda/2\pi$ (Hz)	$-1.3 \pm 1.6 + (0.0 \pm 1.2)i$	0
	$R/2\pi$ (Hz)	$15.15 \pm 0.12 - (0.10 \pm 0.11)i$	15.60
0.05	$\lambda_{EP}/2\pi$ (Hz)	$-22.21 \pm 0.29 - (12.78 \pm 0.24)i$	$-21.91 - 13.42i$
	$\delta\lambda/2\pi$ (Hz)	$1.0 \pm 1.6 + (0.3 \pm 0.7)i$	0
	$R/2\pi$ (Hz)	$15.64 \pm 0.12 + (0.58 \pm 0.17)i$	$15.28 + 0.77i$
0.1	$\lambda_{EP}/2\pi$ (Hz)	$-24.23 \pm 0.29 - (12.22 \pm 0.30)i$	$-23.87 - 12.84i$
	$\delta\lambda/2\pi$ (Hz)	$-0.2 \pm 3.4 - (0.2 \pm 1.1)i$	0
	$R/2\pi$ (Hz)	$15.62 \pm 0.19 + (1.25 \pm 0.19)i$	$15.42 + 1.56i$

Table 7.5: Spectroscopic properties of EP_2 candidates accessed in Sec. 7.2.2.2. λ_{EP}: the degenerate eigenvalue at EP_2, $\delta\lambda$: non-degeneracy of eigenvalues, R: parameter that characterizes the rate at which any state vector of the degenerate system approaches the unique right eigenvector at EP_2 (Eq. (7.4)). Measured value is reported as mean $\pm$ one standard deviation. Theoretical values are obtained by fitting the spectroscopy data used for locating this EP_2. Note: the candidate corresponding to $\angle R = 0$ is also studied in Secs. 7.1, 7.2.1, 7.2.2.1 and 7.3.

shown here were done under similar conditions as others and are of similar quality, one may anticipate such an outcome. As a starting point of this discussion, we expect $\mathrm{Re}(\beta_{\mathrm{deg}}(T > T^*)) = \phi_{B,\mathrm{deg}}$ for $\angle R = 0$ thereby providing a direct access to $\phi_{B,\mathrm{deg}}$. That fails to be the case when $\angle R \neq 0$. In particular for $\angle R \neq 0$, $\mathrm{Re}(\beta_{\mathrm{deg}}(T)) \propto \sqrt{T}$ at large T. Since this diverges, isolating a finite $\phi_{B,\mathrm{deg}}$ therein represents a substantial challenge. The second of half Sec. 2.2.4.3 and references therein provide additional insight to this discussion.

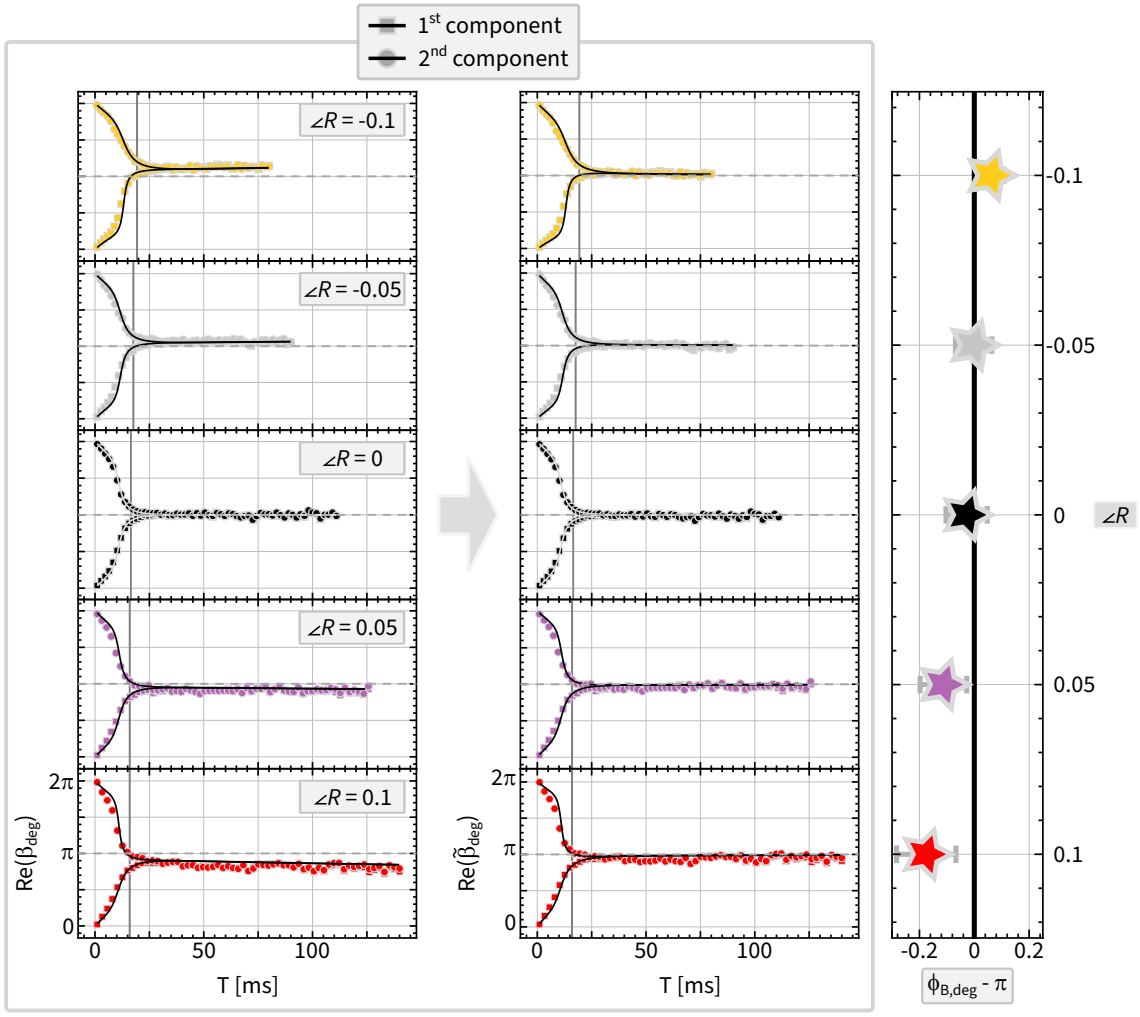

Figure 7.14: Topological character of $\phi_{B,\mathrm{deg}}$ - part IIB(i). First column: $\mathrm{Re}(\beta_{\mathrm{deg}}(T))$ for "simple" non-contractible $\mathcal{C}_{\mathrm{deg}}$ constructed using EP_2 with distinct $\angle R$ values. Top to bottom panels correspond to $\angle R = \{-0.1, -0.05, 0, 0.05, 0.1\}$, respectively. Colored squares and disks: data corresponding to state vector component 1 and 2; solid black curve: corresponding no-free-parameter theory prediction; dashed gray line corresponds to π while the vertical gray line indicates expected $T^* = \pi/2|R|$ for each candidate. We note that all panels shown here share the same X and Y axes as the bottom-most panel. **Second column:** Same as the first column but now showing $\mathrm{Re}(\tilde{\beta}_{\mathrm{deg}}(T)) = \mathrm{Re}(\beta_{\mathrm{deg}}(T) - \sqrt{2\pi RT})$ where the value of R is obtained from spectroscopy measurements at EP_2 as listed in Table 7.5 and shown in Fig. 7.13(b). We note that all panels shown here share the same X and Y axes as the bottom-most panel. **Third column:** $\phi_{B,\mathrm{deg}} - \pi$ estimated from data corresponding to $\mathrm{Re}(\beta_{\mathrm{deg},1}(T))$ (Sec. F.4) for each case shown in first and second columns. Colored stars: mean value of estimated $\phi_{B,\mathrm{deg}} - \pi$; gray fences: standard deviation of estimated $\phi_{B,\mathrm{deg}}$; black line: 0, the expected $\phi_{B,\mathrm{deg}} - \pi$ for non-contractible $\mathcal{C}_{\mathrm{deg}}$ as used in this study. For this measurement, we used the (3,3) and the (5,2) membrane modes. Control parameters that tune to corresponding EP_2 with distinct $\angle R$ are listed in Table 7.4.

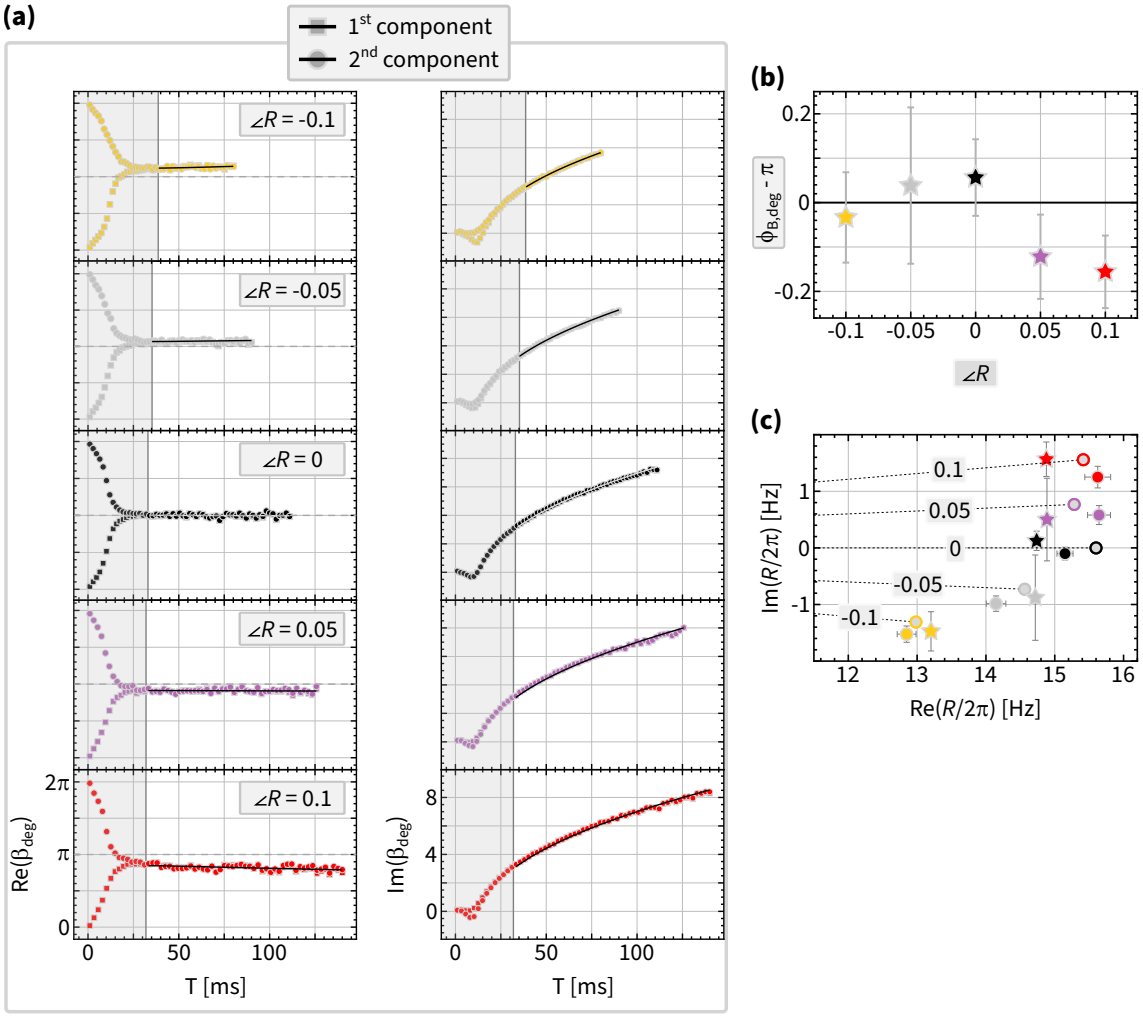

Figure 7.15: Topological character of $\phi_{B,\mathrm{deg}}$ - part IIB(ii). **(a)** $\beta_{\mathrm{deg}}(T)$ for "simple" non-contractible $\mathcal{C}_{\mathrm{deg}}$ constructed using EP_2 with distinct $\angle R$ values. Top to bottom panels correspond to $\angle R = \{-0.1, -0.05, 0, 0.05, 0.1\}$, respectively. First (second) column shows the real (imaginary) part of β_{deg} Colored squares and disks: data corresponding to state vector component 1 and 2; solid black curve: fit to the asymptote of $\beta_{\mathrm{deg}}(T \geq 2T^*)$ (Sec. F.4); dashed gray line in the first column corresponds to π while the vertical gray line indicates expected $2T^* = \pi/|R|$ for each candidate are demarcates the data used for asymptote analysis. We note that all panels shown in the first and the second column share the same X and Y axes as their respective bottom-most panels. **(b)** $\phi_{B,\mathrm{deg}} - \pi$ estimated from the asymptote analysis of $(\beta_{\mathrm{deg}}(T))$ (Sec. F.4) for each case shown in (a). Colored stars: mean value of estimated $\phi_{B,\mathrm{deg}} - \pi$; gray fences: standard deviation of estimated $\phi_{B,\mathrm{deg}}$; black line: 0, the expected $\phi_{B,\mathrm{deg}} - \pi$ for non-contractible $\mathcal{C}_{\mathrm{deg}}$ as used in this study. **(c)** R obtained from the asymptote analysis of $(\beta_{\mathrm{deg}}(T))$ for each case in (a), are shown as colored stars with gray error bars. They are overlaid on panel (b) of Fig. 7.13 alongside the theory expectation (gray disks with same edge color) and corresponding value obtained from spectroscopy measurements at EP_2 (colored disks with gray error bars). For this measurement, we used the (3,3) and the (5,2) membrane modes. Control parameters that tune to corresponding EP_2 with distinct $\angle R$ are listed in Table 7.4.

7.2.2.3 $\mathcal{C}_{\mathrm{deg}}$ with arbitrary R

In this section, we describe measurements of $\phi_{B,\mathrm{deg}}$ for "simple" $\mathcal{C}_{\mathrm{deg}}$ that correspond to EP_2 with arbitrary but constant R. For these measurements we switch over to using the (3,3) and the (5,3) membrane modes. They continue to be tuned and Floquet coupled using two red-detuned tones with parameters $\{P_1, P_2, \delta, \eta, \theta_{12}\}$ as well as a blue-detuned tone with parameters $\{P_4, \Delta_4\}$ to reduce their damping rates. For this exercise, we located several EP_2 candidates as described previously (Sec. 7.1.1) with corresponding R taking arbitrarily chosen values. Their coordinates are listed in Table 7.6 and the corresponding spectroscopic properties are listed in Table 7.7 and illustrated in Fig. 7.16.

	EP_2 coordinates					
Candidate	$P=\sqrt{P_1P_2}$	$\delta/2\pi$	$\sqrt{P_1/P_2}$	$\eta/2\pi$	P_4	$\Delta_4/2\pi$
(i)	5.738	0.038	0.5	-30	15	3
(ii)	8.454	-0.04	0.5	-50	15	3
(iii)	9.451	-0.103	0.5	-50	20	3.25
(iv)	20.83	-0.418	1	-35	45	4
(v)	37.16	-0.484	1.5	-45	35	3.5
(vi)	33.6	-0.565	2	-25	35	3.5

Table 7.6: Coordinates of EP_2 candidates accessed in Sec. 7.2.2.3. The coordinates $P = \sqrt{P_1P_2}$ (units: μW) and δ (units: $2\pi\times$MHz) represent coordinates of the vortex of $\angle D$ obtained from corresponding spectroscopy measurements (see Sec. 7.1.1). Other coordinates $\sqrt{P_1/P_2}$, η ((units: $2\pi\times$Hz)), P_4 (units: μW) and Δ_4 (units: $2\pi\times$MHz) are held fixed to access EP_2 with arbitrary R.

Measurements of real time dynamics were carried out in a similar fashion as described in Sec. 7.1. As an exemplary measurement, we illustrate candidate **(ii)** in Fig. 7.17. Similar to Sec. 7.2.1 we show the quantity $\overline{\beta}_{\mathrm{deg}}(T)$ panel (a) measured for a "simple" non-contractible and contractible $\mathcal{C}_{\mathrm{deg}}$, indicated by $n = 1$ and 2, respectively. Recall that $\mathrm{Re}(\overline{\beta}_{\mathrm{deg}}(T))$ is not constrained within $[0, 2\pi]$ range. While the data for $\mathrm{Re}(\overline{\beta}_{\mathrm{deg}}(T))$ (square and disk symbols) agree reasonably to the corresponding theory prediction (solid black curves), we observe a significant but expected contribution of $\sqrt{T}$-dynamical phase, indicated by dashed black curves. The imaginary component has a similar behavior for

Candidate	Parameter	Measured	Theory
(i)	$\lambda_{EP}/2\pi$ (Hz)	$-23.91 \pm 0.14 - (9.97 \pm 0.13)i$	$-23.59 - 9.90i$
	$\delta\lambda/2\pi$ (Hz)	$-0.99 \pm 0.35 + (1.5 \pm 0.6)i$	0
	$R/2\pi$ (Hz)	$12.52 \pm 0.16 - (2.76 \pm 0.20)i$	$11.69 - 2.62i$
(ii)	$\lambda_{EP}/2\pi$ (Hz)	$-35.32 \pm 0.25 - (18.28 \pm 0.22)i$	$-35.3 - 18.8i$
	$\delta\lambda/2\pi$ (Hz)	$-1.2 \pm 0.8 + (0.2 \pm 1.1)i$	0
	$R/2\pi$ (Hz)	$17.12 \pm 0.21 - (5.30 \pm 0.21)i$	$16.98 - 5.24i$
(iii)	$\lambda_{EP}/2\pi$ (Hz)	$-36.65 \pm 0.24 - (18.82 \pm 0.25)i$	$-36.21 - 19.11i$
	$\delta\lambda/2\pi$ (Hz)	$0.8 \pm 1.1 + (1.1 \pm 1.7)i$	0
	$R/2\pi$ (Hz)	$17.76 \pm 0.21 - (6.82 \pm 0.24)i$	$17.56 - 6.73i$
(iv)	$\lambda_{EP}/2\pi$ (Hz)	$-23.76 \pm 0.20 - (15.54 \pm 0.16)i$	$-23.17 - 15.88i$
	$\delta\lambda/2\pi$ (Hz)	$-0.4 \pm 0.6 + (0.0 \pm 1.8)i$	0
	$R/2\pi$ (Hz)	$13.99 \pm 0.17 - (9.88 \pm 0.17)i$	$13.19 - 8.97i$
(v)	$\lambda_{EP}/2\pi$ (Hz)	$-37.32 \pm 0.21 - (21.10 \pm 0.29)i$	$-36.30 - 21.46i$
	$\delta\lambda/2\pi$ (Hz)	$0.4 \pm 1.0 + (0.6 \pm 2.2)i$	0
	$R/2\pi$ (Hz)	$15.29 \pm 0.19 - (12.02 \pm 0.18)i$	$14.36 - 11.25i$
(vi)	$\lambda_{EP}/2\pi$ (Hz)	$-28.44 \pm 0.14 - (13.12 \pm 0.13)i$	$-28.03 - 13.12i$
	$\delta\lambda/2\pi$ (Hz)	$-1.0 \pm 0.7 + 0.7 \pm 1.3)i$	0
	$R/2\pi$ (Hz)	$9.76 \pm 0.13 - (8.02 \pm 0.13)i$	$9.33 - 7.62i$

Table 7.7: Spectroscopic properties of EP_2 candidates accessed in Sec. 7.2.2.3. λ_{EP}: the degenerate eigenvalue at EP_2, $\delta\lambda$: non-degeneracy of eigenvalues, R: parameter that characterizes the rate at which any state vector of the degenerate system approaches the unique right eigenvector at EP_2 (Eq. (7.4)). Measured value is reported as mean $\pm$ one standard deviation. Theoretical values are obtained by fitting the spectroscopy data used for locating this EP_2.

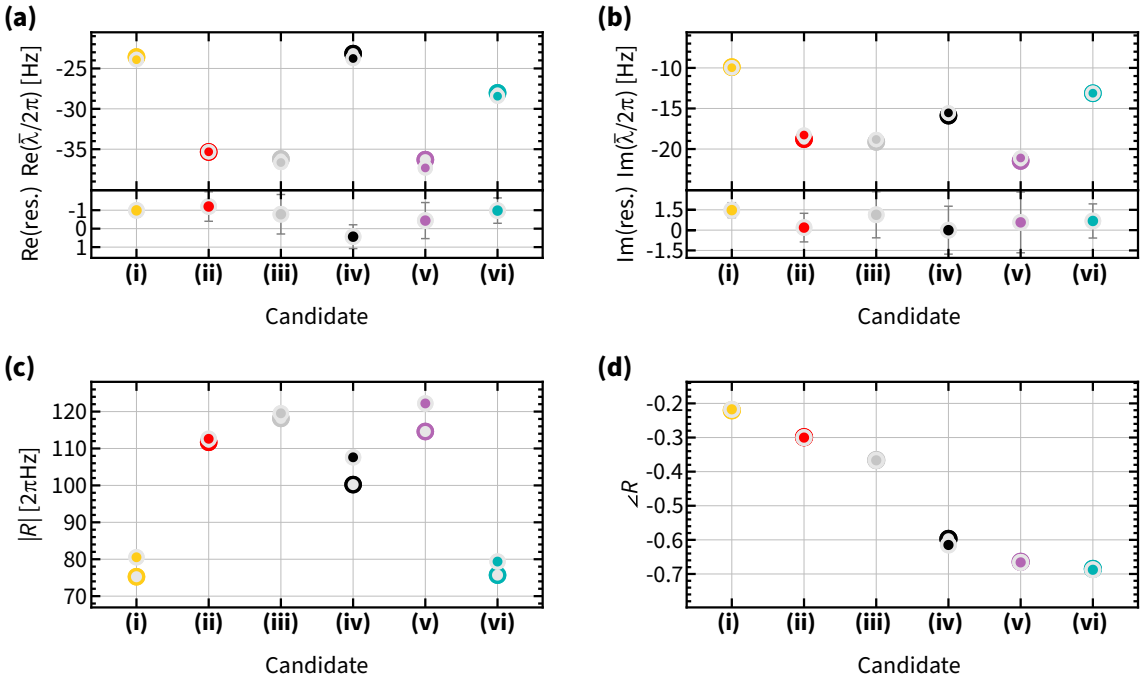

Figure 7.16: Spectroscopically locating EP_2 with arbitrary R. **(a)** Top panel: $\mathrm{Re}(\lambda_{EP})$ and bottom panel: $\mathrm{Re}(\mathrm{res.}) \equiv \mathrm{Re}(\delta\lambda)$ corresponding to EP_2 candidates with arbitrary R. Colored disks: data, grey disk with colored edge: corresponding theory prediction and gray fences: error bars. **(b)** Same as (a) but showing $\mathrm{Im}(\lambda_{EP})$ and $\mathrm{Im}(\mathrm{res.}) \equiv \mathrm{Im}(\delta\lambda)$. **(c,d** Same as (a) but showing $|R|$ and $\angle R$, respectively. For this measurement, we used the (3,3) and the (5,3) membrane modes. Control parameters that tune to corresponding EP_2 with distinct $\angle R$ are listed in Table 7.6.

to all previous cases at large T, i.e, $\mathrm{Im}(\overline{\beta}_{\mathrm{deg}}(T)) \propto \sqrt{T}$. This further illustrated in the bottom half of Fig. 7.17(b) as $\mathrm{Im}(\overline{\beta}_{\mathrm{deg}}(T))/\sqrt{T}$, which visually asymptotes to expected value of $\mathrm{Im}(i\sqrt{2n\pi R})$ shown as dashed black line. Note that we do not quantify this asymptote, and leave it as a leftover analysis.

In order to isolate $\phi_{B,\mathrm{deg}}$ from $\mathrm{Re}(\overline{\beta}_{\mathrm{deg}}(T))$, we apply the first analysis method from Sec. 7.2.2.2, wherein we utilize the spectroscopically measured value of R to eliminate the $\sqrt{T}$-dynamical phase, and subsequently apply asymptote analysis (Sec. F.4.2) to estimate $\phi_{B,\mathrm{deg}}$. The top half of Fig. 7.17(b) shows the real part of $\tilde{\overline{\beta}}_{\mathrm{deg}}(T) = \overline{\beta}_{\mathrm{deg}}(T) - \sqrt{2n\pi\overline{R}T}$ for $n \in \{1, 2\}$, which visually asymptotes to expected $\phi_{B,\mathrm{deg}}$, shown as a dashed black lines. The quantified asymptote is shown in Fig. 7.18, and as such they demonstrate that $\phi_{B,\mathrm{deg}}$ corresponding to a non-contractible and a contractible $\mathcal{C}_{\mathrm{deg}}$ is consistent with a value of π and 0, respectively.

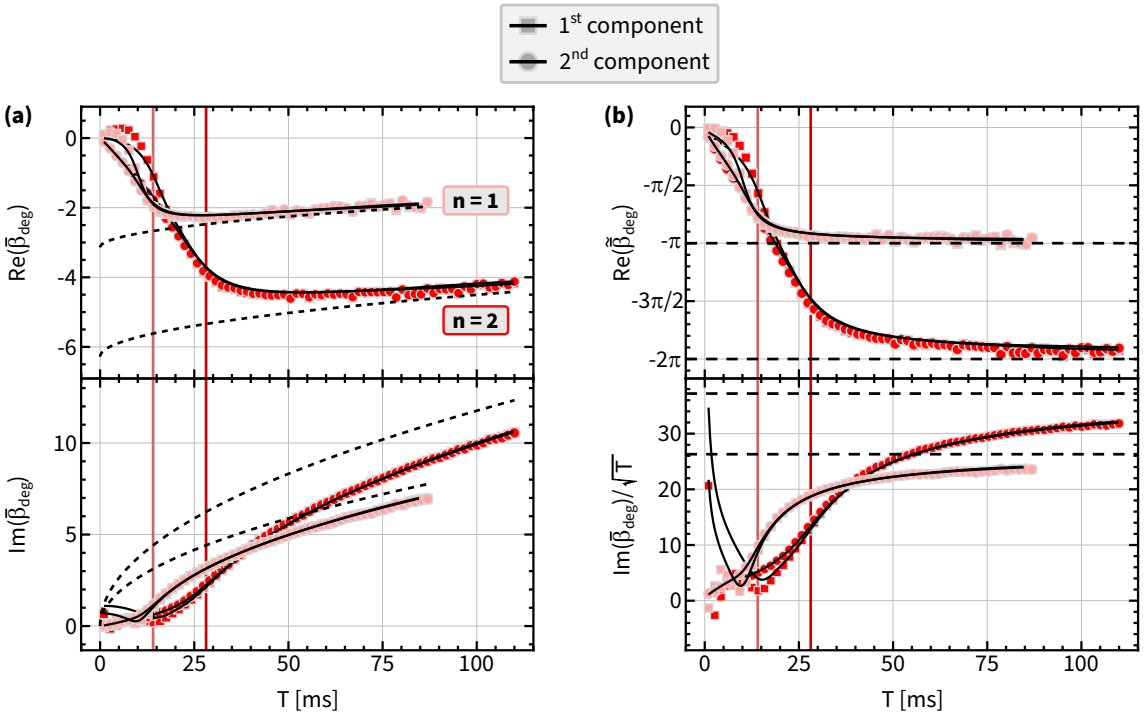

Figure 7.17: Topological character of $\phi_{B,\mathbf{deg}}$ - part IIC(i). **(a)** $\beta_{\mathrm{deg}}(T)$ for "simple" non-contractible ($n = 1$) and contractible ($n = 2$) $\mathcal{C}_{\mathrm{deg}}$ constructed using EP_2 with arbitrary R corresponding to candidate **(ii)**. Top (bottom) panel show real (imaginary) parts. Colored squares and disks: data corresponding to state vector component 1 and 2; solid black curve: corresponding no-free-parameter theory prediction; dashed black curve: corresponds to $\mathrm{Re}(i\sqrt{2n\pi RT}) - n\pi$ in the top panel and $\mathrm{Im}(i\sqrt{2n\pi RT})$ in the bottom panel. The vertical gray pink and red lines indicate expected $T^* = \pi/2|R|$ and $2T^*$, respectively. **(b)** Same as (a) but showing real part of $\tilde{\overline{\beta}}_{\mathrm{deg}}(T) = \overline{\beta}_{\mathrm{deg}}(T) - \sqrt{2n\pi\overline{R}T}$ in the top panel, and $\mathrm{Im}(\overline{\beta}_{\mathrm{deg}}(T))/\sqrt{T}$ in the bottom panel. The dashed black lines here represent $n\pi$ and $\mathrm{Im}(i\sqrt{2\pi R})$ in the top and bottom panel, respectively, the expected asymptotes.

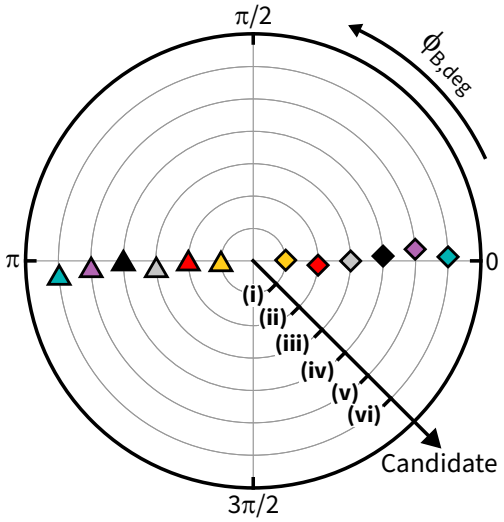

Figure 7.18: Topological character of $\phi_{B,\mathbf{deg}}$ - part IIC(ii). Polar plot of $\phi_{B,\mathrm{deg}}$ estimated for

Figure 7.18: Topological character of $\phi_{B,\mathbf{deg}}$ - part IIC(ii). *continued from previous page*
candidates with arbitrary R values. For each candidate, a "simple" non-contractible and contractible $\mathcal{C}_{\mathrm{deg}}$ was performed. The corresponding estimated $\phi_{B,\mathrm{deg}}$ (Sec. F.4.2) are shown as triangle and diamond symbols, respectively, and they are consistent with a value of π and 0, respectively.

7.2.3 Part III: Varying the manner of $\mathcal{C}_{\mathbf{deg}}$ traversal

For this investigation, we consider a non-contractible $\mathcal{C}_{\mathrm{deg}}$.

1. Similar to "simple" non-contractible $\mathcal{C}_{\mathrm{deg}}$, hold the control parameters that tune to an EP_2 i.e. $\{P_{EP}, \delta_{EP}, \eta, P_4, \Delta_4\}$ fixed.

2. Contrary to "simple" non-contractible $\mathcal{C}_{\mathrm{deg}}$, vary the beat-note phase $\theta_{12}(s)$ with a different functional form i.e., not a linear ramp $\theta_{12}(s) = -2\pi s$ with $0 \leq s \leq 1$. However, one must vary $\theta_{12}(s)$ strictly monotonically from 0 to -2π to ensure the requirement for the existence of a unique least-dissipative eigenvector of H', which is amenable to adiabatic evolution in the large-T limit (see Sec. 2.2.4.3 and Refs. [88, 89]).

Intuitively, it corresponds to rotating $\mathbf{B}^{\mathrm{deg}}_{\mathrm{Re,Im}}$, once around the z-axis but at a variable rate, contrary to its "simple" counterpart, which has a constant rotation rate. For these measurements, we chose the following functional form of $\theta_{12}(s)$:

$$\theta_{12}(s) = -2\pi s - \Delta\phi\ \mathrm{Sin}(\pi s)^2 \tag{7.12}$$

where $\Delta\phi$ is a real-valued parameter. To preserve the strict monotonicity of θ_{12} in Eq. (7.12), $|\Delta\phi| < 2$ is necessary. We chose $\Delta\phi \in \{-1.5, -1, -0.5, 0, 0.5, 1, 1.5\}$ for these measurements, of which all but $\Delta\phi = 0$ correspond to a "non-simple" non-contractible $\mathcal{C}_{\mathrm{deg}}$. These functions are shown in the first column Figs. 7.19 and 7.20.

For these measurements, we employ a different EP_2 location given by: $P = \sqrt{P_1 P_2} =$ 4.30 μW, $\sqrt{P_1/P_2} = 0.68, \delta/2\pi =$ 0.275 MHz, $\eta/2\pi = -17$ Hz for the red-detuned laser tones and $P_4 =$ 8.3 μW, $\Delta_4/2\pi = +3.031$ MHz for the blue-detuned laser tone, while still using the (3,3) and the (5,2) membrane modes. This choice of parameters yet again ensures $\angle R = 0$. We note that this EP_2 location appeared as 'Candidate B' in Sec. 7.2.2.1, and the corresponding spectroscopic quantities are given in Table 7.2.

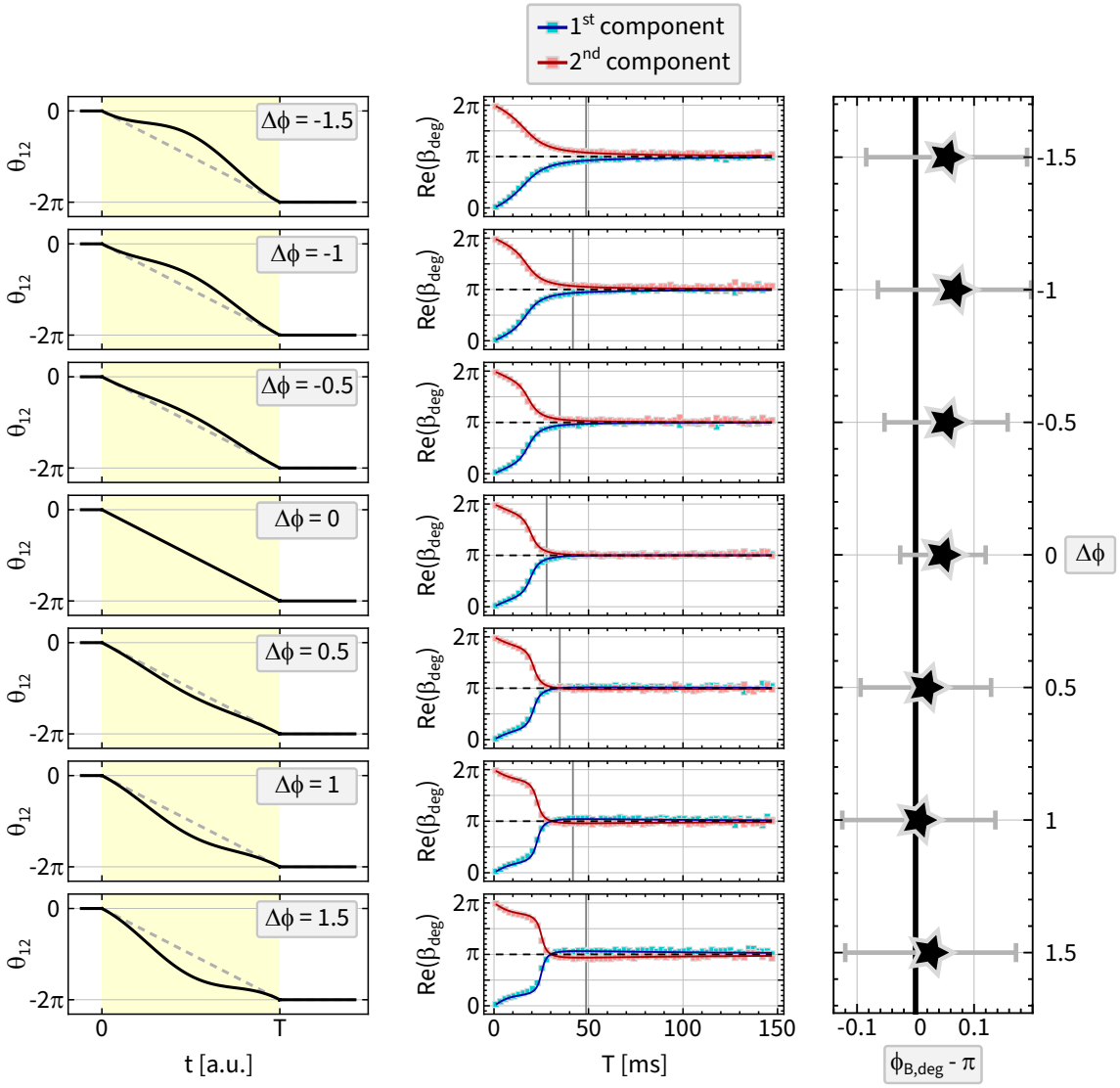

Figure 7.19: Geometric character of $\phi_{B,\mathrm{deg}}$. First column: solid curves show the seven $\theta_{12}(s = t/T)$ described in Sec. 7.2.3. For comparison, the dashed gray line shows $\theta_{12}(t/T) = -2\pi t/T$ that constitutes a "simple" non-contractible $\mathcal{C}_{\mathrm{deg}}$. **Second column:** Cyan (pink) squares show measured $\mathrm{Re}(\beta_{\mathrm{deg},1(2)}(T))$, respectively for the corresponding $\theta_{12}(t/T)$; solid blue and red curves: corresponding no-free-parameter theory predictions; gray vertical line represents $T^* = \pi(1 + |\Delta\phi|/2)/2R$ for each $\theta_{12}(t/T)$ with $\angle R = 0$; dashed black line: π, the expected $\phi_{B,\mathrm{deg}}$ for all $\theta_{12}(t/T)$. **Third column:** $\phi_{B,\mathrm{deg}} - \pi$ for each $\theta_{12}(t/T)$, estimated from data corresponding to $\mathrm{Re}(\beta_{\mathrm{deg},\{1,2\}}(T))$ (Sec. F.4). Black stars: mean value of estimated $\phi_{B,\mathrm{deg}} - \pi$; gray fences: standard deviation of estimated $\phi_{B,\mathrm{deg}}$; black line: 0, the expected $\phi_{B,\mathrm{deg}} - \pi$ for all $\theta_{12}(t/T)$. For this measurement, we used the (3,3) and the (5,2) membrane modes with control parameters that tune it to an EP_2 with $\angle R = 0$ (see Secs. 2.2.4.3, 7.1.3 and 7.1.4): $P = \sqrt{P_1 P_2} =$ 4.30 µW, $\sqrt{P_1/P_2} = 0.68, \delta/2\pi =$ 0.275 MHz, $\eta/2\pi = -17$ Hz for the red-detuned laser tones and $P_4 =$ 8.3 µW, $\Delta_4/2\pi = +3.031$ MHz for the blue-detuned laser tone.

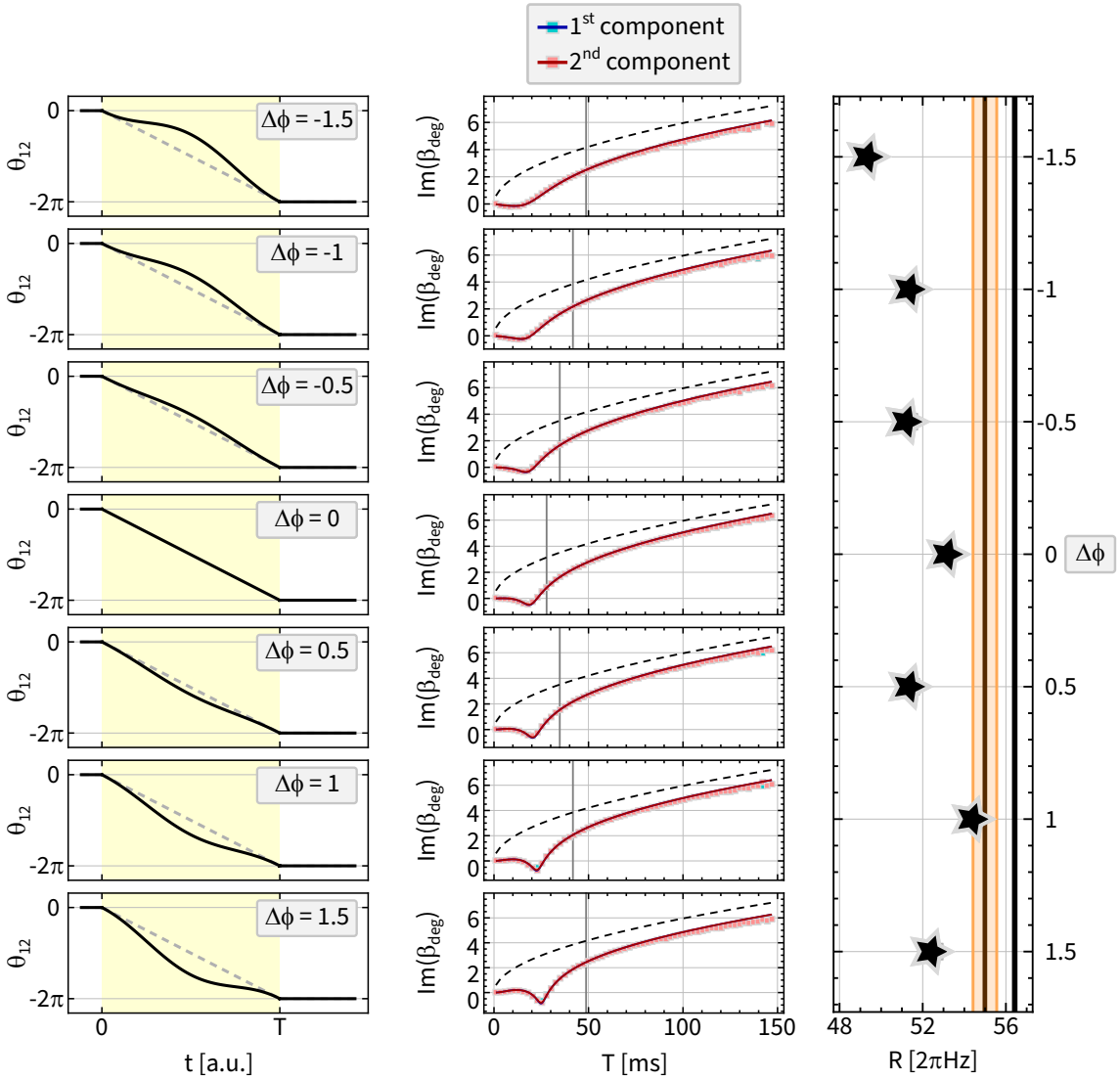

Figure 7.20: $\sqrt{T}$ dynamical phase for distinct traversals of a $\mathcal{C}_{\mathbf{deg}}$. First column: solid curves show the seven $\theta_{12}(s = t/T)$ described in Sec. 7.2.3. For comparison, the dashed gray line shows $\theta_{12}(t/T) = -2\pi t/T$ that constitutes a "simple" non-contractible $\mathcal{C}_{\mathrm{deg}}$. **Second column:** Cyan (pink) squares show measured $\mathrm{Im}(\beta_{\mathrm{deg},1(2)}(T))$, respectively for the corresponding $\theta_{12}(t/T)$; solid blue and red curves: corresponding no-free-parameter theory predictions; gray vertical line represents $T^* = \pi(1 + |\Delta\phi|/2)/2R$ for each $\theta_{12}(t/T)$ with $\angle R = 0$; dashed black line: $\sqrt{2\pi RT}$, the expected $\sqrt{T}$ dynamical phase for all $\theta_{12}(t/T)$. **Third column:** R estimated from data corresponding to $\mathrm{Im}(\beta_{\mathrm{deg},\{1,2\}}(T))$ (Sec. F.4), for each $\theta_{12}(t/T)$. Black stars: mean value of estimated R; gray fences: standard deviation of estimated R; black line: R from theory predictions; dark orange: $|R|$ obtained from spectroscopy measurements at EP_2 (see 'Candidate B' in Table 7.2); orange shaded region: standard deviation of $|R|$ obtained from spectroscopy measurements at EP_2. For this measurement, we used the same membrane modes and the control parameters that tune it to the same EP_2 as in Fig. 7.19.

Measurements of $\beta_{\mathrm{deg},j}(T)$ for $j \in \{1,2\}$ were carried out in the same manner as in Sec. 7.1 and its real and imaginary parts are illustrated in the second panel of Fig. 7.19 and 7.20, respectively. These measurements demonstrate that:

1. The manner in which $\mathrm{Re}/\mathrm{Im}(\beta_{\mathrm{deg},\{1,2\}})$ evolve as function of loop duration T, depends on the functional form of $\theta_{12}(s)$ i.e., how $\mathcal{C}_{\mathrm{deg}}$ is traversed.

2. $\phi_{B,\mathrm{deg}}$ is predicted to depend solely on the topology of $\mathcal{C}_{\mathrm{deg}}$ via its homotopy class. In particular, for this non-contractible $\mathcal{C}_{\mathrm{deg}}$, $\phi_{B,\mathrm{deg}}$ is predicted to be π. This is explicitly shown in the third column of Fig. 7.19 which illustrates $\phi_{B,\mathrm{deg}} \approx \pi$ as estimated from data corresponding to $\mathrm{Re}(\beta_{\mathrm{deg},\{1,2\}}(T))$ (Sec. F.4) for all non-contractible $\mathcal{C}_{\mathrm{deg}}$ discussed here.

3. In addition, for large T, $\mathrm{Im}(\beta_{\mathrm{deg},\{1,2\}})/\sqrt{T}$ is expected to asymptote to $\sqrt{2\pi R}$, independent of the choice of $\theta_{12}(s)$. This is explicitly shown in the third column of Fig. 7.20 which illustrates that R is approximately independent of $\theta_{12}(s)$. The values of R shown here were estimated from data corresponding to $\mathrm{Im}(\beta_{\mathrm{deg},\{1,2\}}(T))$ (Sec. F.4) for all $\theta_{12}(s)$, which agreed well with the theory prediction as well as with the value obtained independently from spectroscopy measurements at EP_2 (see 'Candidate B' in Table 7.2).

4. Following up on our focused discussion about the special case of $\angle R = 0$ in Sec. 2.2.4.3, we expect T^* for which $\mathrm{Re}(\beta_{\mathrm{deg},\{1,2\}}(T > T^*)) = \pi$, to depend on the choice of $\theta_{12}(s)$. In particular, $T^*(\Delta\phi) = \partial_s\theta_{12}(s)_{\max}/4R$ and using Eq. (7.12), we have $T^*(\Delta\phi) = \frac{\pi}{2R}\left(1 + \frac{|\Delta\phi|}{2}\right)$. They are indicated as gray vertical lines in second column of Figs. 7.19 and 7.20, for each $\theta_{12}(s)$ Similar to Sec. 7.1.4, we observe $\mathrm{Re}(\beta_{\mathrm{deg},\{1,2\}}(T \geq 2T^*)) \approx \pi$ and that $\mathrm{Im}(\beta_{\mathrm{deg},\{1,2\}}(T > T^*))$ asymptotes to a $\sqrt{T}$ dependence.

7.3 Robustness of dynamics in $\mathcal{EP}_2$

In this section, we address an important question:

How robust are the features in the dynamics of a system tuned in $\mathcal{EP}_2$?

The topological character of $\phi_{B,\mathrm{deg}}$ demonstrated for a variety of $\mathcal{C}_{\mathrm{deg}}$ (Sec. 7.2) can be construed empirical evidence of its robustness, along with the focused discussion in Sec. 2.2.4.2, here we discuss two additional important aspects. They are:

I. Robustness of $\phi_{B,\mathrm{deg}}$ measurement for a given $\mathcal{C}_{\mathrm{deg}}$.

II. Applicability of the current description for control loops that systematically deviate from the $\mathcal{EP}_2$ subspace.

We now proceed to elaborate both of these aspects below in Secs. 7.3.1 and 7.3.2, respectively.

7.3.1 Robustness of $\phi_{B,\mathrm{deg}}$ measurements

The majority of the measurements reported in this chapter took place over a month[1]. The key ingredients that make this effort possible, are discussed in Chapter 4, in particular Secs. 4.5.4, 4.6.2 and 4.6.3. Here we quantify our ability to precisely, reliably and repeatably: **(i)** locate an EP_2, **(ii)** transport the system along a $\mathcal{C}_{\mathrm{deg}}$ and **(iii)** measure $\phi_{B,\mathrm{deg}}$ (see Sec. 7.1).

Fig. 7.21 illustrates twelve consecutive measurements of $\beta_{\mathrm{deg}}(T)$ and the corresponding estimated values of $\{\phi_{B,\mathrm{deg}}, R\}$ (Sec. F.4). These measurements utilized the same EP_2 and "simple" non-contractible $\mathcal{C}_{\mathrm{deg}}$ as in Sec. 7.1, and were carried out non-stop for a total duration of $\sim$40 hours without any manual interventions. Taking the mean and the standard deviation of all estimated $\phi_{B,\mathrm{deg}}$ values, we obtain $\overline{\phi}_{B,\mathrm{deg}} = 3.127 \pm 0.022 \approx \pi$. Additionally, error bars reported for individual measurements of $\phi_{B,\mathrm{deg}}$ have a mean and standard deviation of 0.065$\pm$0.010. A similar level of repeatability is observed for the measurements of R which show reasonable agreement with the theory value, and also with the value independently obtained from corresponding spectroscopy measurements.

[1]September 05, 2024 - October 06, 2024

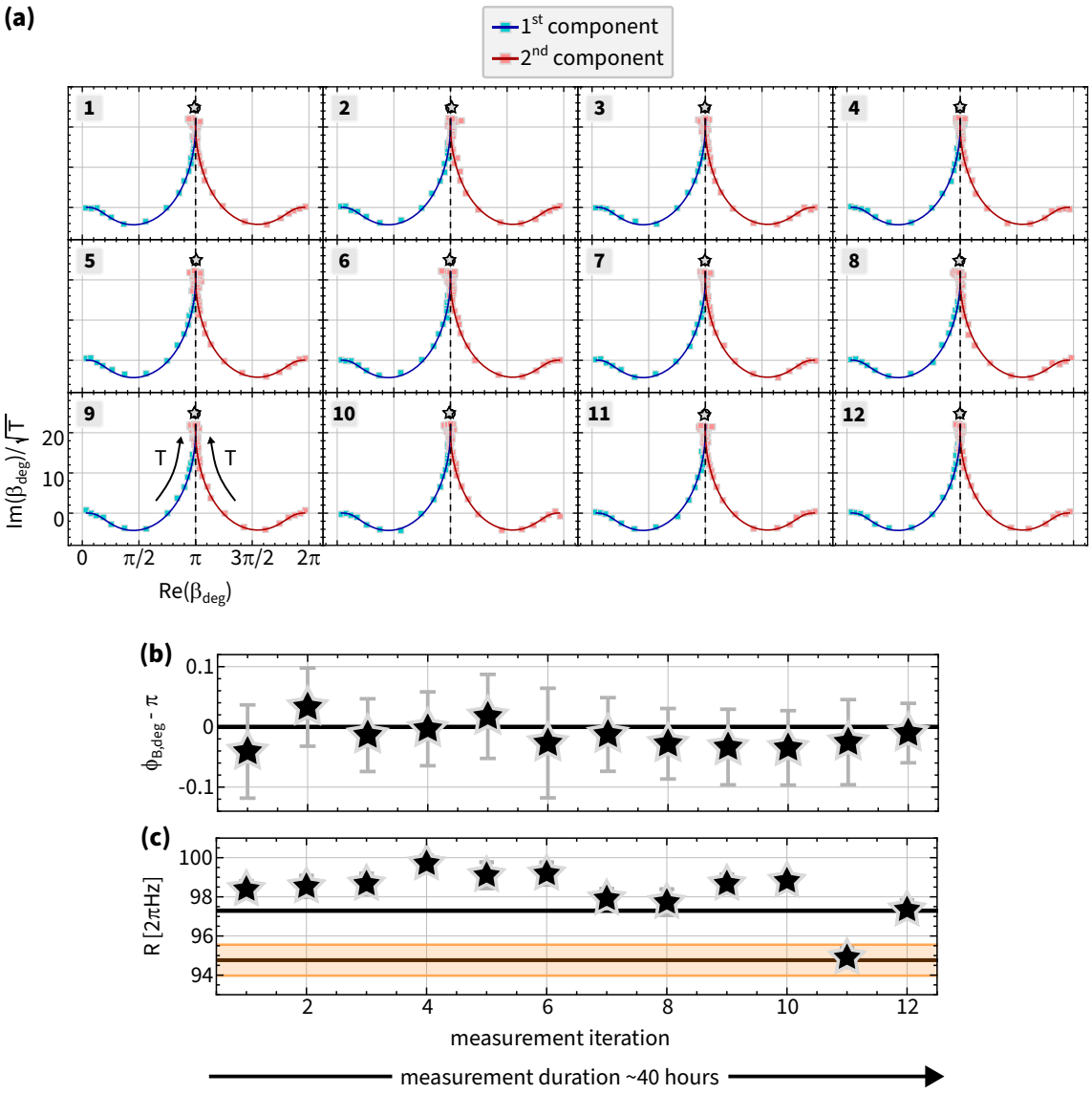

Figure 7.21: $\phi_{B,\mathrm{deg}}$ measured repeatably for over 40 hours. **(a)** Parametric plot of $\mathrm{Im}(\beta_{\mathrm{deg}}(T))/\sqrt{T}$ versus $\mathrm{Re}(\beta_{\mathrm{deg}}(T))$ corresponding to twelve consecutive and non-stop measurements of the same "simple" non-contractible $\mathcal{C}_{\mathrm{deg}}$. Cyan and pink squares: data; solid curves: corresponding no-free-parameter theory predictions; Gray star: estimated value of $\{\phi_{B,\mathrm{deg}}, \sqrt{2\pi R}\}$ (see Sec. F.4), gray fences around the gray star (not visible): error in estimating $\{\phi_{B,\mathrm{deg}}, \sqrt{2\pi R}\}$ (see Sec. F.4), gray disk: theory prediction: $\{\phi_{B,\mathrm{deg}} = \pi, \sqrt{2\pi R} = 24.82\ (2\pi\mathrm{Hz})\}$; dashed black line: $\mathrm{Re}(\beta_{\mathrm{deg}}) = \pi$. Curved black arrows in bottom left panel indicates increasing T and it applies to all panels. We note that all panels shown here share the same X and Y axes as the bottom left panel. **(b)** $\phi_{B,\mathrm{deg}} - \pi$ estimated from each measurement of $\mathrm{Re}(\beta_{\mathrm{deg}}(T))$ shown in panel (a). Black stars: mean value of estimated $\phi_{B,\mathrm{deg}} - \pi$; gray fences: standard deviation of estimated $\phi_{B,\mathrm{deg}}$; black line: 0, the expected $\phi_{B,\mathrm{deg}} - \pi$. **(c)** R estimated from each measurement of $\mathrm{Im}(\beta_{\mathrm{deg}}(T))$ shown in panel (a). Black stars: mean value of estimated R; gray fences: standard deviation of estimated R; black line: R from theory predictions; dark orange: $|R|$ obtained from spectroscopy measurements at EP_2; orange shaded region: standard deviation of $|R|$ obtained from spectroscopy measurements at EP_2. See Sec. F.4 for details of estimating $\phi_{B,\mathrm{deg}}$ and R. For these measurements, we used the same $\mathcal{C}_{\mathrm{deg}}$ as in Sec. 7.1.

In addition, we note that the measurements shown in Figs. {7.9, 7.10} and {7.19, 7.20} were acquired non-stop over a duration of 16 and 30 hours respectively, and as such, they also illustrate the stability of the setup.

7.3.2 Stepping off $\mathcal{EP}_2$

In this section, we investigate real time dynamics when traversing control loops $\mathcal{C}$ that systematically depart from the $\mathcal{EP}_2$ subspace. In particular, we are motivated by the following conceptual puzzle:

- The specific form of adiabatic phase $\phi_{\text{deg}}(T)$ we derived for adiabatic transport in $\mathcal{EP}_2$ (Eq. (2.57)), depends on the quantity R that is seemingly defined only at EP_2.
- Does the adiabatic phase vary discontinuously when we step off $\mathcal{EP}_2$ or is it continuous, i.e,.

$$\phi_{\text{deg}}(T) \xrightarrow{?} \phi(T) \tag{7.13}$$

- If it is continuous, then what takes the role of R when off $\mathcal{EP}_2$, and what is the smooth mapping between $\phi_{\text{deg}}(T)$ and $\phi(T)$?

To elucidate this puzzle further, we note that the theoretical prescription used in Sec. 2.2.4, and in this chapter up until now, uses the Jordan decomposition of H_{deg}, the degenerate dynamical matrix corresponding to $\mathcal{EP}_2$. Mathematically, the Jordan decomposition varies discontinuously when H_{deg} is perturbed off $\mathcal{EP}_2$, to a non-degenerate H. However, it turns out to be a pitfall of the Jordan decomposition itself.

The above issue can be remedied, such that H_{deg} transforms smoothly when perturbed, via other decompositions such as Jordan-Arnold decomposition [96] or Schur decomposition [260]. We theoretically elucidate this matter in Sec. F.2, and experimentally explore the consequences of adiabatic transport off $\mathcal{EP}_2$, below.

7.3.2.1 Systematically deviating from $\mathcal{EP}_2$

For this exercise, we continue to utilize the first EP_2 candidate as in Sec. 7.1 and consider the region around it. Fig. 7.22(a) illustrates the discriminant D on a 2D plane in $P \times \delta$

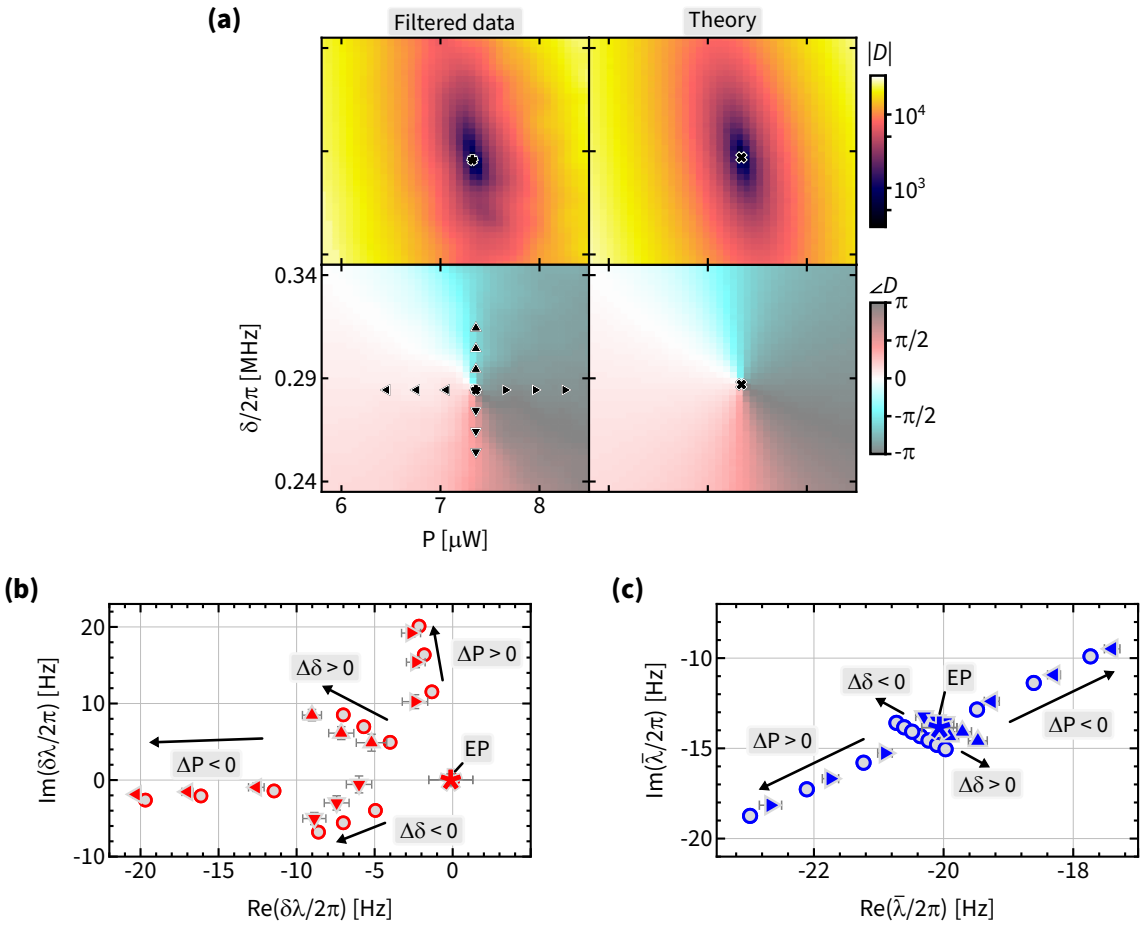

Figure 7.22: Stepping off EP_2. **(a)** $D(P,\delta)$ with $P=\sqrt{P_1P_2}$. Left column: filtered data, black star: experimentally predicted EP_2 location; right column: fit, black cross: theoretically predicted EP_2 location. Top row: $|D|$ (units: $(2\pi\times\text{Hz})^2$), bottom row: $\angle D$ (units: radians). Directional triangles in this panel showing filtered data of $\angle D$ indicate the locations off EP_2 studied in Sec. 7.3.2. **(b)** $\delta\lambda=\lambda_+-\lambda_-$ with $\{\lambda_+,\lambda_-\}$ sorted in their increasing order of real parts, corresponding to EP_2 and locations off the EP_2. Data: star corresponds to EP_2 and directional triangles correspond to the locations off EP_2. Gray disks show the corresponding theory predictions. **(c)** Same as (b) but showing $\overline{\lambda}=(\lambda_++\lambda_-)/2$. Note that for EP_2, $\overline{\lambda}\equiv\lambda_{EP}$. For this measurement, we used the same membrane modes and same the fixed control parameters that tune it to the same EP_2 as in Figs. 7.4-7.10 and 7.21.

with the EP_2 location: $\{P_{EP}, \delta_{EP}\}$ identified by a star and cross symbol in filtered data and theory, respectively. To systematically step off the EP_2, we consider the locations marked with directional triangle symbols in $\angle D$ filtered data panel. Specifically they correspond to $\{P_{\rm pert}, \delta_{\rm pert}\}$ as given by:

Left triangles:

$\{P_{EP} - 0.3\ \mu\text{W}, \delta_{EP}\}, \{P_{EP} - 0.6\ \mu\text{W}, \delta_{EP}\}$ and $\{P_{EP} - 0.9\ \mu\text{W}, \delta_{EP}\}$

Right triangles:

$\{P_{EP} + 0.3\ \mu\text{W}, \delta_{EP}\}, \{P_{EP} + 0.6\ \mu\text{W}, \delta_{EP}\}$ and $\{P_{EP} + 0.9\ \mu\text{W}, \delta_{EP}\}$

Down triangles:

$\{P_{EP}, \delta_{EP} - 2\pi \times\ 10\ \text{kHz}\}, \{P_{EP}, \delta_{EP} - 2\pi \times\ 20\ \text{kHz}\}$ and $\{P_{EP}, \delta_{EP} - 2\pi \times\ 30\ \text{kHz}\}$

Up triangles:

$\{P_{EP}, \delta_{EP} + 2\pi \times\ 10\ \text{kHz}\}, \{P_{EP}, \delta_{EP} + 2\pi \times\ 20\ \text{kHz}\}$ and $\{P_{EP}, \delta_{EP} + 2\pi \times\ 30\ \text{kHz}\}$

and are the focus of this study alongside the EP_2. Panels (b) and (c) of Fig. 7.22 show measured $\delta\lambda = \lambda_+ - \lambda_-$ with $\{\lambda_+, \lambda_-\}$ sorted in their increasing order of real parts and $\overline{\lambda} = (\lambda_+ + \lambda_-)/2$ as directional triangles corresponding to the marked locations in the $P \times \delta$ plane above, respectively. We note that for the EP_2, $\overline{\lambda} \equiv \lambda_{EP}$. All measurements are supplemented with corresponding theory prediction and they are in reasonable agreement.

The next step is to construct the control loops $\mathcal{C}_{\rm pert}$ that systematically deviate from the $\mathcal{EP}_2$ subspace. This is done in a similar fashion as for $\mathcal{C}_{\rm deg}$. Specifically, we consider:

$$\vec{Y}_{\rm pert} \equiv \{P_{\rm pert}, \delta_{\rm pert}, \eta, \theta_{12}, P_4, \Delta_4\} \tag{7.14}$$

and realize "simple" $\mathcal{C}_{\rm pert}$ by the holding the parameters $\{P_s, \delta_s, \eta, P_4, \Delta_4\}$ fixed and varying $\theta_{12}(s) = -2\pi s$, in real time for a duration T, with $0 \leq s = t/T \leq 1$. In Chapter 5 we referred to such loops as "simple" control loops in the "backward" direction. For comparison, these "simple" $\mathcal{C}_{\rm pert}$ are studied alongside a "simple" non-contractible $\mathcal{C}_{\rm deg}$ given by $\vec{Y}_{EP}$ with $\theta_{12}(s) = -2\pi s$.

7.3.2.2 Measuring real time dynamics

We now analogously follow the steps outlined in Sec. 7.1.3 to prepare an initial state $\vec{x}(0)$ that corresponds to the least-dissipative eigenvector of $H'(s,T) = H_{\rm pert}(s) - \mathcal{A}_{\rm pert}(s)/T$, transport $\vec{x}(0)$ along $\mathcal{C}_{\rm pert}$ in real time for a duration T and obtain $\vec{x}(T)$. The state vectors continue to be measured in the basis of uncoupled membrane modes i.e., $(1,0)^{\rm T}$ as the (3,3) mode and $(0,1)^{\rm T}$ as the (5,2) mode. Subsequently, we compare $\vec{x}(T)$ to $\vec{x}(0)$.

The comparison between $\vec{x}(T)$ to $\vec{x}(0)$ is done as described in Sec. 7.1.4 and corresponding to each component of the initial and final state vector we have:

$$\phi_1(T) = i\,{\rm Log}(x_1(T)/x_1(0)) = i\,{\rm Log}(V_1(T)/V_1(0)) \tag{7.15}$$

$$\phi_2(T) = i\,{\rm Log}(x_2(T)/x_2(0)) = i\,{\rm Log}(V_2(T)/V_2(0)) \tag{7.16}$$

where the subscript $i \in [1,2]$ denotes the $i^{\rm th}$ component of the state vector and $V_i(t) = \alpha_i x_i(t)$ denotes the heterodyne voltage measured near $\omega_i^{(0)}$: the bare resonance frequency of $i^{\rm th}$ membrane mode. Subsequently, we define the quantity $\beta(T)$ as:

$$\beta_1(T) = \phi_1(T) - \overline{\lambda} T \tag{7.17}$$

$$\beta_2(T) = \phi_2(T) - \overline{\lambda} T \tag{7.18}$$

For the rest of this discussion, we focus on the behavior of $\beta(T)$ as a function of the amount by which $\mathcal{C}_{\rm pert}$ deviates from the $\mathcal{EP}_2$ subspace.

7.3.2.3 Qualitative features of dynamics off $\mathcal{EP}_2$

For the specific case when $\mathcal{C}_{\rm pert}$ does not deviate from the $\mathcal{EP}_2$ subspace, we have $\mathcal{C}_{\rm pert} \equiv \mathcal{C}_{\rm deg}$ and $\beta(T) \equiv \beta_{\rm deg}(T)$ by construction. This is shown as a reference in the first column of Figs. 7.23 and 7.24 as real and imaginary parts of $\beta_{\rm deg}(T)$, respectively. We note that the EP_2 being accessed here has its corresponding $\angle R = 0$ (see Sec. 7.1) and as result, for $T \geq T^* = \pi/2R$, we expect ${\rm Re}(\beta_{\rm deg}(T)) = \pi$ for this non-contractible $\mathcal{C}_{\rm deg}$. The corresponding data and its analysis corroborates this fact. In addition, we expect ${\rm Im}(\beta_{\rm deg}(T))/\sqrt{T}$ to asymptote to $\sqrt{2\pi R}$, and corresponding data

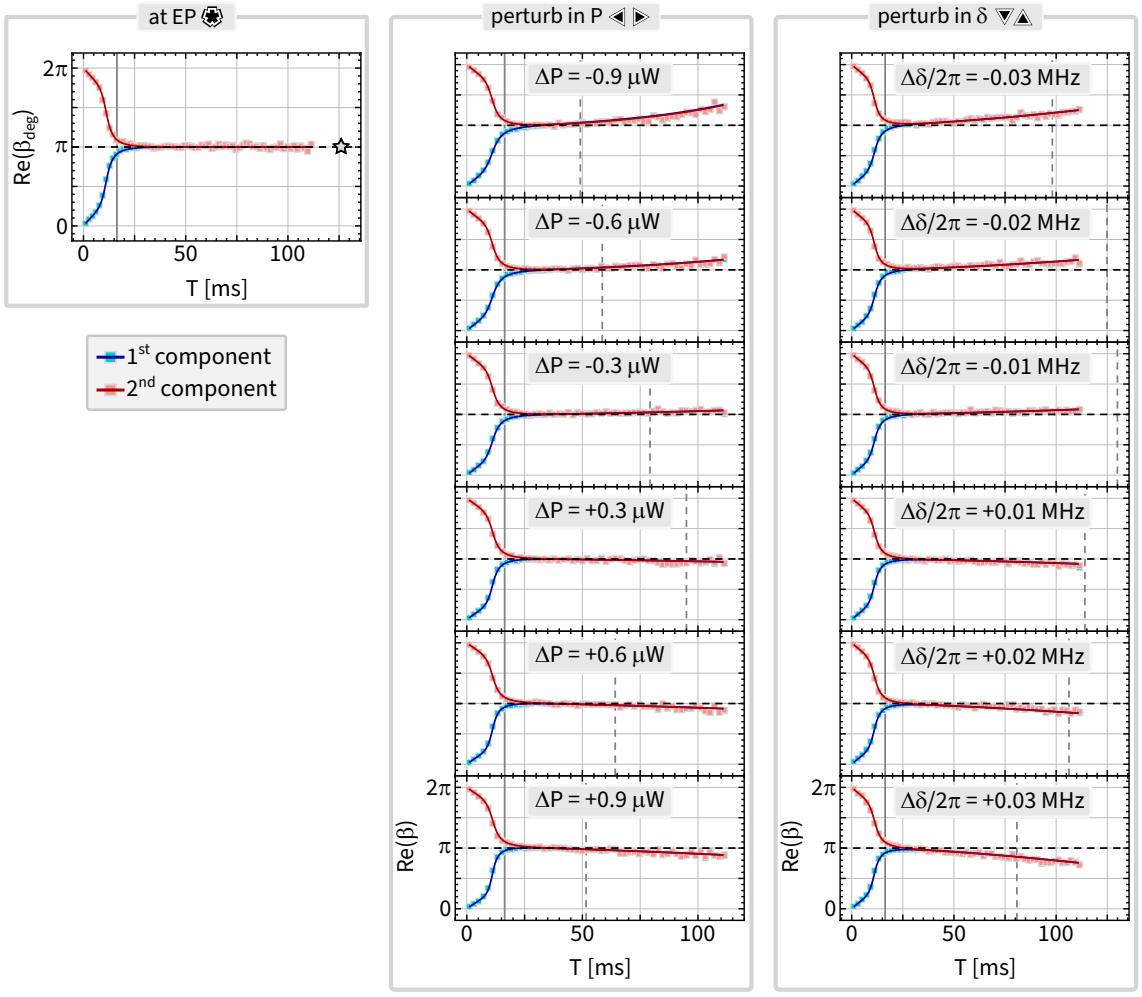

Figure 7.23: Measuring of real time dynamics off $\mathcal{EP}_2$ - part I. First column: $\mathrm{Re}(\beta_{\mathrm{deg}}(T))$ for $\mathcal{C}_{\mathrm{deg}}$, shown as a reference for upcoming measurements off $\mathcal{EP}_2$. Cyan and pink squares: data corresponding to state vector component 1 and 2, respectively; solid curves: corresponding no-free-parameter theory prediction; gray vertical line: $T^* = \pi/2R$ with $\angle R = 0$; dashed black horizontal line: π, the expected $\phi_{B,\mathrm{deg}}$ for this $\mathcal{C}_{\mathrm{deg}}$; gray star: $\phi_{B,\mathrm{deg}}$ estimated from data corresponding to $\mathrm{Re}(\beta_{\mathrm{deg}}(T))$ (see Sec. F.4). **Second column:** Same as first column but showing $\mathrm{Re}(\beta(T))$ corresponding to $\mathcal{C}_{\mathrm{pert}}$ identified by $\{P_{EP} + \Delta P, \delta_{EP}\}$, with dashed gray lines indicating corresponding $T_{\mathrm{ad}} = 2\pi/|\delta\lambda|$. The value of ΔP is indicated for each panel. We note that all panels shown here share the same X and Y axes as the bottom-most panel. **Third column:** Same as second column but for $\mathrm{Re}(\beta(T))$ corresponding to $\mathcal{C}_{\mathrm{pert}}$ identified by $\{P_{EP}, \delta_{EP} + \Delta\delta\}$. The value of $\Delta\delta$ is indicated for each panel. We note that all panels shown here share the same X and Y axes as the bottom-most panel. For this measurement, we used the same membrane modes and same the fixed control parameters that tune it to the same EP_2 as in Figs. 7.4-7.10, 7.21 and 7.22.

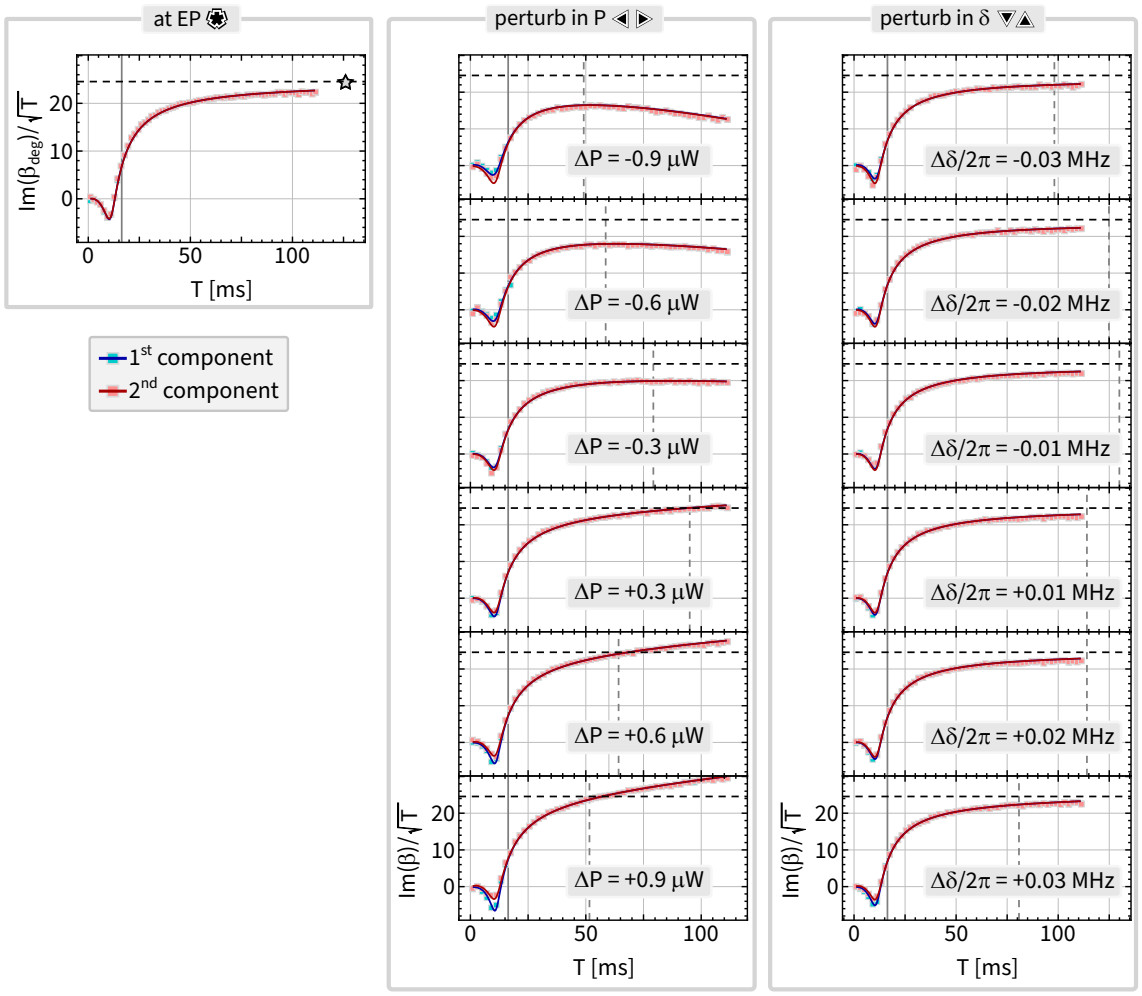

Figure 7.24: Measuring of real time dynamics off $\mathcal{EP}_2$ - part II. First column: $\mathrm{Im}(\beta_{\mathrm{deg}}(T))/\sqrt{T}$ for $\mathcal{C}_{\mathrm{deg}}$, shown as a reference for upcoming measurements off $\mathcal{EP}_2$. Cyan and pink squares: data corresponding to state vector component 1 and 2, respectively; solid curves: corresponding no-free-parameter theory prediction; gray vertical line: $T^* = \pi/2R$ with $\angle R = 0$; dashed black horizontal line: $\sqrt{2\pi R}$, the expected asymptote of $\mathrm{Im}(\beta_{\mathrm{deg}}(T))/\sqrt{T}$; gray star: $\sqrt{2\pi R}$ estimated from data corresponding to $\mathrm{Im}(\beta_{\mathrm{deg}}(T))/\sqrt{T}$ (see Sec. F.4). **Second column:** Same as first column but showing $\mathrm{Im}(\beta(T))/\sqrt{T}$ corresponding to $\mathcal{C}_{\mathrm{pert}}$ identified by $\{P_{EP}+\Delta P, \delta_{EP}\}$, with dashed gray lines indicating corresponding $T_{\mathrm{ad}} = 2\pi/|\delta\lambda|$. The value of ΔP is indicated for each panel. We note that all panels shown here share the same X and Y axes as the bottom-most panel. **Third column:** Same as second column but for $\mathrm{Im}(\beta(T))/\sqrt{T}$ corresponding to $\mathcal{C}_{\mathrm{pert}}$ identified by $\{P_{EP}, \delta_{EP}+\Delta\delta\}$. The value of $\Delta\delta$ is indicated for each panel. We note that all panels shown here share the same X and Y axes as the bottom-most panel. For this measurement, we used the same membrane modes and same the fixed control parameters that tune it to the same EP_2 as in Figs. 7.4-7.10 and 7.21-7.23.

and its analysis is consistent with this expectation.

The second and the third column of Figs. 7.23 and 7.24 show $\beta(T)$ corresponding to $\mathcal{C}_{\text{pert}}$ constructed out of various $\{P_{\text{pert}}, \delta_{\text{pert}}\}$ values. Qualitatively, $\text{Re}(\beta(T))$ deviates from $\text{Re}(\beta_{\text{deg}}(T)) = \pi$ by an amount roughly proportional to the size of the deviation from $\{P_{EP}, \delta_{EP}\}$, a representative point in $\mathcal{EP}_2$ subspace. For $\text{Im}(\beta(T))/\sqrt{T}$ corresponding to $\mathcal{C}_{\text{pert}}$ constructed using $\{P_{\text{pert}}, \delta_{EP}\}$, show a similar trend as its real counterpart. However, for $\text{Im}(\beta(T))/\sqrt{T}$ corresponding to $\mathcal{C}_{\text{pert}}$ constructed out of $\{P_{EP}, \delta_{\text{pert}}\}$, the difference is less apparent. Additionally, we note the various time scales estimated for these measurements. For all cases, we highlight $T^* = \pi/2R$, a prediction for the non-Hermitian degenerate case and $T_{\text{ad}} = 2\pi/|\delta\lambda|$, a prediction for the non-Hermitian non-degenerate case[1]. It is indeed interesting to note that for $T \sim T^*$, $\text{Re}\beta(T) \approx \pi$. We now turn to some quantitative analysis of this data.

7.3.2.4 Quantitative analysis of dynamics off $\mathcal{EP}_2$

For a systematic analysis of $\beta(T)$, we refer to the theoretical discussion in Sec. F.2.2.3 and utilize the analytical expression of $\phi(T)$ (Eq. (F.28)) that appears in the evolution of the state vector initialized as the least-dissipative eigenvector of H' i.e., $\vec{x}(T) = e^{-i\phi(T)}\vec{x}(0)$. For our case, we re-adapt $\phi(T)$ as:

$$\phi(T) = \overline{\lambda}T + \pi + i\sqrt{2\pi(A_r + iA_i)T - \pi^2 - \left(\frac{\delta\lambda T}{2}\right)^2} \tag{7.19}$$

where we replaced complex-valued A with $A_r + iA_i$ where $(A_r, A_i) \in \mathbb{R}$, set $n = 1$, and factored out i from the radical, when compared to Eq(F.28). Consequently,

$$\begin{aligned}\beta(T) &= \phi(T) - \overline{\lambda}T \\ &= \pi + i\sqrt{2\pi(A_r + iA_i)T - \pi^2 - \left(\frac{\delta\lambda T}{2}\right)^2}\end{aligned} \tag{7.20}$$

For $\delta\lambda = 0$, which corresponds to EP_2, Eq. (7.19) reduces to Eq. (2.57) with

[1]For EP_2, the measured $\delta\lambda \approx 0$ results in an empirically estimated $T_{\text{ad}} \approx$ 4 s, well beyond the displayed plot range.

$A_r + iA_i = R$ (see 'Case I' in Sec. F.2.2.3). For this case, since R is real, it is present only in $\mathrm{Im}(\beta_{\mathrm{deg}}(T)) = \sqrt{2\pi RT}$.

For $\delta\lambda \neq 0$, which correspond to perturbations off $\mathcal{EP}_2$, at intermediate time scales we expect a $\sqrt{T}$ like behavior for $\beta(T)$ characterized by $\sqrt{2\pi(A_r + iA_i)T}$ (see 'Case III' in Sec. F.2.2.3), which signifies that the role of R is taken over by $A_r + iA_i$. We also note that with decreasing $\delta\lambda$, i.e., approaching an EP_2, above time scale is expected to increase as $\propto 1/\delta\lambda^2$. Finally, in the adiabatic limit (large T), $\beta(T)$ is expected to be $\mathcal{O}(T)$, the well-known "dynamical phase" result for non-degenerate case [87] (see also: 'Case II' in Sec. F.2.2.3).

Fig. 7.25(a,b) illustrate quantitative analysis of $\beta(T)$. Here we fit the data corresponding to $\beta(2T^* \leq T \leq T_{\mathsf{DAq}})$ to Eq. (7.20) with $\{A_r, A_i\}$ as two real-valued fit parameters. $\delta\lambda$ is independently obtained from corresponding spectroscopy measurements as shown in Fig. 7.22(b). The fits capture the data reasonably well and Fig. 7.25(c) illustrates the fit parameters $\{A_r, A_i\}$ corresponding to each $\beta(T)$ dataset, as directional triangles. The corresponding theory prediction are shown as disks, and the agreement is reasonable.

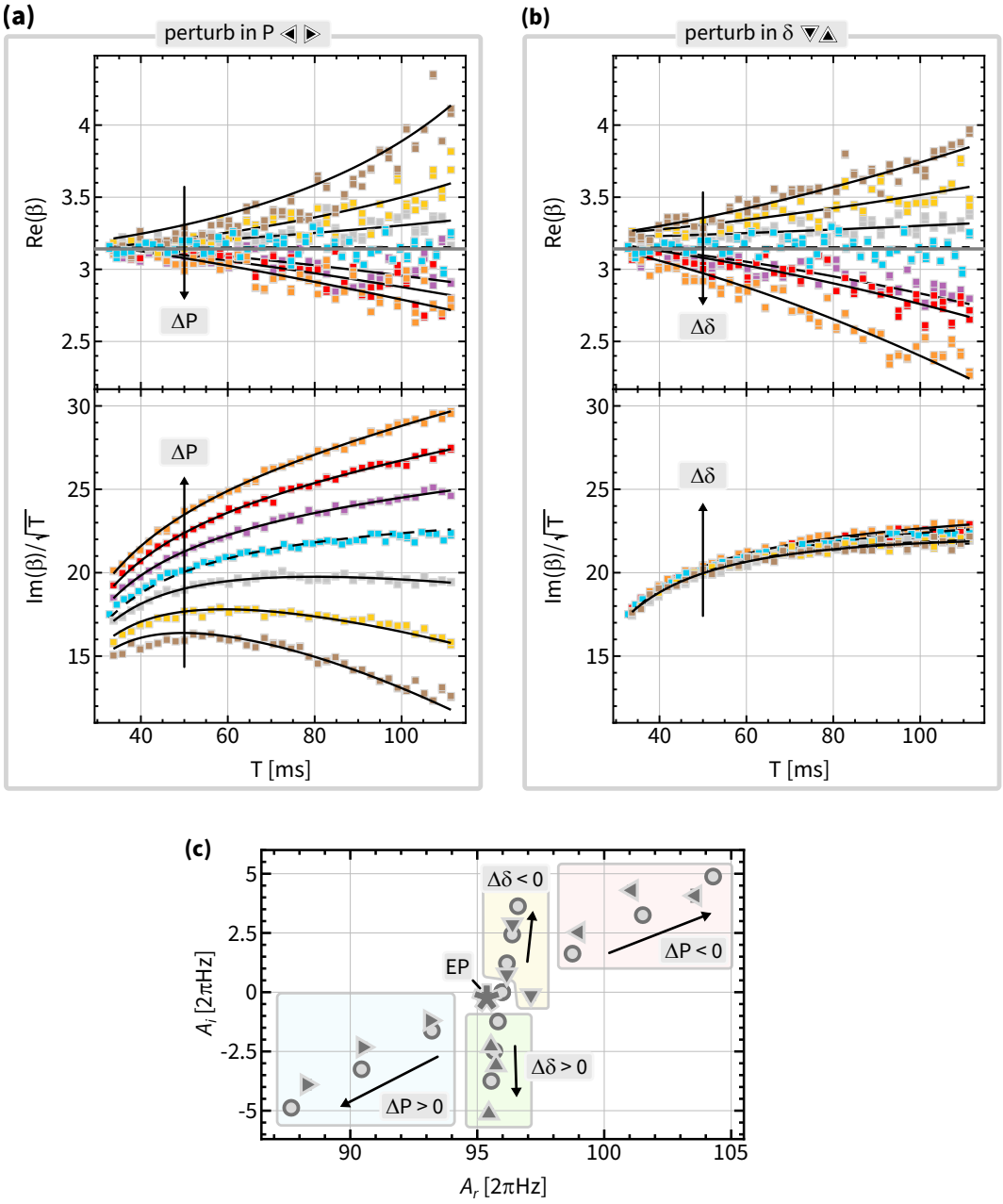

Figure 7.25: Analysis of real time dynamics off $\mathcal{EP}_2$. **(a)** Top panel: $\mathrm{Re}(\beta(T \geq 2T^*))$ for $\mathcal{C}_{\mathrm{pert}}$ constructed using $\{P_{\mathrm{pert}}, \delta_{EP}\}$. Brown to orange squares: data for $\Delta P = P_{\mathrm{pert}} - P_{EP} =$ (-0.9, -0.6, -0.3, 0, 0.3, 0.6, 0.9) μW; solid black lines: fit to Eq. (7.20) for $\Delta P \neq 0$; dashed black line: fit to Eq. (7.20) for $\Delta P = 0$; black arrow indicates increasing ΔP. Bottom panel: same as top panel of (a) but for $\mathrm{Im}(\beta(T \geq 2T^*))/\sqrt{T}$ analysis. **(b)** Top panel: same as the top panel of (a) but for $\mathcal{C}_{\mathrm{pert}}$ constructed using $\{P_{EP}, \delta_{\mathrm{pert}}\}$, with brown to orange squares: data for $\Delta\delta = \delta_{\mathrm{pert}} - \delta_{EP} = 2\pi\times$(-30, -20, -10, 0, 10, 20, 30) kHz and black arrow indicates increasing $\Delta\delta$. Bottom panel: same as top panel of (b) but for $\mathrm{Im}(\beta(T \geq 2T^*))/\sqrt{T}$ analysis. **(c)** Polar plot $a_r + ia_i$. Fit value: star corresponds to EP_2 and directional triangles correspond to the location off EP_2. Gray disk shows corresponding theory predictions. For this measurement, we used the same membrane modes and same the fixed control parameters that tune it to the same EP_2 as in Figs. 7.4-7.10 and 7.21-7.24.

7.4 A novel $\sqrt{T}$-dynamical phase and a $\sqrt{T}$-amplifier

In this section, we detail the $\sqrt{T}$-dynamical phase that is unique to the adiabatic evolution of a degenerate $N = 2$ mode system, and provide some intuition in Sec. 7.4.1. We observe that such a dynamical phase contributes to a "stretched exponential" gain of the state vector amenable to adiabatic evolution and can be of utility in the form of an amplifier (Sec. 7.4.2). Subsequently, we combine the machinery developed in this chapter and Chapter 6 to tune-up this amplifier (Sec. 7.4.3) and demonstrate an analogue of SSGG from Chapter 6 - "steady state $\sqrt{T}$-gain" (SS$\sqrt{T}$G) (Sec. 7.4.4), for an intrinsically damped degenerate harmonic oscillator.

7.4.1 The $\sqrt{T}$-dynamical phase

In this section, we provide some intuition about the $\sqrt{T}$-dynamical phase that appears in the evolution of a degenerate $N = 2$ mode system as predicted in [88, 89], derived in Secs. 2.2.4.3 and A.3.1.2, and its measurements are illustrated in Figs. 7.8-7.12, 7.15, 7.17, 7.20, 7.21 and 7.27.

For an N mode system tuned to N^{th} order degeneracy, it is predicted [88, 89] that the phase $\phi_{\text{deg}}(T)$, acquired by a state vector amenable to adiabatic evolution in $\mathcal{EP}_N$ can be expressed as a Puiseux series. For simplicity, we rewrite Eq. (2.11) below:

$$\phi_{\text{deg}}(T) = \sum_{r=0}^{N} T^{1-r/N} \int_0^1 a_r(s)ds + \mathcal{O}(T^{-1/N}) \tag{7.21}$$

where $a_r(s)$ are complex functions of $H'(s) = J_2 - \mathcal{A}_J(s)/T$, which governs the real time evolution, with $\mathcal{A}_{\text{deg}}$ the matrix of Berry connection and $0 \leq s \leq 1$. The state that is amenable to adiabatic evolution is the one initialized in the least-dissipative eigenvector of H'. The notable terms in $\phi_{\text{deg}}(T)$ as given by the sum in Eq. (7.21) include:

(a) $r = 0$

This term corresponds to the linear dynamical phase i.e., $\mathcal{O}(T)$, characterized by a_0, which is simply $\text{Tr}(H_{\text{deg}})$.

(b) $r = N$

This term corresponds to the geometric phase $\phi_{B,\deg}$ i.e., $\mathcal{O}(T^0)$, characterized by a_N, which is shown to be equal to $\mathrm{Tr}(\mathcal{A}_{\deg})/N$ (Sec. 2.2.4.1).

(c) $1 \leq r < N$

These terms correspond to dynamical phases of fractional order in T, diverge in the $T \to \infty$ limit, and can be considered as giving $\phi_{\deg}$ a "stretched exponential" dependence on T [88, 89]. Since $N \geq 2$, $r = 1$ is the dominant order term i.e., $\mathcal{O}\left(T^{1-1/N}\right)$, characterized by a_1, and has been noticed previously in Ref. [261].

(d) The $\mathcal{O}\left(1/T^{1/N}\right)$ terms and higher are dynamical phases of fractional order in $1/T$, and asymptote to 0 in the $T \to \infty$ limit. Sec. A.3.1.2 provides further details about these dynamical phases for the $N = 2$ case.

For $N = 2$, we expect a $\sqrt{T}$-dynamical phase from Eq. (7.21), which persists in the large T limit, alongside the linear dynamical and geometric phase. Using the parameterization in Sec. 2.2.4.3, the coefficient that characterizes $\sqrt{T}$-dynamical phase corresponding to a control loop in $\mathcal{EP}_2$ ($\mathcal{C}_{\deg}$) is given by $i\int_0^1 \sqrt{2n\pi R}ds$, and we have used this result at various points throughout this chapter, most notably for the case when R is a constant and $\angle R = 0$. We now provide some physical intuition about the quantity R.

7.4.1.1 Physical intuition for the quantity R

The quantity R appears as a scalar multiple of the traceless part of $H_{\deg}$ in Eq. (2.51). For simplicity, we rewrite it below.

$$H_{\deg} = R\begin{bmatrix} 1 & pe^{i\theta} \\ -e^{-i\theta}/p & -1 \end{bmatrix} + \frac{\mathcal{T}}{2}\,\mathbb{I} \tag{7.22}$$

and under a similarity transformation, $M^{-1}H_{\deg}M = \mathcal{T}\,\mathbb{I}/2 + J_2$, where J_2 is a single Jordan block of order 2, and the columns of M are composed of the unique right eigenvector of $H_{\deg}$ at EP_2 given by $\vec{u}_1 = \left(1, -e^{i\theta}/p\right)^{\mathrm{T}}$ and $\vec{u}_2 = \left(c, (1/R - c)e^{i\theta}/p\right)^{\mathrm{T}}$ as the generalized right eigenvector of $H_{\deg}$ with $c \in \mathbb{C}$. Intuitively, R appears as a rate

defining quantity in $H_{\rm deg}$, alongside $\mathcal{T}/2$, albeit with distinct characteristics. To gain further insight, we consider real time evolution in $\mathcal{EP}_2$ without any parameter variation, below. For such a case, $H' = H_{\rm deg}$ and analytic solutions to $i\dot{\vec{c}} = H'\vec{c} = H_{\rm deg}\vec{c}$ are available.

Starting with

$$i\dot{\vec{c}}_J = (\mathcal{T}\,\mathbb{I}/2 + J_2)\,\vec{c}_J \tag{7.23}$$

where $\vec{c}_J = M^{-1}\vec{c}$. Expanding Eq. (7.23) using $\vec{c}_J = (c_{1J}, c_{2J})^{\rm T}$, we have:

$$i\begin{bmatrix}\dot{c}_{1J}\\ \dot{c}_{2J}\end{bmatrix} = \begin{bmatrix}\mathcal{T}/2 & 1\\ 0 & \mathcal{T}/2\end{bmatrix}\begin{bmatrix}c_{1J}\\ c_{2J}\end{bmatrix} \tag{7.24}$$

$$\Rightarrow \begin{cases} i\dot{c}_{1J} = \mathcal{T}c_{1J}/2 + c_{2J} \\ \\ i\dot{c}_{2J} = \mathcal{T}c_{2J}/2 \end{cases} \tag{7.25}$$

Note that $(1,0)^{\rm T}$ is the unique right eigenvector of $\mathcal{T}\,\mathbb{I}/2 + J_2$, while any vector $\propto (a,1)^{\rm T}$ with $a \in \mathbb{C}$ is a generalized right eigenvector. Substituting, $c_{(1,2)J}(t) = \overline{c}_{(1,2)J}(t)e^{-i\mathcal{T}t/2}$ into Eq. (7.25) we have:

$$i\,\dot{\overline{c}}_{1J} = \overline{c}_{2J},\ i\,\dot{\overline{c}}_{2J} = 0 \tag{7.26}$$

which gives

$$\overline{c}_{2J}(t) = \overline{c}_{2J}(0),\ \overline{c}_{1J}(t) = \overline{c}_{1J}(0) - it\,\overline{c}_{2J}(0) \tag{7.27}$$

and consequently,

$$c_{1J}(t) = \overline{c}_{1J}(0)e^{-i\mathcal{T}t/2} - it\,\overline{c}_{2J}(0)e^{-i\mathcal{T}t/2} \tag{7.28}$$

$$c_{2J}(t) = \overline{c}_{2J}(0)e^{-i\mathcal{T}t/2} \tag{7.29}$$

$$\Rightarrow \vec{c}_J(t) = e^{-i\mathcal{T}t/2}\vec{c}_J(0) - it\,\overline{c}_{2J}(0)e^{-i\mathcal{T}t/2}\begin{bmatrix}1\\ 0\end{bmatrix} \tag{7.30}$$

where we suggestively curated Eq. (7.30) as the sum[1] of a state vector $\propto$ initial state vector and a state vector $\propto (1,0)^{\mathrm{T}}$, the unique right eigenvector of $(\mathcal{T}(s)/2)\mathbb{I} + J_2$. Finally, using $\vec{c} = M\vec{c}_J$, we have

$$\vec{c}(t) = e^{-i\mathcal{T}t/2}\vec{c}(0) - iRt\ \ (c_1(0) + e^{i\theta}c_2(0))e^{-i\mathcal{T}t/2}\vec{u}_1 \tag{7.31}$$

where the final state is still the sum of a state vector $\propto$ initial state vector and a state vector $\propto \vec{u}_1$, the unique right eigenvector of H_{deg} with $\vec{c} = (c_1, c_2)^{\mathrm{T}}$.

The result of Eq. (7.31) explicitly furnishes another prediction of non-Hermitian adiabatic theorem for degenerate systems [88, 89]: At large T, $\vec{c}(T) \propto \vec{u}_1$, the unique right eigenvector of H_{deg}. It also highlights two important facts about real time dynamics in $\mathcal{EP}_2$:

1. Real time dynamics in $\mathcal{EP}_2$ is governed by two rates. They are given by the degenerate eigenvalue $\mathcal{T}/2 \propto \mathrm{Tr}(H_{\mathrm{deg}})$ and R, each performing distinct tasks. Note that both the rates are complex, describing how both the amplitude and the phase change in time. The rate $\mathcal{T}/2$ governs the "trivial" dynamics i.e., via $e^{-i\mathcal{T}t/2}$ - which is an overall factor, whereas $|R|$ governs the rate at which any initial state that is linearly independent of the unique right eigenvector, approaches the unique right eigenvector of H_{deg}. Said in another way, the time scale $T_{\mathrm{deg,ad}} \propto 1/|R|$ ensures that the system's dynamics are compatible with the notion of non-Hermitian adiabaticity.

2. For any state vector which is linearly independent of the unique right eigenvector at $t = 0$, there is part in its evolution (Eq. (7.31)) that is proportional to the unique right eigenvector $\vec{u}_1$ of H_{deg}, whose amplitude grows linearly for small time t i.e., $|\vec{v}_1 \cdot \vec{c}(t)| \propto |R|t$, where $\vec{v}_1$ is the unique left eigenvector of H_{deg}.

Finally, one can draw an analogy between R and the quantity $\delta\lambda = \lambda_+ - \lambda_-$ for non-degenerate systems, where $\lambda_\pm$ are the two non-degenerate eigenvalues. Recall that the adiabatic timescale for the non-degenerate case is given by $T_{\mathrm{ND,ad}} \propto 1/|\delta\lambda|$, and we note the apparent similarity of how R and $\delta\lambda$ feature in their respective adiabatic timescales. Now we motivate that R indeed takes a role similar to $\delta\lambda$, when we consider

[1] This method also furnishes the solutions of a simple damped harmonic oscillator undergoing critically damped motion.

time evolution in $\mathcal{EP}_2$ with parameter variation (Secs. 2.2.4.3 and 7.1). For this case, the eigenvalues $\lambda'_{\pm}$ of $H' = J_2 - \mathcal{A}_J/T$ (see Eq. (2.53)) appear symmetrically split as $\lambda'_+ - \lambda'_- \propto \sqrt{R/T}$ in the large T limit.

7.4.2 Defining SS$\sqrt{T}$G

In this section, we utilize the gain from the $\sqrt{T}$-dynamical phase to describe another amplification technique, complimentary to SSGG in Chapter 6. The analysis reveals that a pair of linear but lossy elements when tuned in their degenerate subspace i.e. in $\mathcal{EP}_2$, can produce continuous gain if the tuning is done "slowly" enough, and we refer to this mechanism as steady-state $\sqrt{T}$-gain (SS$\sqrt{T}$G).

To focus this discussion, we consider an $N = 2$ mode degenerate system parameterized by Eq. (7.22) as $H_{\rm deg}(R, p, \theta, \mathcal{T})$, and it is repeatedly tuned around a control loop $\mathcal{C}_{\rm deg,amp}$ in $\mathcal{EP}_2$. Each traversal of $\mathcal{C}_{\rm deg,amp}$ is constrained to have: **(a)** the same winding number $\mathcal{W}$ (i.e., same homotopy class in $\mathcal{EP}_2$) via the same time dependence $s(t/T)$, and **(b)** the same duration T. The following four conditions define SS$\sqrt{T}$G.

(1) There is a unique least-dissipative eigenvector of the dynamical matrix that governs evolution around $\mathcal{C}_{\rm deg,amp}$.

(2) When the system is initialized in this least-dissipative eigenvector at $s = 0$ i.e, at the starting point of $\mathcal{C}_{\rm deg,amp}$, its state after a single traversal of $\mathcal{C}_{\rm deg,amp}$ using $s(t/T)$ in a duration T is given by the initial state multiplied by $e^{-i\phi_{\rm deg}(T)}$, where the complex phase $\phi_{\rm deg}(T)$ is given by:

$$\phi_{\rm deg}(T) = \phi_{\rm LD,deg} - \phi_{B,\rm deg} + \phi_{\rm sqrt,deg} + \mathcal{O}\left(\frac{1}{\sqrt{T}}\right) \tag{7.32}$$

where we expanded Eq. (2.55) in the large T limit. See also Secs. 2.2.4.3 and A.3.1.2.

(3) For each such traversal, this state's linear dynamical phase contributes loss i.e., $\mathrm{Im}(\phi_{\rm LD,deg}) < 0$.

(4) For each traversal, this state's total gain $\mathrm{Im}(\phi_{\rm deg}(T))$ lies in the region $\mathbf{K}$, which

is bounded by:

(i) $T > T^*$

(ii) $\mathrm{Im}(\phi_{\mathrm{deg}}(T)) > 0$

(iii) $\mathrm{Im}(\phi_{\mathrm{deg}}(T)) < \mathrm{Im}(\phi_{\mathrm{LD,deg}}) + \mathrm{Im}(\phi_{\mathrm{sqrt,deg}})$

We now elaborate upon each of these conditions.

For any N mode system, the set of conditions that guarantee the existence of a unique least-dissipative eigenvector of the dynamical matrix that governs evolution in $\mathcal{EP}_N$, is given in Sec. 2.2.4.1. We adapt these conditions for the $N = 2$ mode case by examining arbitrary parametric variation of $H_{\mathrm{deg}}(R, p, \theta, \mathcal{T})$ (Eq. (7.22)), in Sec. A.3.2. For completeness, we note that the measurements for various $\mathcal{C}_{\mathrm{deg}}$ in this chapter utilized constant $\{R, p, \mathcal{T}\}$ with $\mathrm{Re}(R) > 0$ while varying $\theta = \theta_0 + \theta_{12}$ via constant θ_0 and $\theta_{12} = -2n\pi k(s)$ with $n \in \mathbb{N}$, $\partial_s k > 0$ for $0 \leq s \leq 1$ and $k(0) = k(1)$.

Subsequently, if condition (1) is met, condition (2) is met for sufficiently large T. We take $T > T^*$ as the threshold for this condition (see Sec. A.3.2). For the cases studied in this chapter, it reduces to $T^* = n\pi\partial_s k|_{\mathrm{max}}/2\mathrm{Re}(R)$.

Condition (3) requires that the system's linear dynamical phase contributes loss. This condition is included because otherwise the system can serve as steady-state amplifier without the $\sqrt{T}$-dynamical phase (i.e., just by using large T and relying on the linear dynamical phase). For case consider here, condition (3) is satisfied when $\mathrm{Im}\left(T\int_0^1 \frac{\mathcal{T}(s)}{2} ds\right) < 0 \Rightarrow \mathrm{Im}\left(\int_0^1 \mathcal{T}(s) ds\right) < 0$.

Condition (4) identifies the features that $\mathrm{Im}(\phi_{\mathrm{deg}}(T))$ must exhibit upon a single traversal of $\mathcal{C}_{\mathrm{deg,amp}}$ using the time dependence s and duration T, for the system's gain to be attributed to the $\sqrt{T}$-dynamical phase. Each of its sub-conditions has a straightforward physical interpretation.

- Condition (4(i)) ensures that the system's dynamics are compatible with the notion of adiabaticity, and hence described by Eq. (7.32).
- Condition (4(ii)) ensures that the state vector experiences net gain upon each traversal

of $\mathcal{C}_{\mathrm{deg,amp}}$.

- Condition (4(iii)) ensures that the net gain can be attributed to the $\sqrt{T}$-dynamical phase. Specifically, it requires that $\sqrt{T}$-dynamical phase accounts the majority of the difference between the linear dynamical loss $\mathrm{Im}(\phi_{\mathrm{LD,deg}})$ and the net gain. This ensures that the net gain is not attributable to the higher-order terms i.e., $\mathcal{O}\left(1/\sqrt{T}\right)$ in Eq. (7.32).

For a given $\mathcal{C}_{\mathrm{deg,amp}}$ and $s(t/T)$, the conditions (4(i) - 4(iii)) can be visualized by noting that they each bisect the plane spanned by $\mathrm{Im}(\phi_{\mathrm{deg}}(T))$ and T. Together they define a region $\mathbf{K}$ with the following interpretation: for this $\mathcal{C}_{\mathrm{deg,amp}}$ and $s(t/T)$, SS$\sqrt{T}$G results iff T is chosen such that $\mathrm{Im}(\phi_{\mathrm{deg}}(T))$ lies within the $\mathbf{K}$. Fig. 7.26 illustrates the region $\mathbf{K}$.

Finally, we extend SS$\sqrt{T}$G to arbitrarily large T. This is simply accomplished by repeating a $\mathcal{C}_{\mathrm{deg,amp}}$ with a given winding number $\mathcal{W}$, time dependence $s(t/T_{\mathcal{W}})$ and duration $T_{\mathcal{W}}$, n times. This results in a new control loop $\mathcal{C}_{\mathrm{deg,amp,n}}$ with winding number $n\mathcal{W}$, time dependence $s(t/T_{n\mathcal{W}})$ and duration $T_{n\mathcal{W}}$, and the time over which gain is expected to be maintained, is given by $T_{n\mathcal{W}} = nT_{1\mathcal{W}} = nT_{\mathcal{W}}$. This can be seen easily by considering the largest duration for which SS$\sqrt{T}$G may occur (rightmost point on the boundary of $\mathbf{K}$), for a "simple" non-contractible $\mathcal{C}_{\mathrm{deg,amp}}$ (defined by fixed $\{R, p, \mathcal{T}\}$ and $\theta = 2\pi s$). It is given by $\mathrm{Im}(\phi_{\mathrm{deg}}(T_c)) = T_c\,\mathrm{Im}\,(\mathcal{T}/2) + \sqrt{T_c}\,\mathrm{Im}\left(i\sqrt{2\pi R}\right) = 0$ with

$$T_c = \left(\frac{\mathrm{Im}\left(i\sqrt{2\pi R}\right)}{\mathrm{Im}\,(\mathcal{T}/2)}\right)^2 \tag{7.33}$$

Repeating this $\mathcal{C}_{\mathrm{deg,amp}}$, n times (fixed $\{R, p, \mathcal{T}\}$ and $\theta = -2n\pi s \mod 2\pi$), the largest duration $T_c^{(n)}$ for which SS$\sqrt{T}$G may occur is given by

$$T_c^{(n)} = \left(\frac{\mathrm{Im}\left(i\sqrt{2n\pi R}\right)}{\mathrm{Im}\,(\mathcal{T}/2)}\right)^2 = n\left(\frac{\mathrm{Im}\left(i\sqrt{2\pi R}\right)}{\mathrm{Im}\,(\mathcal{T}/2)}\right)^2 = nT_c^{(n=1)} \tag{7.34}$$

We note that this prediction does not contradict the fact that the linear dynamical

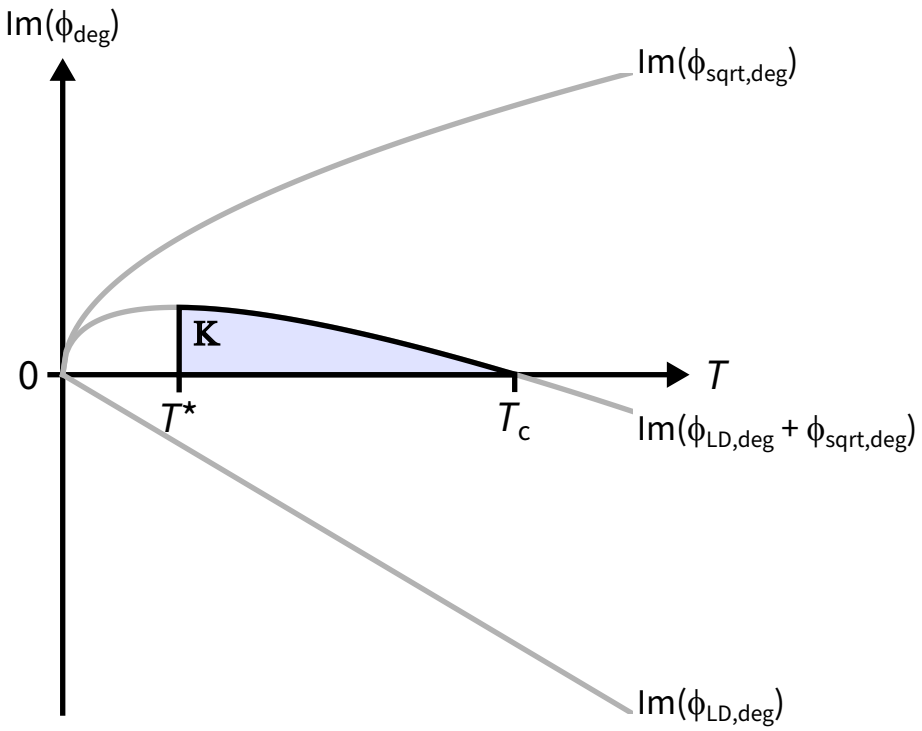

Figure 7.26: Conditions for achieving SS$\sqrt{T}$G. For a given control loop $\mathcal{C}_{\mathrm{deg,amp}}$ in $\mathcal{EP}_2$ with winding number $\mathcal{W}$, its time dependence $s(t/T)$ and its duration T, SS$\sqrt{T}$G occurs iff $\mathrm{Im}(\phi_{\mathrm{deg}}(T))$ lies in the periwinkle shaded region $\mathbf{K}$. $\phi_{\mathrm{LD,deg}}$: the linear dynamical phase, $\phi_{\mathrm{sqrt,deg}}$: the $\sqrt{T}$-dynamical phase and T^* the threshold time duration for $\phi_{\mathrm{deg}}(T)$ to be given by Eq. (7.32), T_c: solution to $\mathrm{Im}(\phi_{\mathrm{LD,deg}} + \phi_{\mathrm{sqrt,deg}}) = 0$, the largest duration for which SS$\sqrt{T}$G may occur, with corresponding gain $= 0$ dB.

phase ($\mathcal{O}(T^1)$) dominates the $\sqrt{T}$-dynamical phase ($\mathcal{O}(\sqrt{T})$), at large T. This is because the prediction applies to a given $\mathcal{C}_{\mathrm{deg,amp}}$, and each choice of n corresponds to a distinct $\mathcal{C}_{\mathrm{deg,amp}}$. Since there is no limit to how large n maybe, $T_{n\mathcal{W}} = nT_{\mathcal{W}}$ can be arbitrarily large i.e., in the steady state.

7.4.2.1 SS$\sqrt{T}$G versus SSGG

In this section, we briefly compare the two independent amplification techniques identified and developed in this thesis, SS$\sqrt{T}$G and SSGG.

Similarities

(a) In both cases the amplification of $\mathcal{O}\left(T^{0\leq\alpha<1}\right)$ competes against the linear dynamical loss of $\mathcal{O}(T)$. Thus, in the $T \to \infty$ limit, linear dynamical loss dominates.

(b) Despite the above condition, one sustains steady state gain i.e., for arbitrarily large T, by simply repeating the corresponding control loop n times, and for both cases, the duration of amplification $T_{\text{amp}} \propto n$.

Differences

(a) SS$\sqrt{T}$G is applicable to $N = 2$ mode degenerate non-Hermitian systems. SSGG is applicable to non-Hermitian non-degenerate systems.

(b) SS$\sqrt{T}$G uses the imaginary part of $\sqrt{T}$-dynamical phase as the source of amplification. SSGG uses the imaginary part of the geometric phase as the source of amplification, which is $\mathcal{O}\left(T^0\right)$.

We also note that SS$\sqrt{T}$G defined here could be adapted to any N mode degenerate non-Hermitian system as SS $\sqrt[N]{T}$G which utilizes the $T^{1-1/N}$ stretched exponential dynamical phase, and that its gain is stronger for larger N.

7.4.3 Tuning up a $\sqrt{T}$-amplifier

In this section, we combine the techniques developed in Secs. 7.1 and 7.4.2 with those utilized in demonstrating SSGG (Sec. 6.3), to establish a platform to demonstrate SS$\sqrt{T}$G.

For this tune-up, we start by locating an EP_2 as described in Sec. 7.1.1. Fig. 7.27(a) illustrates this search. This EP_2 appeared as 'Candidate F' in Sec. 7.2.2.1, and its location is given in Table 7.2. Fig. 7.27(b) illustrates its spectroscopic properties, which are also listed in Table 7.3. Crucially, we note that the degenerate mode corresponding to this EP_2 is damped, thus $\text{Im}(\phi_{\text{LD,deg}}(T)) < 0$ (condition 3 for SS$\sqrt{T}$G, Sec. 7.4.2), and that $\angle R = 0$ for this EP_2. This choice simplifies the discussion as the topological $\phi_{B,\text{deg}}$ and $\sqrt{T}$-amplification appear as independent features of adiabatic evolution in $\mathcal{EP}_2$. However, it does not represent a fundamental constraint. As noted above (Sec. 7.4.1), $\sqrt{T}$-amplification is a general feature of adiabatic evolution in $\mathcal{EP}_2$.

As a next step, we perform real time dynamics in $\mathcal{EP}_2$ as described in Secs. 7.1.2, 7.1.3. In particular we choose a "simple" non-contractible $\mathcal{C}_{\text{deg,amp}}$, and subsequently measure $\phi_{\text{deg}}(T)$. These measurements of $\phi_{\text{deg}}(T)$ are shown in Fig. 7.27(c), and specifically $\text{Im}(\phi_{\text{deg}}(T))$ - the gain experienced by the state vector, initialized as the

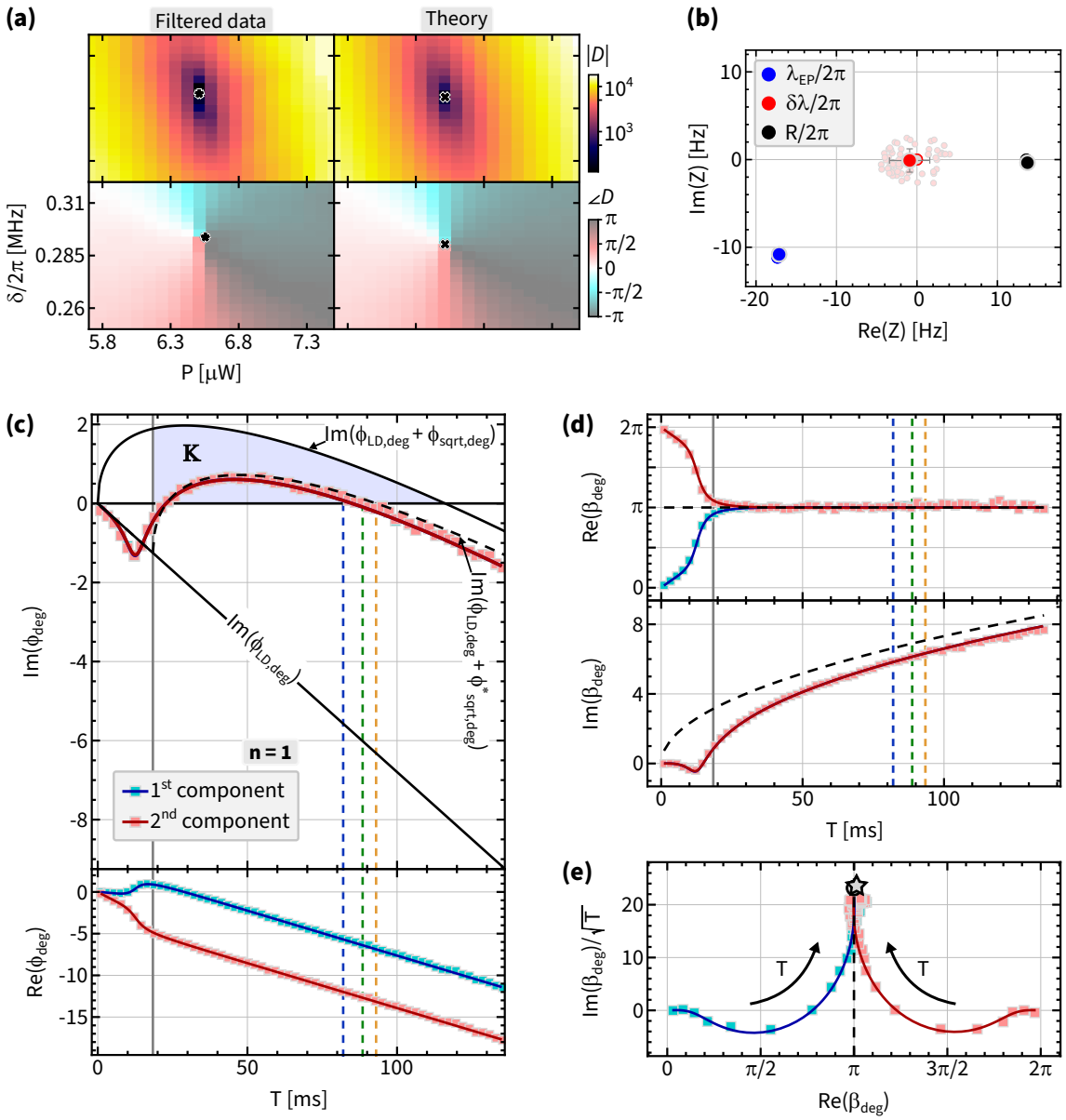

Figure 7.27: Setup for demonstrating SS$\sqrt{T}$G. (a) $D(P, \delta)$ with $P = \sqrt{P_1 P_2}$. Left column: filtered data, black star: experimentally predicted EP_2 location utilized for demonstrating $\sqrt{T}$-amplifier; right column: fit, black cross: corresponding theoretical prediction of the EP_2 location. Top row: $|D|$ (units: $(2\pi \times \mathrm{Hz})^2$), bottom row: $\angle D$ (units: radians). **(b)** Spectroscopy at the EP_2 utilized for demonstrating $\sqrt{T}$-amplifier. Blue disk: $\overline{\lambda}_{EP}$; black disk: $\overline{R}$; red disk: $\delta\lambda$, which is expected to be 0 at EP_2. For each quantity, the theoretical prediction is given by a gray disk with same edge color, the individual measurements are represented as smaller disks with a lighter color shade and the gray fences indicate corresponding error bars. Note: This EP_2 candidate appears as candidate **F** in Sec. 7.2.2.1 and with corresponding $\angle R = 0$. **(c)** Top panel: The gain of state vector initialized as the least-dissipative eigenvector of H': $\mathrm{Im}(\phi_{\mathrm{deg}}(T))$ corresponding to "simple" $\mathcal{C}_{\mathrm{deg,amp}}$ when traversed once. Cyan and pink squares: data corresponding to state vector component 1 and 2, respectively; solid curve: corresponding no-free-parameter theory predictions; periwinkle region: the region $\mathbf{K}$ that produces $\sqrt{T}$-amplification; gray vertical line: $T^* = \pi/2R$ with $\angle R = 0$; lower black line: linear dynamical loss $\mathrm{Im}(\phi_{\mathrm{LD,deg}}(T))$ of the state vector; upper black line: sum of linear dynamical loss $\mathrm{Im}(\phi_{\mathrm{LD,deg}}(T))$ and $\sqrt{T}$-dynamical gain

Figure 7.27: Setup for demonstrating SS$\sqrt{T}$G. *continued from previous page*
$\mathrm{Im}(\phi_{\mathrm{sqrt,deg}}(T)) = \sqrt{2\pi RT}$ of the state vector; dashed black line: $\mathrm{Im}(\phi_{\mathrm{LD,deg}}(T)) + \mathrm{Im}(\phi^*_{\mathrm{sqrt,deg}}(T))$, where $\mathrm{Im}(\phi^*_{\mathrm{sqrt,deg}}(T)) = \mathrm{Im}(i\sqrt{2\pi R(T-T^*)})$. Blue, green and orange dashed vertical lines: values of T used in Fig. 7.28. Bottom panel: same as the top panel but showing corresponding $\mathrm{Re}(\phi_{\mathrm{deg}}(T))$. **(c)** Same as (b) but showing corresponding $\beta_{\mathrm{deg}}(T) = \phi_{\mathrm{deg}}(T) - \phi_{\mathrm{LD,deg}}(T)$. Top (bottom) panel shows real (imaginary) parts. Dashed black curve in top (bottom) panel shows expected $\phi_{B,\mathrm{deg}}$ $(\sqrt{2\pi RT})$. **(d)** Same as (b) but showing a parametric plot of $\mathrm{Im}(\beta_{\mathrm{deg}}(T))/\sqrt{T}$ versus $\mathrm{Re}(\beta_{\mathrm{deg}}(T))$. Gray star: $\{\phi_{B,\mathrm{deg}} = 3.18 \pm 0.08, \sqrt{2\pi R} = 23.09 \pm 0.06\ (2\pi\text{Hz})\}$ estimated from β_{deg} (see Sec. F.4); gray disk: theoretically predicted $\{\phi_{B,\mathrm{deg}} = \pi, \sqrt{2\pi R} = 23.15\ (2\pi\text{Hz})\}$, dashed black line: $\mathrm{Re}(\beta_{\mathrm{deg}}) = \pi$. Curved black arrows indicates increasing T.

least-dissipative eigenvector of H', in the top panel. We observe that despite the loss contributed by $\mathrm{Im}(\phi_{\mathrm{LD,deg}}(T)) < 0$ (lowest black line), the state vector's amplitude experiences a net gain for 23 ms $< T <$ 88.5 ms. Furthermore, $\mathrm{Im}(\phi_{\mathrm{deg}}(T)) > 0$ lies entirely within $\mathbf{K}$ (periwinkle region in Fig. 7.27(c)), and thus we are guaranteed that the gain is attributable to the corresponding $\sqrt{T}$-dynamical phase (condition (4) for SS$\sqrt{T}$G, Sec. 7.4.2). We expect $\mathrm{Im}(\phi_{\mathrm{LD,deg}})$ to dominate at large T, and results in net loss for $T >$ 88.5 ms i.e., $\mathrm{Im}(\phi_{\mathrm{deg}}(T >$ 88.5 ms$)) < 0$.

Finally, we show $\beta_{\mathrm{deg}}(T) = \phi_{\mathrm{deg}}(T) - \phi_{\mathrm{LD,deg}}(T)$ in Fig. 7.27(d,e) which isolate the $\sqrt{T}$-dynamical phase via $\mathrm{Im}(\beta_{\mathrm{deg}}(T))$ and $\phi_{B,\mathrm{deg}}$ via $\mathrm{Re}(\beta_{\mathrm{deg}}(T))$. In particular, we estimate $\{\phi_{B,\mathrm{deg}} = 3.18 \pm 0.08, \sqrt{2\pi R} = 23.09 \pm 0.06\ (2\pi\text{Hz})\}$ (gray star in Fig. 7.27(e), see Sec. F.4), which compares favorably to the theory prediction $\{\phi_{B,\mathrm{deg}} = \pi, \sqrt{2\pi R} = 23.15\ (2\pi\text{Hz})\}$ (gray disk in Fig. 7.27(e)).

7.4.4 Measuring SS$\sqrt{T}$G

In this section, we utilize the setup described above (Sec. 7.4.3) to demonstrate SS$\sqrt{T}$G.

As discussed in Sec. 7.4.1, to obtain net gain via SS$\sqrt{T}$G for arbitrary large times (i.e., in the steady state), one simply repeats $\mathcal{C}_{\mathrm{deg,amp}}$ multiple times. This is demonstrated in Fig. 7.28(a,b), which shows the state vector's amplitude while $\mathcal{C}_{\mathrm{deg,amp}}$ is repeated for $n = 17$ times (corresponding $T \sim 1.5$ s). In particular, the choice of "simple" $\mathcal{C}_{\mathrm{deg,amp}}$ ensures that the amplitude stays constant for its entire duration. This "break-even" condition occurs because $\mathcal{C}_{\mathrm{deg,amp}}$ of duration $T = 88.5$ ms is chosen to provide a near-exact balance between the dynamical loss and the $\sqrt{T}$-gain produced by traversing

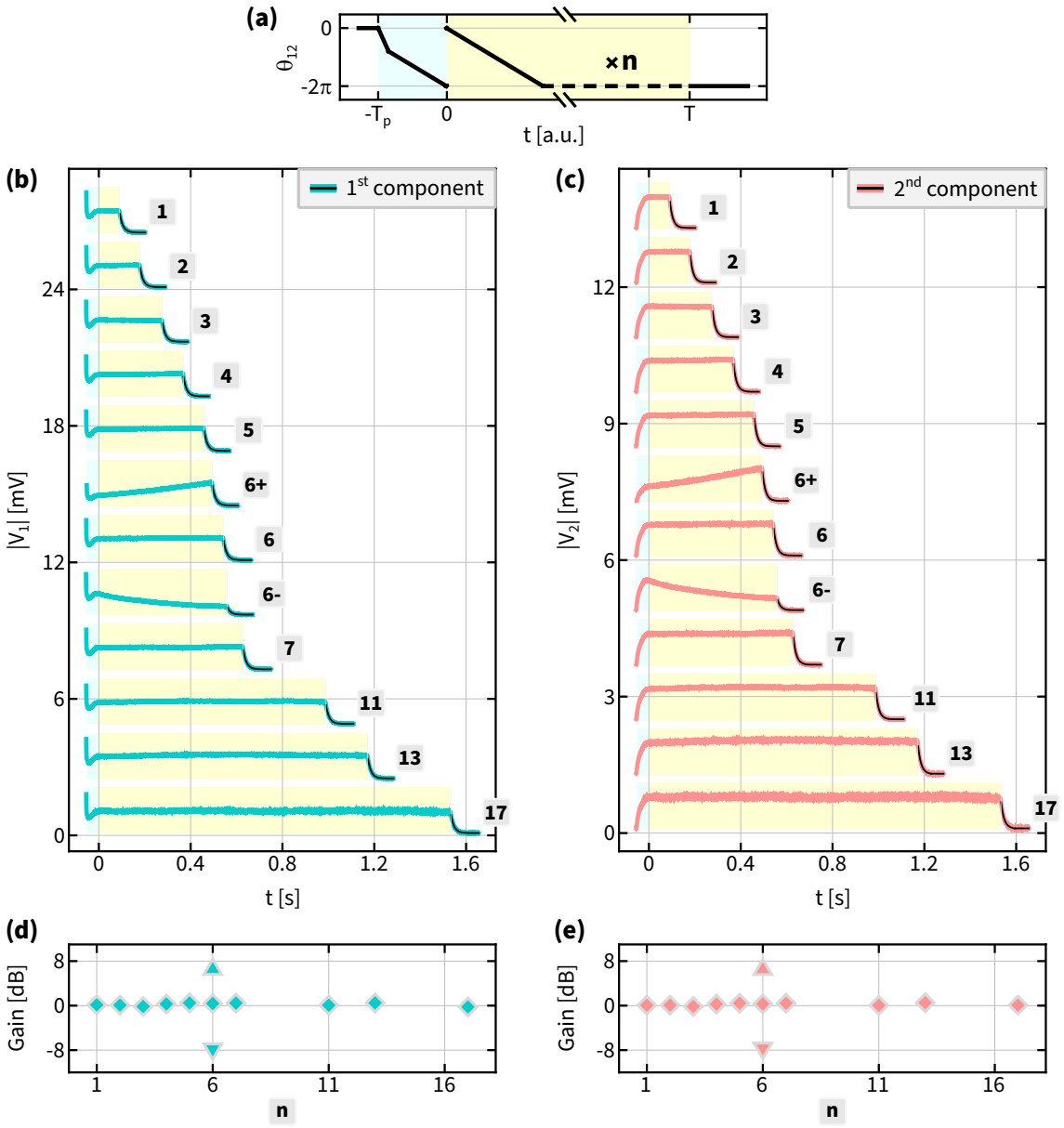

Figure 7.28: Measuring SS$\sqrt{T}$G. (a) $\theta_{12}(t)$ corresponding to $\mathcal{C}_{p,\mathrm{deg}} \,||\, \mathcal{C}_{\mathrm{deg,amp},n}$. **(b)** Cyan curves: data corresponding the amplitude of the state vector initialized as the least-dissipative eigenvector of H', as inferred from its first component when traversing $\mathcal{C}_{\mathrm{deg,amp},n}$ for $T = 88.5$ ms corresponding to $n \in \{1, 2, 3, 4, 5, 6, 7, 11, 13, 17\}$; for $T = 82$ ms corresponding to $n = 6+$; for $T = 93$ ms corresponding to $n = 6-$, respectively. Each curve is vertically onset by 2 mV for clarity. Black curves: fit to ringdown data (Sec. F.3.2). **(c)** Same as (b) but showing the amplitude of the state vector initialized as the least-dissipative eigenvector of H', as inferred from its second component. **(d)** Summary of gain resulting from traversing $\mathcal{C}_{\mathrm{deg,amp},n}$, via the first component of state vector. Diamonds: gain from $\mathcal{C}_{\mathrm{deg,amp},n}$ for $n \in \{1, 2, 3, 4, 5, 6, 7, 11, 13, 17\}$ with $T = 88.5$ ms; up-triangle: gain from $\mathcal{C}_{\mathrm{deg,amp},n}$ for $n = 6+$ with $T = 82$ ms; down-triangle: gain from $\mathcal{C}_{\mathrm{deg,amp},n}$ for $n = 6-$ with $T = 93$ ms. **(e)** Same as (d) but showing gain inferred from the second component of state vector. For this measurement, we used the same membrane modes and the control parameters that tune it to the same EP_2 as in Figs. 7.27.

it (dashed vertical green line in Fig. 7.27(c-top panel)). For smaller (larger) values of T (dashed blue and orange vertical line in Fig. 7.27(c-top panel), respectively), each repetition of $\mathcal{C}_{\rm amp}$ results in net gain (loss).

The measured state vector amplitude corresponding to choosing T as a multiple of "break-even", net gain and net loss $\mathcal{C}_{\rm deg,amp}$ durations (formally $\mathcal{C}_{{\rm deg,amp},n}$, with homotopy class given by their winding number $n \mod 2$.) are illustrated in Fig. 7.28(b,c), as cyan (for the first component of state vector) and pink curves (for the second component of state vector), respectively. The gain obtained by traversing each $\mathcal{C}_{{\rm amp},n}$ are plotted in Fig. 7.28(d,e), corresponding to the first and second component of the state vector, respectively. Finally, in Fig. F.11 we show the phase of the state vector corresponding to $\mathcal{C}_{{\rm deg,amp},n}$ which provides some insight into the phase coherence of the motion undergoing SS$\sqrt{T}$G.

Chapter 8

Conclusion and outlook

In this thesis, we studied a variety of exclusively non-Hermitian features that arise in a system of a few coupled harmonic oscillators, whose parameters are tuned statically and in real time. These include:

1. For a system of $N \geq 2$ oscillators, we showed theoretically how topology arises their eigenvalue spectrum (or eigenspectrum) in Sec. 2.1 and observed a transition in the complexity of the topology when N increases past 2. In Chapter 3, we experimentally demonstrated these features for an $N = 3$ oscillator system, wherein we accessed the full control space that contains a threefold degeneracy EP_3, the twofold degeneracies EP_2 which form a trefoil knot, and varying the control parameters in a loop in the non-degenerate subspace resulted in braiding of eigenvalues, with the braid determined by how the loop encircles the trefoil knot. These braids are shown to form non-Abelian braid group B_3. Finally, using our description, we clarified a number of surprises and anomalous past results regarding eigenvalue permutation resulting from encircling multiple EP_2s, when the encircling is constrained to a 2D control space.

2. In Chapter 5, we measured the complex geometric phase ϕ_B in the adiabatic evolution of a non-degenerate $N = 2$ oscillator non-Hermitian system. While the real part of ϕ_B maybe thought analogous to its Hermitian counterpart, the imaginary part represents a geometric loss/gain which unique to non-Hermitian systems, and is well-defined for open control paths. In Chapter 6, we utilized this geometric gain to demonstrate a

novel form of amplification in the form of 'Steady State Geometric Gain' (SSGG). In particular, we demonstrated a counterintuitive idea that a system of coupled lossy elements subject to "slow" modulation can produce useful gain via SSGG.

3. In Chapter 7, we tuned an $N = 2$ oscillator non-Hermitian system in its degenerate subspace ($\mathcal{EP}_2$), and measured the topological and discrete geometric phase $\phi_{B,\mathrm{deg}}$ in its adiabatic evolution. In addition, we measured a novel $\sqrt{T}$-dynamical phase, a characteristic feature of adiabatic evolution in $\mathcal{EP}_2$. This $\sqrt{T}$-dynamical phase was subsequently cast into another novel form of amplification in the form of 'Steady State $\sqrt{T}$ Gain' (SS$\sqrt{T}$G). Similar to SSGG, SS$\sqrt{T}$G reiterates that a system of degenerate coupled lossy elements subject to "slow" modulation can produce useful gain.

These demonstrations were made possible by the Membrane-in-the-Middle (MIM) optomechanical platform, and Chapter 4 details the construction and operation of one such system. We benefited greatly from its arbitrary tunability, precise in-situ readout, and it conforming to a well established optomechanical theory [175]. As such it continues to be a formidable system of choice to study non-Hermitian physics.

8.1 Possible future directions

We conclude this chapter by listing a few possible directions one may explore with our present MIM platform. To keep this section succinct, we restrict our ideas to those that can be explored with the MIM platform at hand, except for the first entry in this list.

1. Devices based on principle guiding SSGG and SS$\sqrt{T}$G

We start this list by noting that our demonstration of SSGG in Chapter 6 has spawned a new experiment in the Harris lab under the alias of 'Non-Hermitian Photonics' which seeks to demonstrate and develop practical optical devices using the principle guiding SSGG. To add to this endeavor, we warmly recommend utilizing SS$\sqrt{T}$G as well, when possible.

2. Additional insight into non-Hermitian adiabatic evolution.

For a non-Hermitian system, the adiabatic theorem predicts the adiabatic evolution of its unique least-dissipative eigenvector, if such an eigenvector exists (Sec. 2.2.2). Furthermore, during adiabatic evolution along a generic control loop, the system's state tends to transition into the least-dissipative eigenvector (conditional on its existence), for an arbitrary initial state. However, what remains unclear is the specific manner in which this transition happens, and if there are any interesting features in such an evolution, such as a geometric component to it?

Our discussion of non-degenerate non-Hermitian geometric phase for an $N = 2$ mode system suggests a possibility of a complex-valued geometric component in this transition during adiabatic evolution, as illustrated in Figs. 2.6(e), 5.11 and Sec. 5.4, and as such could be explored further both in theory and in experiments. In parallel, one may consider evaluating its similarity or lack thereof, to the effect known as 'geometric component of the transition probability' for their Hermitian counterparts [262–266].

In addition to isolating the corresponding geometric component in the non-degenerate non-Hermitian case, an interesting question could be: At what time scale of such adiabatic evolution, does this geometric component appear as the asymptote? This is motivated by two observations:

(i) $\beta_{--}(T)$ in Fig. 5.11 visually appears to asymptote at longer time than $\beta_{+-}(T)$ and $\beta_{-+}(T)$, which in turn take longer (visually) to asymptote than $\beta_{++}(T) \equiv \beta(T)$.

(ii) Refs.[262, 263] do not seem to provide a model-independent time scale for the Hermitian case.

3. What is the metric tensor for the non-Hermitian case?

Studies of geometric phases often invoke another quantity with geometric character. It is known as the 'quantum metric'[1] [267, 268]. Briefly, while geometric phase is a measure of how an eigenvector "twists" and "turns" in the parameter space, the metric

[1]We note that quantities with a 'quantum' prefix are simply due to the conventional terminology in literature and they may not necessarily reflect uniquely quantum features. However for this section, we conform to the popular terminology.

as its name suggests, is a measure of distances along paths in the parameter space, and the measurement is done using eigenvectors. Formally, the 'quantum metric' is a tensor (g_{ij}) and the corresponding 'quantum distance' (s_{12}) between two points $\boldsymbol{X_1} \equiv (x_1, x_2, ..., x_N)_1$ and $\boldsymbol{X_2} \equiv (x_1, x_2, ..., x_N)_2$ along a path finite $\mathcal{C}$ (that is not necessarily close) in parameter space is given by (also Eq.(33) of Ref. [267])

$$S_{12}(\mathcal{C}) = \int_{\mathcal{C}} ds \left(\sum_{i=1}^{N} \sum_{j=1}^{N} g_{ij} \partial_s x_i \partial_s x_j \right) \tag{8.1}$$

and the combined 'quantum metric' tensor g_{ij} and the Berry curvature (V_{ij}) appear as the 'quantum geometric tensor' $T_{ij} = g_{ij} + iV_{ij}$ [269].

For the Hermitian, case both g_{ij} and V_{ij} are real-valued. In particular, since g_{ij} is involved in providing a measure of distance (which is by definition a positive number), it has positive semi-definite structure. However, when we consider the non-Hermitian case, we have seen that V_{ij} is complex-valued (Eq. (2.28)). What about g_{ij} in the non-Hermitian case?

We conclude this section by noting that there has been a surge in activities involving measurements of the 'quantum geometric tensor' in Hermitian systems [270–275], and Ref. [276] for a non-Hermitian system, as well as several theoretical proposals have appeared recently for the non-Hermitian case [277–281]. A possible route to investigate this topic could be similar to that of Ref. [270][1], wherein we consider an $N = 2$ mode system tuned in real time as follows:

(i) Prepare an initial state $\vec{x}(0)$.

(ii) Tune the system in real time "through" an EP_2 in duration T, for a given value of θ ($\mathcal{C}_\theta$), as shown in Fig. 8.1(a).

(iii) Measure $\vec{x}(T)$ and compute $S(\theta, T) = 1 - |\vec{x}(T) \cdot \vec{x}(0)|^2$, a form equivalent to 'quantum distance' (Eq.(31) of Ref. [267]).

(iv) Repeat steps **(i)**, **(ii)** and **(iii)** as a function of T.

[1] In particular, this was suggested by Charles D. Brown (the lead author of Ref. [270]) himself during Frontiers conference 2024, in Monte Veritá. See Fig. 8.1(b).

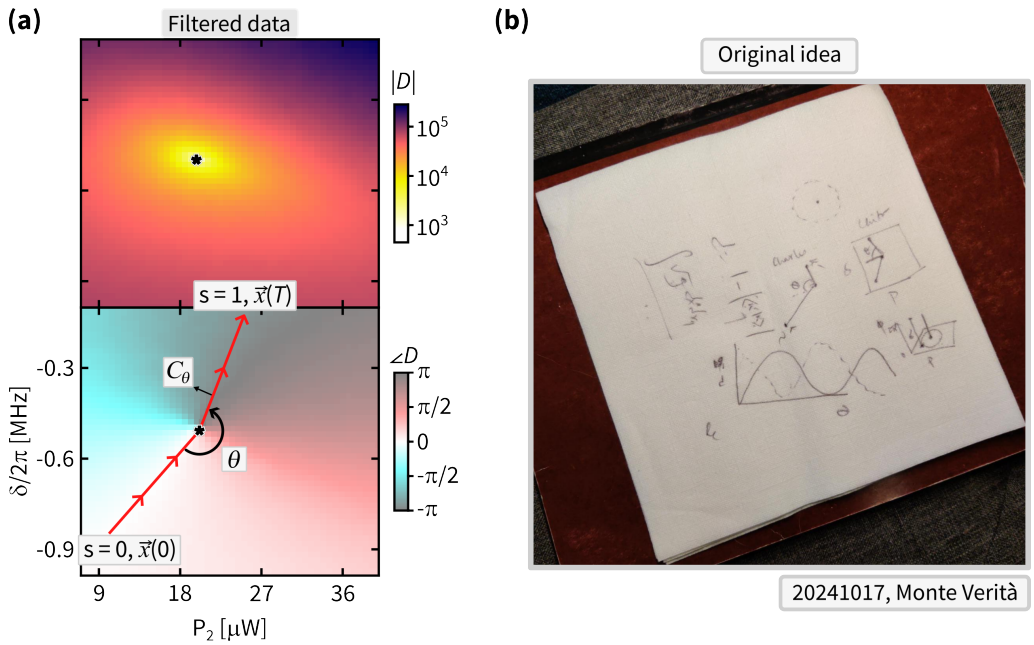

Figure 8.1: A possible route to measure metric tensor for the non-Hermitian case. (a) Schematic for tuning system "through" EP_2 (black star) along $\mathcal{C}_\theta$ (red path; not closed in this case) for a duration T with its starting and end points indicated by $s = 0$ and $s = 1$, respectively with corresponding initial and final states as $\vec{x}(0)$ and $\vec{x}(T)$, respectively. In the background we show a 2D sheet of measured D from Fig. 4.19(d), as a reference. **(b)** The actual photograph of the napkin used to sketch the idea in **(a)**, that was borne out of discussing Ref. [270] with its lead author, Charles D. Brown.

(v) Repeat step **(iv)** as a function of θ (See Fig. 8.1(a)).

In addition, one may even consider trying the above scheme with an $N = 3$ mode system (say using the (3,3); (5,2) and (5,3) membrane modes simultaneously, as described in Sec. 2.3.3 and Chapter 3), involving both EP_2 and EP_3 degeneracies. Finally, one may consider examining a recent work in Ref. [282] about monitoring system's states when control loops "go through" an EP_2 in real time, in light of the above proposal.

4. Measuring the structure of $\mathcal{EP}_2$ via static spectroscopy.

The demonstrations in Chapter 7 were solely based on real time dynamics in $\mathcal{EP}_2$. However, one may desire to measure the structure of $\mathcal{EP}_2$ via static spectroscopy. Such an undertaking is similar in spirit to the work described in Chapter 3. In particular, it could be of interest to measure the $\mathbb{RP}^3$ portion of $\mathcal{EP}_2 \cong \mathbb{RP}^3 \times \mathbb{R}$ for traceless H_{deg}.

For such a measurement, for all points in $\mathcal{EP}_2$ have $\lambda_{\text{deg}} = 0$, by construction,

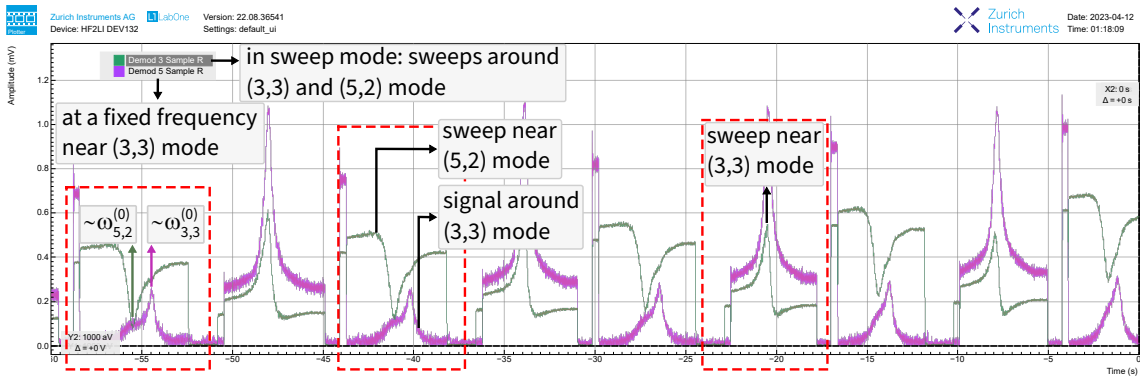

Figure 8.2: A possible route to measure eigenvectors. A screenshot of ZI-HF2 LIA (Sec. 4.6.1.1) during a spectroscopy data run which used susceptibility measurements. Magenta data: amplitude of heterodyne signal measured near the (3,3) membrane mode, using a demodulator (Demod 5) at a fixed frequency near $\omega^{(0)}_{3,3}$; green data: amplitude of heterodyne signal measured near both (3,3) and (5,2) membrane modes, using a demodulator (Demod 3) in "sweep" mode [241]. The sweeps are done in an interleaved fashion, by alternatively switching between frequency ranges near the (3,3) and the (5,2) membrane mode i.e., $\sim \omega^{(0)}_{3,3}$ and $\sim \omega^{(0)}_{5,2}$. Three features are highlighted using dashed red rectangles. Leftmost rectangle: provides a sense of the relative location of the two normal modes within each 'quasi-frequency' band near $\omega^{(0)}_{3,3}$ (magenta data) and near $\omega^{(0)}_{5,2}$ (green data), respectively. Middle rectangle: illustrates what we affectionately call a "*drive here, look there*" measurement, wherein a sweep measurement near $\omega^{(0)}_{5,2}$ (green data) results in characteristic signal near $\omega^{(0)}_{3,3}$ (magenta data). Analyzing data of this kind will provide eigenvectors. Rightmost rectangle: a redundant measurement of susceptibility near $\omega^{(0)}_{3,3}$ by both demodulators. However, the green (magenta) data corresponds to the upper (lower) sideband of the AM modulated heterodyne signal (see 'Heterodyne detection' in Sec. 4.6.1.1).

while the unique right eigenvector $\vec{u}_1$ varies as function of location in $\mathcal{EP}_2$. Therefore, spectroscopy measurements that provide access to eigenvectors are required (and perhaps not limited to an eigenvector indicator like E in Chapters 3, 4 or R in Chapter 7). Although not included in this thesis, one can show that spectroscopy performed using susceptibility measurements of Floquet-coupled non-degenerate membrane modes provide corresponding right eigenvectors. Briefly, this ability comes from measuring susceptibility of Floquet-coupled membrane modes simultaneously at more than one 'quasi-frequency' [283, 284]. In particular, all susceptibility measurements reported in this thesis measure only at one 'quasi-frequency' (which corresponded to the drive frequency), thus precluding this result. However, we include Fig. 8.2 below, that show semi-systematic measurements which if analyzed could provide corresponding eigenvectors alongside eigenvalues. It also remains to be shown if this technique can be adapted when the system is restricted to the $\mathcal{EP}_2$ subspace.

5. Exploring correlated thermal noise in coupled harmonic oscillators.

Continuing in the spirit of studying non-Hermitian systems via spectroscopy measurements, our system would be fairly suitable to characterize the thermal baths to which the individual modes of the system are coupled to. Briefly, for a single damped oscillator in equilibrium with its thermal bath, the Fluctuation-Dissipation theorem (FDT) links the oscillator's damping, its temperature (which is same as the thermal bath's temperature in equilibrium), and thermal force noise [234].

For a collection of damped oscillators, the FDT is usually applied naively "mode-by-mode", with the thermal force noises on each mode taken to be uncorrelated. In practice, this works well for damped systems in which the normal modes (eigenvectors) are sufficiently orthogonal [285, 286].

However, as seen in Chapters 3 and 7, such multimode systems if tuned over their full parameter space, generically contain EP degeneracies. As a result, for such a system when tuned, their eigenvectors are no longer orthogonal and as such N of them are parallel at an EP_N. It will be interesting to study the effect the thermal force noise when this non-orthogonality has a significant contribution. Theoretical work dealing with such multimode systems suggest a modification of the FDT [235], wherein that the thermal baths for each mode can no longer be considered independently, and as such they are correlated. See Ref. [287] for a corresponding experimental study.

In addition to experimentally studying these correlations, an interesting possibility may arise via the following example. Consider an $N = 2$ mode system that is under the influence of the said correlated thermal baths. In such a case, one of the modes can be used as a spectator for the correlated portion of the thermal noise. The correlated portion can be thought as a "common background" for both modes, which can be subtracted from the other mode, thereby gaining an improvement in the sensitivity of thermal noise.

6. Shortcuts-to-adiabaticity (STA) schemes to execute eigenvalue braiding in real time.

As described in Sec. 2.1.1 and Chapter 3, control loops encircling double degeneracies affect eigenvalues to braid. It is natural to ask what role the braids can play in the system's dynamics. A control scheme where one prepares the system in one of its normal modes, and then evolves it along the smoothly connected braid strand would be of considerable interest, as the final state is determined solely by the homotopy class of the control loop, i.e., its topology.

From the outset, real time dynamics involving a system with non-trivially braided eigenvalues (i.e., not identity) is not compatible with non-Hermitian adiabatic evolution, as the identity of least-dissipative eigenmode is not guaranteed to be unique. As a result, during real time evolution, the system undergoes diabatic transitions and the final result cannot be attributed solely to the topology of the control loop [32, 61].

To remedy this situation, one may employ 'shortcuts-to-adiabaticity' (STA) schemes [149]. Recipes such as counter-diabatic driving aim to cancel diabatic transitions by applying additional control parameters [141, 142, 147, 148]. The range of tunability afforded by the MIM platform can be an ideal setting to explore such schemes and affect a truly real time topological operation when eigenvalues braid non-trivially. We note that recently such a scheme was applied to a non-Hermitian system of a single dissipative qubit [76], and it was successful for a range of control loop duration [288]. In addition to STA, one may consider schemes that involve control schemes with tailored non-linearity [64, 289, 290].

7. Adding more tunability to the MIM toolkit.

Our current use of the MIM platform has restricted it to be a linear dispersively-coupled optomechanical system with a single optical mode (in this case $\mathrm{TEM}_{0,0}$); which does not do justice to the rich bounty optomechanical features it possesses. In addition to linear dispersive coupling, one may envision bringing in: **(i)** linear dissipative coupling with a single optical mode, **(ii)** nonlinear dispersive coupling with a single optical mode, **(iii)** linear

dispersive coupling with multiple transverse optical modes i.e., $\mathrm{TEM_{m,n}}$, **(iv)** non-linear dispersive coupling with multiple $\mathrm{TEM_{m,n}}$ optical modes, and so on. Loosely speaking, each of these configurations can bring in new control knobs, in principle, that may allow alternate routes to explore ideas such as STA and studying non-Hermitian systems in new regimes. For example, option **(i)** has the effect of turning the optomechanical coupling rate g_0 from purely real (in the linear dispersive case) to a complex-valued parameter given by the position on the band-structure (see Fig. 4.11(c,d)) [79, 291–294]. We also note that although not mentioned in this thesis, we spent $\sim$1 year exploring STA with our MIM system in configuration given by option **(iii)**. In particular we coupled to a $\mathrm{TEM_{0,0}}$ and a $\mathrm{TEM_{0,1}}$ optical mode and tuned the (4,3) and the (3,4) membrane modes[1]. While we did not accomplish the ultimate goal, our measurements were sense-making and illustrative. Options **(ii)** and **(iv)** are worthy to be explored as just optomechanical systems in their own right, let alone exploring non-Hermitian physics in such a setting. Historically, option **(ii)** has been plagued with the small magnitude of coupling which maybe require substantially larger control powers for its effects to manifest [78], or a redesign based on Refs.[228, 295, 296]. Option **(iv)** is configured to have several optical modes that are nearly degenerate [80, 208, 212], and as such is generally a harder experiment to undertake. We recommend testing and characterizing the present MIM platform first, to evaluate its feasibility.

The above list by no means exhaustive, shows a plethora of things one may pursue with system at hand. They may improve our understanding of various non-Hermitian phenomena, which then in turn may give rise to new practical devices, novel control and sensing techniques. In parallel, we do expect the experimentalists as well as the theorists to have fun with the MIM platform!

Finally, as the author of this thesis, I hope to have conveyed some aspects of non-Hermitian physics which were previously under-appreciated, and possess a clearer understanding now, along with the fact that some of those ideas can be of practical utility, as well as the utility of the MIM platform to explore them.

[1]For this work, we had not figured out a controlled use of the blue detuned control tone, which as shown in Chapters 5, 6 and 7 is a vital control knob.

Appendix

Appendix A

Methods for Chapter 2

A.1 Numerical simulations of N-mode spectral flow

Here we provide details about numerical simulations of spectral flow for the $N = 2$ and 3 cases, as illustrated in Sec. 2.1.2.

A.1.1 $N = 2$

For this case, the characteristic polynomial is given by $p_2(\lambda) = \lambda^2 + \gamma_2$, where we applied the tracelessness condition (Sec. 2.1.3.1). The corresponding eigenvalues are roots of $p_2(\lambda) = 0$, which are given by $\boldsymbol{\lambda} = \{+\sqrt{-\gamma_2}, -\sqrt{-\gamma_2}\}$.

The control loops used for demonstrating spectral flow, as shown in Fig. 2.1(a) are parameterized as:

$$\begin{aligned} \mathrm{Re}(\gamma_2(s)) &= (d-r)\ \mathrm{Sin}(\theta) + r\ \mathrm{Sin}(\theta - 2\pi s) \\ \mathrm{Im}(\gamma_2(s)) &= (d-r)\ \mathrm{Cos}(\theta) + r\ \mathrm{Cos}(\theta - 2\pi s) \end{aligned} \tag{A.1}$$

where $\{d, \theta\}$ denotes the control loop's basepoint in polar coordinates, r its radius and $0 \leq s \leq 1$ parameterizes the position along the loop, with $s = 0$ and $s = 1$ both correspond to its basepoint. For the control loops shown in Fig. 2.1(a), $\{d, \theta\} = \{1, \pi/4\}$ and $r = 0.3, 0.7$ for the red and the blue control loop, respectively. The corresponding $\boldsymbol{\lambda}$

are evaluated numerically for 101 values of s ranging from 0 to 1. They are represented on the complex plane, indicated by $\mathrm{Re}(\lambda)$ and $\mathrm{Im}(\lambda)$ in Fig. 2.1(b,c). Their evolution as a function of s is shown by stacking a copy of the complex plane for each s. The black crosses highlight $\boldsymbol{\lambda}$ at $s = 0$ (the bottom of each plot), which by construction is identical to $\boldsymbol{\lambda}$ at $s = 1$ (the top of each plot). Finally, the braids are colored using a coloring algorithm described in Sec. B.6.1 and also in Refs. [43, 91, 95].

A.1.2 $N = 3$

For this case, the characteristic polynomial is given by $p_3(\lambda) = \lambda^3 + \gamma_2\lambda + \gamma_3$, where we applied the tracelessness condition (Sec. 2.1.3.1) and its corresponding discriminant $D = -4{\gamma_2}^3 - 27{\gamma_3}^2$. For these simulations, we used the following parameterization: $y = -\gamma_2,\ x = \gamma_3$. We begin with a detailed procedure for obtaining and subsequently representing the eigenspectrum degeneracy given by $D = 0$ as shown in Fig. 2.2(c-e). We follow it up with details about the control loops and corresponding eigenvalue braids that illustrate $N = 3$-mode spectral flow as in Figs. 2.3-2.5.

A.1.2.1 Representing the trefoil knot $\mathcal{K}$ in Fig. 2.2(c-e)

The space spanned by x and y can be viewed as $\mathbb{R}^4$ and can be labeled with the Cartesian coordinates $(\mathrm{Re}(x), \mathrm{Im}(x), \mathrm{Re}(y), \mathrm{Im}(y))$. As described in Sec. 2.1.2, any 3-sphere centered at the origin (i.e., at the point $(0, 0, 0, 0)$) contains two-fold degeneracies (EP_2s), and they form a closed curve that is a trefoil knot $\mathcal{K}$. Fig. 2.2(c-e) shows this structure explicitly for three distinct choices of 3-spheres with radii: $r = \{0.5, 1, 1.5\}$, respectively using the standard stereographic projection onto $\mathbb{R}^3$ [107]. In particular, this projection uses the point $(-r, 0, 0, 0)$ as its pole, so that the coordinates X, Y, Z in Fig. 2.2(c-e) are defined via:

$$\mathrm{Re}(x) = r\left(\frac{r^2 - X^2 - Y^2 - Z^2}{r^2 + X^2 + Y^2 + Z^2}\right)$$

$$\mathrm{Im}(x) = \frac{2r^2 Z}{r^2 + X^2 + Y^2 + Z^2}$$

$$\mathrm{Re}(y) = \frac{2r^2 X}{r^2 + X^2 + Y^2 + Z^2}$$

$$\mathrm{Im}(y) = \frac{2r^2 Y}{r^2 + X^2 + Y^2 + Z^2} \tag{A.2}$$

The red, blue and yellow curves in Fig. 2.2(c-e) show locations of the degeneracies within 3-spheres with radii: $r = \{0.5, 1, 1.5\}$, respectively. It is determined by the two constraints $|x|^2 + |y|^2 = r^2$ (which defines the 3-sphere) and $4y^3 - 27x^2 = 0$ (which defines the vanishing of D). It can be seen to form the trefoil knot $\mathcal{K}$.

A.1.2.2 Control loops and eigenvalue braids in Fig. 2.3

The control loops used in Fig. 2.3(a) are parameterized in the cartesian coordinate system $(X, Y, Z)^{\mathrm{T}}$ as:

$$\begin{aligned} X(s) &= (d - r)\ \mathrm{Sin}(\theta)\ \mathrm{Cos}(\phi) + r\ \mathrm{Sin}(\theta + 2\pi s)\ \mathrm{Cos}(\phi) \\ Y(s) &= (d - r)\ \mathrm{Sin}(\theta)\ \mathrm{Sin}(\phi) + r\ \mathrm{Sin}(\theta + 2\pi s)\ \mathrm{Sin}(\phi) \\ Z(s) &= (d - r)\ \mathrm{Cos}(\theta) + r\ \mathrm{Cos}(\theta + 2\pi s) \end{aligned} \tag{A.3}$$

where $\{d, \theta, \phi\}$ denotes the basepoint of the control loop in spherical polar coordinates, r is the loop's radius, and $0 \leq s \leq 1$ parameterizes the position along the loop (i.e., $s = 0$ and $s = 1$ both correspond to the loop's basepoint).

The loops shown in Fig. 2.3(a), have the same basepoint at $(d = 2.5, \theta = 4\pi/9, \phi = -7\pi/9)^{\mathrm{T}}$, which is shown as the black sphere. Control loops from distinct homotopy classes are realized by using $r = 0.12, 0.4$ for $\mathbb{I}$, $r = 0.74$ for σ_1 and $r = 1.2$ for $\sigma_1\sigma_2$. To show the eigenvalue braids in Fig. 2.3(b-e), we first use Eq. (A.2) to convert the loop coordinates from (X, Y, Z) as given in Eq(A.3) to the coordinates $(\mathrm{Re}(x), \mathrm{Im}(x), \mathrm{Re}(y), \mathrm{Im}(y))$. We then find the three roots of $p_3(\lambda) = 0$ for 101 values of s ranging from 0 to 1. For each value of s the three roots (which comprise $\boldsymbol{\lambda}$) are plotted in the complex plane. Their evolution as a function of s is shown by stacking a copy of the complex plane for each value of s. The black crosses highlight $\boldsymbol{\lambda}$ at $s = 0$ (the bottom of each plot), which by construction is identical to $\boldsymbol{\lambda}$ at $s = 1$ (the top of each plot). Finally, the braids are colored using a coloring algorithm described in Sec. B.6.1 and also in Refs. [43, 91, 95].

A.1.2.3 Control loops and eigenvalue braids in Fig. 2.4

The control loops used for showing the non-Abelian character of B_3 as in Fig. 2.4(a) are parameterized in the coordinate system $(X, Y, Z)^{\mathrm{T}}$ as:

$$\begin{aligned} X(s) &= (d-r)\ \mathrm{Sin}(\theta)\ \mathrm{Cos}(\phi) - r\ \mathrm{Sin}(\theta + 2\pi s)\ \mathrm{Cos}(\phi) \\ Y(s) &= (d-r)\ \mathrm{Sin}(\theta)\ \mathrm{Sin}(\phi) - r\ \mathrm{Sin}(\theta + 2\pi s)\ \mathrm{Sin}(\phi) \\ Z(s) &= (d-r)\ \mathrm{Cos}(\theta) + r\ \mathrm{Cos}(\theta + 2\pi s) \end{aligned} \tag{A.4}$$

with basepoint $((d-2r)\ \mathrm{Sin}(\theta)\ \mathrm{Cos}(\phi), (d-2r)\ \mathrm{Sin}(\theta)\ \mathrm{Sin}(\phi), d\ \mathrm{Cos}(\theta))^{\mathrm{T}}$ in cartesian coordinates, r is the loop's radius, and $0 \leq s \leq 1$ parameterizes the position along the loop (i.e., $s = 0$ and $s = 1$ both correspond to the loop's basepoint).

The blue (red) control loop were constructed using in Fig. 2.4(a) used $d = 0(2), \theta = \pi/2(\pi/2), \phi = 2\pi/9(11\pi/9), r = 0.5(0.5)$, respectively and subsequently concatenated. The eigenvalue braids in Fig. 2.4(b,c) are shown in a similar fashion as in Fig. 2.3. However, the braid corresponding to blue (red) portion of concatenated control loops are colored with blue (red) shades, respectively.

A.1.2.4 2D plane $\mathcal{B}$, control loops and eigenvalue braids in Fig. 2.5

The 2D plane $\mathcal{B}$ used in Fig. 2.5(a) is chosen such that it has four points of transverse intersections and one point of non-transverse intersection with the trefoil knot $\mathcal{K}$. This $\mathcal{B}$ is given by $Y + m(Z - Z_0) = 0$, with $m = \tan(-17\pi/36)$ and $Z_0 \approx 0.284$, and it is a plane in the coordinates X, Y, Z. The non-transverse intersection is a result of fine-tuning the parameters m and Z_0, and is included for illustrative purposes.

The three control loops shown in Fig. 2.5(a), ll of which lie in $\mathcal{B}$ and share a common basepoint. Each loop is described by:

$$\begin{aligned} X(s) &= X_b + r[\cos(\phi) - \cos(2\pi s + \phi)] \\ Y(s) &= Y_b + r[\sin(\phi) - \sin(2\pi s + \phi)] \\ Z(s) &= Z_0 - Y(s)/m \end{aligned} \tag{A.5}$$

where $0 \leq s \leq 1$ parameterizes position along a circular path of radius r that starts and stops at the basepoint $(X_b, Y_b, Z_0 - Y_b/m)$. The angle ϕ sets the orientation of the circle's center with respect to the basepoint. The three loops in Fig. 2.5(a) all have their basepoint at $X_b = 0.25$, $Y_b = 0.3$, radii $r = \{0.325, 0.6, 1.1\}$, and orientations $\phi = \{-7\pi/18, 15\pi/36, -13\pi/36\}$ (for the green, red and blue loop respectively).

Fig. 2.5(b) shows the plane $\mathcal{B}$ (i.e., the space spanned by X and Y with $Z = Z_0 - Y/m$), along with the five intersections between $\mathcal{B}$ and $\mathcal{K}$ and the three loops just described. These loops can be seen to enclose zero, one, or two of the five intersections between $\mathcal{B}$ and $\mathcal{K}$.

Finally, the eigenvalue braids in Fig. 2.5(c-e) are shown in a similar fashion as in Fig. 2.3.

A.2 Relation to studies of non-Hermitian band structure

Eigenvalue braiding and knot-like structures corresponding to (eigenvalue) degeneracies have been considered in the context of a non-Hermitian band structure (NHBS) [39, 297–307]. However, there are several qualitative differences between NHBS and the non-Hermitian oscillators considered above: in the physical systems being described, the mathematical concepts relevant to the description, and the generic-ness of the resulting topological structures. We elaborate on these qualitative difference below:

The physical system under consideration in NHBS is a wave propagating in an L - dimensional lattice (in which L is typically 1, 2 or 3) that possesses a combination of non-reciprocity, gain and loss. Propagation in such a lattice can be characterized by bands whose dispersion is given by the complex eigenvalues of a matrix (which plays the role of H). A central question in NHBS is how these eigenvalues depend on the quasimomentum $\vec{k}$ (whose vector components play the role of the control parameters). Theoretical [299, 304, 305] and experimental [39, 306] work has shown that varying $\vec{k}$ in a closed loop may result in non-trivial eigenvalue braids. Theoretical work has shown that, for some lattices with $L = 3$, two-band systems described by 2×2 matrices may exhibit a

trefoil knot of two-fold (eigenvalue) degeneracies within the Brillouin zone [301, 302, 307]. However, we emphasize that these results are distinct from those discussed in previous sections.

This is because in NHBS, the number of control parameters is limited to L, and the control space they span (the analogue of control space $\mathcal{L}_N$ in previous discussions) is topologically non-trivial by assumption, as the Brillouin zone is an L-torus. In contrast, for non-Hermitian oscillators the control space $\mathcal{L}_N$ is topologically trivial, and the number of controls, given by the dimensionality of $\mathcal{L}_N$, is sufficient to span the full space of complex eigenvalues. This results in the direct connection between non-Hermitian oscillators and general complex polynomials (i.e., the characteristic polynomial of H). In particular, the non-trivial structure of the degenerate subspace (of eigenvalues) is a generic feature of $N \times N$ matrices and establishes the correspondence between control loops and the non-Abelian group of eigenvalue braids. This is in contrast to NHBS, in which these features are not generic, but only appear on fine tuning.

Finally, we note that experiments on NHBS so far [39, 306] have been limited to braids realized by two eigenvalues, which correspond to the $N = 2$ case, for which the subspace of (eigenvalue) degeneracies has a trivial geometry (i.e., just a point), and the group formed by the eigenvalue braids B_2 is Abelian. In contrast, the work described here provides description for any N, and for $N > 2$, the subspace of such degeneracies has a non-trivial geometry, and the eigenvalue braids form a non-Abelian group and experimentally demonstrate these features for $N = 3$ in Refs. [43, 91] and in Chapter 3.

A.3 Further remarks on Non-Hermitian geometric phase

Here we provide additional details that supplement our description in Sec.2.2, and some context for other work in this field.

A.3.1 Asymptotic form of the adiabatic phase

In this section, we shed further light on the asymptotic form of the adiabatic phase acquired by the least-dissipative eigenvector[1] for both: **(i)** the non-degenerate (as in illustrated in Sec. 2.2.3), and **(ii)** the degenerate (as illustrated in Sec. 2.2.4) cases, for $N = 2$.

A.3.1.1 Non-degenerate case

The derivation outlined here is similar in principle to the one in Sec. 2.2.4.1. We start with a time dependent dynamical matrix $H(t)$, with a non-zero trace which is diagonalized by a time dependent change of basis $S_D(t)$, i.e., $H_D(t) = S_D^{-1}(t)H(t)S_D(t)$ where

$$H = \lambda \begin{bmatrix} \lambda_+(t) & 0 \\ 0 & \lambda_-(t) \end{bmatrix} \tag{A.6}$$

We require the column vectors of $S_D(t)$ to be normalized (see discussion in Sec. 2.2.3.4) and that $\lambda_\pm(t), S_D(t)$ are T-periodic. In this diagonal basis, Eq. (1.1) becomes

$$i\epsilon\partial_s\vec{c}(s) = (H_D(s) - \epsilon\mathcal{A}(s))\vec{c}(s) \tag{A.7}$$

where $s = t/T, \epsilon = 1/T$ and $A_{ij} = i\vec{v}_i(s).\partial_s\vec{u}_j(s)$ for $i, j \in \{+, -\}$ with $\vec{v}_i$ and $\vec{u}_j$ the left- and right-eigenvectors of H, respectively. $\mathcal{A}$ denotes the matrix of Berry connection.

We now consider a control loop where $\mathrm{Im}(\lambda_+(s)) > \mathrm{Im}(\lambda_-(s))$ for all $s \in [0, 1]$, and correspondingly, $\vec{u}_+(s)$ decays slower than $\vec{u}_-(s)$. The non-Hermitian adiabatic theorem then guarantees that if a state is initialized in $\vec{u}_+(0)$, it will remain in $\vec{u}_+(s)$ for all $s \in [0, 1]$ as $\epsilon \to 0$ [11, 89]. For $\epsilon \to 0$, and we may use time-independent perturbation theory to find the eigenvalues $\lambda'_+(s)$ of $H_D(s) - \epsilon\mathcal{A}(s)$ at every s. Note that $\lambda'_+(s) \to \lambda_+(s)$ as $\epsilon \to 0$. In this case, the phase ϕ accumulated by a state vector is given by Eq. (2.6) (with $\vec{c}(0) = \vec{u}_+(0)$), and can be expressed as a power series in ϵ:

[1] Throughout this appendix, the phrase 'least-dissipative eigenvector' implies the least-dissipative right eigenvector.

$$
\begin{aligned}
\phi &= \frac{1}{\epsilon}\int_0^1 \lambda'_+(s)ds \\
&= \frac{1}{\epsilon}\int_0^1 \lambda_+(s)ds - \int_0^1 i\vec{v}_+(s).\partial_s\vec{u}_+(s)ds \\
&\quad - \epsilon\int_0^1 \frac{\left(\vec{v}_-(s).\partial_s\vec{u}_+(s)\right)\left(\vec{v}_+(s).\partial_s\vec{u}_-(s)\right)}{\lambda_+(s)-\lambda_-(s)}ds \\
&\quad - i\epsilon^2\int_0^1 \frac{\left(\vec{v}_-(s).\partial_s\vec{u}_+(s)\right)\left(\vec{v}_+(s).\partial_s\vec{u}_-(s)\right)\left(\vec{v}_-(s).\partial_s\vec{u}_-(s)-\vec{v}_+(s).\partial_s\vec{u}_+(s)\right)}{(\lambda_+(s)-\lambda_-(s))^2}ds \\
&\quad + \mathcal{O}(\epsilon^3)
\end{aligned}
\tag{A.8}
$$

The first term in this expression is the linear dynamical phase ϕ_D; the second term is the geometric phase ϕ_B; and the subsequent terms approach 0 in the adiabatic limit ($\epsilon \to 0$). In general, the M^{th} term is proportional to ϵ^{M-2} and to a sum of products involving $M-1$ components of A_{ij}, its $M-1$ derivatives.

We now consider ϕ for two cases: ϕ_{rev}, when the control loop is reversed and ϕ_n, when the control loop is repeated $n \in \mathbb{N}$ times. In the first case, we have $s \to 1-s$. For this substitution, each derivative in each term of Eq. (A.8) acquires a factor of (-1) but is otherwise unchanged. Thus each *odd*-ϵ order terms of ϕ_{rev} is equal to the corresponding term in ϕ, while the *even*-ϵ order terms of ϕ_{rev} are the corresponding terms in ϕ multiplied by -1.

The second case is straightforward as substituting $s \to ns$ and applying the T-periodic condition on $\lambda_+(s), \vec{u}(s)$ and $\vec{v}(s)$, the entire equation gets multiplied by n, i.e., $\phi_n = n\phi$.

A.3.1.2 Degenerate case

As shown in Sec. 2.2.4 and in Refs. [88, 89], the phase $\phi_{\text{deg}}(T)$ acquired by the least-dissipative eigenmode of $H' = J_N - \mathcal{A}_{\mathcal{J}}/T$ upon traversing a control loop $\mathcal{C}_{\text{deg}}$ in $\mathcal{EP}_N$

is given by:

$$\phi_{\rm deg}(T) = T\int_0^1 \lambda'_+ ds$$

$$= T\int_0^1 \frac{\mathcal{T}(s)}{2} ds + \sum_{r=1}^{N} \frac{e^{2\pi i \mu r/N}}{T^{r/N-1}} \int_0^1 a_r(s) ds + \mathcal{O}\left(\frac{1}{T^{1/N}}\right) \tag{A.9}$$

$$= \sum_{r=0}^{N} \frac{e^{2\pi i \mu r/N}}{T^{r/N-1}} \int_0^1 a_r(s) ds + \mathcal{O}\left(\frac{1}{T^{1/N}}\right) \tag{A.10}$$

where $\mathcal{T} = \mathrm{Tr}(H_{\rm deg}) = a_0$, $a_{r\geq 1}$ are given by the elements of $\mathcal{A}_J = iM^{-1}\frac{\partial M}{\partial s}$, the matrix of Berry connection and M is an $N \times N$ matrix whose columns are given by the unique right eigenvector of $H_{\rm deg}$ and $N-1$ generalized right eigenvectors. $\mu \in (1, 2, ..., N)$ such that it ensures λ'_+ is the least-dissipative eigenmode of H'.

Subsequently, we identified the $r = N$ term of Eq. (A.9) as the T-independent phase that provides $\phi_{B,\rm deg}$. Below we shed some light on the remaining T-dependent terms of $\phi_{\rm deg}(T)$.

(a) $r = 0$

This term corresponds to the usual linear dynamical phase of $\mathcal{O}(T)$, and is characterized by $\mathcal{T} = \mathrm{Tr}(H_{\rm deg})$.

(b) $1 \leq r < N$

These terms correspond to dynamical phases that fractional powers of $1/T$ that is unique to adiabatic transport in $\mathcal{EP}_N$, and can be considered as providing the "stretched exponential dependence" of $\phi_{\rm deg}(T)$ [88, 89]. The $r = 1$ term at has been noticed previously in Ref. [261].

(c) The $\mathcal{O}\left(1/T^{1/N}\right)$ terms and higher can be thought analogous to the $\mathcal{O}(1/T)$ and higher order contributions for the non-degenerate case as in Eqs. (2.7) and (A.8), that asymptote to zero in the limit $T \to \infty$. Since $N \geq 2$, convergence of $\mathcal{O}(1/T^{1/N})$ (for the degenerate case) is slower than $\mathcal{O}(1/T)$ (for the non-degenerate case).

We now characterize these dynamical phases for the $N = 2$ case as illustrated in Sec. 2.2.4.3. For this exercise we consider "simple" $\mathcal{C}_{\rm deg}$ in $\mathcal{EP}_2$. Specifically, we focus on $\phi_{\rm deg}(T)$ given by Eq. (2.57) and expand it in the large-T limit. This results in

$$\phi_{\rm deg}(T) = T\int_0^1 \frac{\mathcal{T}(s)}{2}ds + n\pi + i\left(2\pi n R\right)^{1/2} T^{1/2} \\ - i\left(\frac{1}{R^{1/2}}\right)\left(\frac{n\pi}{2}\right)^{3/2}\frac{1}{T^{1/2}} - i\frac{(n\pi)^{5/2}}{2^{7/2}R^{3/2}}\frac{1}{T^{3/2}} + \mathcal{O}\left(\frac{1}{T^{5/2}}\right), \tag{A.11}$$

which shows all the expected features discussed above.

A.3.2 Most general control loops for adiabatic transport in $\mathcal{EP}_2$

In this section, we examine the case when all the parameters of the matrix $H_{\rm deg}$ that corresponds to $\mathcal{EP}_2$, are allowed to vary, and then retrieve the most general control loops in $\mathcal{EP}_2$ ($\mathcal{C}_{\rm deg}$) that allow for adiabatic evolution as prescribed in Sec. 2.2.4. For simplicity, we rewrite the corresponding $H_{\rm deg}$ as given in Eqs. (2.51) and (7.22).

$$H_{\rm deg} = R\begin{bmatrix} 1 & pe^{i\theta} \\ -e^{-i\theta}/p & -1 \end{bmatrix} + \frac{\mathcal{T}}{2}\,\mathbb{I} \tag{A.12}$$

with complex-valued parameters $\{R \neq 0, \mathcal{T}\}$ and real-valued parameters $\{p, \theta\}$.

Setting up the problem

To be concrete, here we are interested in $\mathcal{C}_{\rm deg}$ that are beyond the cases studied in Chapter 7, i.e., which solely considered $\mathcal{C}_{\rm deg}$ with fixed $\{R, p, \mathcal{T}\}$ and varied θ in a loop. In this exercise, we allow $\{R, p, \mathcal{T}, \theta\}$ to vary simultaneously and filter out those $\mathcal{C}_{\rm deg}$ that possess a unique least-dissipative eigenvector of the matrix H' that governs evolution along $\mathcal{C}_{\rm deg}$, and thus are amenable to adiabatic transport. By construction, this exercise provides us the set of requirements that a $\mathcal{C}_{\rm deg}$ must fulfill to satisfy condition (1) of SS$\sqrt{T}$G (Sec. 7.4.2). Finally, these results supplement those obtained in Sec. 2.2.4.3.

Calculating H'

The first step is to calculate $H'(s,T) = \mathcal{T}(s)\mathbb{I}/2 + J_2 - \mathcal{A}_J(s)/T$ with $0 \leq s \leq 1$, where the system is varied along a $\mathcal{C}_{\rm deg}$ via its parameters $\vec{W}(s) \equiv (R(s), p(s), \theta(s), \mathcal{T}(s))$ such that $\vec{W}(s=0) = \vec{W}(s=1)$ for a duration T. $\mathcal{A}_J$ is the matrix of Berry connection given by $\mathcal{A}_J = iM^{-1}\frac{\partial M}{\partial s}$ where columns of M are composed of the unique right eigenvector $\vec{u}_1$ and a generalized right eigenvector $\vec{u}_2$ of $H_{\rm deg}$. If we express $\vec{u}_1 = \left(1, -e^{-i\theta}/p\right)^{\rm T}$, $\vec{u}_2$ is constrained by two relations: **(i)** $(H_{\rm deg} - \lambda_{\rm deg}\mathbb{I})\vec{u}_2 = \vec{u}_1$ where $\lambda_{\rm deg} = \mathcal{T}/2$ is the degenerate eigenvalue of $H_{\rm deg}$, and **(ii)** $M^{-1}H_{\rm deg}M = \mathcal{T}(s)\mathbb{I}/2 + J_2$. This results in $\vec{u}_2 = \left(c, (1/R - c)e^{-i\theta}/p\right)^{\rm T}$ with $c \in \mathbb{C}$. Finally, $H'(s,T)$ is given by

$$H'(s) = \begin{bmatrix} \mathcal{T}(s)/2 & 1 \\ 0 & \mathcal{T}(s)/2 \end{bmatrix} - \frac{1}{T}\begin{bmatrix} cR(s)(\partial_s\theta - i\partial_s{\rm Log}(p)) & ic\partial_s{\rm Log}(R) + c(cR(s)-1)(\partial_s\theta - i\partial_s{\rm Log}(p)) \\ -R(s)(\partial_s\theta - i\partial_s{\rm Log}(p)) & -i\partial_s{\rm Log}(R) - (cR(s)-1)(\partial_s\theta - i\partial_s{\rm Log}(p)) \end{bmatrix} \tag{A.13}$$

where we note the manner in which variations in p and R appear in $\mathcal{A}_J$ i.e. as $\partial_s{\rm Log}(p)$ and $\partial_s{\rm Log}(R)$, respectively, while the trace remains absent, as before (Eq. (2.52)).

Constraining $\mathcal{A}_0$, and thereby $\mathcal{C}_{\rm deg}$

To identify the conditions that guarantee the existence of a unique least-dissipative eigenvector of H' for all $s \in [0,1]$, we examine the term corresponding to $\mathcal{A}_0 \equiv \mathcal{A}_{J_{N=2,1}}$. For this case,

$$\mathcal{A}_0(s) = -R(s)(\partial_s\theta - i\partial_s{\rm Log}(p)) \tag{A.14}$$

where note the absence of terms $\propto \partial_s R$ and that complex valued nature of $\mathcal{A}_0$ solely comes for R, as both $\partial_s\theta$ and $\partial_s{\rm Log}(p)$ are real valued quantities.

Adapting the condition on $\mathcal{A}_0$ from Sec. 2.2.4.1 to guarantee a unique least-dissipative eigenvector of H' and Refs. [88, 89], we have:

1. $(\partial_s\theta - i\partial_s \mathrm{Log}(p)) \neq 0$ for all $s \in [0,1]$. Note that $R \neq 0$ needs to be satisfied by-default or else H_{deg} does not correspond to $\mathcal{EP}_2$.

2. $-R(s)(\partial_s\theta - i\partial_s \mathrm{Log}(p))$ does not make a full circuit around the origin as s varies from 0 to 1 via the constraint $|\angle(-R(s)(\partial_s\theta - i\partial_s \mathrm{Log}(p)))| < \pi$, and as such it does not touch or cross the negative real axis.

Calculating $\boldsymbol{\lambda'}$

With the above conditions, we now identify the unique least dissipative eigenvector by examining the eigenvalues $\boldsymbol{\lambda'}$ of H'. They are:

$$\begin{aligned}\lambda'_{\pm}(s) = \frac{\mathcal{T}(s)}{2} - \frac{\partial_s\left[\theta - i\mathrm{Log}(p) - i\mathrm{Log}(R)\right]}{2T} \\ \pm i\frac{\sqrt{-4R(s)T\partial_s[\theta - i\mathrm{Log}(p)] + (\partial_s\left[\mathrm{Log}(p) + \mathrm{Log}(R) + i\theta\right])^2}}{2T}\end{aligned} \tag{A.15}$$

where '$+$' is chosen to denote the least-dissipative eigenvector and '$-$' denotes the other mode.

Calculating $\boldsymbol{\phi_{\mathrm{deg}}(T)}$, isolating $\boldsymbol{\phi_{B,\mathrm{deg}}}$, and the $\boldsymbol{\sqrt{T}}$-dynamical phase

Consequently, if a state were prepared as the unique least-dissipative eigenvector of H' conditional upon its existence for all $s \in [0,1]$, and then evolved adiabatically along $\mathcal{C}_{\mathrm{deg}}$, we expect the final state to be given by $\vec{c}(T) = e^{-i\phi_{\mathrm{deg}}(T)}\vec{c}(0)$, where the complex valued $\phi_{\mathrm{deg}}(T)$ is exactly given by

$$\begin{aligned}\phi_{\mathrm{deg}}(T) &= T\int_0^1 \lambda'_+(s)ds \\ &= T\int_0^1 \frac{\mathcal{T}(s)}{2}ds - \int_0^1 \frac{\partial_s\left[\theta - i\mathrm{Log}(p) - i\mathrm{Log}(R)\right]}{2}ds \\ &+ i\int_0^1 \frac{\sqrt{-4R(s)T\partial_s[\theta - i\mathrm{Log}(p)] + (\partial_s\left[\mathrm{Log}(p) + \mathrm{Log}(R) + i\theta\right])^2}}{2}ds\end{aligned} \tag{A.16}$$

where we used λ'_+ from Eq. (A.15). Upon integrating the T^0 part of $\phi_{\rm deg}(T)$ above, Eq. (A.16) reads

$$\phi_{\rm deg}(T) = T\int_0^1 \frac{\mathcal{T}(s)}{2}ds + n\pi \bmod 2\pi \\ + i\int_0^1 \frac{\sqrt{-4R(s)T\partial_s[\theta - i{\rm Log}(p)] + (\partial_s\left[{\rm Log}(p) + {\rm Log}(R) + i\theta\right])^2}}{2}ds \quad \text{(A.17)}$$

where we have $\int_0^1 {\rm Log}(R)ds = 0$ as R does not wind around the origin via constraints on $\mathcal{A}_0$ with $R(s=0) = R(s=1)$. We also have $\int_0^1 {\rm Log}(p)ds = 0$ as p is real with $p(s=0) = p(s=1)$. As a result, Eq. (A.17) shows that regardless of how "non-straight" a $\mathcal{C}_{\rm deg}$ is, with its "non-straightness" being encoded by $\{R(s), p(s)\}$, $\phi_{B,{\rm deg}}$ is solely given by half the number of times $\theta(s)$ winds by π (modulo 2π), while $\theta(s)/2\pi$ denotes the winding number of $\mathcal{C}_{\rm deg}$ in $\mathcal{EP}_2$.

We also note that the above facts which are specifically derived for an $N=2$ mode system, are consistent with the prediction for any N mode system tuned in its $\mathcal{EP}_N$ subspace (See Sec. 2.2.4.1 and Refs. [88, 89]).

Finally, we note that in the large T limit, the third term of Eq. (A.17), the leading order contribution is $\propto \mathcal{O}\left(\sqrt{T}\right)$ and is characterized by variations in $\{R, p, \theta\}$.

Defining T^* for SS$\sqrt{T}$G

Notice the integrand in the third term of Eq. (A.17). To define T^*, we express it as $\mathcal{I}$ given by

$$\mathcal{I}(s) = \sqrt{\mathcal{I}_1(s)T + \mathcal{I}_2(s)} \quad \text{(A.18)}$$

where $\mathcal{I}_1 = -R(s)\partial_s[\theta - i{\rm Log}(p)]$ and $\mathcal{I}_2 = (\partial_s\left[{\rm Log}(p) + {\rm Log}(R) + i\theta\right])^2/4$. We define T^* as

$$T^* = |\mathcal{I}_2(s)/\mathcal{I}_1(s)|_{\rm max} \quad \text{(A.19)}$$

evaluated for a particular $s \in [0, 1]$ that maximizes T^*. As a result, for $T > T^*$, it allows the third term in Eq. (A.17) to have dominant $\mathcal{O}(\sqrt{T})$ (complex-valued) contribution. Subsequently, its real part may produce SS$\sqrt{T}$G. Notice that $T^* \propto |1/R|$, similar to our discussion in Sec. 7.4.1.1, and as such this definition is compatible with the notion of non-Hermitian adiabaticity.

A.3.3 Geometric phase for control loops that encircle EP_2

In this section, we review the results of geometric phase for control loops that encircle EP_2.

For any N-mode non-Hermitian system, control loops that encircle an EP_2 will result in an eigenvalue braid (Sec. 2.1.1), and to be precise, such an eigenvalue braid will necessarily swap the identity of the least-dissipative eigenvector. As a result, such loops are not in the domain of non-Hermitian adiabatic theorem[1].

Despite this restriction, work on real time evolution along such control loops have developed a notion of "quasi-adiabatic" evolution, that is slow, but not asymptotically slow [28–30]. For concrete examples of such "quasi-adiabatic" evolution, the reader is referred to Chapter 3 of Ref. [94] and Chapter 2 of [188]. In this regime, for a certain class of loops and a particular choice of initial state, the system may end up in a final state that is approximately given by the eigenvalue braid. Most of these works have focused on how the system's energy is transferred between eigenmodes [31, 32, 61, 308, 309]. While a limited number of studies have focused on system's phase [69, 77], a clear picture for geometric phase acquired by a state vector for such control loops, when performed in real time, is yet to emerge.

In parallel to real time evolution, geometric phases for such loops have been investigated via static characterization of system's eigenvectors, both in theory [22, 24, 194, 310, 311] and in experiments [72, 73, 75, 312]. While Ref. [22] theoretically predicts a complex valued geometric phase with a special emphasis on the case that result in a

[1]One may ask: "What if we perform the loop that encircles an EP_2 twice ?" It is an indeed an intriguing question but still falls outside purview of non-Hermitian adiabatic theorem. This is because the strict requirement of the existence of a unique least-dissipative eigenmode was not followed. See Chapter 8 for further discussion.

value of $\pi/2$, the remainder conclude the following: For the $N = 2$ case, control loops that encircle an EP_2, twice, the geometric phase is calculated to be π.

A.4 Mapping the control loops in $\mathcal{EP}_2$ to $\mathbb{R}\mathrm{P}^3$

This section illustrates the control loops $\mathcal{C}_{\mathrm{deg}}$ in $\mathcal{EP}_2$ in $\mathbb{R}\mathrm{P}^3$, the real 3-dimensional projective space. For this illustration, we take $\mathcal{EP}_2$ to be parameterized by H_{deg} in Eq. (2.51), and for simplicity, we set the trace of H_{deg} to be zero. The contents of this section are adapted from Refs. [313, 314].

The starting point for this discussion are two facts about $\mathbb{R}\mathrm{P}^N$, the real N-dimensional projective space [315], which allow us to construct an illustration of $\mathbb{R}\mathrm{P}^3$. They are:

1. $\mathbb{R}\mathrm{P}^N$ has the topology that is obtained by identifying antipodal points[1] of the unit N-sphere, $\mathcal{S}_N$, in $\mathbb{R}^{N+1}$.

2. Alternatively, one may restrict themselves to the "upper hemisphere" of $\mathcal{S}_N$, and identify antipodal points on its bounding "equator". This is done by considering all points in the "lower hemisphere" a double copy of the corresponding points in the "upper hemisphere"[2]. As a result, $\mathbb{R}\mathrm{P}^N$ is topologically equivalent to the closed N-dimensional disk D_N, with antipodal point on its boundary, i.e., $\partial D_N \cong S_{N-1}$, identified.

Additionally, these two descriptions of $\mathbb{R}\mathrm{P}^N$ can be mapped onto each other via a stereographic projection. Using these facts, we illustrate a faithful representation of $\mathbb{R}\mathrm{P}^2$ in Fig. A.1(a,b), and a semi-faithful representation of $\mathbb{R}\mathrm{P}^3$ in Fig. A.1(c,d).

We now turn to representing $\mathcal{C}_{\mathrm{deg}}$ in $\mathbb{R}\mathrm{P}^3$. To accomplish this task, we first work in the picture of the equal length and relatively perpendicular vector pair $\mathbf{B}_{\mathrm{Re,Im}}$, henceforth referred as $\mathbf{B}^{\mathrm{deg}}_{\mathrm{Re,Im}}$. In particular, we parametrically tune $\mathbf{B}^{\mathrm{deg}}_{\mathrm{Re,Im}}$ by changing $\{R, p, \theta\}$, the parameters that specify H_{deg} in Eq. (2.51). We then isolate those smooth parameter variations that affect a pure rotation, i.e, which change orientation of $\mathbf{B}^{\mathrm{deg}}_{\mathrm{Re,Im}}$ while keeping

[1] Diametrically opposite points.
[2] The terms in "$\cdot$" are taken to mean the equivalent object corresponding to an $\mathcal{S}_2$, the unit sphere in $\mathbb{R}^3$.

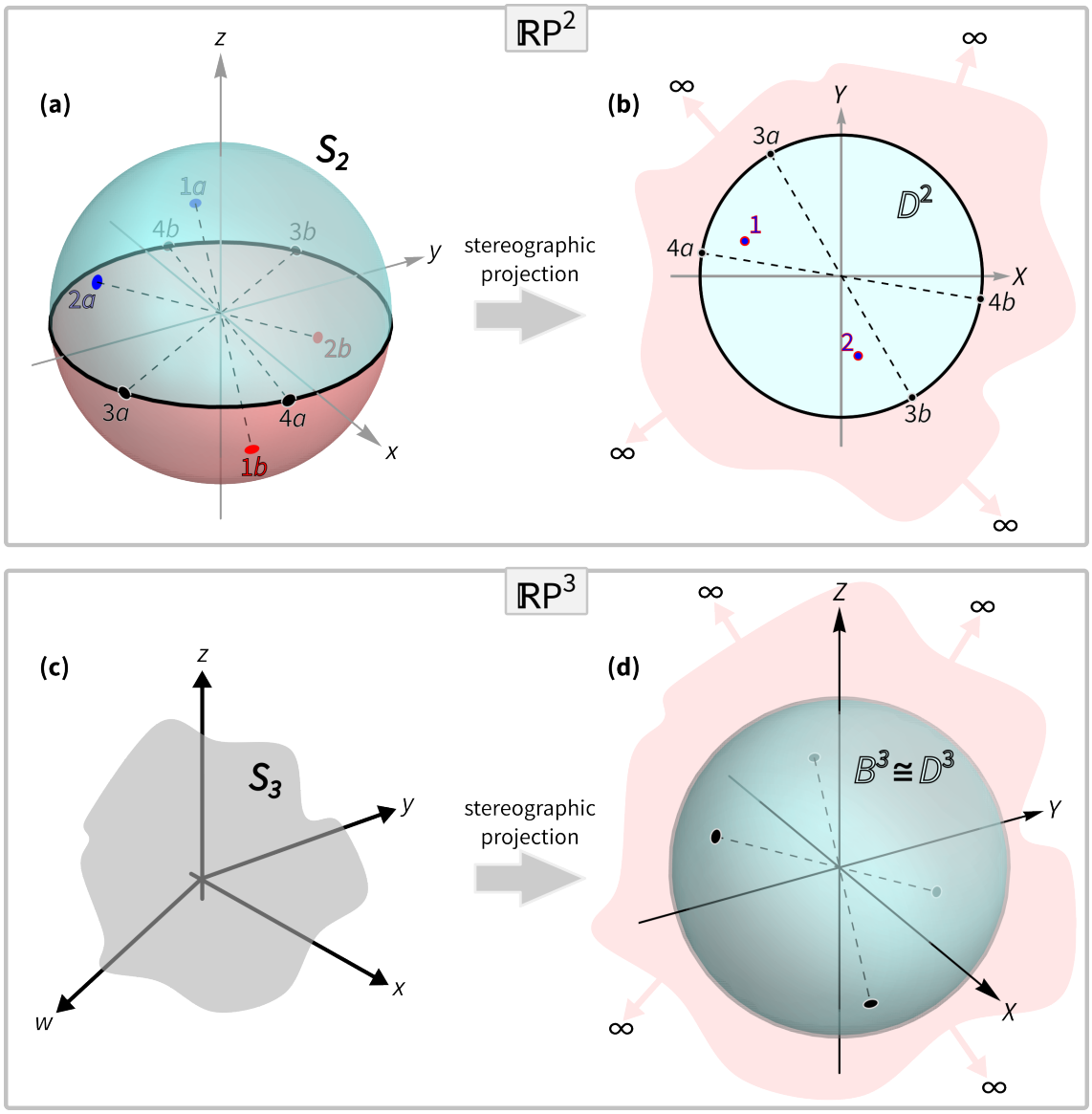

Figure A.1: Representing $\mathbb{RP}^2$ and $\mathbb{RP}^3$. Top panel: Faithful illustration of $\mathbb{RP}^2$ using two complimentary representations. **(a)** $\mathbb{RP}^2$ represented via $\mathcal{S}_2$ in $\mathbb{R}^3$ whose antipodal points are identified. $\mathbb{R}^3$ is spanned by cartesian coordinates (x, y, z), in which resides $\mathcal{S}_2$ with its upper hemisphere (cyan), lower hemisphere (pink), and equator (black circle) identified. The points in the upper hemisphere (here, $1a$ and $2a$) are identified with their antipodes in the lower hemisphere (here, $1b$ and $2b$, respectively). The points on the equator (here, $3a$ and $4a$) are also identified with corresponding antipodes on the equator (here, $3b$ and $4b$, respectively). **(b)** $\mathbb{RP}^2$ represented via the unit disk D^2 in $\mathbb{R}^2$ (spanned by (X, Y)), and is obtained by stereographically projecting $\mathcal{S}_2$ in (a). We used the standard stereographic projection [107], where the south-pole of $\mathcal{S}_2$ is taken as the projection pole. D^2 is composed of the cyan region representing its interior, and the unit circle (black) represents its boundary with antipodal points identified. The pink region that extends to ∞, represents exterior of D^2. The standard stereographic projection has a one-to-one map between an $\mathcal{S}_2$ whose antipodal points are not identified, and $\mathbb{R}^2$ such that the upper (lower) hemisphere of $\mathcal{S}_2$ maps to the interior (exterior) of D^2. However, by constraining

Figure A.1: Representing $\mathbb{RP}^2$ and $\mathbb{RP}^3$. *continued from previous page*
the antipodal points to be identified, the lower hemisphere of $\mathcal{S}_2$ (the exterior of D^2) is simply a double-copy of he upper hemisphere of $\mathcal{S}_2$ (the interior of D^2). Therefore, point-pair $(1a, 1b)$ and $(2a, 2b)$ on $\mathcal{S}_2$, is mapped to the point 1 and 2 in D^2, respectively. The equator of $\mathcal{S}_2$ maps one-to-one to the boundary of D^2, and thus the antipodal point-pairs $(3a, 3b)$ and $(4a, 4b)$. **Bottom panel:** Semi-faithful illustration of $\mathbb{RP}^3$. **(c)** A cartoon illustration of $\mathbb{RP}^3$ represented by $\mathcal{S}_3$ (gray) in $\mathbb{R}^4$ spanned by (w, x, y, z), with its antipodal points identified. **(d)** $\mathbb{RP}^3$ represented via the unit 3-ball B^3 in $\mathbb{R}^3$ (spanned by (X, Y, Z)), obtained by stereographically projecting $\mathcal{S}_3$. The "upper hemisphere" of $\mathcal{S}_3$ is mapped to the interior of B^3 (here, the cyan volume), which by definition of $\mathbb{RP}^3$, is also a map of the "lower hemisphere" of $\mathcal{S}_3$. The exterior of B^3 (here, the pink volume) is simply a double-copy of its interior. The "equator" of $\mathcal{S}_3$ is mapped one-to-one to the surface of B^3 (here, the gray surface), and the antipodal points are identified (here, the black points). Note that $B^3 \cong D^3$. In all panels, the dashed black lines merely serve as a guide to eye.

their length fixed. These pure rotations are subsequently encoded as unit quaternions q as a function of $\{R, p, \theta\}$. By definition, q reside on the surface of a 3-sphere $\mathcal{S}_3$, and $q \to -q$ corresponds to the exact same physical rotation [316]. Therefore, the antipodal points on $\mathcal{S}_3$ given by $(q, -q)$, are identified, and they subsequently are stereographically projected to $\mathbb{R}^3$ as a 3-ball. Tracking such unit quaternion along a closed loop provides a faithful means represent the corresponding $\mathcal{C}_{\rm deg}$ in $\mathbb{RP}^3$. The procedure is described below.

We begin by identifying the $\{R, p, \theta\}$ variations that produce a pure rotation. They are as follows:

(i) Tuning θ produces a pure rotation of $\mathbf{B}^{\rm deg}_{\rm Re,Im}$ around the z-axis.

(ii) Tuning $\angle R \equiv \rho$ has the effect of rotating $\mathbf{B}^{\rm deg}_{\rm Re,Im}$ about the vector $\mathbf{B}^{\rm deg}_{\rm Re} \times \mathbf{B}^{\rm deg}_{\rm Im}$.

(iii) Changing p tunes both the length and the orientation of $\mathbf{B}^{\rm deg}_{\rm Re,Im}$. The pure rotation part amounts to rotating about $\mathbf{B}^{\rm deg}_{\rm Im}$ by an angle $\phi = \mathrm{Arctan}(\mathrm{Sinh}(\mathrm{Log}(p)))$.

We now encode these variations into unit quaternions. We begin by choosing an initial $\mathbf{B}^{\rm deg}_{\rm Re,Im}$ pair with unit norm, and parametrically apply the above three pure rotations, in reverse order. This provides a way to encode any $H_{\rm deg}$ parameterized by Eq. (2.51), up to an overall scalar multiple, and thus the corresponding $\mathcal{C}_{\rm deg}$. For this procedure, we uniquely chose the initial $\mathbf{B}^{\rm deg}_{\rm Re,Im}$ pair given by

$$\mathbf{B}^{\rm deg}_{\rm re} = (0, 0, 1)^{\rm T}$$

$$\mathbf{B}_{\mathrm{im}}^{\mathrm{deg}} = (1,0,0)^{\mathrm{T}} \tag{A.20}$$

which can be expressed as unit quaternions $q_{\mathrm{re,im}}$ as

$$\begin{aligned} q_{\mathrm{re}} &= 0 + 0\mathbf{i} + 0\mathbf{j} + 1\mathbf{k} \\ q_{\mathrm{im}} &= 0 + 1\mathbf{i} + 0\mathbf{j} + 0\mathbf{k} \end{aligned} \tag{A.21}$$

In this basis, pure rotations of step **(iii)**, **(ii)** and **(i)** can be expressed as the unit quaternion q_1, q_2 and q_3, respectively. They are given by

$$q_1 = \mathrm{Cos}(\phi/2) + \mathrm{Sin}(\phi/2)\mathbf{i} + 0\mathbf{j} + 0\mathbf{k} \tag{A.22}$$

$$q_2 = \mathrm{Cos}(\rho/2)q_{\theta,0} - \mathrm{Sin}(\rho/2)q_{\theta,1}\mathbf{i} - \mathrm{Sin}(\rho/2)q_{\theta,2}\,\mathbf{j} - \mathrm{Sin}(\rho/2)q_{\theta,3}\mathbf{k} \tag{A.23}$$

$$q_3 = \mathrm{Cos}(\theta/2) + 0\mathbf{i} + 0\mathbf{j} + \mathrm{Sin}(\theta/2)\mathbf{k} \tag{A.24}$$

where $q_\theta \equiv q_{\theta,0} + q_{\theta,1}\mathbf{i} + q_{\theta,2}\,\mathbf{j} + q_{\theta,3}\mathbf{k} = q_1^{-1}q_{-y}q_1$, with $q_{-y} = 0 + 0\mathbf{i} - 1\mathbf{j} + 0\mathbf{k}$. Subsequently, we have the full quaternion q

$$q = q_3 q_2 q_1 \equiv q_r + q_i\mathbf{i} + q_j\,\mathbf{j} + q_k\mathbf{k} \tag{A.25}$$

that rotates $\mathbf{B}_{\mathrm{Re,Im}}^{\mathrm{deg}}$ as a function $\{R, p, \theta\}$.

At last, we stereographically project q from $\mathcal{S}_3$ to $\mathbb{R}^3$. Taking $q_s = -1 + 0\mathbf{i} + 0\mathbf{j} + 0\mathbf{k}$, i.e., the south pole as the projection pole, we have

$$(X, Y, Z)^{\mathrm{T}} = \left(\frac{q_i}{1+q_r}, \frac{q_j}{1+q_r}, \frac{q_k}{1+q_r}\right)^{\mathrm{T}} \tag{A.26}$$

where we note that $q_r = 0$ corresponds to the "equator" of $\mathcal{S}_3$, which gets mapped to the surface of $\mathbb{R}\mathrm{P}^3$. Additionally, the sign of q_r specifies which member of an antipodal pair $(q, -q)$ is naturally mapped to the interior of $\mathbb{R}\mathrm{P}^3$. Explicitly, for $q_r > 0\,(< 0)$, it is $q\,(-q)$ that is mapped to the interior of $\mathbb{R}\mathrm{P}^3$. These features taken together allow us to plot the corresponding $\mathcal{C}_{\mathrm{deg}}$ in $\mathbb{R}\mathrm{P}^3$, as in Fig. 2.7(b,d).

Appendix B

Methods for Chapter 3

Here we provide additional technical details for the measurements described in Chapter 3, which include their modeling (Sec. B.1), visualizing the data (Secs. B.2 and B.3), data acquisition protocol (Sec. B.4), and data analysis (Secs. B.5 and B.6). We then follow up with a discussion on data fitting and theoretical calculations in Sec. B.7. Finally, we provide the system parameters of the experimental apparatus in Sec. B.8.

B.1 Extracting the spectrum from mechanical susceptibility

In this section, we describe the relationship between the system's eigenvalue spectrum and measurements of the mechanical susceptibility. In particular, we derive the functional form used to fit the susceptibility data as shown in Fig. 3.1(c).

In the frame $\mathcal{R}$ (Sec. 2.3.3), the mechanical modes' response to a force $\boldsymbol{f}(\omega)$ can be written in the Fourier domain as

$$\boldsymbol{c}(\omega) = \boldsymbol{\chi}(\omega)\boldsymbol{f}(\omega) \tag{B.1}$$

where

$$\boldsymbol{\chi}(\omega) = (\omega\mathbb{I} - H)^{-1} \tag{B.2}$$

where $\mathbb{I}$ is the 3 $\times$ 3 identity matrix and H is given in Eq. (2.91). The principle behind the measurements used in this work is to apply a force $\boldsymbol{f}(\omega)$, measure the mechanical response $\boldsymbol{c}(\omega)$, and thus infer the susceptibility $\boldsymbol{\chi}(\omega)$, which contains information about the eigenvalue $\boldsymbol{\lambda}$ and the (complex-valued) amplitude of the mechanical response encode information about eigenvectors and subsequently s_{ij} with $i, j \in \{1, 2, 3\}$.

The measurement of the mechanical response is carried out in the lab frame, where

$$\begin{aligned}\tilde{\boldsymbol{c}}(\tilde{\omega}) = \begin{bmatrix}\tilde{c}_1(\tilde{\omega}) \\ \tilde{c}_2(\tilde{\omega}) \\ \tilde{c}_3(\tilde{\omega})\end{bmatrix} &= \begin{bmatrix}c_1(\tilde{\omega} - \tilde{\omega}_1^{(0)} - \eta) \\ c_2(\tilde{\omega} - \tilde{\omega}_2^{(0)}) \\ c_3(\tilde{\omega} - \tilde{\omega}_3^{(0)} - \eta)\end{bmatrix} \\ &= \begin{bmatrix}\sum_{j=1}^{3} \Big(\boldsymbol{\chi}(\tilde{\omega} - \tilde{\omega}_1^{(0)} - \eta)\Big)_{1,j} \Big(\boldsymbol{f}(\tilde{\omega} - \tilde{\omega}_1^{(0)} - \eta)\Big)_j \\ \sum_{j=1}^{3} \Big(\boldsymbol{\chi}(\tilde{\omega} - \tilde{\omega}_2^{(0)})\Big)_{2,j} \Big(\boldsymbol{f}(\tilde{\omega} - \tilde{\omega}_2^{(0)})\Big)_j \\ \sum_{j=1}^{3} \Big(\boldsymbol{\chi}(\tilde{\omega} - \tilde{\omega}_3^{(0)} - \eta)\Big)_{3,j} \Big(\boldsymbol{f}(\tilde{\omega} - \tilde{\omega}_3^{(0)} - \eta)\Big)_j\end{bmatrix}\end{aligned} \tag{B.3}$$

The force applied to perform susceptibility measurements is sourced from intensity modulation of the probe tone, and is given by

$$\tilde{\boldsymbol{f}}(t) \propto e^{i\tilde{\omega}_{\mathrm{AM}} t} \boldsymbol{g} \tag{B.4}$$

in the lab frame, or equivalently in the Fourier domain,

$$\tilde{\boldsymbol{f}}(\tilde{\omega}) \propto \boldsymbol{g}\, \delta(\tilde{\omega} - \tilde{\omega}_{\mathrm{AM}}) \tag{B.5}$$

where $\boldsymbol{g} \equiv \{g_1, g_2, g_3\}$ is the vector of optomechanical coupling strength between the mechanical modes and the optical cavity mode, and δ denotes the Dirac delta function.

In frame $\mathcal{R}$, it is given by:

$$\boldsymbol{f}(\omega) \propto \begin{bmatrix} g_1\,\delta(\omega - \tilde{\omega}_{\mathrm{AM}} + \tilde{\omega}_1^{(0)} + \eta) \\ g_2\,\delta(\omega - \tilde{\omega}_{\mathrm{AM}} + \tilde{\omega}_2^{(0)}) \\ g_3\,\delta(\omega - \tilde{\omega}_{\mathrm{AM}} + \tilde{\omega}_3^{(0)} + \eta) \end{bmatrix} \tag{B.6}$$

Thus, driving the membrane with a sinusoidal force results in motion at three different frequencies. However, for these measurements, the lock-in amplifier was configured such that it only detects motion at the drive frequency $\tilde{\omega}_{\mathrm{AM}}$, i.e.

$$\tilde{V}(\tilde{\omega}_{\mathrm{AM}}) = \alpha \int f_{\mathrm{LIA}}(\tilde{\omega} - \tilde{\omega}_{\mathrm{AM}})\tilde{\boldsymbol{c}}(\tilde{\omega}).\boldsymbol{g}\, d\tilde{\omega} = \alpha \int_{\tilde{\omega}_{\mathrm{AM}}-\epsilon}^{\tilde{\omega}_{\mathrm{AM}}+\epsilon} \tilde{\boldsymbol{c}}(\tilde{\omega}).\boldsymbol{g}\, d\tilde{\omega} \tag{B.7}$$

where $f_{\mathrm{LIA}}(x)$ is the filter function of the lock-in amplifier, which has an effective bandwidth ϵ, and α is the motion-to-voltage transduction factor.

As a result, we have

$$\begin{aligned} \tilde{V}(\tilde{\omega}_{\mathrm{AM}}) &= \alpha g_1^2 \left(\boldsymbol{\chi}(\tilde{\omega}_{\mathrm{AM}} - \tilde{\omega}_1^{(0)} - \eta)\right) \equiv \tilde{V}_1(\tilde{\omega}_{\mathrm{AM}}) \qquad \text{for } \tilde{\omega}_{\mathrm{AM}} \approx \tilde{\omega}_1^{(0)} \\ &= \alpha g_2^2 \left(\boldsymbol{\chi}(\tilde{\omega}_{\mathrm{AM}} - \tilde{\omega}_2^{(0)} - \eta)\right) \equiv \tilde{V}_2(\tilde{\omega}_{\mathrm{AM}}) \qquad \text{for } \tilde{\omega}_{\mathrm{AM}} \approx \tilde{\omega}_2^{(0)} \\ &= \alpha g_3^2 \left(\boldsymbol{\chi}(\tilde{\omega}_{\mathrm{AM}} - \tilde{\omega}_3^{(0)} - \eta)\right) \equiv \tilde{V}_3(\tilde{\omega}_{\mathrm{AM}}) \qquad \text{for } \tilde{\omega}_{\mathrm{AM}} \approx \tilde{\omega}_3^{(0)} \end{aligned} \tag{B.8}$$

so that only the diagonal components of the susceptibility $\boldsymbol{\chi}(\omega)$ are measured. Each of these diagonal components contains $\boldsymbol{\lambda}$, so in principle it would suffice to measure $\tilde{V}(\tilde{\omega}_{\mathrm{AM}})$ in just one of the frequency ranges (say, around $\tilde{\omega}_3^{(0)}$). However, to make the analysis robust against noise, $\tilde{V}(\tilde{\omega}_{\mathrm{AM}})$ was measured in all three frequency ranges (i.e., around each of the $\tilde{\omega}_{1,2,3}^{(0)}$), and this nominally redundant data was fit to determine $\boldsymbol{\lambda}$.

To explicitly see the relation of the susceptibility $\boldsymbol{\chi}(\omega)$ to the eigenspectrum of H, consider its diagonalization $H = TDT^{-1}$, where

$$D = \begin{bmatrix} \lambda_1 & 0 & 0 \\ 0 & \lambda_2 & 0 \\ 0 & 0 & \lambda_3 \end{bmatrix} \tag{B.9}$$

and the columns of T are composed of right eigenvectors of H. It is straightforward to show that $\boldsymbol{\chi} = T(\omega\mathbb{I} - D)^{-1}T^{-1}$, where $(\omega\mathbb{I} - D)^{-1}$ is diagonal and is given by

$$(\omega\mathbb{I} - D)^{-1} = \begin{bmatrix} \frac{1}{\omega-\lambda_1} & 0 & 0 \\ 0 & \frac{1}{\omega-\lambda_2} & 0 \\ 0 & 0 & \frac{1}{\omega-\lambda_3} \end{bmatrix} \tag{B.10}$$

Subsequently, $\tilde{V}(\tilde{\omega}_{\mathrm{AM}})$ can be explicitly written in terms of $\boldsymbol{\lambda}, T, T^{-1}$ as

$$\begin{aligned}
\tilde{V}_1(\tilde{\omega}) &= \alpha g_1^2 \left(\frac{T_{11}(T^{-1})_{11}}{\tilde{\omega} - \tilde{\omega}_1^{(0)} - \eta - \lambda_1} + \frac{T_{12}(T^{-1})_{21}}{\tilde{\omega} - \tilde{\omega}_1^{(0)} - \eta - \lambda_2} + \frac{T_{13}(T^{-1})_{31}}{\tilde{\omega} - \tilde{\omega}_1^{(0)} - \eta - \lambda_3} \right) \\
\tilde{V}_2(\tilde{\omega}) &= \alpha g_2^2 \left(\frac{T_{21}(T^{-1})_{12}}{\tilde{\omega} - \tilde{\omega}_2^{(0)} - \lambda_1} + \frac{T_{22}(T^{-1})_{22}}{\tilde{\omega} - \tilde{\omega}_2^{(0)} - \lambda_2} + \frac{T_{23}(T^{-1})_{32}}{\tilde{\omega} - \tilde{\omega}_2^{(0)} - \lambda_3} \right) \\
\tilde{V}_3(\tilde{\omega}) &= \alpha g_3^2 \left(\frac{T_{31}(T^{-1})_{13}}{\tilde{\omega} - \tilde{\omega}_3^{(0)} - \eta - \lambda_1} + \frac{T_{32}(T^{-1})_{23}}{\tilde{\omega} - \tilde{\omega}_3^{(0)} - \eta - \lambda_2} + \frac{T_{33}(T^{-1})_{33}}{\tilde{\omega} - \tilde{\omega}_3^{(0)} - \eta - \lambda_3} \right)
\end{aligned} \tag{B.11}$$

and in order to extract information from the susceptibility measurements, these spectra can be fit to the sum of nine complex Lorentzians as

$$\begin{aligned}
\tilde{V}_1(\tilde{\omega}) &= a_1 \left(\frac{s_{11}}{\tilde{\omega} - \tilde{\omega}_1^{(0)} - \eta - \lambda_1} + \frac{s_{12}}{\tilde{\omega} - \tilde{\omega}_1^{(0)} - \eta - \lambda_2} + \frac{s_{13}}{\tilde{\omega} - \tilde{\omega}_1^{(0)} - \eta - \lambda_3} \right) + b_1 \\
\tilde{V}_2(\tilde{\omega}) &= a_2 \left(\frac{s_{21}}{\tilde{\omega} - \tilde{\omega}_2^{(0)} - \lambda_1} + \frac{s_{22}}{\tilde{\omega} - \tilde{\omega}_2^{(0)} - \lambda_2} + \frac{s_{23}}{\tilde{\omega} - \tilde{\omega}_2^{(0)} - \lambda_3} \right) + b_2 \\
\tilde{V}_3(\tilde{\omega}) &= a_3 \left(\frac{s_{31}}{\tilde{\omega} - \tilde{\omega}_3^{(0)} - \eta - \lambda_1} + \frac{s_{32}}{\tilde{\omega} - \tilde{\omega}_3^{(0)} - \eta - \lambda_2} + \frac{s_{33}}{\tilde{\omega} - \tilde{\omega}_3^{(0)} - \eta - \lambda_3} \right) + b_3
\end{aligned} \tag{B.12}$$

where $a_i = \alpha g_i^2$ and $s_{ij} = T_{ij}(T^{-1})_{ji}$, and the three additional (complex-valued) constants b_i represent the lock-in detection background, with $i, j \in \{1, 2, 3\}$. Of the 18 complex parameters in this model $(a_i, b_i, s_{ij}, \lambda_i)$, the amplitudes s_{ij} are constrained by the fact that $TT^{-1} = \mathbb{I} = T^{-1}T$, i.e., $\sum_j T_{ij}(T^{-1})_{ji} = 1 = \sum_j (T^{-1})_{ij}T_{ji}$, which implies that $\sum_j s_{ij} = 1 = \sum_j s_{ji}$. Therefore, the rows and the columns of the matrix

$$S = \begin{bmatrix} s_{11} & s_{12} & s_{13} \\ s_{21} & s_{22} & s_{23} \\ s_{31} & s_{32} & s_{33} \end{bmatrix} \tag{B.13}$$

each add up to unity. These are five different complex constraints on nine complex parameters, leaving behind four independent complex parameters. This is implemented in the model as:

$$\begin{aligned} s_{13} &= 1 - s_{11} - s_{12} \\ s_{23} &= 1 - s_{21} - s_{22} \\ s_{31} &= 1 - s_{11} - s_{21} \\ s_{32} &= 1 - s_{12} - s_{22} \\ s_{33} &= s_{11} + s_{12} + s_{21} + s_{22} - 1 \end{aligned} \tag{B.14}$$

As a result, the global fit of the measured spectra $\tilde{V}_1(\tilde{\omega}), \tilde{V}_2(\tilde{\omega}), \tilde{V}_3(\tilde{\omega})$ to nine complex Lorentzians is implemented with 13 complex fit parameters.

B.2 Projections of the hypersurface $\mathcal{S}$

In this section we describe the two projections of the hypersurface $\mathcal{S}$. They are used for representing data as shown in Fig.3.6 and Figs.B.1 and 3.8-3.16.

B.2.1 Standard stereographic projection

Stereographic projection is a standard means for representing a sphere (typically of one, two or three dimensions) in a Euclidean space with the same number of dimensions. For our purposes, we represent $\mathcal{S}$ by first projecting it onto the unit three-sphere $\mathcal{S}^3$, and then applying the standard stereographic projection of $\mathcal{S}^3$ onto $\mathbb{R}^3$.

The map is constructed by first adimensionalizing the control parameters as:

$$\Psi' = \frac{\Psi}{\Psi_{EP_3}^{(\mathrm{exp})}} - 1 = \left\{ \frac{\delta}{\delta_{EP_3}^{(\mathrm{exp})}}, \frac{P_1}{P_{1,EP_3}^{(\mathrm{exp})}}, \frac{P_2}{P_{2,EP_3}^{(\mathrm{exp})}}, \frac{P_3}{P_{3,EP_3}^{(\mathrm{exp})}} \right\} - 1 \tag{B.15}$$

and then normalizing it as $\Psi'' = \Psi'/||\Psi'||$, where $||\cdot||$ is the conventional L^2 norm. Note that we implicitly used the fact that $\Psi_{EP_3}^{(\exp)}$ lies inside the four-volume bounded by $\mathcal{S}$.

The next step involves transforming Ψ'' under a 4D rotation R, specified below. The new unit vector $R\Psi'' \equiv \{x, z, w, y\}$ is then stereographically projected onto the 3D cartesian coordinates $\{X, Y, Z\}$ as $X = \frac{x}{1-w}, Y = \frac{y}{1-w}, Z = \frac{z}{1-w}$. The choice of R corresponds to modifying pole for the stereographic projection, by rotating the standard one: $\Psi''_{\text{standard pole}} = \{0, 0, 1, 0\}$. The specific choice was made to optimize the visualization of the experimentally identified trefoil knot, and it corresponds to $\Psi''_{\text{new pole}} = \{0.1, -0.83, 0.55, 0\}$, or $\Psi_{\text{new pole}} = \{2\pi \times 55 \text{ kHz}, 22\ \mu\text{W}, 596\ \mu\text{W}, 304\ \mu\text{W}\}$.

B.2.2 "Rectilinear stereographic" projection

This projection is isomorphic to the standard stereographic projection, but provides a more intuitive representation of the dimensionful experimental parameters Ψ. Illustrative animations that describe this projection are shown in Refs. [199, 201]. This projection consists of the following steps:

1. We select one of the eight cuboids that constitute $\mathcal{S}$, and simply rescale its axes such that it forms a unit-length cube. This is the central cube in Figs. 3.6(b), bottom panels of Figs.3.8-3.10 and Fig. B.1(a).

2. Each of the six cuboids adjacent to the first one is also rescaled to form a unit-length cube, which is then attached to the first cube on their common 2D face. The resulting 'six-way cross' faithfully represents the connections of the central cube to its six neighbors.

3. To faithfully represent the connections among these six neighbors, a bilinear transformation (see Sec.6.5.1 of Ref. [95]) is applied to each, deforming each cube into a truncated square pyramid. The transformation is chosen so that the 2D faces that are common to any two of these neighbors are made to touch. These seven hexahedrons (the central cube and the six truncated square pyramids surrounding it) can readily be labeled by their original dimensionful axes. Together they form the bounding box as shown in Figs. 3.6(b), 3.8-3.10(bottom panel) and B.1(a).

4. The final cuboid is mapped to the exterior of the bounding box through a nonlinear mapping, and extends to infinity (as does the standard stereographic projection described above).

As will be described in Sec. B.4, there are no EP_2s in the two cuboids that correspond to constant P_1. We choose the minimum and maximum P_1 cuboid to be the interior cubical hexahedron and the exterior region, respectively. This choice conveniently places all of the EP_2s in the six truncated square pyramids, facilitating a clear view of the knot. Refs. [201, 202] shows animated views of the data and the fit shown in this projection.

B.3 Description of 2D control spaces used in the case study

This section describes the three 2D control spaces used in studying the effect of restricted control spaces as described in Sec. 3.3.1.1. Each of these consists of the union of two or three of the "sheets" described therein and in Sec. B.4.

The 2D control space shown in Fig. 3.14 ($\mathcal{B}^{(1)}$) is the union of two sheets. In the first sheet, P_3 and δ are fixed to 78 μW and $2\pi\times$ 60 kHz, respectively. In the second sheet, P_3 and δ are fixed to 78 μW and $2\pi\times$ 75.6 kHz, respectively. The 2D control space shown in Fig. 3.15 ($\mathcal{B}^{(2)}$) is the union of three sheets. The first two are the same as for $\mathcal{B}^{(1)}$, and the third sheet consists of fixing P_2 and δ to 289 μW and $2\pi\times$ 75.6 kHz, respectively. The 2D control space shown in Fig. 3.16 ($\mathcal{B}^{(3)}$) is the union of two sheets: the second sheet from $\mathcal{B}^{(1)}$ and the third sheet from $\mathcal{B}^{(2)}$.

The three sheets used to form $\mathcal{B}^{(1)}$, $\mathcal{B}^{(2)}$, and $\mathcal{B}^{(3)}$ are shown in Fig. B.1. One of its views uses the standard stereographic projection (Sec. B.2.1) as in Figs.3.14-3.16. The other view uses the "rectilinear stereographic" projection (Sec. B.2.2), which provides an intuitive interpretation of the 2D control spaces in terms of the experimental parameters $\Psi = \{\delta, P_1, P_2, P_3\}$.

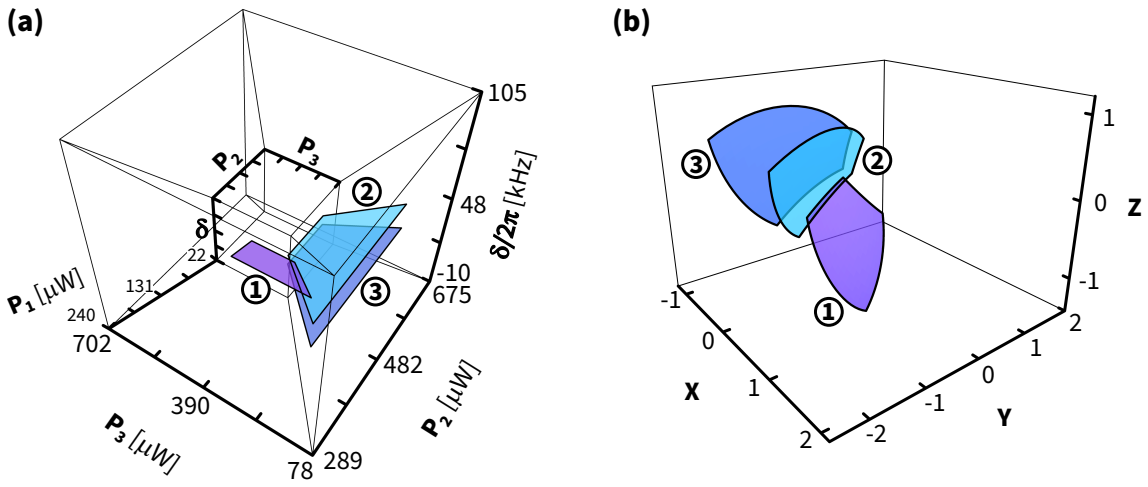

Figure B.1: Sheets that constitute the case study of 2D control spaces. The sheets used to form the 2D control spaces shown in Figs. 3.14, 3.15 and 3.16. Sheets ② and ③ are joined to make $\mathcal{B}^{(1)}$ in Fig. 3.14(a). Sheets ①, ② and ③ are joined to make $\mathcal{B}^{(2)}$ in Fig. 3.15(a). Sheets ① and ② are joined to make $\mathcal{B}^{(3)}$ in Fig. 3.16(a). **(a)** The three sheets, shown in the "rectilinear stereographic" projection of the hypersurface $\mathcal{S}$. **(b)** The same sheets, shown in the standard stereographic projection as used in Figs. 3.14, 3.15 and 3.16.

B.4 Rastering the hypersurface $\mathcal{S}$

The hypersurface $\mathcal{S}$ described in the main text is the boundary of a 4D hyperrectangle, which in turn is a union of eight cuboids, which we refer to as "faces". Each of these 3D faces is spanned by three components of Ψ (for e.g. $\{P_1, P_2, P_3\}$) which range from their minimum value to their maximum value (given below), while the remaining component of Ψ (in this example it would be δ) is held fixed at either its minimum or its maximum value. As a result, the 3D faces span the ranges:

$$\begin{aligned} \text{-10 kHz} &\leq \delta/2\pi \leq \text{ 105.6 kHz} \\ \text{22 } \mu\text{W} &\leq P_1 \leq \text{240 } \mu\text{W} \\ \text{289 } \mu\text{W} &\leq P_2 \leq \text{675 } \mu\text{W} \\ \text{78 } \mu\text{W} &\leq P_3 \leq \text{702 } \mu\text{W} \end{aligned} \tag{B.16}$$

For ease of analysis, eigenspectra were measured by densely rastering Ψ within sixty-one 2D sheets, each lying within one of the eight 3D faces. The locations of these sheets are shown in Fig. 3.6, and the actual data from all sixty-one sheets are shown in Ref.

[200].

As can be seen from Fig. 3.6, no 2D sheets lie within the two faces having constant P_1. This is because the optomechanical model (Sec. 2.3.3) predicts that EP_2 lie only in the other six faces. The absence of EP_2 in the two faces with constant P_1 was confirmed by measuring eigenspectra at several hundred locations in these two faces. They are however not shown.

B.5 Data analysis I: 2D sheets

In this section, we describe the algorithms used to locate EPs in the 2D data sheets which include their processing in the form of outlier rejection and Gaussian filtering, in order for the algorithms to perform effectively.

As described in the main text, each measurement of a mechanical spectrum, i.e., with the control parameters Ψ set to a particular value, is fit to extract the corresponding $\boldsymbol{\lambda}$ and S. These quantities are then converted to d, D, E and Θ, for this value of Ψ. The quantity Θ is defined as:

$$\Theta = x/y = \frac{2\prod_{i=1}^{3}\overline{\lambda_i}}{\sum_{i=1}^{3}\overline{\lambda_i}^2} \tag{B.17}$$

where x, y are the coefficients of the characteristics polynomial for a $N = 3$-mode system (Sec. 2.1.2) and $\overline{\lambda_i} = \lambda_i - \sum_{i=1}^{3}\lambda_i/3$ for $i \in \{1, 2, 3\}$. $\overline{\boldsymbol{\lambda}}$ denotes the eigenvalues of the traceless version of H. As described in Sec. 3.2.3, $\mathrm{Arg}(\Theta) = \vartheta$ in Eq. (3.8) provides a useful coordinate along the trefoil knot.

Almost all the analysis used in this study is based on densely rastering two components of Ψ while keeping the other two fixed, resulting in a "2D sheet" in which $d(\Psi), D(\Psi), E(\Psi)$ and $\Theta(\Psi)$ are displayed. Analyzing the data in these sheets allows for identifying EP_3 and EP_2 locations. It is usually straightforward to identify EPs as vanishing magnitudes of $d(\Psi), D(\Psi), E(\Psi)$ or phase-winding of $D(\Psi), E(\Psi)$ as shown in Figs. 3.3, 3.7(first column) and in Ref. [200].

However, to apply a uniform approach to locating these points, we use a minima-finding algorithm and a vortex-finding algorithm. These algorithms can be adversely impacted by noise in the data and by occasional outlier data points. The noise we refer to is the apparently Gaussian random pixel-to-pixel variations visible in Figs. 3.3, 3.7(first column) i.e., superposed on the smooth behavior similar to the corresponding theory plots Figs. 3.5, 3.7(third column), respectively. The outliers we refer to are the few pixels whose values differ drastically from their neighbors in the Figs. 3.3, 3.7(first column). As a result, we apply outlier rejection followed by Gaussian filtering to each of the quantities $d(\Psi), D(\Psi), E(\Psi)$ and $\Theta(\Psi)$, yielding their filtered versions $\overline{d}(\Psi), \overline{D}(\Psi), \overline{E}(\Psi)$ and $\overline{\Theta}(\Psi)$, which are shown in Figs. 3.4, 3.7(second column), 3.14-3.16, and also in Ref. [200]. For the complex-valued quantities D, E and Θ, the real and imaginary parts are treated separately and then recombined.

A minima identification algorithm (Sec. B.5.3) is applied to $\overline{d}$ locate the EP_3 point as described in Sec. 3.2.1. Minima identification is also applied to the magnitudes of D and E to locate the EP_2 points in the hypersurface $\mathcal{S}$. A phase-vortex identification algorithm (Sec. B.5.4) is applied to the complex arguments of D and E, also to locate the EP_2 points in $\mathcal{S}$. Lastly, the complex argument of $\overline{\Theta}$ at each EP_2 is the value of ϑ used to color the corresponding point in Figs. 3.8,3.9 and 3.10.

The complete data set consisting of the sixty-one 2D sheets used to search for EP_2 points in the hypersurface $\mathcal{S}$ is shown in Ref. [200]. The data set of six 2D sheets used to identify the EP3 point is shown in Figs. 3.3 and 3.4.

B.5.1 Outlier rejection

Outliers in $f(\Psi)$ were identified using a Tukey Fence. This algorithm tags a data point at Ψ as an outlier if the value of $f(\Psi)$ is outside the range $Q_1 - q \times (Q_3 - Q_1), Q_3 + q \times (Q_3 - Q_1)$, where the first Q_1 and the third Q_3 quartiles are defined over a 5 pixel $\times$ 5 pixel neighborhood of Ψ within the 2D sheet under consideration. For Ψ near the edge of the sheet, the neighborhood is clipped appropriately.

In order to ensure that only the extreme outliers are tagged, we set $q = 6$. By way of illustration, if the data were Gaussian distributed, this value of q would correspond to

tagging values beyond 8.7 standard deviations as outliers.

Each and every tagged outlier is inspected manually to eliminate the possibility of a false tag. The value of each "true" outlier is subsequently replaced with the median of its 5 pixel $\times$ 5 pixel neighborhood. In the end, $\sim$200 out of $\sim$27,000 measurements (i.e. $\sim 0.8\%$) of $\{D, E, \Theta\}$ were rejected as outliers. An illustrative discussion on outlier filtering our dataset is given in Ref. [95](Pg:151-153).

B.5.2 Gaussian filtering

Following the outlier rejection described above, the data in each 2D sheet is convolved with a 2D Gaussian kernel with half-width at half-maxima HWHM $= 1.87$ pixels. The filter kernel is clipped and re-normalized appropriately for pixels that lie near the edge of the sheet.

B.5.3 Minima identification

For any quantity $f(\Psi)$ (which may be $\overline{d}(\Psi)$, $|\overline{D}(\Psi)|$, or $|\overline{E}(\Psi)|$), a minimum is initially tagged at any value of Ψ at which f is the minimum over its 3 pixel $\times$ 3 pixel neighborhood. Since some of these initial tags are caused by noise, we only accept tags at which the magnitude of the second derivative is larger than a specific threshold. In particular, we require $|f''(\Psi)| > \zeta$, where the threshold ζ is chosen to be $\langle |f''| \rangle + 2\sigma_{|f''|}$, with the mean $\langle ... \rangle$ and standard deviation σ of $|f''|$, evaluated over the entire data sheet.

The Ψ that are tagged in this way are reported as the experimentally identified minima. When this analysis is applied to $\overline{d}(\Psi)$, the minima correspond to experimental estimates of the EP_3 location. When this analysis is applied to $|\overline{D}(\Psi)|$ and $|\overline{E}(\Psi)|$, the minima correspond to the experimentally identified EP_2 points. At each identified minimum of $|\overline{D}|$ and $|\overline{E}|$, the value of $\mathrm{Arg}(\overline{\Theta})$ at that location is reported as the measured ϑ for that EP_2. These points are explicitly shown in Figs. 3.8(a,c) and 3.10(a,c).

B.5.4 Phase-Vortex identification

For each phase function $\mathrm{Arg}(D)$ and $\mathrm{Arg}(E)$, the algorithm starts with a location Ψ within the sheet and then considers the closed counter-clockwise path defined by the eight nearest neighbors of Ψ. The point Ψ is tagged as a phase-vortex if the unwrapped phase along this closed path changes by $\pm 2\pi$.

It sometimes happens that this approach tags several neighboring Ψ as phase-vortices. To determine whether this results from pixelation of the data, or because different portions of the knot actually intersect the sheet in close-by locations, we algorithmically cluster any adjacent points identified as phase-vortices based on their value of ϑ, which serves to distinguish different parts of the knot from each other[1]. For each cluster identified in this way, the mean value of Ψ is reported as the experimentally identified phase-vortex EP_2. Also, the mean value of $\mathrm{Arg}(\overline{\Theta})$ for each cluster is reported as the measured ϑ for that EP_2. These points are explicitly shown in Figs. 3.8(b,d) and 3.10(b,d).

It should be noted that all the phase-vortices identified in this work show a winding of $\pm 2\pi$ along the closed path constructed above. This is expected for $\mathrm{Arg}(D)$ and $\mathrm{Arg}(E)$, as $\lambda_i(\Psi) \sim (\Psi - \Psi_{EP_2})^{1/2}$ in the neighborhood of an EP_2 point at Ψ_{EP_2} [21, 26].

B.6 Data analysis II: eigenvalue braids

In this section, we discuss a crucial aspect of representing the eigenvalues braids namely how their strands are colored, both for the experimental data as illustrated in Fig. 3.11(middle row) and Figs.3.12-3.16, and also for the theoretical calculations as shown in Fig.2.1, Figs.2.3-2.5 and Fig. 3.11(bottom row).

B.6.1 Coloring the braid strands

Coloring individual braids strands of the eigenvalue braids is an important aspect of our experimental data analysis, as well as for theory calculations. This allows us to represent

[1]We used "FindClusters" function of Mathematica [317] with method as "Agglomerate" and Chebyshev distance as the distance function. Prior to clustering we algorithmically ensured that ϑ is interpreted as 2π periodic quantity.

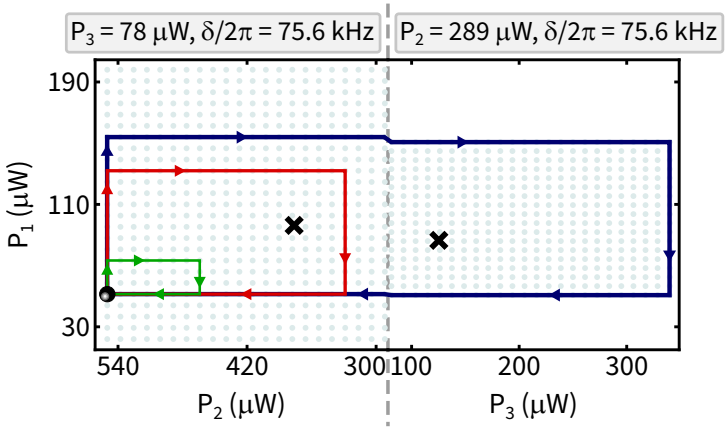

Figure B.2: Assembling the control loops for Fig. 3.11 The three control loops in Fig. 3.11(a-c) were assembled from data taken in the two 2D sheets shown here. The two sheets' common border is shown as the dashed gray line. Each small light blue disc represents a value of Ψ at which $\boldsymbol{\lambda}$ was measured (i.e., a 'pixel' in the 2D sheet). The black crosses show the location of the EP_2 in these sheets as determined by the minima-finding algorithm.

them unambiguously, and helps discern their braid equivalence classes both visually and algorithmically.

To describe the algorithm that colors the individual braid strands, we focus on a particular dataset of experimentally measured braids as a representative example: the data shown in Fig. 3.11. However, we note that every eigenvalue braid described in this thesis, both experimentally measured or theoretically obtained, was subject to this analysis. The data shown in Fig. 3.11 is realized by stepping the control parameters Ψ around the loops shown in panels (a-c), which in turn were assembled from data taken in two of the sixty-one 2D sheets. These loops are further elucidated in Fig. B.2, where the two 2D sheets are assembled around their common edge and each gray disc represents a value of Ψ at which $\boldsymbol{\lambda}$ is measured. The green, red and blue rectangles show the control loops that are produced by selecting 21, 59 and 123 of these pixels, respectively and the black disk represents the common starting point. The discrete variable ξ indexes the pixels along the control loop. For e.g.: $1 \leq \xi \leq 59$ for the red loop in Fig. 3.11(b).

However, coloring the individual strands is potentially ambiguous. This is a consequence of the fact Ψ is always stepped by a finite amount between measurements, while the components of $\boldsymbol{\lambda}$ at a particular value of Ψ are associated with specific components of $\boldsymbol{\lambda}$ at some other Ψ only via the fact that $\boldsymbol{\lambda}$ is a smooth function of Ψ, so long as Ψ

is not an EP [21, 26].

Consequently, if the steps in Ψ are sufficiently fine and the corresponding measurements of $\boldsymbol{\lambda}$ have reasonably less noise, then the individual identity of a braid strand would be evident in each step of Ψ. Conversely, if Ψ is stepped unreasonably coarsely, or the measurements of $\boldsymbol{\lambda}$ are noisy, the identification of each braid strand would not be evident in a straightforward manner.

We ensured that the steps in Ψ were sufficiently fine as evident in Fig. 3.11(d-f) and for all other eigenvalue braid measurements, and the system stability and measurement protocols ensured that the noise in $\boldsymbol{\lambda}$ is sufficiently low. As a result, it may be straightforward to visually identify, connect and thereby color the individual braid strands. However, to ensure uniformity in data analysis and avoid potential ambiguities, we implemented this "coloring" of the braid strands using a simple algorithm. Specifically, with each increment of ξ i.e., from ξ to $\xi + 1$, each component of $\boldsymbol{\lambda}(\xi + 1)$ is associated with a component of $\boldsymbol{\lambda}(\xi)$ such that sum of the distances

$$Q = \sum_{i,j=1}^{3} |\lambda_i(\xi + 1) - \lambda_j(\xi)|^2 \tag{B.18}$$

is the minimum with $\xi > 1$. More precisely, Q is minimized over the six possible choices for identifying the components of $\boldsymbol{\lambda}(\xi + 1)$ with those of $\boldsymbol{\lambda}(\xi)$. Repeating this process for every value of ξ, the braid strands are tracked and colored. Lastly, for the very first index i.e. $\xi = 1$, we explicitly specify a ordering given by the increasing order of $\mathrm{Im}(\lambda_i)$ for $i \in \{1, 2, 3\}$.

B.7 Data fitting and theoretical calculations

In this section, we describe fitting data to the three-mode optomechanical model as described in Sec. 2.3.3, and using the fitted model to produce theory plots as shown in Figs. 3.5 and 3.7(third column), and theory curves as shown in Figs. 3.8, 3.9, and 3.11.

B.7.1 Fitting the EP_2 locations to optomechanical model

This section describes the fit of the three-mode optomechanical model to the 291 experimentally identified EP_2 points shown in Figs.3.8-3.10. These locations are denoted here as $\Psi_{EP_2}^{(\mathrm{exp},\ell)}$, with $1 \leq \ell \leq 291$.

The best-fit parameters $\boldsymbol{g}$ and κ for the model are obtained by minimizing the cost function

$$C(\boldsymbol{g},\kappa) = \sum_{\ell=1}^{291} |\Psi_{EP_2}^{(\mathrm{exp},\ell)} - \Psi_{EP_2}^{(\mathrm{thy},\ell)}(\boldsymbol{g},\kappa)|^2 \tag{B.19}$$

where the sums define a distance between the experiment and theory, which is adimensionalized by the experimentally determined EP_3 coordinates given by $\Psi_{EP_3}^{(\mathrm{exp})} = \left\{\delta_{EP_3}^{(\mathrm{exp})}, P_{1,EP_3}^{(\mathrm{exp})}, P_{2,EP_3}^{(\mathrm{exp})}, P_{3,EP_3}^{(\mathrm{exp})}\right\}$. In particular, for

$$\Psi_{EP_2}^{(\mathrm{exp},\ell)} = \left\{\delta_{EP_2}^{(\mathrm{exp},\ell)}, P_{1,EP_2}^{(\mathrm{exp},\ell)}, P_{2,EP_2}^{(\mathrm{exp},\ell)}, P_{3,EP_2}^{(\mathrm{exp},\ell)}\right\} \tag{B.20}$$

and

$$\Psi_{EP_2}^{(\mathrm{thy},\ell)} = \left\{\delta_{EP_2}^{(\mathrm{thy},\ell)}, P_{1,EP_2}^{(\mathrm{thy},\ell)}, P_{2,EP_2}^{(\mathrm{thy},\ell)}, P_{3,EP_2}^{(\mathrm{thy},\ell)}\right\} \tag{B.21}$$

this dimensionless distance (squared) is given by

$$\begin{aligned} |\Psi_{EP_2}^{(\mathrm{exp},\ell)} - \Psi_{EP_2}^{(\mathrm{thy},\ell)}(\boldsymbol{g},\kappa)|^2 = &\left(\frac{\delta_{EP_2}^{(\mathrm{exp},\ell)} - \delta_{EP_2}^{(\mathrm{thy},\ell)}}{\delta_{EP_3}^{(\mathrm{exp})}}\right)^2 + \left(\frac{P_{1,EP_2}^{(\mathrm{exp},\ell)} - P_{1,EP_2}^{(\mathrm{thy},\ell)}}{P_{1,EP_3}^{(\mathrm{exp})}}\right)^2 \\ &+ \left(\frac{P_{2,EP_2}^{(\mathrm{exp},\ell)} - P_{2,EP_2}^{(\mathrm{thy},\ell)}}{P_{2,EP_3}^{(\mathrm{exp})}}\right)^2 + \left(\frac{P_{3,EP_2}^{(\mathrm{exp},\ell)} - P_{3,EP_2}^{(\mathrm{thy},\ell)}}{P_{3,EP_3}^{(\mathrm{exp})}}\right)^2 \end{aligned} \tag{B.22}$$

Here, $\Psi_{EP_2}^{(\mathrm{thy},\ell)}(\boldsymbol{g},\kappa)$ in the EP_2 point found numerically as a root of the discriminant $D(\Psi,\boldsymbol{g},\kappa)$ (Sec. B.7.2) in a neighborhood of $\Psi_{EP_2}^{(\mathrm{exp},\ell)}$ and within its 2D data sheet. For example, if $\Psi_{EP_2}^{(\mathrm{exp},\ell)}$ is identified in a data sheet that rasters P_1 and P_2 while holding δ

and P_3 fixed, the numerical root is found in the neighborhood given by

$$(0.65\ P_{1,EP_2}^{(\mathrm{exp},\ell)},\ 1.35\ P_{1,EP_2}^{(\mathrm{exp},\ell)}) \times (0.65\ P_{2,EP_2}^{(\mathrm{exp},\ell)},\ 1.35\ P_{2,EP_2}^{(\mathrm{exp},\ell)}) \tag{B.23}$$

at the same fixed values of δ and P_3. $\Psi_{EP_2}^{(\mathrm{thy},\ell)}(\boldsymbol{g},\kappa)$ is evaluated with $\kappa_{\mathrm{in}}/\kappa = 0.267$, and $\tilde{\boldsymbol{\lambda}}^{(0)}$ held equal to the values determined from single-tone DBA measurements as described in Sec. 4.4.3 and given in Table B.1.

The minimization of $C(\boldsymbol{g},\kappa)$ is implemented numerically on a high-performance cluster[1]. The best-fit parameters so obtained are

$$\begin{aligned} \boldsymbol{g} &= 2\pi \times \{0.1979,\ 0.3442,\ 0.3092\}\ \mathrm{Hz} \\ \kappa &= 2\pi \times\ 173.84\ \mathrm{kHz} \end{aligned} \tag{B.24}$$

These parameters are used to produce the 'best-fit knot' shown as the continuous curve in Figs. 3.8 and 3.9. This curve is generated by using the best-fit values of $\boldsymbol{g}$ and κ given above to calculate $\boldsymbol{\lambda}$ on 16,000 2D sheets in $\mathcal{S}$. On each sheet, the EP_2 points are identified as the roots of the discriminant D, found numerically as described in the Sec. B.7.2. At each of these EP_2 points, ϑ is also calculated. Finally, these points are colored according to ϑ and are connected by straight line segments.

The values of the parameters $\boldsymbol{g}$ and κ given above are also used to generate the theory plots in Figs. 3.5, 3.7 (third column) and in Ref. [200].

B.7.2 Theory plots of D and E

H as given in Eq. (2.91) can be numerically diagonalized at a given Ψ to find the eigenvalues $\boldsymbol{\lambda}(\Psi)$. Similarly, we calculate $S(\Psi)$ from the matrix T associated with this diagonalization (Secs. 2.1.3.2). The theoretical $D(\Psi)$ and $E(\Psi)$ so evaluated are illustrated in Figs. 3.5, 3.7 (third column) and in Ref. [200].

The cyan squares in the theory plots of these figures mark the roots of D, which correspond to EP_2s. The roots are found numerically. To make the numerical root-

[1] *Grace* cluster in Yale Center for Research Computing

finding tractable, the EP_2 degeneracy of H is cast as a system of equations

$$\begin{aligned} \mathrm{Re}(D) &= 0 \\ \mathrm{Im}(D) &= 0 \end{aligned} \tag{B.25}$$

where D is the discriminant of the characteristic polynomial p_H of H. Crucially, the initial guess to the numerical root finding is given by identifying phase-vortices in the calculated $\angle D$. The theory plots and theory curves are obtained from the three-mode optomechanical mode and using the best-fit parameters Eq. (B.24) as obtained in Sec. B.7.1.

B.8 System parameters

This section gives the values of the various parameters in the three-mode optomechanical model of the experimental three-mode system, as described in Sec. 2.3.3. The parameters values are obtained from device controllers, cavity spectroscopy (see Refs. [93–95, 188]), single-tone DBA characterization (as described in Sec. 4.4.3 and illustrated in Fig. B.3), or by fitting the knot of EP_2s (as described Sec. B.7.1). The value and source of each parameter is explicitly given in Table B.1.

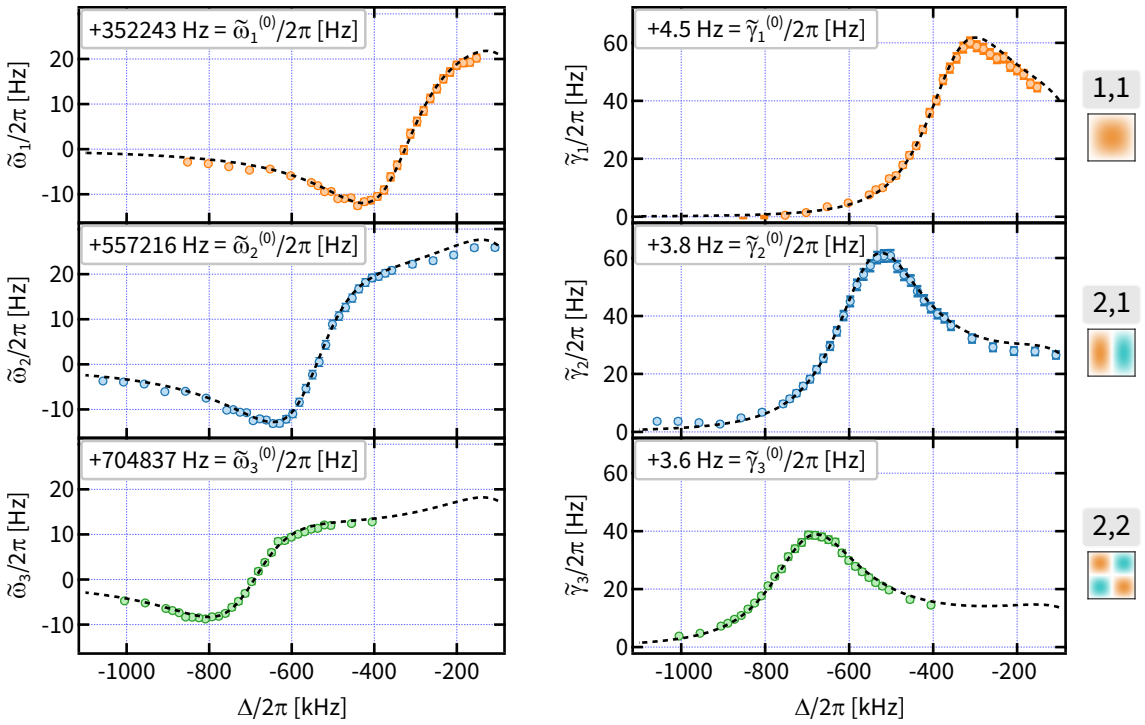

Figure B.3: Characterizing the optomechanical coupling via DBA measurements. For this measurement, the cavity is driven with a single control tone, whose detuning (from the cavity resonance) is Δ. Each panel shows the measured deviation of the (real or imaginary part of the) mechanical mode's eigenvalue from its bare value (i.e., from the relevant component of $\tilde{\boldsymbol{\lambda}}^{(0)}$, whose numerical value is given in each panel, respectively). The error bars show the 1σ confidence interval for each data point. A global fit to standard optomechanical theory gives the bare resonance frequencies $\tilde{\boldsymbol{\lambda}}^{(0)}$ and the optomechanical couplings $\boldsymbol{g}$. The identity of each mode is given as $\{i, j\}$, each index denoting the number of anti-nodes of its vibration along its length and width, respectively. A representative colormap its vibration is provided.

Parameter	Value	Source
λ (nm)	1064	Laser controller
$\kappa/2\pi$ (kHz)	173.8 (189.7)	Knot fitting (Single-tone DBA)
$\kappa_{\mathrm{in}}/2\pi$ (kHz)	46.4	Cavity spectroscopy
$\tilde{\omega}_1^{(0)}/2\pi$ (Hz)	352243.3 $\pm$ 0.1	Single-tone DBA
$\tilde{\omega}_2^{(0)}/2\pi$ (Hz)	557216.8 $\pm$ 0.1	Single-tone DBA
$\tilde{\omega}_3^{(0)}/2\pi$ (Hz)	704836.7 $\pm$ 0.1	Single-tone DBA
$\tilde{\gamma}_1^{(0)}/2\pi$ (Hz)	4.4 $\pm$ 0.1	Single-tone DBA
$\tilde{\gamma}_2^{(0)}/2\pi$ (Hz)	3.8 $\pm$ 0.1	Single-tone DBA
$\tilde{\gamma}_3^{(0)}/2\pi$ (Hz)	3.6 $\pm$ 0.1	Single-tone DBA
$g_1/2\pi$ (Hz)	0.1979 (0.1980)	Knot fitting (Single-tone DBA)
$g_2/2\pi$ (Hz)	0.3442 (0.3040)	Knot fitting (Single-tone DBA)
$g_3/2\pi$ (Hz)	0.3092 (0.3000)	Knot fitting (Single-tone DBA)

Table B.1: System parameters. λ: the laser wavelength. κ: the optical cavity linewidth. κ_{in}: the optical cavity input coupling rate. $\tilde{\omega}_i^{(0)}$: the bare resonance frequency of the i^{th} mechanical mode (i.e., in the absence of any optomechanical effects). $\tilde{\gamma}_i^{(0)}$: the bare energy damping rate of the i^{th} mechanical mode. g_i: the optomechanical coupling rate between the optical cavity and the i^{th} mechanical mode. For bare resonance frequencies ($\omega^{(0)}$), energy damping rates ($\gamma^{(0)}$) and optomechanical coupling rates (g), the subscript denotes the mechanical mode: 1$\rightarrow$(1,1), 2$\rightarrow$(2,1), 3$\rightarrow$(2,2).

Appendix C

Methods for Chapter 4

C.1 Mode-matching routine

Here we provide a numerical routine that solves for the distance between the collimator and the lens ($d = x_1 + y_1 + x_2$) and the distance between the lens and the input cavity mirror (z_3), as discussed in Sec. 4.2.2.

```
In[•]:= ClearAll["Global`*"]
```

step 1

```
In[•]:= (*Quick reminder of Gaussian Beam Propagation*)
```

$$\begin{pmatrix} q_{col} \\ 1 \end{pmatrix} = k . M_{ABCD} . \begin{pmatrix} q_c \\ 1 \end{pmatrix}$$

$$\text{or} \begin{pmatrix} q_c \\ 1 \end{pmatrix} = \frac{1}{k} . (M_{ABCD})^{-1} . \begin{pmatrix} q_{col} \\ 1 \end{pmatrix}$$

step 2

```
In[•]:= (*list all parameters*)
```

```
In[•]:= (*given parameters*)
λ = 1550 × 10^-9; (*m, laser wavelength*)
tm = 4 × 10^-3; (*m, thickness of both cavity mirrors*)
ROC = 50 × 10^-3; (*m, radius of curvature of both cavity mirrors, a symmetric cavity*)
Lc = 7 × 10^-3; (*m, length of cavity*)
n = 1.444; (*refractive index cavity mirrors' substrate*)
flens = +175 × 10^-3; (*m, focal length of convex lens, assuming thin*)
```

In[•]:= (*measured parameters*)

zRcol = 81.38×10^{-3}; (*Rayleigh range of the collimator*)

In[•]:= (*derived parameters*)

qcol = + $\bar{\imath}$ zRcol; (*complex beam parameter of the collimator at its waist, purely imaginary*)

$$zRc = \sqrt{\frac{Lc}{2}\left(ROC - \frac{Lc}{2}\right)};$$ (*Rayleigh range of the cavity mode, for symmetric cavity*)

qc = $\bar{\imath}$ zRc; (*complex beam parameter of the cavity mode – at its waist, purely imaginary*)

$$fm = \frac{-ROC}{n-1}$$ (*lensing due to curvature of cavity mirrors, here it acts like a convex lens*) ;

step 3

In[•]:= (*some simplifications: $z_1 + y_1 + z_2 = d$*)

In[•]:= (*construct ABCD matrix as follows: M1. Beam travels distance d in air starting from z =
0. Reflections from plane mirrors 1,2 are trivial i.e. $M_{reflection} = I_{2x2}$,
M2. Beam gets focussed by a thin lens with focal length flens, M3. Beam travels a further distance z3,
in air to reach cavity mirror's flat face, M4. Beam travels in cavity mirror substrate of thickness tm,
M5. Beam gets focussed due cavity mirror's curvature,
M6. Beam travels a further distance Lc / 2 in air and gets focussed to the size of cavity's waist*)

$$M1 = \begin{pmatrix} 1 & d \\ 0 & 1 \end{pmatrix}; M2 = \begin{pmatrix} 1 & 0 \\ \frac{-1}{flens} & 1 \end{pmatrix}; M3 = \begin{pmatrix} 1 & z3 \\ 0 & 1 \end{pmatrix}; M4 = \begin{pmatrix} 1 & \frac{tm}{n} \\ 0 & 1 \end{pmatrix}; M5 = \begin{pmatrix} 1 & 0 \\ \frac{-1}{fm} & 1 \end{pmatrix}; M6 = \begin{pmatrix} 1 & \frac{Lc}{2} \\ 0 & 1 \end{pmatrix};$$

MABCD = M1.M2.M3.M4.M5.M6;

step 4

In[•]:= (*define q_f as $\begin{pmatrix} q_f \\ 1 \end{pmatrix} = M_{ABCD} \cdot \begin{pmatrix} q_c \\ 1 \end{pmatrix}$*)

$$qf = \frac{MABCD[\![1,1]\!]\,qc + MABCD[\![1,2]\!]}{MABCD[\![2,1]\!]\,qc + MABCD[\![2,2]\!]};$$

qfRe = ComplexExpand [Re [qf]] ;

qfIm = ComplexExpand [Im [qf]] ;

In[•]:= (*solve for $q_f = q_{col}$, a complex equation (or 2 real equations) ,
solutions provide values of d and z3 in meters, acceptable values of d and z3 are real and positive*)

sol = Quiet [NSolve [qfIm == zRcol && qfRe == 0 && d ≥ 0 && z3 ≥ 0 && d ∈ Reals && x ∈ Reals, {d, z3}]] ;

prettyprint = Text[Style[TableForm[{{"f_{lens} (mm)", "d (cm)", "z_3 (cm)"},
{flens * 10^3, (d /. sol[[1]]) * 10^2, (z3 /. sol[[1]]) * 10^2}}], FontFamily → "Source Sans Code"]]

f_{lens} (mm)	d (cm)	z_3 (cm)
175	62.6194	23.327

C.2 Membrane modes

Here we illustrate and identify the membrane modes discussed in Chapter 3: section 4.3.These include modes starting from $(i, j) \equiv$ (1,1) , all the way up to $(i, j) \equiv$ (8,3);(3,8), with all the drumhead modes in-between. Figs. C.1, C.2 and C.3 illustrate their Brownian spectra and corresponding fits to the squared modulus of the sum of N Lorentzians and a constant offset representing the detection background, following ref.[192]. Here N denotes the order of degeneracy. The fit returns the peak positions and the widths of the Lorentzians which correspond to the modes' resonance frequencies (f_{ij}) and energy damping rates (γ_{ij}), respectively and detailed further in section 4.3. As mentioned before, we cannot distinguish (i, j) from (j, i) mode, representing the ambiguity in this identification.

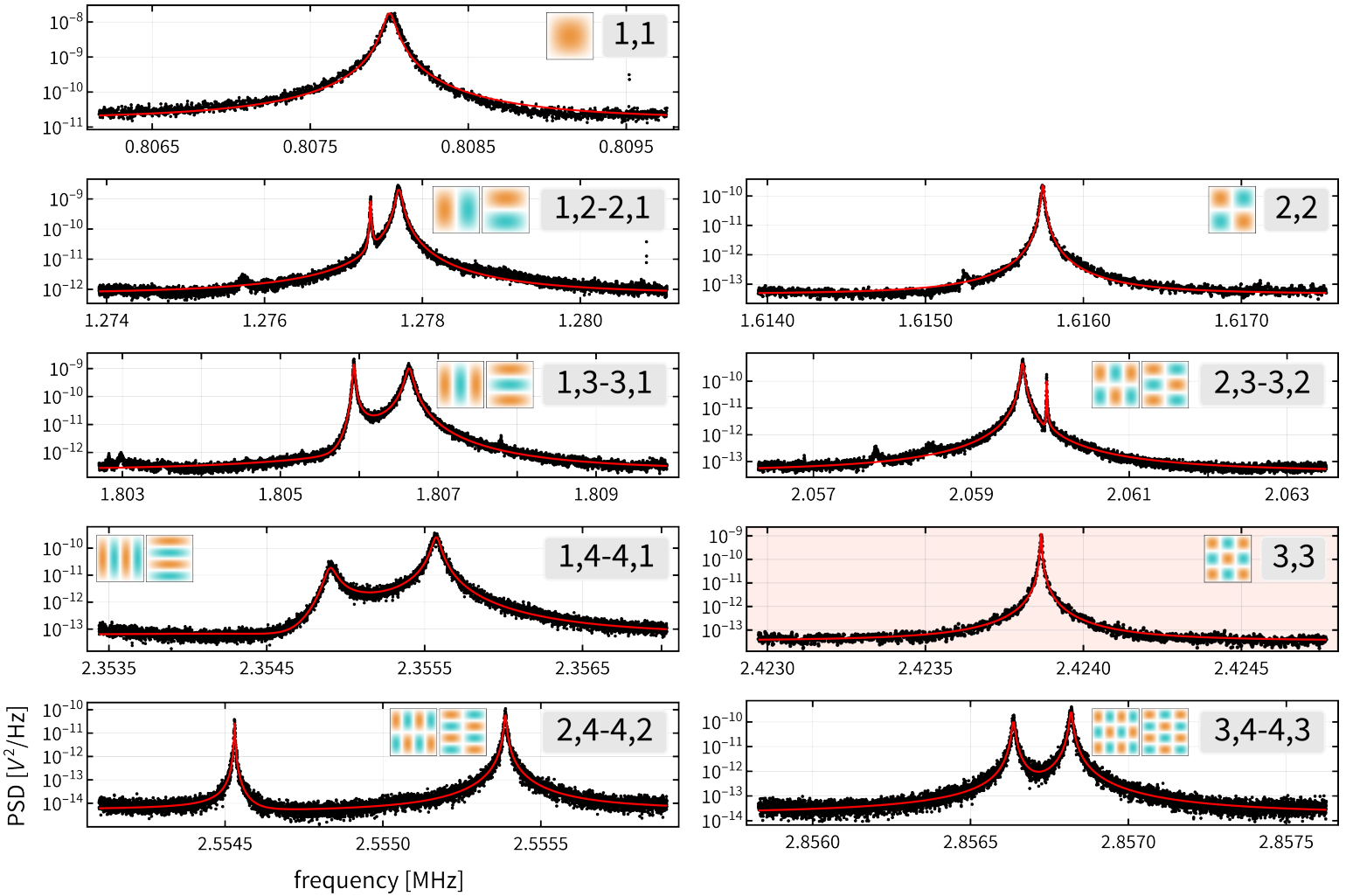

Figure C.1: Membrane modes - set I. This set includes modes from (1,1) at ∼0.8 MHz to (4,3);(3,4) at ∼2.85 MHz. For each panel, data: black points, fit: red curve, inset: mode profiles calculated using Equation 4.7 at t = 0; $\phi = 0$, and mode indices. Note that we cannot identity (i,j) from (j,i) mode. (3,3) mode is highlighted for its use in Chapters 5, 6 and 7.

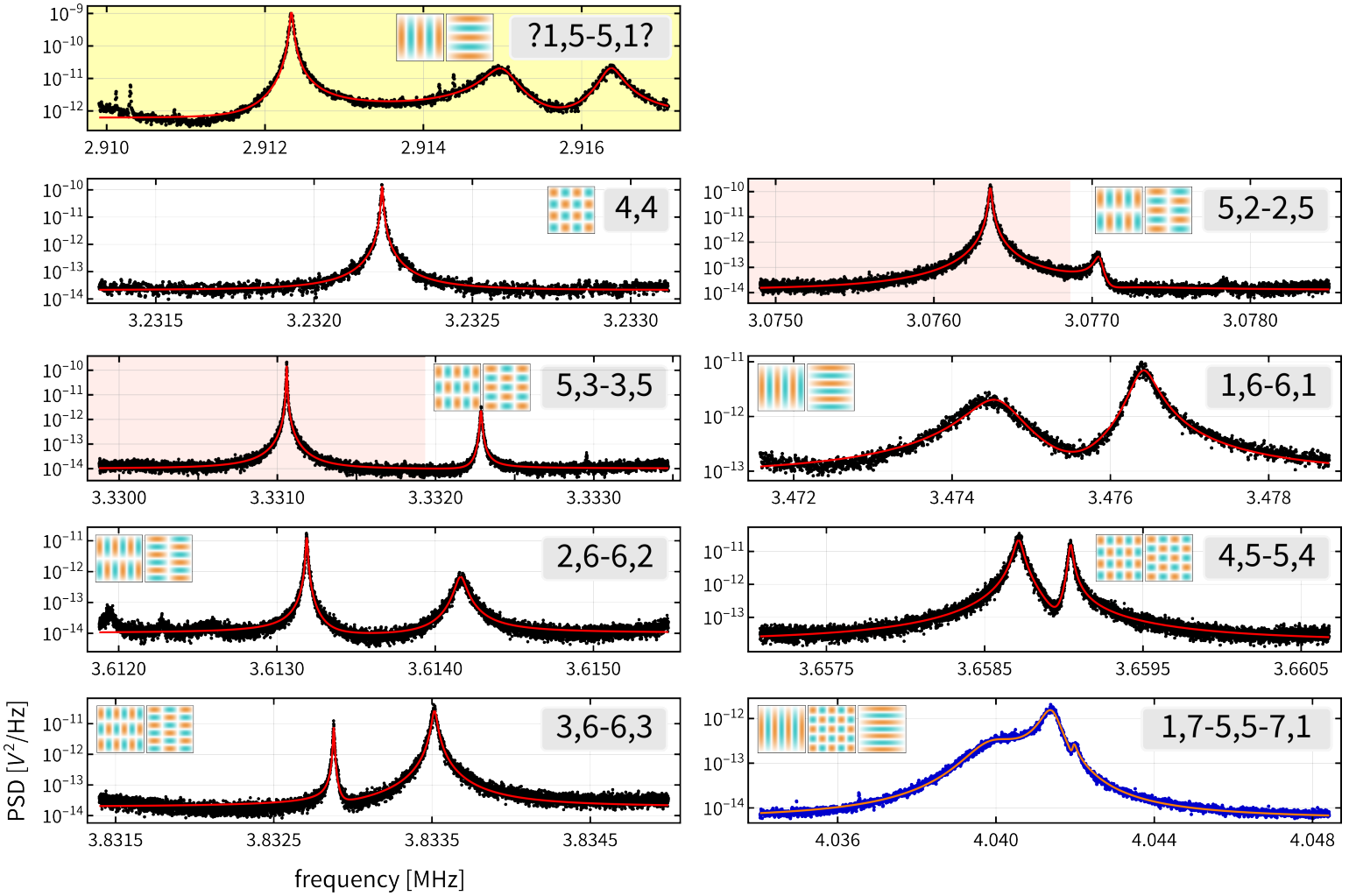

Figure C.2: Membrane modes - set II. This set includes modes from controversial (5,1);(1,5) at ∼2.9 MHz to (7,1);(5,5);(1,7) at ∼4 MHz. For each panel, data: black points, fit: red curve, inset: mode profiles calculated using Equation 4.7 at t = 0; $\phi = 0$, and mode indices. Note that we cannot identity (i,j) from (j,i) mode. (5,2) and (5,3) modes are highlighted for their use in Chapters 5, 6 and 7.

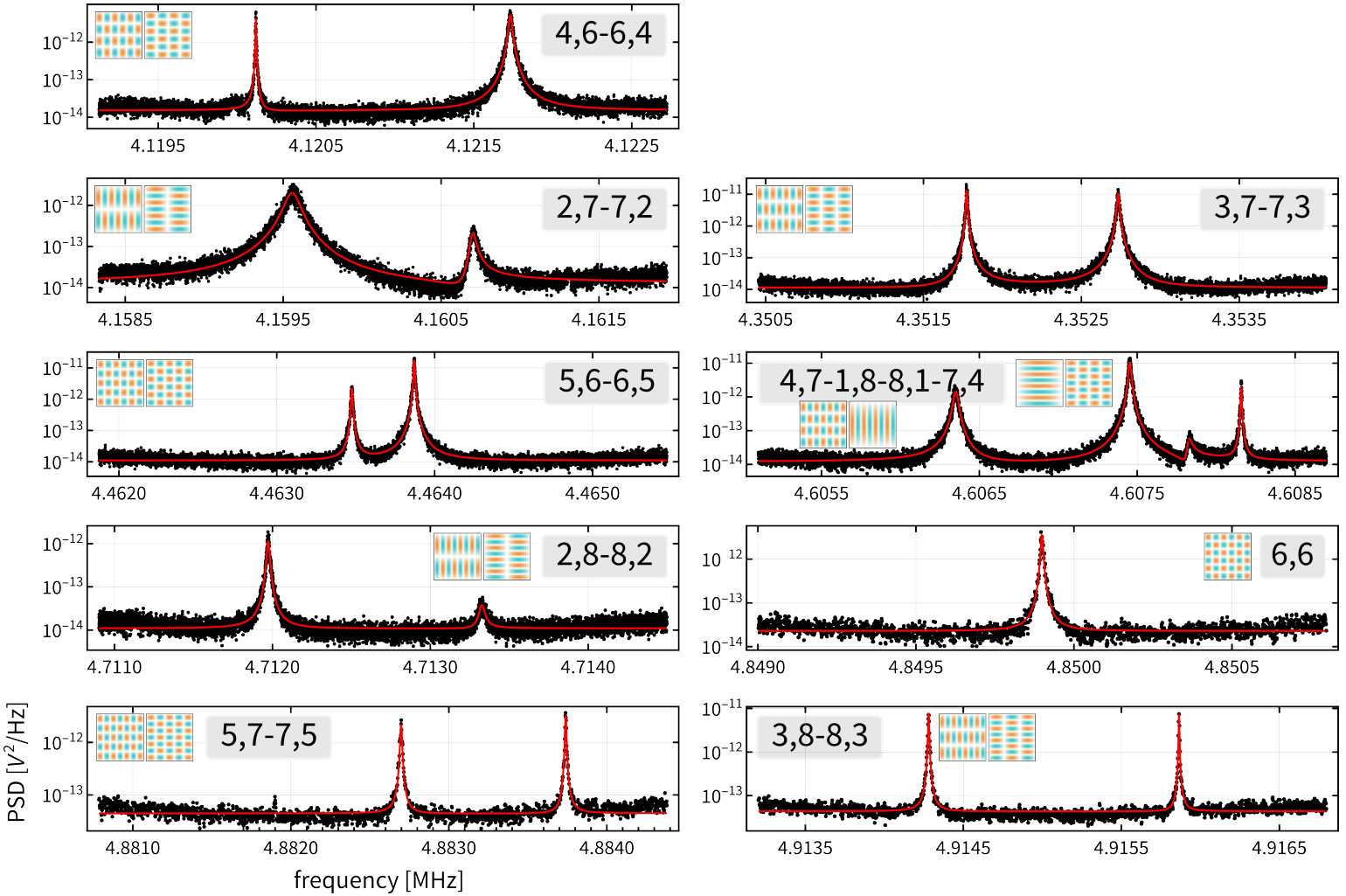

Figure C.3: Membrane modes - set III. This set includes modes from (6,4);(4,6) at ∼4.1 MHz to (8,3);(3,8) at ∼4.9 MHz. For each panel, data: black points, fit: red curve, inset: mode profiles calculated using Equation 4.7 at t = 0; $\phi = 0$, and mode indices. Note that we cannot identity (i,j) from (j,i) mode.

C.3 Non-tunability of (2,5) and (3,5) membrane modes

Here we illustrate the non-tunability of (2,5) and (3,5) membrane modes via DBA, as mentioned in Chapter 3: section 4.4.3.

These measurements follow the same protocol as DBA characterization (section 4.4.3) except we measure the Brownian spectrum of these modes along side their nominally degenerate partners as function of control parameters. Here, we fixed the control laser power $P_1 = 30(33)$ μW for (2,5)((3,5)) mode measurement, and varied its detuning from cavity resonance Δ_1 over a $\sim 4\kappa$ range: -9 MHz to -0.25 MHz. We infer their eigenvalues by fitting the spectra to the squared modulus of the sum of two Lorentzians and a constant offset representing the detection background, following ref.[192]. The fit returns the peak positions and the widths of the Lorentzians which represent the mode's resonance frequencies (ω_{ij}) and energy damping rates (γ_{ij}), respectively. Subsequently, we have the eigenvalues $\lambda_{ij} = \omega_{ij} - i\gamma_{ij}/2$, which then are algorithmically ordered to depend smoothly on parameters. These ordered eigenvalues are fit to the expected radiation pressure and photothermal DBA and extract several system parameters, crucially the optomechanical coupling g for the (2,5) and (3,5) modes. The fits to ordered eigenvalues are illustrated in Fig. C.4 and the fitted system parameters are listed in Table C.1.

The lack of discernible optical spring and damping of (2,5) and (3,5) modes are corroborated by the their small fitted g. Furthermore, they are separated from (5,2) and (5,3) by $\sim$0.7 kHz and $\sim$1 kHz, respectively. With such parameters, we expect control powers of $\mathcal{O}$(1 mW) to possibly 'hybridize' [211]. For all measurements described in Chapters 5, 6 and 7, used control powers $<$50 μW. Hence, we can safely ignore (2,5) and (3,5) in the experiments that involve the pairs: (3,3), (5,2) and (3,3), (5,3), respectively. In addition, we note that (2,5) and (3,5) have similar fitted photothermal coefficient A, compared to the (5,2) and (5,3) counterparts, respectively. However, as described in Sec.4.4.3.1, the photothermal effect simply shifts the mechanical modes' frequencies and does not cause 'hybridization'. Formally, they appear only in the diagonal of H in Eq.(2.81). Thus, we continue to treat it with disdain, as described before (Sec.4.4.3.1).

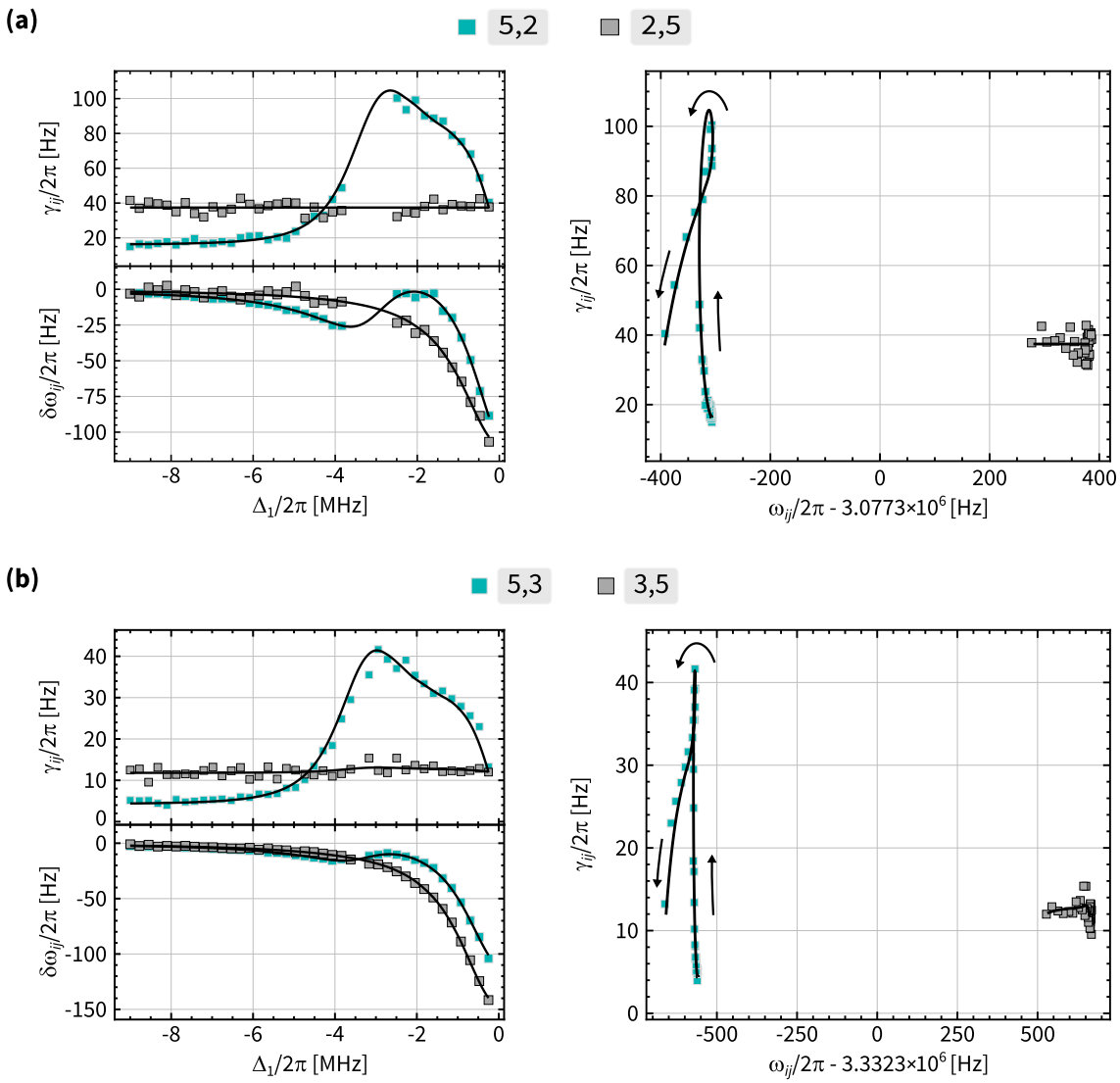

Figure C.4: Non-tunability of (2,5) and (3,5) modes. (a) DBA characterization (2,5) and (5,2) modes, simultaneously. Left top (bottom) panel: modes' damping (shift in frequency) vs. Δ_1, and right panel: parametric plot of damping vs. frequency, black arrows indicate the direction of increasing Δ_1. For all panels, data: gray squares for (2,5) mode, blue squares for (5,2) mode, fit to DBA: black curve. DBA includes only radiation pressure for damping, while it includes both radiation pressure and photothermal effect for frequency and its shift. This measurement used $P_1 = 30$ μW. **(b)** Same as (a) but for (3,5) and (5,3) modes, simultaneously. For all panels, data: gray squares for (3,5) mode, blue squares for (5,3) mode. This measurement used $P_1 = 33$ μW.

Parameter	Estimated value
$\kappa/2\pi$ (MHz)	2.26 $\pm$ 0.04
$g_{2,5}/2\pi$ (Hz)	0.01 $\pm$ 0.5
$g_{5,2}/2\pi$ (Hz)	4.04 $\pm$ 0.04
$A_{2,5}/2\pi$ (μHz)	-4.53 $\pm$ 0.20
$A_{5,2}/2\pi$ (μHz)	-4.45 $\pm$ 0.20
$\Delta_{\mathrm{o}}/2\pi$ (kHz)	-18 $\pm$ 19

(a)

Parameter	Estimated value
$\kappa/2\pi$ (MHz)	2.24 $\pm$ 0.03
$g_{3,5}/2\pi$ (Hz)	0.50 $\pm$ 0.20
$g_{5,3}/2\pi$ (Hz)	2.69 $\pm$ 0.04
$A_{3,5}/2\pi$ (μHz)	-5.52 $\pm$ 0.18
$A_{5,3}/2\pi$ (μHz)	-4.19 $\pm$ 0.18
$\Delta_{\mathrm{o}}/2\pi$ (kHz)	-37 $\pm$ 13

(b)

Table C.1: Fit parameters obtained from DBA characterization of (a) (2,5) and (b) (3,5) modes. Also reported are the corresponding fit parameters for their nominally degenerate partners in (a) and (b), respectively. The estimated value is given as fit value $\pm$ fit error reported as one standard deviation.

C.4 Fits to optomechanical model

Here we provide a detailed view of fits to optomechanical model as described in sections 4.5.1 and 4.5.3. The data corresponding to the discriminant D and trace $\mathcal{T}$ were fit using least-square minimization routine [236] and the corresponding fit parameters are given in Table 4.5. The data and fit corresponding to Figs. 4.15, 4.16 and 4.19 are illustrated in Figs. C.5, C.6 and C.7, respectively.

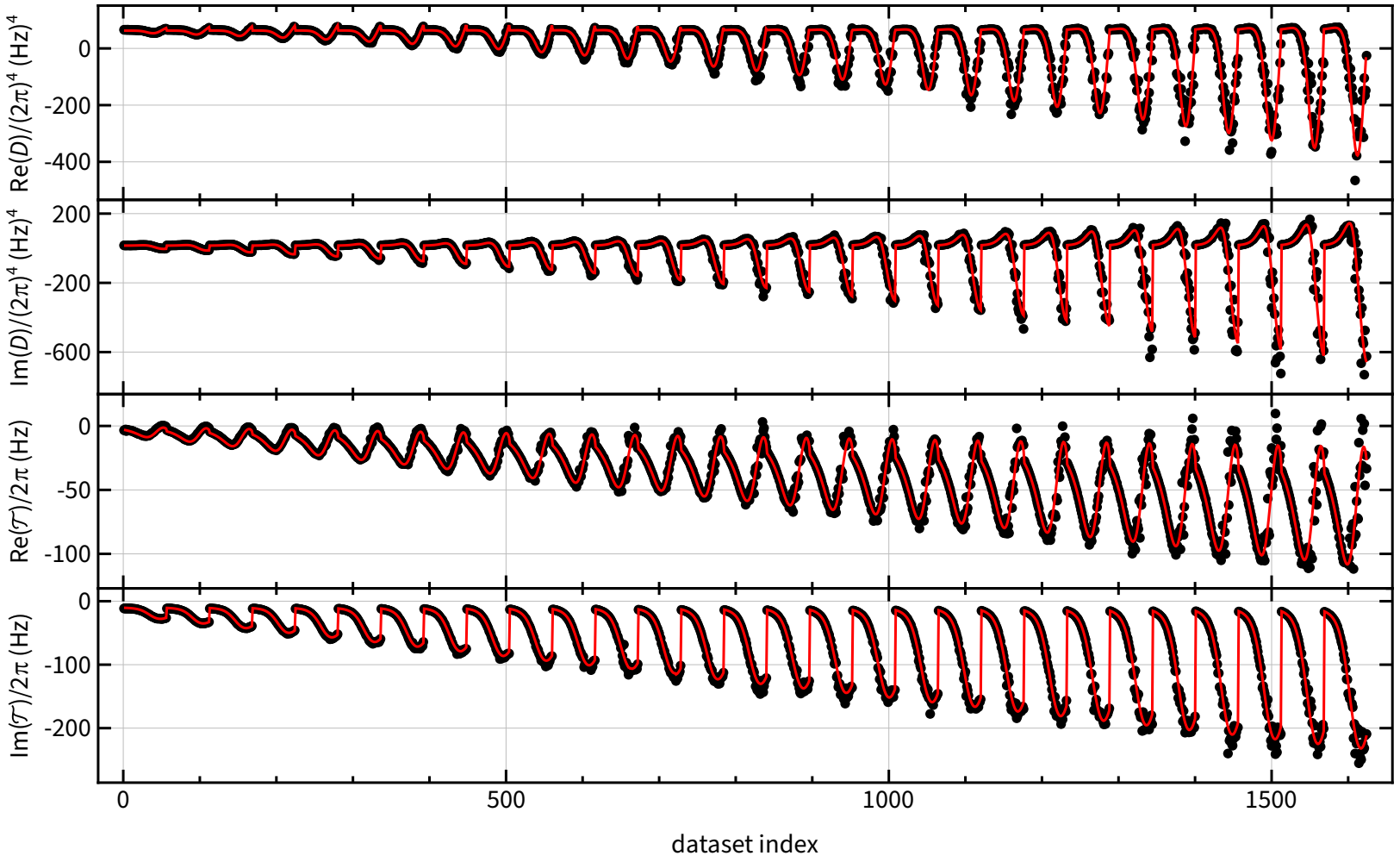

Figure C.5: Fit to optomechanical model corresponding to Fig. 4.15. Top panel: $\mathrm{Re}(D)$ vs. dataset index. Data (black points) and fit (red curve). The control parameter P increases from top to bottom and δ decreases from left to right. Second panel: same as the top panel but for $\mathrm{Im}(D)$. Third panel: same as the top panel but for $\mathrm{Re}(\mathcal{T})$. Bottom panel: same as the top panel but for $\mathrm{Im}(\mathcal{T})$. The corresponding fit parameter are listed in Table 4.5.

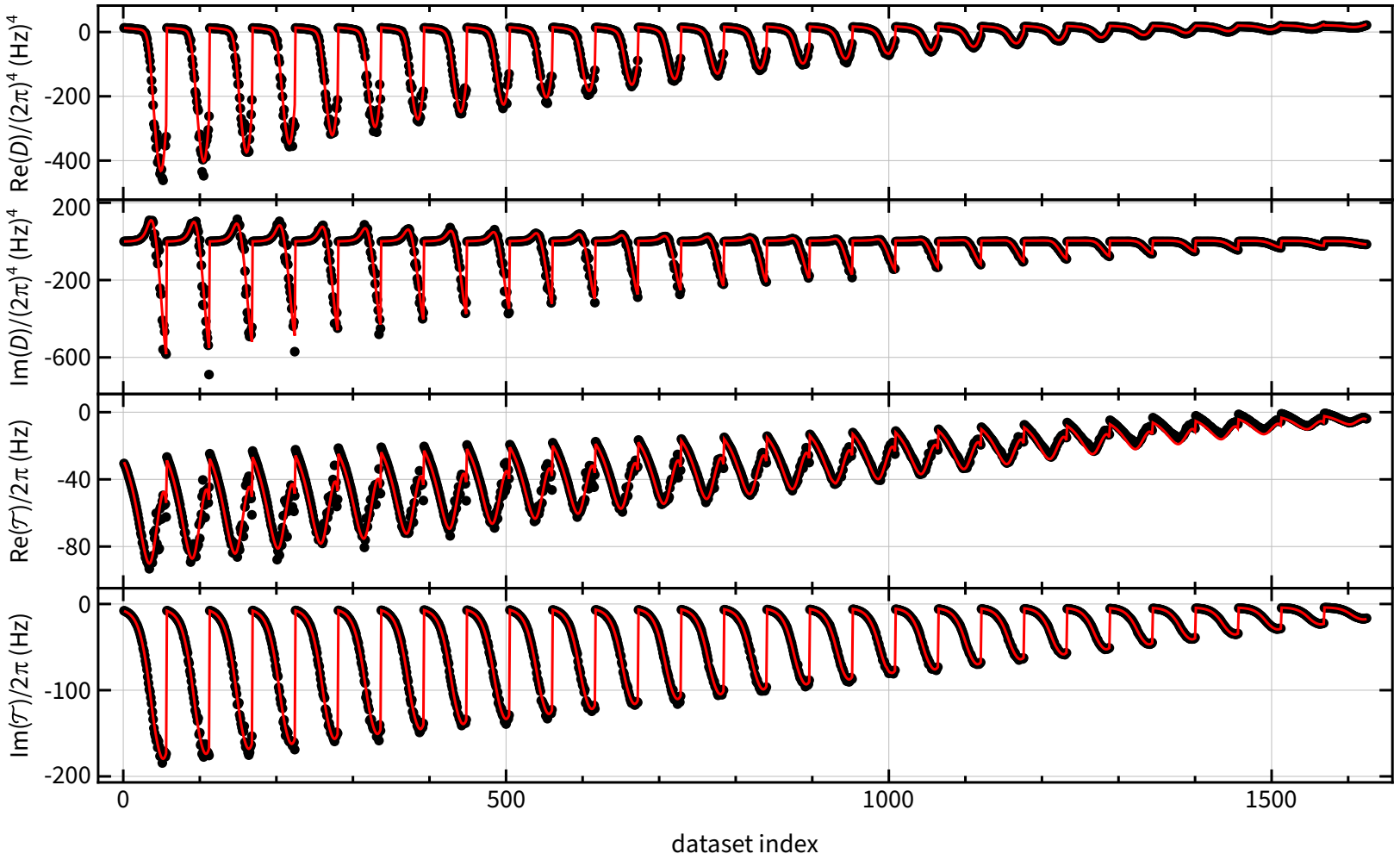

Figure C.6: Fit to optomechanical model corresponding to Fig. 4.16. Top panel: $\mathrm{Re}(D)$ vs. dataset index. Data (black points) and fit (red curve). The control parameter P increases from bottom to top and δ increases from left to right. Second panel: same as the top panel but for $\mathrm{Im}(D)$. Third panel: same as the top panel but for $\mathrm{Re}(\mathcal{T})$. Bottom panel: same as the top panel but for $\mathrm{Im}(\mathcal{T})$. The corresponding fit parameter are listed in Table 4.5.

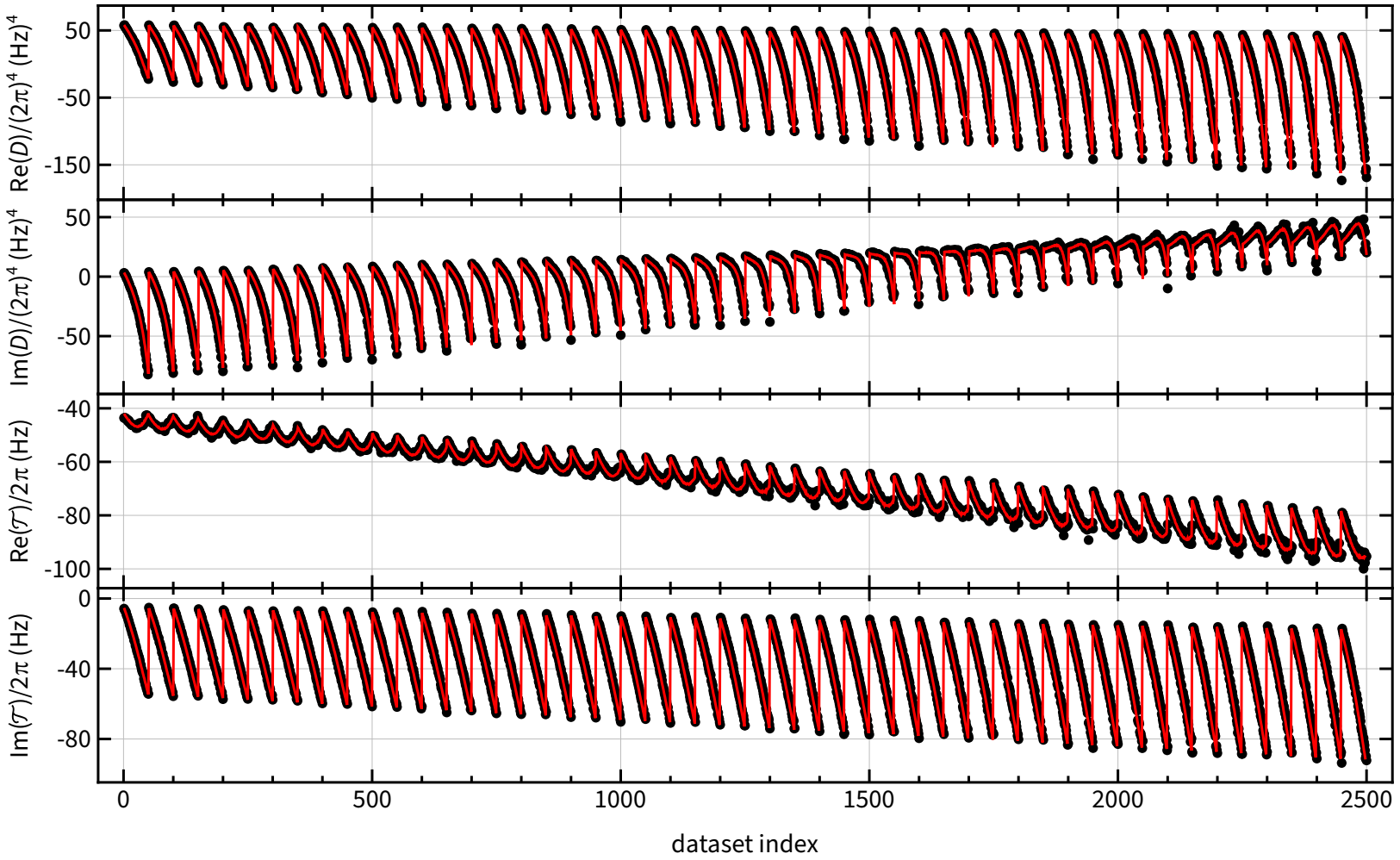

Figure C.7: Fit to optomechanical model corresponding to Fig. 4.19. Top panel: $\mathrm{Re}(D)$ vs. dataset index. Data (black points) and fit (red curve). The control parameter P increases from bottom to top and δ increases from left to right. Second panel: same as the top panel but for $\mathrm{Im}(D)$. Third panel: same as the top panel but for $\mathrm{Re}(\mathcal{T})$. Bottom panel: same as the top panel but for $\mathrm{Im}(\mathcal{T})$. The corresponding fit parameter are listed in Table 4.5.

C.5 Instrument calibrations

In this section, we describe various instrument calibrations that are necessary for appropriate tuning and tapping of control parameters, as well as setting system parameters. These include calibrating the VOAs, the AOMs and various photodetectors as shown in the optical and electrical setups above (Figs.4.21 and 4.22).

C.5.1 VOA calibration

This is accomplished straightforwardly by the experimental setup as shown in Fig. C.8(a). The calibration involves tuning the DC voltage input (V_{DC}) to the VOA and monitoring the power of the output light for given input light power. Fig. C.8(b) illustrates the result of this calibration for the VOA used in the setup shown in Fig. 4.22 and it matches favorably with its vendor specification [318]. Three independent VOAs are utilized in our setup to stabilize the probe, the LO and the overall control powers (Sec. 4.6.2.3), each calibrated as above. In order to ensure a nominally linear slope of the error signal used for this stabilization, we set $V_{\mathrm{DC}} \approx$ 1.8 V for all VOAs.

C.5.2 AOM calibration

For our experiments, we utilize an AOM in the probe path to output a constant probe power and a separate AOM in the control path to tune control parameters statically and in real time. The probe AOM is thus driven by a constant RF drive: 2.5 V_{pp} at 83 MHz which results in a probe power $P_{\mathrm{probe}} = 7$ μW measured at the input to the cavity for all measurements reported in this thesis.

Each of control tones described in Sec. 4.6.1.2 require systematic tuning of their powers and their corresponding calibrations are dealt on an individual basis. The control AOM calibration protocol is executed as follows:

1. The protocol begins by calibrating the photodetector used for tapping the control tones' powers: PD8 in Fig. 4.22. For this step, we apply an RF drive to the control AOM at 80 MHz with various drive amplitudes. The corresponding control power is

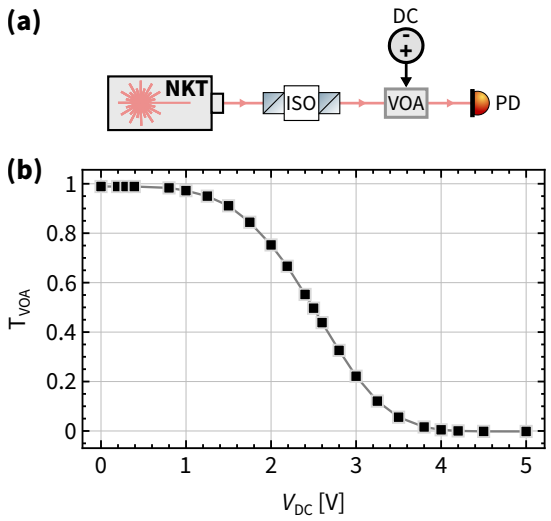

Figure C.8: VOA calibration. (a). Schematic of the setup used for characterizing the variable optical attenuator: VOA. ISO: isolator, DC: power supply that provides DC voltage to tune the VOA, PD: photodetector. **(b)** Transmitted power normalized to input power (T_{VOA}) versus tuning DC voltage (V_{DC}). Data: black squares joined by gray straight lines.

measured at two locations: one at the input to the cavity using a power-meter[1] in units of power, and the other by PD8 as a voltage. These two measurements provide a power-to-voltage calibration for PD8 via a linear fit. Fig. C.9(a) illustrates this calibration.

2. For a control tone say $\{\Delta_1, P_1\}$, we prepare a rectangular grid of corresponding to RF drive amplitude (V_{c1}) and frequency (f_{c1}) values. Typically, we vary $\{V_{\mathrm{c1}}, f_{\mathrm{c1}}\}$ as: 2.5 mV $\leq V_{\mathrm{c1}} \leq$ 0.5 V in 25 steps and 72 MHz $\leq f_{\mathrm{c1}} \leq$ 83 MHz in 25 steps, respectively. The range of these parameters are sufficiently large to provide access to all $\{\Delta_1, P_1\}$ used in this thesis. Each RF drive parameter is applied to the control AOM for a programmed duration, typically 5 s and the corresponding tap voltage ($V_{\mathrm{tap,1}}$) is measured by PD8 and recorded via input 1 of PM (see Fig. 4.22) for 1 s duration at 1000 samples/s.

The aim here is to find the relation between P_1 and V_{c1} as well as between Δ_1 and f_{c1}. By construction, $\Delta_1/2\pi =$ 83 MHz $- f_{\mathrm{c1}}$. So the remaining bit is accomplished in two steps. We first calibrate out the f_{c1} dependence of the control AOM output. This is done by fitting $\overline{V}_{\mathrm{tap,1}}$ to a 6^{th} order polynomial as a function of f_{c1} ($v_1(f_{\mathrm{c1}})$),

[1]THORLABS S132C and THORLABS PM400

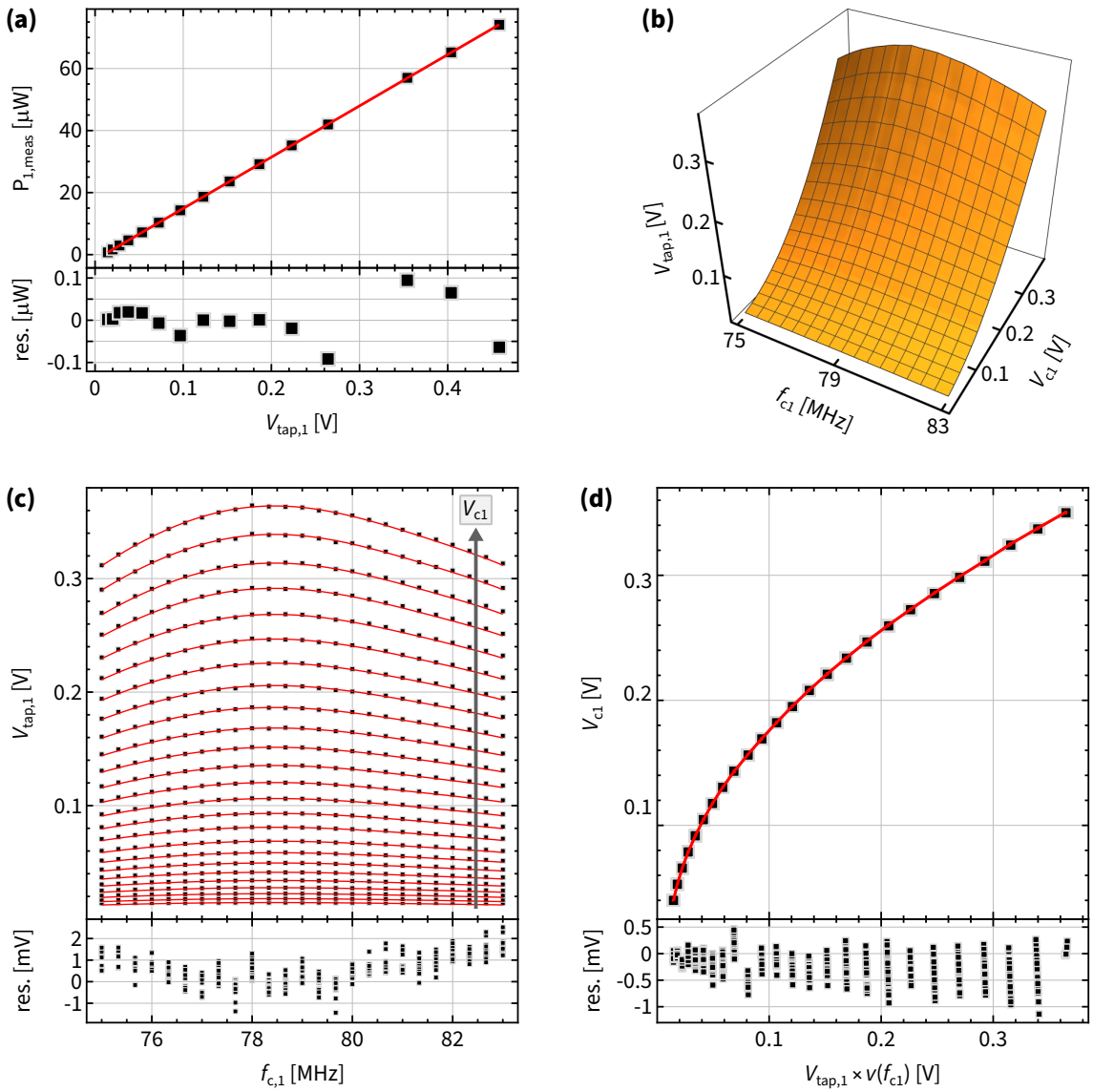

Figure C.9: Control AOM calibration. **(a)** Step I of the procedure to calibrate the tap photodetector (PD8 in Fig. 4.22). The top panel shows measured P_1 versus tap voltage ($V_{\mathrm{tap},1}$). Data: black squares; red curve: linear fit to the data. Bottom panel shows fit residuals corresponding to the measurement and fit in the top panel. **(b)** Data corresponding to step II of the calibration procedure. Orange plane shows $V_{\mathrm{tap},1}$ versus AOM RF drive amplitude (V_{c1}) and frequency (f_{c1}). The data points are connected by straight lines to their nearest neighbors that form the edges of rectangles, which are subsequently filled in orange color [319]. **(c)** Calibrating the AOM's RF drive frequency (f_{c1}) dependence. Top panel shows data as a function of f_{c1} using black squares and the red curve shows a 6^{th} order polynomial fit ($v(f_{\mathrm{c1}})$) to the data. Gray arrow indicates increasing V_{c1}. The bottom panel show fit residuals corresponding to the measurement and fit in the top panel. **(d)** Calibrating AOM's RF drive amplitude (V_{c1}) to output the appropriate control power via $V_{\mathrm{tap},1}$. Top panel shows V_{c1} as a function of $V_{\mathrm{tap},1} \times v(f_{\mathrm{c1}})$ using black squares and the red curve shows a 6^{th} order polynomial fit to the data. The bottom panel show fit residuals corresponding to the measurement and fit in the top panel. This calibration shown here corresponds to the first control tone: $\{\Delta_1, P_1\}$.

where $\overline{V}_{\mathrm{tap},1}$ is obtained by normalizing $V_{\mathrm{tap},1}$ to its maximum value for a given V_{c1}. Subsequently, we fit V_{c1} to a 10^{th} order polynomial as a function of $V_{\mathrm{tap},1} \times v_1(f_{\mathrm{c1}})$. Fig. C.9(b,c,d) shows data corresponding to $V_{\mathrm{tap},1}(V_{\mathrm{c1}}, f_{\mathrm{c1}})$, data and fit corresponding to $\overline{V}_{\mathrm{tap},1}(f_{\mathrm{c1}})$ as well as data, and fit corresponding to $V_{\mathrm{c1}}(V_{\mathrm{tap},1} \times v_1(f_{\mathrm{c1}}))$, respectively. Finally, using the power-to-voltage calibration in the previous step, we can connect P_1 to V_{c1} via $V_{\mathrm{tap},1}$ and thereby completing the calibration for a control tone, here $\{\Delta_1, P_1\}$.

3. Step 2 is repeated for control tones: $\{\Delta_2, P_2\}$, $\{\Delta_4, P_4\}$ and $\{\Delta_{\mathrm{pt}}, P_{\mathrm{pt}}\}$. The corresponding rectangular grid of RF drive parameters stay the same for $\{\Delta_2, P_2\}$ and $\{\Delta_{\mathrm{pt}}, P_{\mathrm{pt}}\}$. For $\{\Delta_4, P_4\}$, the f_{c1} part of the grid is tweaked to 85 MHz $\leq f_{\mathrm{c1}} \leq$ 88 MHz in 25 steps.

4. The final step of this calibration is to connect the tap readings of PD8 and the power-meter to the photodetector that measures transmitted light, PD3 in Fig. 4.22. This allows for an independent tap measure of the control tone power which tracks the optical setup beyond PD8. As a concrete example, we note that beyond PD8, the setup consists of several polarization sensitive parts as well as free space components, which in turn can be detrimentally affected by changes in experimental condition like the temperature and by construction, are not recorded by PD8. To mitigate this issue, we apply the first control tone given by $\{\Delta_1/2\pi = -$ 3 MHz$, P_1 =$ 10 μW$\}$ as reported independently by the power-meter, and record the corresponding PD3 reading $V_{\tau 0}$ (via input 3 of PM in Fig. 4.22). This reading is subsequently utilized in control power stabilization as described in Sec. 4.6.2.3.

Appendix D

Methods for Chapter 5

Here we provide additional technical details for measurements described in Chapter 5. This includes a detailed protocol for measuring $\beta(T)$ for a control loop (Sec. D.1), extracting the state vector via ringdown measurements (Sec. D.2), measuring the propagator matrix $U(T)$ for a control loop (Sec. D.3) and estimating ϕ_B via the asymptote of $\beta(T)$ (Sec. D.4). Finally, we provide the system parameters of the experimental apparatus in Sec. D.5.

D.1 Protocol for measuring $\beta(T)$

In this section, we provide details of the protocol used to measure the phase accumulated by the membrane's oscillations when its control parameters are varied along a path. The phase is determined from measurements of $\beta(T)$, which is summarized in the following steps:

1. The control parameters are tuned to their values at the beginning of the control path, setting the system's dynamical matrix H to its initial value at $t = 0$ i.e.,$H(t = 0)$.

2. A drive is applied at frequency ω_{d} to ring the membrane up to its initial state vector $\vec{c}^{(a)}$.

3. The drive is turned off. This defines $t = 0$.

4. While the membrane rings down i.e., it evolves under the time-independent dynamical matrix $H(0)$, we record the heterodyne signal demodulated by two oscillators at frequencies $\omega_1^{\rm mod} = \omega_{\rm d}$ and $\omega_2^{\rm mod}$. This measurement corresponds to the first column of Figs. D.1, D.2, 5.1 and 5.2.

5. Steps **2** and **3** are repeated. But now once the drive is turned off, the control parameters are tuned in real time along a chosen control path for a duration T (for e.g., by setting $\theta_{12}(t) = 2\pi t/T$), such that the system evolves under a time-dependent dynamical matrix $H(t)$. For $t > T$, the membrane is allowed to ring down (i.e., it evolves under $H(T)$), and we record the heterodyne signal demodulated by the same two oscillators $\omega_1^{\rm mod} = \omega_{\rm d}$ and $\omega_2^{\rm mod}$. This measurement corresponds to the second column of Figs. D.1, D.2, 5.1 and 5.2.

6. We repeat the measurements described above, alternating between free ringdown (step **4**) and the control path (step **5**). Typically 50 – 500 measurements of each type are "complex-averaged" (discussed later) to increase the signal-to-noise ratio (SNR).

7. We fit the "free ringdown" data to extract the initial state vector $\vec{c}^{(a)}(0)$ immediately after the drive is turned off, and the "control path" data to extract the state vector $\vec{c}^{(a)}(T)$ after a control path of duration T is performed (see Sec. D.2).

8. In order to determine the four complex components of the propagator matrix $U(T)$ (defined by $\vec{c}^{(a)}(T) = U(T)\vec{c}^{(a)}(0)$), we measure the evolution of two linearly independent initial state vectors. Thus, we repeat steps **2** – **7** above, choosing a different value for the drive frequency $\omega_{\rm d}$, which rings the membrane up to an initial state vector $\vec{c}^{(b)}(0)$ that is linearly independent of $\vec{c}^{(a)}(0)$. The state vectors $\{\vec{c}^{(a)}(0), \vec{c}^{(b)}(0), \vec{c}^{(a)}(T), \vec{c}^{(a)}(T)\}$ yield sufficient information to determine the propagator in the "forward" direction: $U_{\circlearrowleft}(T)$ (see Sec. D.3).

9. We repeat the entire series of measurements described in steps **2** to **8**, varying the control path duration T to determine $U_{\circlearrowleft}$ as a function T.

10. We repeat the series of measurements described in steps **1** to **9**, except that we apply the "time reversed" version of the control path from the above measurements. For example, if the "forward" circuit was defined by $\theta_{12}(t) = 2\pi t/T$, the "time reversed"

circuit would be defined by $\theta_{12}(t) = -2\pi t/T$ (see Sec. 5.1 and the third column of Figs. D.1, D.2, 5.1 and 5.2). This measurement gives the "time reversed" propagator $U_{\circlearrowleft}(T)$.

11. From these data, we calculate $\beta(T) = -i\,\mathrm{Log}(U_{++,\circlearrowleft}/U_{++,\circlearrowleft})/2$ which (up to a choice of the branch of the complex logarithm, see Sec. D.4) tends to the complex geometric phase $\phi_{B,\circlearrowleft}$ at large T. Here the least-dissipative eigenmode is denoted by the subscript $+$.

The entire sequence described above constitutes the measurement of $\beta(T)$ for a given control path.

Prior to performing this measurement sequence, we measure the Brownian motion spectrum with the control tones off to obtain the bare mechanical frequencies $\omega_{1,2}^{(0)}$ (Sec. 4.3.1). We then perform a measurement of the membrane's susceptibility with the control tones on to extract the frequencies Λ_{ij} for $i, j \in \{1, 2\}$ (Sec. 2.3.2 and Eq. (2.82)). This static spectroscopy is also performed intermittently during a measurement sequence to track any drift in the system parameters that may occur during data acquisition. A typical measurement of $\beta(T)$ for a given control path (see for example Figs. 5.3 and 5.4) lasts $\sim$4 hours, during which the static spectroscopy measurement is performed every 15 minutes. The drive and demodulation frequencies (discussed below) are updated based on these measurements.

The measured values of Λ_{ij} are also utilized to set and update the drive frequency ω_{d} and set the demodulation frequency $\omega_1^{\mathrm{mod}} = \omega_{\mathrm{d}}$ and ω_2^{mod}. Specifically, we choose ω_{d} to be the real part of Λ_{ij}. Any choice of the four values of $\mathrm{Re}(\Lambda_{ij})$ results in a distinct initialization of the membrane's state vector. However, to reconstruct the propagator matrix U for a control path of duration T, we measure the initial and the final state vectors for two linearly independent initializations of the state vector. They are the $\vec{c}^{(a)}(0)$ and $\vec{c}^{(b)}(0)$ introduced in steps **2** and **8**. To ensure that $\vec{c}^{(a)}(0)$ and $\vec{c}^{(b)}(0)$ are linearly independent to a degree sufficient to accurately determine the propagator, we initialize $\vec{c}^{(a)}(0)$ with $\omega_{\mathrm{d}} = \mathrm{Re}(\Lambda_{1j}) \approx \omega_1^{(0)}$ and $\vec{c}^{(b)}(0)$ with $\omega_{\mathrm{d}} = \mathrm{Re}(\Lambda_{2j}) \approx \omega_2^{(0)}$.

Similarly, the demodulation frequency is chosen from among the four $\mathrm{Re}(\Lambda_{ij})$ with

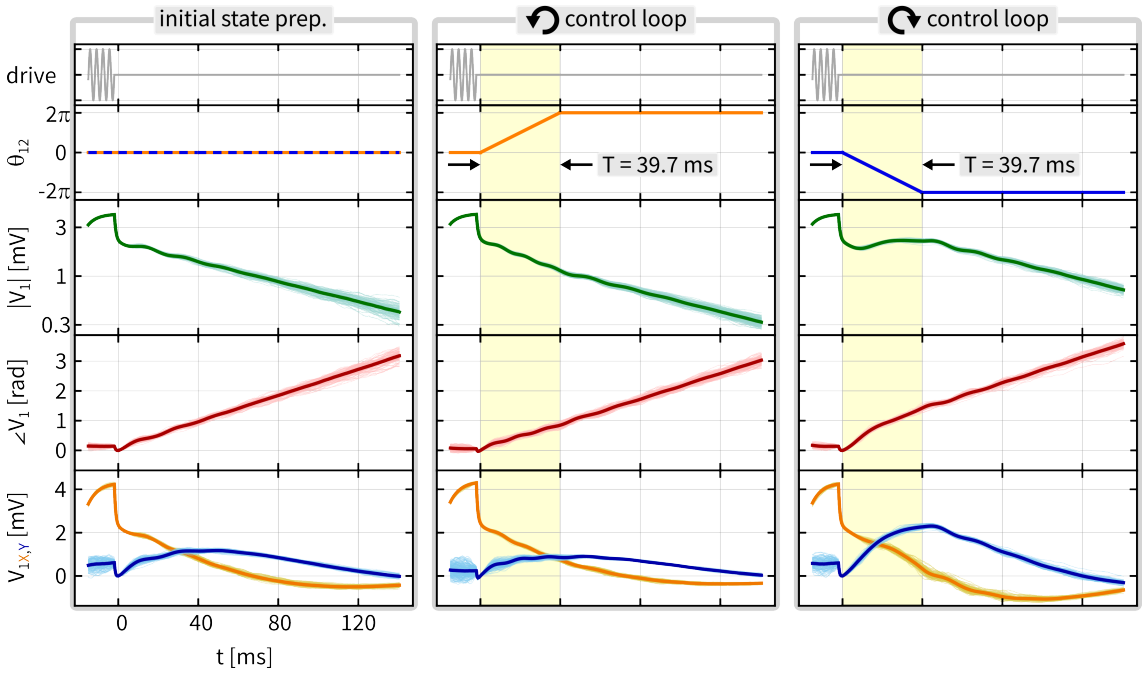

Figure D.1: Complex-averaging for state vectors $\vec{c}^{(a)}(0)$ and $\vec{c}^{(a)}(T)$. First column: measurements for $\vec{c}^{(a)}(0)$ i.e, with no control loop. **Second column**: measurements for $\vec{c}^{(a)}(T)$ with control loop in "forward" direction. **Third column**: measurements for $\vec{c}^{(a)}(T)$ with control loop in "backward" direction. For all columns, gray curves: a schematic of the driving force applied to the membrane, which is switched off at $t = 0$. Orange curve in second column: a plot of the beat-note phase $\theta_{12}(t)$, for the control loop in the "forward" direction. Blue curve in second column: a plot of the beat-note phase $\theta_{12}(t)$, for the control loop in the "backward" direction. Solid green, red, dark-orange and dark-blue curves: the "complex-averaged" magnitude, the phase, the in-phase and the quadrature part of the heterodyne signal, respectively and for measurements shown in each column. The faint colored counterparts correspond to the individual traces. For this measurement, we used the same membrane modes and the same other control parameters as in Figs. 5.1-5.4, 5.9 and 5.11.

one being equal to ω_{d}. Specifically, we choose $\omega_1^{\mathrm{mod}} = \mathrm{Re}(\Lambda_{1j}) \approx \omega_1^{(0)}$ and $\omega_1^{\mathrm{mod}} = \mathrm{Re}(\Lambda_{1j}) \approx \omega_1^{(0)}$.

D.1.1 Complex averaging of ringdown measurements

When averaging multiple records of the heterodyne signal $V(t)$ with the i^{th} record denoted as $V_i(t)$, it is important to account for the phase of $V_i(t)$. For each $V_i(t)$, we reference the phase at the end of the drive to zero, i.e. we set $\angle V_i(0) = 0$. This ensures that, upon averaging, coherent motion of the membrane induced by the drive is in-phase for all i, while the incoherent noise will tend to average to zero. It is also important to choose the same reference time (i.e., the end of the drive) for both the "free ringdown" measurement and the "control path" measurement, as this ensures that the state vectors $\vec{c}^{(a)}(0)$ and

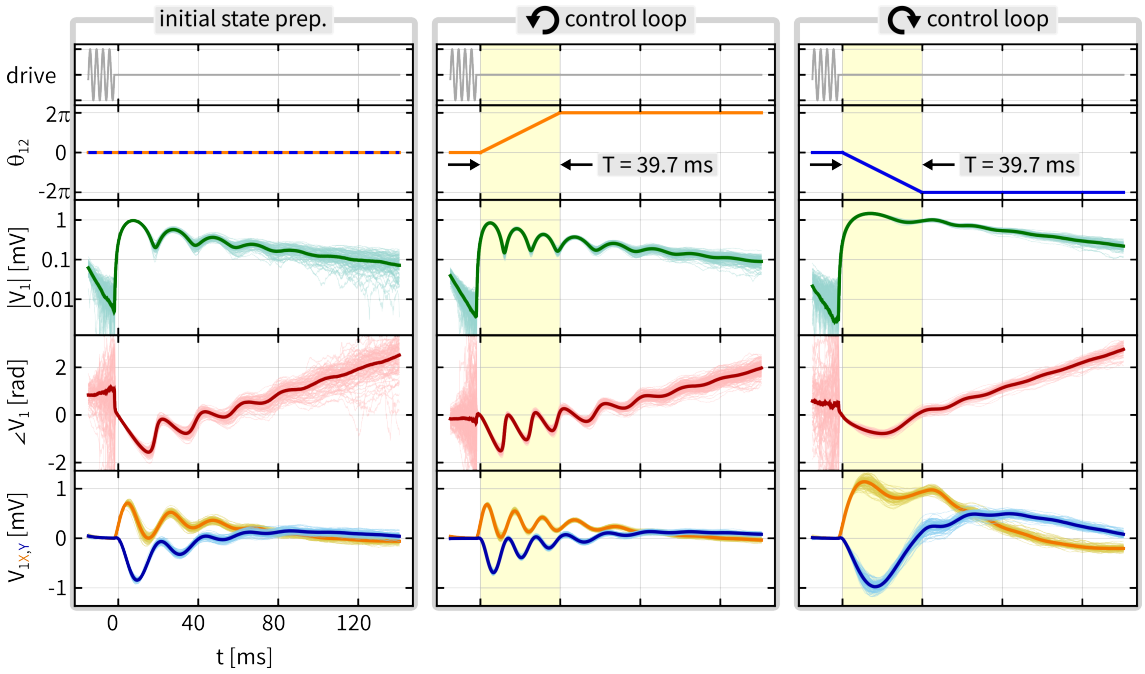

Figure D.2: Complex-averaging for state vectors $\vec{c}^{(b)}(0)$ and $\vec{c}^{(b)}(T)$.First column: measurements for $\vec{c}^{(b)}(0)$ i.e, with no control loop. **Second column**: measurements for $\vec{c}^{(b)}(T)$ with control loop in "forward" direction. **Third column**: measurements for $\vec{c}^{(b)}(T)$ with control loop in "backward" direction. For all columns, gray curves: a schematic of the driving force applied to the membrane, which is switched off at $t = 0$. Orange curve in second column: a plot of the beat-note phase $\theta_{12}(t)$, for the control loop in the "forward" direction. Blue curve in second column: a plot of the beat-note phase $\theta_{12}(t)$, for the control loop in the "backward" direction. Solid green, red, dark-orange and dark-blue curves: the "complex-averaged" magnitude, the phase, the in-phase and the quadrature part of the heterodyne signal, respectively and for measurements shown in each column. The faint colored counterparts correspond to the individual traces. For this measurement, we used the same membrane modes and the same other control parameters as in Figs. D.1, 5.1-5.4, 5.9 and 5.11.

$\vec{c}^{(a)}(T)$ have a common phase reference. This averaging protocol is illustrated in Figs. D.1 and D.1, which correspond to the measurements of state vectors $\{\vec{c}^{(a)}(0), \vec{c}^{(a)}(T)\}$ and $\{\vec{c}^{(b)}(0), \vec{c}^{(b)}(T)\}$, respectively, where the individual measurements (faint lines) are plotted along with the averaged result (thick lines). These measurements correspond to ones shown in Figs. D.1 and D.2, respectively. This averaging protocol is affectionately named "complex-averaging".

D.2 Extracting state vector from ringdown measurements

In this section, we describe the procedure to extract the membrane's state vector via ringdown measurements. In particular, we derive the functional form used to fit the ringdown data as shown in Figs. 5.1 and 5.2.

When the control parameters are held fixed and the drive is off, the free ringdown of the membrane modes may be written in the lab frame as a solution of $\vec{c}_{\mathrm{lab}}(t)$ in Eq. (2.75). However, it is more straightforward to first solve for $\vec{c}(t)$ in the frame $\mathcal{R}$ as in Eq. (2.80), and then apply the unitary transformation $S_{\mathcal{R}}^{-1}$ (Eq. (2.79)) to convert the motional amplitudes in the frame $\mathcal{R}$ to the lab frame.

In order to solve for $\vec{c}(t)$ in frame $\mathcal{R}$, we rewrite Eq. (2.80) as:

$$\dot{\vec{c}}_{\mathrm{D}} = -iH_{\mathrm{D}}\vec{c}_{\mathrm{D}} \tag{D.1}$$

where we have introduced the state vector in a frame where the system's dynamical matrix H is diagonal. Specifically, we have

$$\begin{aligned} \vec{c}_{\mathrm{D}}(t) &= (\overline{c}_{+}(t), \overline{c}_{-}(t))^{\mathrm{T}} = S_{\mathrm{D}}^{-1}\vec{c}(t) \\ H_{\mathrm{D}} &= \begin{bmatrix} \lambda_{+} & 0 \\ 0 & \lambda_{-} \end{bmatrix} = S_{\mathrm{D}}^{-1} H S_{\mathrm{D}} \end{aligned} \tag{D.2}$$

where $\overline{c}_i(t)$ is the complex motional amplitude of normal mode $i \in \{+, -\}$, $\lambda_{\pm}$ are the eigenvalues of the system in frame $\mathcal{R}$, and the columns (rows) of $S_{\mathrm{D}}(S_{\mathrm{D}}^{-1})$ are composed of the normalized right (left) eigenvectors of H. We emphasize that $H, H_{\mathrm{D}}, S_{\mathrm{D}}, S_{\mathrm{D}}^{-1}$ are time-independent because the control parameters are held fixed before the start of the control path (for state initialization) and at the end of the control path (for post-control

path ringdown). The solution of Eq. (D.1) is

$$\vec{c}_{\mathrm{D}}(t) = \begin{bmatrix} \overline{c}_{+} e^{-i\lambda_{+} t} \\ \overline{c}_{-} e^{-i\lambda_{-} t} \end{bmatrix} \tag{D.3}$$

with $\overline{c}_i$: the complex motional amplitude of normal mode $i \in \{+, -\}$ at the instant when the radiation pressure drive is turned off. Expanding S_{D} as

$$S_{\mathrm{D}} = \begin{bmatrix} u_{11} & u_{12} \\ u_{21} & u_{22} \end{bmatrix} \tag{D.4}$$

gives

$$\vec{c}(t) = S_{\mathrm{D}} \vec{c}_{\mathrm{D}}(t) = \begin{bmatrix} u_{11}\overline{c}_{+} e^{-i\lambda_{+} t} + u_{12}\overline{c}_{-} e^{-i\lambda_{-} t} \\ u_{21}\overline{c}_{+} e^{-i\lambda_{+} t} + u_{22}\overline{c}_{-} e^{-i\lambda_{-} t} \end{bmatrix} \tag{D.5}$$

and subsequently, we have

$$\begin{aligned} \vec{c}_{\mathrm{lab}}(t) &= S_{\mathcal{R}}^{-1}(t)\vec{c}(t) = S_{\mathcal{R}}^{-1}(t) S_{\mathrm{D}} \vec{c}_{\mathrm{D}}(t) \\ &= \begin{bmatrix} u_{11}\overline{c}_{+} e^{-i(\lambda_{+} + \omega_1^{(0)} + \eta/2)t} + u_{12}\overline{c}_{-} e^{-i(\lambda_{-} + \omega_1^{(0)} + \eta/2)t} \\ u_{21}\overline{c}_{+} e^{-i(\lambda_{+} + \omega_2^{(0)} - \eta/2)t} + u_{22}\overline{c}_{-} e^{-i(\lambda_{-} + \omega_2^{(0)} - \eta/2)t} \end{bmatrix} \end{aligned} \tag{D.6}$$

Or, more succinctly via Eq. (2.82)

$$\vec{c}_{\mathrm{lab}}(t) = \begin{bmatrix} u_{11}\overline{c}_{+} e^{-i\Lambda_{1+} t} + u_{12}\overline{c}_{-} e^{-i\Lambda_{1-} t} \\ u_{21}\overline{c}_{+} e^{-i\Lambda_{2+} t} + u_{22}\overline{c}_{-} e^{-i\Lambda_{2-} t} \end{bmatrix} \tag{D.7}$$

This motion is transduced onto the optical field, converted into an electronic signal, and measured by the lock-in amplifier (LIA) as $\rho\chi_c(\omega)\vec{g} \cdot \vec{c}_{\mathrm{lab}}(t)$, where ρ is the transduction gain[1], $\chi_c(\omega)$ is the optical cavity susceptibility and $\vec{g} = (g_1, g_2)$ is the vector of optomechanical coupling strengths, $(\cdot)$ is the usual dot product and $\rho\chi_c(\omega)\vec{g}$ as a whole represents the detection vector. This signal is then demodulated by the LIA at frequen-

[1]The transduction gain also depends on demodulation frequency, and is omitted solely for notational simplicity.

cies ω_1^{mod} and ω_2^{mod} and low-pass filtered with bandwidth $BW \ll |\omega_1^{(0)} - \omega_2^{(0)}|$. See also Secs. 2.3.1.2, B.1 and 4.6.1.1. The corresponding demodulated (complex-valued) signals at ω_1^{mod} and ω_2^{mod} are:

$$\begin{aligned} V_1(t) &= \rho\chi_c(\omega_1^{\mathrm{mod}})g_1\left(W(\Lambda_{1+},\omega_1^{\mathrm{mod}})u_{11}\overline{c}_+e^{-i\Lambda_{1+}t} + W(\Lambda_{1-},\omega_1^{\mathrm{mod}})u_{12}\overline{c}_-e^{-i\Lambda_{1-}t}\right) \\ V_2(t) &= \rho\chi_c(\omega_2^{\mathrm{mod}})g_2\left(W(\Lambda_{2+},\omega_2^{\mathrm{mod}})u_{21}\overline{c}_+e^{-i\Lambda_{2+}t} + W(\Lambda_{2-},\omega_2^{\mathrm{mod}})u_{22}\overline{c}_-e^{-i\Lambda_{2-}t}\right) \end{aligned} \tag{D.8}$$

respectively, where $W(\lambda,\omega) = (1 + i(\mathrm{Re}(\lambda) - \omega)\tau_{BW})^{-n}$ is the low-pass filter function for a signal at frequency $\mathrm{Re}(\lambda)$ that is demodulated by a local oscillator, oscillating at frequency ω with a low-pass filter whose order, bandwidth and time-constant are given by n, BW and τ_{BW}, respectively. For all the measurements shown in this chapter and Chapter 6, $n =$ 1, $BW =$ 250 Hz , $\tau_{BW} = (2\pi BW)^{-1} =$ 0.637 ms.

Additionally, the LIA has a settling time τ_{settle} (corresponding to the 99% settling time) that depends on n and τ_{BW}. For all the measurements in this chapter and Chapter 6, $\tau_{\mathrm{settle}} =$ 2.934 ms. To accommodate this, we exclude from any fits the data in an interval τ_{settle} after the start of a ringdown. τ_{settle} is explicitly shown as the light-gray region in Figs. 5.1 and 5.2.

Both $V_{1,2}(t)$ contain equivalent information about the complex motional amplitudes $\overline{c}_\pm$, up to in-principle known multiplicative factors $(\chi_c(\omega), W(\lambda,\omega), g_i, u_{ij})$ with $i,j \in \{1,2\}$ and an overall scaling factor ρ. Recall that the motional eigenstates $\overline{c}_\pm$ at $t = 0$ are extracted from measurements of "simple" ringdowns, i.e. ringdowns without a control path. The signals $V_{1,2}(t)$ recorded in such a measurement (Eq. (D.8)) are fit to:

$$\begin{aligned} V_1(t) &= b_1 + W(\Lambda_{1+},\omega_1^{\mathrm{mod}})A_{11}(0)e^{-i\Lambda_{1+}t} + W(\Lambda_{1-},\omega_1^{\mathrm{mod}})A_{12}(0)e^{-i\Lambda_{1-}t} \\ V_2(t) &= b_2 + W(\Lambda_{2+},\omega_2^{\mathrm{mod}})A_{21}(0)e^{-i\Lambda_{2+}t} + W(\Lambda_{2-},\omega_2^{\mathrm{mod}})A_{22}(0)e^{-i\Lambda_{2-}t} \end{aligned} \tag{D.9}$$

respectively. Here, $\lambda_\pm, b_i, A_{ij}(0)$ with $i,j \in \{1,2\}$ are the eight complex-valued fit parameters, which denote the system's eigenvalues, the heterodyne signal's background, and the amplitudes of decaying exponentials, respectively. To be clear, $\lambda_\pm$ appear implic-

itly in Eq. (D.9) by way of Eq. (2.82). By comparing Eqs. (D.8) and (D.9), the complex amplitudes at $t = 0$ can be written as

$$\begin{aligned}\overline{c}_+(0) &= \frac{A_{11}(0)}{\rho\chi_c(\omega_1^{(0)})g_1u_{11}} = \frac{A_{21}(0)}{\rho\chi_c(\omega_2^{(0)})g_2u_{21}} \\ \overline{c}_-(0) &= \frac{A_{12}(0)}{\rho\chi_c(\omega_1^{(0)})g_1u_{12}} = \frac{A_{22}(0)}{\rho\chi_c(\omega_2^{(0)})g_2u_{22}}\end{aligned} \tag{D.10}$$

which underlines the fact that $V_{1,2}(t)$ contain redundant information about the motional amplitude. In practice, we simply use the fit parameters obtained from the fit to $V_1(t)$ i.e., $A_{11}(0)$ and $A_{12}(0)$ in this case and subsequently calculate $\overline{c}_\pm(0)$. We justify this choice below.

Expressions similar to Eq. (D.9) are used to extract amplitudes of the motional eigenstates at $t = T$ i.e., $\overline{c}_\pm(T)$, from the data corresponding to ringdown after a control path. However, for large T, the motion may decay significantly before the completion of the control path, resulting in low SNR and potentially compromising the quality of the fit. In practice, we observe that the signal near $\omega_1^{(0)}$, and correspondingly $V_1(t)$, tends to have a larger SNR than V_2 near $\omega_2^{(0)}$ after control paths of long duration. Thus, to obtain the complex motional amplitudes at the end of the control path, we fit only $V_1(t)$.

Additionally, we use only three complex fit parameters $\{b_i, A_{11}(T), A_{12}(T)\}$ in this fit, while fixing the eigenvalues $\lambda_\pm$ to the values obtained by fitting the corresponding initialization ringdown data. We justify the choice of fixing the eigenvalues during the fit by noting that **(a)** for all control paths in this chapter and in Chapter 6, the eigenvalues at the beginning of the control path are equal to the eigenvalues at the end of the control path, and **(b)** the individual measurements of "complex-averaged" datasets were interleaved between initialization and control path ringdowns, which reduces the impact of systematic errors caused by temporal drifts. Finally from this fit, we obtain the complex motional amplitudes at $t = T$ as follows:

$$\overline{c}_+(T) = \frac{A_{11}(T)}{\rho\chi_c(\omega_1^{(0)})g_1u_{11}},\ \ \overline{c}_-(T) = \frac{A_{12}(T)}{\rho\chi_c(\omega_1^{(0)})g_1u_{12}} \tag{D.11}$$

D.3 Measuring the propagator matrix $U(T)$

In this section, we describe the procedure to reconstruct the full propagator $U(T)$ via the state vector measurements as described in Secs. D.1 and D.2.

As described previously (Sec. D.1), in order to reconstruct the full propagator $U(T)$ for a control path of duration T, we measure the initial and the final state vectors for two linearly independent initializations of the state vectors $\vec{c}^{(a)}$ and $\vec{c}^{(b)}$. Thus, for every value of T, we measure $\{\overline{c}_+^{(a)}(0), \overline{c}_-^{(a)}(0), \overline{c}_+^{(a)}(T), \overline{c}_-^{(a)}(T)\}$ and $\{\overline{c}_+^{(b)}(0), \overline{c}_-^{(b)}(0), \overline{c}_+^{(b)}(T), \overline{c}_-^{(b)}(T)\}$. The equation that connects the initial and final complex amplitudes is given by:

$$\begin{bmatrix} \overline{c}_+(T) \\ \overline{c}_-(T) \end{bmatrix} = U(T) \begin{bmatrix} \overline{c}_+(0) \\ \overline{c}_-(0) \end{bmatrix} \tag{D.12}$$

where $U(T)$ is the complex-valued propagator matrix. Explicitly,

$$U(T) = \begin{bmatrix} U_{++}(T) & U_{+-}(T) \\ U_{-+}(T) & U_{--}(T) \end{bmatrix} \tag{D.13}$$

The two initializations $\vec{c}^{(a)}(0)$ and $\vec{c}^{(b)}(0)$ result in four linearly independent equations relating the initial and final complex amplitudes:

$$\begin{aligned} \overline{c}_+^{(a)}(T) &= U_{++}(T)\overline{c}_+^{(a)}(0) + U_{+-}(T)\overline{c}_-^{(a)}(0) \\ \overline{c}_+^{(b)}(T) &= U_{++}(T)\overline{c}_+^{(b)}(0) + U_{+-}(T)\overline{c}_-^{(b)}(0) \\ \overline{c}_-^{(a)}(T) &= U_{-+}(T)\overline{c}_+^{(a)}(0) + U_{--}(T)\overline{c}_-^{(a)}(0) \\ \overline{c}_-^{(b)}(T) &= U_{-+}(T)\overline{c}_+^{(b)}(0) + U_{--}(T)\overline{c}_-^{(b)}(0) \end{aligned} \tag{D.14}$$

These four equations are sufficient to solve for $U(T)$, whose elements are given by:

$$U_{++}(T) = \frac{\overline{c}_+^{(a)}(T)\overline{c}_-^{(b)}(0) - \overline{c}_+^{(b)}(T)\overline{c}_-^{(a)}(0)}{\overline{c}_+^{(a)}(0)\overline{c}_-^{(b)}(0) - \overline{c}_+^{(b)}(0)\overline{c}_-^{(a)}(0)}$$

$$U_{+-}(T) = \frac{\bar{c}_+^{(a)}(T)\bar{c}_+^{(b)}(0) - \bar{c}_+^{(b)}(T)\bar{c}_+^{(a)}(0)}{\bar{c}_-^{(a)}(0)\bar{c}_+^{(b)}(0) - \bar{c}_-^{(b)}(0)\bar{c}_+^{(a)}(0)}$$

$$U_{-+}(T) = \frac{\bar{c}_-^{(a)}(T)\bar{c}_-^{(b)}(0) - \bar{c}_-^{(b)}(T)\bar{c}_-^{(a)}(0)}{\bar{c}_+^{(a)}(0)\bar{c}_-^{(b)}(0) - \bar{c}_+^{(b)}(0)\bar{c}_-^{(a)}(0)}$$

$$U_{--}(T) = \frac{\bar{c}_-^{(a)}(T)\bar{c}_+^{(b)}(0) - \bar{c}_-^{(b)}(T)\bar{c}_+^{(a)}(0)}{\bar{c}_-^{(a)}(0)\bar{c}_+^{(b)}(0) - \bar{c}_-^{(b)}(0)\bar{c}_+^{(a)}(0)} \tag{D.15}$$

Using the relation between the motional amplitude and the amplitudes of the heterodyne signal (Eqs. (D.10) and(D.11)), Eq. (D.15) can be further simplified to:

$$U_{++}(T) = \left(\frac{A_{11}^{(a)}(T)A_{12}^{(b)}(0) - A_{11}^{(b)}(T)A_{12}^{(a)}(0)}{A_{11}^{(a)}(0)A_{12}^{(b)}(0) - A_{11}^{(b)}(0)A_{12}^{(a)}(0)}\right)\frac{u_{11}(0)}{u_{11}(T)}$$

$$U_{+-}(T) = \left(\frac{A_{11}^{(a)}(T)A_{11}^{(b)}(0) - A_{11}^{(b)}(T)A_{11}^{(a)}(0)}{A_{12}^{(a)}(0)A_{11}^{(b)}(0) - A_{12}^{(b)}(0)A_{11}^{(a)}(0)}\right)\frac{u_{12}(0)}{u_{11}(T)}$$

$$U_{-+}(T) = \left(\frac{A_{12}^{(a)}(T)A_{12}^{(b)}(0) - A_{12}^{(b)}(T)A_{12}^{(a)}(0)}{A_{11}^{(a)}(0)A_{12}^{(b)}(0) - A_{11}^{(b)}(0)A_{12}^{(a)}(0)}\right)\frac{u_{11}(0)}{u_{12}(T)}$$

$$U_{--}(T) = \left(\frac{A_{12}^{(a)}(T)A_{11}^{(b)}(0) - A_{12}^{(b)}(T)A_{11}^{(a)}(0)}{A_{12}^{(a)}(0)A_{11}^{(b)}(0) - A_{12}^{(b)}(0)A_{11}^{(a)}(0)}\right)\frac{u_{12}(0)}{u_{12}(T)} \tag{D.16}$$

where $A_{ij}^{(k)}(t')$ are the motional amplitudes at $t' = 0$ or $t' = T$ that are returned by fitting the ringdown the heterodyne signal (Sec. D.2) and u_{ij} are given in Eq. (D.4) with $i, j \in \{1, 2\}$.

Notably, the propagator matrix $U(T)$ depends only on the choice of gauge for the eigenvectors that compose S_{D}. Since the adiabatic theorem is only applicable to the mode with least loss [11], only the diagonal component corresponding to the least-dissipative eigenmode (denoted by subscript $++$) contains information about the geometric phase ϕ_B. For closed control loops, we choose $u_{ij}(0) = u_{ij}(T)$, as $t = 0$ and $t = T$ correspond to the same point in parameter space, and consequently, $U_{++}(T)$ and $U_{--}(T)$ are independent of u_{ij} (Eq. (D.16)). These measurements are shown in Fig. 5.3. The off-diagonal elements of $U(T)$ i.e., $U_{+-}(T)$ and $U_{-+}(T)$ use the u_{ij} calculated from the

optomechanical model, and in a gauge where u_{ij} is real-valued.

While the least-dissipative eigenmode (which is amenable to adiabatic evolution) is the main focus of this chapter, we note that the absence of an adiabatic limit for the more damped mode is formally given by $U_{--}(T) \ll U_{+-}(T)$ for large T. This is illustrated in Fig. 5.3(c,d).

D.4 Estimating the asymptote of $\beta(T)$

In this section, we describe data analyses that estimate the asymptote of the measured $\beta(T)$ (Sec. D.1) and important features related to the definition of real-valued phases modulo 2π. The theoretical description that guides our analysis is given in Sec. 2.2.3.1 and A.3.1.

D.4.1 The asymptotic form of the accumulated phase

The expected asymptotic form of the accumulated phase for the least-dissipative state while adiabatically evolving along a control path is given in Eq. (A.8). As a result, in the large T limit we can express the phase acquired along each direction i.e., "forward: $\circlearrowleft$" and "backward: $\circlearrowright$" of a control path, as follows (see also Eq. (2.7) and (D.17)):

$$\begin{aligned}\phi_{\circlearrowleft}(T) &= 2\pi n_{\circlearrowleft} + q_D T - \phi_B + \frac{q_1}{T} + \frac{q_2}{T^2} + \mathcal{O}\left(\frac{1}{T^3}\right)\\ \phi_{\circlearrowright}(T) &= 2\pi n_{\circlearrowright} + q_D T + \phi_B + \frac{q_1}{T} - \frac{q_2}{T^2} + \mathcal{O}\left(\frac{1}{T^3}\right)\end{aligned} \tag{D.17}$$

where $n_{\circlearrowleft}$ and $n_{\circlearrowright}$ are arbitrary integers that correspond to the choice of a branch of the complex logarithm of $\tilde{\phi}(T) = -i\,\mathrm{Log}(U_{++}(T))$. In other words, they reflect the fact that (real-valued) phases are defined modulo 2π. In the following, we describe our convention for the choice of the complex logarithm's branch.

The quantity $\beta(T) = (\phi_{\circlearrowleft} - \phi_{\circlearrowright})/2$ contains only terms of even order in T and the

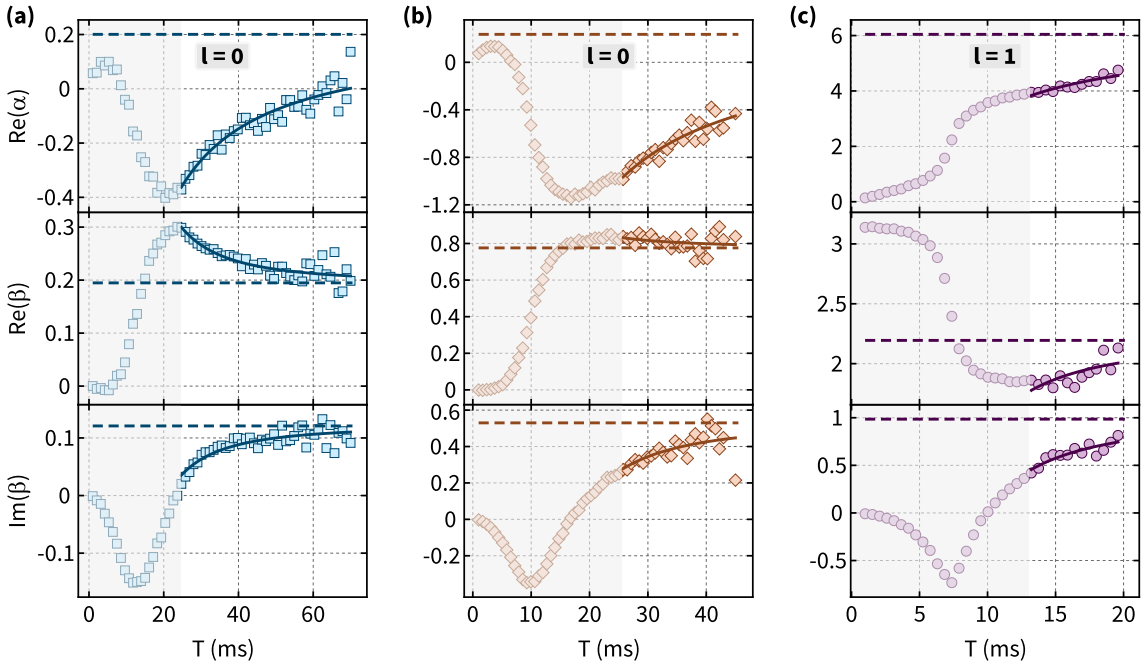

Figure D.3: Examples of asymptote analysis of $\mathrm{Re}(\alpha(T))$ and $\beta(T)$. Shaded region: data excluded from asymptote analysis. **(a)** An example of a measurement in which 2/3 of the data was included in the asymptote analysis. This is Option (2) of Sec. D.4. **(b)** An example of a measurement in which data corresponding to $T \geq 8/|\lambda_+ - \lambda_-|$ was included in the asymptote analysis. This is Option (1) of Sec. D.4. **(c)** An example of a measurement in which 1/3 of the data was included in the asymptote analysis. This is Option (3) of Sec. D.4. Top row: $\mathrm{Re}(\alpha(T))$, Middle and bottom rows: $\mathrm{Re}(\beta(T))$ and $\mathrm{Im}(\beta(T))$, respectively. Points: data, solid curve: fit, dashed line: fitted asymptote, which is used to calculate ϕ_B. For $\mathrm{Re}(\alpha(T))$, this asymptote is binned to determine the integer l as in Fig.. For these measurements, we used the (3,3) and the (5,2) membrane modes with common control parameters: $P_1 = P_2 = P, \eta/2\pi = -$ 50 Hz and $P_4 = 0$, thus Δ_4 is not applicable. For panel (a), $P =$ 17.5 μW, $\delta/2\pi = -1.5$ MHz. For panel (b), $P =$ 17.5 μW, $\delta/2\pi = -0.75$ MHz. For panel (c), $P =$ 20 μW, $\delta/2\pi = -0.25$ MHz.

first three terms in the expansion of $\beta(T)$, in the large-T limit are of the form

$$\beta(T) = \pi(n_{\circlearrowleft} - n_{\circlearrowright}) + \phi_B - \frac{q_2}{T^2} + \mathcal{O}\left(\frac{1}{T^4}\right) \tag{D.18}$$

Ignoring the first term, this is the fit function used to determine ϕ_B from the data as described in Sec. 5.1 and Fig. 5.4, using the complex coefficient q_2 and complex ϕ_B as fit parameters. This shows that without further processing, ϕ_B can only be estimated modulo π from $\beta(T)$.

However, ϕ_B maybe determined modulo 2π by inspecting the quantity $\alpha(T) = \phi_{\circlearrowleft} +$

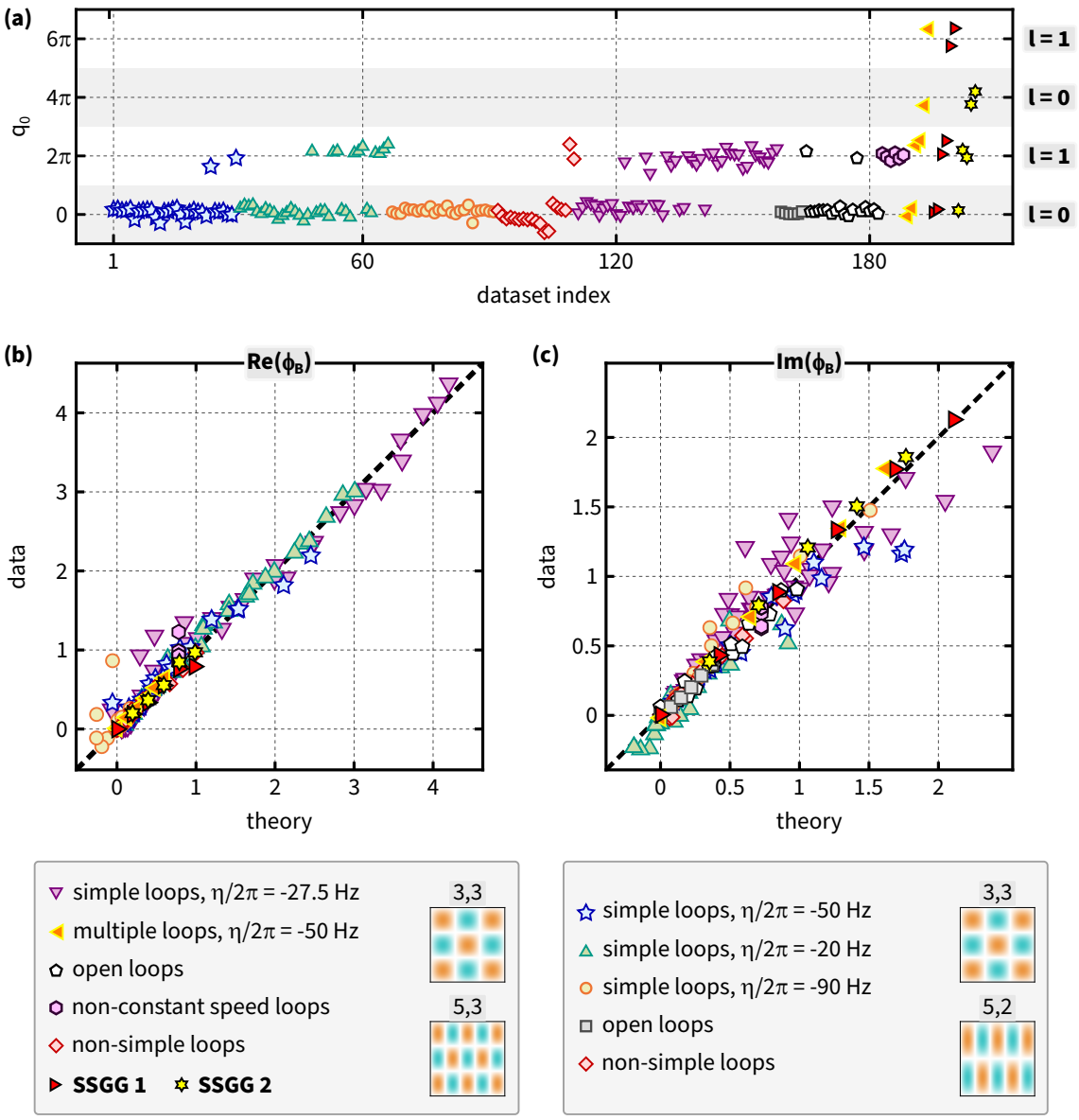

Figure D.4: Summary of all ϕ_B measurements. A collation of all measurements of ϕ_B for this chapter and Chapter 6. ϕ_B are estimated via asymptote analysis of $\mathrm{Re}(\alpha(T))$ and $\beta(T)$ as described in Sec. D.4. **(a)** The fit parameter q_0 obtained by asymptote fitting $\mathrm{Re}(\alpha(T))$. Its value is binned to obtain the integer l. Specifically, we take $l = 0$ for $-\pi < q_0 \leq \pi$ and $3\pi < q_0 \leq 5\pi$ (gray bands), and $l = 1$ for $\pi < q_0 \leq 3\pi$. **(b,c)** The real and the imaginary parts of ϕ_B, respectively. The estimated values are the fit parameters of the asymptote fit to $\beta(T) + l\pi$. They are plotted against the no-free-parameter theory prediction of ϕ_B. Lower panels: the legend for the upper panels. They indicate the pair of membrane modes, the value of η for "simple" control loops, control loops with varying manner of traversal, "non-simple" control loops, multiple loops, open control paths and a foreshadowing of the Geometric amplifier measurements from Chapter 6 (labeled as SSGG).

$\phi_{\circlearrowleft}$, which contains only odd order terms in T:

$$\mathrm{Re}(\alpha(T)) = 2\pi(n_{\circlearrowright} + n_{\circlearrowleft}) + 2\mathrm{Re}(q_D)T + \frac{2q_1}{T} + \mathcal{O}\left(\frac{1}{T^3}\right) \tag{D.19}$$

For every data set that we use to determine $\beta(T)$, we also determine $\alpha(T)$. We then fit $\mathrm{Re}(\alpha(T))$ to large T to $q_0 + 2\mathrm{Re}(q_D)T + 2q_{1,\mathrm{Re}}/T$ with q_0 and $q_{1,\mathrm{Re}}$ as real fit parameters and $q_D = -\int_0^1 \lambda_+(s)ds$ is known from state initialization data (Secs. D.1 and D.2). The measured $\mathrm{Re}(\alpha(T))$ are the corresponding fits are shown in the top row of Fig. D.3. Rounding the best-fit value of $q_0/2\pi$ to the nearest integer then provides $(n_{\circlearrowright} + n_{\circlearrowleft})$. Since the integers $(n_{\circlearrowright} + n_{\circlearrowleft})$ and $(n_{\circlearrowright} - n_{\circlearrowleft})$ have the same sign, we define $l = (n_{\circlearrowright} + n_{\circlearrowleft}) \bmod 2$. All values of the complex Berry phase ϕ_B shown here are equal to $l\pi$ plus the T-independent complex-valued fit coefficient of $\beta(T)$.

Fig. D.4 shows the best-fit value of q_0 resulting from fits to $\mathrm{Re}(\alpha(T))$ for every measurement for complex ϕ_B. These values of q_0 are binned to $l = 0$ for $-\pi < q_0 \leq \pi$ and $3\pi < q_0 \leq 5\pi$ (gray regions) and $l = 1$ for $\pi < q_0 \leq 3\pi$ (white region).

D.4.2 Determining the large-T asymptote of the data

In this section, we describe our protocol to decide what portion of a dataset is used for asymptote analysis, as described in the previous section. For the power series expansions described above to be valid, the data used for fitting must be sufficiently far into the adiabatic regime (corresponding to large T). However, for most control paths, the membrane's motion decays. In practice this sets an upper limit to T (beyond which the membrane's motion is indistinguishable from its thermal fluctuations) which we denote T_{SNR}. The value of T_{SNR} depends upon the control path, as the normal modes' decay rate depends upon the control tones' powers and detuning.

To address this, for each control path we perform asymptotic fits to $\mathrm{Re}(\alpha(T))$ and $\beta(T)$ for $T_{\mathrm{min}} < T < T_{\mathrm{SNR}}$ using one of the three possible options for T_{min}:

Option (1). $T_{\mathrm{min}} = 8/|\lambda_+ - \lambda_-|$. Here, $1/|\lambda_+ - \lambda_-|$ is a typical time scale associated with adiabaticity in non-Hermitian systems.

Option (2). For those control paths in which Option (1) results in $T_{\min} < T_{\mathrm{SNR}}/3$, we instead use $T_{\min} = T_{\mathrm{SNR}}/3$.

Option (3). For those control paths in which Option (1) leaves insufficient data for the asymptotic fit, we instead use $T_{\min} = 2T_{\mathrm{SNR}}/3$.

D.5 System parameters

This section gives the values of the various parameters in the two-mode optomechanical model that describes the experimental two-mode system, as described in Sec. 2.3.2 with the addition of the photothermal effect (Sec. 4.4.3.1). The parameter values are obtained from device controllers (Secs. 4.4.3 and 4.6.1), cavity spectroscopy (Sec. 4.2.3.3) and two/three-tone mechanical spectroscopy characterization (or multi-tone DBA: see Secs. 4.5.1, 4.5.3 and Figs. C.5-C.7, 4.15, 4.16 and 4.19). The value and the drift range of each parameter along with its source is given in Table D.1.

Parameter	Value	Drift range	Source
λ (nm)	1549.95	0.01	Laser controller
$\kappa/2\pi$ (MHz)	2.32	0.05	Multi-tone DBA
ϵ	0.85	0.01	Cavity spectroscopy
$\kappa_{\mathrm{in}}/\kappa$	0.41	0.01	Cavity spectroscopy
$\tilde{\omega}_1^{(0)}/2\pi$ (Hz)	2423969	20	Bare Brownian
$\tilde{\omega}_2^{(0)}/2\pi$ (Hz)	3076488	20	Bare Brownian
$\tilde{\omega}_3^{(0)}/2\pi$ (Hz)	3331064	20	Bare Brownian
$\tilde{\gamma}_1^{(0)}/2\pi$ (Hz)	3.6	0.5	Bare Brownian
$\tilde{\gamma}_2^{(0)}/2\pi$ (Hz)	16.2	0.5	Bare Brownian
$\tilde{\gamma}_3^{(0)}/2\pi$ (Hz)	3.4	0.5	Bare Brownian
$g_1/2\pi$ (Hz)	4.4	0.1	Multi-tone DBA
$g_2/2\pi$ (Hz)	3.9	0.1	Multi-tone DBA
$g_3/2\pi$ (Hz)	2.6	0.1	Multi-tone DBA
$A_1/2\pi$ (μHz)	-2.8	0.5	Multi-tone DBA
$A_2/2\pi$ (μHz)	-4.0	0.5	Multi-tone DBA
$A_3/2\pi$ (μHz)	-3.6	0.5	Multi-tone DBA
$\Delta_0/2\pi$ (kHz)	-10	10	Multi-tone DBA

Table D.1: System parameters. λ: the laser wavelength, its drift range represents three separate instances of static tuning that were made over time while performing measurements reported in this chapter and Chapter 6. κ: the optical cavity linewidth. ϵ: the cavity-mode-matching efficiency. κ_{in}: the optical cavity input coupling rate. $\tilde{\omega}_i^{(0)}$: the bare resonance frequency of the i^{th} mechanical mode (i.e., in the absence of any optomechanical effects). $\tilde{\gamma}_i^{(0)}$: the bare energy damping rate of the i^{th} mechanical mode. g_i: the optomechanical coupling rate between the optical cavity and the i^{th} mechanical mode. A_i: the photothermal coupling rate between the optical cavity and the i^{th} mechanical mode. Δ_0: detuning offset of the control tones from the optical cavity resonance(see Sec. 4.4.3 and 4.6.1). For bare resonance frequencies ($\omega^{(0)}$), energy damping rates ($\gamma^{(0)}$), optomechanical coupling rates (g) and photothermal coupling rates (A), the subscript denotes the mechanical mode: 1→(3,3), 2→(5,2), 3→(5,3). The best-fit values are given for a typical day. Small drifts in these parameters are tracked throughout the measurements prescribed in this chapter and Chapter 6, and are included in all comparisons with theory. The third column gives the extent of the parameters' drift over several months, while the fourth column provides the source of these parameter values.

Appendix E

Methods for Chapter 5

E.1 Additional views of SSGG data

Here we provide additional views of the SSGG data shown in panel (d) of Figs. 6.9 and 6.11. For each complex averaged trace shown in panel (d) of Fig. 6.9 (Fig. 6.11), Figs. E.1-E.4 (Figs. E.5-E.8) illustrate the corresponding individual traces, showing the amplitude as well as the phase of the mechanical motion. These illustrations provide a tangible evidence of phase-coherence of the mechanical motion undergoing SSGG, and its loss thereof with increasing duration of control loops ($\mathcal{C}_{\mathrm{amp},n}$) that produce SSGG.

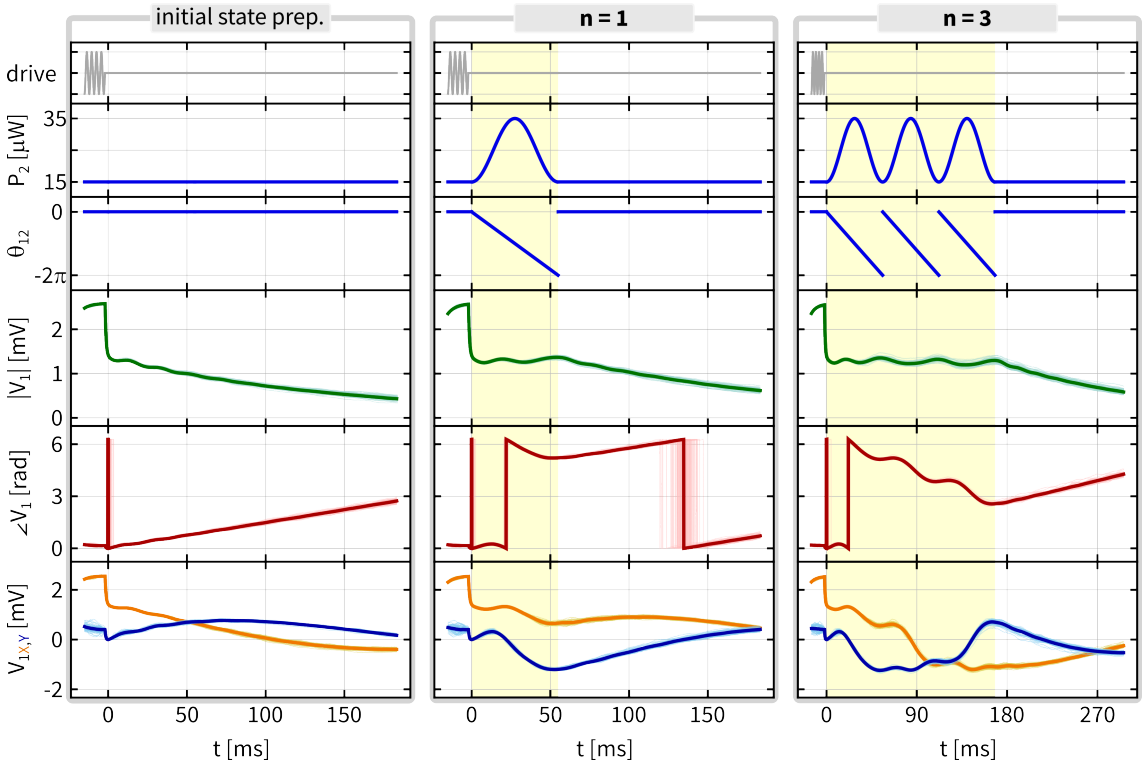

Figure E.1: Preparation of the initial state vector $\vec{c}^{(a)}(0)$, and its evolution to $\vec{c}^{(a)}(T)$ along control loops that produce SSGG - family I, part I. First column: measurements for $\vec{c}^{(a)}(0)$ i.e, with no control loop. **Second column**: measurements for $\vec{c}^{(a)}(T)$ for $\mathcal{C}_{\mathrm{amp},1}$ with gain ~ 0 dB. **Third column**: measurements for $\vec{c}^{(a)}(T)$ for $\mathcal{C}_{\mathrm{amp},3}$ with gain ~ 0 dB. For all columns, first row: a schematic of the driving force applied to the membrane, which is switched off at $t = 0$; second row: a plot control power $P_2(t)$ and third row: a plot of the beat-note phase $\theta_{12}(t)$, for the respective initialization/control loop. Solid green, red, dark-orange and dark-blue curves: the "complex-averaged" magnitude, the phase, the in-phase and the quadrature part of the heterodyne signal, respectively and for measurements shown in each column. The faint colored counterparts correspond to the individual traces. For this measurement, we used the same membrane modes and the same other control parameters as in Figs. 6.8, 6.9, 6.12, 6.14 and 6.15.

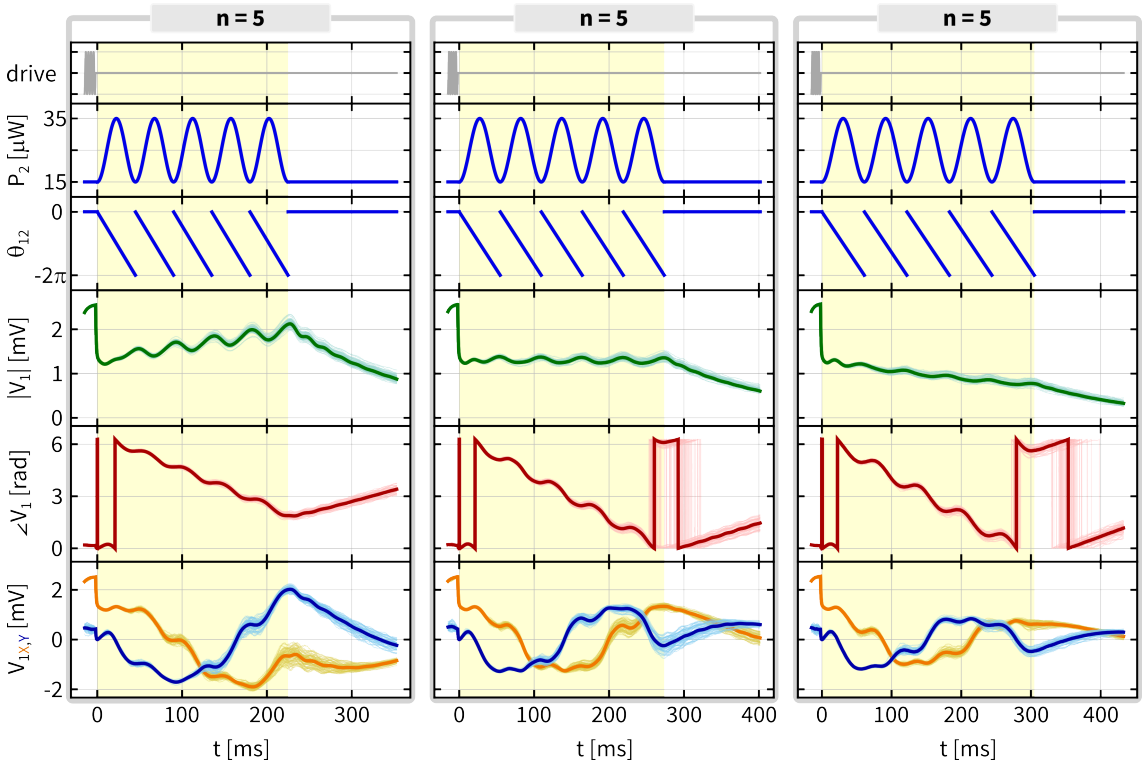

Figure E.2: Evolution to state vector $\vec{c}^{(a)}(T)$ along control loops that produce SSGG - family I, part II. First column: measurements for $\vec{c}^{(a)}(T)$ for $\mathcal{C}_{\mathrm{amp},5}$ with gain > 0 dB. **Second column**: measurements for $\vec{c}^{(a)}(T)$ for $\mathcal{C}_{\mathrm{amp},5}$ with gain ~ 0 dB. **Third column**: measurements for $\vec{c}^{(a)}(T)$ for $\mathcal{C}_{\mathrm{amp},5}$ with gain < 0 dB. For all columns, first row: a schematic of the driving force applied to the membrane, which is switched off at $t = 0$; second row: a plot control power $P_2(t)$ and third row: a plot of the beat-note phase $\theta_{12}(t)$, for the respective initialization/control loop. Solid green, red, dark-orange and dark-blue curves: the "complex-averaged" magnitude, the phase, the in-phase and the quadrature part of the heterodyne signal, respectively and for measurements shown in each column. The faint colored counterparts correspond to the individual traces. For this measurement, we used the same membrane modes and the same other control parameters as in Figs. E.1, 6.8, 6.9, 6.12, 6.14 and 6.15.

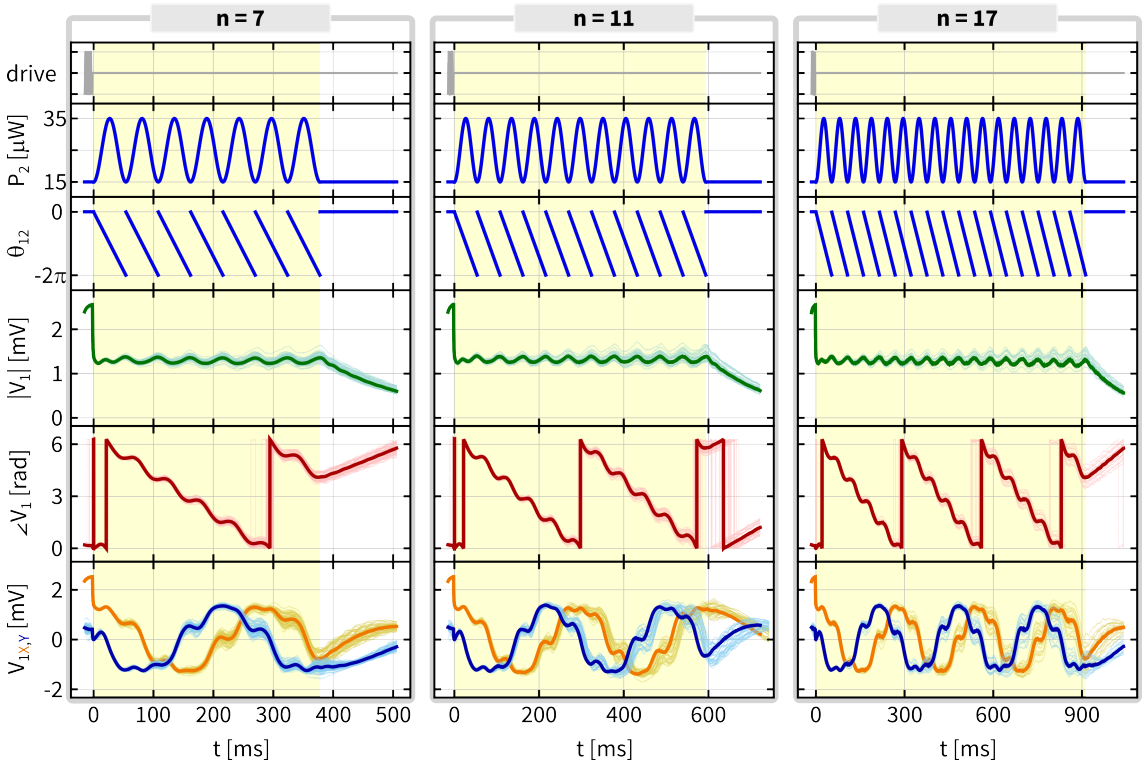

Figure E.3: Evolution to state vector $\vec{c}^{(a)}(T)$ along control loops that produce SSGG - family I, part III. First column: measurements for $\vec{c}^{(a)}(T)$ for $\mathcal{C}_{\mathrm{amp},7}$ with gain $\sim$ 0 dB. **Second column**: measurements for $\vec{c}^{(a)}(T)$ for $\mathcal{C}_{\mathrm{amp},11}$ with gain $\sim$ 0 dB. **Third column**: measurements for $\vec{c}^{(a)}(T)$ for $\mathcal{C}_{\mathrm{amp},17}$ with gain $\sim$ 0 dB. For all columns, first row: a schematic of the driving force applied to the membrane, which is switched off at $t = 0$; second row: a plot control power $P_2(t)$ and third row: a plot of the beat-note phase $\theta_{12}(t)$, for the respective initialization/control loop. Solid green, red, dark-orange and dark-blue curves: the "complex-averaged" magnitude, the phase, the in-phase and the quadrature part of the heterodyne signal, respectively and for measurements shown in each column. The faint colored counterparts correspond to the individual traces. For this measurement, we used the same membrane modes and the same other control parameters as in Figs. E.1, E.2, 6.8, 6.9, 6.12, 6.14 and 6.15.

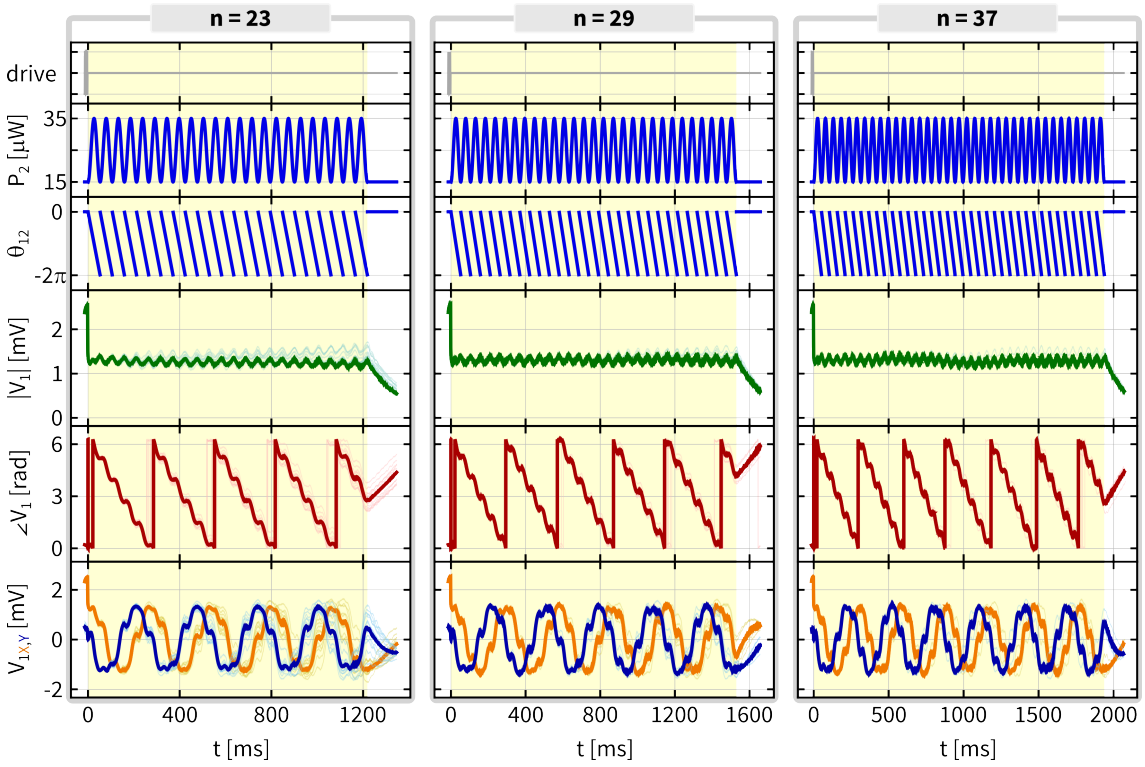

Figure E.4: Evolution to state vector $\vec{c}^{(a)}(T)$ along control loops that produce SSGG - family I, part IV. First column: measurements for $\vec{c}^{(a)}(T)$ for $\mathcal{C}_{\mathrm{amp},23}$ with gain $\sim$ 0 dB. **Second column**: measurements for $\vec{c}^{(a)}(T)$ for $\mathcal{C}_{\mathrm{amp},29}$ with gain $\sim$ 0 dB. **Third column**: measurements for $\vec{c}^{(a)}(T)$ for $\mathcal{C}_{\mathrm{amp},37}$ with gain $\sim$ 0 dB. For all columns, first row: a schematic of the driving force applied to the membrane, which is switched off at $t = 0$; second row: a plot control power $P_2(t)$ and third row: a plot of the beat-note phase $\theta_{12}(t)$, for the respective initialization/control loop. Solid green, red, dark-orange and dark-blue curves: the "complex-averaged" magnitude, the phase, the in-phase and the quadrature part of the heterodyne signal, respectively and for measurements shown in each column. The faint colored counterparts correspond to the individual traces. For this measurement, we used the same membrane modes and the same other control parameters as in Figs. E.1-E.3, 6.8, 6.9, 6.12, 6.14 and 6.15.

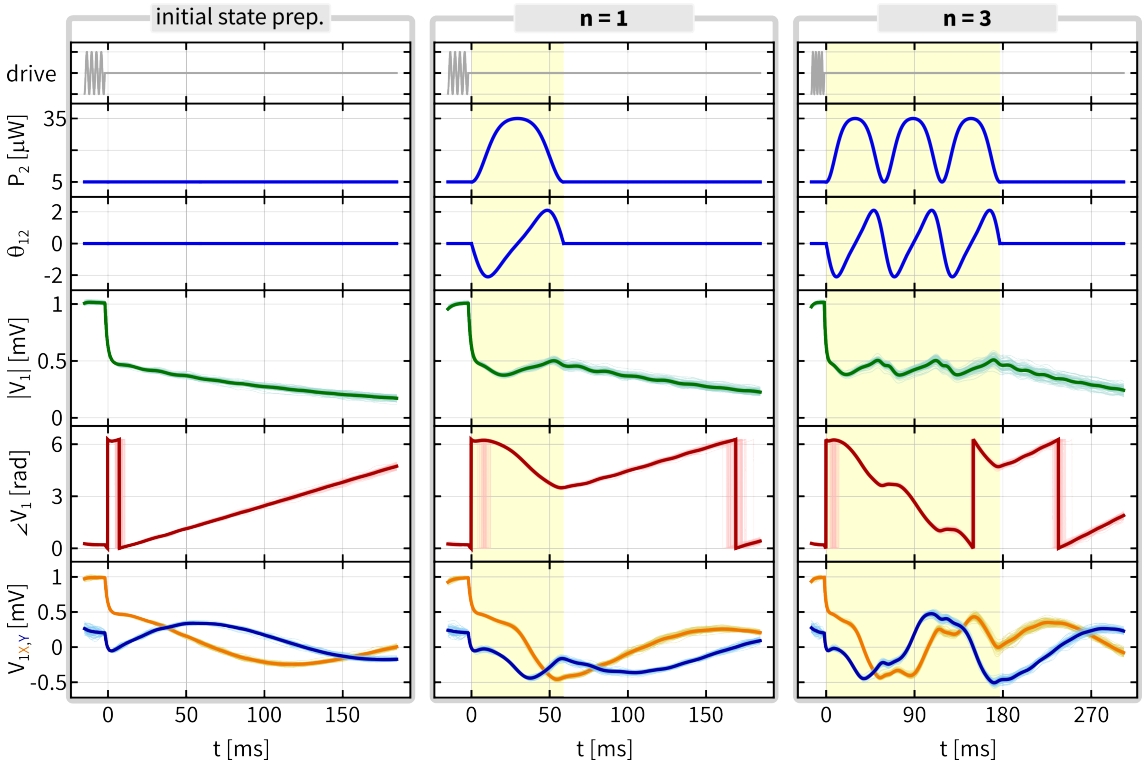

Figure E.5: Preparation of the initial state vector $\vec{c}^{(a)}(0)$, and its evolution to $\vec{c}^{(a)}(T)$ along control loops that produce SSGG - family II, part I. First column: measurements for $\vec{c}^{(a)}(0)$ i.e, with no control loop. **Second column**: measurements for $\vec{c}^{(a)}(T)$ for $\mathcal{C}_{\mathrm{amp},1}$ with gain ~ 0 dB. **Third column**: measurements for $\vec{c}^{(a)}(T)$ for $\mathcal{C}_{\mathrm{amp},3}$ with gain ~ 0 dB. For all columns, first row: a schematic of the driving force applied to the membrane, which is switched off at $t = 0$; second row: a plot control power $P_2(t)$ and third row: a plot of the beat-note phase $\theta_{12}(t)$, for the respective initialization/control loop. Solid green, red, dark-orange and dark-blue curves: the "complex-averaged" magnitude, the phase, the in-phase and the quadrature part of the heterodyne signal, respectively and for measurements shown in each column. The faint colored counterparts correspond to the individual traces. For this measurement, we used the same membrane modes and the same other control parameters as in Figs. 6.10, 6.11 and 6.13.

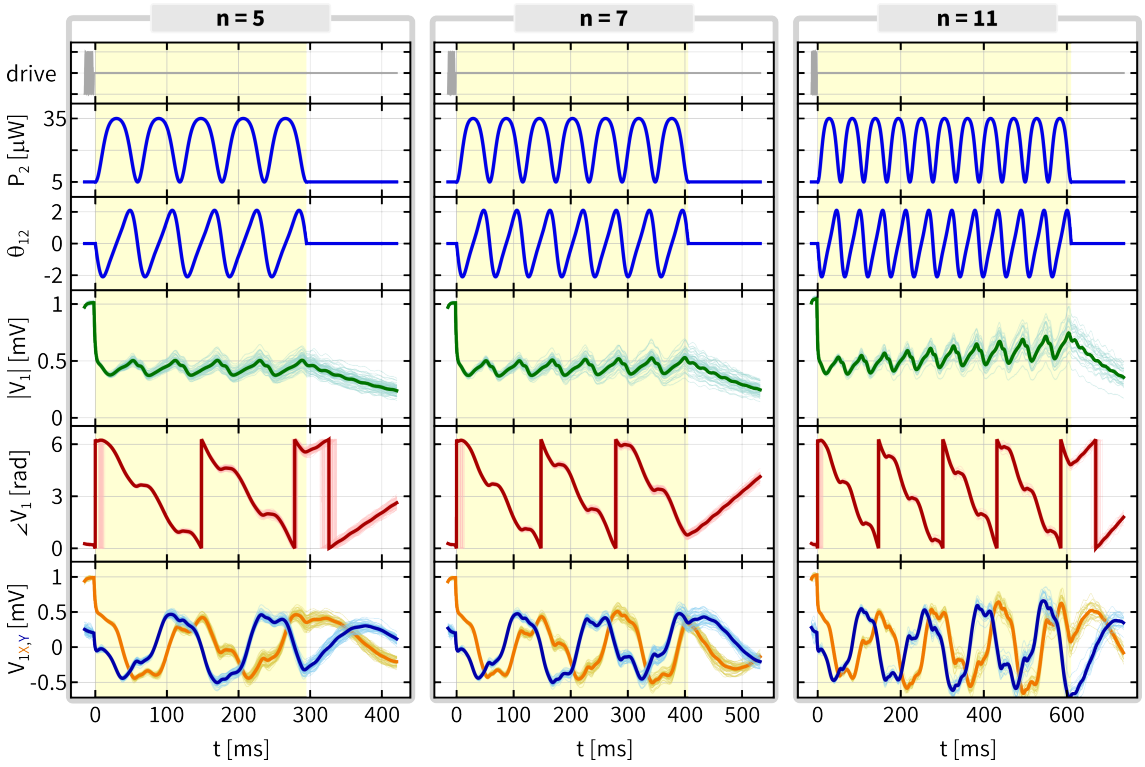

Figure E.6: Evolution to state vector $\vec{c}^{(a)}(T)$ along control loops that produce SSGG - family II, part II. First column: measurements for $\vec{c}^{(a)}(T)$ for $\mathcal{C}_{\mathrm{amp},5}$ with gain $\sim$ 0 dB. **Second column**: measurements for $\vec{c}^{(a)}(T)$ for $\mathcal{C}_{\mathrm{amp},7}$ with gain $\sim$ 0 dB. **Third column**: measurements for $\vec{c}^{(a)}(T)$ for $\mathcal{C}_{\mathrm{amp},11}$ with gain $>$ 0 dB. For all columns, first row: a schematic of the driving force applied to the membrane, which is switched off at $t = 0$; second row: a plot control power $P_2(t)$ and third row: a plot of the beat-note phase $\theta_{12}(t)$, for the respective initialization/control loop. Solid green, red, dark-orange and dark-blue curves: the "complex-averaged" magnitude, the phase, the in-phase and the quadrature part of the heterodyne signal, respectively and for measurements shown in each column. The faint colored counterparts correspond to the individual traces. For this measurement, we used the same membrane modes and the same other control parameters as in Figs. E.5, 6.10, 6.11 and 6.13.

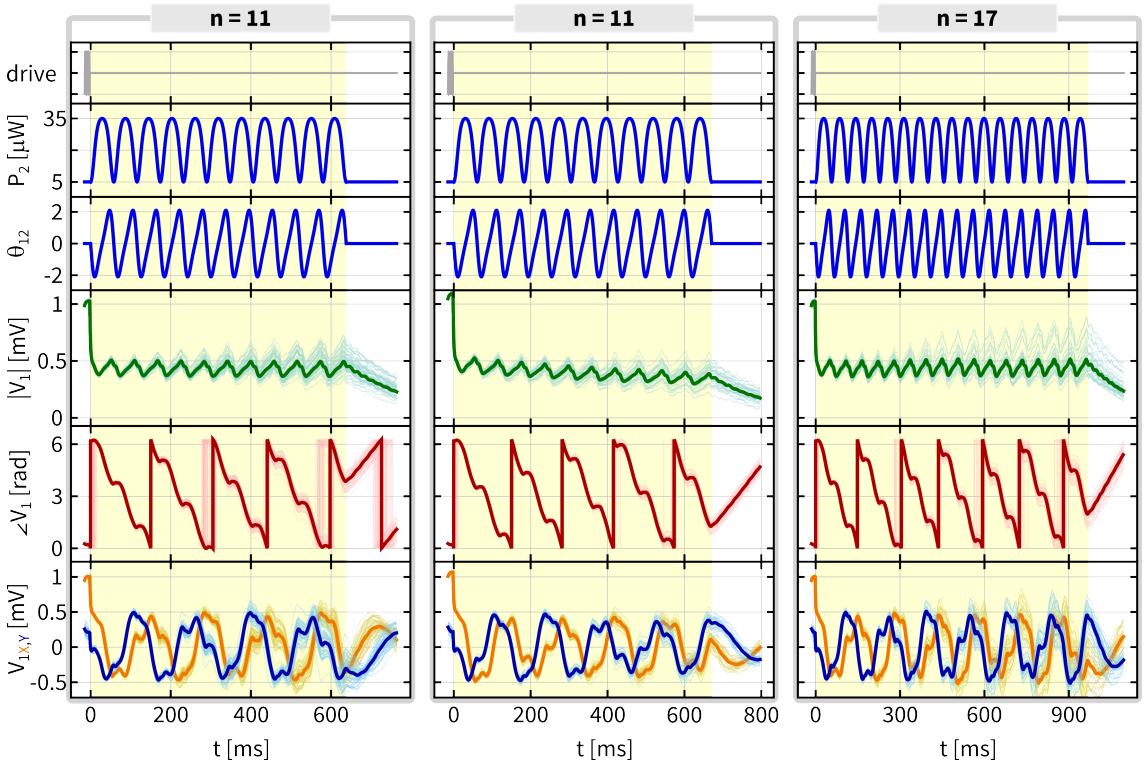

Figure E.7: Evolution to state vector $\vec{c}^{(a)}(T)$ along control loops that produce SSGG - family II, part III. First column: measurements for $\vec{c}^{(a)}(T)$ for $\mathcal{C}_{\mathrm{amp},11}$ with gain ~ 0 dB. **Second column**: measurements for $\vec{c}^{(a)}(T)$ for $\mathcal{C}_{\mathrm{amp},11}$ with gain < 0 dB. **Third column**: measurements for $\vec{c}^{(a)}(T)$ for $\mathcal{C}_{\mathrm{amp},17}$ with gain ~ 0 dB. For all columns, first row: a schematic of the driving force applied to the membrane, which is switched off at $t = 0$; second row: a plot control power $P_2(t)$ and third row: a plot of the beat-note phase $\theta_{12}(t)$, for the respective initialization/control loop. Solid green, red, dark-orange and dark-blue curves: the "complex-averaged" magnitude, the phase, the in-phase and the quadrature part of the heterodyne signal, respectively and for measurements shown in each column. The faint colored counterparts correspond to the individual traces. For this measurement, we used the same membrane modes and the same other control parameters as in Figs. E.5, E.6, 6.10, 6.11 and 6.13.

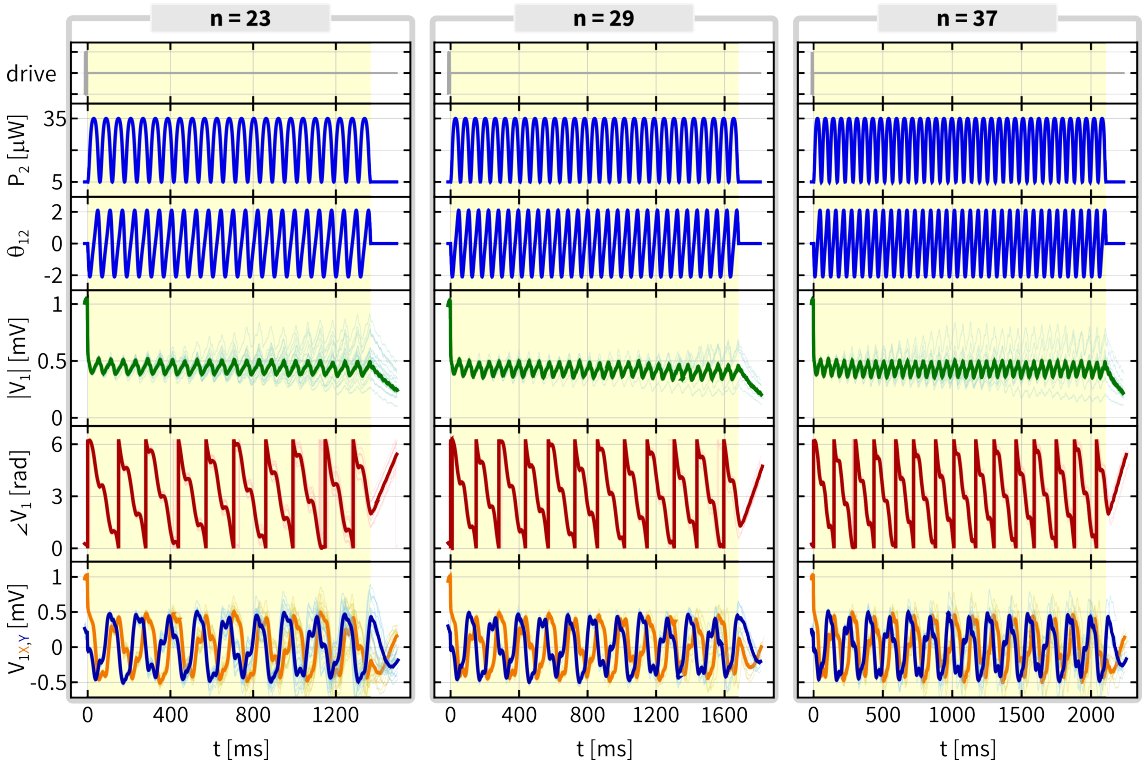

Figure E.8: Evolution to state vector $\vec{c}^{(a)}(T)$ along control loops that produce SSGG - family IV, part III. First column: measurements for $\vec{c}^{(a)}(T)$ for $\mathcal{C}_{\mathrm{amp},23}$ with gain $\sim$ 0 dB. **Second column**: measurements for $\vec{c}^{(a)}(T)$ for $\mathcal{C}_{\mathrm{amp},29}$ with gain $\sim$ 0 dB. **Third column**: measurements for $\vec{c}^{(a)}(T)$ for $\mathcal{C}_{\mathrm{amp},37}$ with gain $\sim$ 0 dB. For all columns, first row: a schematic of the driving force applied to the membrane, which is switched off at $t = 0$; second row: a plot control power $P_2(t)$ and third row: a plot of the beat-note phase $\theta_{12}(t)$, for the respective initialization/control loop. Solid green, red, dark-orange and dark-blue curves: the "complex-averaged" magnitude, the phase, the in-phase and the quadrature part of the heterodyne signal, respectively and for measurements shown in each column. The faint colored counterparts correspond to the individual traces. For this measurement, we used the same membrane modes and the same other control parameters as in Figs. E.5-E.7, 6.10, 6.11 and 6.13.

Appendix F

Methods for Chapter 7

Here we provide additional technical details for the measurements described in Chapter 7. These include: **(i)** a detailed description of initial state preparation (Sec. F.1) following up on Sec. 7.1.3.1; **(ii)** elucidating a pitfall of Jordan decomposition used in Chapters 2 and herein, and subsequently remedying it using Schur decomposition (Sec. F.2);**(iii)** extracting state vectors, λ_{EP} and R by fitting corresponding ringdown measurements (Sec. F.3), **(iv)** estimating the asymptote of $\beta_{\mathrm{deg}}(T)$ to obtain $\{\phi_{B,\mathrm{deg}}, R\}$ (Sec. F.4), **(v)** additional views of SS$\sqrt{T}$G data (Sec. F.5), and **(vi)** list the system parameters of the experimental apparatus as setup for this chapter in Sec. F.6.

F.1 Initial state preparation

In this section, we detail the procedure for preparing the initial state that is prescribed [88, 89] for adiabatic evolution in $\mathcal{EP}_2$. We begin by providing intuition for how one may prepare the initial state as the least-dissipative eigenvector of H', the matrix that governs evolution in $\mathcal{EP}_2$ (Sec. F.1.1). We then describe and evaluate two protocols that can accomplish this task (Sec. F.1.2). Finally, we describe measurements to verify the chosen protocol for initial state preparation (Sec. F.1.3).

F.1.1 Non-Hermitian Adiabatic theorem is our ally

The intuition for how one may prepare the initial state as the least-dissipative eigenvector of H' is straightforward. One simply has to recall a key feature of the non-Hermitian adiabatic theorem (Sec. 2.2.2.2) i.e., during adiabatic evolution along a generic control loop, the system's state tends to transition into the least-dissipative eigenvector (conditional on its existence). This transition is irrespective of the initial state except for the trivial case when the initial state is already the least-dissipative eigenvector.

This feature is encoded in Eq. (2.9) and corrections to its right hand side are $\mathcal{O}(1/T^{\alpha})$ where $T \gg 1$ is the duration of control loop and $\alpha > 0$. For the non-degenerate case, $\alpha = 1$ [27] and $\alpha = 1-1/N$ for the N-fold degenerate N mode system [88]. Therefore, a protocol that incorporates the non-Hermitian adiabatic evolution is guaranteed to prepare the initial state as the least-dissipative eigenvector of H'.

F.1.2 Two protocols for initial state preparation

In this section, we describe and evaluate two protocols for initial state preparation.

Protocol I

The first protocol applies to any generic control loop $\mathcal{C}_{\text{gen}}$ that allows for non-Hermitian adiabatic evolution. To describe this protocol, we consider a $\mathcal{C}_{\text{gen}}$ traversed once in duration T_1. The protocol proceeds as follows:

Steps

(1) At time $t = -mT_1 \equiv -T_{p1}$, prepare an arbitrary initial state $\vec{x}(t = -mT_1)$ with $m \in \mathbb{N}$.

(2) For duration mT_1, traverse m repetitions of $\mathcal{C}_{\text{gen}}$, while $\vec{x}(t = -mT_1)$ evolves to $\vec{x}(0)$. For large T_1, this step prepares $\vec{x}(0)$ as the least dissipative eigenvector of $H'(s = 0)$ corresponding to $\mathcal{C}_{\text{gen}}$ traversed $n \in \mathbb{N}$ times in duration $T = nT_1$, with sufficient accuracy [11, 88].

Subsequently, $\mathcal{C}_{\rm gen}$ can be traversed $n \in \mathbb{N}$ times in duration $T = nT_1$, while $\vec{x}(0)$ evolves to $\vec{x}(T)$, and the rest of the story follows from the adiabatic theorem.

Evaluation

To systematically evaluate this protocol, we consider the "simple" $\mathcal{C}_{\rm deg}$ studied in Sec. 7.1. For this exercise, we take $m = 1$ such that $T_{p1} = T_1$, and as a first step, we numerically simulate $\vec{x}(-T_{p1} \leq t \leq 0)$ for a specific duration of $\mathcal{C}_{\rm deg}$ traversal.

The cyan region in Fig. F.1(a) sketches the initial state preparation protocol, while panels (b) and (c) show Bloch sphere representation [320] of $\vec{x}(t)$ corresponding to $\vec{x}(-T_{p1}) = (1,0)^{\rm T}$ and $(0,1)^{\rm T}$, respectively, for $T_{p1} = T_1 =$ 100 ms. In both cases, $\vec{x}(-T_{p1})$, shown as the orange arrow, evolves as the black curve that represents $\vec{x}(-T_{p1} \leq t \leq 0)$, and approaches the least-dissipative eigenvector of $H'(s=0)$ corresponding to $\mathcal{C}_{\rm deg}$, shown as the green arrow.

To quantify this approach, we calculate the fidelity $\mathcal{F}$ of $\vec{x}(t)$ being the least-dissipative right eigenvector $\vec{u}'_+(t)$ of $H'(t)$. It is given by $\mathcal{F}(t) = |\vec{v}'_+(t) \cdot \vec{x}(t)|^2$, where $\vec{v}'_+(t)$ is the corresponding least-dissipative left eigenvector, and we enforce $\vec{v}'_\pm(t) \cdot \vec{u}'_\pm(t) = 1$ and $\vec{v}'_\pm(t) \cdot \vec{u}'_\mp(t) = 0$, where $\vec{v}'_-(t)$ and $\vec{u}'_-(t)$ represent the other left and right eigenvectors of H', respectively. Fig. F.1(d-top) shows $1 - \mathcal{F}(t) = |\vec{v}'_-(t) \cdot \vec{x}(t)|^2$ calculated[1] for both cases that are illustrated in panels (b) and (c). We take $1 - \mathcal{F}(0)$ to be the first figure of merit for this initial state preparation protocol. For this protocol, $1 - \mathcal{F}(0) < 10^{-12}$. We consider this value to be overwhelmingly small, and quite possibly beyond our measurement capabilities.

Additionally, we track the amplitude of the state vector during this protocol. All the work described in this chapter utilizes a system of damped harmonic oscillators, and it is a practical consideration that the decay of the state vector amplitude be nominally small, such that the prepared initial state vector has sufficient signal-to-noise ratio, for further processing and experimentation. Fig. F.1(d-bottom) shows the state vector amplitude $|\vec{x}(-T_{p1} \leq t \leq 0)|$ with $|\vec{x}(-T_{p1})| = 1$. We take $|\vec{x}(0)|$ to be the second figure of merit for this initial state preparation protocol. For this protocol, $|\vec{x}(0)| \sim$ 0.2. We consider

[1] Starting with $\mathcal{F} = |\vec{v}'_+ \cdot \vec{x}|^2$, we have $1 - \mathcal{F} = 1 - |\vec{v}'_+ \cdot \vec{x}|^2 = |\vec{v}'_+ \cdot \vec{x}|^2 + |\vec{v}'_- \cdot \vec{x}|^2 - |\vec{v}'_+ \cdot \vec{x}|^2 = |\vec{v}'_- \cdot \vec{x}|^2$.

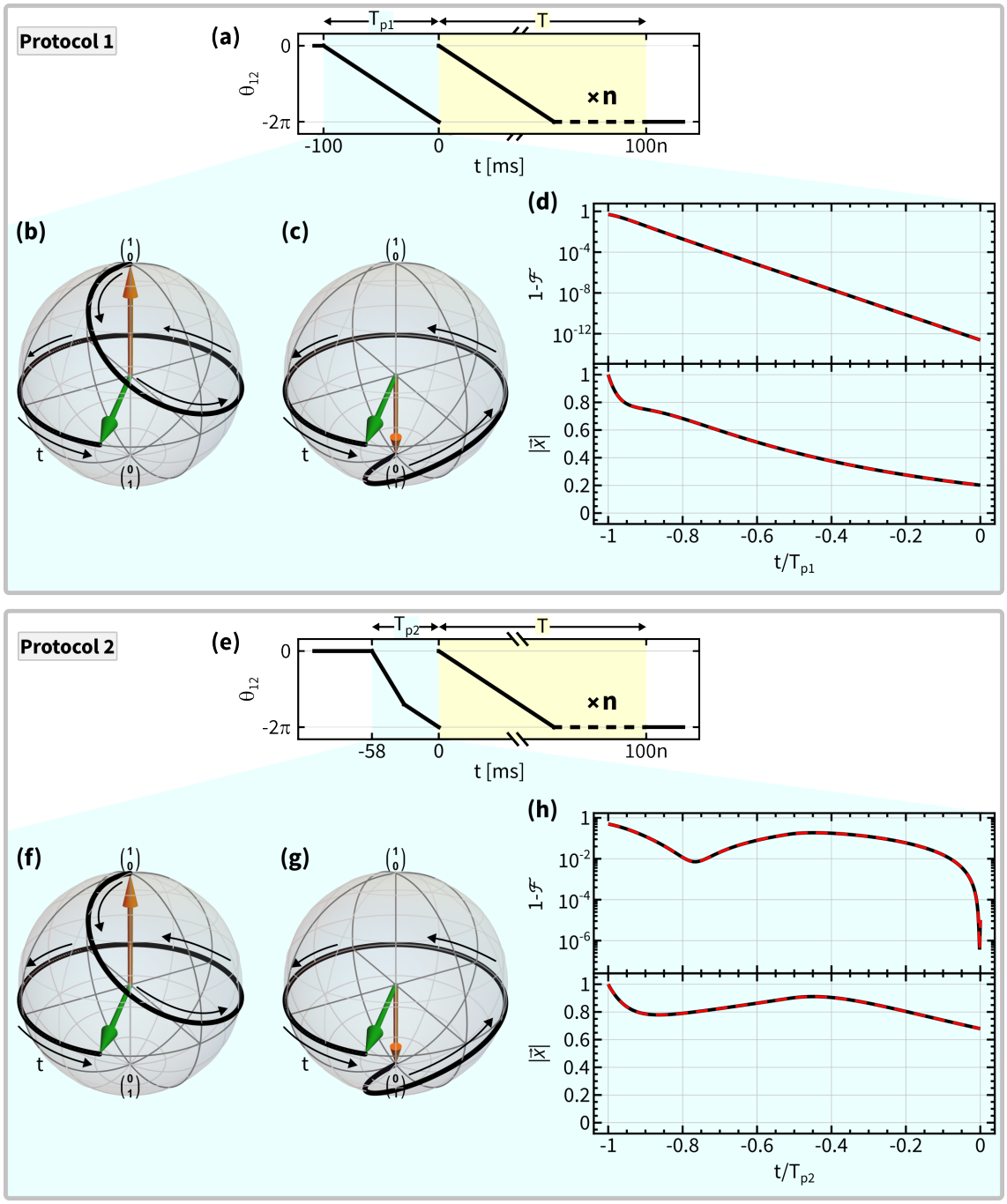

Figure F.1: Evaluating initial state preparation protocols - part I. Top panel: protocol I. **(a)** $\theta_{12}(t)$ (black curve), with cyan and yellow regions corresponding to initial state preparation ($-T_{p1} \leq t < 0$) and $\mathcal{C}_{\text{deg}}$ ($0 \leq t \leq T$), respectively. **(b)** Bloch sphere representation of numerically simulated $\vec{x}(t)$ during initial state preparation with $\vec{x}(-T_{p1}) = (1,0)^{\text{T}}$. The curved arrows indicate $-T_{p1} \leq t < 0$. **(c)** Same as (b) but for $\vec{x}(-T_{p1}) = (0,1)^{\text{T}}$. **(d)** Numerically simulated $1 - \mathcal{F}(t)$ (top panel) and $|\vec{x}(t)|$ (bottom panel) during initial state preparation. Black and dashed red curves correspond to $\vec{x}(-T_{p1}) = (1,0)^{\text{T}}$ and $(0,1)^{\text{T}}$, respectively. **Bottom panel:** Same as the top panel but for initial state preparation protocol II. For these simulations, $T_{p1} = 100$ ms, $T = 100n$ ms with $n \in \mathbb{N}$, and we used the same $\mathcal{C}_{\text{deg}}$ as in Sec. 7.1.

this value to be insufficient for further processing and experimentation. Refs. [321, 322] show an interactive view of Fig. F.1(a-d).

As a next step for evaluating this protocol, we repeat the above exercise as a function of $T_1 = T/n$. Fig. F.2(a-c) illustrates the protocol, its corresponding parameters and the resulting figures of merit, respectively. Both figures of merit are show expected trends:

(a) The infidelity $1 - \mathcal{F}(0)$ reduces with increasing T_1, as predicted by Refs. [11, 88]. However, we do not analyze its explicit dependence on T_1 in this work, and relegate it for future studies. At large T_1, $1 - \mathcal{F}(0)$ is agnostic to the choice of $\vec{x}(-T_{p1})$, in this example. However, this is not a general result, but rather specific given the choice of $\mathcal{C}_{\text{deg}}$.

(b) The prepared state vector amplitude $|\vec{x}(0)|$ reduces with increasing T_1. This is due to linear dynamical loss dominating at large T_1. The non-monotonic behavior at intermediate values of T_1 is due to the interplay between the gain from $\sqrt{T}$-dynamical phase and linear dynamical loss. Finally, $|\vec{x}(0)|$ is also agnostic to the choice of $\vec{x}(-T_{p1})$, in this example. However, this is not a general result, but rather specific given the choice of $\mathcal{C}_{\text{deg}}$.

Result and discussion

In conclusion, we find that this protocol is conceptually simple but has a crucial shortcoming namely the insufficient value of $|\vec{x}(0)|$ for large T_1, thus making it less practical for our purposes. The situation exacerbates if we take $m > 1$, which by construction, requires m times the preparation duration, which in turn incurs e^m times the linear dynamical loss. One alternative could be to explore $\mathcal{C}_{\text{deg}}$ with less linear dynamical loss. The other alternative could be to try a modified initial state preparation protocol that requires smaller preparation durations, i.e., small T_p, thereby reducing the effect of linear dynamical loss. We took the second approach, and it is detailed below.

Protocol II

This protocol aims to improve on its predecessor by retaining sufficient state vector amplitude $|\vec{x}(0)|$ for large T_1, while maintaining reasonable values of preparation fidelity.

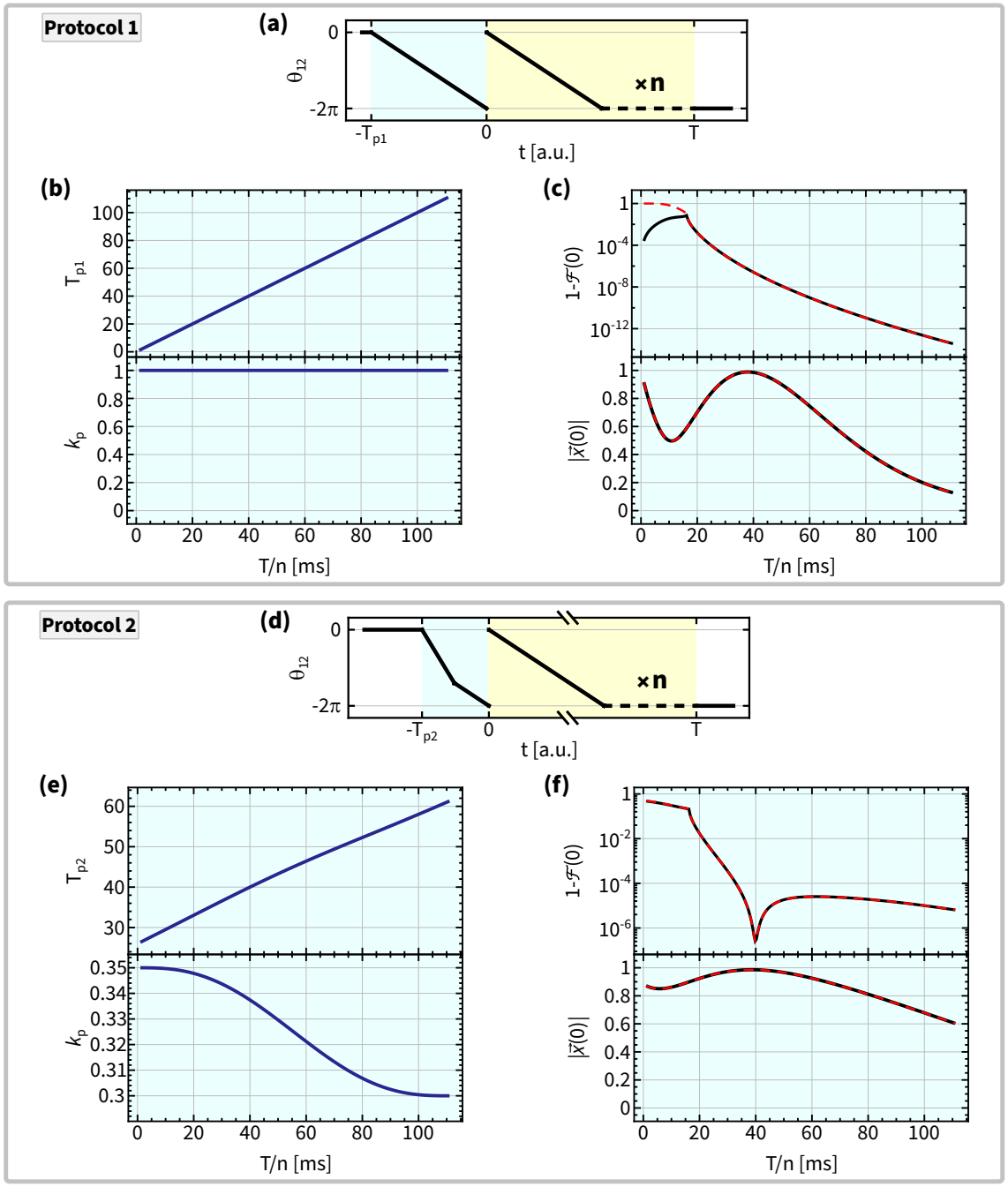

Figure F.2: Evaluating initial state preparation protocols - part II. Top panel: protocol I. **(a)** $\theta_{12}(t)$ (black curve), with cyan and yellow regions corresponding to initial state preparation ($-T_{p1} \leq t < 0$) and $\mathcal{C}_{\rm deg}$ ($0 \leq t \leq T$), respectively. **(b)** T_{p1} (top panel) and k_p (bottom panel) versus $T_1 = T/n$. For this case, $T_{p1} = T_1$ and $k_p = 1$. **(c)** Numerically simulated $1 - \mathcal{F}(0)$ (top panel) and $|\vec{x}(0)|$ (bottom panel) versus T_1. Black and dashed red curves correspond to $\vec{x}(-T_{p1}) = (1, 0)^{\rm T}$ and $(0, 1)^{\rm T}$, respectively, for all values of T_{p1}. **Bottom panel:** Same as the top panel but for initial state preparation protocol II. For this case, k_p and T_{p2} are specified by T_1 via Eqs. (F.3) and (F.4), respectively. For these simulations, we used the same $\mathcal{C}_{\rm deg}$ as in Sec. 7.1.

We impose $|\vec{x}(0)| > 0.5$ and $1 - \mathcal{F}(0) < 2 \times 10^{-4}$ as the corresponding thresholds for a viable candidate. For this protocol, we focus only on the $\mathcal{C}_{\rm deg}$s utilized in this chapter. They are parameterized by $\vec{Y}_{EP} \equiv \{P_{EP}, \delta_{EP}, \eta, \theta_{12}, P_4, \Delta_4\}$ with fixed values of $\{P_{EP}, \delta_{EP}, \eta, P_4, \Delta_4\}$ and $\theta_{12}(s) = 2n\pi k(s) \bmod 2\pi$, with $0 \leq s = t/T \leq 1$, $n \in \mathbb{N}$, $0 \leq k(s) \leq 1$, $\partial_s k > 0$ and $\partial_s k|_{s=0} = \partial_s k|_{s=1} = 2\pi n/T$. To describe this protocol, we consider a $\mathcal{C}_{\rm deg}$ with $n = 1$, and denoted by $\mathcal{C}_{\rm deg,1}$, which is traversed in duration T_1. The protocol proceeds as follows:

Steps

(1) At time $t = -T_{p2}$, prepare $\vec{x}(t = -T_{p2})$ as $(1, 0)^{\rm T}$ or $(0, 1)^{\rm T}$.

(2) For $-T_{p2} \leq t < (k_p - 1)T_1$, vary $\theta_{12}(t)$ as

$$\theta_{12}(t) = \frac{-2\pi k_p (t + T_{p2})}{T_{p2} - (1 - k_p)T_1} \tag{F.1}$$

with $0 \leq k_p \leq 1$, while $\vec{x}(t = -T_{p2})$ evolves to $\vec{x}(t = (k_p - 1)T_1)$. Intuitively, this step provides some initial amplification to $\vec{x}(t = -T_{p2})$ via the $\sqrt{T}$-dynamical phase.

(3) For $(k_p - 1)T_1 \leq t \leq 0$, vary $\theta_{12}(t)$ as

$$\theta_{12}(t) = -2\pi - \frac{2\pi t}{T_1} \tag{F.2}$$

while $\vec{x}(t = (k_p - 1)T_1)$ evolves to $\vec{x}(t = 0)$. Intuitively, this step steers the nominally amplified $\vec{x}(t = (k_p - 1)T_1)$ from the previous step, to the least-dissipative eigenvector of $H'(s = 0)$ corresponding to $\mathcal{C}_{\rm deg,1}$ traversed in duration T_1. By construction, this step also prepares the initial state as the least-dissipative eigenvector of $H'(s = 0)$ corresponding to $n > 1$ repetitions of $\mathcal{C}_{\rm deg,1}$ traversed in duration $T = nT_1$ with $n \in \mathbb{N}$.

Note that $\theta_{12}(t)$ in Eqs. (F.1) and (F.2) can be succinctly expressed via Eq. (7.2). The corresponding values of k_p and T_{p_2} are specified via

$$k_p(T_1) = k_{p,1} - (k_{p,1} - k_{p,0}) \left(6 \left(\frac{T_1}{T_{1,\mathrm{m}}} \right)^5 - 15 \left(\frac{T_1}{T_{1,\mathrm{m}}} \right)^4 + 10 \left(\frac{T_1}{T_{1,\mathrm{m}}} \right)^3 \right) \tag{F.3}$$

and

$$T_{p2}(T_1, k_p) = k_p(T_1) T_1 + (1 - k_p(T_1)) T_0, \tag{F.4}$$

respectively, where the constants $\{k_{p,0}, k_{p,1}\}$ denote the minimum and the maximum value of k_p, $T_{1,\mathrm{m}}$ denotes the largest value of T_1 for which $\mathcal{C}_{\mathrm{deg},1}$ is traversed, and $T_0 > 0$ denotes a constant duration characterizing T_{p2}. We note that in this parameterization, the previous protocol corresponds to $k_{p,0} = k_{p,1} = 1$.

Finally, we take the steps **(2)** and **(3)** together to constitute a preparation control loop $\mathcal{C}_{p,\mathrm{deg}}$ in $\mathcal{EP}_2$ traversed in duration $T_{p2}(T_1, k_p)$, (Sec. 7.1.3.1), and as such it is uniquely specified for a $\mathcal{C}_{\mathrm{deg}}$ traversed in a duration $T = nT_1$.

Evaluation

To systematically evaluate this protocol and compare it with its predecessor, we continue studying the "simple" $\mathcal{C}_{\mathrm{deg}}$ studied in Sec. 7.1, and repeat the numerical simulations from the previous case.

The cyan region in Fig. F.1(e) sketches this initial state preparation protocol, while panels (f) and (g) show Bloch sphere representation of $\vec{x}(-T_{p2} \leq t \leq 0)$ corresponding to $\vec{x}(-T_{p2}) = (1,0)^{\mathrm{T}}$ and $(0,1)^{\mathrm{T}}$, respectively, for $T_{p2} = 58$ ms. The parameters that characterize this procedure: $k_p = 0.3$, $T_1 = T_{1,\mathrm{m}} = 100$ ms and $T_0 = 40$ ms. In both cases, $\vec{x}(-T_{p1})$, shown as the orange arrow, evolves as the black curve that represents $\vec{x}(-T_{p1} \leq t \leq 0)$, and approaches the least-dissipative eigenvector of $H'(s = 0)$ corresponding to $\mathcal{C}_{\mathrm{deg}}$, shown as the green arrow. The corresponding values of $1 - \mathcal{F}(t)$ and $|\vec{x}(t)|$ are shown in the top and the bottom panel of Fig. F.1(h), respectively. The two resulting figures of merit read $1 - \mathcal{F}(0) \sim 10^{-5}$ and $|\vec{x}(0)| \sim 0.67$, and both of these values are considered acceptable. Refs. [323, 324] show an interactive view of Fig.

F.1(e-h).

We subsequently repeat these numerically simulations as a function of $T_1 = T/n$. Fig. F.2(d-f) illustrates the protocol, its corresponding parameters and figures of merit, respectively. For these simulations, $k_{p,0} = 0.3$, $k_{p,1} = 0.35$, $T_{1,\mathrm{m}} = 111.35$ ms and $T_0 = 40$ ms. Both figures of merit indicate favorable outcomes as $1 - \mathcal{F}(0) < 2 \times 10^{-4}$ for $T_1 > 30$ ms, and $|\vec{x}(0)| \geq 0.6$ for all T_1.

Result and discussion

The above simulations indicate that this initial state preparation protocol remedies the shortcoming of its predecessor albeit with lower but still reasonable state preparation fidelity. A potential avenue for improvement would be to reduce $1-\mathcal{F}(0)$ values of $T_1 <$ 30 ms, and as such we believe that the inflated value of $1 - \mathcal{F}(0)$ for $T_1^* \leq T_1 < 2T_1^*$ where $T_1^* = \pi/2R$ ($\sim$16 ms for this $\mathcal{C}_{\mathrm{deg}}$), is the reason for the transient behavior of $\mathrm{Re}(\beta(T_1^* \leq T_1 < 2T_1^*))$ in Fig. 7.8(c) as opposed to a sharp cusp in Fig. 2.8(b).

However, we did not attempt any further improvements and proceeded forward with this initial state protocol, for studying all $\mathcal{C}_{\mathrm{deg}}$ in this chapter. Finally, we also note that we adapt this protocol studying $\mathcal{C}_{\mathrm{pert}}$ in Sec. 7.3.2, simply by replacing $\vec{Y}_{EP}$ with $\vec{Y}_{\mathrm{pert}}$ given by Eq. (7.14), with $\theta_{12}(t)$ as in Eq. (7.2).

F.1.3 Experimental verification

The measurements of real-dynamics in $\mathcal{EP}_2$ illustrated in this chapter, along with their reasonable agreement to theory maybe taken as an experimental verification of the initial state preparation protocol we have employed, i.e, Protocol II. Regardless, in this section, we provide an explicit experimental demonstration of this initial state preparation protocol.

These measurements constitute traversing $\mathcal{C}_{p,\mathrm{deg}}$ in real time, while monitoring the state vector. Operationally, this protocol reads:

(1) Select a duration T for which a $\mathcal{C}_{\mathrm{deg}}$ is to be traversed in real time. By construction, we have $T_1 = T/n$, the duration of the corresponding $\mathcal{C}_{\mathrm{deg},1}$. Subsequently, compute

$T_{p_2} \equiv T_p$, the corresponding duration of $\mathcal{C}_{p,\mathrm{deg}}$ as given by Eqs. (F.3) and (F.4).

(2) At time $t = -T_p$, prepare $\vec{x}(t = -T_p)$ as $(1,0)^{\mathrm{T}}$ or $(0,1)^{\mathrm{T}}$. Subsequently, measure $\vec{x}(-T_p)$.

(3) For a value of $t \in (-T_p, 0]$, traverse $\mathcal{C}_{p,\mathrm{deg}}$ by varying $\theta_{12}(t)$ as in Eq. (7.2) and evolve $\vec{x}(t = -T_p)$ to $\vec{x}(t)$. Subsequently, measure $\vec{x}(t)$.

(4) Repeat step **(3)** as a function of $t \in (-T_p, 0]$. For each occurrence of step **(3)**, we require it to be preceded by step **(2)**.

(5) Repeat steps **(1-4)** as a function of T.

In addition, we note that the state vector measurement protocol stays unchanged from Secs. 7.1.3.1, 7.1.3.2 and F.3.2.

Figs. F.3-F.5(b-e) illustrate measurements corresponding to initial state preparation for $\mathcal{C}_{\mathrm{deg}}$ studied in Sec. 7.1 for twelve distinct values of T. Note that for this $\mathcal{C}_{\mathrm{deg}}$, $n = 1$ and therefore $T = T_1$. In each panel, we show estimated $\vec{x}(t)$ in the Bloch sphere coordinates, $1 - \mathcal{F}(t)$ and $|\vec{x}(t)|$ corresponding to $\vec{x}(-T_p) = (1,0)^{\mathrm{T}}$, where $-T_p \leq t \leq 0$.

We note that until now, we did not require to fully specify $\vec{x}(t) = (x_1(t), x_2(t))^{\mathrm{T}}$, but rather its components $V_i(t) \propto x_i(t)$, where V_i is the measured heterodyne signal and the proportionality constant is α_i: the motion-to-voltage transduction factor (Secs. 7.1.4 and F.3.2) with $i \in [1,2]$. This is because we were solely concerned with comparing $\vec{x}(T) = (x_1(T), x_2(T))^{\mathrm{T}}$ to $\vec{x}(0) = (x_1(0), x_2(0))^{\mathrm{T}}$. As such α_i is a common factor, and none of our results depend on it except for the current case.

To specify $\vec{x}(t) = (x_1(t), x_2(t))^{\mathrm{T}}$ completely, we utilize estimated value of $\vec{\alpha} = (\alpha_1, \alpha_2)^{\mathrm{T}}$ given by (also in Sec. D.2)

$$\alpha_i = \rho_i(\omega_i)\chi_c(\omega_i)g_i \tag{F.5}$$

where ρ_i is the transduction gain [94, 188, 209] and χ_c is the optical cavity susceptibility at frequency $\omega_i \simeq \omega_i^{(0)}$: the bare resonance frequency of i^{th} membrane mode, with g_i denoting the optomechanical coupling strength and $i \in [1,2]$. We note that both

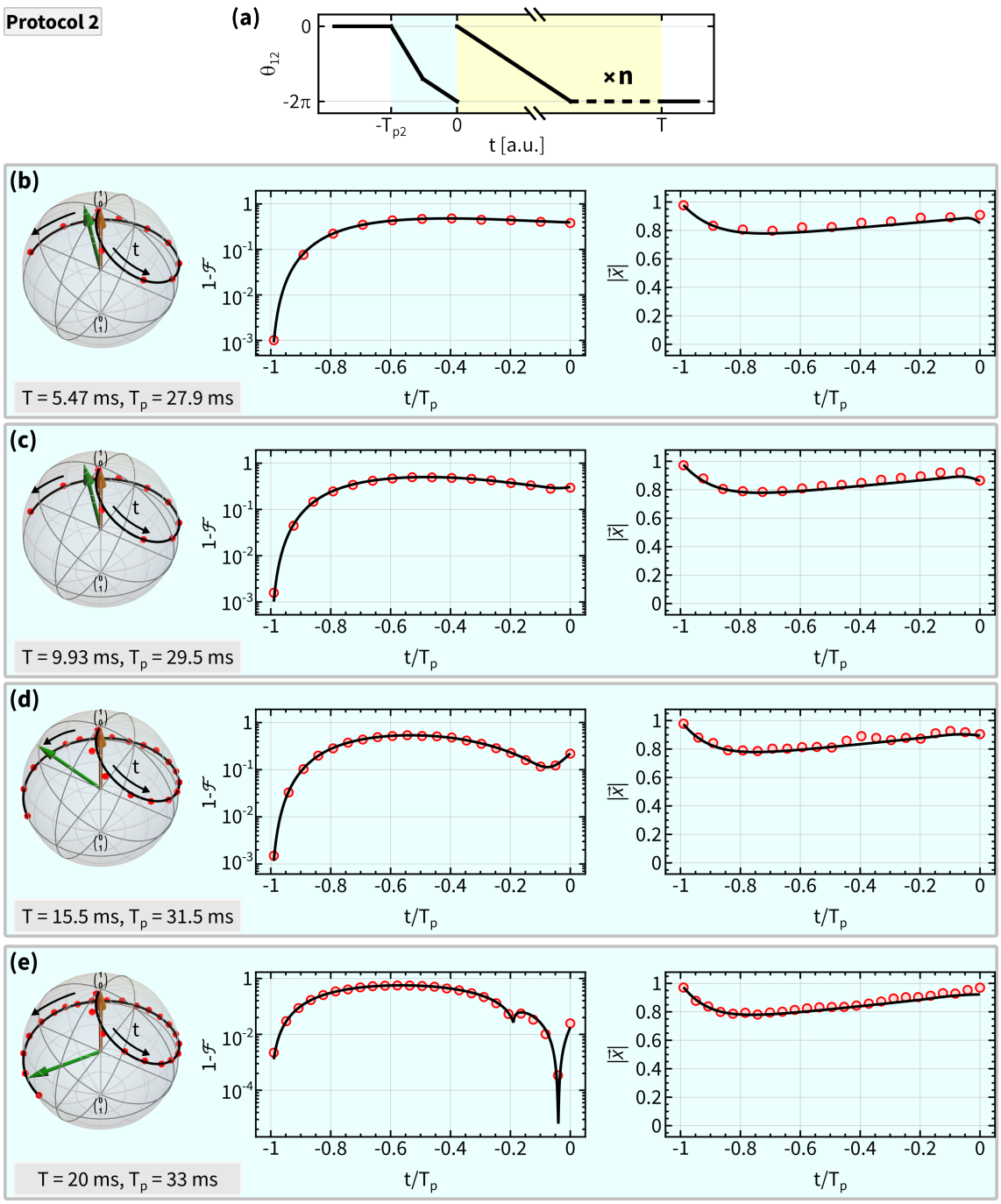

Figure F.3: Experimental verification of initial state preparation protocol II - part I. (a) $\theta_{12}(t)$ (black curve), with cyan and yellow regions corresponding to initial state preparation protocol II ($-T_p \leq t < 0$) and $\mathcal{C}_{\text{deg}}$ ($0 \leq t \leq T$), respectively. **(b)** Bloch sphere representation of $\vec{x}(t)$ (left), $1 - \mathcal{F}(t)$ (middle) and $|\vec{x}(t)|$ (right) for $\vec{x}(-T_p) = (1, 0)^{\text{T}}$. Red points show estimated values from measured heterodyne signal and estimated motion-to-voltage transduction. See text in Sec. F.1.3 for assumptions. Black curves show corresponding no-free-parameter theory prediction. For this panel, $T_1 = T/n$ and T_p are indicated in the bottom left gray box. **(c-e)** Same as panel (b) but for increasing values of T_1. For these measurements, we used the same $\mathcal{C}_{\text{deg}}$ as in Sec. 7.1.

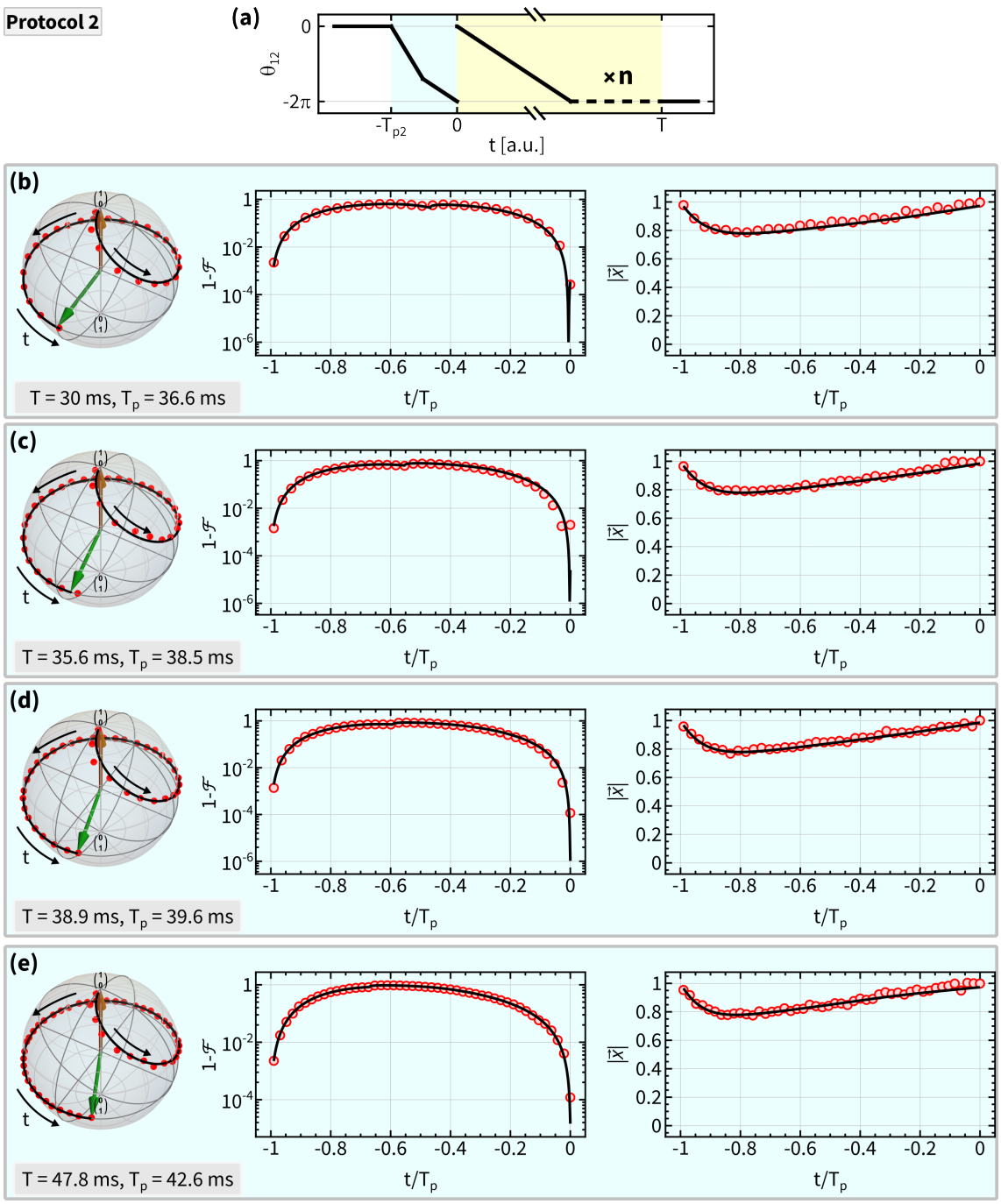

Figure F.4: Experimental verification of initial state preparation protocol II - part II. (a) $\theta_{12}(t)$ (black curve), with cyan and yellow regions corresponding to initial state preparation protocol II ($-T_p \leq t < 0$) and $\mathcal{C}_{\text{deg}}$ ($0 \leq t \leq T$), respectively. **(b)** Bloch sphere representation of $\vec{x}(t)$ (left), $1 - \mathcal{F}(t)$ (middle) and $|\vec{x}(t)|$ (right) for $\vec{x}(-T_p) = (1, 0)^{\text{T}}$. Red points show estimated values from measured heterodyne signal and estimated motion-to-voltage transduction. See text in Sec. F.1.3 for assumptions. Black curves show corresponding no-free-parameter theory prediction. For this panel, $T_1 = T/n$ and T_p are indicated in the bottom left gray box. **(c-e)** Same as panel (b) but for increasing values of T_1. For these measurements, we used the same $\mathcal{C}_{\text{deg}}$ as in Sec. 7.1.

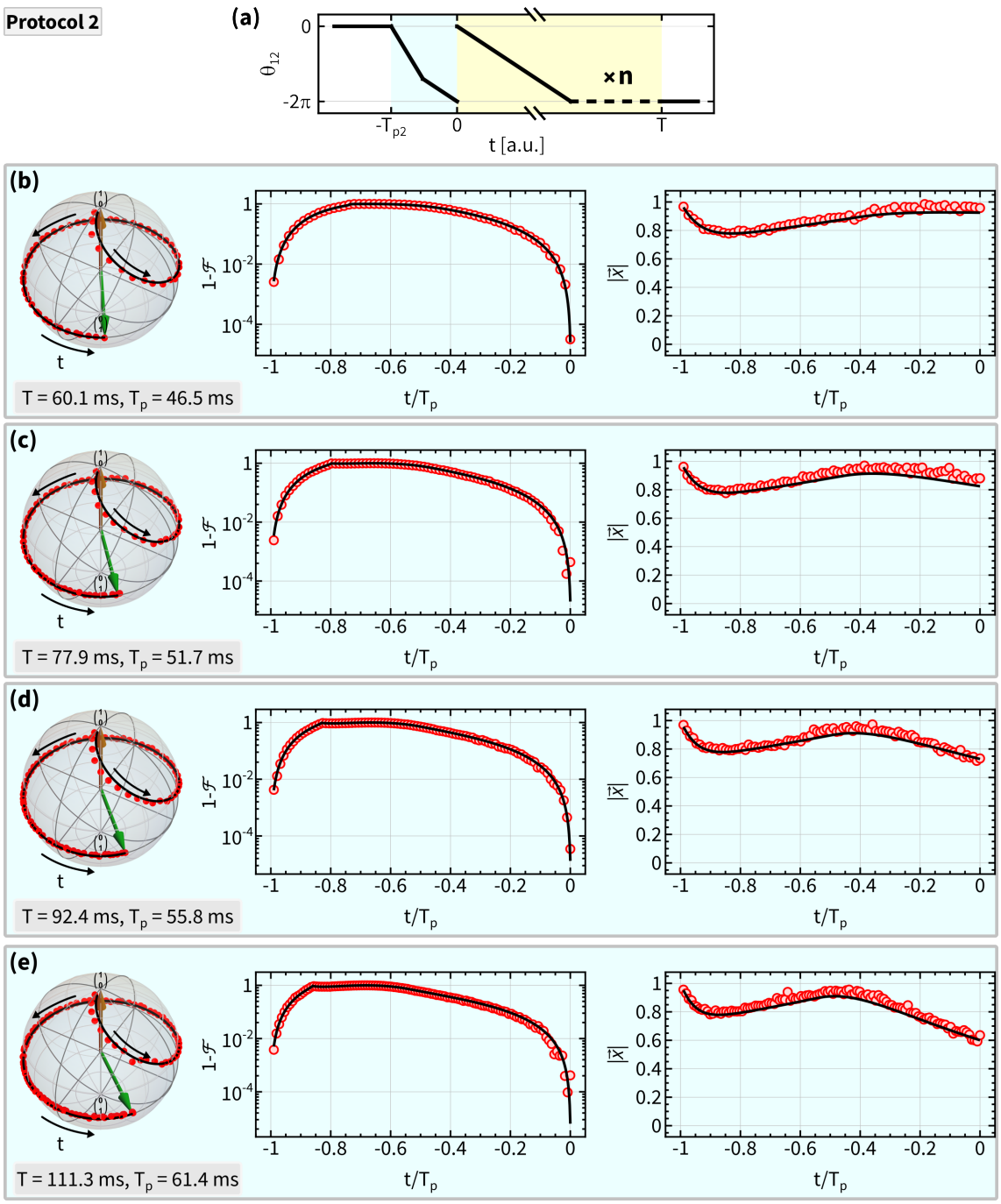

Figure F.5: Experimental verification of initial state preparation protocol II - part III. (a) $\theta_{12}(t)$ (black curve), with cyan and yellow regions corresponding to initial state preparation protocol II ($-T_p \leq t < 0$) and $\mathcal{C}_{\text{deg}}$ ($0 \leq t \leq T$), respectively. **(b)** Bloch sphere representation of $\vec{x}(t)$ (left), $1 - \mathcal{F}(t)$ (middle) and $|\vec{x}(t)|$ (right) for $\vec{x}(-T_p) = (1, 0)^{\text{T}}$. Red points show estimated values from measured heterodyne signal and estimated motion-to-voltage transduction. See text in Sec. F.1.3 for assumptions. Black curves show corresponding no-free-parameter theory prediction. For this panel, $T_1 = T/n$ and T_p are indicated in the bottom left gray box. **(c-e)** Same as panel (b) but for increasing values of T_1. For these measurements, we used the same $\mathcal{C}_{\text{deg}}$ as in Sec. 7.1.

$\chi_c(\omega_i) = (\kappa/2 - i\omega_i)^{-1}$ via κ: the cavity linewidth, and g_i are obtained from characterization of the MIM system (Secs. 4.4.2 and 4.4.3). However, ρ_i requires additional characterizations, which were unfortunately not undertaken. In this light, we make the assumption that $\rho_1(\omega_1) = \rho_2(\omega_2)$ which amounts to assuming:

(a) Both bare[1] mechanical modes are in thermal equilibrium with their respective baths, and the modes and their baths are at the same temperature.

(b) The photodetector gain at $\omega_1 \simeq \omega_1^{(0)}$ is equal to the photodetector gain at $\omega_2 \simeq \omega_2^{(0)}$.

Under this assumption, we estimate $\vec{x}(t) = (x_1(t), x_2(t))^{\mathrm{T}}$ as

$$x_1(t) = \frac{V_{1p}(t)}{V_{1i}(-T_p)}$$
$$x_2(t) = \left(\frac{\chi_c(\omega_1)g_1}{\chi_c(\omega_2)g_2}\right)\left(\frac{V_{2p}(t)}{V_{1i}(-T_p)}\right) \tag{F.6}$$

where $V_{1i}(-T_p)$ denotes the heterodyne signal corresponding to independent measurement of $x_1(-T_p)$, while $V_{1p}(t)$ and $V_{2p}(t)$ denote the heterodyne signal corresponding to measurements of $x_1(t)$ and $x_2(t)$ for $t \in (T_p, 0]$, respectively[2]. As a result, it is this estimated $\vec{x}(t) = (x_1(t), x_2(t))^{\mathrm{T}}$ that is shown in Figs. F.3-F.5(b-e). We also note that in order to calculate $1 - \mathcal{F}$, we utilized the dot product of theoretically predicted $\vec{v}'_-(t)$ and estimated $\vec{x}(t)$ for $t \in (T_p, 0]$.

Finally, we show the estimated values of the figures of merits, i.e, $1 - \mathcal{F}(0)$ and $|\vec{x}(0)|$ in panels (b) and (c) of Fig. F.6. We find the estimated $1 - \mathcal{F}(0)$ to be sufficiently small for our purposes. The agreement to theory is qualitatively reasonable, and given our assumption above, any further inference is not straightforward. The estimated $|\vec{x}(0)|$ is also sufficient for our purposes, and is in good agreement with theoretical prediction.

[1] To be precise, bare here means the membrane modes in the presence of the probe and the LO beams. We expect the probe beam ($P_{\mathrm{probe}} = 7$ μW, $\Delta_0/2\pi \approx -0.05$ MHz) to produce a ∼10 Hz photothermal spring shift, ∼1 Hz spring shift due to radiation pressure DBA and ∼0.5 Hz damping due to radiation pressure DBA.

[2] Note that in Eq. (F.6), we are not required know the precise value of the temperature or the photodetector gain. However, Ref. [188] lists values of our photodetector's gain at two frequencies separated by ∼1 MHz around 20 MHz (the same frequency range of our detection), and they differ by 9 parts in 10^4.

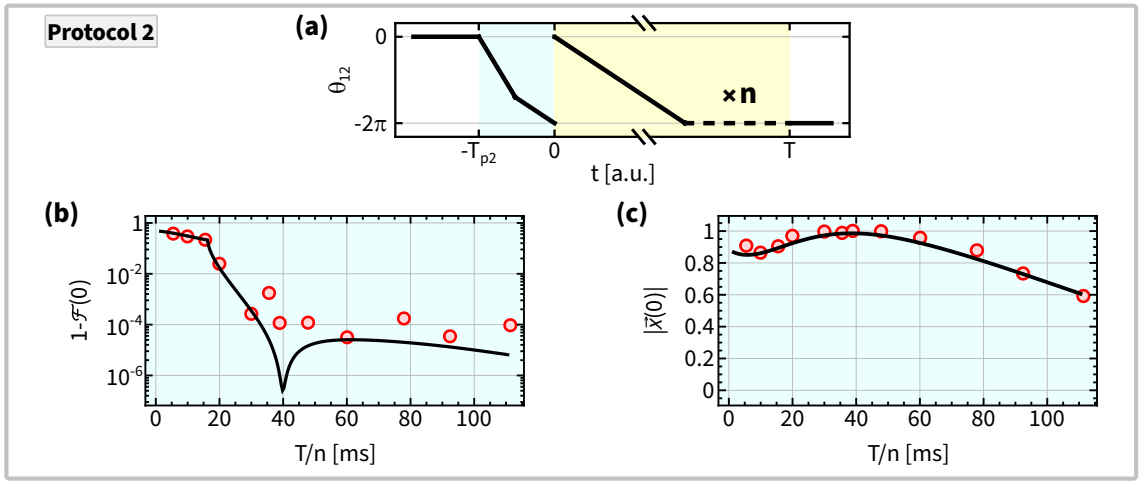

Figure F.6: Experimental verification of initial state preparation protocol II - part IV. (a) $\theta_{12}(t)$ (black curve), with cyan and yellow regions corresponding to initial state preparation protocol II ($-T_p \leq t < 0$) and $\mathcal{C}_{\rm deg}$ ($0 \leq t \leq T$), respectively. **(b)** $1 - \mathcal{F}(0)$ versus $T_1 = T/n$. Red points show estimated values from measured heterodyne signal and estimated motion-to-voltage transduction. See text in Sec. F.1.3 for assumptions. Black curve show corresponding no-free-parameter theory prediction. **(c)** Same as (b) but showing $|\vec{x}(0)|$. For these measurements, we used the same $\mathcal{C}_{\rm deg}$ as in Sec. 7.1.

F.2 On Jordan and Schur decompositions

In this section, we highlight a pitfall that one generically encounters when using the Jordan decomposition to study perturbations of degenerate matrices (Sec. F.2.1). We remedy this issue by utilizing Schur decomposition (Sec. F.2.2).

F.2.1 A pitfall of Jordan decomposition

In so far (except in Sec. 7.3.2), we have studied dynamics of an $N = 2$ mode system tuned in its degenerate subspace $\mathcal{EP}_2$ under the similarity transformation given by $M^{-1}H_{\rm deg}M = \mathcal{T}\,\mathbb{I}/2 + J_2$ (see Eq. (7.22)), where $H_{\rm deg}$ is the dynamical matrix of the degenerate system, the columns of M are given by the unique right eigenvector and a specific choice of generalized right eigenvector of $H_{\rm deg}$. J_2 is a 2×2 Jordan block, and in this case it is the Jordan normal form of $H_{\rm deg}$, and is referred to as the Jordan decomposition [152]. Subsequently, the matrix that governs evolution in $\mathcal{EP}_2$ is given by $H' = M^{-1}H_{\rm deg}M - iM^{-1}\partial_s M/T = \mathcal{T}\,\mathbb{I}/2 + J_2 - \mathcal{A}_J/T$.

However, when we smoothly perturb away from EP (here EP_2), we observe that

$$H_{\rm deg} = R\begin{bmatrix} 1 & pe^{i\theta} \\ -e^{-i\theta}/p & -1 \end{bmatrix} + \frac{\mathcal{T}}{2}\,\mathbb{I} \longrightarrow H = \begin{bmatrix} A & Be^{i\theta} \\ Ce^{-i\theta} & -A \end{bmatrix} + \frac{\mathcal{T}}{2}\,\mathbb{I} \tag{F.7}$$

i.e., $H_{\rm deg}$ varies smoothly to a non-degenerate and non-defective H (see also Sec. 2.2.4.3). However, when they are Jordan decomposed,

$$\begin{bmatrix} \mathcal{T}/2 & 1 \\ 0 & \mathcal{T}/2 \end{bmatrix} \longrightarrow \begin{bmatrix} \lambda_+ & 0 \\ 0 & \lambda_- \end{bmatrix} \tag{F.8}$$

represents a discontinuous mapping of $\mathcal{T}\,\mathbb{I}/2 + J_2$ to $\mathrm{Diag}(\lambda_+, \lambda_-)$ with $\lambda_\pm = \mathcal{T}/2 \pm \sqrt{A^2 + BC}$, via the discontinuous $1 \to 0$ mapping in the upper right. To be precise, this discontinuous mapping is regardless the size of perturbation. Also, recall that for Jordan decomposition of the non-degenerate and non-defective H, its corresponding M's columns are the linearly independent right eigenvectors of H.

The above exercise illustrates that such a discontinuous mapping between the normal form of a defective matrix to a non-defective one, is indeed a drawback of Jordan decomposition, and as such is less suitable for experimental purposes where one approaches EP degeneracy with a finite precision. To remedy this issue, we turn to Schur decomposition [260], below. We also note that there exist other techniques to remedy this problem, for example: the Jordan-Arnold decomposition [96].

F.2.2 Schur decomposition

This section is divided into three parts. The first part provides a quick primer on Schur decomposition. The second part shows that there exists a Schur decomposition that varies smoothly when H is tuned to and around an EP_2, thereby remedying the above pitfall. In the final part, we re-derive the result of Sec. 2.2.4.3 using Schur decomposition, thereby allowing to predict the outcomes of "stepping off" $\mathcal{EP}_2$ in Sec. 7.3.2.

F.2.2.1 A quick primer

Every complex matrix H has a Schur decomposition [260]. There exists a unitary matrix U and an upper triangular matrix T such that $U^{\dagger}HU = T_U$, where $(^{\dagger})$ denotes conjugate transpose. In what follows, we restrict this exercise solely to 2×2 matrices, the main focus of Chapter 7.

Schur decomposition of a normal matrix H, for e.g. Hermitian, is specified by U whose columns are the orthonormal eigenvectors of H and $T = \mathrm{Diag}(\lambda_+, \lambda_-)$ where $\lambda_{+,-}$ are the eigenvalues of H.

However, when H corresponds to an EP (here EP_2), i.e., $H \equiv H_{\mathrm{deg}}$ and thus defective, the orthonormal basis that specifies U is obtained by Gram-Schmidt processing [325] of the non-orthogonal basis of the Jordan normal form. The first column of U (denoted $\boldsymbol{u_1}$), is the normalized unique right eigenvector, and its second column (denoted $\boldsymbol{u_2}$), is a normalized generalized right eigenvector[1]. The above steps constitute Schur decomposition of H_{deg}, which results in

$$U_{\mathsf{A}}^{\dagger} H_{\mathrm{deg}} U_{\mathsf{A}} = \begin{bmatrix} \mathcal{T}/2 & \rho \\ 0 & \mathcal{T}/2 \end{bmatrix} \equiv T_U \tag{F.9}$$

where for specificity and later use, the unitary matrix is denoted by U_{A}, and $\rho = \overline{\boldsymbol{u}}_{\boldsymbol{1}} \cdot H_{\mathrm{deg}} \cdot \boldsymbol{u_2} \in \mathbb{C}^{\times}$ with $\overline{\boldsymbol{u}}_i$ denoting the i^{th} row of $U_{\mathsf{A}}^{\dagger}$. Note that the above transformation can be ambiguous up to a unitary change of basis[2]. Observe that under a unitary change of basis, i.e., $\boldsymbol{u_i} \to e^{i\varphi_i}\boldsymbol{u_i}$ with $\varphi_i \in \mathbb{R}$ and $i \in \{1, 2\}$, the diagonal entry of T_U remains invariant, but $\rho \to e^{-i(\varphi_1 - \varphi_2)}$. Therefore, only $|\rho|$ is invariant to basis transformations in a Schur decomposition. Finally, we also note that $\mathrm{Tr}(H_{\mathrm{deg}}^{\dagger} H_{\mathrm{deg}}) = \mathrm{Tr}(T_U^{\dagger} T_U) = |\mathcal{T}|^2/2 + |\rho|^2$, which provides a way to compute $|\rho|$ in a basis independent manner, i.e.,

$$|\rho| = \sqrt{\mathrm{Tr}(H_{\mathrm{deg}}^{\dagger} H_{\mathrm{deg}}) - |\mathrm{Tr}(H_{\mathrm{deg}})|^2/2} \tag{F.10}$$

[1] We note that this particular choice of the generalized right eigenvector can be different from the one used in the Jordan decomposition.

[2] Since U is unitary, unitary change of basis constitute all allowed basis transformations.

F.2.2.2 A smoothly varying Schur decomposition near EP_2

Now in order to show that there exists a Schur decomposition that varies smoothly when H is tuned to and around an EP_2, we utilize the Jordan-Arnold decomposition [96]. It shows than under perturbation away from EP_2, there exists a smooth basis (potentially non-orthonormal) in H in which it has a Jordan-Arnold normal form J_A given by

$$J_A(x) = \begin{bmatrix} \mathcal{T}/2 & 1 \\ x & \mathcal{T}/2 \end{bmatrix} \tag{F.11}$$

where $x \in \mathbb{C}$ depends smoothly on H. This form (smoothly) reduces to J_2 (i.e., the Jordan normal form), at an EP_2, i.e., $x = 0$. Furthermore, one may intuit x to be proportional to the strength of perturbation from an EP_2, by noting the eigenvalues of $J_A : \mathcal{T}/2 \pm \sqrt{x}$. However, the appearance of '1' in the upper right is a convenience, and one can very well choose a smooth orthonormal basis in H such that

$$S(x, \rho) = \begin{bmatrix} \mathcal{T}/2 & \rho \\ x & \mathcal{T}/2 \end{bmatrix} \tag{F.12}$$

is the Jordan-Arnold normal form, and to be specific, we chose the orthonormal basis to be the one used for Schur decomposition of $H \equiv H_{\text{deg}}$ in Eq. (F.9), i.e. $S(x, \rho) = U_{\mathsf{A}}^{\dagger} H U_{\mathsf{A}}$. Similar to J_A, this normal form approaches an EP_2 smoothly, i.e., when $x \to 0$.

Now what is left to be shown is to find another smooth orthonormal basis U_{B}, to reduce $S(x, \rho)$ into an upper triangular form. As a result, one can combine these two smooth orthonormal basis transformations to specify a single smooth orthonormal basis transformation $U_{\mathsf{final}} = U_{\mathsf{B}} U_{\mathsf{A}}$, and Schur decompose any H, smoothly to an upper triangular matrix $T_U(x, \rho)$.

It is straightforward to obtain U_{B}. The eigenvalues of $S(x, \rho)$ are $\lambda_{\pm} = \mathcal{T}/2 \pm \sqrt{x\rho}$, and the non-orthogonal eigenvectors are $\boldsymbol{v}_{\pm} = (1, \pm\sqrt{x/\rho})^{\mathrm{T}} / \sqrt{1 + |x/\rho|}$. Depending on which basis one starts out with ($\boldsymbol{v}_+$ or $\boldsymbol{v}_-$), one obtains two different orthonormal

bases via Gram Schmidt process. For concreteness, we pick $\boldsymbol{u}_1 = \boldsymbol{v}_+$ first, and obtain

$$U_{\mathsf{B}} = \frac{1}{\sqrt{1+|x/\rho|}} \begin{bmatrix} 1 & -\sqrt{x^*/\rho^*} \\ \sqrt{x/\rho} & 1 \end{bmatrix} \tag{F.13}$$

where $(^*)$ denotes the complex conjugation and finally,

$$T_U(x,\rho) = \begin{bmatrix} \mathcal{T}/2 + \sqrt{x\rho} & \rho\sqrt{1-|x/\rho|} \\ 0 & \mathcal{T}/2 - \sqrt{x\rho} \end{bmatrix} \tag{F.14}$$

which varies smoothly with x, and to explicitly highlight the remedial of the pitfall in Sec. F.2.1, smooth perturbations away from EP_2, i.e.,

$$H_{\rm deg} = R \begin{bmatrix} 1 & pe^{i\theta} \\ -e^{-i\theta}/p & -1 \end{bmatrix} + \frac{\mathcal{T}}{2}\,\mathbb{I} \longrightarrow H = \begin{bmatrix} A & Be^{i\theta} \\ Ce^{-i\theta} & -A \end{bmatrix} + \frac{\mathcal{T}}{2}\,\mathbb{I}$$

can be Schur decomposed using the unitary $U_{\mathsf{final}} = U_{\mathsf{B}} U_{\mathsf{A}}$, which results in a smoothly varying upper triangular form, i.e.,

$$\begin{bmatrix} \mathcal{T}/2 & \rho \\ 0 & \mathcal{T}/2 \end{bmatrix} \longrightarrow \begin{bmatrix} \mathcal{T}/2 + \sqrt{x\rho} & \rho\sqrt{1-|x/\rho|} \\ 0 & \mathcal{T}/2 - \sqrt{x\rho} \end{bmatrix} \equiv \begin{bmatrix} \lambda_+ & \rho\sqrt{1-|x/\rho|} \\ 0 & \lambda_- \end{bmatrix}$$

F.2.2.3 Adiabatic transport revisited using Schur decomposition

With above machinery in hand, we now proceed to re-examine the case in Sec. 2.2.4.3. For this examination, we consider a system with its dynamical matrix H as in Eq. (2.14)

$$H(s) = \begin{bmatrix} A & Be^{i\theta(s)} \\ Ce^{-i\theta(s)} & -A \end{bmatrix} + \mathcal{T}\,\mathbb{I}/2 \tag{F.15}$$

and restrict ourselves to the case of "simple" control loops given by fixed parameters $(A, B, C, \mathcal{T}) \in \mathbb{C}$ and real-valued $\theta(s) = -2n\pi s \bmod 2\pi$ with $0 \le s \le 1$, and tuned for a duration T. The corresponding eigenvalues of $H(s)$ are $\lambda_\pm = \mathcal{T}/2 \pm \sqrt{A^2 + BC} \equiv$

$\mathcal{T}/2 \pm \delta\lambda/2$ and the system's evolution is simply

$$i\epsilon\partial_s \vec{c} = H\,\vec{c} \tag{F.16}$$

as in Eq. (1.1), where $\vec{c}$ is the state vector being evolved and $\epsilon = 1/T$.

Applying Schur decomposition to $H(s)$, reduces it to an upper triangular matrix $T_U(s)$ via a unitary transformation given by $T_U(s) = U(s)^\dagger H(s) U(s)$ where

$$T_U(s) = \begin{bmatrix} \mathcal{T}/2 + \delta\lambda/2 & \rho(s) \\ 0 & \mathcal{T}/2 - \delta\lambda/2 \end{bmatrix} \tag{F.17}$$

and we chose

$$U(s) = \frac{1}{\sqrt{1+|u|^2}} \begin{bmatrix} 1 & -u^* \\ ue^{-i\theta(s)} & e^{-i\theta(s)} \end{bmatrix} \tag{F.18}$$

where

$$u = \frac{C}{A + \sqrt{A^2 + BC}} \equiv \frac{C}{A + \delta\lambda/2}, \tag{F.19}$$

$$\begin{aligned} \rho &= B - (A + \sqrt{A^2 + BC})u^* \\ &= B - C^* \frac{A + \sqrt{A^2 + BC}}{\left(A + \sqrt{A^2 + BC}\right)^*} \equiv B - C^* \frac{A + \delta\lambda/2}{(A + \delta\lambda/2)^*} \end{aligned} \tag{F.20}$$

and we note that ρ is independent of s in this case. We also note the algebraic relation

$$\frac{\rho u}{1+|u|^2} - \frac{\delta\lambda}{2}\left(\frac{1-|u|^2}{1+|u|^2}\right) = -A \tag{F.21}$$

Subsequently, the equation of motion as given by Eq. (F.16) transforms to

$$i\epsilon\partial_s \vec{c}_U = H'\vec{c}_U = (T_U - \epsilon\mathcal{A}_U)\vec{c}_U \tag{F.22}$$

where $\vec{c} = U\vec{c}_U$, and $\mathcal{A}_U = iU^\dagger \frac{\partial U}{\partial s}$, and explicitly

$$\mathcal{A}_U(s) = \frac{\partial_s \theta}{1+|u|^2} \begin{bmatrix} |u|^2 & u^* \\ u & 1 \end{bmatrix} \tag{F.23}$$

Following our prescription from Secs. 2.2.4.1 and 2.2.4.3, we compute the eigenvalues $\boldsymbol{\lambda'}$ of $H' = T_U - \epsilon \mathcal{A}_U$. They are given by

$$\lambda_\pm(s) = \frac{\mathcal{T}}{2} - \frac{\partial_s \theta}{2T} \pm \sqrt{\frac{\delta\lambda^2}{4} + \frac{(\partial_s\theta)^2}{4T^2} + \frac{A\partial_s\theta}{T}} \tag{F.24}$$

or

$$\lambda_\pm(s) = \frac{\mathcal{T}}{2} - \frac{\partial_s \theta}{2T} \pm \sqrt{\frac{\delta\lambda^2}{4} + \frac{(\partial_s\theta)^2}{4T^2} - \frac{\rho u \partial_s\theta}{T(1+|u|^2)} + \frac{\delta\lambda\,\partial_s\theta}{2T}\left(\frac{1-|u|^2}{1+|u|^2}\right)} \tag{F.25}$$

where '+' is chosen to denote the least-dissipative eigenvector of H', and the second form, i.e, Eq. (F.25) uses the relation in Eq. (F.21). Finally, we compute $\phi_+(T) = T\int_0^1 \lambda_+(s)ds$, the phase acquired by a state vector initialized at the least dissipative eigenvector of H', which is given by

$$\phi_+(T) = \frac{\mathcal{T}T}{2} - \int_0^1 \frac{\partial_s\theta}{2} ds + \int_0^1 ds\sqrt{\delta\lambda^2T^2/4 + (\partial_s\theta)^2/4 + A\partial_s\theta\, T} \tag{F.26}$$

$$= \frac{\mathcal{T}T}{2} + n\pi \bmod 2\pi + \int_0^1 ds\sqrt{\delta\lambda^2T^2/4 + (\partial_s\theta)^2/4 + A\partial_s\theta\, T} \tag{F.27}$$

$$= \frac{\mathcal{T}T}{2} + n\pi \bmod 2\pi + \sqrt{\delta\lambda^2T^2/4 + n^2\pi^2 - 2n\pi AT} \tag{F.28}$$

where we suggestively evaluated the sum in three steps. In Eq. (F.26) we merely substituted Eq. (F.24). Then Eq. (F.27) evaluated the second term trivially, as it is an integral of a total derivative, and finally in Eq. (F.28) we substituted $\theta(s) = -2n\pi s \bmod 2\pi$.

To appreciate the power of Eqs. (F.27) and (F.28), we evaluate it in several limiting cases which are described below.

Case I: $\delta\lambda = 0$

This case corresponds to being at an EP_2 with $H \to H_{\rm deg}$, and using the relation in Eq. (F.7), we have $\{A \to R, B \to Rp, C \to -R/p\}$, as in Sec. 2.2.4.3. The corresponding $\phi_+ \equiv \phi_{\rm deg}$ reads

$$\phi_{\rm deg}(T) = \frac{\mathcal{T}T}{2} + n\pi \bmod 2\pi + i\sqrt{2n\pi RT - n^2\pi^2} \tag{F.29}$$

as in Eq. (2.57), with A in Eq. (F.28) replaced with R. The first term $\propto T$ is the usual linear dynamical phase, the second term $\propto T^0$ specifies $-\phi_{B,\rm deg}$, and at large $\phi_{\rm deg}$ has a unique $\sqrt{T}$-dynamical phase. We also note that in this case Eq. (F.21) reduces to

$$\frac{\rho u}{1+|u|^2} \to -R, \tag{F.30}$$

and in particular, Eqs. (F.21) and (F.30) form the basis of extracting R from spectroscopy measurements at EP_2 (Sec. F.3.3).

Case II: $\delta\lambda \neq 0$, and at large T

This corresponds to the non-degenerate case as considered in Sec. 2.2.3 and Chapters 5 and 6. For large T, we Taylor expand either of the Eqs. (F.27) and (F.28) to obtain

$$\begin{aligned}\phi_+(T) = \frac{(\mathcal{T}+\delta\lambda)T}{2} + n\pi\left(1 - \frac{A}{\delta\lambda/2}\right) \bmod 2\pi + \frac{1}{T}\left(\frac{1}{4\delta\lambda} - \frac{A^2}{\delta\lambda^3}\right)\int_0^1 (\partial_s\theta)^2 ds \\ + \frac{1}{T^2}\left(\frac{A}{2\delta\lambda^3} - \frac{4A^3}{\delta\lambda^5}\right)\int_0^1 (\partial_s\theta)^3 ds + \mathcal{O}\left(\frac{1}{T^3}\right)\end{aligned} \tag{F.31}$$

or

$$\begin{aligned}\phi_+(T) = \frac{(\mathcal{T}+\delta\lambda)T}{2} + n\pi\left(1 - \frac{A}{\delta\lambda/2}\right) \bmod 2\pi + \frac{4n^2\pi^2}{T}\left(\frac{1}{4\delta\lambda} - \frac{A^2}{\delta\lambda^3}\right) \\ + \frac{8n^3\pi^3}{T^2}\left(\frac{A}{2\delta\lambda^3} - \frac{4A^3}{\delta\lambda^5}\right) + \mathcal{O}\left(\frac{1}{T^3}\right)\end{aligned} \tag{F.32}$$

where we substituted $\theta(s) = 2n\pi s \bmod 2\pi$ in Eq. (F.31) to obtain Eq. (F.32).

This furnishes the well-known result for the non-degenerate case with its first term

$\propto T$ is usual linear dynamical phase, the second term $\propto T^0$ specifies $-\phi_{B,+}$ [12, 87], and the remaining terms represent dynamical phases that asymptote to zero at large T.

Case III: $\delta\lambda$ systematically perturbed from zero, and at intermediate T

This represents the cases studied in Sec. 7.3.2 and as such it aims to connect the two seemingly independent descriptions, i.e., the degenerate case ($\delta\lambda = 0$) in Sec. 2.2.4.3, and the non-degenerate case ($\delta\lambda \neq 0$) in the large T limit (Sec. 2.2.3). This disconnect maybe understood as follows:

- **Case I** is solely concerned with $\delta\lambda = 0$ and is a relatively new result borne out of the works of Ref. [88, 89], wherein adiabatic transport in $\mathcal{EP}_N$ (here $\mathcal{EP}_2$) is uniquely elucidated for the first time.
- **Case II** is a well-known topic of investigation. However, it is generically the case that such studies stop at the first two terms of Eq. (F.31) or (F.32), i.e., $\mathcal{O}(T)$ and $\mathcal{O}(T^0)$. But one may be curious about when $\delta\lambda \to 0$, and naively applying Eq. (F.31) or (F.32) leads us nowhere. In particular, it predicts that the geometric phase diverges for control loops where $\delta\lambda \to 0$. This is indeed in contradiction to the theoretical results of Ref. [88, 89] and the experimental demonstration in this chapter.

To address this disconnect, we examine Eq. (F.28) at intermediate values of T when $\delta\lambda \sim 0$ but not exactly zero.

In particular, we focus on the radicand of the third term in Eq. (F.28) given by

$$\phi_{+,3}(T)^2 = \delta\lambda^2 T^2/4 + n^2\pi^2 - 2n\pi AT \tag{F.33}$$

and observe that for $0 < T < \frac{8n\pi A}{\delta\lambda^2}$, $|2n\pi AT| > |\delta\lambda^2 T^2/4|$. In this range of T, $\phi_{+,3}(T)^2$ a dominant linear dependence on T, and thus $\phi_+(T) - \mathcal{T}T/2$ has a dominant $\sqrt{T}$ dependence. This $\sqrt{T}$ (sub-linear) dependence is a unique behavior, applies to all cases of study i.e., whether or not $\delta\lambda$ is zero and its range increases as $1/\delta\lambda^2$. Finally, for $T \gg \frac{8n\pi A}{\delta\lambda^2}$, $\phi_+(T) - \mathcal{T}T/2$ is $\mathcal{O}(T)$, the well-known result in the adiabatic limit.

F.3 Data acquisition, processing and fitting

In this section, we provide details data acquisition and its processing (Sec. F.3.1) followed by fitting routines employed to extract the initial and final state vectors (Sec. F.3.2) as well as the spectroscopic quantities at and around EP_2 (Sec. F.3.3).

F.3.1 Data acquisition and processing

All measurements reported in this chapter are derived from ringdown measurements of the membrane modes in presence or in absence of control and auxiliary laser tones. They are classified by the purpose serve and are listed below:

(a) Bare ringdowns

These measurements are performed in absence of any control or auxiliary laser tones and provide the bare resonance frequency $\omega^{(0)}$ and the bare damping rate $\gamma^{(0)}$ of the membrane modes. The timing sequence for these measurements are same as Fig. 7.3(third column) except that the control and auxiliary laser tones are off. These measurement are fit to $Ae^{(i\rho - i\omega^{(0)}t - \gamma^{(0)}t/2)}$ with $\{A, \rho, \omega^{(0)}, \gamma^{(0)}\}$ are real valued fit parameters. The value of $\omega^{(0)}$ for each membrane mode is then utilized to set the demodulation frequencies for subsequent data acquisition.

(b) Ringdowns for state vector measurement

These measurements are performed in presence of the auxiliary laser tone which does not couple individual membrane modes. The key feature that enables these measurements is the instantaneous[1] switching between control laser tones to the auxiliary tone (see Sec. 4.6.1.2). The instantaneous switching at time $t = t_0$ can be intuited as the "sudden approximation" of quantum mechanics [3] which has no effect on the state vector at $t = t_0$. Thus, setting up a ringdown measurement for $t_0 \leq t \leq t_{\mathsf{DAq}}$ allows us to infer the state vector at $t = t_0$. The timing sequence for these measurements is illustrated

[1]The switching time scale is ∼50 ns due to the cAOM (Fig. 4.22). It is comparable to the ringdown time of the MIM cavity $1/\kappa$: representative timescale of optomechanical interactions. However, our data sampling interval is ≥50 µs, thereby making us insensitive to any optical transients.

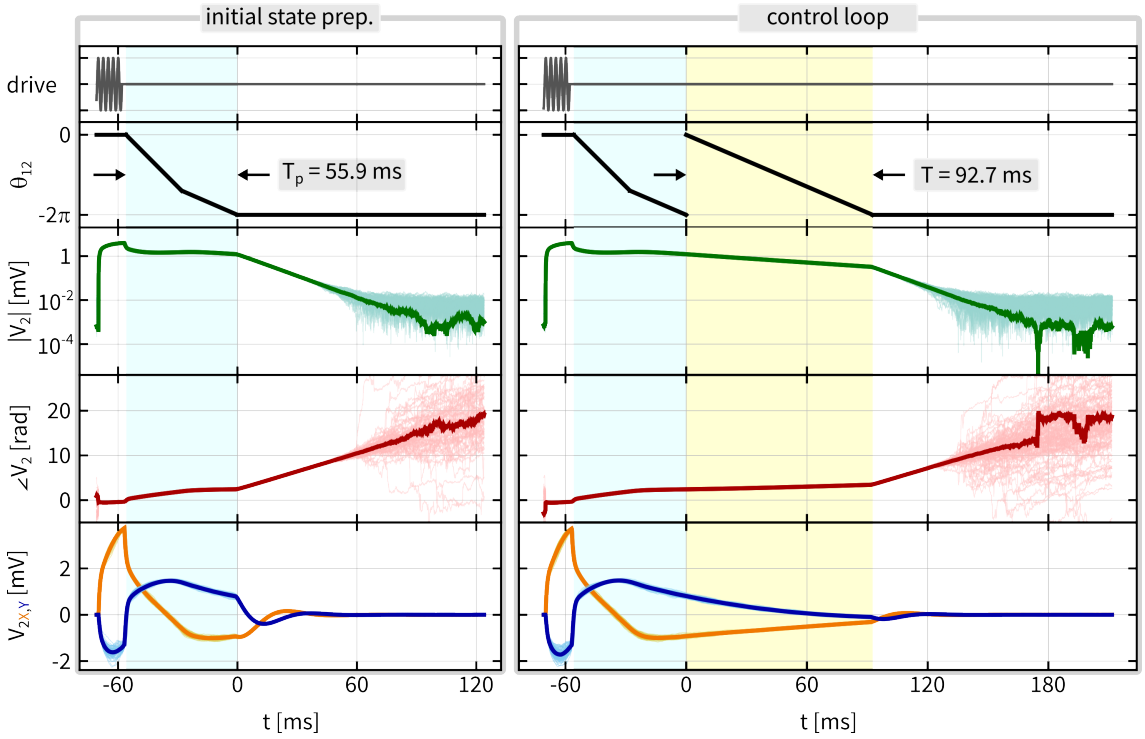

Figure F.7: Complex averaging for the initial state vector $\vec{x}(0)$, and its evolution to $\vec{x}(T)$ along a control loop in $\mathcal{EP}_2$: state vector component I. First column: measurements for the first component of $\vec{x}(0)$ obtained by transporting $\vec{x}(-T_p)$ along $\mathcal{C}_{p,\mathrm{deg}}$. **Second column:** measurements for the first component of $\vec{x}(T)$ obtained by transporting $\vec{x}(0)$ along a "simple" non-contractible $\mathcal{C}_{\mathrm{deg}}$. For both columns, dark gray curves: a schematic of the driving force applied to the membrane, which is switched off at $t = -T_p - T_{\mathrm{wait}}$. $T_{\mathrm{wait}} =$ 2 ms is a programmed delay used in these measurements; black curves: $\theta_{12}(t)$ corresponding to $\mathcal{C}_{p,\mathrm{deg}}$ (left column), and $\mathcal{C}_{p,\mathrm{deg}} \,||\, \mathcal{C}_{\mathrm{deg}}$ (right column). Solid green, red, dark-orange and dark-blue curves: the "complex-averaged" magnitude, the phase, the in-phase and the quadrature part of the heterodyne signal, respectively and for measurements shown in each column. The faint colored counterparts correspond to the individual traces. The duration of initial state preparation, the control loop and the LIA settling are indicated as cyan, yellow and gray shaded regions, respectively. For this measurement, we used the same membrane modes and the control parameters that tune it to the same EP_2 as in Figs. F.1-F.6, 7.4-7.10 and 7.21.

in Fig. 7.3 (first and second column) The corresponding fitting procedure is detailed in Sec. F.3.2. Finally, we note that the auxiliary tone is applied to mitigate parasitic photothermal transients as detailed in Secs. 4.4.3.1, 4.5.3 and Eq. (4.16).

(c) Ringdowns for spectroscopy at and around EP_2

These measurements are done in presence of the control laser tones that provide optical spring, optical damping and Floquet coupling for the membrane modes. Their timing sequence is given in Fig. 7.3(third column) and the fitting routine in Sec. Sec. F.3.3.

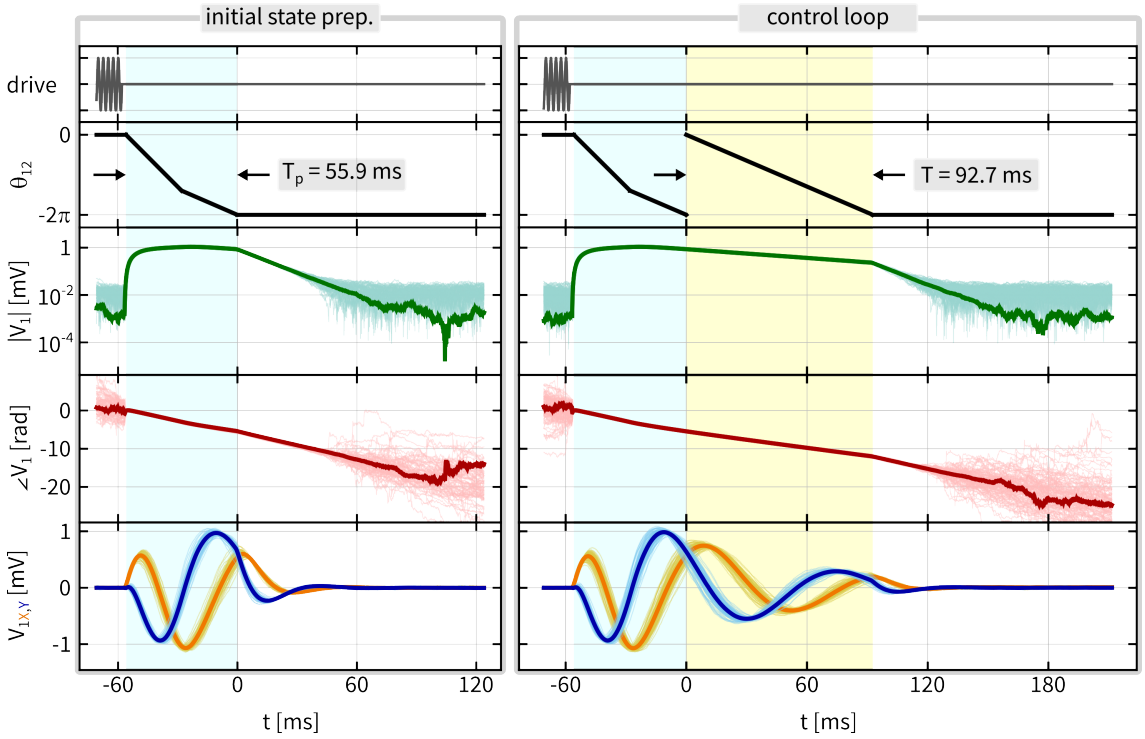

Figure F.8: Complex averaging for the initial state vector $\vec{x}(0)$, and its evolution to $\vec{x}(T)$ along a control loop in $\mathcal{EP}_2$: state vector component II. First column: measurements for the second component of $\vec{x}(0)$ obtained by transporting $\vec{x}(-T_p)$ along $\mathcal{C}_{p,\mathrm{deg}}$. **Second column:** measurements for the second component of $\vec{x}(T)$ obtained by transporting $\vec{x}(0)$ along a "simple" non-contractible $\mathcal{C}_{\mathrm{deg}}$. For both columns, dark gray curves: a schematic of the driving force applied to the membrane, which is switched off at $t = -T_p - T_{\mathrm{wait}}$. $T_{\mathrm{wait}} =$ 2 ms is a programmed delay used in these measurements; black curves: $\theta_{12}(t)$ corresponding to $\mathcal{C}_{p,\mathrm{deg}}$ (left column), and $\mathcal{C}_{p,\mathrm{deg}} \,||\, \mathcal{C}_{\mathrm{deg}}$ (right column). Solid green, red, dark-orange and dark-blue curves: the "complex-averaged" magnitude, the phase, the in-phase and the quadrature part of the heterodyne signal, respectively and for measurements shown in each column. The faint colored counterparts correspond to the individual traces. The duration of initial state preparation, the control loop and the LIA settling are indicated as cyan, yellow and gray shaded regions, respectively. For this measurement, we used the same membrane modes and the control parameters that tune it to the same EP_2 as in Figs. F.1-F.7, 7.4-7.10 and 7.21.

We note that each ringdown measurement is subject to "complex averaging" as detailed in Sec. D.1.1. In general, we acquire 70-80 individual copies of ringdown measurements for the initial state preparation step, 50-500 individual copies for the control loop traversal step, 50 individual copies for spectroscopy at EP_2 step and ∼30 individual bare ringdowns, which are then subject to complex averaging and subsequent analysis. An exemplary illustration of this procedure is shown in Figs. F.7 and F.8 for state vector measurement and Fig. F.9 for corresponding spectroscopy at EP_2. For each datapoint corresponding to a measurement of $\beta_{\mathrm{deg}}(T)$, all three types of ringdowns are performed including the bare ringdowns to keep track of bare membrane parameters over time. Prior

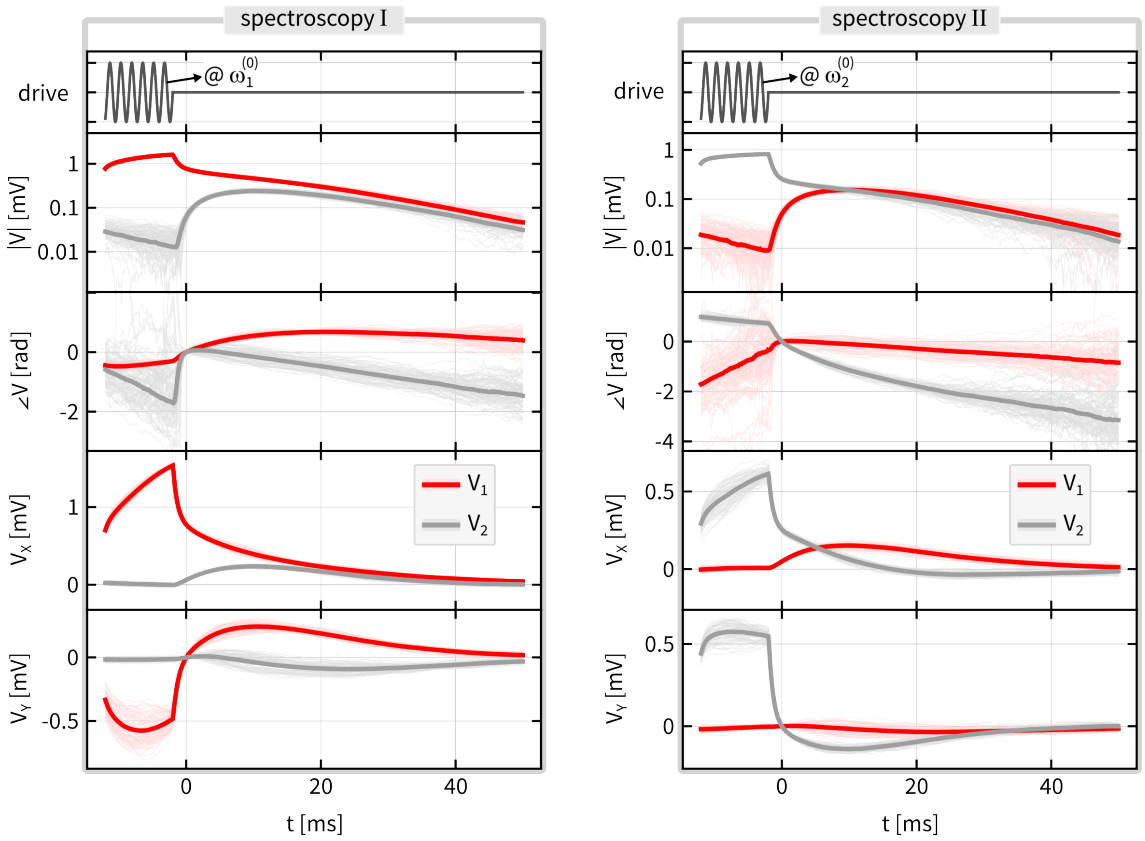

Figure F.9: Complex averaging for spectroscopy at EP_2. First column: first half of the measurements that determine λ_{EP} and R at EP_2. **Second column:** second half of the measurements that determine λ_{EP} and R at EP_2. For first and second columns, dark gray curves: a schematic of the driving force applied to the membrane near (3,3) and (5,2) membrane modes, respectively, which is switched off at $t = -T_{\text{wait}}$. $T_{\text{wait}} =$ 2 ms is a programmed delay used in these measurements; Second to fifth rows in both columns shows the magnitude, the phase, the in-phase and the quadrature part of the heterodyne signal near (3,3) membrane mode as red curves and (5,2) membrane mode as gray curves, respectively. The faint colored counterparts correspond to the individual traces. The duration of the LIA settling is indicated as the gray shaded region. For this measurement, we used the same membrane modes and the control parameters that tune it to the same EP_2 as in Figs. F.1-F.8, 7.4-7.10 and 7.21.

to each ringdown measurement, the control parameters are tapped, software stabilized and re-tapped as described in Sec. 4.6.2.3.

F.3.2 Fitting ringdowns for state vector estimation

Fitting ringdowns that correspond to state vector measurements is a straightforward affair. This simplicity is provided by our measurement protocol as described in Sec. 7.1 and above.

In presence of the auxiliary laser tone, a state vector $\vec{x}$ evolves via:

$$\dot{\vec{x}} = -iH_{\rm pt}\vec{x} \tag{F.34}$$

$$\Rightarrow \begin{bmatrix}\dot{x}_1\\ \dot{x}_2\end{bmatrix} = \begin{bmatrix}\lambda_{\rm pt,1} & 0\\ 0 & \lambda_{\rm pt,2}\end{bmatrix}\begin{bmatrix}x_1\\ x_2\end{bmatrix} \tag{F.35}$$

where in the second step we expanded out the vectors and the matrix. For all measurements reported in this chapter we use an auxiliary laser[1] with constant power $P_{\rm pt}$ and detuning from cavity resonance $\Delta_{\rm pt}$. Consequently the corresponding complex eigenvalues $\{\lambda_{\rm pt,1}, \lambda_{\rm pt,2}\}$ are constants given by DBA effect via Eq. (2.77) and the photothermal effect (Sec. 4.4.3.1). As a result $\{x_1, x_2\}$ is simply given by:

$$\begin{aligned} x_1(t) &= x_1(t_0)e^{-i\lambda_{\rm pt,1}(t-t_0)}\\ x_2(t) &= x_2(t_0)e^{-i\lambda_{\rm pt,2}(t-t_0)}\end{aligned} \tag{F.36}$$

where $x_i(t_0)$ is the constant complex amplitude of the $i^{\rm th}$ component of the state at the instant $t = t_0$. For our purposes, $t_0 = 0$: corresponds to the initial state vector and $t_0 = T$: corresponds to the final state vector.

As detailed in Sec. D.2, the above motional amplitude is transduced into an electrical signal and measured by the lock-in amplifier at two demodulation frequencies $\omega_1^{\rm mod} \approx \omega_1^{(0)}$ and $\omega_2^{\rm mod} \approx \omega_2^{(0)}$, with the being signal low-pass filtered with a bandwidth $BW \ll |\omega_1^{(0)} - \omega_2^{(0)}|$. The corresponding demodulated (complex-valued) signals are given by:

$$\begin{aligned} V_1(t) &= W\left(\lambda_{\rm pt,1}, \omega_1^{\rm mod}\right)\left(\alpha_1 x_1(t_0)e^{-i\lambda_{\rm pt,1}(t-t_0)}\right)\\ V_2(t) &= W\left(\lambda_{\rm pt,2}, \omega_2^{\rm mod}\right)\left(\alpha_2 x_2(t_0)e^{-i\lambda_{\rm pt,2}(t-t_0)}\right)\end{aligned} \tag{F.37}$$

respectively, where α is motion to electrical signal transduction factor and $W(\lambda, \omega) = (1 + i(\mathrm{Re}(\lambda) - \omega)\tau_{BW})^{-n}$ is the low-pass filter function for a signal at frequency $\mathrm{Re}(\lambda)$ that is demodulated by a local oscillator, oscillating at frequency ω with a low-pass filter

[1]For all measurements in this chapter, the value of $\Delta_{\rm pt}/2\pi \sim$ -0.5 MHz, and the corresponding $P_{\rm pt}$ is such that the intracavity optical amplitude is constant for $-t_{\rm drive} - T_p \leq t \leq t_{\rm DAq}$.

whose order, bandwidth and time-constant are given by n, BW and τ_{BW}, respectively. Additionally, the LIA has a settling time τ_{settle} (corresponding to the 99% settling time), that depends on n and τ_{BW}. To accommodate this, we exclude from any fits the data in an interval τ_{settle} after the start of a ringdown. τ_{settle} is explicitly shown as light-gray region in Figs. 7.4 and 7.5.

The signals $V_{1,2}(t)$ in Eq. (F.37) are fit to:

$$\begin{aligned} V_1(t) &= b_1 + W(\lambda_{\text{pt},1}, \omega_1^{\text{mod}}) \left(A_1(t_0) e^{-i\lambda_{\text{pt},1}(t-t_0)}\right) \\ V_2(t) &= b_2 + W(\lambda_{\text{pt},2}, \omega_2^{\text{mod}}) \left(A_2(t_0) e^{-i\lambda_{\text{pt},2}(t-t_0)}\right) \end{aligned} \tag{F.38}$$

respectively, with $\{b_i, \lambda_{\text{pt},i}, A_i\}$ with $i \in \{1, 2\}$ are the six complex-valued parameters, which denote the heterodyne signal's background, the system's eigenvalues in presence of the auxiliary tone, and the amplitudes of decaying exponentials, respectively. For the initial state preparation case with $t_0 = 0$, $\{b_i, \lambda_{\text{pt},i}, A_i\}$ with $i \in \{1, 2\}$ are taken as complex fit parameters, whereas to obtain the final state vector i.e., for $t_0 = T$, only $\{b_i, A_i\}$ with $i \in \{1, 2\}$ are taken as complex fit parameters. The corresponding $\lambda_{\text{pt},i}$ are fixed parameters set by the value obtained by fitting the corresponding initial state preparation ringdown measurement. We justify this choice of fixing $\lambda_{\text{pt},i}$ for the latter case by noting that **(a)** for all control paths used in this chapter, $\lambda_{\text{pt},i}$ are the same at the start and at the end, and **(b)** the two classes of measurements are done in sequence to mitigate the impact of systematic errors due to temporal drifts.

From the fits that determine the initial and the final states, we obtain:

$$x_1(0) = A_1(0)/\alpha_1 \;\; ; \;\; x_2(0) = A_2(0)/\alpha_2 \tag{F.39}$$

$$x_1(T) = A_1(T)/\alpha_1 \; ; \; x_2(T) = A_2(T)/\alpha_2 \tag{F.40}$$

These amplitudes subsequently get utilized to compare $\vec{x}(T)$ to $\vec{x}(0)$, as detailed in Sec. 7.1.4. Figs. 7.4 and 7.5 illustrate the fits to the ringdown data corresponding to initial and final state vector measurements

F.3.3 Ringdown spectroscopy fitting at and around EP_2

In this section, we describe our fitting procedure to extract nearly degenerate eigenvalues and state vector amplitudes proportional to nearly degenerate eigenvectors at and around EP_2, from ringdown measurements.

F.3.3.1 Initial setup

Our procedure utilizes two key facts:

(i) We can only approach an EP_2 with a finite precision and accuracy.

(ii) Any matrix whether degenerate and defective or non-degenerate and non-defective, can be Schur decomposed (Sec. F.2.2.1), and the Schur decomposed form varies smoothly with parameters (Sec. F.2.2.2).

Using **(i)**, we can always in-principle diagonalize the dynamical matrix H that governs the system as $H_D = S_D^{-1} H S_D$ and explicitly

$$H_{\mathrm{D}} = \begin{bmatrix} \lambda_+ & 0 \\ 0 & \lambda_- \end{bmatrix} \tag{F.41}$$

and we chose

$$S_{\mathrm{D}} = \begin{bmatrix} 1 & v_2 e^{i\theta} \\ v_1 e^{-i\theta} & 1 \end{bmatrix} \tag{F.42}$$

where $(1, v_1 e^{-i\theta})^{\mathrm{T}}$ and $(v_2 e^{i\theta}, 1)^{\mathrm{T}}$ are the two eigenvectors of H, which in turn is taken to be of the form given by Eq. (F.15), i.e., the "simple" control loop parameterization. Here $(v_1, v_2) \in \mathbb{C}$ and θ is real-valued. Re-expressing H as $H = S_D H_D S_D^{-1}$, and explicitly

$$H = \frac{1}{1 - v_1 v_2} \begin{bmatrix} \lambda_+ - v_1 v_2 \lambda_- & -e^{i\theta} v_2 (\lambda_+ - \lambda_-) \\ e^{-i\theta} v_1 (\lambda_+ - \lambda_-) & -v_1 v_2 \lambda_+ + \lambda_- \end{bmatrix} \tag{F.43}$$

which becomes crucial for the next steps.

Now applying Schur decomposition on H in Eq. (F.43), using the unitary U given

by

$$U = \frac{1}{\sqrt{1+|v_1|^2}} \begin{bmatrix} 1 & -v_1^* \\ v_1 e^{-i\theta} & e^{-i\theta} \end{bmatrix}, \tag{F.44}$$

the upper triangular $T_U = U^\dagger H U$ reads

$$T_U = \begin{bmatrix} \lambda_+ & -\frac{(v_1^*+v_2)(\lambda_+-\lambda_-)}{1-v_1 v_2} \\ 0 & \lambda_- \end{bmatrix} \tag{F.45}$$

and we identify the upper right entry as

$$\rho = -\frac{(v_1^*+v_2)(\lambda_+-\lambda_-)}{1-v_1 v_2} \tag{F.46}$$

Substituting ρ given by Eq. (F.46) in Eq. (F.21), we have

$$A \equiv R_{\text{eff}} = (\lambda_+ - \lambda_-)\left(\frac{1}{1-v_1 v_2} - \frac{1}{2}\right) \tag{F.47}$$

and as such, this form of $A \equiv R_{\text{eff}}$ is tractable via the ringdown spectroscopy measurements, as shown below. Notice that A by definition, varies smoothly around an EP_2, and takes the role of R at EP_2. As result, the right hand side of Eq. (F.47) is also expected to vary smoothly at and around EP_2.

With this setup in place, we now describe the specific manner in which we perform and fit such ringdown spectroscopy measurements, below.

F.3.3.2 Measurement and fitting routine

The ringdown spectroscopy measurements are similar to those corresponding to the initial state preparation in Chapter 5 (Sec. D.2), with the additional fact that the initial state vector is proportional to $(1,0)^{\mathrm{T}}$ or $(0,1)^{\mathrm{T}}$, when expressed in the basis of uncoupled membrane modes. This is accomplished by turning off all control tones that mediate coupling between the two chosen membrane modes, and mechanically driving one of them for programmed time duration until $t = 0$. The corresponding procedure for ringdown

spectroscopy of membrane modes is sketched in Fig. 7.3 (third column) while Fig. 7.6 shows an exemplary ringdown spectroscopy measurement at an EP_2. Its first and second column corresponds to initial state vector being $(1,0)^{\mathrm{T}}$ and $(0,1)^{\mathrm{T}}$, respectively.

At $t = 0$, all control tone parameters are set to their fixed target values[1] and are turned on, while the initial state vector rings down. This ringdown can be represented as

$$\vec{x}(t) = S_{\mathcal{R}}^{-1}(t) S_{\mathrm{D}} \vec{x}_{\mathrm{D}}(t) = \begin{bmatrix} x_+ e^{-i\Lambda_{1+}t} + v_2 x_- e^{-i\Lambda_{1-}t} \\ v_1 x_+ e^{-i\Lambda_{2+}t} + x_- e^{-i\Lambda_{2-}t} \end{bmatrix} \tag{F.48}$$

in the lab frame, with $x_D(t) = (x_+ e^{-i\lambda_+ t}, x_- e^{-i\lambda_- t})^{\mathrm{T}}$, S_D given by Eq. (F.42) and $S_{\mathcal{R}}$ given by Eq. (2.79). For the two independent state vector initializations, i.e., $\vec{x}^{(1)}(0) \propto (1,0)^{\mathrm{T}}$ and $\vec{x}^{(2)}(0) \propto (0,1)^{\mathrm{T}}$, we retrieve the following relations:

$$x_-^{(1)} = -v_1 x_+^{(1)} \tag{F.49}$$

and

$$x_+^{(2)} = -v_2 x_-^{(2)}, \tag{F.50}$$

respectively, with $^{(i)}$ indicating i^{th} initialization with $i \in \{1,2\}$.

The above motion is transduced onto the optical field, converted into an electronic signal, measured and demodulated by the lock-in amplifier (LIA) at two frequencies, $\omega_1^{\mathrm{mod}} \sim \omega_1^{(0)}$ and $\omega_2^{\mathrm{mod}} \sim \omega_2^{(0)}$, where $\omega_i^{(0)}$ is the bare resonance frequency of i^{th} membrane mode. The corresponding demodulated (complex-valued) signals are given by:

$$\begin{aligned} V_1(t) &= \alpha_1 \left(W(\Lambda_{1+}, \omega_1^{\mathrm{mod}}) x_+ e^{-i\Lambda_{1+}t} + W(\Lambda_{1-}, \omega_1^{\mathrm{mod}}) v_2 x_- e^{-i\Lambda_{1-}t} \right) \\ V_2(t) &= \alpha_2 \left(W(\Lambda_{2+}, \omega_2^{\mathrm{mod}}) v_1 x_+ e^{-i\Lambda_{2+}t} + W(\Lambda_{2-}, \omega_2^{\mathrm{mod}}) x_- e^{-i\Lambda_{2-}t} \right) \end{aligned} \tag{F.51}$$

respectively, where α and $W(\lambda, \omega)$ are defined in Sec. F.3.2. Similar to Sec. F.3.2, the data within the 99% settling time of the LIA (τ_{settle}) interval is excluded from all fits. τ_{settle} is explicitly shown as light-gray region in Figs. 7.6.

[1] Quick reminder: for spectroscopy measurement we set the beat-note phase $\theta_{12} = 0$.

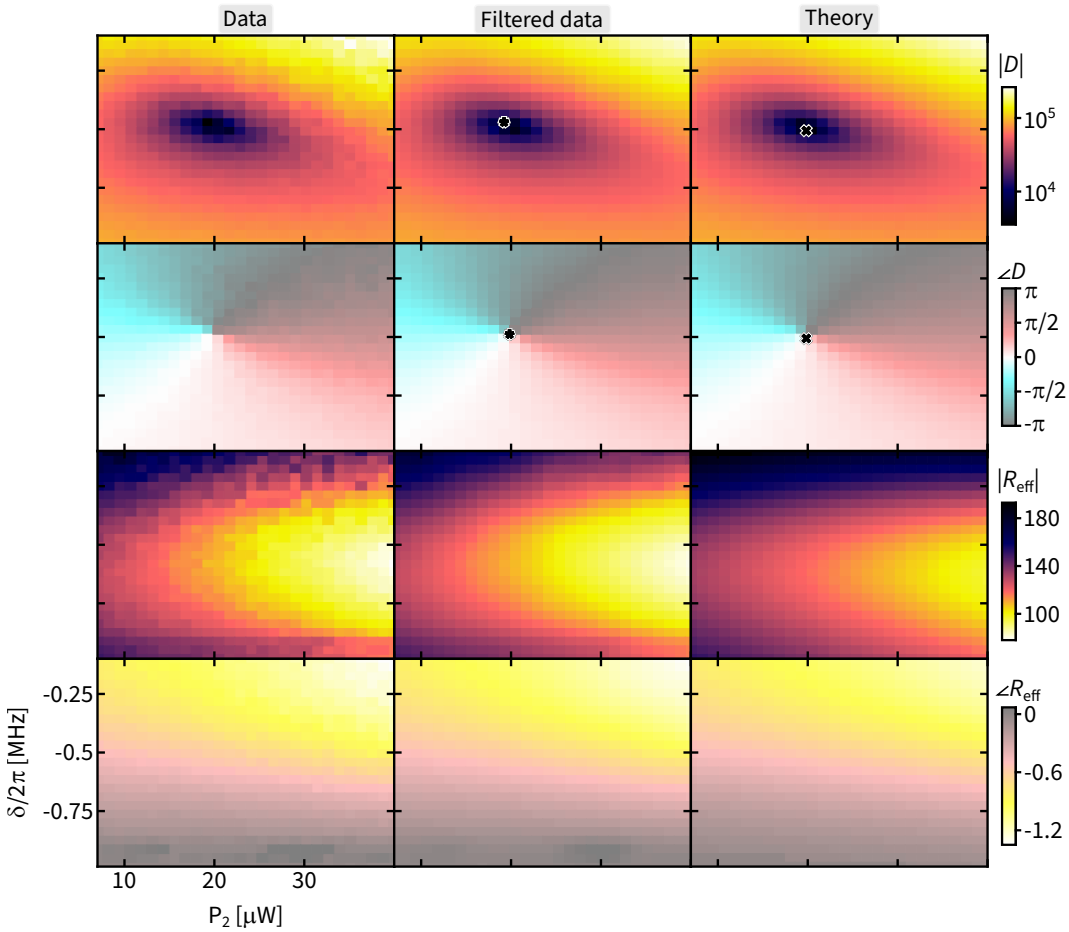

Figure F.10: Ringdown spectroscopy of R_{eff}. $D(P_2, \delta)$ and $R_{\text{eff}}(P_2, \delta)$ (Eq. (F.47)). Left column: data; middle column: filtered data, black star: experimentally predicted EP_2 location; right column: fit, black cross: theoretically predicted EP_2 location. For this measurement, we used the (3,3) and the (5,3) membrane modes with fixed control parameters: $P_1 = 30$ μW, $\eta/2\pi = -45$ Hz for the red-detuned laser tones and $P_4 =$ 33.5 μW, $\Delta_4/2\pi = +3.5$ MHz for the blue-detuned laser tone.

Using Eqs. (F.49) and (F.50), we adapt Eq. (F.51) to encode the two independent state vector initializations as:

$$V_1^{(1)}(t) = \alpha_1 x_+^{(1)} \left(W(\Lambda_{1+}, \omega_1^{\text{mod}}) e^{-i\Lambda_{1+}t} - W(\Lambda_{1-}, \omega_1^{\text{mod}}) v_1 v_2 e^{-i\Lambda_{1-}t} \right)$$
$$V_2^{(1)}(t) = \alpha_2 v_1 x_+^{(1)} \left(W(\Lambda_{2+}, \omega_2^{\text{mod}}) e^{-i\Lambda_{2+}t} - W(\Lambda_{2-}, \omega_2^{\text{mod}}) e^{-i\Lambda_{2-}t} \right) \tag{F.52}$$

and

$$V_1^{(2)}(t) = \alpha_1 v_2 x_-^{(2)} \left(-W(\Lambda_{1+}, \omega_1^{\text{mod}}) e^{-i\Lambda_{1+}t} + W(\Lambda_{1-}, \omega_1^{\text{mod}}) e^{-i\Lambda_{1-}t} \right)$$
$$V_2^{(2)}(t) = \alpha_2 x_-^{(2)} \left(-W(\Lambda_{2+}, \omega_2^{\text{mod}}) v_1 v_2 e^{-i\Lambda_{2+}t} + W(\Lambda_{2-}, \omega_2^{\text{mod}}) e^{-i\Lambda_{2-}t} \right) \tag{F.53}$$

respectively. Upon further algebraic simplifications, the two sets of heterodyne signals $\left(V_1^{(1)}(t), V_2^{(1)}(t)\right)$ and $\left(V_1^{(2)}(t), V_2^{(2)}(t)\right)$ above, are subsequently fit to:

$$\begin{aligned} V_1^{(1)}(t) &= A^{(1)}\left(W(\Lambda_{1+}, \omega_1^{\text{mod}})e^{-i\Lambda_{1+}t} - W(\Lambda_{1-}, \omega_1^{\text{mod}})ke^{-i\Lambda_{1-}t}\right) + b_1^{(1)} \\ V_2^{(1)}(t) &= C^{(1)}\left(W(\Lambda_{2+}, \omega_2^{\text{mod}})e^{-i\Lambda_{2+}t} - W(\Lambda_{2-}, \omega_2^{\text{mod}})e^{-i\Lambda_{2-}t}\right) + b_2^{(1)}, \end{aligned} \tag{F.54}$$

and

$$\begin{aligned} V_1^{(2)}(t) &= \frac{k\,A^{(1)}C^{(2)}}{C^{(1)}}\left(-W(\Lambda_{1+}, \omega_1^{\text{mod}})e^{-i\Lambda_{1+}t} + W(\Lambda_{1-}, \omega_1^{\text{mod}})e^{-i\Lambda_{1-}t}\right) + b_1^{(2)} \\ V_2^{(2)}(t) &= C^{(2)}\left(-W(\Lambda_{2+}, \omega_2^{\text{mod}})ke^{-i\Lambda_{2+}t} + W(\Lambda_{2-}, \omega_2^{\text{mod}})e^{-i\Lambda_{2-}t}\right) + b_2^{(2)}, \end{aligned} \tag{F.55}$$

where $\{b_i^{(j)}, \lambda_\pm, A^{(1)}, C^{(1)}, C^{(2)}, k\}$ with $i, j \in \{1, 2\}$ are ten complex-valued fit parameters. The $b_i^{(j)}$s for $i, j \in \{1, 2\}$ encode the heterodyne signal's background, $\lambda_\pm$ the eigenvalues. To be clear, $\lambda_\pm$ appear implicitly in Eq. (F.54) and (F.55) by way of Eq. (2.82). The parameters $\{A^{(1)}, C^{(1)}, C^{(2)}\}$ denote the common complex amplitude, and $k = v_1 v_2$. Subsequently, the fitted $\{\lambda_+, \lambda_-, k\}$ are used to compute R_{eff} as given in Eq. (F.47). Fig. F.10 illustrates measured $R_{\text{eff}}(P_2, \delta)$ alongside $D(P_2, \delta)$. Its agreement to the theoretically predicted R_{eff}, also shown in Fig. F.10, is reasonable. Finally, by performing and ringdown measurements as close as possible to an EP_2 (Sec. 7.1.1) thus provides λ_{EP} and R as given in Eqs. (7.3) and (7.4), respectively.

F.4 Estimating the asymptote of $\boldsymbol{\beta_{\text{deg}}(T)}$

In this section, we describe the much awaited asymptote analysis of $\beta_{\text{deg}}(T)$ and $\overline{\beta}_{\text{deg}}(T)$ that provide estimate for $\phi_{B,\text{deg}}$ and R. Throughout this chapter we have utilized three distinct variants of asymptote analysis depending on the case under consideration. They are described below.

F.4.1 Case I: $\angle R = 0$

For this case, we consider $\beta_{\rm deg}(T \geq 2T^*)$. T^* corresponds to the duration of $\mathcal{C}_{\rm deg}$ traversal, for which $\beta_{\rm deg}(T^*) = \phi_{B,\rm deg}$. For $\mathcal{C}_{\rm deg}$ defined via $\vec{Y}_{EP}$ (Eq.(7.1)) and $\theta_{12}(s)$ with $0 \leq s \leq 1$, we have $T^* = \partial_s \theta_{12}(s)|_{\rm max}/4R$. In the case of "simple" $\mathcal{C}_{\rm deg}$ with $\theta_{12}(s) = 2\pi n s \mod 2\pi$, $T^* = n\pi/2R$.

Subsequently, for $\mathcal{C}_{\rm deg}$ with 2π winding of $\theta_{12}(s)$, $\phi_{B,\rm deg}$ is estimated as the mean and standard deviation of both ${\rm Re}(\beta_{{\rm deg},1}(2T^* \leq T \leq T_{\sf DAq}))$ and ${\rm Re}(\beta_{{\rm deg},2}(2T^* \leq T \leq T_{\sf DAq}))$ taken together. $T_{\sf DAq}$ denotes the maximum duration of $\mathcal{C}_{\rm deg}$ for which we acquired data. This exercise is illustrated in Figs. 7.8(d), 7.19(third column), 7.11(a,c-first column), 7.12 and 7.21(a,b-first row). For the case studied in Sec. 7.2.1 that corresponds to $\mathcal{C}_{\rm deg}$ with $2n\pi$ winding of $\theta_{12}(s)$, we deployed $\overline{\beta}_{\rm deg}(T)$. Here, $\phi_{B,\rm deg}$ is estimated as the mean and standard deviation of $\phi_{B,{\rm deg},1}$ and $\phi_{B,{\rm deg},2}$, where $\phi_{B,{\rm deg},i}$ is given by the mean and standard deviation of ${\rm Re}(\overline{\beta}_{{\rm deg},i}(2T^* \leq T \leq T_{\sf DAq})) \mod 2\pi$. This is shown in Fig. 7.10(a).

To obtain R from measurements involving $\mathcal{C}_{\rm deg}$ with 2π winding of $\theta_{12}(s)$, we simultaneously fit both ${\rm Im}(\beta_{{\rm deg},1}(2T^* \leq T \leq T_{\sf DAq})/\sqrt{T})$ and ${\rm Im}(\beta_{{\rm deg},2}(2T^* \leq T \leq T_{\sf DAq})/\sqrt{T})$ to $C + a/T$ with $\{C, a\}$ as real-valued fit parameters. R is then reported as the $C^2/2\pi$. The result of this analysis is illustrated in Figs. 7.8(d), 7.20(third column), 7.11(b,c-second column), 7.12 and 7.21(a,b-second row). For the case studied in Sec. 7.2.1 that involves $\mathcal{C}_{\rm deg}$ with $2n\pi$ winding of $\theta_{12}(s)$, we simultaneously fit ${\rm Im}(\overline{\beta}_{{\rm deg},1}(2T^* \leq T \leq T_{\sf DAq})/\sqrt{T})$ and ${\rm Im}(\overline{\beta}_{{\rm deg},2}(2T^* \leq T \leq T_{\sf DAq})/\sqrt{T})$ to the same function as above. Subsequently, R is given by $C^2/2n\pi$. This is shown in Fig. 7.10(b,c).

F.4.2 Case II: $\angle R \neq 0$

As described in Sec. 7.2.2.2, data corresponding to this case are analyzed via two distinct methods. In addition, we redefine T^* to accommodate the complex value of R as $T^* = \partial_s \theta_{12}(s)|_{\rm max}/4|R|$. This can be thought analogously to the non-degenerate case where the adiabatic time-scale $T_{\rm ad} \propto 1/|\delta\lambda|$, where we note the appearance of $|.|$. For this entire study, we considered "simple" non-contractible $\mathcal{C}_{\rm deg}$ with $\theta_{12}(s) = 2\pi s$ and as a

result $T^* = \pi/2|R|$.

The first method utilizes the value of R obtained from spectroscopy measurements at EP_2, denoted as $\overline{R}$. We then define $\tilde{\beta}_{\mathrm{deg}}(T) = \beta_{\mathrm{deg}}(T) - \sqrt{2\pi\overline{R}T}$. $\phi_{B,\mathrm{deg}}$ is subsequently obtained by taking the mean and the standard deviation of both components of $\mathrm{Re}(\tilde{\beta}_{\mathrm{deg}}(2T^* \leq T \leq T_{\mathsf{DAq}}))$. This exercise is illustrated in Figs. 7.14, 7.17 and 7.18.

For the second method we simultaneously fit both components of the complex valued $\beta_{\mathrm{deg}}(2T^* \leq t \leq T_{\mathsf{DAq}})$ to $a + i\sqrt{(b_r + ib_i)T - \pi^2}$ as prescribed by Eq. (2.57), with $\{a, b_r, b_i\}$ as real-valued fit parameters. We then estimate $\phi_{B,\mathrm{deg}} = a$ and $R = b_r + ib_i$. Fig. 7.15 illustrates this analysis method.

F.5 Additional views of SS$\sqrt{T}$G data

Here we provide additional views of the SS$\sqrt{T}$G data shown in panels (b,c) of Fig. 7.28. For each trace that shows the amplitude of the state vector undergoing SS$\sqrt{T}$G in Fig. 7.28(b,c), Fig. F.11(b,c) shows the corresponding phase of the state vector undergoing SS$\sqrt{T}$G, respectively. These illustrations provide a some evidence of phase-coherence of the motion undergoing SS$\sqrt{T}$G, and its loss thereof with increasing duration of control loops ($\mathcal{C}_{\mathrm{deg,amp},n}$) that produce SS$\sqrt{T}$G. Similar to its SSGG counterpart, SS$\sqrt{T}$G is a linear and phase-insensitive process and thereby the phase will diffuse [251–254].

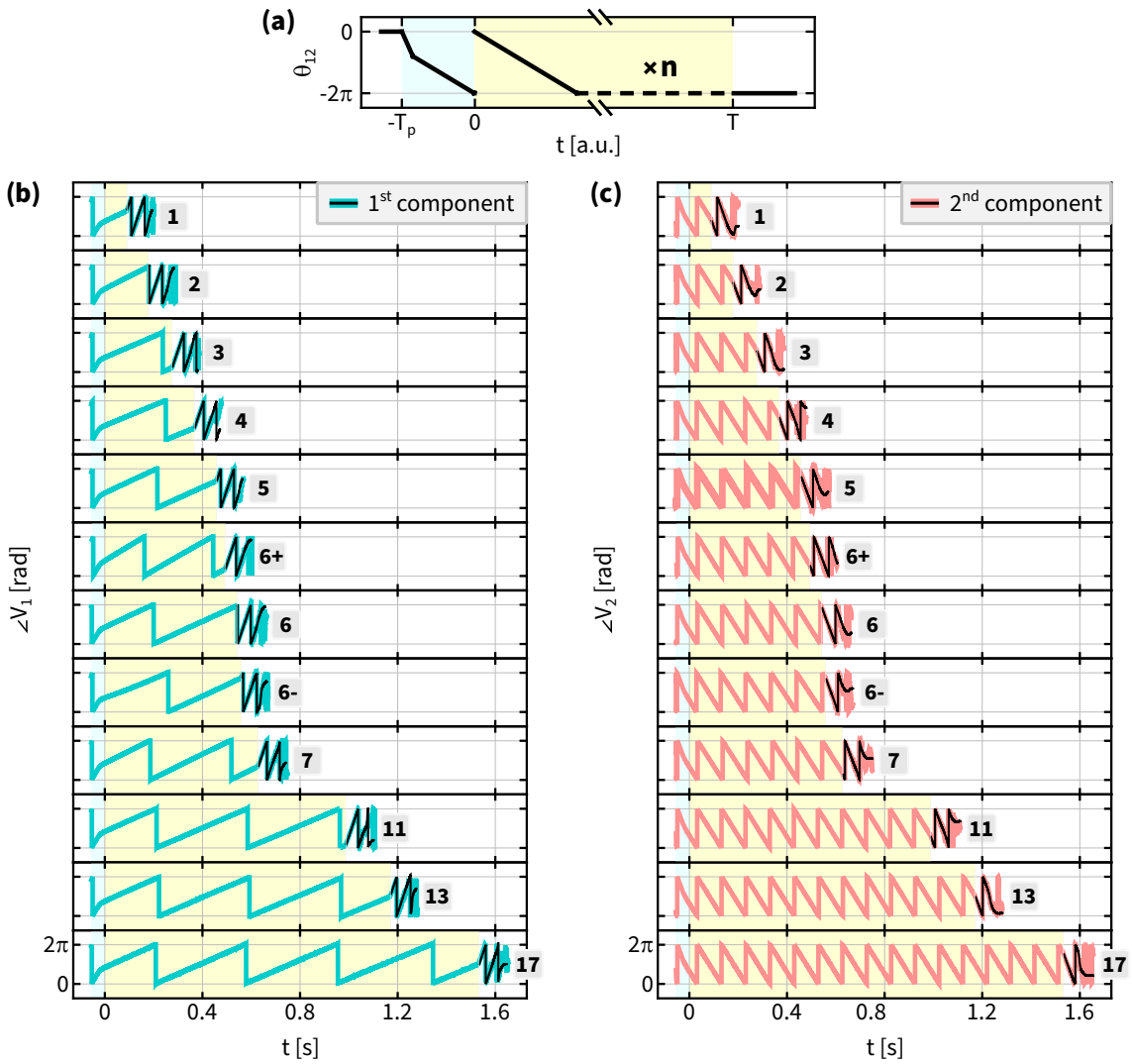

Figure F.11: Tracking the phase of motion undergoing SS$\sqrt{T}$G. (a) $\theta_{12}(t)$ corresponding to $\mathcal{C}_{p,\mathrm{deg}} \mid\mid \mathcal{C}_{\mathrm{deg,amp},n}$. **(b)** Cyan curves: data corresponding the phase of the state vector initialized as the least-dissipative eigenvector of H', as inferred from its first component when traversing $\mathcal{C}_{\mathrm{deg,amp},n}$ for $T = 88.5$ ms corresponding to $n \in \{1, 2, 3, 4, 5, 6, 7, 11, 13, 17\}$; for $T = 82$ ms corresponding to $n =$ 6+; for $T = 93$ ms corresponding to $n =$ 6−, respectively. Black curves: fit to ringdown data (Sec. F.3.2). We note that all panels shown here share the same X and Y axes as the bottom-most panel. **(c)** Same as (b) but showing the phase of the state vector initialized as the least-dissipative eigenvector of H', as inferred from its second component. We note that all panels shown here share the same X and Y axes as the bottom-most panel. For this measurement, we used the same membrane modes and the control parameters that tune it to the same EP_2 as in Figs. 7.27 and 7.28.

F.6 System parameters

In this section, we tabulate various parameters that appear the two-mode optomechanical model that describes the experimental two-mode system utilized in this chapter, as described in Sec. 2.3.2, with the addition of the photothermal effect (Sec. 4.4.3.1). The values of these parameters are obtained from device controllers (Secs. 4.4.3 and 4.6.1), cavity spectroscopy measurements (Sec. 4.2.3.3) and mechanical spectroscopy measurements of the bare modes as well as of the coupled modes in and around all the EP_2 accessed in this chapter (referred to as multi-tone DBA, see also discussion in Sec. 7.1.1). These values are listed in Table F.1. See also Sec. 4.6.3 for a complimentary study evaluating the experimental setup's stability over the same time period during which most of the data presented in this chapter was acquired.

Parameter	Value	Sample size	Source
λ (nm)	1549.987	1	Laser controller
$\kappa/2\pi$ (MHz)	2.221 $\pm$ 0.067	21	Multi-tone DBA
ϵ	0.85	1	Cavity spectroscopy
$\kappa_{\mathrm{in}}/\kappa$	0.41	1	Cavity spectroscopy
$\tilde{\omega}_1^{(0)}/2\pi$ (Hz)	2423438 $\pm$ 8	21	Bare Ringdown
$\tilde{\omega}_2^{(0)}/2\pi$ (Hz)	3075815 $\pm$ 10	21	Bare Ringdown
$\tilde{\omega}_3^{(0)}/2\pi$ (Hz)	3330590 $\pm$ 6	11	Bare Ringdown
$\tilde{\gamma}_1^{(0)}/2\pi$ (Hz)	4.3 $\pm$ 0.3	21	Bare Ringdown
$\tilde{\gamma}_2^{(0)}/2\pi$ (Hz)	16.5 $\pm$ 0.1	21	Bare Ringdown
$\tilde{\gamma}_3^{(0)}/2\pi$ (Hz)	3.58 $\pm$ 0.06	11	Bare Ringdown
$g_1/2\pi$ (Hz)	4.86 $\pm$ 0.10	21	Multi-tone DBA
$g_2/2\pi$ (Hz)	4.07 $\pm$ 0.09	21	Multi-tone DBA
$g_3/2\pi$ (Hz)	2.63 $\pm$ 0.03	11	Multi-tone DBA
$A_1/2\pi$ (μHz)	4.49 $\pm$ 0.16	21	Multi-tone DBA
$A_2/2\pi$ (μHz)	5.64 $\pm$ 0.31	21	Multi-tone DBA
$A_3/2\pi$ (μHz)	4.56 $\pm$ 0.25	11	Multi-tone DBA
$\Delta_0/2\pi$ (kHz)	-53.2 $\pm$ 12.8	21	Multi-tone DBA

Table F.1: System parameters. λ: the laser wavelength. κ: the optical cavity linewidth. ϵ: the cavity-mode-matching efficiency. κ_{in}: the optical cavity input coupling rate. $\tilde{\omega}_i^{(0)}$: the bare resonance frequency of the i^{th} mechanical mode (i.e., in the absence of any optomechanical effects). $\tilde{\gamma}_i^{(0)}$: the bare energy damping rate of the i^{th} mechanical mode. g_i: the optomechanical coupling rate between the optical cavity and the i^{th} mechanical mode. A_i: the photothermal coupling rate between the optical cavity and the i^{th} mechanical mode. Δ_0: detuning offset of the control tones from the optical cavity resonance(see Sec. 4.4.3 and 4.6.1). For bare resonance frequencies ($\omega^{(0)}$), energy damping rates ($\gamma^{(0)}$), optomechanical coupling rates (g) and photothermal coupling rates (A), the subscript denotes the mechanical mode: 1→(3,3), 2→(5,2), 3→(5,3). Each value is reported as the mean $\pm$ one standard deviation in the second column, over the sample size indicated in the third column. The source of these parameter values are indicated in the fourth column.

Bibliography

[1] H. Goldstein, C.P. Poole, and J.L. Safko. *Classical Mechanics*. Addison Wesley, 2002. URL https://books.google.com/books?id=tJCuQgAACAAJ.

[2] David J Griffiths. *Introduction to electrodynamics*. Pearson, Boston, MA, 2013. URL https://cds.cern.ch/record/1492149.

[3] Ramamurti Shankar. *Principles of quantum mechanics*. Plenum, New York, NY, 1980. URL https://cds.cern.ch/record/102017.

[4] W.H. Zurek. *Decoherence and Quantum Darwinism: From Quantum Foundations to Classical Reality*. Cambridge University Press, 2025. URL https://books.google.com/books?id=PBAP0QEACAAJ.

[5] Rudolph Emil Kalman. A new approach to linear filtering and prediction problems. *Journal of Basic Engineering*, 82(1):35, 1960. URL http://dx.doi.org/10.1115/1.3662552.

[6] S.H. Strogatz. *Nonlinear Dynamics and Chaos: With Applications to Physics, Biology, Chemistry, and Engineering*. CRC Press, 2018. URL https://books.google.com/books?id=A0paDwAAQBAJ.

[7] Antonio M. Puertas, Juan E. Trinidad-Segovia, Miguel A. Sánchez-Granero, Joaquim Clara-Rahora, and F. Javier de las Nieves. Linear response theory in stock markets. *Scientific Reports*, 11(1):23076, Nov 2021. URL https://doi.org/10.1038/s41598-021-02263-6.

[8] Aparna Guria. *On Some Inventory Problems with delay in payments in different environments*. PhD thesis, Vidyasagar University, 2013.

[9] Wikipedia contributors. Characteristic polynomial — Wikipedia, the free encyclopedia, 2025. URL https://en.wikipedia.org/w/index.php?title=Characteristic_polynomial&oldid=1330025490.

[10] M. Born and V. Fock. Beweis des adiabatensatzes. *Zeitschrift für Physik*, 51(3): 165–180, Mar 1928. URL https://doi.org/10.1007/BF01343193.

[11] G Nenciu and G Rasche. On the adiabatic theorem for nonself-adjoint hamiltonians. *Journal of Physics A: Mathematical and General*, 25(21):5741, Nov 1992. URL https://dx.doi.org/10.1088/0305-4470/25/21/027.

[12] Michael Victor Berry. Quantal phase factors accompanying adiabatic changes. *Proceedings of the Royal Society of London. A. Mathematical and Physical Sciences*, 392(1802):45–57, 1984. URL https://royalsocietypublishing.org/doi/abs/10.1098/rspa.1984.0023.

[13] Michael Berry. Geometric phase memories. *Nature Physics*, 6(3):148–150, Mar 2010. URL https://www.nature.com/articles/nphys1608.

[14] Lev Davidovich Landau. 7 - A THEORY OF ENERGY TRANSFER ON COLLISIONS. In D. TER HAAR, editor, *Collected Papers of L.D. Landau*, pages 52–59. Pergamon, 1965. URL https://www.sciencedirect.com/science/article/pii/B9780080105864500122.

[15] Lev Davidovich Landau. 9 - A THEORY OF ENERGY TRANSFER. II. In D. TER HAAR, editor, *Collected Papers of L.D. Landau*, pages 63–66. Pergamon, 1965. URL https://www.sciencedirect.com/science/article/pii/B9780080105864500146.

[16] Clarence Zener. Non-adiabatic crossing of energy levels. *Proceedings of the Royal Society of London. Series A, Containing Papers of a Mathematical and Physical Character*, 137(833):696–702, 09 1932. URL https://doi.org/10.1098/rspa.1932.0165.

[17] E.C.G. Stückelberg. theory of Inelastic Collisions between Atoms. *Helvetica Physica Acta*, 5:369–423, 1932.

[18] Ettore Majorana. Atomi orientati in campo magnetico variabile. *Il Nuovo Cimento (1924-1942)*, 9(2):43–50, Feb 1932. URL https://doi.org/10.1007/BF02960953.

[19] V. Weisskopf and E. Wigner. Berechnung der natürlichen Linienbreite auf Grund der Diracschen Lichttheorie. *Zeitschrift fur Physik*, 63(1-2):54–73, January 1930.

[20] E. B. Davies. Dynamics of a multilevel wigner-weisskopf atom. *Journal of Mathematical Physics*, 15(12):2036–2041, 12 1974. URL https://doi.org/10.1063/1.1666578.

[21] Tosio Kato. *Perturbation theory for linear operators*. Classics in Mathematics (CLASSICS, volume 132). Springer, Berlin, 1995. URL https://link.springer.com/book/10.1007/978-3-642-66282-9.

[22] Ch. Miniatura, C. Sire, J. Baudon, and J. Bellissard. Geometrical phase factor for a non-hermitian hamiltonian. *Europhysics Letters*, 13(3):199, Oct 1990. URL https://dx.doi.org/10.1209/0295-5075/13/3/002.

[23] W.D. Heiss. Phases of wave functions and level repulsion. *The European Physical Journal D - Atomic, Molecular and Optical Physics*, 7(1):1–4, August 1999. URL http://dx.doi.org/10.1007/s100530050339.

[24] W. D. Heiss. Repulsion of resonance states and exceptional points. *Phys. Rev. E*, 61:929–932, Jan 2000. URL https://link.aps.org/doi/10.1103/PhysRevE.61.929.

[25] M. V. Berry. Physics of Nonhermitian Degeneracies. *Czechoslovak Journal of Physics*, 54(10):1039–1047, October 2004. URL https://link.springer.com/article/10.1023/B:CJOP.0000044002.05657.04.

[26] T. Kato. *A Short Introduction to Perturbation Theory for Linear Operators*. Springer New York, 2012. URL https://link.springer.com/book/10.1007/978-1-4612-5700-4.

[27] G. Nenciu. Linear adiabatic theory. exponential estimates. *Communications in Mathematical Physics*, 152(3):479–496, Mar 1993. URL https://doi.org/10.1007/BF02096616.

[28] Raam Uzdin, Alexei Mailybaev, and Nimrod Moiseyev. On the observability and asymmetry of adiabatic state flips generated by exceptional points. *Journal of Physics A: Mathematical and Theoretical*, 44(43):435302, Oct 2011. URL https://dx.doi.org/10.1088/1751-8113/44/43/435302.

[29] M V Berry and R Uzdin. Slow non-hermitian cycling: exact solutions and the stokes phenomenon. *Journal of Physics A: Mathematical and Theoretical*, 44(43):435303, oct 2011. URL https://doi.org/10.1088/1751-8113/44/43/435303.

[30] Thomas J. Milburn, Jörg Doppler, Catherine A. Holmes, Stefano Portolan, Stefan Rotter, and Peter Rabl. General description of quasiadiabatic dynamical phenomena near exceptional points. *Phys. Rev. A*, 92:052124, Nov 2015. URL https://link.aps.org/doi/10.1103/PhysRevA.92.052124.

[31] Jörg Doppler, Alexei A. Mailybaev, Julian Böhm, Ulrich Kuhl, Adrian Girschik, Florian Libisch, Thomas J. Milburn, Peter Rabl, Nimrod Moiseyev, and Stefan Rotter. Dynamically encircling an exceptional point for asymmetric mode switching. *Nature*, 537(7618):76–79, July 2016. URL http://dx.doi.org/10.1038/nature18605.

[32] H. Xu, D. Mason, Luyao Jiang, and J. G. E. Harris. Topological energy transfer in an optomechanical system with exceptional points. *Nature*, 537(7618):80–83, July 2016. URL http://dx.doi.org/10.1038/nature18604.

[33] Carl M. Bender and Stefan Boettcher. Real spectra in non-hermitian hamiltonians having $\mathcal{PT}$ symmetry. *Phys. Rev. Lett.*, 80:5243–5246, Jun 1998. URL https://link.aps.org/doi/10.1103/PhysRevLett.80.5243.

[34] R. El-Ganainy, K. G. Makris, D. N. Christodoulides, and Ziad H. Musslimani. Theory of coupled optical pt-symmetric structures. *Opt. Lett.*, 32(17):2632–2634, Sep 2007. URL https://opg.optica.org/ol/abstract.cfm?URI=ol-32-17-2632.

[35] K. G. Makris, R. El-Ganainy, D. N. Christodoulides, and Z. H. Musslimani. Beam dynamics in $\mathcal{PT}$ symmetric optical lattices. *Phys. Rev. Lett.*, 100:103904, Mar 2008. URL https://link.aps.org/doi/10.1103/PhysRevLett.100.103904.

[36] A. Guo, G. J. Salamo, D. Duchesne, R. Morandotti, M. Volatier-Ravat, V. Aimez, G. A. Siviloglou, and D. N. Christodoulides. Observation of $\mathcal{PT}$-symmetry breaking in complex optical potentials. *Phys. Rev. Lett.*, 103:093902, Aug 2009. URL https://link.aps.org/doi/10.1103/PhysRevLett.103.093902.

[37] Christian E. Rüter, Konstantinos G. Makris, Ramy El-Ganainy, Demetrios N. Christodoulides, Mordechai Segev, and Detlef Kip. Observation of parity–time symmetry in optics. *Nature Physics*, 6(3):192–195, Mar 2010. URL https://doi.org/10.1038/nphys1515.

[38] Turning loss into gain. *Nature Photonics*, 11(12):741–741, Dec 2017. URL https://doi.org/10.1038/s41566-017-0067-2.

[39] Bo Zhen, Chia Wei Hsu, Yuichi Igarashi, Ling Lu, Ido Kaminer, Adi Pick, Song-Liang Chua, John D. Joannopoulos, and Marin Soljačić. Spawning rings of exceptional points out of dirac cones. *Nature*, 525(7569), 2015. URL http://dx.doi.org/10.1038/nature14889.

[40] Hengyun Zhou, Chao Peng, Yoseob Yoon, Chia Wei Hsu, Keith A. Nelson, Liang Fu, John D. Joannopoulos, Marin Soljačić, and Bo Zhen. Observation of bulk fermi arc and polarization half charge from paired exceptional points. *Science*, 359 (6379):1009–1012, March 2018. URL http://dx.doi.org/10.1126/science.aap9859.

[41] Alexander Cerjan, Sheng Huang, Mohan Wang, Kevin P. Chen, Yidong Chong, and Mikael C. Rechtsman. Experimental realization of a weyl exceptional ring. *Nature Photonics*, 13(9):623–628, June 2019. URL http://dx.doi.org/10.1038/s41566-019-0453-z.

[42] Emil J. Bergholtz, Jan Carl Budich, and Flore K. Kunst. Exceptional topology of non-hermitian systems. *Rev. Mod. Phys.*, 93:015005, Feb 2021. URL https://link.aps.org/doi/10.1103/RevModPhys.93.015005.

[43] Yogesh S. S. Patil, Judith Höller, Parker A. Henry, Chitres Guria, Yiming Zhang, Luyao Jiang, Nenad Kralj, Nicholas Read, and Jack G. E. Harris. Measuring the knot of non-hermitian degeneracies and non-commuting braids. *Nature*, 607(7918): 271–275, July 2022. URL http://dx.doi.org/10.1038/s41586-022-04796-w.

[44] Haiping Hu, Shikang Sun, and Shu Chen. Knot topology of exceptional point and non-hermitian no-go theorem. *Phys. Rev. Res.*, 4:L022064, Jun 2022. URL https://link.aps.org/doi/10.1103/PhysRevResearch.4.L022064.

[45] Kun Ding, Chen Fang, and Guancong Ma. Non-hermitian topology and exceptional-point geometries. *Nature Reviews Physics*, 4(12):745–760, October 2022. URL http://dx.doi.org/10.1038/s42254-022-00516-5.

[46] Liang Feng, Ye-Long Xu, William S. Fegadolli, Ming-Hui Lu, José E. B. Oliveira, Vilson R. Almeida, Yan-Feng Chen, and Axel Scherer. Experimental demonstration of a unidirectional reflectionless parity-time metamaterial at optical frequencies. *Nature Materials*, 12(2):108–113, Feb 2013. URL https://doi.org/10.1038/nmat3495.

[47] M. Brandstetter, M. Liertzer, C. Deutsch, P. Klang, J. Schöberl, H. E. Türeci, G. Strasser, K. Unterrainer, and S. Rotter. Reversing the pump dependence of a laser at an exceptional point. *Nature Communications*, 5(1):4034, Jun 2014. URL https://doi.org/10.1038/ncomms5034.

[48] Dimitrios L. Sounas, Romain Fleury, and Andrea Alù. Unidirectional cloaking based on metasurfaces with balanced loss and gain. *Phys. Rev. Appl.*, 4:014005, Jul 2015. URL https://link.aps.org/doi/10.1103/PhysRevApplied.4.014005.

[49] Bo Peng, Şahin Kaya Özdemir, Matthias Liertzer, Weijian Chen, Johannes Kramer, Huzeyfe Yılmaz, Jan Wiersig, Stefan Rotter, and Lan Yang. Chiral modes and directional lasing at exceptional points. *Proceedings of the National Academy of Sciences*, 113(25):6845–6850, 2016. URL https://www.pnas.org/doi/abs/10.1073/pnas.1603318113.

[50] Zi Jing Wong, Ye-Long Xu, Jeongmin Kim, Kevin O'Brien, Yuan Wang, Liang Feng, and Xiang Zhang. Lasing and anti-lasing in a single cavity. *Nature Photonics*, 10 (12):796–801, Dec 2016. URL https://doi.org/10.1038/nphoton.2016.216.

[51] Liang Feng, Ramy El-Ganainy, and Li Ge. Non-hermitian photonics based on parity–time symmetry. *Nature Photonics*, 11(12):752–762, Dec 2017. URL https://doi.org/10.1038/s41566-017-0031-1.

[52] Ramy El-Ganainy, Konstantinos G. Makris, Mercedeh Khajavikhan, Ziad H. Musslimani, Stefan Rotter, and Demetrios N. Christodoulides. Non-hermitian physics and pt symmetry. *Nature Physics*, 14(1):11–19, Jan 2018. URL https://doi.org/10.1038/nphys4323.

[53] Chun-Hui Liu, Hui Jiang, and Shu Chen. Topological classification of non-hermitian systems with reflection symmetry. *Phys. Rev. B*, 99:125103, Mar 2019. URL https://link.aps.org/doi/10.1103/PhysRevB.99.125103.

[54] Kohei Kawabata, Ken Shiozaki, Masahito Ueda, and Masatoshi Sato. Symmetry and topology in non-hermitian physics. *Phys. Rev. X*, 9:041015, Oct 2019. URL https://link.aps.org/doi/10.1103/PhysRevX.9.041015.

[55] Yang Cao, Yang Li, and Xiaosen Yang. Non-hermitian bulk-boundary correspondence in a periodically driven system. *Phys. Rev. B*, 103:075126, Feb 2021. URL https://link.aps.org/doi/10.1103/PhysRevB.103.075126.

[56] Clara C. Wanjura, Matteo Brunelli, and Andreas Nunnenkamp. Correspondence between non-hermitian topology and directional amplification in the presence of disorder. *Phys. Rev. Lett.*, 127:213601, Nov 2021. URL https://link.aps.org/doi/10.1103/PhysRevLett.127.213601.

[57] Clara C. Wanjura. *Non-Hermitian Topology and Directional Amplification in Driven-Dissipative Cavity Arrays*. PhD thesis, University of Cambridge, 2022. URL https://doi.org/10.17863/CAM.90051.

[58] Matteo Brunelli, Clara C. Wanjura, and Andreas Nunnenkamp. Restoration of the non-hermitian bulk-boundary correspondence via topological amplification. *SciPost Physics*, 15(4), October 2023. URL http://dx.doi.org/10.21468/SciPostPhys.15.4.173.

[59] Jesse J. Slim, Clara C. Wanjura, Matteo Brunelli, Javier del Pino, Andreas Nunnenkamp, and Ewold Verhagen. Optomechanical realization of the bosonic kitaev chain. *Nature*, 627(8005):767–771, March 2024. URL http://dx.doi.org/10.1038/s41586-024-07174-w.

[60] Julius T. Gohsrich, Ayan Banerjee, and Flore K. Kunst. The non-hermitian skin effect: A perspective. *Europhysics Letters*, 150(6):60001, jun 2025. URL https://doi.org/10.1209/0295-5075/addf77.

[61] H. Xu, D. Mason, Luyao Jiang, and J. G. E. Harris. Topological dynamics in an optomechanical system with highly non-degenerate modes. *arXiv:1703.07374*, 2017. URL https://arxiv.org/abs/1703.07374.

[62] Hossein Hodaei, Absar U. Hassan, Steffen Wittek, Hipolito Garcia-Gracia, Ramy El-Ganainy, Demetrios N. Christodoulides, and Mercedeh Khajavikhan. Enhanced sensitivity at higher-order exceptional points. *Nature*, 548(7666):187–191, Aug 2017. URL https://doi.org/10.1038/nature23280.

[63] Weijian Chen, Şahin Kaya Özdemir, Guangming Zhao, Jan Wiersig, and Lan Yang. Exceptional points enhance sensing in an optical microcavity. *Nature*, 548(7666): 192–196, Aug 2017. URL https://doi.org/10.1038/nature23281.

[64] Sid Assawaworrarit, Xiaofang Yu, and Shanhui Fan. Robust wireless power transfer using a nonlinear parity–time-symmetric circuit. *Nature*, 546(7658):387–390, Jun 2017. URL https://doi.org/10.1038/nature22404.

[65] Mohammad-Ali Miri and Andrea Alù. Exceptional points in optics and photonics. *Science*, 363(6422):eaar7709, 2019. URL https://www.science.org/doi/abs/10.1126/science.aar7709.

[66] Hoi-Kwan Lau and Aashish A. Clerk. Fundamental limits and non-reciprocal approaches in non-hermitian quantum sensing. *Nature Communications*, 9(1), October 2018. URL http://dx.doi.org/10.1038/s41467-018-06477-7.

[67] Jan Wiersig. Review of exceptional point-based sensors. *Photon. Res.*, 8(9):1457–1467, Sep 2020. URL https://opg.optica.org/prj/abstract.cfm?URI=prj-8-9-1457.

[68] Q. Zhong, S.K. Ozdemir, A. Eisfeld, A. Metelmann, and R. El-Ganainy. Exceptional-point-based optical amplifiers. *Phys. Rev. Appl.*, 13:014070, Jan 2020. URL https://link.aps.org/doi/10.1103/PhysRevApplied.13.014070.

[69] Maryam Abbasi, Weijian Chen, Mahdi Naghiloo, Yogesh N. Joglekar, and Kater W. Murch. Topological quantum state control through exceptional-point proximity. *Phys. Rev. Lett.*, 128:160401, Apr 2022. URL https://link.aps.org/doi/10.1103/PhysRevLett.128.160401.

[70] Fahri Emre Öztürk, Tim Lappe, Göran Hellmann, Julian Schmitt, Jan Klaers, Frank Vewinger, Johann Kroha, and Martin Weitz. Observation of a non-hermitian phase transition in an optical quantum gas. *Science*, 372(6537):88–91, April 2021. URL http://dx.doi.org/10.1126/science.abe9869.

[71] Entong Zhao, Zhiyuan Wang, Chengdong He, Ting Fung Jeffrey Poon, Ka Kwan Pak, Yu-Jun Liu, Peng Ren, Xiong-Jun Liu, and Gyu-Boong Jo. Two-dimensional

non-hermitian skin effect in an ultracold fermi gas. *Nature*, 637(8046):565–573, January 2025. URL http://dx.doi.org/10.1038/s41586-024-08347-3.

[72] C. Dembowski, H.-D. Gräf, H. L. Harney, A. Heine, W. D. Heiss, H. Rehfeld, and A. Richter. Experimental observation of the topological structure of exceptional points. *Phys. Rev. Lett.*, 86:787–790, Jan 2001. URL https://link.aps.org/doi/10.1103/PhysRevLett.86.787.

[73] C. Dembowski, B. Dietz, H.-D. Gräf, H. L. Harney, A. Heine, W. D. Heiss, and A. Richter. Encircling an exceptional point. *Phys. Rev. E*, 69:056216, May 2004. URL https://link.aps.org/doi/10.1103/PhysRevE.69.056216.

[74] Rodion Kononchuk, Jizhe Cai, Fred Ellis, Ramathasan Thevamaran, and Tsampikos Kottos. Exceptional-point-based accelerometers with enhanced signal-to-noise ratio. *Nature*, 607(7920):697–702, Jul 2022. URL https://doi.org/10.1038/s41586-022-04904-w.

[75] Weiyuan Tang, Kun Ding, and Guancong Ma. Direct measurement of topological properties of an exceptional parabola. *Phys. Rev. Lett.*, 127:034301, Jul 2021. URL https://link.aps.org/doi/10.1103/PhysRevLett.127.034301.

[76] M. Naghiloo, M. Abbasi, Yogesh N. Joglekar, and K. W. Murch. Quantum state tomography across the exceptional point in a single dissipative qubit. *Nature Physics*, 15(12):1232–1236, October 2019. URL http://dx.doi.org/10.1038/s41567-019-0652-z.

[77] Weijian Chen, Maryam Abbasi, Yogesh N. Joglekar, and Kater W. Murch. Quantum jumps in the non-hermitian dynamics of a superconducting qubit. *Physical Review Letters*, 127(14), September 2021. URL http://dx.doi.org/10.1103/PhysRevLett.127.140504.

[78] J. D. Thompson, B. M. Zwickl, A. M. Jayich, Florian Marquardt, S. M. Girvin, and J. G. E. Harris. Strong dispersive coupling of a high-finesse cavity to a micromechanical membrane. *Nature*, 452(7183):72–75, March 2008. URL http://dx.doi.org/10.1038/nature06715.

[79] A M Jayich, J C Sankey, B M Zwickl, C Yang, J D Thompson, S M Girvin, A A Clerk, F Marquardt, and J G E Harris. Dispersive optomechanics: a membrane inside a cavity. *New Journal of Physics*, 10(9):095008, September 2008. URL http://dx.doi.org/10.1088/1367-2630/10/9/095008.

[80] J. C. Sankey, C. Yang, B. M. Zwickl, A. M. Jayich, and J. G. E. Harris. Strong and tunable nonlinear optomechanical coupling in a low-loss system. *Nature Physics*, 6(9):707–712, June 2010. URL http://dx.doi.org/10.1038/nphys1707.

[81] M. Underwood, D. Mason, D. Lee, H. Xu, L. Jiang, A. B. Shkarin, K. Børkje, S. M. Girvin, and J. G. E. Harris. Measurement of the motional sidebands of a nanogram-scale oscillator in the quantum regime. *Physical Review A*, 92(6), December 2015. URL http://dx.doi.org/10.1103/PhysRevA.92.061801.

[82] W D Heiss. Chirality of wavefunctions for three coalescing levels. *Journal of Physics A: Mathematical and Theoretical*, 41(24):244010, Jun 2008. URL https://dx.doi.org/10.1088/1751-8113/41/24/244010.

[83] Gilles Demange and Eva-Maria Graefe. Signatures of three coalescing eigenfunctions. *Journal of Physics A: Mathematical and Theoretical*, 45(2):025303, Dec 2011. URL https://dx.doi.org/10.1088/1751-8113/45/2/025303.

[84] Jung-Wan Ryu, Soo-Young Lee, and Sang Wook Kim. Analysis of multiple exceptional points related to three interacting eigenmodes in a non-hermitian hamiltonian. *Phys. Rev. A*, 85:042101, Apr 2012. URL https://link.aps.org/doi/10.1103/PhysRevA.85.042101.

[85] W D Heiss and G Wunner. A model of three coupled wave guides and third order exceptional points. *Journal of Physics A: Mathematical and Theoretical*, 49(49): 495303, Nov 2016. URL https://dx.doi.org/10.1088/1751-8113/49/49/495303.

[86] Jan Schnabel, Holger Cartarius, Jörg Main, Günter Wunner, and Walter Dieter Heiss. $\mathcal{PT}$-symmetric waveguide system with evidence of a third-order exceptional point. *Phys. Rev. A*, 95:053868, May 2017. URL https://link.aps.org/doi/10.1103/PhysRevA.95.053868.

[87] J. C. Garrison and E. M. Wright. Complex geometrical phases for dissipative systems. *Physics Letters A*, 128(3-4):177–181, March 1988. URL https://linkinghub.elsevier.com/retrieve/pii/037596018890905X.

[88] J. Höller, N. Read, and J. G. E. Harris. Non-hermitian adiabatic transport in spaces of exceptional points. *Phys. Rev. A*, 102:032216, Sep 2020. URL https://link.aps.org/doi/10.1103/PhysRevA.102.032216.

[89] Judith Höller. *Topological Quantization of Berry Phases in Quantum and Classical Systems*. PhD thesis, Yale University, 2020. URL https://www.proquest.com/docview/2572595301.

[90] Nicholas Read. Topological phases and quasiparticle braiding. *Physics Today*, page 38–43, Jul 2012. URL https://physicstoday.aip.org/features/topological-phases-and-quasiparticle-braiding.

[91] Chitres Guria, Qi Zhong, Sahin Kaya Ozdemir, Yogesh S. S. Patil, Ramy El-Ganainy, and Jack Gwynne Emmet Harris. Resolving the topology of encircling multiple exceptional points. *Nature Communications*, 15(1), February 2024. URL http://dx.doi.org/10.1038/s41467-024-45530-6.

[92] J. R. Lane, C. Guria, J. Höller, T. D. Montalvo, Y. S. S. Patil, and J. G. E. Harris. Complex berry phase and steady-state geometric amplification in non-hermitian systems, 2025. URL https://arxiv.org/abs/2503.23197.

[93] Mitchell J. Underwood. *Cryogenic Optomechanics with a Silicon Nitride Membrane*. PhD thesis, Yale University, 2016. URL https://harrislab.yale.edu/files/thesis/Underwood_Thesis.pdf.

[94] David R. Mason. *Dynamical Behavior near Exceptional Points in an Optomechanical System*. PhD thesis, Yale University, 2018. URL https://harrislab.yale.edu/files/thesis/Mason_Thesis.pdf.

[95] Parker Henry. *Measuring the Knot of Non-Hermitian Degeneracies and Non-Abelian Braids*. PhD thesis, Yale University, 2022. URL https://harrislab.yale.edu/files/thesis/Henry_Thesis.pdf.

[96] V. I. Arnold. On matrices depending on parameters. *Russian Mathematical Surveys*, 26(2):29, 1971. URL https://iopscience.iop.org/article/10.1070/RM1971v026n02ABEH003827.

[97] Wikipedia contributors. Homeomorphism — Wikipedia, the free encyclopedia, 2025. URL https://en.wikipedia.org/w/index.php?title=Homeomorphism&oldid=1328300518.

[98] R. Fox and L. Neuwirth. The braid groups. *Mathematica Scandinavica*, 10:119–126, 1962. URL https://www.mscand.dk/article/view/10518.

[99] V. I. Arnold. *Vladimir I. Arnold, Collected Works Vol. II*. Springer-Verlag, 2014. URL https://link.springer.com/book/10.1007/978-3-642-31031-7.

[100] gmoss. Mathematics StackExchange: Isotopy and Homotopy, 2013. URL https://math.stackexchange.com/questions/296170/isotopy-and-homotopy.

[101] Agatha Mallett. Deformation Retract of Punctured Torus, 2013. URL https://www.youtube.com/watch?v=j2HxBUaoaPU.

[102] E. Artin. Theory of braids. *Annals of Mathematics*, 48(1):101–126, 1947.

[103] Wikipedia contributors. Isomorphism — Wikipedia, the free encyclopedia, 2025. URL https://en.wikipedia.org/w/index.php?title=Isomorphism&oldid=1319141431.

[104] Yong-Shi Wu. General theory for quantum statistics in two dimensions. *Phys. Rev. Lett.*, 52:2103–2106, Jun 1984. URL https://link.aps.org/doi/10.1103/PhysRevLett.52.2103.

[105] Wikipedia contributors. 3-sphere — Wikipedia, the free encyclopedia, 2025. URL https://en.wikipedia.org/w/index.php?title=3-sphere&oldid=1318091345. [Online; accessed 17-January-2026].

[106] J. Milnor. *Singular Points of Complex Hypersurfaces*. Annals of Mathematics Studies. Princeton University Press, 1968. URL https://press.princeton.edu/books/paperback/9780691080659/singular-points-of-complex-hypersurfaces.

[107] Wikipedia contributors. Stereographic projection — Wikipedia, the free encyclopedia, 2025. URL https://en.wikipedia.org/w/index.php?title=Stereographic_projection&oldid=1321947812.

[108] J.R. Weeks. *The Shape of Space: How to Visualize Surfaces and Three-dimensional Manifolds*. Monographs and textbooks in pure and applied mathematics. M. Dekker, 1985. URL https://books.google.com/books?id=mVHvAAAAMAAJ.

[109] Wikipedia contributors. N-sphere Wikipedia, the free encyclopedia, 2025. URL https://en.wikipedia.org/w/index.php?title=N-sphere&oldid=1328221352.

[110] C.C. Adams. *The Knot Book*. W.H. Freeman, 1994. URL https://bookstore.ams.org/KNOT.

[111] J. W. Alexander and G. B. Briggs. On types of knotted curves. *Annals of Mathematics*, 28(1/4):562–586, 1926. URL http://www.jstor.org/stable/1968399.

[112] Wikipedia contributors. Reidemeister move — Wikipedia, the free encyclopedia. https://en.wikipedia.org/w/index.php?title=Reidemeister_move&oldid=1338046066, 2026. [Online; accessed 18-February-2026].

[113] Victor Guillemin and Alan Pollack. *Differential topology*. Prentice-Hall Inc., Englewood Cliffs, N.J., 1974. URL https://bookstore.ams.org/view?ProductCode=CHEL/370.H.

[114] S. Kalajdzievski. *An Illustrated Introduction to Topology and Homotopy*. CRC Press, 2015. URL https://www.amazon.com/Illustrated-Introduction-Topology-Homotopy/dp/1439848157.

[115] R. Gilmore. *Catastrophe Theory for Scientists and Engineers*. A Wiley-Interscience publication. Wiley, 1981. URL https://www.sciencedirect.com/science/article/abs/pii/092056328790017X.

[116] Hua-Zhou Chen, Tuo Liu, Hong-Yi Luan, Rong-Juan Liu, Xing-Yuan Wang, Xue-Feng Zhu, Yuan-Bo Li, Zhong-Ming Gu, Shan-Jun Liang, He Gao, Ling Lu, Li Ge, Shuang Zhang, Jie Zhu, and Ren-Min Ma. Revealing the missing dimension at an exceptional point. *Nature Physics*, 16(5):571–578, May 2020. URL https://www.nature.com/articles/s41567-020-0807-y.

[117] Michael Victor Berry and Mark Wilkinson. Diabolical points in the spectra of triangles. *Proceedings of the Royal Society of London. A. Mathematical and Physical Sciences*, 392(1802):15–43, 1984. URL https://royalsocietypublishing.org/doi/abs/10.1098/rspa.1984.0022.

[118] Wikipedia contributors. Pauli matrices — Wikipedia, the free encyclopedia. https://en.wikipedia.org/w/index.php?title=Pauli_matrices&oldid=1335668226, 2026. [Online; accessed 18-February-2026].

[119] Carl M Bender, M V Berry, and Aikaterini Mandilara. Generalized PT symmetry and real spectra. *Journal of Physics A: Mathematical and General*, 35(31):L467, jul 2002. URL https://doi.org/10.1088/0305-4470/35/31/101.

[120] Carl M. Bender and Philip D. Mannheim. PT symmetry and necessary and sufficient conditions for the reality of energy eigenvalues. *Physics Letters A*, 374(15):1616–1620, 2010. URL https://www.sciencedirect.com/science/article/pii/S0375960110001933.

[121] Eric J. Pap, Daniël Boer, and Holger Waalkens. Non-abelian nature of systems with multiple exceptional points. *Phys. Rev. A*, 98:023818, Aug 2018. URL https://link.aps.org/doi/10.1103/PhysRevA.98.023818.

[122] Xu-Lin Zhang and C. T. Chan. Dynamically encircling exceptional points in a three-mode waveguide system. *Communications Physics*, 2(1):63, Jun 2019. URL https://doi.org/10.1038/s42005-019-0171-3.

[123] Arnab Laha, Dinesh Beniwal, Sibnath Dey, Abhijit Biswas, and Somnath Ghosh. Third-order exceptional point and successive switching among three states in an optical microcavity. *Phys. Rev. A*, 101:063829, Jun 2020. URL https://link.aps.org/doi/10.1103/PhysRevA.101.063829.

[124] Ievgen I. Arkhipov, Adam Miranowicz, Fabrizio Minganti, Şahin K. Özdemir, and Franco Nori. Dynamically crossing diabolic points while encircling exceptional

curves: A programmable symmetric-asymmetric multimode switch. *Nature Communications*, 14(1):2076, Apr 2023. URL https://doi.org/10.1038/s41467-023-37275-5.

[125] Anton Montag and Flore K. Kunst. Symmetry-induced higher-order exceptional points in two dimensions. *Phys. Rev. Res.*, 6:023205, May 2024. URL https://link.aps.org/doi/10.1103/PhysRevResearch.6.023205.

[126] Arpan Roy, Arnab Laha, Abhijit Biswas, Bishnu P Pal, Somnath Ghosh, and Adam Miranowicz. Dynamically encircled higher-order exceptional points in an optical fiber. *Physica Scripta*, 100(4):045529, Mar 2025. URL https://dx.doi.org/10.1088/1402-4896/adbea6.

[127] E M Graefe, U Günther, H J Korsch, and A E Niederle. A non-hermitian $\mathcal{PT}$ symmetric bose–hubbard model: eigenvalue rings from unfolding higher-order exceptional points. *Journal of Physics A: Mathematical and Theoretical*, 41(25): 255206, May 2008. URL http://dx.doi.org/10.1088/1751-8113/41/25/255206.

[128] Kun Ding, Guancong Ma, Meng Xiao, Z. Q. Zhang, and C. T. Chan. Emergence, coalescence, and topological properties of multiple exceptional points and their experimental realization. *Phys. Rev. X*, 6:021007, Apr 2016. URL https://link.aps.org/doi/10.1103/PhysRevX.6.021007.

[129] Hossein Hodaei, Absar U. Hassan, Steffen Wittek, Hipolito Garcia-Gracia, Ramy El-Ganainy, Demetrios N. Christodoulides, and Mercedeh Khajavikhan. Enhanced sensitivity at higher-order exceptional points. *Nature*, 548(7666):187–191, Aug 2017. URL https://doi.org/10.1038/nature23280.

[130] H. Jing, Ş K. Özdemir, H. Lü, and Franco Nori. High-order exceptional points in optomechanics. *Scientific Reports*, 7(1):3386, Jun 2017. URL https://doi.org/10.1038/s41598-017-03546-7.

[131] Qi Zhong, Mercedeh Khajavikhan, Demetrios N. Christodoulides, and Ramy El-Ganainy. Winding around non-hermitian singularities. *Nature Communications*, 9 (1):4808, Nov 2018. URL https://doi.org/10.1038/s41467-018-07105-0.

[132] F Wilczek and A Shapere. *Geometric Phases in Physics*. WORLD SCIENTIFIC, 1989. URL https://www.worldscientific.com/doi/abs/10.1142/0613.

[133] Eliahu Cohen, Hugo Larocque, Frédéric Bouchard, Farshad Nejadsattari, Yuval Gefen, and Ebrahim Karimi. Geometric phase from Aharonov–Bohm to Pancharatnam–Berry and beyond. *Nature Reviews Physics*, 1(7):437–449, June 2019. URL http://dx.doi.org/10.1038/s42254-019-0071-1.

[134] Michael Berry. Anticipations of the geometric phase. *Physics Today*, 43(12):34–40, Dec 1990. URL https://doi.org/10.1063/1.881219.

[135] SNS Sciences. Sir Michael Berry FRS, Geometric phases old and new, 2025. URL https://www.youtube.com/watch?v=Mb-x5_IpDvI.

[136] Michael Berry. A geometric-phase timeline. *Opt. Photon. News*, 35(3):42–49, Mar 2024. URL https://www.optica-opn.org/abstract.cfm?URI=opn-35-3-42.

[137] Y. Aharonov and J. Anandan. Phase change during a cyclic quantum evolution. *Phys. Rev. Lett.*, 58:1593–1596, Apr 1987. URL https://link.aps.org/doi/10.1103/PhysRevLett.58.1593.

[138] Barry Simon. Holonomy, the quantum adiabatic theorem, and berry's phase. *Phys. Rev. Lett.*, 51:2167–2170, Dec 1983. URL https://link.aps.org/doi/10.1103/PhysRevLett.51.2167.

[139] Don N. Page. Geometrical description of berry's phase. *Phys. Rev. A*, 36:3479–3481, Oct 1987. URL https://link.aps.org/doi/10.1103/PhysRevA.36.3479.

[140] Joseph Samuel and Rajendra Bhandari. General setting for berry's phase. *Phys. Rev. Lett.*, 60:2339–2342, Jun 1988. URL https://link.aps.org/doi/10.1103/PhysRevLett.60.2339.

[141] Mustafa Demirplak and Stuart A. Rice. Adiabatic population transfer with control fields. *The Journal of Physical Chemistry A*, 107(46):9937–9945, 2003. URL https://doi.org/10.1021/jp030708a.

[142] M V Berry. Transitionless quantum driving. *Journal of Physics A: Mathematical and Theoretical*, 42(36):365303, Aug 2009. URL https://dx.doi.org/10.1088/1751-8113/42/36/365303.

[143] David Vanderbilt. *Berry Phases in Electronic Structure Theory: Electric Polarization, Orbital Magnetization and Topological Insulators*. Cambridge University Press, 2018. URL https://doi.org/10.1017/9781316662205.

[144] Raffaele Resta. Manifestations of berry's phase in molecules and condensed matter. *Journal of Physics: Condensed Matter*, 12(9):R107, Mar 2000. URL https://dx.doi.org/10.1088/0953-8984/12/9/201.

[145] Tosio Kato. On the adiabatic theorem of quantum mechanics. *Journal of the Physical Society of Japan*, 5(6):435–439, 1950. URL https://doi.org/10.1143/JPSJ.5.435.

[146] G Dattoli, R Mignani, and A Torre. Geometrical phase in the cyclic evolution of non-hermitian systems. *Journal of Physics A: Mathematical and General*, 23(24): 5795, Dec 1990. URL https://dx.doi.org/10.1088/0305-4470/23/24/020.

[147] Mustafa Demirplak and Stuart A. Rice. Assisted adiabatic passage revisited. *The Journal of Physical Chemistry B*, 109(14):6838–6844, 2005. URL https://doi.org/10.1021/jp040647w.

[148] Mustafa Demirplak and Stuart A. Rice. On the consistency, extremal, and global properties of counterdiabatic fields. *The Journal of Chemical Physics*, 129(15): 154111, Oct 2008. URL https://doi.org/10.1063/1.2992152.

[149] D. Guéry-Odelin, A. Ruschhaupt, A. Kiely, E. Torrontegui, S. Martínez-Garaot, and J. G. Muga. Shortcuts to adiabaticity: Concepts, methods, and applications. *Rev. Mod. Phys.*, 91:045001, Oct 2019. URL https://link.aps.org/doi/10.1103/RevModPhys.91.045001.

[150] Frank Wilczek and A. Zee. Appearance of gauge structure in simple dynamical systems. *Phys. Rev. Lett.*, 52:2111–2114, Jun 1984. URL https://link.aps.org/doi/10.1103/PhysRevLett.52.2111.

[151] M. S. Sarandy and D. A. Lidar. Abelian and non-abelian geometric phases in adiabatic open quantum systems. *Phys. Rev. A*, 73:062101, Jun 2006. URL https://link.aps.org/doi/10.1103/PhysRevA.73.062101.

[152] Wikipedia contributors. Jordan decomposition — Wikipedia, the free encyclopedia, 2011. URL https://en.wikipedia.org/w/index.php?title=Jordan_normal_form&oldid=1315233498.

[153] Wikipedia contributors. Puiseux series — Wikipedia, the free encyclopedia, 2025. URL https://en.wikipedia.org/w/index.php?title=Puiseux_series&oldid=1305725857.

[154] A. Hatcher. *Algebraic Topology*. Algebraic Topology. Cambridge University Press, 2002. URL https://books.google.com/books?id=BjKs86kosqgC.

[155] M. V. Berry. Interpreting the anholonomy of coiled light. *Nature*, 326(6110): 277–278, Mar 1987. URL https://doi.org/10.1038/326277a0.

[156] M. V. Berry. Quantum Adiabatic Anholonomy, 1990. URL https://michaelberryphysics.wordpress.com/wp-content/uploads/2013/07/berry198.pdf.

[157] M. V. Berry. Some geometric phases: transparencies for three lectures at CERN, 1993. URL https://cds.cern.ch/record/282618/files/AT00000125.pdf.

[158] Alexander I Nesterov and F Aceves de la Cruz. Complex magnetic monopoles, geometric phases and quantum evolution in the vicinity of diabolic and exceptional points. *Journal of Physics A: Mathematical and Theoretical*, 41(48):485304, Oct 2008. URL https://dx.doi.org/10.1088/1751-8113/41/48/485304.

[159] S. Massar. Applications of the complex geometric phase for metastable systems. *Phys. Rev. A*, 54:4770–4774, Dec 1996. URL https://link.aps.org/doi/10.1103/PhysRevA.54.4770.

[160] Yaashnaa Singhal, Enrico Martello, Shraddha Agrawal, Tomoki Ozawa, Hannah Price, and Bryce Gadway. Measuring the adiabatic non-hermitian berry phase in feedback-coupled oscillators. *Phys. Rev. Res.*, 5:L032026, Aug 2023. URL https://link.aps.org/doi/10.1103/PhysRevResearch.5.L032026.

[161] Julien. Physics StackExchange: How to prove $\det(e^A) = e^{\mathrm{tr}(A)}$?, 2013. URL https://math.stackexchange.com/questions/322640/how-to-prove-det-leftea-right-e-operatornametra.

[162] Jean Gallier. *The Quaternions and the Spaces S3, SU(2), SO(3), and* $\mathbb{RP}^3$, pages 281–300. Springer New York, New York, NY, 2011. URL https://doi.org/10.1007/978-1-4419-9961-0_9.

[163] Orlin Stoytchev. Topology of so(3) for kids, 2023. URL https://arxiv.org/abs/2310.19665.

[164] P. J. Leek, J. M. Fink, A. Blais, R. Bianchetti, M. Göppl, J. M. Gambetta, D. I. Schuster, L. Frunzio, R. J. Schoelkopf, and A. Wallraff. Observation of berry's phase in a solid-state qubit. *Science*, 318(5858):1889–1892, 2007. URL https://www.science.org/doi/abs/10.1126/science.1149858.

[165] S. Berger, M. Pechal, S. Pugnetti, A. A. Abdumalikov, L. Steffen, A. Fedorov, A. Wallraff, and S. Filipp. Geometric phases in superconducting qubits beyond the two-level approximation. *Phys. Rev. B*, 85:220502, Jun 2012. URL https://link.aps.org/doi/10.1103/PhysRevB.85.220502.

[166] M. Pechal, S. Berger, A. A. Abdumalikov, J. M. Fink, J. A. Mlynek, L. Steffen, A. Wallraff, and S. Filipp. Geometric phase and nonadiabatic effects in an electronic harmonic oscillator. *Phys. Rev. Lett.*, 108:170401, Apr 2012. URL https://link.aps.org/doi/10.1103/PhysRevLett.108.170401.

[167] S. Berger, M. Pechal, P. Kurpiers, A. A. Abdumalikov, C. Eichler, J. A. Mlynek, A. Shnirman, Yuval Gefen, A. Wallraff, and S. Filipp. Measurement of geometric dephasing using a superconducting qubit. *Nature Communications*, 6(1):8757, Oct 2015. URL https://doi.org/10.1038/ncomms9757.

[168] Simone Gasparinetti, Simon Berger, Abdufarrukh A. Abdumalikov, Marek Pechal, Stefan Filipp, and Andreas J. Wallraff. Measurement of a vacuum-induced geometric phase. *Science Advances*, 2(5):e1501732, 2016. URL https://www.science.org/doi/abs/10.1126/sciadv.1501732.

[169] Shimon Kolkowitz, Ania C. Bleszynski Jayich, Quirin P. Unterreithmeier, Steven D. Bennett, Peter Rabl, J. G. E. Harris, and Mikhail D. Lukin. Coherent sensing of a mechanical resonator with a single-spin qubit. *Science*, 335(6076):1603–1606, 2012. URL https://www.science.org/doi/abs/10.1126/science.1216821.

[170] Shimon J. Kolkowitz. *Nanoscale sensing with individual nitrogen-vacancy centers in diamond*. PhD thesis, Harvard University, 2014. URL https://lukin.physics.harvard.edu/sites/g/files/omnuum6416/files/lukin/files/shimon_kolkowitz_thesis.pdf.

[171] Wikipedia contributors. Cauchy–schwarz inequality — Wikipedia, the free encyclopedia, 2026. URL https://en.wikipedia.org/w/index.php?title=Cauchy%E2%80%93Schwarz_inequality&oldid=1331683631. [Online; accessed 16-January-2026].

[172] Tobias J. Kippenberg and Kerry J. Vahala. Cavity opto-mechanics. *Optics Express*, 15(25):17172, 2007. URL http://dx.doi.org/10.1364/OE.15.017172.

[173] Florian Marquardt and Steven M. Girvin. Optomechanics. *Physics*, 2(40):40, 2009. URL https://physics.aps.org/articles/v2/40.

[174] Pierre Meystre. A short walk through quantum optomechanics. *Annalen der Physik*, 525(3):215–233, 2013. URL https://onlinelibrary.wiley.com/doi/abs/10.1002/andp.201200226.

[175] Markus Aspelmeyer, Tobias J. Kippenberg, and Florian Marquardt. Cavity optomechanics. *Reviews of Modern Physics*, 86(4):1391–1452, December 2014. URL http://dx.doi.org/10.1103/RevModPhys.86.1391.

[176] Pierre-François Cohadon, Jack Harris, Florian Marquardt, and Leticia Cugliandolo. *Quantum Optomechanics and Nanomechanics: Lecture Notes of the Les Houches Summer School: Volume 105, August 2015*. Oxford University Press, 03 2020. URL https://doi.org/10.1093/oso/9780198828143.001.0001.

[177] P. Verlot, A. Tavernarakis, T. Briant, P.-F. Cohadon, and A. Heidmann. Backaction amplification and quantum limits in optomechanical measurements. *Phys. Rev. Lett.*, 104:133602, Mar 2010. URL https://link.aps.org/doi/10.1103/PhysRevLett.104.133602.

[178] Vladimir B. Braginsky, Yuri I. Vorontsov, and Kip S. Thorne. Quantum nondemolition measurements. *Science*, 209(4456):547–557, 1980. URL https://www.science.org/doi/abs/10.1126/science.209.4456.547.

[179] Carlton M. Caves. Quantum-mechanical radiation-pressure fluctuations in an interferometer. *Phys. Rev. Lett.*, 45:75–79, Jul 1980. URL https://link.aps.org/doi/10.1103/PhysRevLett.45.75.

[180] B. P. Abbott, LIGO Scientific Collaboration, and Virgo Collaboration. Observation of gravitational waves from a binary black hole merger. *Phys. Rev. Lett.*, 116: 061102, Feb 2016. URL https://link.aps.org/doi/10.1103/PhysRevLett.116.061102.

[181] J. D. Teufel, T. Donner, M. A. Castellanos-Beltran, J. W. Harlow, and K. W. Lehnert. Nanomechanical motion measured with an imprecision below that at the standard quantum limit. *Nature Nanotechnology*, 4(12):820–823, Dec 2009. URL https://doi.org/10.1038/nnano.2009.343.

[182] Jasper Chan, T. P. Mayer Alegre, Amir H. Safavi-Naeini, Jeff T. Hill, Alex Krause, Simon Gröblacher, Markus Aspelmeyer, and Oskar Painter. Laser cooling of a nanomechanical oscillator into its quantum ground state. *Nature*, 478, Oct 2011. URL https://doi.org/10.1038/nature10461.

[183] J. D. Teufel, T. Donner, Dale Li, J. W. Harlow, M. S. Allman, K. Cicak, A. J. Sirois, J. D. Whittaker, K. W. Lehnert, and R. W. Simmonds. Sideband cooling of micromechanical motion to the quantum ground state. *Nature*, 475(7356): 359–363, Jul 2011. URL https://doi.org/10.1038/nature10261.

[184] T. P. Purdy, R. W. Peterson, and C. A. Regal. Observation of radiation pressure shot noise on a macroscopic object. *Science*, 339(6121):801–804, 2013. URL https://www.science.org/doi/abs/10.1126/science.1231282.

[185] Massimiliano Rossi, David Mason, Junxin Chen, Yeghishe Tsaturyan, and Albert Schliesser. Measurement-based quantum control of mechanical motion. *Nature*, 563(7729):53–58, Nov 2018. URL https://doi.org/10.1038/s41586-018-0643-8.

[186] David Mason, Junxin Chen, Massimiliano Rossi, Yeghishe Tsaturyan, and Albert Schliesser. Continuous force and displacement measurement below the standard quantum limit. *Nature Physics*, 15(8):745–749, Aug 2019. URL https://doi.org/10.1038/s41567-019-0533-5.

[187] Shlomi Kotler, Gabriel A. Peterson, Ezad Shojaee, Florent Lecocq, Katarina Cicak, Alex Kwiatkowski, Shawn Geller, Scott Glancy, Emanuel Knill, Raymond W. Simmonds, José Aumentado, and John D. Teufel. Direct observation of deterministic macroscopic entanglement. *Science*, 372(6542):622–625, 2021. URL https://www.science.org/doi/abs/10.1126/science.abf2998.

[188] Luyao Jiang. *Nonreciprocal dynamics in a cryogenic optomechanical system*. PhD thesis, Yale University, 2020. URL https://harrislab.yale.edu/files/thesis/Luyao_Thesis.pdf.

[189] Yiming Zhang. Building an optomechanical platform for third order exceptional point physics. Bachelor's thesis, Yale University, 2022.

[190] Mark S. Rudner and Netanel H. Lindner. The floquet engineer's handbook. *arXiv:2003.08252*, 2020. URL https://arxiv.org/abs/2003.08252.

[191] Jack G.E. Harris. A pedagogical introduction to the emergence of topology in non-Hermitian dynamics. Jack Harris Lab Journal Club, November 2019.

[192] H. Xu, Luyao Jiang, A. A. Clerk, and J. G. E. Harris. Nonreciprocal control and cooling of phonon modes in an optomechanical system. *Nature*, 568(7750):65–69, April 2019. URL http://dx.doi.org/10.1038/s41586-019-1061-2.

[193] Holger Cartarius, Jörg Main, and Günter Wunner. Exceptional points in the spectra of atoms in external fields. *Phys. Rev. A*, 79:053408, May 2009. URL https://link.aps.org/doi/10.1103/PhysRevA.79.053408.

[194] Soo-Young Lee, Jung-Wan Ryu, Sang Wook Kim, and Yunchul Chung. Geometric phase around multiple exceptional points. *Phys. Rev. A*, 85:064103, Jun 2012. URL https://link.aps.org/doi/10.1103/PhysRevA.85.064103.

[195] Kun Ding, Z. Q. Zhang, and C. T. Chan. Coalescence of exceptional points and phase diagrams for one-dimensional $\mathcal{PT}$-symmetric photonic crystals. *Phys. Rev. B*, 92:235310, Dec 2015. URL https://link.aps.org/doi/10.1103/PhysRevB.92.235310.

[196] Kun Ding, Guancong Ma, Meng Xiao, Z. Q. Zhang, and C. T. Chan. Emergence, coalescence, and topological properties of multiple exceptional points and their experimental realization. *Phys. Rev. X*, 6:021007, Apr 2016. URL https://link.aps.org/doi/10.1103/PhysRevX.6.021007.

[197] Shubo Wang, Bo Hou, Weixin Lu, Yuntian Chen, Z. Q. Zhang, and C. T. Chan. Arbitrary order exceptional point induced by photonic spin–orbit interaction in coupled resonators. *Nature Communications*, 10(1):832, Feb 2019. URL https://doi.org/10.1038/s41467-019-08826-6.

[198] Zhicheng Xiao, Huanan Li, Tsampikos Kottos, and Andrea Alù. Enhanced sensing and nondegraded thermal noise performance based on $\mathcal{PT}$-symmetric electronic circuits with a sixth-order exceptional point. *Phys. Rev. Lett.*, 123:213901, Nov 2019. URL https://link.aps.org/doi/10.1103/PhysRevLett.123.213901.

[199] Yogesh SS Patil. SuppVideo1, 2022. URL https://www.youtube.com/watch?v=2HsIo1OgZFA.

[200] Yogesh SS Patil. SuppVideo5, 2022. URL https://www.youtube.com/watch?v=8h8sxCRgufg.

[201] Yogesh SS Patil. SuppVideo2, 2022. URL https://www.youtube.com/watch?v=j8sBhf2pZuA.

[202] Yogesh SS Patil. SuppVideo3, 2022. URL https://www.youtube.com/watch?v=4-4OqfkHQpk.

[203] David Kramer. Helium prices surge to record levels as shortage continues. *Physics Today*, 76(9):18–20, 09 2023. URL https://doi.org/10.1063/PT.3.5305.

[204] Justin Lane, Chitres Guria, Yiming Zhang, Yogesh S. Patil, and Jack G. Harris. An improved optomechanical system for measuring the trefoil knot of degeneracies near a triple exceptional point. In *Abstracts*, APS Meeting, page K33.007, March 2022. URL https://meetings.aps.org/Meeting/MAR22/Session/K33.7.

[205] Rob Campbell. The Principle of Kinematic Constraint, 2016. URL https://practicalprecision.com/kinematic-constraint/.

[206] Srivatsan Chakram. *Dissipation and Nonlinear Mechanics in Ultrahigh Quality Factor Membrane Resonators*. PhD thesis, Cornell University, 2015. URL https://ecommons.cornell.edu/items/e332a474-0ed7-42d3-b023-52c3b824a9ce.

[207] Jeff D. Thompson. Strong coupling between a micromechanical resonator and an optical cavity. Bachelor's thesis, Yale University, 2007.

[208] J. C. Sankey, A. M. Jayich, B. M. Zwickl, C. Yang, and J. G. E. Harris. *Improved "Position squared" readout using degenerate cavity modes*, pages 131–149. World Scientific, 2009. URL https://www.worldscientific.com/doi/abs/10.1142/9789814273008_0014.

[209] A M Jayich, J C Sankey, K Børkje, D Lee, C Yang, M Underwood, L Childress, A Petrenko, S M Girvin, and J G E Harris. Cryogenic optomechanics with a si3n4 membrane and classical laser noise. *New Journal of Physics*, 14(11):115018, Nov 2012. URL https://dx.doi.org/10.1088/1367-2630/14/11/115018.

[210] N. E. Flowers-Jacobs, S. W. Hoch, J. C. Sankey, A. Kashkanova, A. M. Jayich, C. Deutsch, J. Reichel, and J. G. E. Harris. Fiber-cavity-based optomechanical device. *Applied Physics Letters*, 101(22):221109, Nov 2012. URL https://doi.org/10.1063/1.4768779.

[211] A.B. Shkarin, N.E. Flowers-Jacobs, S.W. Hoch, A.D. Kashkanova, C. Deutsch, J. Reichel, and J.G.E. Harris. Optically mediated hybridization between two mechanical modes. *Physical Review Letters*, 112(1), January 2014. URL http://dx.doi.org/10.1103/PhysRevLett.112.013602.

[212] D. Lee, M. Underwood, D. Mason, A. B. Shkarin, S. W. Hoch, and J. G. E. Harris. Multimode optomechanical dynamics in a cavity with avoided crossings. *Nature Communications*, 6(1):6232, Feb 2015. URL https://doi.org/10.1038/ncomms7232.

[213] T P Purdy, R W Peterson, P-L Yu, and C A Regal. Cavity optomechanics with si3n4 membranes at cryogenic temperatures. *New Journal of Physics*, 14(11):115021, Nov 2012. URL https://dx.doi.org/10.1088/1367-2630/14/11/115021.

[214] R. W. Andrews, R. W. Peterson, T. P. Purdy, K. Cicak, R. W. Simmonds, C. A. Regal, and K. W. Lehnert. Bidirectional and efficient conversion between microwave and optical light. *Nature Physics*, 10(4):321–326, March 2014. URL http://dx.doi.org/10.1038/nphys2911.

[215] T. P. Purdy, P.-L. Yu, N. S. Kampel, R. W. Peterson, K. Cicak, R. W. Simmonds, and C. A. Regal. Optomechanical raman-ratio thermometry. *Phys. Rev. A*, 92:031802, Sep 2015. URL https://link.aps.org/doi/10.1103/PhysRevA.92.031802.

[216] Robert W. Peterson. *Quantum measurement backaction and upconverting microwave signals with mechanical resonators*. PhD thesis, University of Colorado, 2017. URL https://jila.colorado.edu/sites/default/files/2019-03/rwpthesis_jila.pdf.

[217] H. Kogelnik and T. Li. Laser beams and resonators. *Appl. Opt.*, 5(10):1550–1567, Oct 1966. URL https://opg.optica.org/ao/abstract.cfm?URI=ao-5-10-1550.

[218] J. Gallego, S. Ghosh, S. K. Alavi, W. Alt, M. Martinez-Dorantes, D. Meschede, and L. Ratschbacher. High-finesse fiber fabry–perot cavities: stabilization and mode matching analysis. *Applied Physics B*, 122(3), March 2016. URL http://dx.doi.org/10.1007/s00340-015-6281-z.

[219] Eric D. Black. An introduction to pound–drever–hall laser frequency stabilization. *American Journal of Physics*, 69(1):79–87, 01 2001. URL https://doi.org/10.1119/1.1286663.

[220] Moku. Laser Lock Box, 2025. URL https://liquidinstruments.com/products/integrated-instruments/laser-lock-box/.

[221] Christina J. Hood, H. J. Kimble, and Jun Ye. Characterization of high-finesse mirrors: Loss, phase shifts, and mode structure in an optical cavity. *Phys. Rev. A*, 64:033804, Aug 2001. URL https://link.aps.org/doi/10.1103/PhysRevA.64.033804.

[222] Benjamin M. Zwickl. *Progress Toward Observation of Radiation Pressure Shot Noise*. PhD thesis, Yale University, 2011. URL https://harrislab.yale.edu/files/thesis/Zwickl_Thesis.pdf.

[223] Anna D. Kashkanova. *Optomechanics with Superfluid Helium*. PhD thesis, Yale University, 2017. URL https://harrislab.yale.edu/files/thesis/Kashkanova_Thesis.pdf.

[224] Dalziel J. Wilson. *Cavity Optomechanics with High-Stress Silicon Nitride Films*. PhD thesis, California Institute of Technology, 2012. URL https://thesis.library.caltech.edu/7162/2/DJW_thesis_draft_final.pdf.

[225] B. M. Zwickl, W. E. Shanks, A. M. Jayich, C. Yang, A. C. Bleszynski Jayich, J. D. Thompson, and J. G. E. Harris. High quality mechanical and optical properties of commercial silicon nitride membranes. *Applied Physics Letters*, 92(10), March 2008. URL http://dx.doi.org/10.1063/1.2884191.

[226] S. Chakram, Y. S. Patil, L. Chang, and M. Vengalattore. Dissipation in ultrahigh quality factor sin membrane resonators. *Phys. Rev. Lett.*, 112:127201, Mar 2014. URL https://link.aps.org/doi/10.1103/PhysRevLett.112.127201.

[227] P.-L. Yu, K. Cicak, N. S. Kampel, Y. Tsaturyan, T. P. Purdy, R. W. Simmonds, and C. A. Regal. A phononic bandgap shield for high-q membrane microresonators. *Applied Physics Letters*, 104(2):023510, 01 2014. URL https://doi.org/10.1063/1.4862031.

[228] Christoph Reinhardt, Tina Müller, Alexandre Bourassa, and Jack C. Sankey. Ultralow-noise sin trampoline resonators for sensing and optomechanics. *Phys. Rev. X*, 6:021001, Apr 2016. URL https://link.aps.org/doi/10.1103/PhysRevX.6.021001.

[229] Y. Tsaturyan, A. Barg, E. S. Polzik, and A. Schliesser. Ultracoherent nanomechanical resonators via soft clamping and dissipation dilution. *Nature Nanotechnology*, 12(8):776–783, Aug 2017. URL https://doi.org/10.1038/nnano.2017.101.

[230] C. Reetz, R. Fischer, G.G.T. Assumpcao, D.P. McNally, P.S. Burns, J.C. Sankey, and C.A. Regal. Analysis of membrane phononic crystals with wide band gaps and low-mass defects. *Phys. Rev. Appl.*, 12:044027, Oct 2019. URL https://link.aps.org/doi/10.1103/PhysRevApplied.12.044027.

[231] M. J. Bereyhi, A. Beccari, R. Groth, S. A. Fedorov, A. Arabmoheghi, T. J. Kippenberg, and N. J. Engelsen. Hierarchical tensile structures with ultralow mechanical dissipation. *Nature Communications*, 13(1):3097, Jun 2022. URL https://doi.org/10.1038/s41467-022-30586-z.

[232] Nils Johan Engelsen, Alberto Beccari, and Tobias Jan Kippenberg. Ultrahigh-quality-factor micro- and nanomechanical resonators using dissipation dilution. *Nature Nanotechnology*, 19(6):725–737, Jun 2024. URL https://doi.org/10.1038/s41565-023-01597-8.

[233] G B Shaw. Degeneracy in the particle-in-a-box problem. *Journal of Physics A: Mathematical, Nuclear and General*, 7(13):1537, Sep 1974. URL https://dx.doi.org/10.1088/0305-4470/7/13/008.

[234] Herbert B. Callen and Richard F. Greene. On a theorem of irreversible thermodynamics. *Phys. Rev.*, 86:702–710, Jun 1952. URL https://link.aps.org/doi/10.1103/PhysRev.86.702.

[235] Richard F. Greene and Herbert B. Callen. On a theorem of irreversible thermodynamics. ii. *Phys. Rev.*, 88:1387–1391, Dec 1952. URL https://link.aps.org/doi/10.1103/PhysRev.88.1387.

[236] Wolfram Research. NonlinearModelFit, 2025. URL https://reference.wolfram.com/language/ref/NonlinearModelFit.html.

[237] Thomas M. Karg. *Strong light-mediated coupling between a membrane oscillator and an atomic spin ensemble*. PhD thesis, University of Basel, 2020. URL https://atom.physik.unibas.ch/fileadmin/user_upload/atom_physik/Publications/Theses/PhD_thesis_Thomas_Karg.pdf.

[238] Chun T. Ngai. *Coherent feedback cooling of nanomechanical membrane with atomic spins*. PhD thesis, University of Basel, 2023. URL https://atom.physik.unibas.ch/fileadmin/user_upload/atom_physik/Publications/Theses/PhD_Thesis_ChunTat_Ngai.pdf.

[239] Maryse Ernzer. *Optical coherent feedback control of a mechanical oscillator*. PhD thesis, University of Basel, 2024. URL https://atom.physik.unibas.ch/fileadmin/user_upload/atom_physik/Publications/Theses/PhD_Thesis_Maryse_Ernzer.pdf.

[240] Sameer Sonar, Vitaly Fedoseev, Matthew J. Weaver, Fernando Luna, Elger Vlieg, Harmen van der Meer, Dirk Bouwmeester, and Wolfgang Löffler. Strong thermo-mechanical squeezing in a far-detuned membrane-in-the-middle system. *Phys. Rev.*

A, 98:013804, Jul 2018. URL https://link.aps.org/doi/10.1103/PhysRevA.98.013804.

[241] Zurich Instruments. HF2 user manual, 2025. URL https://docs.zhinst.com/pdf/ziHF2_UserManual.pdf.

[242] S. Pancharatnam. Generalized theory of interference, and its applications. *Proceedings of the Indian Academy of Sciences - Section A*, 44(5):247–262, Nov 1956. URL https://doi.org/10.1007/BF03046050.

[243] Thomas van Dijk, Hugo F. Schouten, and Taco D. Visser. Geometric interpretation of the pancharatnam connection and non-cyclic polarization changes. *J. Opt. Soc. Am. A*, 27(9):1972–1976, Sep 2010. URL https://opg.optica.org/josaa/abstract.cfm?URI=josaa-27-9-1972.

[244] Atsuo Morinaga, Akinori Monma, Kazuhito Honda, and Masao Kitano. Berry's phase for a noncyclic rotation of light in a helically wound optical fiber. *Phys. Rev. A*, 76:052109, Nov 2007. URL https://link.aps.org/doi/10.1103/PhysRevA.76.052109.

[245] T. van Dijk, H.F. Schouten, W. Ubachs, and T.D. Visser. The pancharatnam-berry phase for non-cyclic polarization changes. *Opt. Express*, 18(10):10796–10804, May 2010. URL https://opg.optica.org/oe/abstract.cfm?URI=oe-18-10-10796.

[246] Zhifan Zhou, Yair Margalit, Samuel Moukouri, Yigal Meir, and Ron Folman. An experimental test of the geodesic rule proposition for the noncyclic geometric phase. *Science Advances*, 6(9):eaay8345, 2020. URL https://www.science.org/doi/abs/10.1126/sciadv.aay8345.

[247] Aleksi Leinonen, Antti Hannonen, Henri Partanen, Janne Heikkinen, Tero Setälä, Ari T. Friberg, and Tommi K. Hakala. Noncyclic continuous pancharatnam—berry phase in dual-beam interference. *Communications Physics*, 6(1), Jun 2023. URL https://www.nature.com/articles/s42005-023-01249-2.

[248] Wolfram Research. ListPointPlot3D, 2025. URL https://reference.wolfram.com/language/ref/ListPointPlot3D.html.

[249] Wolfram Research. ConvexHullMesh, 2020. URL https://reference.wolfram.com/language/ref/ConvexHullMesh.html.

[250] Konstantin Yu Bliokh. The appearance of a geometric-type instability in dynamic systems with adiabatically varying parameters. *Journal of Physics A: Mathematical and General*, 32(13):2551, Apr 1999. URL https://dx.doi.org/10.1088/0305-4470/32/13/007.

[251] H. A. Haus and J. A. Mullen. Quantum noise in linear amplifiers. *Phys. Rev.*, 128: 2407–2413, Dec 1962. URL https://link.aps.org/doi/10.1103/PhysRev.128.2407.

[252] H. Heffner. The fundamental noise limit of linear amplifiers. *Proceedings of the IRE*, 50(7):1604–1608, 1962.

[253] Carlton M. Caves. Quantum limits on noise in linear amplifiers. *Phys. Rev. D*, 26: 1817–1839, Oct 1982. URL https://link.aps.org/doi/10.1103/PhysRevD.26.1817.

[254] Andy Chia, Michal Hajdušek, Rosario Fazio, Leong-Chuan Kwek, and Vlatko Vedral. Phase diffusion and the small-noise approximation in linear amplifiers: Limitations and beyond. *Quantum*, 3:200, November 2019. URL https://doi.org/10.22331/q-2019-11-04-200.

[255] Wikipedia. Plate trick, 2025. URL https://en.wikipedia.org/w/index.php?title=Plate_trick&oldid=1309939089.

[256] tparker. Physics stackexchange: What exactly does the belt/plate trick demonstrate?, 2019. URL https://physics.stackexchange.com/questions/516513/what-exactly-does-the-belt-plate-trick-demonstrate.

[257] Dr. Trefor Bazett. Dirac's Belt Trick: Why a 2π rotation twists space but a 4π rotation fixes it, 2022. URL https://www.youtube.com/watch?v=EgsUDby0X1M.

[258] VisualMath. What is...Dirac's belt trick?, 2022. URL https://www.youtube.com/watch?v=5ysSYR2DsdI.

[259] NoahExplainsPhysics. Dirac's belt trick, Topology, and Spin ½ particles, 2021. URL https://www.youtube.com/watch?v=ACZC_XEyg9U.

[260] Wikipedia contributors. Schur decomposition — Wikipedia, the free encyclopedia, 2025. URL https://en.wikipedia.org/w/index.php?title=Schur_decomposition&oldid=1301204104.

[261] Alain Joye. General adiabatic evolution with a gap condition. *Communications in Mathematical Physics*, 275(1):139–162, Oct 2007. URL https://doi.org/10.1007/s00220-007-0299-y.

[262] Michael Victor Berry. Geometric amplitude factors in adiabatic quantum transitions. *Proceedings of the Royal Society of London. Series A: Mathematical and Physical Sciences*, 430(1879):405–411, 08 1990. URL https://doi.org/10.1098/rspa.1990.0096.

[263] J. W. Zwanziger, S. P. Rucker, and G. C. Chingas. Measuring the geometric component of the transition probability in a two-level system. *Phys. Rev. A*, 43: 3232–3240, Apr 1991. URL https://link.aps.org/doi/10.1103/PhysRevA.43.3232.

[264] Rob Tycko. Geometry of probabilities confirmed. *Physics World*, 4(9):33, sep 1991. URL https://doi.org/10.1088/2058-7058/4/9/25.

[265] D. Bouwmeester, G. P. Karman, N. H. Dekker, C. A. Schrama, and J. P. Woerdman. Observation of the geometric amplitude factor in an optical system. *Journal of Modern Optics*, 43(10):2087–2103, 1996. URL https://doi.org/10.1080/09500349608232872.

[266] D. Bouwmeester, G. P. Karman, C. A. Schrama, and J. P. Woerdman. Observation of interference in transitions due to local geometric phases. *Phys. Rev. A*, 53:985–989, Feb 1996. URL https://link.aps.org/doi/10.1103/PhysRevA.53.985.

[267] Michael V. Berry. THE QUANTUM PHASE, FIVE YEARS AFTER, 1989. URL https://michaelberryphysics.wordpress.com/wp-content/uploads/2013/07/berry187.pdf.

[268] J. P. Provost and G. Vallee. Riemannian structure on manifolds of quantum states. *Communications in Mathematical Physics*, 76(3):289–301, Sep 1980. URL https://doi.org/10.1007/BF02193559.

[269] Ran Cheng. Quantum geometric tensor (fubini-study metric) in simple quantum system: A pedagogical introduction, 2013. URL https://arxiv.org/abs/1012.1337.

[270] Charles D. Brown, Shao-Wen Chang, Malte N. Schwarz, Tsz-Him Leung, Vladyslav Kozii, Alexander Avdoshkin, Joel E. Moore, and Dan Stamper-Kurn. Direct geometric probe of singularities in band structure. *Science*, 377(6612):1319–1322, 2022. URL https://www.science.org/doi/abs/10.1126/science.abm6442.

[271] Xinsheng Tan, Dan-Wei Zhang, Zhen Yang, Ji Chu, Yan-Qing Zhu, Danyu Li, Xiaopei Yang, Shuqing Song, Zhikun Han, Zhiyuan Li, Yuqian Dong, Hai-Feng Yu, Hui Yan, Shi-Liang Zhu, and Yang Yu. Experimental measurement of the quantum metric tensor and related topological phase transition with a superconducting qubit. *Phys. Rev. Lett.*, 122:210401, May 2019. URL https://link.aps.org/doi/10.1103/PhysRevLett.122.210401.

[272] Min Yu, Pengcheng Yang, Musang Gong, Qingyun Cao, Qiuyu Lu, Haibin Liu, Shaoliang Zhang, Martin B Plenio, Fedor Jelezko, Tomoki Ozawa, Nathan Goldman, and Jianming Cai. Experimental measurement of the quantum geometric tensor using coupled qubits in diamond. *National Science Review*, 7(2):254–260, Nov 2019. URL https://doi.org/10.1093/nsr/nwz193.

[273] A. Gianfrate, O. Bleu, L. Dominici, V. Ardizzone, M. De Giorgi, D. Ballarini, G. Lerario, K. W. West, L. N. Pfeiffer, D. D. Solnyshkov, D. Sanvitto, and G. Malpuech. Measurement of the quantum geometric tensor and of the anomalous hall drift. *Nature*, 578(7795):381–385, Feb 2020. URL https://doi.org/10.1038/s41586-020-1989-2.

[274] Mingu Kang, Sunje Kim, Yuting Qian, Paul M. Neves, Linda Ye, Junseo Jung, Denny Puntel, Federico Mazzola, Shiang Fang, Chris Jozwiak, Aaron Bostwick, Eli Rotenberg, Jun Fuji, Ivana Vobornik, Jae-Hoon Park, Joseph G. Checkelsky, Bohm-Jung Yang, and Riccardo Comin. Measurements of the quantum geometric tensor in solids. *Nature Physics*, 21(1):110–117, Jan 2025. URL https://doi.org/10.1038/s41567-024-02678-8.

[275] Sunje Kim, Yoonah Chung, Yuting Qian, Soobin Park, Chris Jozwiak, Eli Rotenberg, Aaron Bostwick, Keun Su Kim, and Bohm-Jung Yang. Direct measurement of the quantum metric tensor in solids. *Science*, 388(6751):1050–1054, 2025. URL https://www.science.org/doi/abs/10.1126/science.ado6049.

[276] Javier Cuerda, Jani M. Taskinen, Nicki Källman, Leo Grabitz, and Päivi Törmä. Observation of quantum metric and non-hermitian berry curvature in a plasmonic lattice. *Phys. Rev. Res.*, 6:L022020, Apr 2024. URL https://link.aps.org/doi/10.1103/PhysRevResearch.6.L022020.

[277] Y.-M. Robin Hu, Elena A. Ostrovskaya, and Eliezer Estrecho. Generalized quantum geometric tensor in a non-hermitian exciton-polariton system *Invited*. *Opt. Mater. Express*, 14(3):664–686, Mar 2024. URL https://opg.optica.org/ome/abstract.cfm?URI=ome-14-3-664.

[278] Javier Cuerda, Jani M. Taskinen, Nicki Källman, Leo Grabitz, and Päivi Törmä. Pseudospin-orbit coupling and non-hermitian effects in the quantum geometric tensor of a plasmonic lattice. *Phys. Rev. B*, 109:165439, Apr 2024. URL https://link.aps.org/doi/10.1103/PhysRevB.109.165439.

[279] Chao Chen Ye, W. L. Vleeshouwers, S. Heatley, V. Gritsev, and C. Morais Smith. Quantum metric of non-hermitian su-schrieffer-heeger systems. *Phys. Rev. Res.*, 6:023202, May 2024. URL https://link.aps.org/doi/10.1103/PhysRevResearch.6.023202.

[280] Jun-Feng Ren, Jing Li, Hai-Tao Ding, and Dan-Wei Zhang. Identifying non-hermitian critical points with the quantum metric. *Phys. Rev. A*, 110:052203, Nov 2024. URL https://link.aps.org/doi/10.1103/PhysRevA.110.052203.

[281] Kai Chen and Jie Zhu. Non-hermitian quantum geometric tensor and nonlinear electrical response, 2025. URL https://arxiv.org/abs/2509.11765.

[282] N. J. Lambert, A. Schumer, J. J. Longdell, S. Rotter, and H. G. L. Schwefel. Coherent control of magnon–polaritons using an exceptional point. *Nature Physics*, 21(10):1570–1577, Oct 2025. URL https://doi.org/10.1038/s41567-025-02998-3.

[283] Judith Höller. MIM knot notes. Harris Lab MIM notes, 2019.

[284] Chitres Guria. Full driven spectrum V3. Harris Lab MIM notes, Apr 2023.

[285] Francesco Fogliano, Benjamin Besga, Antoine Reigue, Laure Mercier de Lépinay, Philip Heringlake, Clement Gouriou, Eric Eyraud, Wolfgang Wernsdorfer, Benjamin Pigeau, and Olivier Arcizet. Ultrasensitive nano-optomechanical force sensor operated at dilution temperatures. *Nature Communications*, 12(1):4124, Jul 2021. URL https://doi.org/10.1038/s41467-021-24318-y.

[286] Johannes Piotrowski, Dominik Windey, Jayadev Vijayan, Carlos Gonzalez-Ballestero, Andrés de los Ríos Sommer, Nadine Meyer, Romain Quidant, Oriol Romero-Isart, René Reimann, and Lukas Novotny. Simultaneous ground-state cooling of two mechanical modes of a levitated nanoparticle. *Nature Physics*, 19(7): 1009–1013, Jul 2023. URL https://doi.org/10.1038/s41567-023-01956-1.

[287] Laure Mercier de Lépinay, Benjamin Pigeau, Benjamin Besga, and Olivier Arcizet. Eigenmode orthogonality breaking and anomalous dynamics in multimode nano-optomechanical systems under non-reciprocal coupling. *Nature Communications*, 9(1):1401, Apr 2018. URL https://doi.org/10.1038/s41467-018-03741-8.

[288] Serra Erdamar, Maryam Abbasi, Weijian Chen, Niklas Hörnedal, Aurélia Chenu, and Kater W. Murch. Exploring the topology of a non-hermitian superconducting qubit using shortcuts to adiabaticity, 2025. URL https://arxiv.org/abs/2508.10122.

[289] Eva Maria Graefe and Hans Jürgen Korsch. Crossing scenario for a nonlinear non-hermitian two-level system. *Czechoslovak Journal of Physics*, 56(9):1007–1020, Sep 2006. URL https://doi.org/10.1007/s10582-006-0396-8.

[290] Haiwen Wang, Sid Assawaworrarit, and Shanhui Fan. Dynamics for encircling an exceptional point in a nonlinear non-hermitian system. *Opt. Lett.*, 44(3):638–641, Feb 2019. URL https://opg.optica.org/ol/abstract.cfm?URI=ol-44-3-638.

[291] Florian Elste, S. M. Girvin, and A. A. Clerk. Quantum noise interference and backaction cooling in cavity nanomechanics. *Phys. Rev. Lett.*, 102:207209, May 2009. URL https://link.aps.org/doi/10.1103/PhysRevLett.102.207209.

[292] Talitha Weiss, Christoph Bruder, and Andreas Nunnenkamp. Strong-coupling effects in dissipatively coupled optomechanical systems. *New Journal of Physics*, 15 (4):045017, apr 2013. URL https://doi.org/10.1088/1367-2630/15/4/045017.

[293] Yariv Yanay, Jack C. Sankey, and Aashish A. Clerk. Quantum backaction and noise interference in asymmetric two-cavity optomechanical systems. *Phys. Rev. A*, 93: 063809, Jun 2016. URL https://link.aps.org/doi/10.1103/PhysRevA.93.063809.

[294] Juliette Monsel, Anastasiia Ciers, Sushanth Kini Manjeshwar, Witlef Wieczorek, and Janine Splettstoesser. Dissipative and dispersive cavity optomechanics with a frequency-dependent mirror. *Phys. Rev. A*, 109:043532, Apr 2024. URL https://link.aps.org/doi/10.1103/PhysRevA.109.043532.

[295] Catvu H. Bui, Jiangjun Zheng, S. W. Hoch, Lennon Y. T. Lee, J. G. E. Harris, and Chee Wei Wong. High-reflectivity, high-q micromechanical membranes via guided resonances for enhanced optomechanical coupling. *Applied Physics Letters*, 100 (2):021110, 01 2012. URL https://doi.org/10.1063/1.3658731.

[296] Vincent Dumont, Simon Bernard, Christoph Reinhardt, Alex Kato, Maximilian Ruf, and Jack C. Sankey. Flexure-tuned membrane-at-the-edge optomechanical system. *Opt. Express*, 27(18):25731–25748, Sep 2019. URL https://opg.optica.org/oe/abstract.cfm?URI=oe-27-18-25731.

[297] K. G. Makris, R. El-Ganainy, D. N. Christodoulides, and Z. H. Musslimani. Beam dynamics in $\mathcal{PT}$ symmetric optical lattices. *Phys. Rev. Lett.*, 100:103904, Mar 2008. URL https://link.aps.org/doi/10.1103/PhysRevLett.100.103904.

[298] Alexander Szameit, Mikael C. Rechtsman, Omri Bahat-Treidel, and Mordechai Segev. $\mathcal{PT}$-symmetry in honeycomb photonic lattices. *Phys. Rev. A*, 84:021806, Aug 2011. URL https://link.aps.org/doi/10.1103/PhysRevA.84.021806.

[299] Daniel Leykam, Konstantin Y. Bliokh, Chunli Huang, Y. D. Chong, and Franco Nori. Edge modes, degeneracies, and topological numbers in non-hermitian systems. *Phys. Rev. Lett.*, 118:040401, Jan 2017. URL https://link.aps.org/doi/10.1103/PhysRevLett.118.040401.

[300] Wei Chen, Hai-Zhou Lu, and Jing-Min Hou. Topological semimetals with a double-helix nodal link. *Phys. Rev. B*, 96:041102, Jul 2017. URL https://link.aps.org/doi/10.1103/PhysRevB.96.041102.

[301] Ren Bi, Zhongbo Yan, Ling Lu, and Zhong Wang. Nodal-knot semimetals. *Phys. Rev. B*, 96:201305, Nov 2017. URL https://link.aps.org/doi/10.1103/PhysRevB.96.201305.

[302] Johan Carlström and Emil J. Bergholtz. Exceptional links and twisted fermi ribbons in non-hermitian systems. *Phys. Rev. A*, 98:042114, Oct 2018. URL https://link.aps.org/doi/10.1103/PhysRevA.98.042114.

[303] Huitao Shen, Bo Zhen, and Liang Fu. Topological band theory for non-hermitian hamiltonians. *Phys. Rev. Lett.*, 120:146402, Apr 2018. URL https://link.aps.org/doi/10.1103/PhysRevLett.120.146402.

[304] Charles C. Wojcik, Xiao-Qi Sun, Tomá š Bzdušek, and Shanhui Fan. Homotopy characterization of non-hermitian hamiltonians. *Phys. Rev. B*, 101:205417, May 2020. URL https://link.aps.org/doi/10.1103/PhysRevB.101.205417.

[305] Haiping Hu and Erhai Zhao. Knots and non-hermitian bloch bands. *Phys. Rev. Lett.*, 126:010401, Jan 2021. URL https://link.aps.org/doi/10.1103/PhysRevLett.126.010401.

[306] Kai Wang, Avik Dutt, Charles C. Wojcik, and Shanhui Fan. Topological complex-energy braiding of non-hermitian bands. *Nature*, 598(7879):59–64, Oct 2021. URL https://doi.org/10.1038/s41586-021-03848-x.

[307] Xiao Zhang, Guangjie Li, Yuhan Liu, Tommy Tai, Ronny Thomale, and Ching Hua Lee. Tidal surface states as fingerprints of non-hermitian nodal knot metals. *Communications Physics*, 4(1):47, Mar 2021. URL https://doi.org/10.1038/s42005-021-00535-1.

[308] Youngsun Choi, Jae Woong Yoon, Jong Kyun Hong, Yeonghwa Ryu, and Seok Ho Song. Direct observation of time-asymmetric breakdown of the standard adiabaticity around an exceptional point. *Communications Physics*, 3(1):140, December 2020. URL https://www.nature.com/articles/s42005-020-00409-y.

[309] Zhujing Xu, Xingyu Gao, Jaehoon Bang, Zubin Jacob, and Tongcang Li. Non-reciprocal energy transfer through the casimir effect. *Nature Nanotechnology*, 17 (2):148–152, December 2021. URL http://dx.doi.org/10.1038/s41565-021-01026-8.

[310] W.D. Heiss and H.L. Harney. The chirality of exceptional points. *The European Physical Journal D*, 17(2):149–151, November 2001. URL http://dx.doi.org/10.1007/s100530170017.

[311] Alexei A. Mailybaev, Oleg N. Kirillov, and Alexander P. Seyranian. Geometric phase around exceptional points. *Phys. Rev. A*, 72:014104, Jul 2005. URL https://link.aps.org/doi/10.1103/PhysRevA.72.014104.

[312] T. Gao, E. Estrecho, K. Y. Bliokh, T. C. H. Liew, M. D. Fraser, S. Brodbeck, M. Kamp, C. Schneider, S. Höfling, Y. Yamamoto, F. Nori, Y. S. Kivshar, A. G. Truscott, R. G. Dall, and E. A. Ostrovskaya. Observation of non-hermitian degeneracies in a chaotic exciton-polariton billiard. *Nature*, 526(7574):554–558, Oct 2015. URL https://doi.org/10.1038/nature15522.

[313] Justin R. Lane. What does $\mathcal{EP}_2$ look like in our limited space? Harris Lab MIM notes, Oct 2022.

[314] Justin R. Lane. Mapping to the $\mathbb{RP}^3$ ball. Harris Lab MIM notes, May 2024.

[315] Wikipedia contributors. Real projective space — Wikipedia, the free encyclopedia, 2025. URL https://en.wikipedia.org/w/index.php?title=Real_projective_space&oldid=1306786174.

[316] Wikipedia contributors. Quaternions and spatial rotation — Wikipedia, the free encyclopedia, 2025. URL https://en.wikipedia.org/w/index.php?title=Quaternions_and_spatial_rotation&oldid=1318439832.

[317] Wolfram Research. FindClusters, 2020. URL https://reference.wolfram.com/language/ref/FindClusters.html.

[318] THORLABS. V1550A-SpecSheet, 2023. URL https://www.thorlabs.com/drawings/5139d2c1771f5c98-C0E44812-94A6-92FD-4237A6798B637C5D/V1550A-SpecSheet.pdf.

[319] Wolfram Research. ListPlot3D, 2025. URL https://reference.wolfram.com/language/ref/ListPlot3D.html.

[320] Wikipedia contributors. Bloch sphere — Wikipedia, the free encyclopedia, 2025. URL https://en.wikipedia.org/w/index.php?title=Bloch_sphere&oldid=1329354443.

[321] Chitres Guria. Initial state preparation Protocol I, Initial state: $(1,0)^{\mathsf{T}}$, 2026. URL https://www.youtube.com/watch?v=SagyeJxLHcs.

[322] Chitres Guria. Initial state preparation Protocol I, Initial state: $(0,1)^{\mathsf{T}}$, 2026. URL https://www.youtube.com/watch?v=K69zON8LKSg.

[323] Chitres Guria. Initial state preparation Protocol II, Initial state: $(1,0)^{\mathsf{T}}$, 2026. URL https://www.youtube.com/watch?v=4uvlVdHwLug.

[324] Chitres Guria. Initial state preparation Protocol II, Initial state: $(0,1)^{\mathsf{T}}$, 2026. URL https://www.youtube.com/watch?v=pOaUCVCSy8A.

[325] Wikipedia contributors. Gram–Schmidt process — Wikipedia, The Free Encyclopedia, 2025. URL https://en.wikipedia.org/w/index.php?title=Gram%E2%80%93Schmidt_process&oldid=1321869664.